

DESIGN AND CONTROL OF ADAPTIVE CIVIL STRUCTURES

EDITED BY: Gennaro Senatore and Ian F. C. Smith
PUBLISHED IN: Frontiers in Built Environment





frontiers

Frontiers eBook Copyright Statement

The copyright in the text of individual articles in this eBook is the property of their respective authors or their respective institutions or funders. The copyright in graphics and images within each article may be subject to copyright of other parties. In both cases this is subject to a license granted to Frontiers.

The compilation of articles constituting this eBook is the property of Frontiers.

Each article within this eBook, and the eBook itself, are published under the most recent version of the Creative Commons CC-BY licence.

The version current at the date of publication of this eBook is CC-BY 4.0. If the CC-BY licence is updated, the licence granted by Frontiers is automatically updated to the new version.

When exercising any right under the CC-BY licence, Frontiers must be attributed as the original publisher of the article or eBook, as applicable.

Authors have the responsibility of ensuring that any graphics or other materials which are the property of others may be included in the CC-BY licence, but this should be checked before relying on the CC-BY licence to reproduce those materials. Any copyright notices relating to those materials must be complied with.

Copyright and source acknowledgement notices may not be removed and must be displayed in any copy, derivative work or partial copy which includes the elements in question.

All copyright, and all rights therein, are protected by national and international copyright laws. The above represents a summary only. For further information please read Frontiers' Conditions for Website Use and Copyright Statement, and the applicable CC-BY licence.

ISSN 1664-8714

ISBN 978-2-88971-292-2

DOI 10.3389/978-2-88971-292-2

About Frontiers

Frontiers is more than just an open-access publisher of scholarly articles: it is a pioneering approach to the world of academia, radically improving the way scholarly research is managed. The grand vision of Frontiers is a world where all people have an equal opportunity to seek, share and generate knowledge. Frontiers provides immediate and permanent online open access to all its publications, but this alone is not enough to realize our grand goals.

Frontiers Journal Series

The Frontiers Journal Series is a multi-tier and interdisciplinary set of open-access, online journals, promising a paradigm shift from the current review, selection and dissemination processes in academic publishing. All Frontiers journals are driven by researchers for researchers; therefore, they constitute a service to the scholarly community. At the same time, the Frontiers Journal Series operates on a revolutionary invention, the tiered publishing system, initially addressing specific communities of scholars, and gradually climbing up to broader public understanding, thus serving the interests of the lay society, too.

Dedication to Quality

Each Frontiers article is a landmark of the highest quality, thanks to genuinely collaborative interactions between authors and review editors, who include some of the world's best academicians. Research must be certified by peers before entering a stream of knowledge that may eventually reach the public - and shape society; therefore, Frontiers only applies the most rigorous and unbiased reviews.

Frontiers revolutionizes research publishing by freely delivering the most outstanding research, evaluated with no bias from both the academic and social point of view. By applying the most advanced information technologies, Frontiers is catapulting scholarly publishing into a new generation.

What are Frontiers Research Topics?

Frontiers Research Topics are very popular trademarks of the Frontiers Journals Series: they are collections of at least ten articles, all centered on a particular subject. With their unique mix of varied contributions from Original Research to Review Articles, Frontiers Research Topics unify the most influential researchers, the latest key findings and historical advances in a hot research area! Find out more on how to host your own Frontiers Research Topic or contribute to one as an author by contacting the Frontiers Editorial Office: frontiersin.org/about/contact

DESIGN AND CONTROL OF ADAPTIVE CIVIL STRUCTURES

Topic Editors:

Gennaro Senatore, École Polytechnique Fédérale de Lausanne, Switzerland

Ian F. C. Smith, École Polytechnique Fédérale de Lausanne, Switzerland

Citation: Senatore, G., Smith, I. F. C., eds. (2021). Design and Control of Adaptive Civil Structures. Lausanne: Frontiers Media SA. doi: 10.3389/978-2-88971-292-2

Table of Contents

04	<i>Editorial: Design and Control of Adaptive Civil Structures</i> Gennaro Senatore and Ian F. C. Smith
06	<i>Experimental Testing of a Small-Scale Truss Beam That Adapts to Loads Through Large Shape Changes</i> Arka P. Reksowardojo, Gennaro Senatore and Ian F. C. Smith
22	<i>Using Influence Matrices as a Design and Analysis Tool for Adaptive Truss and Beam Structures</i> Simon Steffen, Stefanie Weidner, Lucio Blandini and Werner Sobek
34	<i>A General Model for Both Shape Control and Locomotion Control of Tensegrity Systems</i> Huiying Cai, Meijia Wang, Xian Xu and Yaozhi Luo
46	<i>Integrating Ionic Electroactive Polymer Actuators and Sensors Into Adaptive Building Skins – Potentials and Limitations</i> Raphael Neuhaus, Nima Zahiri, Jan Petrs, Yasaman Tahouni, Jörg Siegert, Ivica Kolaric, Hanaa Dahy and Thomas Bauernhansl
68	<i>Fast and Optimized Calculation of the Cable Pretension Forces in Arch Bridges With Suspended Deck</i> Mariano Modano, Arnas Majumder, Filipe Santos, Raimondo Luciano and Fernando Fraternali
79	<i>Force and Shape Control Strategies for Minimum Energy Adaptive Structures</i> Gennaro Senatore and Arka P. Reksowardojo
107	<i>Adaptive Concrete Beams Equipped With Integrated Fluidic Actuators</i> Christian Kelleter, Timon Burghardt, Hansgeorg Binz, Lucio Blandini and Werner Sobek
120	<i>A Case Study on Design and Optimization of Adaptive Civil Structures</i> Florian Geiger, Jan Gade, Malte von Scheven and Manfred Bischoff
133	<i>Optimal Static Load Compensation With Fault Tolerance in Nonlinear Adaptive Structures Under Input and State Constraints</i> Julia L. Wagner, Andreas Gienger, Charlotte Stein, Philipp Arnold, Cristina Tarín, Oliver Sawodny and Michael Böhm
151	<i>Vibration Suppression Through Variable Stiffness and Damping Structural Joints</i> Qinyu Wang, Gennaro Senatore, Kaspar Jansen, Arjan Habraken and Patrick Teuffel
173	<i>Inherent Adaptive Structures Using Nature-Inspired Compound Elements</i> Mohammad Reza Chenaghlo, Mohammad Kheirollahi, Karim Abedi, Ahmad Akbari and Aydin Fathpour
186	<i>Motion Design With Efficient Actuator Placement for Adaptive Structures that Perform Large Deformations</i> Renate Sachse, Florian Geiger, Malte von Scheven and Manfred Bischoff



Editorial: Design and Control of Adaptive Civil Structures

Gennaro Senatore* and Ian F. C. Smith

Applied Computing and Mechanics Laboratory (IMAC), School of Architecture, Civil and Environmental Engineering (ENAC), Swiss Federal Institute of Technology (EPFL), Lausanne, Switzerland

Keywords: adaptive structures, adaptive facades, sustainable design, structural optimization, structural sensing, structural control, vibration control, shape morphing

Editorial on the Research Topic

Design and Control of Adaptive Civil Structures

The environmental impact of buildings and civil infrastructure has become an important topic owing to significant non-renewable material use and the greenhouse gas emissions (GHG) that are required for sourcing, extraction, component manufacturing, transport, fabrication and operation. This Research Topic investigates new design strategies, control methods and applications for structures that adapt to loading events and other environmental actions through sensing and actuation. Actuation is most often implemented at the component scale. Strategic integration of active components enables modification of structural behavior under loading to fulfill control objectives. When included during design, adaptation enables a significant improvement in performance because the structure can sense and react to change of external stimuli and thus it can operate optimally under different conditions.

Adaptation is carried out in various ways. For example, the inherently adaptive features of nature-inspired compound elements are integrated into structures to reduce the response under seismic excitations and to mitigate the onset of instability in long-span structures (Chenaghlu et al.). Variable stiffness and damping properties of components made of viscoelastic material (e.g., shape memory polymers) have been investigated in the form of structural joints for vibration control. Actuation through thermal energy causes a significant stiffness reduction and a parallel increase of damping which results in the shift of the structure natural frequencies and an increase in damping ratios. This semi-active control strategy is effective for multi-story buildings and bridges under various excitations such as pedestrian/vehicular traffic and earthquakes (Wang et al.). In Kelleter et al. numerical and experimental studies are carried out on concrete beams equipped with multiple disc-shaped fluidic actuators. Controlled expansion of the fluidic actuators enables the reduction of bending-induced stress and compensation of displacements. Adaptation has been investigated to design multifunctional façade components. In Neuhaus et al. experimental studies have been carried out on the integration of ionic electroactive polymer actuators (IEPA) in adaptive membrane building skins. Actuation of small apertures provides ventilation control and humidity regulation. At the same time, the embedded devices work as sensors for load monitoring. Experimental studies show the potential and limitations of IEPA for adaptive building skins.

Integration of linear actuators into truss and frame structures enables the implementation of many control strategies. Generally, controlled length changes of the actuators allow for the internal force flow and the structural shape to be manipulated to fulfill a control objective. In Cai et al. this strategy has been employed for shape control as well as locomotion of tensegrity structures. A formulation based on genetic algorithms and dynamic relaxation is developed to determine optimal control commands for shape control of a double-layered tri-prism tensegrity structure, as well as optimal gaits and motion paths of a six-strut locomotive tensegrity structure.

OPEN ACCESS

Edited and reviewed by:

Branko Glisic,
Princeton University, United States

*Correspondence:

Gennaro Senatore
gennarosenatore@gmail.com

Specialty section:

This article was submitted to
Structural Sensing, Control and Asset
Management,
a section of the journal
Frontiers in Built Environment

Received: 23 June 2021

Accepted: 29 June 2021

Published: 09 July 2021

Citation:

Senatore G and Smith IFC (2021)
Editorial: Design and Control of
Adaptive Civil Structures.
Front. Built Environ. 7:729752.
doi: 10.3389/fbuil.2021.729752

In the context of civil structures, force and shape control through linear actuators have been employed to counteract the effect of loading through stress homogenization and compensation of displacements. In Steffen et al. the use of actuation influence matrices is employed to evaluate how forces and displacements are modified by the length change of actuators that are installed either in series or in parallel with structural elements. This analysis quantifies the effect of the structural topology on actuator efficacy with regard to force and displacement compensation for optimal actuator placement. In Modano et al. a method based on influence matrices is formulated to determine optimal tension forces in the stays of through-type arch bridges with suspended deck. The objective is to obtain a target moment distribution over the deck that mitigates stress under loading. Owing to the reduced model formulation, this process has potential for a real-time control strategy using the bridge stays as active tendons. In Geiger et al. a formulation for optimal element sizing and computation of control commands is applied to design truss and frame structures equipped with linear actuators. The actuator placement is predetermined and actuators are installed in series with the structural elements. Both truss and frame structures are studied. Case studies show significant mass savings can be achieved through control of displacements for stiffness governed structures, confirming findings of previous work on similar adaptive structural types. Numerical and experimental studies are carried out in Wagner et al. on optimal load compensation of a 1:18 scaled high-rise building model equipped with actuators installed in parallel with some of the columns and in series with some of the diagonal bracing elements. The displacements are measured through a camera system. Actuator failure scenarios are simulated to quantify control performance degradation and to test the reconfiguration capability of the controller.

In Reksowardojo et al. experimental studies are carried out on a small-scale prototype structure that is designed to counteract the effect of loading through shape morphing. Instead of having one unique geometrical configuration that is the best fit to resist the envelope of peak loads, the structure is designed to “morph” into a shape that is optimal to take each load occurrence. The optimal shape changes as the load changes. Load control through shape adaptation enables significant stress homogenization so that the design is no longer dominated by peak demands. This way, material utilization is maximized and thus the embodied energy is reduced. A similar approach is taken in Sachse et al. that presents heuristic methods useful to identify a subset of external or internal actuator locations that enable control of the structure through a required motion path between two geometric configurations. An optimal deformation path between an initial undeformed geometry and a prescribed deformed configuration is identified. Actuator placement is carried out through heuristics that minimize the elastic energy (i.e., cost of deformation) integrated over the optimal motion path.

Generally, structural adaptation enables a significant reduction of material input since the structure no longer relies exclusively on passive load-bearing resistance. However, adaptation might require significant operational energy input. In Senatore and Reksowardojo an integrated structure-control optimization process is formulated to design minimum energy adaptive structures. The design objective

is whole-life energy minimization including a share embodied in the material and a share for the operation of the active system. Minimum energy solutions are obtained through combined element sizing and actuator placement optimization. Actuators are installed in series with structural elements and at the supports. Four control strategies are compared through simulations on a slender high-rise structure and an arch bridge. Results show that minimum energy solutions achieve significant material as well as total energy (or carbon equivalent) savings compared with optimized passive structures.

This Research Topic has opened up a series of interesting new avenues. Consideration of material, energy and carbon costs is not only important for new construction but also to existing buildings and infrastructure. Most structures typically have a significant reserve capacity that is often not utilized before the end of service. Among possible future work, retrofitting active systems could be an effective means of ensuring safety and improving the behavior of aging structures. Structural adaptation could be employed to help diagnosis as well as to increase reserve capacity through active stress homogenization. Some of the methods described in this Research Topic could be repurposed for optimal retrofitting of sensing and actuation technologies to extend the service life of existing structures and in so doing deferring the disposal of embodied energy and carbon.

The work contained in this Research Topic demonstrates that current knowledge of methods for optimal integration of sensing and actuation technology in structures could lead to widespread adoption and large-scale applications. Adaptation enables new design and improved performance using less material, carbon and energy resources. For this reason, adaptive structures have great potential to reduce adverse environmental impacts caused by the construction industry.

AUTHOR CONTRIBUTIONS

GS curated this Research Topic with contribution of IS. GS was actively involved in reviewing all articles. GS wrote the first draft of the editorial. GS and IS contributed to the review, revised and approved the submitted version of the editorial.

ACKNOWLEDGMENTS

The editors would like to thank all contributors to this Research Topic as well as the reviewers and Frontiers Editorial Team.

Conflict of Interest: The authors declare that the research was conducted in the absence of any commercial or financial relationships that could be construed as a potential conflict of interest.

Copyright © 2021 Senatore and Smith. This is an open-access article distributed under the terms of the Creative Commons Attribution License (CC BY). The use, distribution or reproduction in other forums is permitted, provided the original author(s) and the copyright owner(s) are credited and that the original publication in this journal is cited, in accordance with accepted academic practice. No use, distribution or reproduction is permitted which does not comply with these terms.



Experimental Testing of a Small-Scale Truss Beam That Adapts to Loads Through Large Shape Changes

Arka P. Reksowardojo*, Gennaro Senatore and Ian F. C. Smith

Applied Computing and Mechanics Laboratory (IMAC), School of Architecture, Civil and Environmental Engineering (ENAC), Swiss Federal Institute of Technology (EPFL), Lausanne, Switzerland

OPEN ACCESS

Edited by:

Landolf Rhode-Barbarigos,
University of Miami, United States

Reviewed by:

Nan Hu,
The Ohio State University,
United States
Marios C. Phocas,
University of Cyprus, Cyprus

*Correspondence:

Arka P. Reksowardojo
arka.reksowardojo@epfl.ch

Specialty section:

This article was submitted to
Structural Sensing,
a section of the journal
Frontiers in Built Environment

Received: 07 May 2019

Accepted: 27 June 2019

Published: 10 July 2019

Citation:

Reksowardojo AP, Senatore G and
Smith IFC (2019) Experimental Testing
of a Small-Scale Truss Beam That
Adapts to Loads Through Large
Shape Changes.
Front. Built Environ. 5:93.
doi: 10.3389/fbuil.2019.00093

Adaptive structures have the ability to modify their shape and internal forces through sensing and actuation in order to maintain optimal performance under changing actions. Previous studies have shown that substantial whole-life energy savings with respect to traditional passive designs can be achieved through well-conceived adaptive design strategies. The whole-life energy comprises an embodied part in the material and an operational part for structural adaptation. Structural adaptation through controlled large shape changes allows a significant stress redistribution so that the design is not governed by extreme loads with long return periods. This way, material utilization is maximized and embodied energy is reduced. A design process based on shape optimization has been formulated to obtain shapes that are optimal for each load case. A geometrically non-linear force method is employed to control the structure into required shapes. This paper presents the experimental testing of a small-scale prototype adaptive structure produced by this design process. The structure is a simply supported planar truss. Shape adaptation is achieved through controlled length changes of turnbuckles that strategically replace some of the structural elements. The stress is monitored by strain sensors fitted on some of the truss elements. The nodal coordinates are monitored by an optical tracking system. Numerical predictions and measurements have a minimum Pearson correlation of 0.86 which indicates good accordance. Although scaling effects have to be further investigated, experimental testing on a small-scale prototype has been useful to assess the feasibility of the design and control methods outlined in this work. Results show that stress homogenization through controlled large shape changes is feasible.

Keywords: adaptive structures, shape control, actuator placement optimization, structural sensing, structural optimization

INTRODUCTION

Civil structures are designed to meet strength and deformation criteria for critical load cases. Since extreme and thus rarely occurring loads have to be accounted for, the structural capacity is not fully utilized for most of the service life of the structure. The construction sector, however, is a major contributor to the global energy demand (Straube, 2006) as well as a major consumer of

raw materials (United Nations Environmental Programme, 2007), and therefore it is of growing importance to minimize environmental impacts of load-bearing structures.

Structural adaptation through sensing and actuation is a potential solution. If the structure is able to counteract the effect of loads through active control, it can be designed to maintain optimal performance as the external load changes (Yao, 1972; Soong, 1988). The potential of structural adaptation as a means to mitigate the dynamic response during the occurrence of extreme loads (e.g., earthquakes, strong winds) has been subject of extensive research (Skelton et al., 1992; Reinhorn et al., 1993; Soong and Cimellaro, 2009). More recently, the potential of using adaptation to design structures with a better material utilization has been investigated (Sobek and Teuffel, 2001; Cimellaro et al., 2008). A new design criterion for adaptive structures has been introduced in Senatore et al. (2019), which is “whole-life” energy comprising a part embodied in the material and another part for control and adaptation. It was shown that substantial whole-life energy savings can be achieved through adaptive design strategies (Senatore et al., 2018). Instead of relying solely on passive resistance provided by material and form, strategically located actuators change the internal forces and shape of the structure to ensure safety and serviceability. Since actuation is only employed for rarely occurring loading, reduction in material embodied energy can be achieved with a small increase in control operational energy as a trade-off. It was shown that whole-life energy savings as high as 70% can be achieved through this design strategy (Senatore et al., 2018a,b).

Shape optimization is usually employed to optimize the geometry of structures under worst load cases (Gil and Andreu, 2000; Wang et al., 2002; Shea and Smith, 2006). When applied to reticular structures, the optimization process can lead to large modifications of nodal coordinates starting from an initial layout, to an extent that the internal forces are manipulated significantly (Descamps and Coelho, 2013). Through this process, shapes resembling arches, catenaries, and lenticular configurations have been found to be efficient in terms of material utilization (Gil and Andreu, 2000). Using a similar approach (Pedersen and Nielsen, 2003), it was shown that small but strategic adjustments of the shape result in weight savings up to 35% without changing the main geometric features. However, the geometry obtained through these methods is fixed and thus, the structural capacity is only partially utilized under peak demands.

Shape control involving large shape changes has been studied numerically and experimentally for deployable and tensegrity structures (Tibert, 2002; Fest et al., 2003; Veuve et al., 2015). In this context, large shape changes have been achieved through mechanisms. However, the use of mechanisms based on moving parts often results in a significant penalty due to the weight of the joints and increased control complexity (Campanile, 2003). Shape control through flexibility has received little attention both theoretically and experimentally. Shape and force control of a reticular adaptive structure has been successfully tested in Senatore et al. (2018); however, geometric non-linearity was not accounted for. Formulations of geometrically non-linear shape and force control exist (Yuan et al., 2016), nonetheless experimental validation is still lacking.

Recent work has investigated the efficacy of structural adaptation through large shape changes (Reksowardojo et al., 2018). Numerical studies have shown that a substantial amount of embodied energy can be saved with respect to structures that are able to adapt through small shape changes. Through large geometry reconfiguration, the internal forces can be redistributed effectively and thus, the design is not governed by extreme loading. This paper presents details of the experimental testing of a small-scale prototype adaptive structure produced by the methods presented in Reksowardojo et al. (2018). The prototype tested in this work is a simply-supported planar-truss beam. Shape adaptation is achieved through controlled length changes of turnbuckles that strategically replace some of the structural elements. Strain sensors and an optical tracking system are employed to monitor element stress and nodal displacements. The aim of this work is to validate experimentally the feasibility of shape and force control through the process outlined in Reksowardojo et al. (2018) on a small-scale prototype. Results from this test will inform future research on larger scale adaptive structures.

DESIGN METHOD

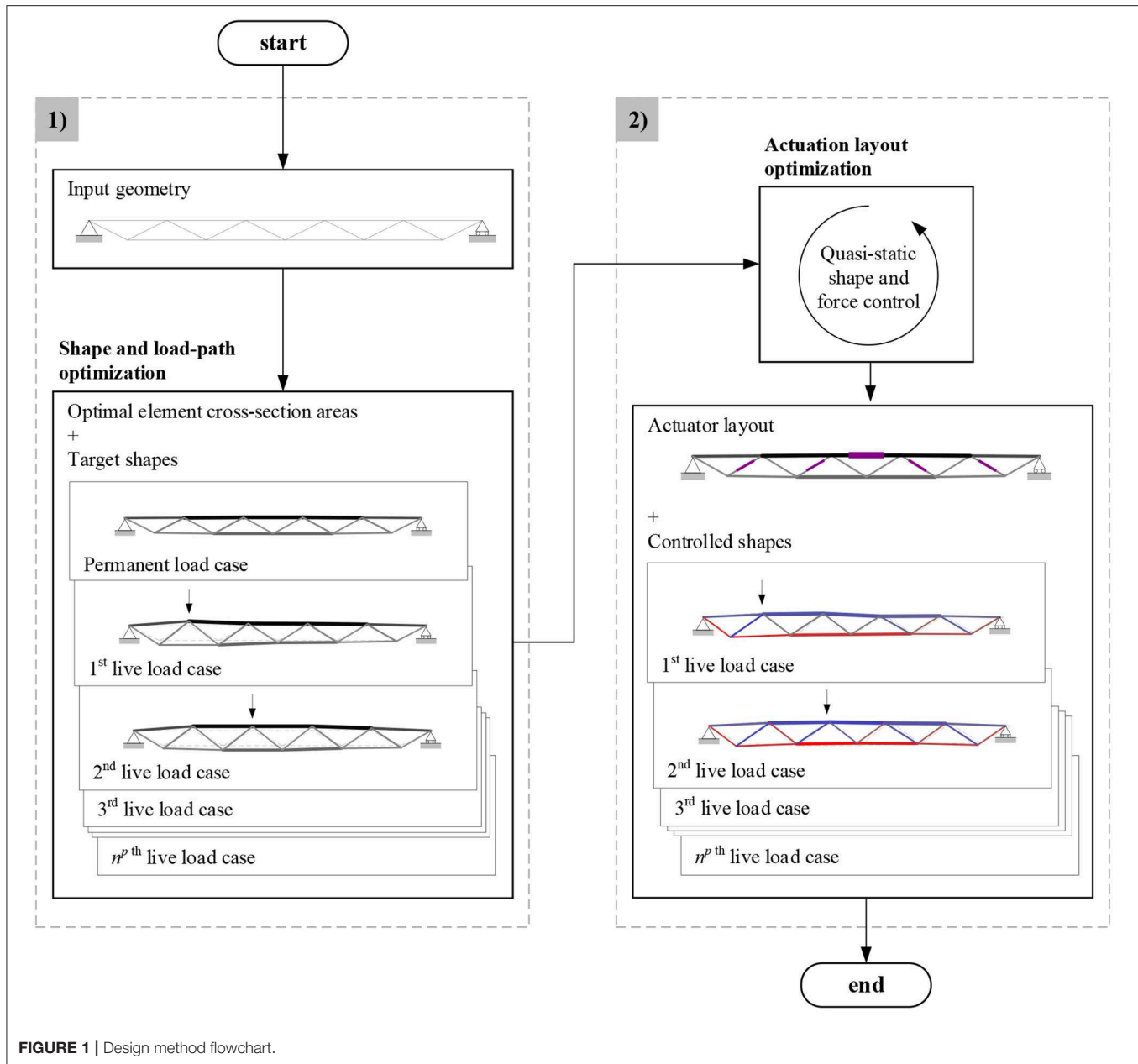
The design method consists of two parts: (1) optimization of the geometry, internal forces and element cross-section areas to minimize the structure embodied energy, (2) optimal actuator placement to control the structure into the optimal shapes obtained in (1) through quasi-static, non-linear geometric shape and force control. The design process is illustrated in **Figure 1**. The design method is formulated for reticular structures and this study only deals with such structures. The actuators are assumed to be linear actuators integrated into the structure by replacing selected elements. This design method has been formulated for structures subjected to slowly changing loads (e.g., snow load). The control methods adopted in this formulation are for quasi-static or low frequency loading hence the dynamic response of the structure is not taken into account.

Shape and Load-Path Optimization

The structure is designed to have an optimal shape and an optimal internal load path against each load case. This process, denoted by χ , is a mapping between external load \mathbf{p} and target shapes \mathbf{d}^t as well as internal forces \mathbf{f}^t that are optimized to maximize material utilization:

$$\begin{aligned}\chi : \mathbf{p}_j &\rightarrow \left(\mathbf{f}_j^t, \mathbf{d}_j^t \right) \quad \forall j = 0, 1, \dots, n^p \\ \mathbf{p}_j &\mapsto \mathbf{f}_j^t(\mathbf{p}_j) \\ \mathbf{p}_j &\mapsto \mathbf{d}_j^t(\mathbf{p}_j)\end{aligned}\quad (1)$$

The superscript t stands for “target.” The inputs are the structural topology, i.e., a set of n^n nodes connected by n^e elements, support conditions, loading and controlled degrees of freedom n^{cd} . The controlled degrees of freedom identify the nodal positions that will be varied during shape optimization and that will be controlled through actuation. The initial shape of the structure (i.e., initial node coordinates) is defined as $\mathbf{d}^{input} \in \mathbb{R}^{n^d}$. The



design variables are element cross-section areas $\alpha \in \mathbb{R}^{n^e}$, internal forces $\mathbf{f}^t \in \mathbb{R}^{n^e}$ and nodal positions $\mathbf{d}^t \in \mathbb{R}^{n^d}$:

$$\mathbf{x} = \left[\alpha \quad \mathbf{f}_0^t \cdots \mathbf{f}_j^t \cdots \mathbf{f}_{n^p}^t \quad \mathbf{d}_0^t \cdots \mathbf{d}_j^t \cdots \mathbf{d}_{n^p}^t \right]^T \quad (2)$$

The objective is to minimize the embodied energy of the structure subject to force equilibrium and stress constraints including element buckling:

$$\min_{\mathbf{x}} \sum_{i=1}^{n^e} g_i \alpha_i l_{i0} \rho_i \quad (3)$$

s.t.

$$\mathbf{A}_j \mathbf{f}_j^t = \mathbf{p}_j, \quad (4)$$

$$f_{ij}^t \leq \sigma_i^t \alpha_i; \quad f_{ij}^t \geq \max \left(\sigma_i^c \alpha_i, -\frac{\pi^2 E I_i}{l_{ij}^2} \right), \quad (5)$$

$$\mathbf{d}^l \leq \mathbf{d}^t \leq \mathbf{d}^u; \quad \alpha^l \leq \alpha \quad (6)$$

The index i refers to the i th element, j to the j th load case, n^e is the number of elements and n^p is the total number of load cases. In Equation (2) g_i is the material energy intensity (Hammond and Jones, 2008) and ρ_i the density of the i th element. The term l_{ij} is the length of the i th element for the j th load case. The second moment of area I_i is a function of the cross-section area α_i . E , σ^t and σ^c are the Young's modulus, admissible tensile and

compressive stress respectively. $\mathbf{A}_j \in \mathbb{R}^{n^d \times n^e}$, \mathbf{f}_j and \mathbf{p}_j are the equilibrium matrix, internal forces and external load for the j th load case. Upper and lower bounds are set in order to avoid potential convergence issues caused by node position reversal or merging as well as to ensure control feasibility. The output of this process includes the element cross-section areas α as well as the optimal forces \mathbf{f}_j^* and nodal positions \mathbf{d}_j^* for each load case.

At this stage, geometric compatibility between element deformations and nodal displacements is not accounted for and thus, the resulting target shapes may not be compatible. Geometric compatibility is a non-linear constraint which can cause convergence difficulties and hence, it is often ignored in structural optimization. For a passive structure, the omission of this constraint might result in a configuration that does not meet serviceability limits (e.g., deflection) under loading. For adaptive structures, disaggregation of force equilibrium and geometric compatibility is a key aspect (Senatore et al., 2019). Geometric compatibility is instead enforced through a controlled shape change. This way, a structure can be designed to meet strength requirements passively but serviceability constraints are met through adaptation i.e., shape and internal force control.

Actuation Layout Optimization

The second step of the design process is to obtain an actuator layout (i.e., placement) that is optimal to control the structure into the target shapes obtained in section Shape and Load-Path Optimization. The objective is to maximize the similarity between shapes controlled via actuation $\Delta \mathbf{d}^c$ and the target shapes obtained in section Shape and Load-Path Optimization subject to ultimate limit state (ULS) constraints:

$$\min_{\mathbf{y}} 1 - Q, \quad (7)$$

s.t.

$$f_i^c \leq \sigma_i^t \alpha_i; f_i^c \geq \max \left(\sigma_i^c \alpha_i, -\frac{\pi^2 E I_i}{l_i^2} \right), \quad (8)$$

where:

$$Q = \frac{1}{n^p} \sum_{j=1}^{n^p} \frac{(\Delta \mathbf{d}_j^c)^T \Delta \mathbf{d}_j^t}{(\Delta \mathbf{d}_j^c)^T \Delta \mathbf{d}_j^c + (\Delta \mathbf{d}_j^t)^T \Delta \mathbf{d}_j^t - (\Delta \mathbf{d}_j^c)^T \Delta \mathbf{d}_j^t} \quad (9)$$

$\Delta \mathbf{d}^t$ is the nodal displacement vector to move from the deformed shape to the target shape \mathbf{d}^t . $\Delta \mathbf{d}^c$ is the nodal displacement vector to move from the deformed shape to the shape obtained through control (section Quasi-Static, Non-linear Geometric Shape, and Force Control). Both equilibrium and geometric compatibility must be considered at this stage. The design variable $\mathbf{y} \in \mathbb{Z}^{n^{act}}$ is a vector containing the indices of the active elements and n^{act} is the number of actuators. Q is a similarity criterion (Tanimoto, 1958) which is employed in this work to measure the difference between two vectors in terms of shape features and node positions. The index Q takes a value between 0 and 1.

The optimization stated in Equations (8)–(10) is combinatorial and thus, when the number of structural elements is large a full enumeration is impossible. Optimal

actuator placement is carried out using a global search method called constrained simulated annealing (CSA) (Wah and Wang, 1999). A heuristic based on a measure of efficacy for each element to contribute toward the attainment of the optimal shapes through its length changes (Senatore et al., 2019) is employed to generate the initial candidate solution and to define the neighborhood structure i.e., the set of feasible solutions “close” to the current solution.

Quasi-Static, Non-linear Geometric Shape, and Force Control

The structure has to be controlled through actuator commands $\Delta \mathbf{l}$ that cause a change of internal forces $\Delta \mathbf{f}^c$ and nodal displacement $\Delta \mathbf{d}^c$ that approximate the target ones ($\Delta \mathbf{f}^t$, $\Delta \mathbf{d}^t$):

$$\phi^{-1}: (\Delta \mathbf{f}_j^t, \Delta \mathbf{d}_j^t) \rightarrow \Delta \mathbf{l}_j \quad \forall j = 1, \dots, n^p. \quad (10)$$

Since large shape changes modify equilibrium conditions, control commands must be computed through a method that considers geometric non-linearity. In addition, because shape adaptation does not rely on mechanisms with defined kinematics, given an actuator layout there are generally infinite solutions in terms of length changes to approximate a required shape change. A possible strategy is to find the minimum actuator length changes that deform the structure into a target shape. This is an inverse problem having a non-trivial solution.

For small deformations, the relationship between element length changes $\Delta \mathbf{l}$ to shape changes $\Delta \mathbf{d}$ and internal force changes $\Delta \mathbf{f}$ can be expressed as:

$$\Delta \mathbf{f} = \mathbf{S}_f \Delta \mathbf{l}, \quad (11)$$

$$\Delta \mathbf{d} = \mathbf{S}_d \Delta \mathbf{l}, \quad (12)$$

where \mathbf{S}_f and \mathbf{S}_d are the force and displacement sensitivity matrices (Senatore et al., 2019). In this work, \mathbf{S}_f and \mathbf{S}_d are computed using a force method based on singular value decomposition of the equilibrium matrix (Pellegrino, 1993; Luo and Lu, 2006; Yuan et al., 2016). Once the force and displacement sensitivity matrices are known, ϕ^{-1} is formulated as a constrained minimization of the difference between the controlled ($\Delta \mathbf{d}^c$, $\Delta \mathbf{f}^c$) and optimal configuration ($\Delta \mathbf{d}^t$, $\Delta \mathbf{f}^t$):

$$\min_{\Delta \mathbf{l}} \left\| \mathbf{S} \cdot \{\Delta \mathbf{l}\} - \begin{Bmatrix} \Delta \mathbf{d}^t \\ \Delta \mathbf{f}^t \\ \mathbf{0} \end{Bmatrix} \right\|^2, \quad (13)$$

s.t.

$$f_{ij} \leq \sigma_i^t \alpha_i; f_{ij} \geq \max \left(\sigma_i^c \alpha_i, -\frac{\pi^2 E I_i}{l_{ij}^2} \right), \quad (14)$$

where the term \mathbf{S} is:

$$\mathbf{S} = [\mathbf{S}_d \quad \mathbf{S}_f \quad \mathbf{I}]^T. \quad (15)$$

When geometrical non-linearity is accounted for, \mathbf{S}_d and \mathbf{S}_f have to be updated as the geometry of the structure changes. The

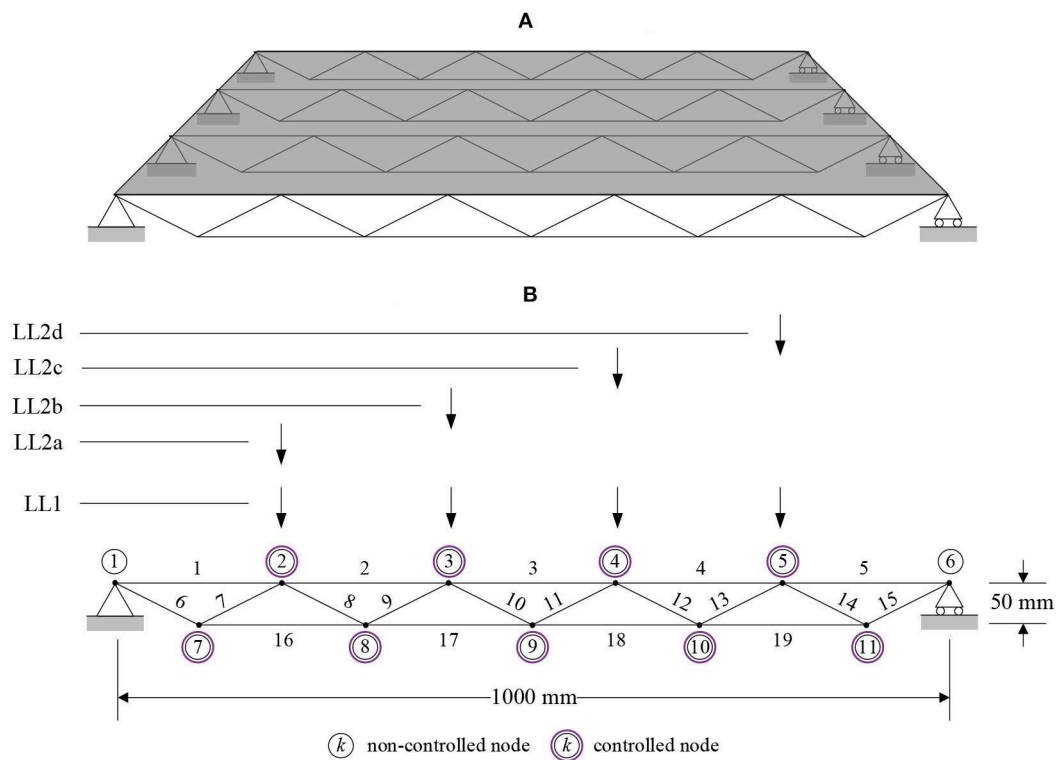


FIGURE 2 | Description of the case study. **(A)** Roof structure case study. **(B)** Loading, node and element numberings.

Newton-Raphson scheme is employed to iterate to convergence which is reached when the change of forces $\|\Delta \mathbf{f}^c - \Delta \mathbf{f}'\|^2$ and displacements $\|\Delta \mathbf{d}^c - \Delta \mathbf{d}'\|^2$ between two consecutive iterations are smaller than a set tolerance, where $\Delta \mathbf{f}'$ and $\Delta \mathbf{d}'$ are the change of forces and shape at next iteration.

NUMERICAL CASE STUDY

The prototype structure tested in this study is a planar simply-supported truss which can be thought of as a part of the roof system shown in **Figure 2A**. The truss has a span of 1,000 mm and a 20:1 span-to-depth ratio. It consists of 19 elements connected through 11 nodes of which two are constrained as indicated in the diagram shown in **Figure 2B**. The truss is statically determinate. All elements have a solid cylindrical section and are made of aluminum with a Young's modulus of 72.4 GPa.

Due to the small scale of this structure its self-weight is negligible. Two live loads (LL) are considered: (1) a uniformly distributed load of 10 N applied on all top chord nodes (LL1); (2) a moving load discretized by four point loads of 20 N applied on each node of the top chord in turn (LL2a–2L2d).

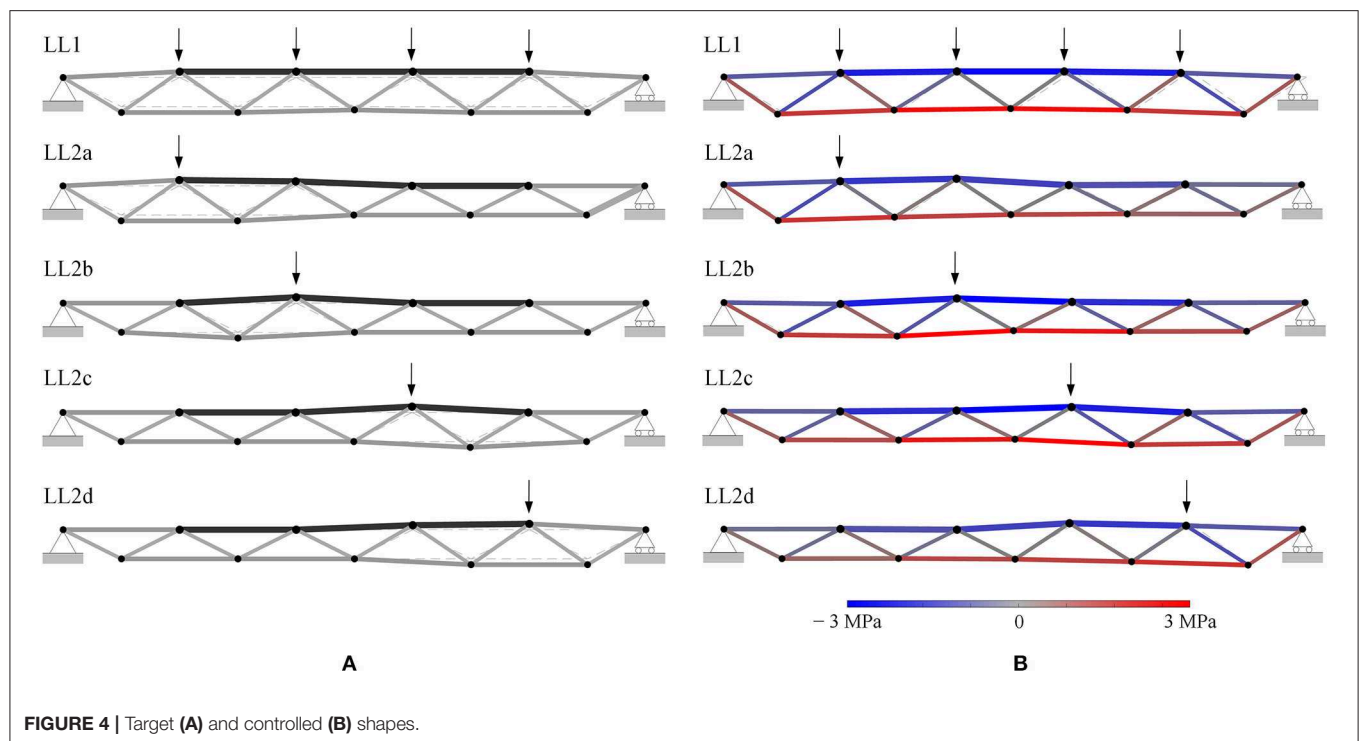
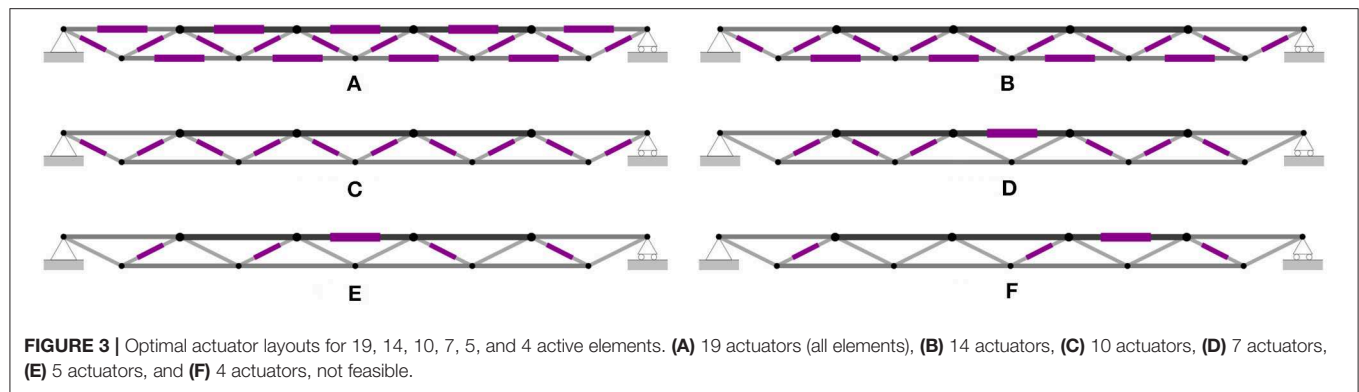
All nodes except the supports are allowed to shift vertically with an upper bound $\Delta \mathbf{d}^u$ and a lower bound $\Delta \mathbf{d}^l$ set to ± 15 mm. The lower bound for the element radius is set to 1 mm. The first step of the method outlined in section Shape and Load-Path Optimization produces a structure whose embodied energy is

reduced by 17% with respect to an identical weight-optimized passive structure.

A low number of actuators is generally preferred in order to reduce monetary cost and control complexity. A minimum number of actuators is determined by applying sequentially the actuator layout optimization process (section Actuation Layout Optimization), each time decreasing the number of actuators until no solution can be obtained that satisfies ULS requirements. **Figure 3** shows the layouts obtained for 19, 14, 10, 7, 5, and 4 actuators.

No feasible solution (ULS satisfied) can be found for layouts made of less than 5 actuators. The layout shown in **Figure 3F** is an infeasible solution for 4 actuators. With this layout, the maximum element demand/capacity ratio is 1.26. With 5 actuators the maximum element demand/capacity ratio of 0.83. The 5-actuator solution is therefore chosen as the optimal actuator layout (**Figure 3E**). This solution was obtained after 413 iterations in 651 s on an Intel Core i7, 3.60 GHz. This layout has been verified through a full enumeration (11,628 candidate solutions) which has taken ~ 5 h.

The target shapes are shown in **Figure 4A**. For comparison, **Figure 4B** shows the controlled shapes (5-actuator layout) with the element stress mapped onto the geometry. Optimal shapes and controlled shapes are very similar but not identical. There is a maximum distance of 11.8 mm for node 8 between target and controlled shape under LL2b. **Table 1** gives the actuator length changes for all load cases.

**TABLE 1 |** Actuator length changes.

Actuator #	Length change Δl (mm)				
	LL1	LL2a	LL2b	LL2c	LL2d
3	-16	-7	-2	-2	-7
7	17	14	4	0	0
9	15	13	9	0	0
12	15	0	0	9	13
14	17	0	0	4	14

In order to show stress redistribution through active control, the adaptive solution is compared to an identical weight-optimized passive structure. In this context, stress homogenization is understood as a reduction of magnitude

and variability. For example, it is clear from **Figure 4** that through shape control the depth of the structure increases in the proximity of the point of application of the external load. If the structure is thought of as a beam, this results in a better resistance against bending moment.

Figure 5 shows the element stress for the passive (a) and adaptive (b) structures. For brevity, LL2c and LL2d are not shown since they are mirror of LL2b and LL2a. Tensile and compressive stress are indicated in red and blue, respectively. The mean for each data set is shown as a horizontal dashed line. Stress variability is quantified through standard deviation. The width of the shaded band, whose centerline is the mean value of each data set, is twice the standard deviation.

The element stress in the adaptive structure is consistently lower than that of the passive structure. The maximum mean reduction for tensile and compressive stress are 33 and 34%, respectively (both in LL1). The same applies to stress variability.

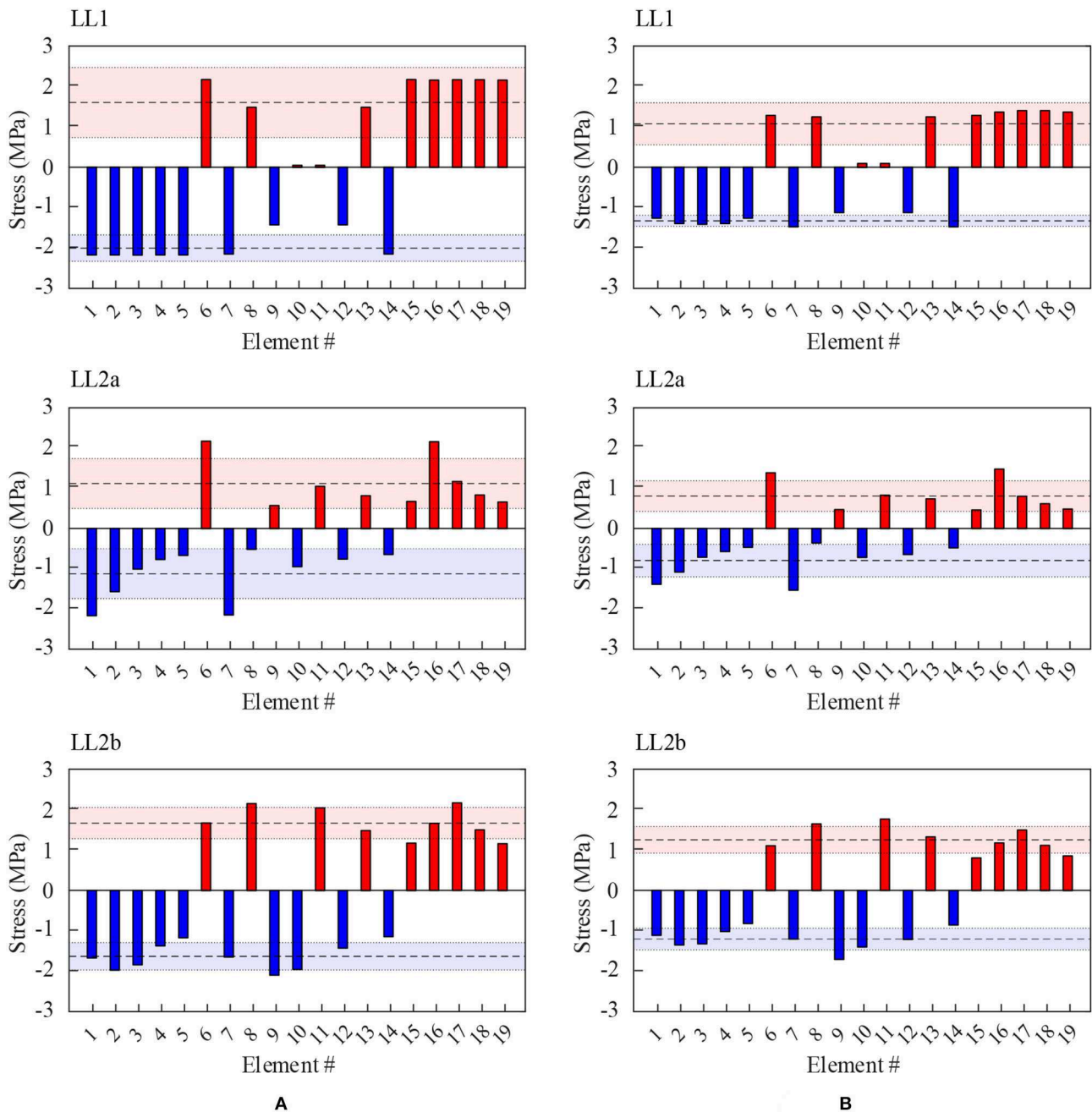


FIGURE 5 | Element stress in passive (A) and adaptive (B) structure.

LL1 and LL2b have the smallest variability through shape control for compressive and tensile stress, respectively. Stress homogenization can be appreciated the most in LL1. The stress of element 8, 9, 12, and 13 remains similar to that of the corresponding elements in the passive structure. However, the stress of element 1 ~ 7 and 14 ~ 19 decrease. Similarly, in LL2a, the stress of element 6, 7, and 16 decrease significantly while the stress for the other elements remain practically the same. There is no stress reversal between the passive and adaptive structure.

EXPERIMENTAL TESTING

Setup

The aim of this test is to assess the applicability of the design method outlined in section Shape and Load-Path Optimization and Actuation Layout Optimization to a real structure, as well as the accuracy of the numerical methods for shape control outlined in section Quasi-Static, Non-linear Geometric Shape, and Force Control. A prototype structure was built based on

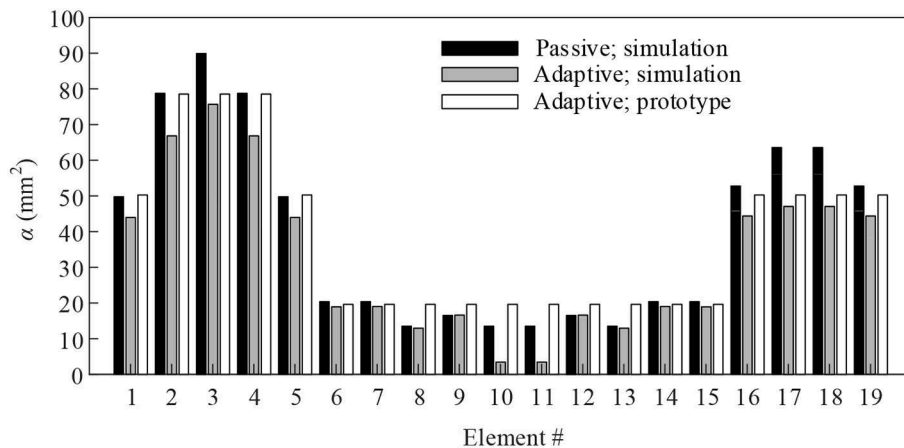


FIGURE 6 | Optimal cross-section sizing.

the model described in section Numerical Case Study. **Figure 6** shows a bar chart comparing the cross section area between the passive and adaptive structure obtained through simulation with the built prototype. Assuming the density of aluminum is $2,649 \text{ kg/m}^3$, the mass of the passive and adaptive structure is 0.35 and 0.28 kg, respectively. The element cross sections of the built prototype have been sized-up to match commercial availability. The total mass of the prototype is 0.32 kg, of which the mass of the actuators comprises 1%.

The active elements are five turnbuckles that are fitted on element 3, 7, 9, 12, and 14 according to the 5-actuator layout obtained in section Numerical Case Study. Each turnbuckle consists of a shaft hosting two rods of opposite threads (left and right). This way, rotating the shaft can either shorten or lengthen the turnbuckle (i.e., contraction or extension) depending on the rotation direction.

The joints are fabricated through additive manufacturing using a polymer-based material (polyether block amide) with a Young's modulus of 82 MPa. The low stiffness of this material was chosen to ease shape reconfiguration, which in this case is manually operated through the turnbuckles. Due to the planarity of the truss, to avoid out-of-plane deflections, two acrylic posts are placed at 300 mm from both ends as shown in **Figure 7A**. These posts are in direct contact with the structure allowing only in-plane movements. Although not shown in **Figure 7A**, the right support can slide horizontally through a pin-slot joint.

Elements 1, 2, 4, 5, 16, 17, 18, and 19 are instrumented with strain sensors. Only 8 out of 19 elements are instrumented because it was not practical to install strain gauges on the 5 mm diameter bracing elements and on the turnbuckles. **Figure 7B** shows the location of both actuators and strain sensors. **Figure 8** is a close-up taken at mid-span showing some of the turnbuckles and strain sensors.

For each element, two strain gauges are placed diametrically opposed to one another in a quarter-bridge configuration. The strain of the i th element is computed as $\varepsilon_i = (\varepsilon_i^a + \varepsilon_i^b)/2$ where ε_i^a and ε_i^b are the strains measured at each gauge position. By

doing so, flexural effects are rejected, since strains of opposing signs cancel each other. To reduce the effect of out-of-plane actions, the gauges are placed parallel to the truss main plane. The strain gauges used in this test have a resistance of $350 \Omega \pm 0.35\%$ and a gauge factor of $2.06 \pm 1.0\%$. The gauges are manufactured by Hottinger Baldwin Messtechnik (HBM).

The node position is monitored using an optical tracking system by OptiTrack comprising four cameras and reflective targets that are placed on the nodes. The optical system is able to track the node position within a $\pm 0.025 \text{ mm}$ precision. Data acquisition of strains and nodal positions was carried out with a sampling rate of 10 Hz using National Instruments PXIe-8840 with Intel Core i7, 2.60 GHz quad-core. Loading consists of weights of 1 kg ($\approx 10 \text{ N}$) and 2 kg ($\approx 20 \text{ N}$) for LL1 and LL2, respectively which are applied on the nodes using hooks.

SIMULATED vs. MEASURED CONTROLLED SHAPES

The structure static response under loading is measured and compared to the numerical predictions obtained in section Numerical Case Study. Element strains and nodal positions are measured before and after shape control. **Figure 9** shows the difference between $\Delta \mathbf{d}^{cm}$ and $\Delta \mathbf{d}^{cs}$ (measured and simulated controlled shape changes) represented by thick and dashed lines respectively (**Figure 4B**). Referring to the similarity criterion given in Equation (10), a similarity of 0.78 is obtained between $\Delta \mathbf{d}^{cs}$ and $\Delta \mathbf{d}^{cm}$. **Table 2A** gives the maximum Euclidean distance between the nodes of \mathbf{d}^{cs} and \mathbf{d}^{cm} (measured and simulated controlled shapes) as well as the norm of the difference between $\Delta \mathbf{d}^{cs}$ and $\Delta \mathbf{d}^{cm}$. There was a maximum of 12.2 mm for node 8 between \mathbf{d}^{cs} and \mathbf{d}^{cm} under LL2b.

The measured structure response under shape control is consistent with the numerical predictions (section Numerical Case Study); an overall reduction of tensile and compressive stress is observed. This reduction is caused by the increase in depth in proximity of the point of application of the external load.

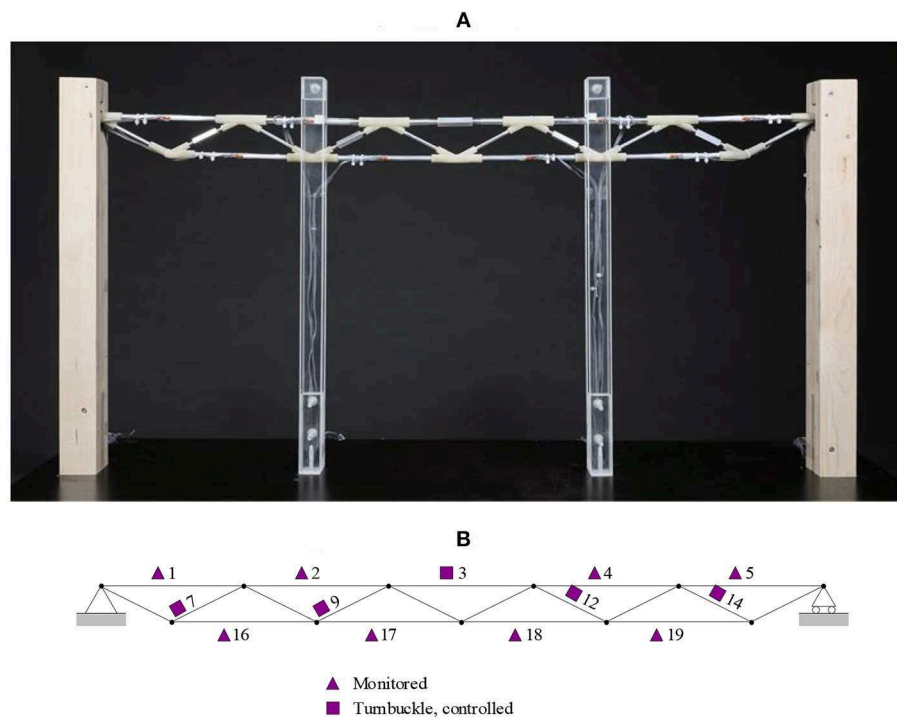


FIGURE 7 | Experimental setup. (A) Structure and supports. (B) Location of sensors and turnbuckles.

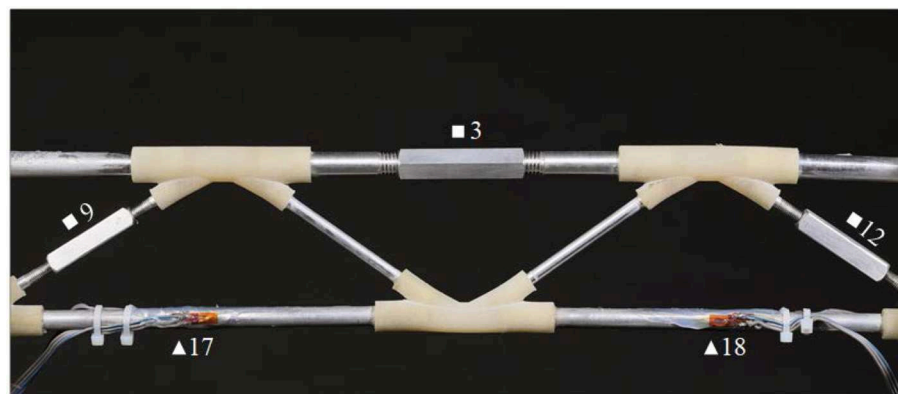


FIGURE 8 | Sensors and turnbuckles fitted in the truss.

The bar charts in **Figure 10** compare element stresses obtained from simulation and the measured ones for all load cases. For brevity, LL2c and LL2d are not shown since they mirror LL2b and LL2a, respectively. The element stress predicted by simulations before and after control is shown in white and gray respectively. The element stress measured before and after control is indicated by hatching.

Table 2B shows the Pearson correlation (Hollander and Wolfe, 1973) between measured and predicted change of stress (the change of stress before and after control). A strong correlation between measurement and prediction is obtained for all load cases.

Tables 3A,B give metrics related to predicted and measured element stress distribution respectively. When assessing the effect of shape control (i.e., stress reduction and homogenization) predicted through simulations in Simulated vs. Measured Controlled Shapes (**Figure 5**), it was observed that both mean and standard deviation of the element stress are lower in the adaptive compared to the weight-optimized passive structure. Generally, this is also observed through measurement. The mean of the stress is lower for all load cases. The maximum mean reduction for tensile and compressive stress are 25% (LL1) and 32% (LL2d), respectively. However, the standard deviations for compressive stress for LL1, LL2a, and LL2d is higher for the adaptive structure

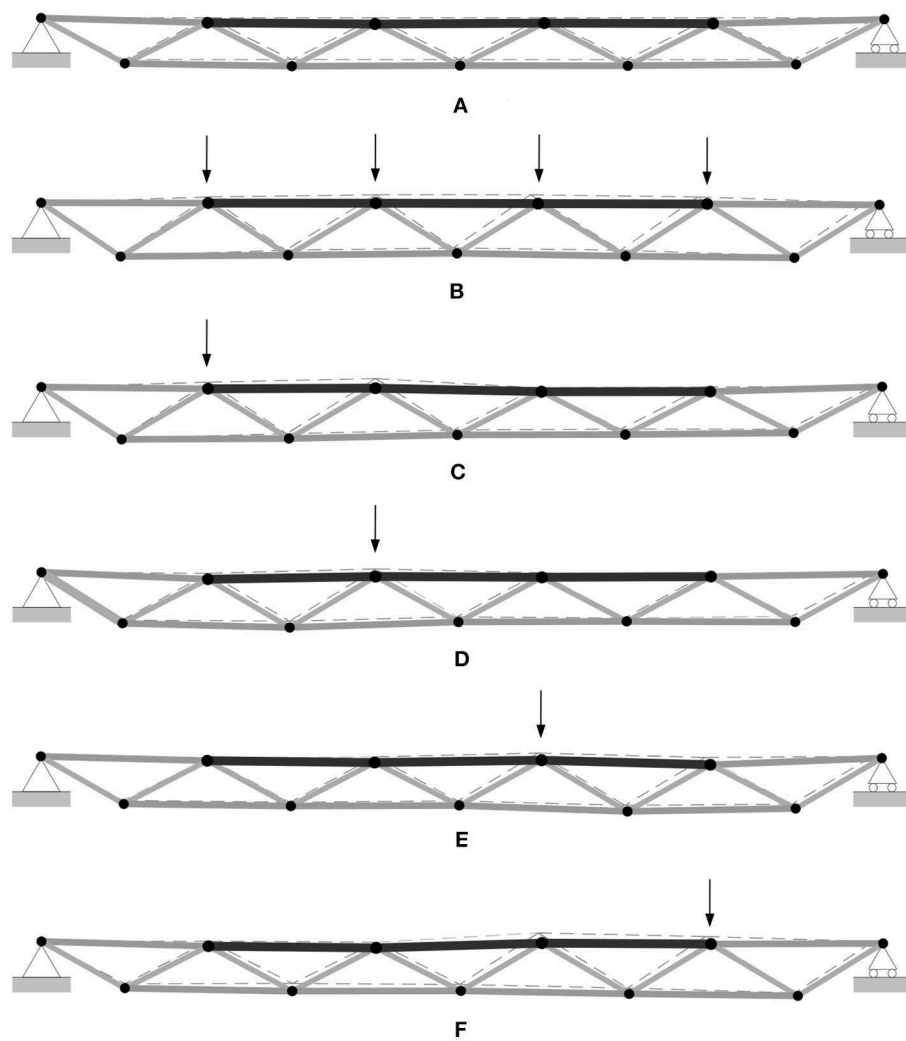


FIGURE 9 | Controlled shapes: measurement (thick lines) vs. simulation (dashed lines). **(A)** No load, **(B)** LL1, **(C)** LL2a, **(D)** LL2b, **(E)** LL2c, and **(F)** LL2d.

TABLE 2 | Discrepancy between measurement and simulation.

Load case	No load	LL1	LL2a	LL2b	LL2c	LL2d
(A) NODAL COORDINATES						
$\ \Delta \mathbf{d}^{cm} - \Delta \mathbf{d}^{cs}\ _2$ (mm)	19.8	21.9	19.6	22.4	23.5	23.4
Max. node distance (mm)	7.9	10.6	11.5	12.2	11.7	12.1
(B) CHANGE OF STRESS						
Pearson correlation measure	-	0.99	0.86	0.93	0.94	0.90

because the element cross sections had to be changed due to commercial availability. The symbol “▲” in Table 3 indicates cases where mean or standard deviation of the element stress in the adaptive structure is higher than in the weight-optimized passive structure.

To implement a control system based on the optimization process outlined in section Shape and Load-Path Optimization,

the external load \mathbf{p} has to be sensed in order to compute the target shapes \mathbf{d}^t . When the internal forces and the shape of the structure are known, the external loads \mathbf{p} can be inferred through force equilibrium:

$$\mathbf{A}\mathbf{f} = \mathbf{p} \quad (16)$$

where \mathbf{A} is the equilibrium matrix which is iteratively updated based on the measured nodal positions, \mathbf{f} is the vector of internal forces obtained directly through strain measurement. Because the structure undergoes a large shape change, the equilibrium matrix \mathbf{A} cannot be kept constant. For example, if \mathbf{A} is not updated as the shape changes, the sensed external load \mathbf{p} may appear to vary even if it is kept constant.

Since only 8 out of 19 elements are instrumented with strain gauges, the forces in non-instrumented elements are obtained through nodal equilibrium. Force equilibrium can be expressed as a homogeneous linear system for a node whose degree of

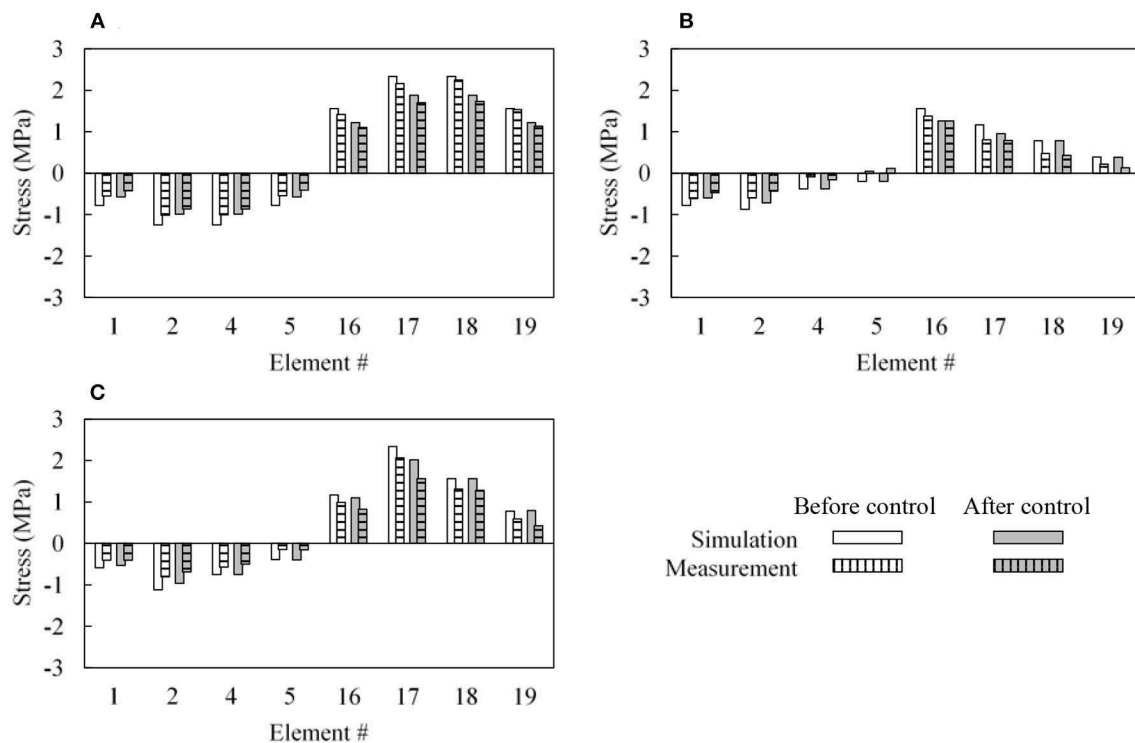


FIGURE 10 | Element stress. (A) LL1, (B) LL2a, and (C) LL2b.

TABLE 3 | Element stress passive vs. adaptive structure.

Metric	Stress passive/stress adaptive (MPa/MPa)				
	LL1	LL2a	LL2b	LL2c	LL2d
(A) SIMULATION					
Mean tensile	1.61/1.08	1.12/0.81	1.67/1.26	1.67/1.26	1.12/0.81
Mean compressive	-2.00/-1.32	-1.12/-0.80	-1.63/-1.20	-1.63/-1.20	-1.12/-0.80
Standard deviation tensile	0.87/0.52	0.62/0.38	0.39/0.33	0.39/0.33	0.62/0.38
Standard deviation compressive	0.33/0.14	0.62/0.40	0.34/0.27	0.34/0.27	0.62/0.40
(B) MEASUREMENT					
Mean tensile	1.65/1.23	1.11/0.88	1.72/1.32	1.72/1.34	1.11/0.91
Mean compressive	-1.71/-1.18	-0.92/-0.68	-1.47/-1.02	-1.47/-1.06	-0.92/-0.62
Standard deviation tensile	0.95/0.70	0.61/0.53	0.61/0.40	0.61/0.43	0.61/0.55
Standard deviation compressive	0.41/0.54 ▲	0.39/0.55 ▲	0.63/0.44	0.63/0.47	0.39/0.56 ▲

freedoms are not constrained (i.e., it is not a support) and when no external load is applied on it:

$$Af = 0 \quad (17)$$

Node 7, 8, 9, 10, and 11 satisfy these criteria (Figure 2B), therefore the forces in elements 6 to 15 can be computed through Equation (18). It is not possible to compute the force in element 3 using Equation (18) because it connects node 3 and 4 where the external load is applied. In this case, force equilibrium is an underdetermined linear system with more unknowns than equations. Therefore, the force in

element 3 is inferred through linear regression. The input dataset is obtained through simulation, the known values of f are the independent variables. Load cases LL1 and LL2 were investigated.

Figure 11A shows the comparison between applied (continuous) and predicted (scatter) external load on node 2 (load case LL2a) when no shape control was carried out. A 20 N load was applied incrementally in four steps of 5 N. Load prediction was carried out 10 times per second. The external load predicted for node 2 was in good agreement with the applied one, with a maximum error of 1.1 N when the load magnitude

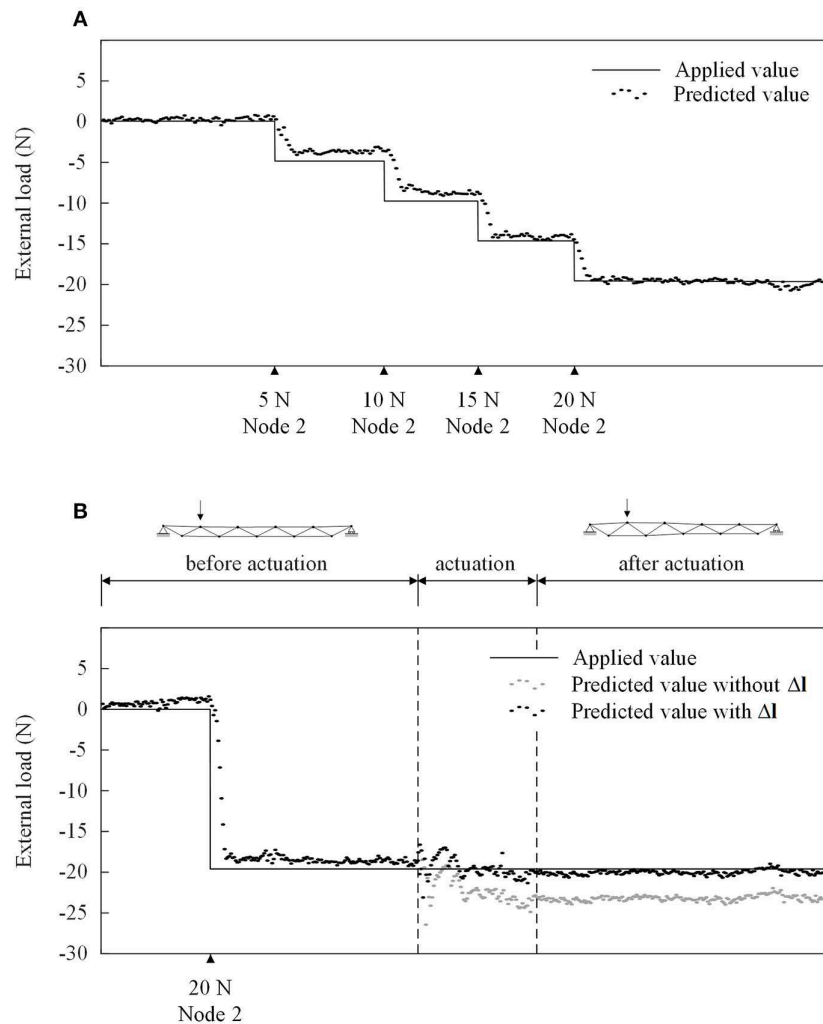


FIGURE 11 | External load on node 2 (load case LL2a). **(A)** No shape control. **(B)** Shape control.

reaches 20 N. Despite no load was applied on node 3, 4, and 5, spurious vertical loads of 1.8 N magnitude were predicted.

Figure 11B shows the comparison between applied and predicted values for the external load when the structure is subjected to a 20 N load (applied in one step) on node 2 before and after control. Shape control was carried out by applying the length changes Δl for load case LL2a. By using a linear regression model that considers only the known values of \mathbf{f} as the independent variables, prediction of the external load \mathbf{p} had a maximum error of 4 N as shown by the gray scatter plot in **Figure 11B**. Load prediction was more accurate when the length changes Δl were also included in the independent variables in order to obtain the forces in non-instrumented elements. As shown by the black scatter plot in **Figure 11B**, the predicted load is close to the applied one even after shape control with a maximum error of 0.6 N. As in the previous case, despite no load was applied on node 3, 4, and 5, spurious vertical loads of 2.3 N magnitude were predicted.

Similarly, for load case LL1, 10 N loads were applied to node 2, 3, 4, and 5 sequentially and when no shape control was carried out. **Figure 12A** shows the comparison between the applied (continuous) and predicted (scatter) external load. The external load was predicted with good accuracy, with a maximum error of 2 N for node 4. Prediction error varied when adjacent nodes were loaded. For example, the load predicted on node 2 is on average 9.2 N. However, when the load is applied on node 2 and 3 simultaneously the predicted value was 9.7 N.

When shape control is carried out under LL1, the external load was predicted with good accuracy, with a maximum error of 2.3 N for node 4. Higher prediction errors occurred during actuation, as shown in **Figure 12B**, which involved manual adjustment of several turnbuckles.

DISCUSSION

This work has presented experimental testing of a small-scale adaptive planar truss that counteracts loading through controlled

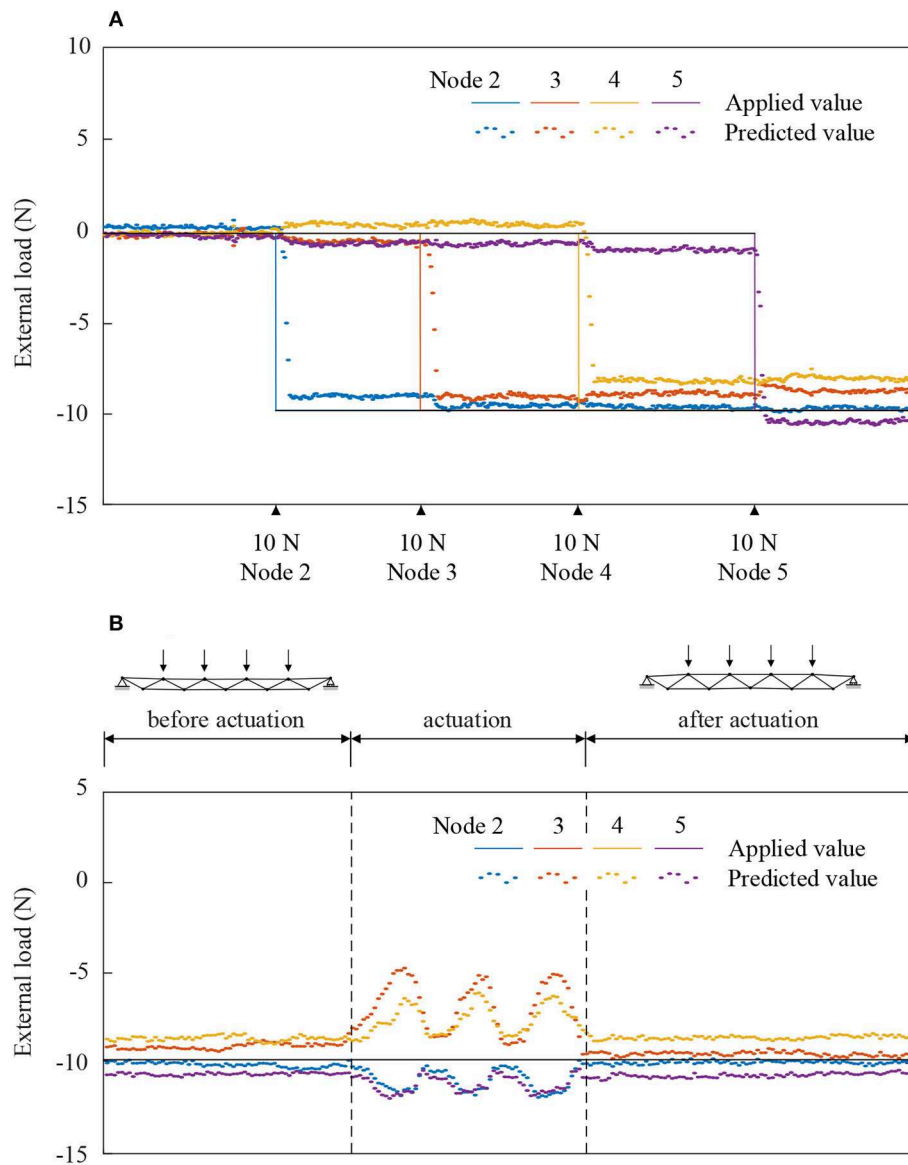


FIGURE 12 | External load on node 2, 4, 6, and 8 (load case LL1). **(A)** No shape control. **(B)** Shape control.

large shape changes. This structure was designed using a design method outlined in section Design Method, which involves a shape optimization process, through which an optimal shape is obtained for each load case. This way the design is not governed by peak loads. Stress homogenization through shape control allows a structure to operate closer to design limits maximizing material utilization and thus saving embodied energy with respect to a passive structure.

Stress homogenization has been quantified by comparing the mean and standard deviation of the element stress for the adaptive structure to those of an equivalent weight-optimized passive structure. Although the cross-section of the elements in the adaptive structure are smaller than those in the passive one, both mean and standard deviation of the stress are lower for the

adaptive thanks to shape control. The maximum mean reduction for tensile and compressive stress are 25 and 32%, respectively. Experimental results show good agreement with numerical simulations. A minimum Pearson correlation coefficient of 0.86 has been observed. The formulation outlined in this study treats the element cross section area as continuous variables. However, the element cross sections are subject to commercial availability. Future works could look into implementing a similar optimization process by treating the element cross sections as discrete variables using mixed-integer programming.

Shape and force control based on the formulation outlined in this paper requires knowledge of the external load. In this work, the external load was inferred from sparse strain measurements (only 8 elements instrumented out of 19) complemented by

an optical tracking system. The optical system was essential to close the information gap caused by sparse instrumentation, especially in situations where nodal coordinates varied through shape control. However, the use of machine vision may pose a reliability risk in practice as the monitoring of nodal coordinates may fail when multiple reflective markers are occluded. Methods that mitigate this failure could be subject of future investigation.

Since experimental testing was carried out at a small scale, the effect of the structure self-weight and that of the actuators is negligible. However, this effect becomes significant with scale, especially due to the weight of the actuators, and thus it is important to include it in optimization and control. An approach proposed in Senatore et al. (2019) is to estimate the weight of an actuator by assuming it is proportional to the required force capacity.

CONCLUSIONS

The results of this study lead to the following conclusions:

- Experimental testing on a small-scale prototype has demonstrated that stress homogenization through large-shape changes is feasible. This enables an adaptive structure to operate closer to design limits maximizing material utilization and thus saving embodied energy with respect to a passive structure.
- The geometrically non-linear force method (NFM) outlined in section Quasi-Static, Non-linear Geometric Shape and Force Control offers an efficient way to control the shape of a reticular structure under quasi-static loading as shown by the good accordance between simulation and measurement.
- Detection of the applied loading is necessary for non-linear shape and force control.

It is expected that tests on similar full-scale reticular structures designed using the design method outlined in this work will lead

to similar conclusions. Experimental testing at a small scale has allowed model validation without including the effect of node stiffness on internal forces and nodal displacements, as well as how this effect behaves with scale. For this reason, further work will involve testing on a larger scale prototype adaptive structure.

DATA AVAILABILITY

The raw data supporting the conclusions of this manuscript will be made available by the authors, without undue reservation, to any qualified researcher.

AUTHOR CONTRIBUTIONS

GS set up research objectives and directions with contribution from IS. Method implementation were carried out by AR and GS. AR carried out simulations and experimental tests. AR wrote the first draft of the paper with GS and IS actively involved in the rest of the writing process. All authors contributed to manuscript revision, reviewed and approved the final version.

FUNDING

The authors thankfully acknowledge the Swiss National Science Foundation who provided core funding for this research via project 200021_182033 (Structural Adaptation through Large Shape Changes) and the Swiss Government Excellence Scholarship (ESKAS-Nr: 2016.0749).

ACKNOWLEDGMENTS

The authors would also like to acknowledge EPFL technicians Armin Krkic, Gérald Rouge, Gilles Guignet and photographer Alain Herzog for their contributions.

REFERENCES

- Campanile, L. F. (2003). "Using compliant and active materials to adapt structural geometry - challenges and good reasons," in *14th International Conference on Adaptive Structures* (Seoul).
- Cimellaro, G. P., Soong, T. T., and Reinhorn, A. M. (2008). "Optimal integrated design of controlled structures," in *The 14th World Conference on Earthquake Engineering* (Beijing).
- Descamps, B., and Coelho, R. F. (2013). A lower-bound formulation for the geometry and topology optimization of truss structures under multiple loading. *Struct. Multidiscipl. Optimiz.* 48, 49–58. doi: 10.1007/s00158-012-0876-3
- Fest, E., Shea, K., Domer, B., and Smith, I. F. C. (2003). Adjustable tensegrity structures. *J. Struct. Eng.* 129, 515–526. doi: 10.1061/(ASCE)0733-9445(2003)129:4(515)
- Gil, L., and Andreu, A. (2000). Shape and cross-section optimisation of a truss structure. *Comput. Struct.* 79, 681–689. doi: 10.1016/S0045-7949(00)00182-6
- Hammond, G., and Jones, C. (2008). Embodied energy and carbon in construction materials. *Proc. Inst. Civil Eng. Energy* 161, 87–98. doi: 10.1680/ener.2008.161.2.87
- Hollander, M., and Wolfe, D. A. (1973). *Nonparametric Statistical Methods*. New York, NY: John Wiley & Sons.
- Luo, Y., and Lu, J. (2006). Geometrically non-linear force method for assemblies with infinitesimal mechanisms. *Comput. Struct.* 84, 2194–2199. doi: 10.1016/j.compstruc.2006.08.063
- Pedersen, N. L., and Nielsen, A. K. (2003). Optimization of practical trusses with constraints on eigenfrequencies, displacements, stresses, and buckling. *Struct. Multidiscipl. Optimiz.* 25, 436–445. doi: 10.1007/s00158-003-0294-7
- Pellegrino, S. (1993). Structural computations with the singular value decomposition of the equilibrium matrix. *Int. Solids Struct.* 30, 3025–3035. doi: 10.1016/0020-7683(93)90210-X
- Reinhorn, A. M., Soong, T. T., Riley, M. A., and Lin, R. C. (1993). Full-scale implementation of active control. II: installation and performance. *J. Struct. Eng.* 119, 1935–1960. doi: 10.1061/(ASCE)0733-9445(1993)119:6(1935)
- Reksowardojo, A. P., Senatore, G., and Smith, I. F. C. (2018). "Actuator layout optimization for adaptive structures performing large shape changes," in *Advanced Computing Strategies for Engineering. EG-ICE 2018. Lecture Notes in Computer Science, Vol. 10864*, eds I. F. C. Smith and B. Domer (Lausanne; Cham: Springer), 111–129.
- Senatore, G., Duffour, P., and Winslow, P. (2018a). Energy and cost analysis of adaptive structures: case studies. *J. Struct. Eng. ASCE* 144:04018107. doi: 10.1061/(ASCE)ST.1943-541X.0002075

- Senatore, G., Duffour, P., and Winslow, P. (2018b). Exploring the application domain of adaptive structures. *Eng. Struct.* 167, 608–628. doi: 10.1016/j.engstruct.2018.03.057
- Senatore, G., Duffour, P., and Winslow, P. (2019). “Synthesis of minimum energy adaptive structures,” in *Structural and Multidisciplinary Optimization*, ed P. Wang (Heidelberg: Springer Berlin Heidelberg).
- Senatore, G., Duffour, P., Winslow, P., and Wise, C. (2018). Shape control and whole-life energy assessment of an infinitely stiff prototype adaptive structure. *Smart Mater. Struct.* 27:015022. doi: 10.1088/1361-665X/aa8cb8
- Shea, K., and Smith, I. F. C. (2006). Improving full-scale transmission tower design through topology and shape optimization. *Struct. Eng.* 132, 781–790. doi: 10.1061/(ASCE)0733-9445(2006)132:5(781)
- Skelton, R., Hanks, B., and Smith, M. (1992). Structure redesign for improved dynamic response. *J. Guid. Control Dyn.* 15, 1271–1278. doi: 10.2514/3.20979
- Sobek, W., and Teuffel, P. (2001). “Adaptive systems in architecture and structural engineering,” in *Proc. SPIE 4330, Smart Structures and Materials 2001: Smart Systems for Bridges, Structures, and Highways* (Newport Beach, CA).
- Soong, T. T. (1988). Active structural control in civil engineering. *Eng. Struct.* 10, 74–84. doi: 10.1016/0141-0296(88)90033-8
- Soong, T. T., and Cimellaro, G. P. (2009). Future directions in structural control. *Struct. Control Health Monit.* 16, 7–16. doi: 10.1002/stc.291
- Straube, J. (2006 October, 24). Green building and sustainability. *Building Science Digests*.
- Tanimoto, T. T. (1958). *An Elementary Mathematical Theory of Classification and Prediction*. New York, NY: IBM.
- Tibert, G. (2002). *Deployable Tensegrity Structures for Space Applications*. (Doctoral dissertation). Royal Institute of Technology, Stockholm.
- United Nations Environmental Programme (2007). *Buildings and Climate Change: Status, Challenges and Opportunities*. United Nations Environmental Programme, Sustainable Consumption and Production Branch, Paris.
- Veuve, N. W., Safei, S. D., and Smith, I. F. C. (2015). Deployment of a tensegrity footbridge. *J. Struct. Eng.* 141, 1–8. doi: 10.1061/(ASCE)ST.1943-541X.0001260
- Wah, B. W., and Wang, T. (1999). “Constrained simulated annealing with applications in nonlinear continuous constrained global optimization,” in *Proceedings 11th International Conference on Tools with Artificial Intelligence* (Chicago, IL).
- Wang, D., Zhang, W. H., and Jiang, J. S. (2002). Truss shape optimization with multiple displacement constraints. *Comput. Methods Appl. Mech. Eng.* 191, 3597–3612. doi: 10.1016/S0045-7825(02)00297-9
- Yao, J. T. P. (1972). Concept of structural control. *J. Struct. Divis.* 98, 1567–1574.
- Yuan, X., Liang, X., and Li, A. (2016). Shape and force control of prestressed cable-strut structures based on nonlinear force method. *Adv. Struct. Eng.* 19, 1917–1926. doi: 10.1177/1369433216652411

Conflict of Interest Statement: The authors declare that the research was conducted in the absence of any commercial or financial relationships that could be construed as a potential conflict of interest.

Copyright © 2019 Reksowardojo, Senatore and Smith. This is an open-access article distributed under the terms of the Creative Commons Attribution License (CC BY). The use, distribution or reproduction in other forums is permitted, provided the original author(s) and the copyright owner(s) are credited and that the original publication in this journal is cited, in accordance with accepted academic practice. No use, distribution or reproduction is permitted which does not comply with these terms.

NOMENCLATURE

A	Equilibrium matrix
E	Young's modulus
I	Second moment of area
Q	Tanimoto similarity index
S_d	Shape influence matrix
S_f	Force influence matrix
d^t	Optimal (target) shape
d^{cm}	Controlled shape (measured)
d^{cs}	Controlled shape (simulated)
d^{input}	Initial shape
f	Internal forces
f^t	Optimal (target) forces
Δd^C	Controlled shape change
Δd^{cm}	Controlled shape change (measured)
Δd^{cs}	Controlled shape change (simulated)
Δd^t	Target (optimal) shape change
Δf	Change of internal forces
Δf^C	Controlled change of internal forces
Δf^t	Target (optimal) change of internal forces
g	Material energy intensity
i	i th element
j	j th load case
l	Element length
Δl	Control commands (actuator length changes)
n^{act}	Number of actuators
n^{cd}	Number of controlled degrees of freedom
n^d	Number of degrees of freedom
n^e	Number of elements
n^n	Number of nodes
n^p	Number of load cases
p	External load
x	Design variable vector: α , f , Δd
y	Actuator positions (actuator layout)
α	Element cross-section areas
X	Mapping between external load and shapes
ϕ	Computation of internal forces and shape given control commands
ϕ^{-1}	Computation of control commands given target internal forces and shape
ρ	Material density
σ^C	Ultimate compressive stress
σ^t	Ultimate tensile stress
CSA	Constrained simulated annealing
LL	Live load
NFM	Non-linear force method



Using Influence Matrices as a Design and Analysis Tool for Adaptive Truss and Beam Structures

Simon Steffen*, Stefanie Weidner, Lucio Blandini and Werner Sobek

Institute for Lightweight Structures and Conceptual Design (ILEK), University of Stuttgart, Stuttgart, Germany

OPEN ACCESS

Edited by:

Gennaro Senatore,
École Polytechnique Fédérale de
Lausanne, Switzerland

Reviewed by:

Ehsan Noroozinejad Farsangi,
Graduate University of Advanced
Technology, Iran
Michele Betti,
University of Florence, Italy

*Correspondence:

Simon Steffen
simon.steffen@ilek.uni-stuttgart.de

Specialty section:

This article was submitted to
Computational Methods in Structural
Engineering,
a section of the journal
Frontiers in Built Environment

Received: 28 February 2020

Accepted: 06 May 2020

Published: 23 June 2020

Citation:

Steffen S, Weidner S, Blandini L and
Sobek W (2020) Using Influence
Matrices as a Design and Analysis
Tool for Adaptive Truss and Beam
Structures. *Front. Built Environ.* 6:83.
doi: 10.3389/fbuil.2020.00083

Due to the already high and still increasing resource consumption of the building industry, the imminent scarcity of certain building materials and the occurring climate change, new resource- and emission-efficient building technologies need to be developed. This need for new technologies is further amplified by the continuing growth of the human population. One possible solution proposed by researchers at the University of Stuttgart, and which is currently further examined in the context of the Collaborative Research Centre (SFB) 1244 *Adaptive Skins and Structures for the Built Environment of Tomorrow* is that of adaptivity. The integration of sensors, actuators, and a control unit enables structures to react specifically to external loads, when needed (e.g., in the case of high but rare loads). For example, adaptivity in load-bearing structures allows for a reduction of deflections or a homogenization of stresses. This in its turn allows for ultra-lightweight structures with significantly reduced material consumption and emissions. To reach ultra-lightweight structures, i.e., adaptive load-bearing structures, two key questions need to be answered. First, the question of optimal actuator placement and, second, which type of typology (truss, frame, etc.) is most effective. One approach for finding the optimal configuration is that of the so-called influence matrices. Influence matrices, as introduced in this paper, are a type of sensitivity matrix, which describe how and to which extend various properties of a given load-bearing structure can be influenced by different types of actuation principles. The method of influence matrices is exemplified by a series of studies on different configurations of a truss structure.

Keywords: adaptivity, actuator placement, typology, optimization, finite element method, sensitivity, influence matrices

INTRODUCTION

The cement industry alone causes 5.4% (United Nations Environment Programme, 2019; Kelleter et al., 2020) of the global emissions of greenhouse gases and up to 10% of the total anthropogenic CO₂ emissions (Scrivener et al., 2018). Overall, the building industry accounts for 35% of all global CO₂ emissions, thus being a significant contributor to the ongoing climate change. Furthermore, 35% of the global energy consumption can be attributed to the built environment and 50% of the global resource consumption (UNEP, 2011; Sobek, 2016), leading to an ongoing depletion of vital resources, like sand (Peduzzi, 2014). The global growth of population and the increasing wealth in several parts of the world further intensify this effect (UN, 2019). Therefore, new building technologies and solutions are needed, which allow

for a substantial reduction in emissions and resource consumption. Adaptive load-bearing structures, meaning structures with integrated active elements, i.e., sensors and actuators, have been put forward as a promising approach. The integration of such active elements allows an adaptive structure to monitor its stress state and to react accordingly. In case of rarely occurring, high external loads, the structure may induce forces counteracting those from the external load, respectively change its stiffness distribution to homogenize stresses and strains (Sobek and Teuffel, 2001; Senatore et al., 2018a), induce counter deformations (Sobek et al., 2002; Senatore et al., 2018b; Kelleter et al., 2020), or generate shape changes to establish a more efficient load transfer (Neuhaeuser et al., 2013; Reksowardojo et al., 2019), thus increasing structural performance. Due to this increase in performance, the passive elements of the adaptive structure can be dimensioned for lower, more frequently occurring loads, which reduces the structures' resource consumption and embodied energy while using comparatively little operational energy (Senatore et al., 2018c; Schlegel et al., 2019). While there are early examples of supporting structures with integrated active components (e.g., Domke, 1992), most studies concentrate on the possibilities of active control of the dynamic properties of a given structure (Soong and Manolis, 1987; Reinhorn et al., 1992; Holnicki-Szulc et al., 1998; Issa et al., 2010). The manipulation of quasi-static deflections and internal forces with the declared goal of a resource- and emission-efficient design as formulated in Sobek et al. (2006) and Sobek (2016) is still relatively new. This approach separates adaptive systems into three different states: first, the passive state, in which the structure acts as a conventional system under external load; second, the active state, in which the structure is subjected to actuation; and third, the adaptive state, the superposition of passive and active states. The adaptive state is the desired state of an adaptive system, which has to be established through actuation (active state) from a given passive state. Achieving load-bearing structures with an optimal resource and emission efficiency requires precise knowledge about the optimal amount and position of actuators for a given structure. Teuffel (2004) offers a first approach for truss structures, the *load path management*, which is built upon in Senatore et al. (2019) to optimize the structure in regards to overall energy consumption using the integrated force method (Patnaik, 1973), resulting in a new integral formulation to optimize adaptive structure in regards to overall energy consumption. Reksowardojo et al. (2020) presents a method for stress homogenization through large shape changes, i.e., geometric non-linearity, for trusses. In Wagner et al. (2018) and Böhm et al. (2019), Gramian-based approaches are described, which select actuated elements with the help of a greedy algorithm. Underlying the above mentioned methods are matrices, which contain information on how a given structure can be influenced by the actuation of each individual structural element. These sensitivity matrices, or influence matrices—analogue to the theory of influence lines—are used to determine the optimal actuator placement. In this paper, the reverse approach is tested. Investigating how variations of a load-bearing structure affect the contents of influence matrices generates answers for the overarching question: which topologies

(respectively typologies) of truss and beam structures are most efficient for adaptive structures?

In *Derivation*, a general form of influence matrices is derived, which is further specified in *Influence Matrices of Axial Forces*, for the two actuation types presented in *Derivation*. In *Example*, different configurations of the same basic truss structure are analyzed using the beforehand derived influence matrices, highlighting how individual changes to a structural system correlate with its adaptability. The results are summarized and discussed in *Result Discussion and Generalization*. *Large Scale Prototype High Rise* provides a concise description of an experimental high-rise building, which will be used for further experimental validation of the actuation concepts and the findings of this paper. A conclusion and outlook are given in *Conclusion*.

INFLUENCE MATRICES

Actuation Types

In this paper, two different types of linear actuation are considered (**Figure 1**)—serial actuation (a) and parallel actuation (b). In the case of serial actuation, an actuator is integrated into the load path of the structure, whereas parallel actuation adds an actuator parallel to an existing passive element (Weidner et al., 2018). The actuator force resulting from actuator extension is defined as positive and the actuator force from retraction as negative.

Derivation

For a given adaptive load-bearing structure, with n degrees of freedom and m actuators, the linear system of equations for static equilibrium can be written as

$$Kq = f = f_{\text{ext}} + f_{\text{act}} \quad (1)$$

where $K \in \mathbb{R}^{n \times n}$ is the stiffness matrix, $q \in \mathbb{R}^n$ is the vector of deformation, and $f \in \mathbb{R}^n$ is the force vector—separated into external forces f_{ext} and actuation forces f_{act} . As influence matrices investigate how a given structure reacts to actuation, the external forces f_{ext} can be set to zero. The vector of actuation forces f_{act} is calculated from an input matrix $B \in \mathbb{R}^{n \times m}$, which maps the actuator forces $u \in \mathbb{R}^m$ of the individual actuator elements onto the respective global degrees of freedom as nodal forces

$$f_{\text{act}} = Bu \quad (2)$$

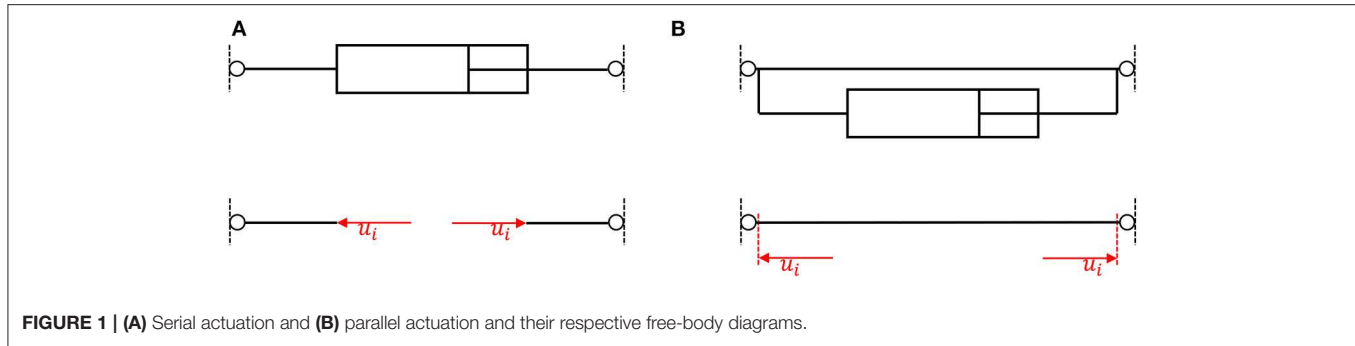
Each column vector $b_i \in \mathbb{R}^n$

$$B = (b_1 \ b_2 \ \dots \ b_i \ \dots \ b_{m-1} \ b_m) \quad (3)$$

thus describes the orientation and the connectivity of each respective actuator element. Any output $y \in \mathbb{R}^p$ of interest can be calculated from the vector of deformations q using

$$y = Cq \quad (4)$$

where $C \in \mathbb{R}^{p \times n}$ is an output matrix that has to be computed according to the desired output y . In case of serial actuation, a



second output matrix, the feedthrough matrix $D \in \mathbb{R}^{p \times m}$, may be required, which takes the actuation forces \mathbf{u} into account:

$$\mathbf{y} = \mathbf{C}\mathbf{q} + \mathbf{D}\mathbf{u} \quad (5)$$

Integrating Equations (1) and (2) into Equation (5) and setting \mathbf{f}_{ext} to zero yields

$$\mathbf{y} = (\mathbf{C}\mathbf{K}^{-1}\mathbf{B} + \mathbf{D})\mathbf{u} \quad (6)$$

To compute the influence of the actuation, each structural element is successively actuated by a unit load (number of actuators m = number of elements), expanding the load vector \mathbf{u} into a matrix:

$$\mathbf{u} = (\mathbf{u}_1, \mathbf{u}_2, \dots, \mathbf{u}_i, \dots, \mathbf{u}_{m-1}, \mathbf{u}_m) = \begin{pmatrix} 1 & 0 & \dots & 0 & 0 \\ 0 & 1 & \dots & 0 & 0 \\ \vdots & \vdots & \ddots & \vdots & \vdots \\ 0 & 0 & \dots & 1 & 0 \\ 0 & 0 & \dots & 0 & 1 \end{pmatrix} = \mathbf{I} \quad (7)$$

with \mathbf{I} being the identity matrix in $\mathbb{R}^{m \times m}$ and \mathbf{u}_i therefore denoting the actuation of the i th element. Substituting the above into Equation (6) provides the equation, with which influence matrices $\mathbf{E} \in \mathbb{R}^{p \times m}$ are calculated:

$$\mathbf{E} = \mathbf{C}\mathbf{K}^{-1}\mathbf{B} + \mathbf{D} \quad (8)$$

Influence matrices can also be used to calculate the required actuation forces \mathbf{u} for any desired (adaptive) state $\mathbf{y}_{\text{adaptive}}$ from a given passive state $\mathbf{y}_{\text{passiv}}$ (cf. Sobek et al., 2006) using

$$\mathbf{y}_{\text{adaptive}} = \mathbf{y}_{\text{passiv}} + \mathbf{y}_{\text{active}} = \mathbf{C}\mathbf{K}^{-1}\mathbf{f}_{\text{ext}} + \mathbf{E}\mathbf{u} \quad (9)$$

and solving for \mathbf{u}

$$\mathbf{u} = \mathbf{E}^+(\mathbf{y}_{\text{adaptive}} - \mathbf{C}\mathbf{K}^{-1}\mathbf{f}_{\text{ext}}) \quad (10)$$

with $(\cdot)^+$ denoting the Moore–Penrose Pseudoinverse (Penrose, 1955).

Influence Matrices of Axial Forces

The influence matrix of axial forces due to parallel linear actuation $\mathbf{E}_{N,p}$,

$$\mathbf{E}_{N,p} = \mathbf{C}_N\mathbf{K}^{-1}\mathbf{B} \quad (11)$$

describes how the axial forces of a given load-bearing structure can be manipulated by parallel linear actuation of each individual element. The output matrix $\mathbf{C}_N \in \mathbb{R}^{m \times m}$ therefore needs to calculate the axial forces from the resulting vector of deformation \mathbf{q} and can be computed as

$$\mathbf{C}_N = (\mathbf{B}\mathbf{K}_{\text{elem}})^T \quad (12)$$

where $\mathbf{K}_{\text{elem}} \in \mathbb{R}^{m \times m}$ is a diagonal matrix, containing the axial stiffness of each element of the load-bearing structure. Accordingly, the influence matrix of axial forces due to serial linear actuation $\mathbf{E}_{N,s}$ computes the equivalent for serial linear actuation:

$$\mathbf{E}_{N,s} = \mathbf{C}_N\mathbf{K}^{-1}\mathbf{B} + \mathbf{D}_N \quad (13)$$

In this case, the additional feedthrough matrix $\mathbf{D}_N \in \mathbb{R}^{m \times m}$ is needed, subtracting the unit load of actuation once from the axial forces in the actuator element, as the axial load of a serial actuator is equivalent to the already applied force couple of nodal loads (cf. Figure 1).

$$\mathbf{D}_N = \begin{pmatrix} -1 & 0 & \dots & 0 & 0 \\ 0 & -1 & \dots & 0 & 0 \\ \vdots & \vdots & \ddots & \vdots & \vdots \\ 0 & 0 & \dots & -1 & 0 \\ 0 & 0 & \dots & 0 & -1 \end{pmatrix} = -\mathbf{I} \quad (14)$$

Thus, the entry $e_{N,ij}$ of the i th row and j th column of the influence matrix of axial forces \mathbf{E}_N depicts the axial force in element i due to actuation of the element j . For truss structures the influence matrix of axial forces due to serial linear actuation $\mathbf{E}_{N,s}$ is equivalent to the negative inverse of the redundancy matrix $\mathbf{R} \in \mathbb{R}^{m \times m}$ described in Ströbel (1996) and Wagner et al. (2018).

$$\mathbf{E}_{N,s} = \mathbf{C}_N\mathbf{K}^{-1}\mathbf{B} + \mathbf{D}_N = -\mathbf{R}^T \quad (15)$$

Further types of influence matrices can be derived from Equation (8), e.g., an influence matrix of deformations, or one of bending moments. Similarly, other actuation types can be examined if their actuation principle can be formulated according to Equation (2).

Example

To showcase the method of influence matrices, different variations of the modular truss structure displayed in **Figure 2** have been investigated. Each module was 1 m wide and high. The structural members were initially assigned an E modulus of 100 MPa and a quadratic cross-section of 0.01 m^2 (cf. **Table 1**). The structures were modeled in ANSYS Mechanical APDL 17.2, using *link180* and *beam188* elements. The computation and analyses of influence matrices were done with MATLAB R2018a.

Statically Determinate Substructure

The resulting influence matrix of axial forces due to serial linear actuation $E_{N,s}$ is depicted in **Figure 2**. The matrix can be divided into three sections: the left section E_{1-5} , which corresponds to the lowest module, a middle matrix E_{6-8} containing only zeros, equating to elements 6–8, and the right part E_{9-14} , which matches the top module. It can further be observed that the ranks of the left (E_{1-5}) and right (E_{9-14}) section each are equal to 1, which corresponds to the degree of static indeterminacy n_s of each substructure, meaning that *one* linearly independent state of axial forces can be induced by serial actuation in the respective modules of the truss. Summing the ranks of each submatrix results in a rank of 2, which is equal to the degree of static indeterminacy n_s of the overall truss structure. Thus, to manipulate *both* states of axial forces, *two* linear serial actuators are needed, with one actuator placed in each statically indeterminate subsystem (cf. Teuffel, 2004; Wagner et al., 2018). Integrating a serial actuator in the statically determinate middle section will not allow any manipulation of forces (only of

displacements and rotations) as the extension or retractions of a linear actuator is not constrained. It is equally not possible to manipulate any axial forces in the top substructure by serial actuation of an element in the bottom one and vice versa. If the goal of the adaptation is the manipulation of axial forces, it might be most efficient to choose one of the diagonals in each subsystem as actuator, as a serial actuation of those elements results in roughly twice the change in axial forces, given the same actuation force (cf. **Figure 2**). This correlates with the increased redundancy of the elements in the given configuration (cf. Equation 15, resp. Wagner et al., 2018). Assuming the linear theory, the resulting axial forces from actuation can be calculated by multiplying the columns of the chosen actuators with the desired actuation force and vectorially summing the results (cf. Equation 9). As stated above, a degree of static indeterminacy n_s of *one* means *one* linearly independent state of axial forces. Adding an additional serial actuator into the top or bottom substructure will not enable a second state of axial forces. However, it allows for the control of an additional degree of freedom (Teuffel, 2004). Additional serial actuators can also be used to compensate the axial forces induced by actuation, thus enabling constraint free deflections and rotations in statically indeterminate structures. For example, serially actuating element 1 and 4 by the same force, but one by extension and one by retraction, will result in an inclination of the upper part of the load-bearing structure, without inducing any axial forces.

TABLE 1 | Overview of the initially chosen structural properties of the example structure.

Module height	Module width	Young's modulus	Cross-sectional area	Moment of inertia
1 m	1 m	100 MPa	0.01 m^2	$8.33\text{e-}6 \text{ m}^4$

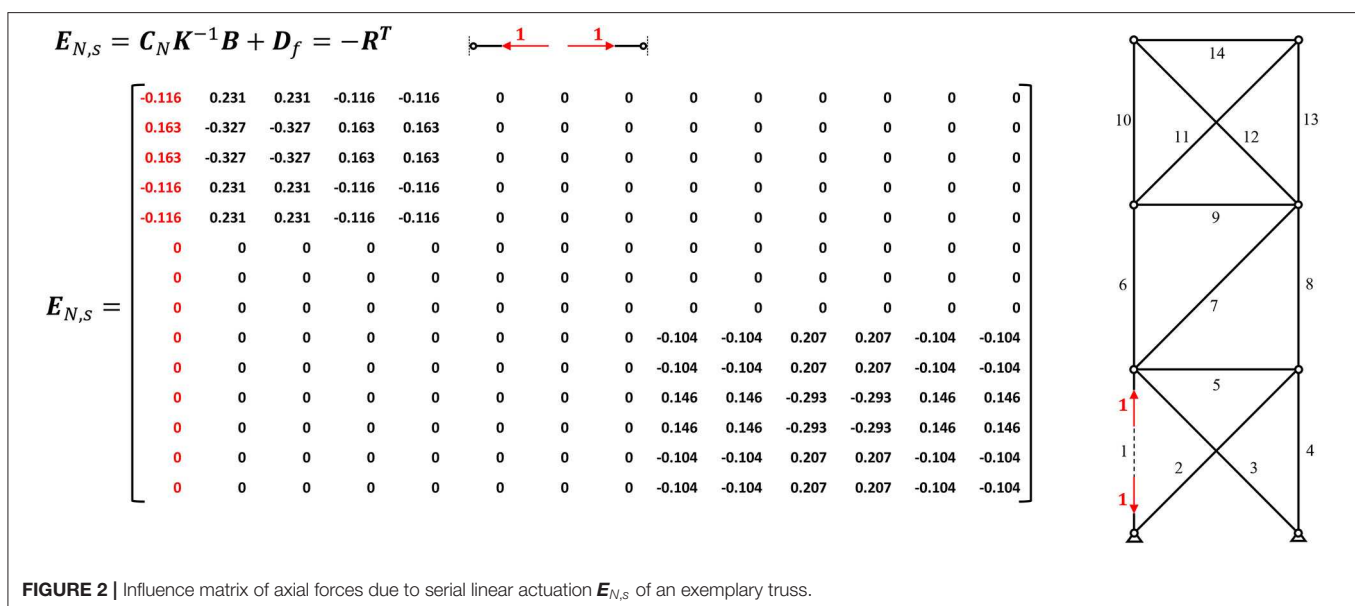
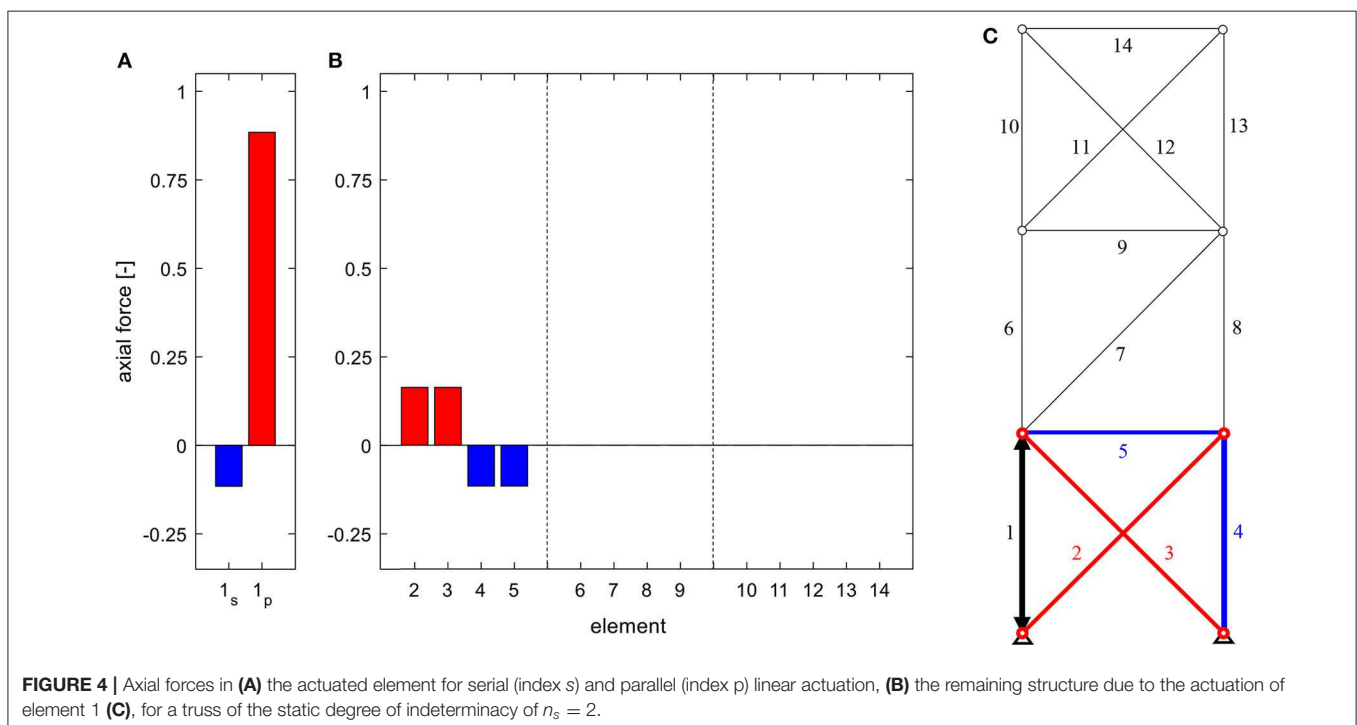
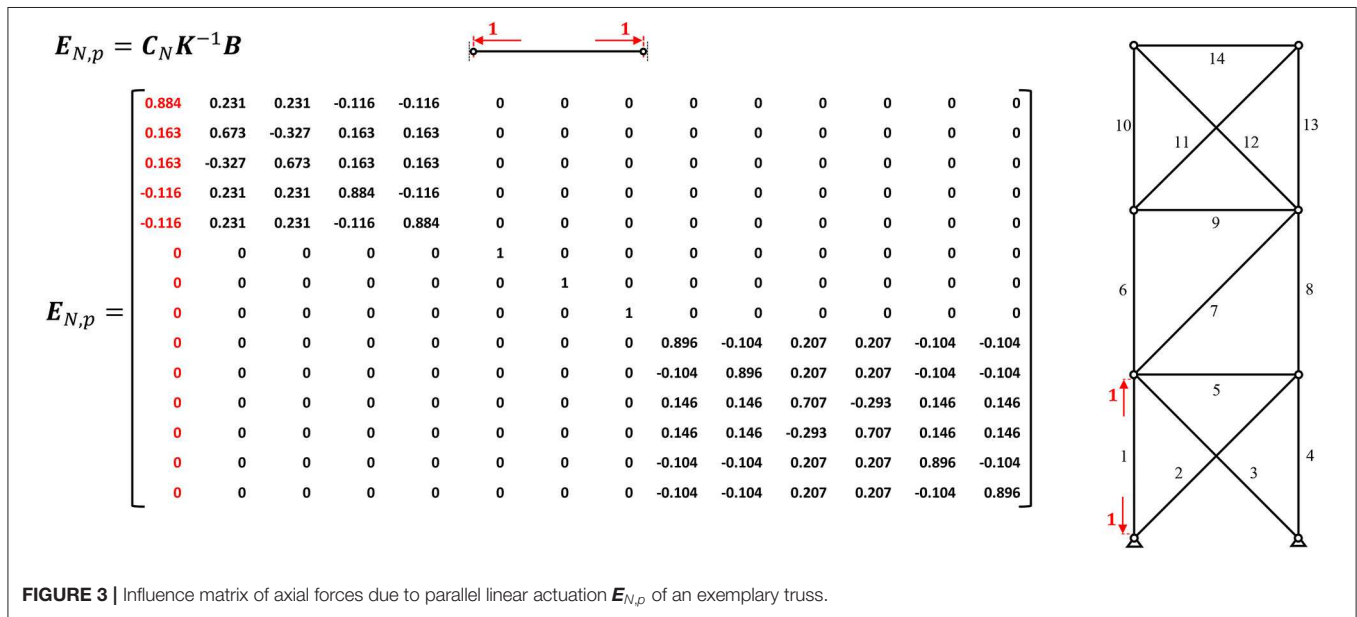
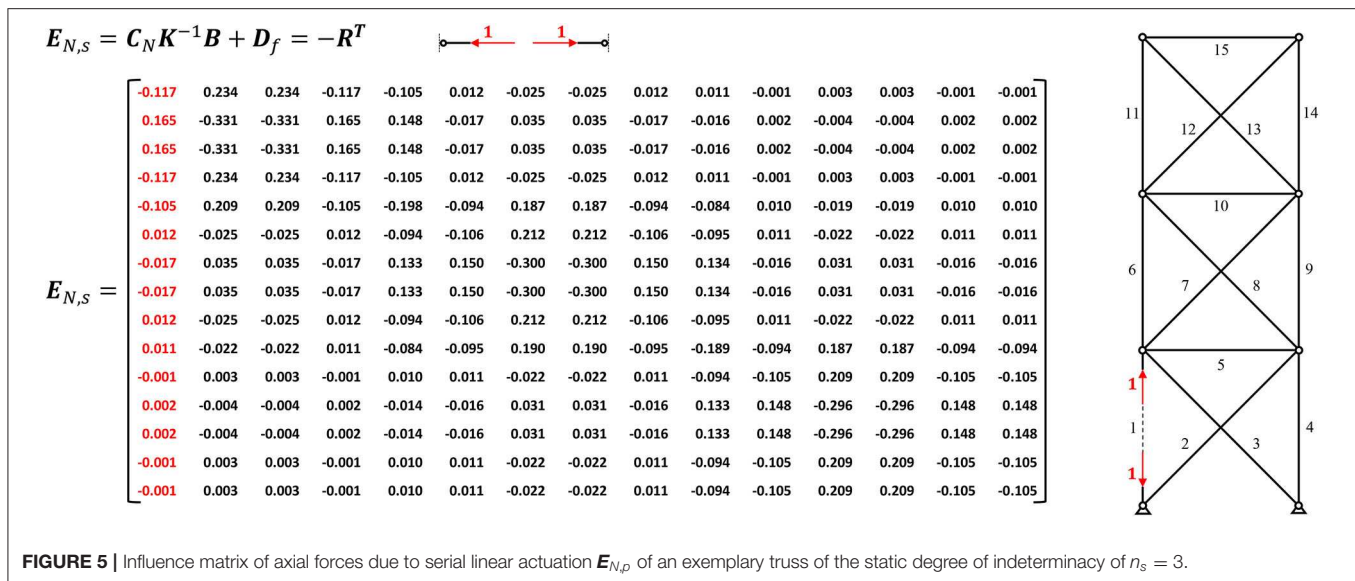


Figure 3 depicts the influence matrix of axial forces due to parallel linear actuation $E_{N,p}$, which can be structured into the same three sections. However, the rank of this matrix is equal to the number of columns, respectively the number of elements. Parallel actuation, thus, always induces a linearly independent state of axial forces, as parallel actuation adds an additional load-bearing element, the actuator, to the existing structure. An extension or retraction of the actuator is primarily constrained by the parallel passive element, resulting in a comparably high axial force in the passive element, with

reversed sign. In case of a statically determinate substructures, the passive element constitutes the only constraint, therefore leading to a complete short circuiting of the actuation force along the passive element (cf. **Figure 3**, columns 6–8). The effect that serial or parallel actuation has on the remaining passive load-bearing structure is identical, assuming identical actuation forces (cf. **Figures 2, 3**). The additional state of axial forces therefore only applies to the parallel actuated element. However, this allows for a (nearly) isolated force manipulation of individual elements, which can be preferable. **Figure 4** graphs





the resulting axial forces of the truss structure for serial and parallel actuation of element 1 (Figure 4C) in the actuated element (Figure 4A) and the remaining load-bearing structure (Figure 4B).

Statically Indeterminate Truss—Homogenous Stiffness Distribution

For the first variation, a second diagonal is added to the middle module (cf. Figure 5), thus changing the substructure's static determinacy from determinate to indeterminate and increasing the overall degree of static indeterminacy n_s to three, which corresponds to the rank of the influence matrix of axial forces due to serial linear actuation $E_{N,s}$ for this system. Changing from statically determinate to indeterminate means constraining the substructure, disabling it from deforming freely and enabling an additional state of axial forces of the middle module, which can be manipulated.

Thus, the separation of substructures (cf. Figure 2) is removed—the influence matrix is filled with non-zero values (see Figure 5). Actuation of an element in a neighboring substructure also affects the axial forces in the adjacent module (cf. Figure 6). However, in the given configuration of the load-bearing structure with homogenous stiffness distribution, the constraint can be compensated along two substructures, leading to negligible axial forces in the top module. Statically determinate substructures, as described in *Statically Determinate Substructure*, completely isolate the influence area of force actuation on chosen elements or substructures.

Statically Indeterminate Truss—Rigid Joints

Next, the pinned joints are exchanged for rigid connections (cf. Figure 7). As a two-dimensional load-bearing structure, the degree of static indeterminacy is increased from 3 to 27, meaning there are now 27 linearly independent states of the internal force variables (combined states of axial forces, shear forces, and bending moments), but only 15 elements available

for linear actuation. The imposed constrained of the rigid joints, however, is very similar to that of the pinned connections in Figure 6, as the chosen quadratic cross-section is comparably flexible (cf. Table 1). The result is an almost identical state of axial forces, although shear forces and bending moments are also manipulated. Changing the stiffness of all elements equally, for example by choosing a material with a different Young's modulus, would have the same effect. Changing the shape of the cross-section to one with the same cross-sectional area, but with a higher area moment of inertia ($I = 5.34e-4 \text{ m}^4$) and therefore increasing the ratio of flexural stiffness to axial stiffness, would constrain the deformations differently, thus resulting in different states of internal variables (cf. Figure 8).

While the overall stiffness of the structure is increased through the rigid joints, the stiffness distribution within the structure is still homogenous. Therefore, as in *Statically Indeterminate Truss—Homogenous Stiffness Distribution*, the resulting constraint forces from an actuation in the bottom module can still be compensated along the lower two modules, disabling the manipulation of forces or bending moments in the top module.

Statically Indeterminate Truss—Varied Stiffness Distribution

Using the truss with pinned joints in *Statically Indeterminate Truss—Homogenous Stiffness Distribution* as base, the stiffness of all diagonals is now increased by a factor of 10 (cf. Table 1).

Increasing the stiffness of the diagonals increases, in turn, the constraint on the actuated column in Figure 9, resulting in an amplified state of axial forces due to actuation in the bottom module. As the diagonals in both upper substructures are also stiffened, their imposed constraint increases as well, in relation to that of the columns and cross girder. This leads to a further distribution of the influence of actuation. However, there are still only three linearly independent states of axial forces, as the static indeterminacy remains at $n_s = 3$. The increased constraint also

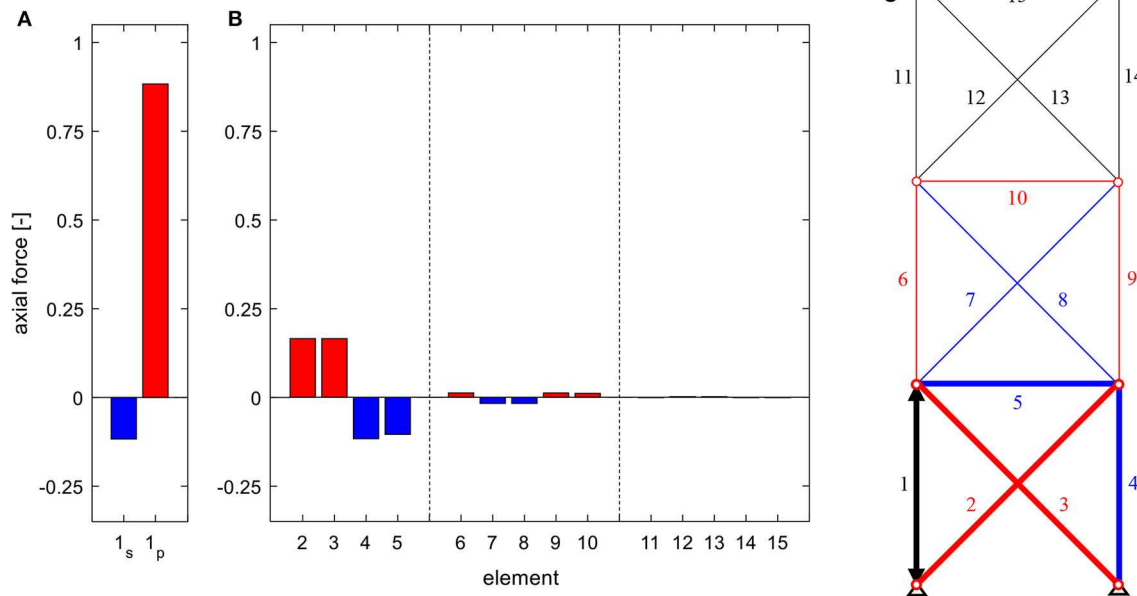


FIGURE 6 | Axial forces in (A) the actuated element for serial (index s) and parallel (index p) linear actuation, (B) the remaining structure due to the actuation of element 1 (C), for a truss of the static degree of indeterminacy of $n_s = 3$.

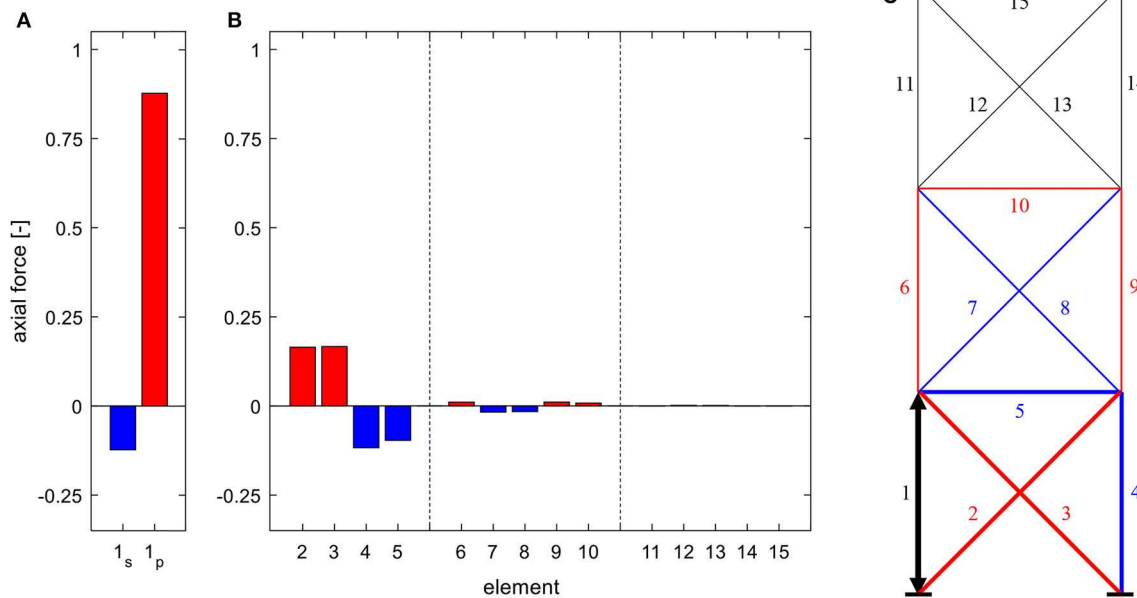
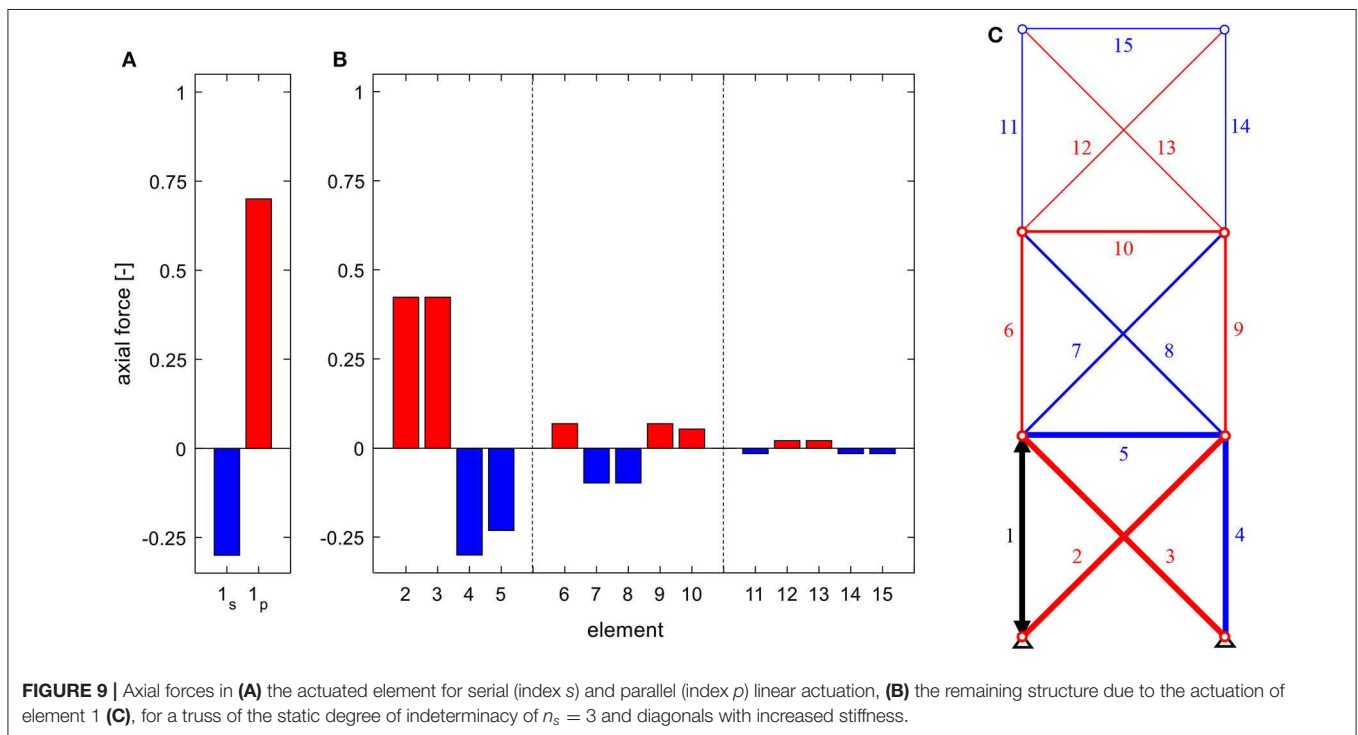
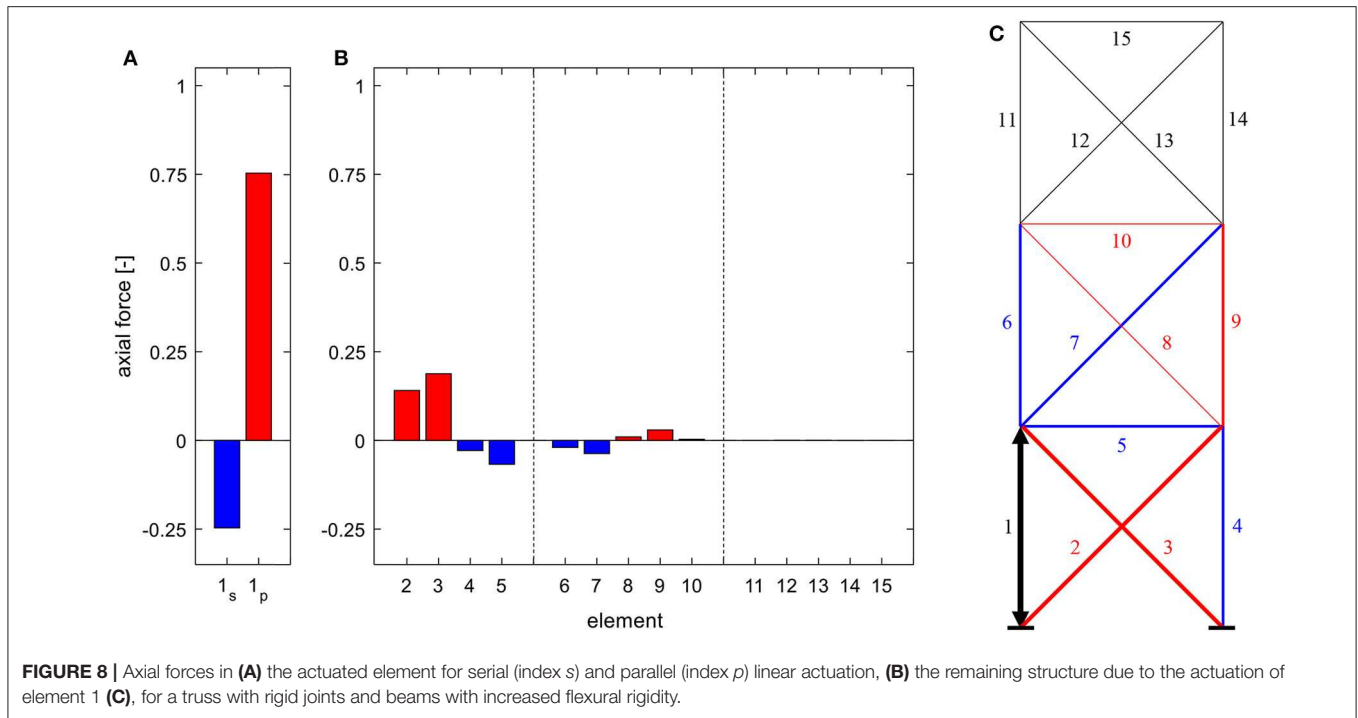


FIGURE 7 | Axial forces in (A) the actuated element for serial (index s) and parallel (index p) linear actuation, (B) the remaining structure due to the actuation of element 1 (C), for a truss with rigid joints.

shows in the resulting axial forces in the actuated element of this variation (cf. **Figure 7A**). In the case of serial actuation, the actuated element experiences a larger compressive force due to the increased constraint described above. In the case of parallel actuation, however, the resulting tensile force is decreased, in comparison to previous system variations. The effect of short

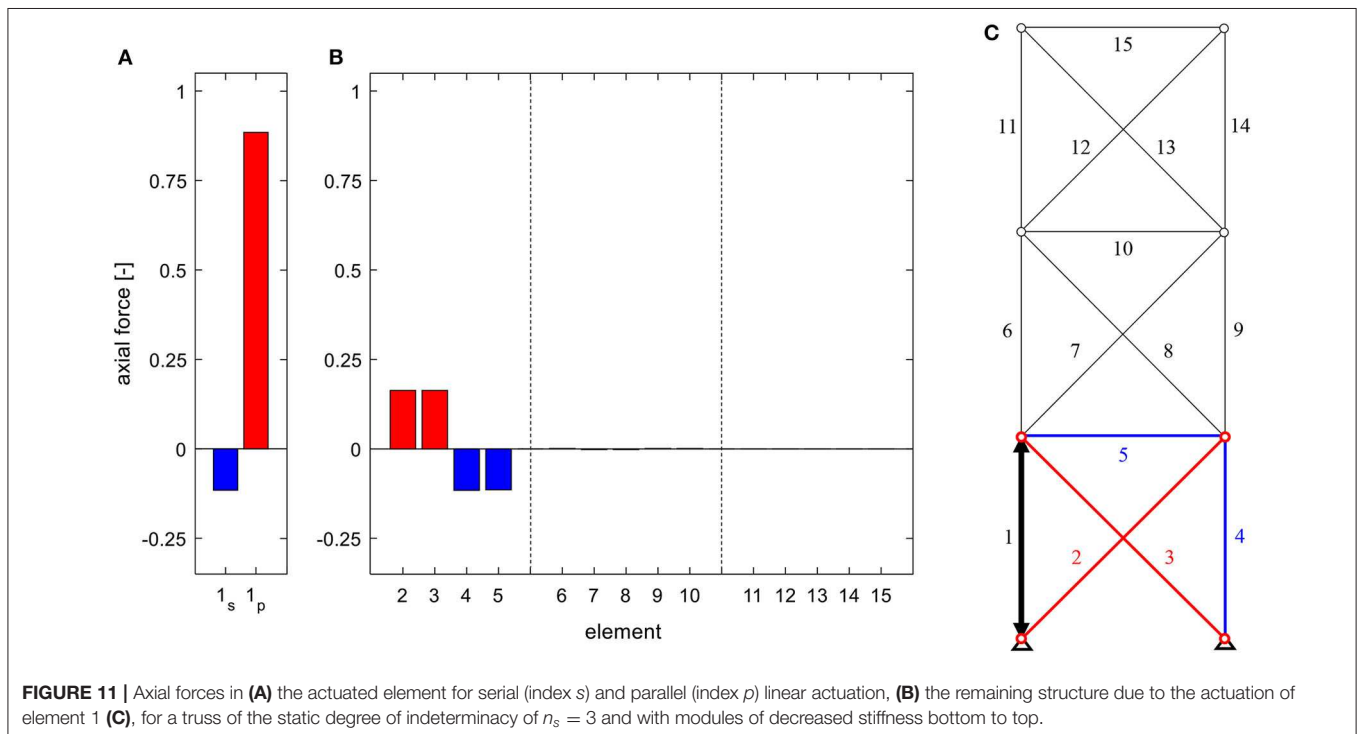
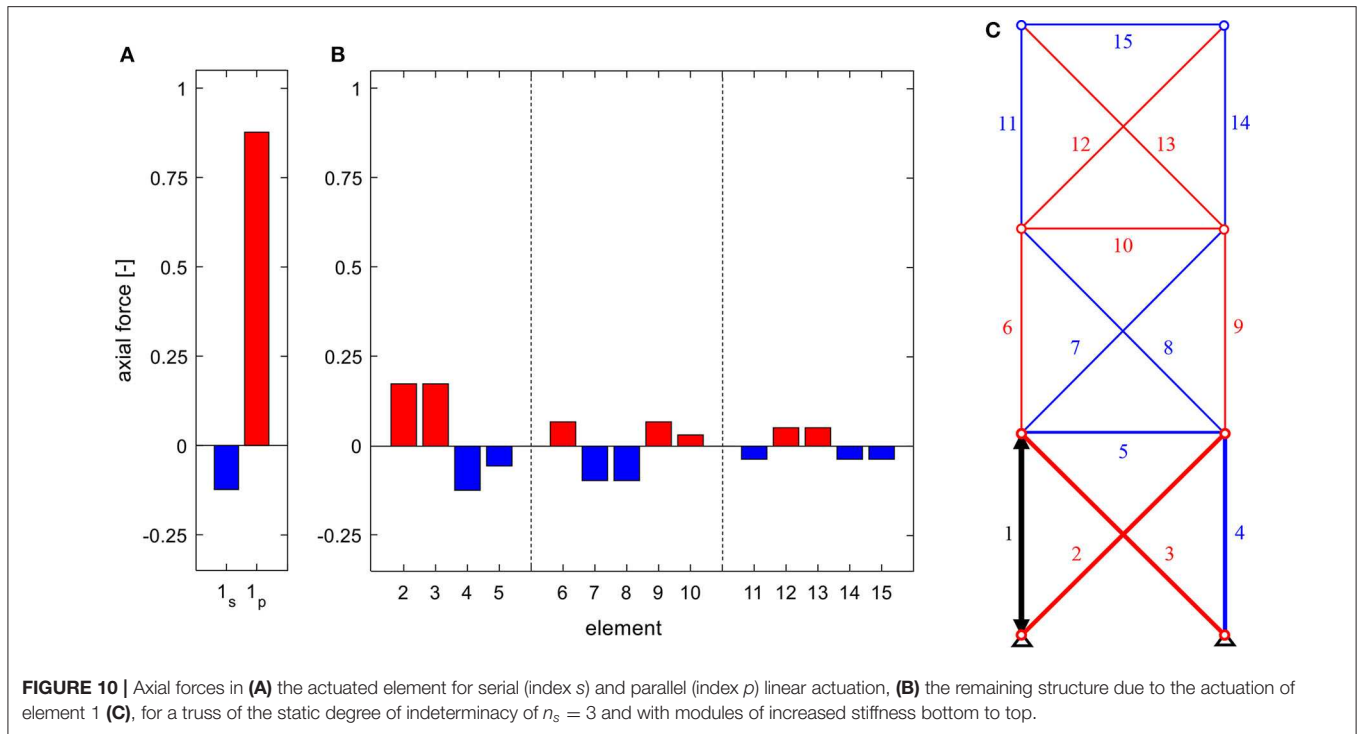
circuiting when using parallel actuation, which was prevalent before, is now less dominant, as the ratio of constraint imposed by the parallel passive element and the remaining connected load-bearing structure shifted toward the latter.

Increasing the stiffness of each module from bottom to top, each by a factor of 10, also expands the influence of actuation



of axial forces (resp. internal force variables) for actuators in the bottom module (cf. **Figure 10**). Although the constraint forces from actuation can still be (partially) compensated along each substructure, the increasing stiffness of each module results in higher axial forces.

Inverting the stiffness distribution, however, encourages a short circuiting of the actuation forces in the bottom module (cf. **Figure 11**). The induced constraint can be fully compensated, similarly to the system in *Statically Determinate Substructure*. The difference being, that, in



this case, the influence of actuation of an element in the top module would still extend to the bottom module (equivalent to configuration in **Figure 10**). Careful placement of comparatively stiff elements or substructures in statically indeterminate systems can thus be used to control the area of influence of actuation forces, to create unilateral expansion

of the influence, and to isolate the influence of actuation to certain substructures.

Module-Overlapping Structural Elements

Lastly, two diagonal bracings of the lower two modules (one of each) are replaced by one overlapping bracing (**Figure 12**).

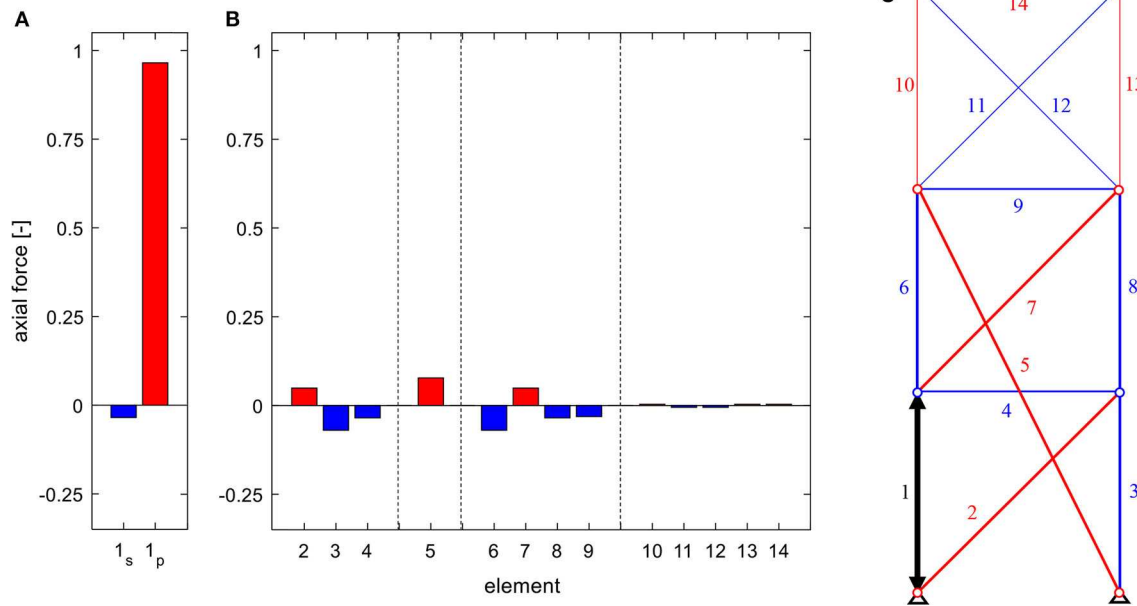


FIGURE 12 | Axial forces in (A) the actuated element for serial (index *s*) and parallel (index *p*) linear actuation, (B) the remaining structure due to the actuation of element 1 (C), for a truss with module-overlapping bracing.

Cross-sections and Young's moduli are reset to the initial values (Table 1). In this configuration, the axial force, which is induced by actuation of element 1, cannot be short circuited inside the bottom module, due to the elimination of the diagonal. The force is distributed into the structure along elements 4, 6, and 7, before it can be short circuited, respectively transferred to the supports through elements 2 and 7, the result being an even distribution of axial forces in both subsystems. Conversely, forces from actuation of element 3 would be primarily short circuited and transferred to the support through element 2, resulting in only negligible forces in the middle module. The overlapping diagonal merges two statically determinate substructures to one statically indeterminate module. This configuration is also comparatively flexible, as the resulting axial forces through linear actuation are relatively small and the force from parallel linear actuation is nearly fully short circuited along the parallel passive element. The top module, again, is connected comparably flexible, resulting in minimal axial forces.

Overlapping elements can therefore be used to connect individual modules, allowing for a further distribution of the influence of actuation. Likewise, removing or adding certain elements from, respectively, to a structure controls the possible load paths, which are activated through actuation.

RESULT DISCUSSION AND GENERALIZATION

Through actuation, an actuator performs a motion, e.g., extension or retraction in case of linear actuators. If this motion can be performed freely, no internal force variables, e.g., axial

forces, can be manipulated; only rigid body motions can be induced. If the motion is constrained, internal force variables, i.e., actuation forces, are activated, leading to deformations (and rigid body motions). The load-bearing structure is statically indeterminate. The degree of static indeterminacy corresponds to the number of linearly independent states of internal force variables, which can be manipulated through actuation. Placing serial actuators into a substructure of an ideal truss, in a number greater its static (in)determinacy, allows for constraint free rigid body motions. In the case of beam structures, it is not necessarily possible to actuate all states by linear actuators alone. The forces and moments induced by actuation have to be transferred to the supports or short circuited inside the load-bearing structure. These load paths—and therefore the sphere of influence—can be controlled by the topology, meaning the configuration of elements, the stiffness distribution, and the static (in)determinacy. For example, strategically placing statically determinate substructures or indeterminate modules with reduced stiffness limits the sphere of influence, while overlapping elements or elements with comparatively higher stiffness can be used to further distribute the influence of actuation. Parallel actuation always generates a linearly independent state of internal force variables, due to the parallel connection of the actuator to the passive element, which also inverts the resulting force in the parallel passive element compared to the actuation force. These basic principles underlie the algorithms listed in *Introduction*. Applying them directly in the design process of adaptive load-bearing structures should therefore result in adaptive topologies (resp. typologies) with increased resource and emission efficiency. Influence matrices can be used for additional analysis, for example

to quantify the effects of actuation, allowing the designer to further optimize their load-bearing structure in regards of its adaptability. The method is presumed most effective in the early conception phase of load-bearing structures and on smaller (sub)systems with a limited number of structural elements.

LARGE-SCALE PROTOTYPE HIGH RISE

The method of influence matrices was developed during the interdisciplinary design process of a large-scale adaptive high-rise prototype, which is currently being realized on an experimental platform at the University of Stuttgart. Upon its completion, it will be the world's largest adaptive structure with a total height of 36 m, consisting of 12 identical floors, which are separated into four similar units (Weidner et al., 2018). Eight hydraulic cylinders are implemented as parallel actuators in the columns of unit 1 and 2 and a further 16 serially incorporated hydraulic actuators in the structure's diagonal bracing (eight in unit 1, and four in each unit 2 and 3) complete the actuator placement. Movements and changes in the stress state of the structure are tracked by a multitude of strain gauges, inertial measurement units (IMUs), and 16 LED tracking sensors. Oscillation of the tower through wind is calculated to reach a deflection of maximum 30 mm at the topmost point. Through actuation, deflections of up to 140 mm become possible. The whole building will be subject of investigation for multiple research projects, throughout its lifetime. One focus of its conception, therefore, lies on the adaptability of the structure and the exchangeability of structural (and façade-) elements. This enables a comfortable dismantling process and also the possibility of removing structural elements and replacing them with elements of different materials or new actuation concepts, which result from the ongoing and upcoming research in the Collaborative Research Centre 1244 *Adaptive Skins and Structures for the Built Environment of Tomorrow*, allowing for large-scale tests of different configuration of the 12-story experimental high-rise building, according to the findings of different methods, such as the influence matrices. The concepts for actuation introduced above have been experimentally tested and validated in a prototype frame and published in Weidner et al. (2019).

CONCLUSION

In this paper, a general method of influence matrices is derived and specified for the case of axial forces for serial and parallel linear actuations. Influence matrices are a type of sensitivity

matrices, which underlie most optimization algorithms that search for the optimal actuator placement in a given load-bearing structure. Influence matrices quantify how a chosen actuation principle affects certain properties of the structure, respectively how changes in the topology of the structure affect the influence of the actuation, i.e., its adaptability. This is exemplified through studies of different configurations of an exemplary truss structure. Such an analysis indicates how the topology of adaptive load-bearing structures should be changed and where to implement which actuation principle in order to increase the adaptability of the structure and thus improve resource and energy efficiency. Future work will include further development and discussion of the presented method of influence matrices (e.g., combination of multiple elements into one actuation unit), the derivation and analyses of further actuation principles, the large-scale experimental validation of the actuation principles and presented findings through tests on the introduced experimental high-rise building, and the conception of adaptive structural typologies based on the presented findings.

DATA AVAILABILITY STATEMENT

The datasets generated for this study are available on request to the corresponding author.

AUTHOR CONTRIBUTIONS

WS initiated the research project, including the planning of the experimental high rise, whose design process SW coordinated. SW and SS also contributed in the planning phase of the high-rise, throughout which, under guidance of WS and LB, the presented method was developed. The first draft was written by SS and SW, with the former focusing on the presented method and the latter on the presentation of the experimental high rise. All authors contributed to the article and approved the submitted version.

FUNDING

The authors gratefully acknowledge the generous funding of this work by the German Research Foundation (DFG–Deutsche Forschungsgemeinschaft) as part of the Collaborative Research Centre 1244 (SFB) Adaptive Skins and Structures for the Built Environment of Tomorrow/project A06 and Z01 (Project number: 279064222).

REFERENCES

- Böhm, M., Wagner, J., Steffen, S., Sobek, W., and Sawodny, O. (2019). "Homogenizability of element utilization in adaptive structures," in 2019 IEEE 15th International Conference on Automation Science and Engineering (CASE) (Vancouver, BC, Canada: IEEE), 1263–1268. doi: 10.1109/COASE.2019.8843066
- Domke, H. (1992). *Aktive Tragwerke*. Leverkusen: Springer. 7–37. doi: 10.1007/978-3-322-85350-9_1
- Holnicki-Szulc, J., Mackiewicz, A., and Kolakowski, P. (1998). Design of adaptive structures for improved load capacity. *AIAA J.* 36, 471–476. doi: 10.2514/2.388
- Issa, J., Mukherjee, R., and Shaw, S. W. (2010). Vibration suppression in structures using cable actuators. *J. Vib. Acoust.* 132:031006. doi: 10.1115/1.4000783

- Kelleter, C., Burghardt, T., Binz, H., Blandini, L., and Sobek, W. (2020). Adaptive concrete beams equipped with integrated fluidic actuators. *Front. Built Environ.* 6:91. doi: 10.3389/fbuil.2020.00091
- Neuhaeuser, S., Weickgenannt, M., Witte, C., Haase, W., Sawodny, O., and Sobek, W. (2013). Stuttgart smartshell—a full scale prototype of an adaptive shell structure. *J. Int. Assoc. Shell Spat. Struct.* 54, 259–270.
- Patnaik, S. (1973). An integrated force method for discrete analysis. *Int. J. Numer. Methods Eng.* 6, 237–251. doi: 10.1002/nme.1620060209
- Peduzzi, P. (2014). *Sand, Rarer Than One Thinks*. Sioux Falls, SD: UNEP Global Environmental Alert Service (GEAP).
- Penrose, R. (1955). A generalized inverse for matrices. *Math. Proc. Camb. Philos. Soc.* 51, 406–413. doi: 10.1017/S0305004100030401
- Reinhorn, A. M., Soong, T. T., Riley, M. A., Wang, Y. P., Aizawa, et al. (1992). *Active Bracing System: A Full Scale Implementation of Active Control*. Buffalo, NY: National Center for Earthquake Research (NCEER).
- Reksowardojo, A. P., Senatore, G., and Smith, I. F. C. (2019). Experimental testing of a small-scale truss beam that adapts to loads through large shape changes. *Front. Built Environ.* 5:93. doi: 10.3389/fbuil.2019.00093
- Reksowardojo, A. P., Senatore, G., and Smith, I. F. C. (2020). Design of structures that adapt to loads through large shape changes. *J. Struct. Eng.* 146:04020068. doi: 10.1061/(ASCE)ST.1943-541X.0002604
- Schlegl, F., Honold, C., Leistner, S., Albrecht, S., Roth, D., Leistner, P., et al. (2019). Integration of LCA in the planning phases of adaptive buildings. *Sustainability* 11:4299. doi: 10.3390/su11164299
- Scrivener, K. L., John, V. M., and Gartner, E. M. (2018). Eco-efficient cements: potential economically viable solutions for a low-CO₂ cement-based materials industry. *Cem. Concr. Res.* 114, 2–26. doi: 10.1016/j.cemconres.2018.03.015
- Senatore, G., Duffour, P., and Winslow, P. (2018a). Energy and cost assessment of adaptive structures: case studies. *J. Struct. Eng.* 144:04018107. doi: 10.1061/(ASCE)ST.1943-541X.0002075
- Senatore, G., Duffour, P., and Winslow, P. (2018b). Exploring the application domain of adaptive structures. *Eng. Struct.* 167, 608–628. doi: 10.1016/j.engstruct.2018.03.057
- Senatore, G., Duffour, P., and Winslow, P. (2019). Synthesis of minimum energy adaptive structures. *Struct. Multidiscip. Optim.* 60, 849–877. doi: 10.1007/s00158-019-02224-8
- Senatore, G., Duffour, P., Winslow, P., and Wise, C. (2018c). Shape control and whole-life energy assessment of an ‘infinitely stiff’ prototype adaptive structure. *Smart Mater. Struct.* 27, 015022. doi: 10.1088/1361-665X/aa8cb8
- Sobek, W. (2016). Ultra-lightweight construction. *Int. J. Space Struct.* 31, 74–80. doi: 10.1177/0266351116643246
- Sobek, W., and Teuffel, P. (2001). “Adaptive systems in architecture and structural engineering,” in *Proceedings of SPIE—The International Society for Optical Engineering*, ed S. C. Liu (Newport Beach, CA), 36–45. doi: 10.1117/12.434141
- Sobek, W., Teuffel, P., Weilandt, A., and Lemaitre, C. (2006). “Adaptive and lightweight,” in *Adaptables 2006: Proceedings of the Joint CIB, Tensinet, IASS international Conference on Adaptability in Design and Construction*, Vol. 2 (Eindhoven: Eindhoven University of Technology), 6.38–6.42.
- Sobek, W., Teuffel, P., and Landauer, A. (2002). *Stuttgarter Träger*. Stuttgart: Inst. Für Leichtbau Entwurf. Konstr. Univ. Stuttg.
- Soong, T. T., and Manolis, G. D. (1987). Active structures. *J. Struct. Eng.* 113, 2290–2302. doi: 10.1061/(ASCE)0733-9445(1987)113:11(2290)
- Ströbel, D. (1996). *Die Anwendung der Ausgleichsrechnung auf Elastomechanische Systeme*. Stuttgart: University of Stuttgart.
- Teuffel, P. (2004). *Entwerfen Adaptiver Strukturen*. Stuttgart: University of Stuttgart. doi: 10.18419/opus-195
- UN (2019). *World Economic Situation and Prospects as of Mid-2019*. 30. New York, NY: United Nations.
- UNEP (2011). *Decoupling Natural Resource Use and Environmental Impacts From Economic Growth*. Nairobi: UNEP.
- United Nations Environment Programme (2019). *The Emissions Gap Report 2019*. Available online at: <https://www.unenvironment.org/resources/emissions-gap-report-2019> (accessed February 13, 2020).
- Wagner, J. L., Gade, J., Heidingsfeld, M., Geiger, F., von Scheven, M., Böhm, M., et al. (2018). On steady-state disturbance compensability for actuator placement in adaptive structures. *Automation* 66, 591–603. doi: 10.1515/auto-2017-0099
- Weidner, S., Kelleter, C., Sternberg, P., Haase, W., Geiger, F., Burghardt, T., et al. (2018). The implementation of adaptive elements into an experimental high-rise building. *Steel Constr.* 11, 109–117. doi: 10.1002/stco.2018.10019
- Weidner, S., Steffen, S., and Sobek, W. (2019). The integration of adaptive elements into high-rise structures. *Int. J. High-Rise Build.* 8, 95–100. doi: 10.21022/IJHRB.2019.8.2.95

Conflict of Interest: The authors declare that the research was conducted in the absence of any commercial or financial relationships that could be construed as a potential conflict of interest.

Copyright © 2020 Steffen, Weidner, Blandini and Sobek. This is an open-access article distributed under the terms of the Creative Commons Attribution License (CC BY). The use, distribution or reproduction in other forums is permitted, provided the original author(s) and the copyright owner(s) are credited and that the original publication in this journal is cited, in accordance with accepted academic practice. No use, distribution or reproduction is permitted which does not comply with these terms.



A General Model for Both Shape Control and Locomotion Control of Tensegrity Systems

Huiying Cai^{1,2}, Meijia Wang¹, Xian Xu^{1*} and Yaozhi Luo¹

¹ Space Structures Research Center, Department of Civil Engineering, Zhejiang University, Hangzhou, China, ² 5th Comprehensive Architectural Design Institutes, Zhejiang Province Institute of Architectural Design and Research, Hangzhou, China

OPEN ACCESS

Edited by:

Gennaro Senatore,
École Polytechnique Fédérale de
Lausanne, Switzerland

Reviewed by:

Fernando Fraternali,
University of Salerno, Italy
Landolf Rhode-Barbarigos,
University of Miami, United States

*Correspondence:

Xian Xu
xian_xu@zju.edu.cn

Specialty section:

This article was submitted to
Computational Methods in Structural
Engineering,
a section of the journal
Frontiers in Built Environment

Received: 27 February 2020

Accepted: 28 May 2020

Published: 30 June 2020

Citation:

Cai H, Wang M, Xu X and Luo Y
(2020) A General Model for Both
Shape Control and Locomotion
Control of Tensegrity Systems.
Front. Built Environ. 6:98.
doi: 10.3389/fbuil.2020.00098

Tensegrity systems composed of tension and compression elements have the potential for use in configurable structures and locomotive robots. In this work, we propose a general mathematical model for controllable tensegrity structures. Additionally, a method combining a genetic algorithm (GA) and dynamic relaxation method (DRM) is developed to solve the model. Our proposed model and method are applied to a typical shape controlled tensegrity and a typical locomotive tensegrity system. Firstly, the shape control of a two-stage tri-prism tensegrity is considered, and a collision-free path with minimum energy consumption is identified by using our approach. Secondly, gait design and path planning of a six-strut tensegrity is considered, and optimal gaits and motion paths are obtained by using our approach. The generality and feasibility of the proposed approach is conceptually verified in these implementations.

Keywords: controllable tensegrity, optimization model, shape control, gait design, path planning

INTRODUCTION

Tensegrity systems are a class of special prestressed pin-jointed bar assembly, composed of compression elements and tension elements. A distinguishing feature of tensegrity structures is that their shape and mechanical properties can be actively controlled by prestressing their structural elements, making them good candidates for structural systems requiring controllable shapes and mechanical properties, such as smart structures (Shea et al., 2002; Fest et al., 2003; Motro, 2003; Al Sabouni-Zawadzka, 2014), deployable structures (Fazli and Abedian, 2011; Veuve et al., 2015; Kan et al., 2018; Oh et al., 2018), tunable metamaterials (Fraternali et al., 2014; Amendola et al., 2018; Liu et al., 2019), and robots (Paul et al., 2006; Mirlitz et al., 2015; Kim et al., 2017; Cera and Agogino, 2018; Park et al., 2019; Wang et al., 2019). The actuators of a controllable tensegrity structure can usually be idealized as active members with variable rest lengths. The main problem to be solved in the control of a tensegrity system given an actuation configuration is determining the actuations (i.e., rest length changes of the active members) required to drive the structural system from its initial state to the target state.

If the actuations are imposed on the structural system very slowly and the structural system remains in static equilibrium throughout the control process, it is deemed a quasi-static system and the control problem can be interpreted as that of finding a static equilibrated path to connect the initial and target states. Most recent studies on shape control of tensegrity structures have treated it as a quasi-static process (Shea et al., 2002; Sultan et al., 2002; Xu et al., 2014). In particular, the prestressable equilibrium manifold of symmetrical prism tensegrity structures can be identified analytically, and then feasible control paths can be determined based on the equilibrium manifold using a search strategy (Sultan et al., 2002; Sultan and Skelton, 2003). For general cases in which the equilibrium manifold cannot easily be determined, an algorithm based on rapidly-exploring random trees has been proposed to find feasible actuation sets for the shape control of tensegrity systems (Xu et al., 2014). Form-finding methods, such as dynamic relaxation method (Fest et al., 2003) and non-linear force method (Xu and Luo, 2009) have been used to track the quasi-static motion of shape controlled tensegrities. Meanwhile, the dynamic effect have to be considered in the studies of locomotive tensegrity systems, due to the stronger actuations and environmental interactions involved in such systems. The potential for using tensegrity structures as locomotive systems has recently attracted considerable attention. A tensegrity swimmer was developed to achieve propulsive performance with closed-loop control (Bliss et al., 2013). Omer et al. (2011) proposed a 2D tensegrity robot to mimic caterpillar locomotion. Böhm and Zimmermann (2013) proposed a vibration-driven mobile tensegrity robot. The DuCTT (Duct Climbing Tetrahedral Tensegrity) with the ability to traverse complex duct systems was presented and demonstrated (Friesen et al., 2014, 2016). Spherical tensegrity robots with potential application in planetary explorers (SunSpiral et al., 2013; Sabelhaus et al., 2015) have been most intensively studied (Khazanov et al., 2013; Kim, 2016; Luo and Liu, 2017; Lu et al., 2019). To track the dynamic motion of locomotive tensegrities, Runge-Kutta method (Rovira and Tur, 2009), multi-body kinematic and dynamic simulation (Lin et al., 2016), and commercial physical engine (Zhao et al., 2017) have been used. Different descriptions and formulations are usually used for the shape control and the locomotion control problems of tensegrity systems, due to the difference in their application scenarios and the difference in the academic background of the researchers. In this paper, both the shape controlled tensegrity systems and the locomotive tensegrity systems will be modeled by the same mathematical formulations and a DRM-based motion tracking algorithm applicable for both quasi-static and dynamic motions will be adopted.

This paper is laid out as follows: section Model for Controllable Tensegrity Systems presents the general mathematical model for controllable tensegrity systems. In section Control Optimization Method, a method incorporating a GA-based optimization scheme with a DRM-based motion tracking algorithm is developed to solve the model. The proposed model and method are implemented in a tensegrity system shape control application in section Shape Control. Section Locomotion Control presents the application of the

proposed model and method to locomotive control in tensegrity systems. Finally, section Discussion concludes the study.

MODEL FOR CONTROLLABLE TENSEGRITY SYSTEMS

For a tensegrity system composed of n nodes and n_c elements, an element's type is given by the element type vector $\mathbf{D} = [D_1, D_2, \dots, D_{n_c}]$ where D_i is defined as:

$$D_i = \begin{cases} 1, & \text{for compression element} \\ 0, & \text{for tension element} \end{cases} \quad (1)$$

For a controllable tensegrity system with n_a ($n_a \leq n_c$) active elements, the locations of the active elements are described by an active element location vector $\mathbf{D}_A = [D_{A1}, D_{A2}, \dots, D_{A n_c}]$, where

$$D_{Ai} = \begin{cases} 1, & \text{for active element} \\ 0, & \text{for passive element} \end{cases} \quad (2)$$

in which “active element” means the element whose length can be actively changed by actuators, and “passive element” means the element whose length cannot be actively changed. The active element location vector satisfies that sum $(\mathbf{D}_A) = n_a$.

The control strategy of a controllable tensegrity system can be described by an actuating function Δ . During a given time period $[t_s, t_f]$, the actuating function of the i^{th} member is defined as $e_i = f_i(t)$, where f_i is a continuous function of time t . Then, the actuating function Δ is written as

$$\Delta = \{e_1, e_2, \dots, e_{n_c}\} \quad (3)$$

where $e_i \in [-e_i^s, e_i^l]$, in which e_i^s and e_i^l are the allowable shortening and elongation for the i^{th} member, respectively. Note that $e_i^s = e_i^l = 0$ for passive members ($D_{Ai} = 0$). The rest length change ranges of the elements can be expressed as $\mathbf{E} = \{[-e_1^s, e_1^l], [-e_2^s, e_2^l], \dots, [-e_{n_c}^s, e_{n_c}^l]\}$. Hence, at any time, the rest length change function of the controllable tensegrity system is required to satisfy the condition that $\Delta \in \mathbf{E}$.

The rest length of members \mathbf{L}_R^t at time t satisfies

$$\mathbf{L}_R^t = \mathbf{L}_R^{t_s} + \Delta^t \quad (4)$$

The internal force F_i^t of the i^{th} member is determined by

$$F_i^t = \frac{E_i A_i (L_{Gi}^t - L_{Ri}^t)}{L_{Ri}^t} \quad (5)$$

where E_i , A_i , L_{Gi}^t , and L_{Ri}^t are the elasticity modulus, cross-sectional area, deformed length, and rest length of the i^{th} member, respectively. Meanwhile, the internal force F_i^t of the i^{th} member is required to be within the strength limitations, i.e.,

$$F_i^l \leq F_i^t \leq F_i^u \quad (6)$$

where F_i^l and F_i^u are the lower bound and upper bound of the strength of the i^{th} member, respectively. Specifically, F_i^l and F_i^u are given by

$$\begin{aligned} F_i^l &= -\min(F_{ci}, F_{bi}) \text{ and } F_i^u = 0, \text{ for } D_i = 1 \\ F_i^l &= 0 \text{ and } F_i^u = F_{ti}, \text{ for } D_i = 0 \end{aligned} \quad (7)$$

where F_{ci} , F_{bi} , and F_{ti} are the compression strength, buckling strength, and tension strength of the i^{th} member, respectively. Having defined $\Omega_f = \left\{ [F_1^l, F_1^u], [F_2^l, F_2^u], \dots, [F_{n_c}^l, F_{n_c}^u] \right\}$, the strength constraint on the members of the controllable tensegrity system can be written as $\mathbf{F}^t \in \Omega_f$.

The equilibrium equation of the tensegrity system at time t is written as

$$\mathbf{A}^t \mathbf{F}^t = \mathbf{F}_e^t \quad (8)$$

where \mathbf{A}^t ($n_r \times n_c$) is the equilibrium matrix, \mathbf{F}_e^t ($n_r \times 1$) is the external nodal load vector, and n_r is the number of degrees of freedom. Hence, the unbalanced nodal force \mathbf{R}^t of the system at time t can be expressed as

$$\mathbf{R}^t = \mathbf{F}_e^t - \mathbf{A}^t \mathbf{F}^t \quad (9)$$

Then, according to Newton's second law:

$$\mathbf{R}^t = \mathbf{M} \ddot{\mathbf{U}}^t + \mathbf{C} \dot{\mathbf{U}}^t \quad (10)$$

where \mathbf{M} is the nodal mass matrix of the system, \mathbf{C} is the viscous damping of the system, and \mathbf{U} is the matrix of nodal coordinates of the system.

Substituting Equation (9) into Equation (10) yields

$$\mathbf{F}_e^t - \mathbf{A}^t \mathbf{F}^t = \mathbf{M} \ddot{\mathbf{U}}^t + \mathbf{C} \dot{\mathbf{U}}^t \quad (11)$$

The control objective of the system is case-dependent. It could be a special requirement of the nodal displacement, locomotion distance, or the energy cost to generate the required shape adjustment or motion. Since it is usually a function of the control strategy, it can be conceptually represented as $G(\Delta)$.

Based on the above definitions of the control strategy, constraints, and control objective, a general model for the controllable tensegrity system can be written as

$$\begin{cases} \text{find } \Delta \\ \min G(\Delta) \\ \text{s.t.} \\ \mathbf{F}_e^t - \mathbf{A}^t \mathbf{F}^t = \mathbf{M} \ddot{\mathbf{U}}^t + \mathbf{C} \dot{\mathbf{U}}^t \\ \Delta \in \mathbf{E} \\ \mathbf{U} \in \Omega_s \\ \mathbf{F}^t \in \Omega_f \\ C(\Delta) \end{cases} \quad (12)$$

where Ω_s represents free space in an environment where the controllable system does not interfere with boundaries or obstacles, and $C(\Delta)$ represents the additional constraints on the system in specific situations.

CONTROL OPTIMIZATION METHOD

Motion Tracking

An incremental procedure based on the dynamic relaxation method (Xu and Luo, 2013) is adopted to simulate the motion of the controllable tensegrity system under a given actuation. The duration of the actuation is discretized by a given time increment of Δt . The state of the system is tracked by a DRM procedure that starts from a known state at time t and ends with a new state at time $t + \Delta t$ after a time increment of Δt . Step by step, the motion of the system under the given actuation is discretely depicted. Details of the DRM-based motion tracking procedure are given in the following paragraph.

Under a given actuation Δ^t , the residual force \mathbf{R}^t of the system is determined by Equation (9). According to Equation (10), for a node j in the direction x at time t , we have

$$R_{jx}^t = M_j \ddot{u}_{jx}^t + C_{jx} \dot{u}_{jx}^t \quad (13)$$

where R_{jx}^t represents the residual force of node j in the direction x , and is a component of \mathbf{R}^t ; M_j represents the equivalent nodal mass of node j ; and C_{jx} represents the damping of node j in the direction x . The nodal acceleration can be approximated in centered finite difference form as

$$\ddot{u}_{jx}^t = \frac{\dot{u}_{jx}^{t+\Delta t/2} - \dot{u}_{jx}^{t-\Delta t/2}}{\Delta t} \quad (14)$$

Substituting Equation (14) into Equation (13), the nodal velocity at $t + \Delta t/2$ can be expressed as

$$\dot{u}_{jx}^{t+\Delta t/2} = \dot{u}_{jx}^{t-\Delta t/2} + \frac{\Delta t}{M_j} (R_{jx}^t - C_{jx} \dot{u}_{jx}^t) \quad (15)$$

Then, the nodal coordinate at $t + \Delta t$ can be expressed as

$$u_{jx}^{t+\Delta t} = u_{jx}^{\Delta t} + \dot{u}_{jx}^{t+\Delta t/2} \Delta t \quad (16)$$

By setting $t = t + \Delta t$, the actuation Δ^t , equilibrium matrix \mathbf{A}^t , internal force \mathbf{F}^t , external force \mathbf{F}_e^t , and residual force \mathbf{R}^t can be updated accordingly. The above central difference process repeats until $t = t_f$. The numerical stability of this central difference process is guaranteed by using a time increment Δt no larger than $\sqrt{\frac{2M}{S}}$, where S is the highest direct stiffness of any node relative to adjacent nodes (Barnes, 1999). For quasi-static problems, the motion tracking can be interpreted as a series of form-finding processes (Xu and Luo, 2013). In each form-finding process, a sub-iteration scheme is implemented whereby each time step is iterated so that convergence is achieved for each time step (Senatore and Piker, 2015). Fictitious values for mass, stiffness, and damping are used to improve the performance of the algorithm for convergence to the static solution (Zhang et al., 2006). In particular, a technique called "kinetic damping" is usually adopted to expedite the convergence of algorithm (Barnes, 1999; Zhang et al., 2006). Note that the real value for stiffness should be substituted

into the each form-found system to evaluate whether the stress and stability limits of the structural elements are met. For dynamic problems, real values for mass, stiffness, and damping are used by the algorithm. The effectiveness of it in dealing with dynamic problems has been demonstrated by a similar procedure called “finite particle method” (Yu and Luo, 2009; Yu et al., 2011). Note that a DRM-based scheme for both quasi-static analysis and dynamic analysis also has been proposed by Senatore and Piker (2015).

An internal collision-detecting strategy proposed in the literature (Xu et al., 2014) is used here to check whether there is internal collision between any pair of elements. This must be avoided, since any internal collision may cause the moving system to become stuck. As a result, the motion tracking algorithm stops if an internal collision is detected, and the path and corresponding actuation are deemed infeasible. On the other hand, collision between the structural system and its environment is allowed and must be accounted for. The penalty

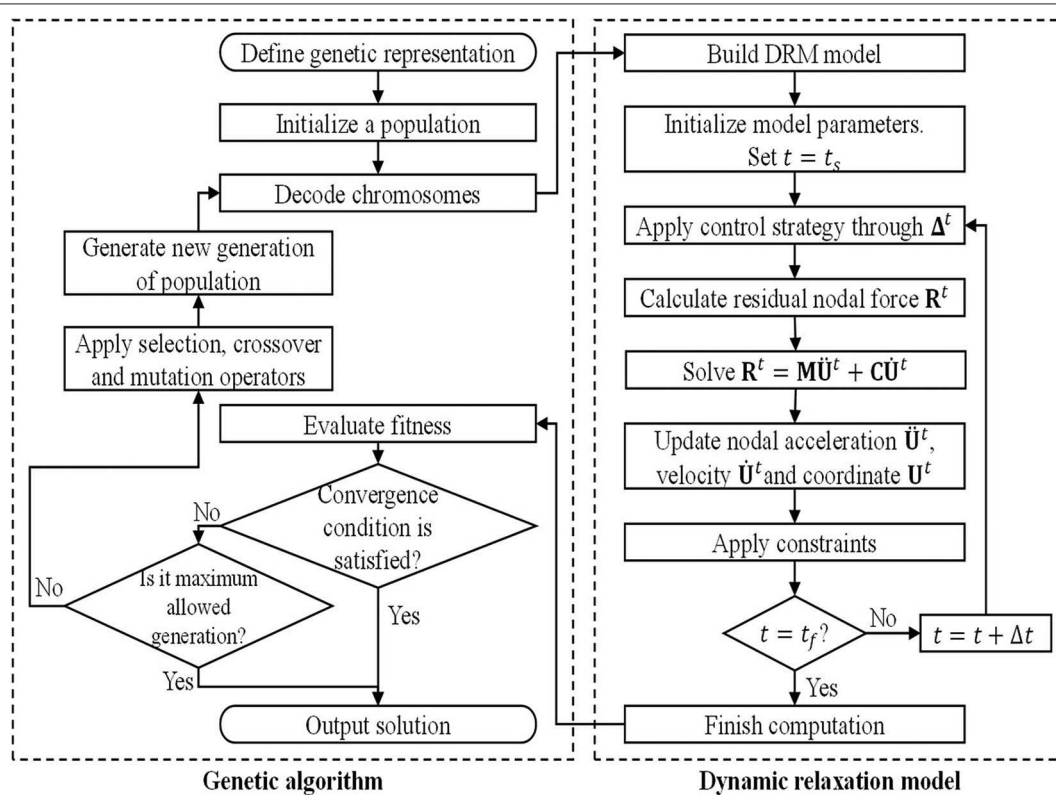


FIGURE 1 | Flowchart of the solving method.

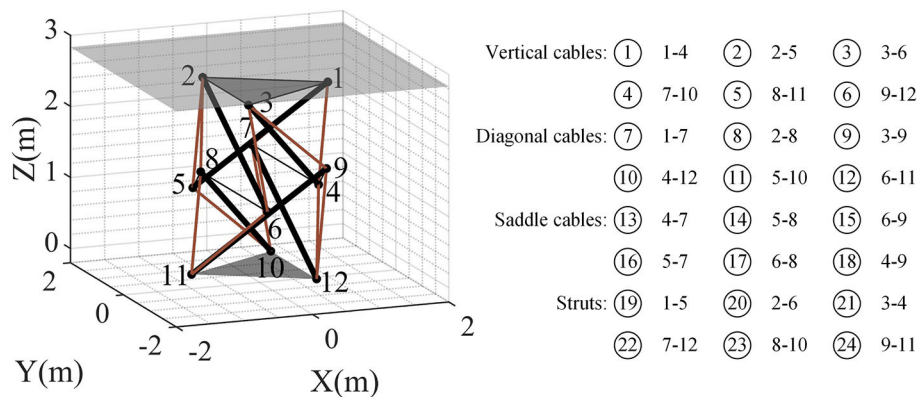


FIGURE 2 | Shape-controlled double-layered tri-prism tensegrity structure.

function method (Oden and Kikuchi, 1982; Papadopoulos and Taylor, 1992) is used to consider the interaction between the structural system and its environment. An obstacle in the environment is assumed to be a series of surfaces covered with springs, and the nodes of the tensegrity structure are allowed to penetrate the surface. The normal contact force F_n between the node and the surface is evaluated by

$$F_n = k_n \delta \quad (17)$$

where δ is the penetration depth; and k_n is the virtual normal stiffness of the surface. The friction force F_f between the node and the surface is determined by

$$F_f = \mu F_n \quad (18)$$

where μ is the friction coefficient.

Optimization Algorithm

To find a control strategy that minimizes the given objective, an optimization algorithm is required. The control problem modeled by Equation (12) is essentially a problem of combinatorial optimization, and the search domain is usually very large. Direct search algorithms such as evolutionary algorithms, simulated annealing algorithms, and genetic algorithms are considered suitable for this problem. Without loss of generality, a genetic algorithm is adopted here.

Solution Flowchart

Combining the DRM-based motion tracking method and GA-based optimization algorithm, the flowchart of the algorithm is as shown in **Figure 1**. The main steps of the algorithm are as follows:

- (1) Define the genetic representation and the fitness function; initialize a population.
- (2) Decode the chromosomes.
- (3) For each individual, build a numerical model of the corresponding tensegrity system for DRM; initialize the parameters of the numerical tensegrity model, and set $t = t_s$; perform Step (4) to Step (6).
- (4) Apply a control strategy to the numerical tensegrity model through the actuating function Δ^t .
- (5) Calculate the residual nodal force \mathbf{R}^t ; solve Equation (11) by the central difference method; update the nodal acceleration $\ddot{\mathbf{U}}^t$, nodal velocity $\dot{\mathbf{U}}^t$, and nodal coordinate \mathbf{U}^t ; apply constraints.
- (6) If $t = t_f$, go to Step (7); otherwise, set $t = t + \Delta t$, and go to Step (4).
- (7) Evaluate the fitness of the population. If the population satisfies the convergence condition or the number of generations reaches the maximum permissible, go to Step (9); otherwise, go to Step (8).
- (8) Apply the selection, crossover, and mutation operators, and create a new generation. Then, go to Step (2).
- (9) Output the solutions.

TABLE 1 | Nodal coordinates of the double-layered tri-prism tensegrity system.

Nodes	Initial location			Target location		
	x (m)	y (m)	z (m)	x (m)	y (m)	z (m)
1	1.000	0.000	2.534	2.248	−0.379	1.392
2	−0.500	0.866	2.534	2.244	1.164	2.178
3	−0.500	−0.866	2.534	1.079	−0.037	2.624
4	0.966	0.259	1.034	0.596	0.143	0.300
5	−0.707	0.707	1.034	0.200	0.577	0.645
6	−0.259	−0.966	1.034	0.402	−0.216	1.570
7	0.259	0.966	1.500	0.484	1.470	0.452
8	−0.966	−0.259	1.500	−0.419	−0.255	1.887
9	0.707	−0.707	1.500	1.128	−0.066	1.065
10	0.500	0.866	0.000	0.500	0.866	0.000
11	−1.000	0.000	0.000	−1.000	0.000	0.000
12	0.500	−0.866	0.000	0.500	−0.866	0.000

SHAPE CONTROL

Shape-Controlled Tensegrity System

The feasibility of the proposed model and method in solving tensegrity system shape control problems is tested in a double-layered tri-prism tensegrity structure, which is used as a typical example of a shape-controlled tensegrity system in a previous study (Xu et al., 2014). As shown in **Figure 2**, the shape-controlled tensegrity consists of 12 nodes, 6 compression members, and 18 tension members. The initial locations and target locations of the nodes are given in **Table 1**. The tension members comprise six vertical cables, six diagonal cables, and six saddle cables. The connectivities of the elements are also shown in **Figure 2**. The triangle bottom and top of the tensegrity structure are assumed to be rigid, and the three bottom nodes is fixed to the ground. There is a ceiling at $z = 2.830$ m in the space.

Properties of the members used for the shape-controlled tensegrity structure are given in **Table 2**. A fictitious nodal mass of 1.00 is assumed because the dynamics of the system was not considered in this shape control problem. A linear stiffness of 2×10^5 N/m for struts and a linear stiffness of 200 N/m for cables are assumed. The “kinetic damping” is used to expedite the convergence of the DRM. The GA’s parameters are set as follows: The population size is 50; the selection type is stochastic universal sampling; the crossover type is two-point; the crossover probability is 1; the mutation probability is 0.7 divided by bits of coding; the maximum number of generations is 200. The algorithm stops when the number of generations reach the maximum number specified.

Vertical and diagonal cables are used as active elements whose rest lengths can actively change in the ranges of 0.40–3.20 m and 0.05–4.00 m, respectively. The control strategy represented by the actuating function is simplified using the following approach: The actuating function for an active element is divided into a series of actuating steps; in each step the rest length of the active element is assumed to be linearly changed. Given the initial rest

TABLE 2 | Properties of members of the double-layered tri-prism tensegrity system.

Type of members	Rest length (m)	Mass (kg)	Linear stiffness (N/m)	Prestress (N)	Compressive strength (N)	Tensile strength (N)
Struts	2.380	1	2×10^5	-100.12	-400	400
Vertical cables	1.523	0	200	38.90	0	400
Diagonal cables	1.598	0	200	38.27	0	400
Saddle cables	1.103	0	200	58.67	0	400

length, initial time, end time, and the rest length at the end of each step, the linear actuating function of the element in each step is easily determined. Denoting the rest length change of the element i in the k^{th} step as e_{ik} , the actuating function of an element with q steps can be expressed as $\mathbf{e}_i (e_{i1}, e_{i2}, \dots, e_{iq})$. Further assuming that all the active elements possess the same division of actuating steps, i.e., all have q steps and the start time and end time of each step are the same for all active elements, the actuating function of the system can be expressed as $\Delta\{\mathbf{e}_1, \mathbf{e}_2, \dots, \mathbf{e}_{nc}\}$.

Path Optimization

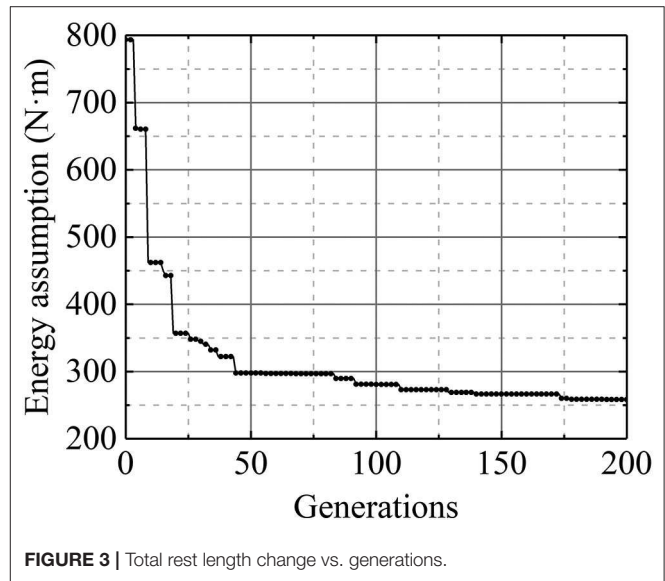
The requirement to be collision-free is considered as an additional constraint, expressed as $\mathbf{S} \in \Omega_c$, in which \mathbf{S} represents the state of the system and Ω_c represents the states without internal collision. The target state of the control is imposed as a further constraint that $\mathbf{U}^f = \mathbf{U}_{\text{target}}$. The target state, i.e., the target location of nodes, is given in **Table 1**. This corresponds to change the center of the top triangle of the double-layered tensegrity from the initial position (0.000, 0.000, and 2.534) to (1.857, 0.249, and 2.065). The energy cost of the control strategy is used as the objective which can be expressed as:

$$G(\Delta) = \sum_{t=t_s}^{t_f} \sum_{i=1}^{n_c} \left| \frac{1}{2} (F_i^t + F_i^{t-\Delta t})(e_i^t - e_i^{t-\Delta t}) \right| \quad (19)$$

where n_c is the number of elements; F_i^t and $F_i^{t-\Delta t}$ are the internal forces of the i^{th} element at times t and $t-\Delta t$, respectively; and e_i^t and $e_i^{t-\Delta t}$ are the rest length changes of the i^{th} element at times t and $t-\Delta t$, respectively. The control model is rewritten as

$$\left\{ \begin{array}{l} \text{find } \Delta \\ \min G(\Delta) = \sum_{t=t_s}^{t_f} \sum_{i=1}^{n_c} \left| \frac{1}{2} (F_i^t + F_i^{t-\Delta t})(e_i^t - e_i^{t-\Delta t}) \right| \\ \text{s.t.} \\ \mathbf{F}_e^t - \mathbf{A}^t \mathbf{F}^t = \mathbf{M} \ddot{\mathbf{U}}^t + \mathbf{C} \dot{\mathbf{U}}^t \\ \Delta \in \mathbf{E} \\ \mathbf{U} \in \Omega_s \\ \mathbf{F}^t \in \Omega_f \\ \mathbf{S} \in \Omega_c \\ \mathbf{U}^f = \mathbf{U}_{\text{target}} \end{array} \right. \quad (20)$$

The reciprocal of the objective, i.e., $1/G(\Delta)$, is selected as the fitness for the GA. The number of actuating steps is assumed to be 2, i.e., $q = 2$. The computation is carried out on a personal computer with a Intel Core i7-4790k CPU @ 4.0

**FIGURE 3** | Total rest length change vs. generations.

GHz and 16 GB RAM. It has taken 293 min to carry out the 200-generation revolution. It is observed that the total energy assumption decreases rapidly in the first 46 generations and then converges slowly on 258.17 N·m (**Figure 3**). The optimal control strategy, corresponding to the minimum energy cost, is shown in **Table 3**, and the equilibrium configuration at the end of each actuating step of the optimal control strategy is shown in **Figure 4**. The motion trajectory of the center of upper triangle during the control is shown in **Figure 5**, in which the thick blue line represents the optimal path generated by the optimal control strategy, and the thin red lines represent 10 feasible paths generated by 10 feasible control strategies found in the evolution process. It is observed that the motion path generated by the optimal control strategy is much shorter than those generated by the unoptimized control strategies.

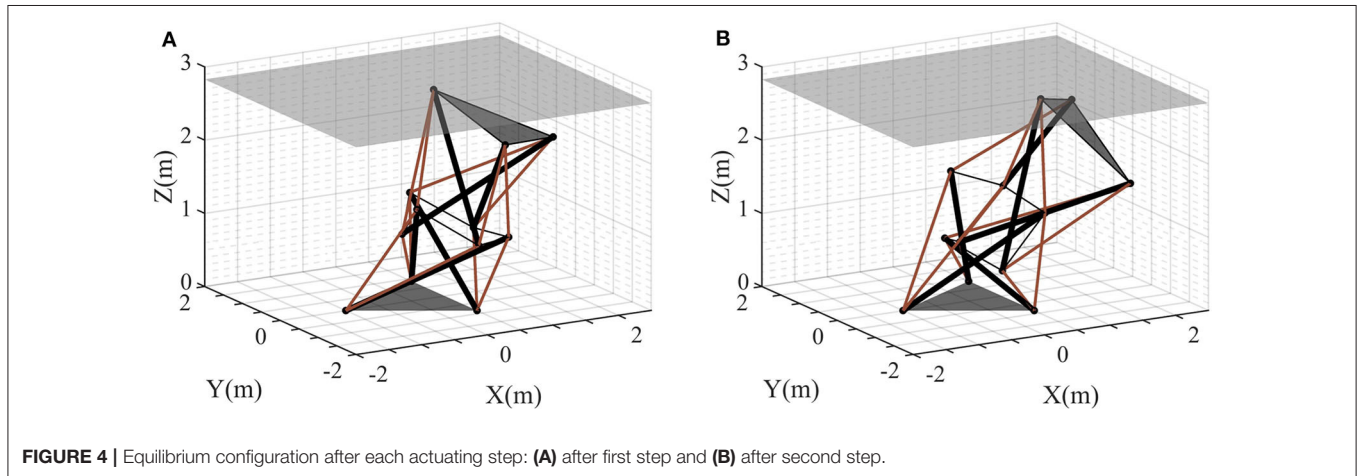
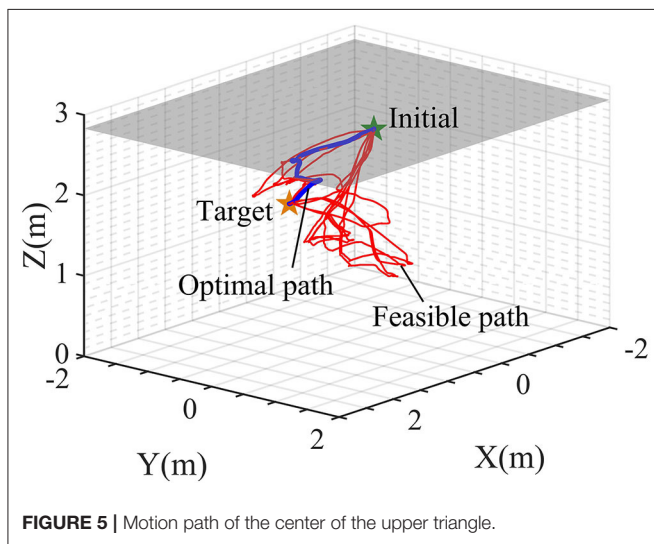
LOCOMOTION CONTROL

Locomotive Tensegrity System

The application of the proposed model and method to locomotion control in tensegrity systems is tested in a six-strut locomotive tensegrity structure. As shown in **Figure 6**, the tensegrity system comprises 12 nodes, 6 compression elements, and 24 tension elements. The connectivities and numbers of the

TABLE 3 | Optimal control strategy for the double-layered tri-prism tensegrity structure.

Actuating steps	Rest length change in active elements (m)											
	1	2	3	4	5	6	7	8	9	10	11	12
Step 1	0.195	0.519	−0.034	−0.270	0.323	−0.512	0.688	0.576	0.085	0.282	−0.803	0.616
Step 2	0.696	1.277	−0.104	−0.793	0.581	0.122	1.317	1.624	0.151	−0.864	−1.344	0.707

**FIGURE 4** | Equilibrium configuration after each actuating step: (A) after first step and (B) after second step.**FIGURE 5** | Motion path of the center of the upper triangle.

elements are also shown in **Figure 6**. The 24 tension elements generate a pattern of 20 triangles on the outer surface of the structure. Eight of the surface triangles, each of which is closed by elements, are called closed triangles (TC). The other triangles are called opened triangles (TO) because each has only two tension elements and one edge of the triangle is open. For instance, as shown in **Figure 6**, the triangle with nodes 3, 7, and 12 is a TC, and the triangle with nodes 3, 11, and 12 is a TO. In the ideal state without external load and gravity, the compression elements and the tension elements have the same geometrical

length. As a result, in the ideal state all the TCs and TOs are identical.

The six compression elements are used as active elements, with an actuating range of $[-5, 5]$ cm. The actuating speed is assumed to be 10 mm/s. The rest lengths of elements at the initial state and the mechanical properties of the elements are as shown in **Table 4**. The initial state of the system is obtained by applying gravity to the ideal state. A damping coefficient of 0.01 is assumed for the elements. Environmental parameters are set as follows: A stiffness of 1,000 N/m, and a friction coefficient of 0.5 are assumed for the ground; the gravitational acceleration is -9.8 m/s^2 .

Gait Design

The gait of the locomotive tensegrity structure is designed to satisfy the conditions that (1) the system acquires a certain amount of motion after the gait; and (2) the rest lengths of active elements are not changed before and after the gait, i.e.,

$$\Delta^{t_f} = \Delta^{t_s} \quad (21)$$

The motion of the system can be expressed by the displacement of the mass center as $\Delta u_c^t = \|\mathbf{u}_c^t - \mathbf{u}_c^{t_s}\|$, in which $\mathbf{u}_c = [u_{cx}, u_{cy}, u_{cz}]$ is the coordinate of the mass center.

Regarding the symmetry of the tensegrity system, there are two basic stand states in the locomotive system: the TC state and the TO state. As indicated by the names, the tensegrity structure stands on the ground with a TC in the TC state, and with a TO in the TO state.

There are two typical types of gaits for the six-strut locomotive tensegrity system, namely crawling gaits, and rolling gaits (Li et al., 2017). It can be easily recognized that rolling gaits usually generate a larger motion than crawling gaits. To obtain rolling gaits rather than crawling gaits, the objective function for gait design is defined to maximize the horizontal motion of the mass center of the system, i.e.,

$$G(\Delta) = \frac{1}{\Delta u_{cxy}^{t_f} + 1}, \Delta u_{cxy}^{t_f} = \sqrt{(u_{cx}^{t_f} - u_{cx}^{t_s})^2 + (u_{cy}^{t_f} - u_{cy}^{t_s})^2} \quad (22)$$

where $\Delta u_{cxy}^{t_f}$ is the horizontal motion distance of the mass center at time t_f ; $u_{cx}^{t_s}$ and $u_{cy}^{t_s}$ are the x and y coordinates of the mass center at time t_s ; and $u_{cx}^{t_f}$ and $u_{cy}^{t_f}$ are the x and y coordinates of the mass center at time t_f . An additional constraint on the number of active elements used in the gait is adopted to impose control on the number of active elements used in the motion. The additional constraint is written as

$$n_a = N_a \quad (23)$$

where n_a is the number of active elements used in the gait, and N_a is an integer constant no larger than 6, specified by the designer.

Substituting the above objective in Equation (22) and additional constraints Equations (21) and (23) into Equation

(12), an optimization model for the gait design can be obtained:

$$\begin{cases} \text{find } \Delta \\ \min G(\Delta) = \frac{1}{\Delta u_{cxy}^{t_f} + 1} \\ \text{s.t.} \\ \mathbf{F}_e^t - \mathbf{A}^t \mathbf{F}^t = \mathbf{M} \ddot{\mathbf{U}}^t + \mathbf{C} \dot{\mathbf{U}}^t \\ \Delta \in \mathbf{E} \\ \mathbf{U} \in \Omega_s \\ \mathbf{F}^t \in \Omega_f \\ \Delta^{t_f} = \Delta^{t_s} \\ n_a = N_a \end{cases} \quad (24)$$

The method proposed in this paper is used to solve this model. The GA used here adopts a maximum number of generations of 100, and the other parameters of it are same as those used in section Shape Control. The computations are carried out with the

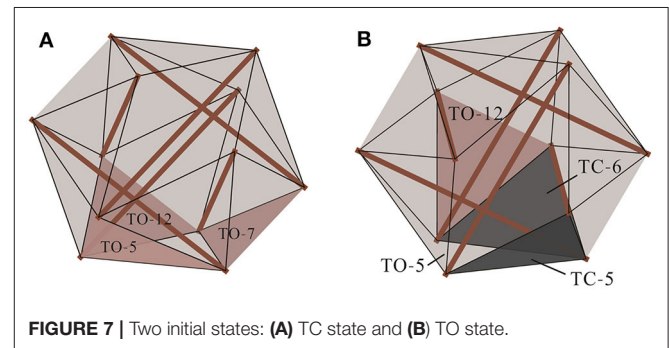


FIGURE 7 | Two initial states: (A) TC state and (B) TO state.

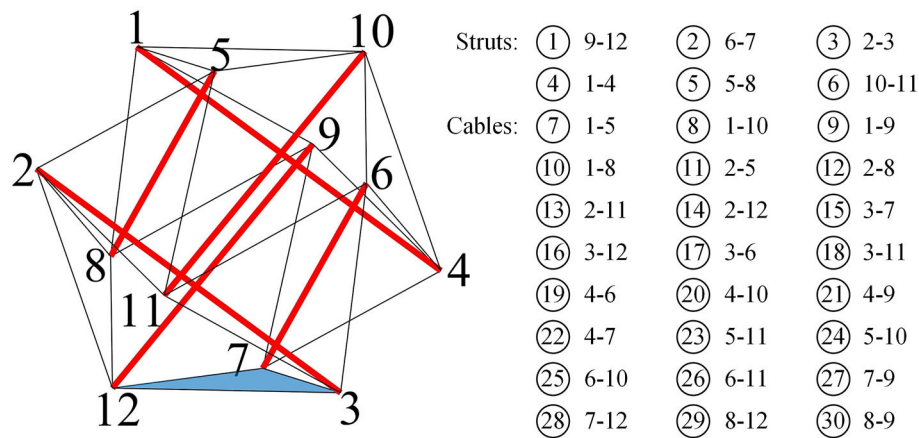


FIGURE 6 | Six-strut tensegrity system.

TABLE 4 | Rest lengths at initial state and mechanical properties of elements.

Type of members	Rest length (m)	Mass (kg)	Linear stiffness (N/m)	Prestress (N)	Compressive strength (N)	Tensile strength (N)
Struts	0.20	0.065	2×10^5	-31.36	-150	150
cables	0.12	0.001	205	12.80	-150	150

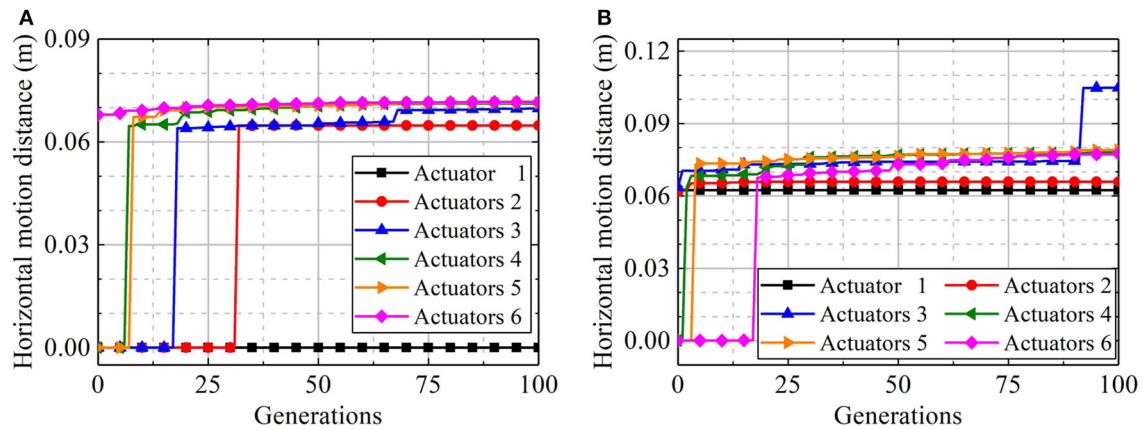


FIGURE 8 | Motion distance vs. generations: **(A)** TC state and **(B)** TO state.

TABLE 5 | Locomotive gait for the six-strut tensegrity structure.

Gait number	Gait type	Actuating length (cm)						Motion distance (cm)
		1	2	3	4	5	6	
1	TC-6→ TO-5	-4.22	5.28	–	–	–	–	6.48
2	TC-6→ TO-7	5.30	–	-4.15	–	–	–	6.48
3	TC-6→ TO-12	–	-4.67	4.84	–	–	–	6.41
4	TO-5→ TC-5	5.30	–	–	–	–	–	6.24
5	TO-5→ TC-6	–	–	–	–	–	5.30	6.24
6	TO-5→ TC-5→ TO-12	–	-4.56	3.73	–	–	5.28	10.48

same computer used in section Shape Control. Two cases, using the TC state and TO state, as the initial state, are considered. The number of stand triangles and triangles adjacent to the stand triangle are shown in **Figure 7**. In each case, six computations, corresponding to $N_a = 1, 2, 3, 4, 5$, and 6 , are performed. The evolution process of the mass center's horizontal motion distance in the computations are shown in **Figure 8**. In the case using the TC state as the initial state, three typical gaits that, respectively, drive the system rolling from the current stand triangle to the three adjacent triangles are found (**Table 5**). The motion distance of the mass center generated by these gaits is in the range 6.40–6.50 cm. In the case using the TO state as the initial state, there are also three gait types. Two respectively, drive the system rolling from the initial stand triangle to two of the three adjacent triangles, whereas the third drives the system rolling twice, from the initial stand triangle to an adjacent triangle, and then to an adjacent triangle again (**Table 5**). The motion distance of the mass center generated by the single-rolling gaits is 6.24 cm. The motion distance of the mass center generated by the double-rolling gait is 10.48 cm; about 1.68 times that generated by the single-rolling gaits.

Motion Path Planning

For a given initial and target location pairing, there are generally two approaches to realizing motion from the initial to the target location. One is connecting the initial location to the

target location using several basic gaits, as given in **Table 5**. This approach is suitable for regular movement on flat terrains with given maps, and a geometry-based algorithm has previously been verified for finding the path for locomotion of a six-strut tensegrity robot (Lu et al., 2019). The other approach is a direct search for a control strategy able to drive movement of the system from the initial location to the target location. This approach is considered more flexible than the first, but normally carries greater computational cost because it has to numerically track motion within the path planning scheme. In the current work, the second approach is adopted. The locations $A(x_A, y_A)$ and $B(x_B, y_B)$ are defined as the initial location and the target location.

The objective function is defined as:

$$G(\Delta) = \begin{cases} d, & \text{if } d > \varepsilon \\ 0, & \text{if } d \leq \varepsilon \end{cases} \quad (25)$$

where d is the distance between the current location and the target location, and ε is a positive small constant.

The aforementioned additional constraint of no internal collision is included. The motion path planning model can thus

be written as

$$\begin{cases} \text{find } \Delta \\ \min G(\Delta) = \begin{cases} d, & \text{if } d > \varepsilon \\ 0, & \text{if } d \leq \varepsilon \end{cases} \\ \text{s.t.} \\ \mathbf{F}_e^t - \mathbf{A}^t \mathbf{F}^t = \mathbf{M} \ddot{\mathbf{U}}^t + \mathbf{C} \dot{\mathbf{U}}^t \\ \Delta \in \mathbf{E} \\ \mathbf{U} \in \Omega_s \\ \mathbf{F}^t \in \Omega_f \\ \Delta^{t_f} = \Delta^{t_s} \end{cases} \quad (26)$$

The initial location is set as A (0, 0) and the target location as B (0.1, 0.1). The starting time is set as $t_s = 0$, the end time as $t_f = 150$ s, and the positive small constant ε as 0.0005 m. Time is discretized by an interval of 1 s. The GA used here adopts the same set of parameters as used in section Gait Design. It has taken 1,750 min to complete 75 generations on the same computer as that used for the motion path planning optimization.

The evolution of the average and minimum objectives in the computation is shown in **Figure 9**. The minimum distance

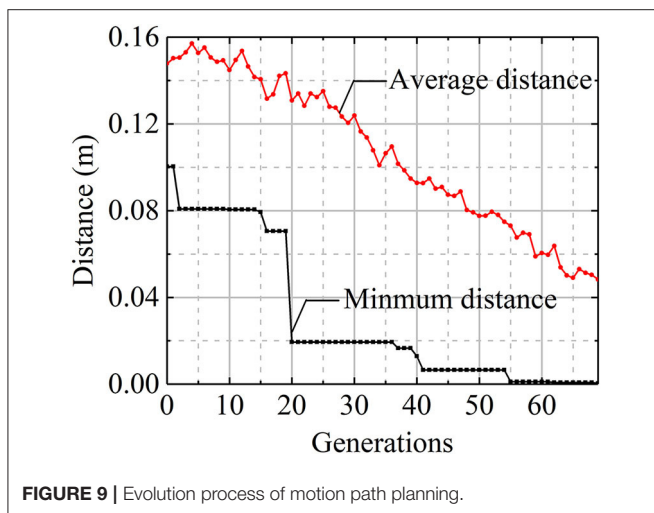


FIGURE 9 | Evolution process of motion path planning.

between the current and the target location decreases to 0.0004 m in the 69th generation. The individual corresponding to the minimum objective in the last generation is the optimal control strategy, represented by the rest length change spectra of the six active elements, as shown in **Figure 10A**. The motion trajectory of the system's mass center under the optimal control strategy is shown in **Figure 10B**. Further investigation into the motion reveals that the system experiences three complete rolls and the stand triangle shifts from TC-6 (3, 7, 12) to TO-7 (3, 4, 7), TC-8 (4, 7, 9), and finally TO-11 (7, 8, 9). Besides the rolling movements, some crawls and shape adjustments occurs, resulting in small-scale movements, as indicated by the red dashed-line rectangles in **Figure 10B**.

DISCUSSION

In this paper, the generality of the proposed model is ensured by the following factors: It does not deliberately distinguish between the shape-controlled tensegrity structure and the locomotive tensegrity structure. A unified dynamic formulation is used for the controllable tensegrity structure, though the shape control process is usually deemed to be quasi-static. The DRM-based algorithm using the central difference explicit scheme can track both the deformations and global rigid body motions of tensegrity systems. Conceptual expressions of the subjective and constraints were adopted. The control problem for a controllable tensegrity structure was interpreted as a combinational optimization problem. A similar optimization model was used for shape-controlled tensegrity structures in previous studies (Xu and Luo, 2009; Xu et al., 2014). However, in the current work, quasi-static behavior was assumed for the structural system, and the global rigid body motion of the structural system was eliminated by proper restraints. To some extent, the proposed model may be considered an extension of the previous model.

The global optimization algorithm used in the paper, i.e., the GA, worked well in the shape control example in section Shape Control and the locomotion control example in section Locomotion Control. In both examples, the number of control steps was provided in advance. Situations in which

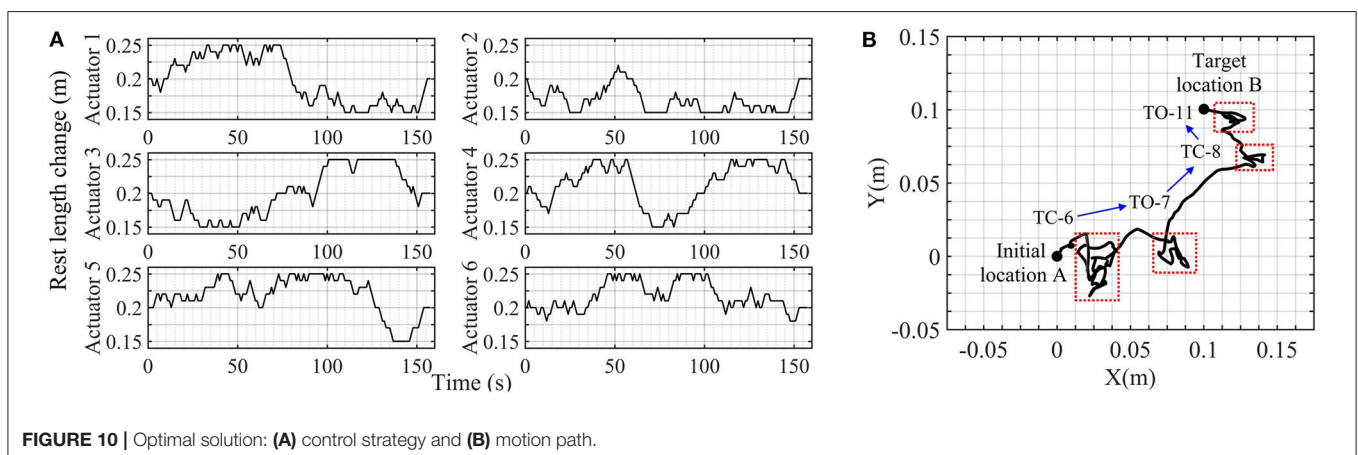


FIGURE 10 | Optimal solution: (A) control strategy and (B) motion path.

the number of control steps cannot be determined in advance, as in the path planning situations considered in the literature (Xu et al., 2014; Lu et al., 2019), are difficult to handle with a GA. Further considering that there is no constraint on the number of control steps in the mathematical model given in Equation (12), the generality of the GA does not match that of the model. Various other global optimization algorithms besides a GA could be used, based on the specific application.

CONCLUSION

In this paper, a general model for both shape control and locomotion control of tensegrity systems is proposed. A method combining GA and DRM was adopted to solve the model. The proposed model and method were applied to typical tensegrity system shape and locomotion control problems. The results demonstrate that both the shape control problem of a double-layered tri-prism tensegrity structure, and the locomotion control problem of a six-strut tensegrity structure can be modeled by the proposed model, and solved by the proposed method. We believe the proposed model is also suitable for control problems in other types of tensegrity system. The applicability of the proposed

GA-based method to control problems of higher complexity and larger scale than those presented in this work could be subject of future investigation.

DATA AVAILABILITY STATEMENT

All datasets generated for this study are included in the article/supplementary material.

AUTHOR CONTRIBUTIONS

HC developed the model and method for the controllable tensegrity. XX proposed the main idea of the paper. MW assisted HC in the numerical computations in the applications. YL developed the DRM-based algorithm for dynamic tensegrity. All authors contributed to the article and approved the submitted version.

FUNDING

This work was supported by the Natural Science Foundation of Zhejiang Province (LR17E080001) and the Natural Science Foundation of China (51578494).

REFERENCES

- Al Sabouni-Zawadzka, A. (2014). Active control of smart tensegrity structures. *Arch. Civil Eng.* 60, 517–534. doi: 10.2478/ace-2014-0034
- Amendola, A., Krushynska, A., Daraio, C., Pugno, N. M., and Fraternali, F. (2018). Tuning frequency band gaps of tensegrity mass-spring chains with local and global prestress. *Int. J. Solids Struct.* 155, 47–56. doi: 10.1016/j.ijsolstr.2018.07.002
- Barnes, M. R. (1999). Form finding and analysis of tension structures by dynamic relaxation. *Int. J. Space Struct.* 14, 89–104. doi: 10.1260/0266351991494722
- Bliss, T., Iwasaki, T., and Bart-Smith, H. (2013). Central pattern generator control of a tensegrity swimmer. *IEEE/ASME Trans. Mech.* 18, 586–597. doi: 10.1109/TMECH.2012.2210905
- Böhm, V., and Zimmermann, K. (2013). “Vibration-driven mobile robots based on single actuated tensegrity structures,” in *Proceedings - IEEE International Conference on Robotics and Automation*. (Karlsruhe), doi: 10.1109/ICRA.2013.6631362
- Cera, B., and Agogino, A. M. (2018). “Multi-cable rolling locomotion with spherical tensegrities using model predictive control and deep learning,” in: *IEEE International Conference on Intelligent Robots and Systems* (Madrid), 6595–6600. doi: 10.1109/IROS.2018.8594401
- Fazli, N., and Abedian, A. (2011). Design of tensegrity structures for supporting deployable mesh antennas. *Scientia Iranica* 18, 1078–1087. doi: 10.1016/j.scient.2011.08.006
- Fest, E., Shea, K., Domer, B., and Smith, I. F. C. (2003). Adjustable tensegrity structures. *J. Struct. Eng.* 129, 515–526. doi: 10.1061/(ASCE)0733-9445(2003)129:4(515)
- Fraternali, F., Carpentieri, G., Amendola, A., Skelton, R. E., and Nesterenko, V. F. (2014). Multiscale tunability of solitary wave dynamics in tensegrity metamaterials. *Appl. Phys. Lett.* 105:201903. doi: 10.1063/1.4902071
- Friesen, J., Pogue, A., Bewley, T., Oliveira, M. D., Skelton, R., and Sunspir, V. (2014). “DuCTT: a tensegrity robot for exploring duct systems,” in *Proceedings - IEEE International Conference on Robotics and Automation* (Hong Kong), 4222–4228. doi: 10.1109/ICRA.2014.6907473
- Friesen, J. M., Glick, P., Fanton, M., Manovi, P., and Sunspir, V. (2016). “The second generation prototype of a duct climbing tensegrity robot, DuCTv2,” in *Proceedings - IEEE International Conference on Robotics and Automation* (Stockholm), 2123–2128. doi: 10.1109/ICRA.2016.7487361
- Kan, Z., Peng, H., Chen, B., and Zhong, W. (2018). Nonlinear dynamic and deployment analysis of clustered tensegrity structures using a positional formulation FEM. *Compos. Struct.* 187, 241–258. doi: 10.1016/j.compstruct.2017.12.050
- Khazanov, M., Humphreys, B., Keat, W., and Rieffel, J. (2013). “Exploiting dynamical complexity in a physical tensegrity robot to achieve locomotion,” in *The Twelfth European Conference on Artificial Life* (East Lansing, MI), 965–972. doi: 10.7551/978-0-262-31709-2-ch144
- Kim, K. (2016). *On the locomotion of spherical tensegrity robots* (PhD dissertation). University of California, Berkeley, CA, United States.
- Kim, K., Moon, D., Bin, J. Y., and Agogino, A. M. (2017). “Design of a spherical tensegrity robot for dynamic locomotion,” in *IEEE International Conference on Intelligent Robots and Systems* (Vancouver, BC), 450–455. doi: 10.1109/IROS.2017.8202192
- Li, B., Du, W., and Liu, W. (2017). “Dynamic modeling and controlling for the crawling motion of the 6-strut tensegrity robot,” in *2017 IEEE 7th Annual International Conference on CYBER Technology in Automation, Control, and Intelligent Systems* (CYBER) (Honolulu, HI: IEEE). doi: 10.1109/CYBER.2017.8446093
- Lin, C., Li, D., and Zhao, Y. (2016). “Tensegrity robot dynamic simulation and kinetic strategy programming,” in *2016 IEEE Chinese Guidance, Navigation and Control Conference* (CGNCC) (Nanjing), 2394–2398.
- Liu, K., Zegard, T., Pratapa, P. P., and Paulino, G. H. (2019). Unraveling tensegrity tessellations for metamaterials with tunable stiffness and bandgaps. *J. Mech. Phys. Solids* 131, 147–166. doi: 10.1016/j.jmps.2019.05.006
- Lu, Y., Xu, X., and Luo, Y. (2019). Path planning for rolling locomotion of polyhedral tensegrity robots based on Dijkstra algorithm. *J. Int. Assoc. Shell Spatial Struct.* 60, 271–284. doi: 10.20898/j.iaass.2019.2.02.037
- Luo, A., and Liu, H. (2017). Analysis for feasibility of the method for bars driving the ball tensegrity robot. *J. Mech. Robotics* 9:051010. doi: 10.1115/1.4037565
- Mirletz, B. T., Bhandal, P., Adams, R. D., Agogino, A. K., Quinn, R. D., and SunSpir, V. (2015). Goal-directed CPG-based control for tensegrity spines with many degrees of freedom traversing irregular terrain. *Soft Robotics* 2, 165–176. doi: 10.1089/soro.2015.0012
- Motro, R. (2003). *Tensegrity: Structural Systems for the Future*. London: Kogan Page Science. doi: 10.1016/B978-190399637-9/50038-X

- Oden, J. T., and Kikuchi, N. (1982). Finite element methods for constrained problems in elasticity. *Int. J. Numerical Methods Eng.* 18, 701–725. doi: 10.1002/nme.1620180507
- Oh, C. L., Choong, K. K., Nishimura, T., Kim, J. Y., and Zain, M. R. (2018). Tapered three-stage deployable tensegrity model. *J. Phys. Conf. Ser.* 1130:012031. doi: 10.1088/1742-6596/1130/1/012031
- Omer, O., Offer, S., Amir, A., and Uri, B. (2011). “A model of caterpillar locomotion based on assure tensegrity structures,” in *ASME 2011 International Design Engineering Technical Conferences and Computers and Information in Engineering Conference* (Washington, DC).
- Papadopoulos, P., and Taylor, R. L. (1992). A mixed formulation for the finite element solution of contact problems. *Comput. Methods Appl. Mech. Eng.* 94, 373–389. doi: 10.1016/0045-7825(92)90061-N
- Park, S., Park, E., Yim, M., Kim, J., and Seo, T. (2019). Optimization-based nonimpact rolling locomotion of a variable geometry truss. *IEEE Robotics Automation Lett.* 4, 747–752. doi: 10.1109/LRA.2019.2892596
- Paul, C., Valero-Cuevas, F. J., and Lipson, H. (2006). Design and control of tensegrity robots for locomotion. *IEEE Trans. Robotics* 22, 944–957. doi: 10.1109/TRO.2006.878980
- Rovira, A. G., and Tur, J. M. M. (2009). Control and simulation of a tensegrity-based mobile robot. *Robotics Auton. Syst.* 57, 526–535. doi: 10.1016/j.robot.2008.10.010
- Sabelhaus, A. P., Bruce, J., Caluwaerts, K., Manovi, P., and Sunspiral, V. (2015). “System design and locomotion of SUPERball, an untethered tensegrity robot,” in *Proceedings - IEEE International Conference on Robotics and Automation* (Seattle, WA), 2867–2873. doi: 10.1109/ICRA.2015.7139590
- Senatore, G., and Piker, D. (2015). Interactive real-time physics: an intuitive approach to form-finding and structural analysis for design and education. *Comput. Aided Design* 61, 32–41. doi: 10.1016/j.cad.2014.02.007
- Shea, K., Fest, E., and Smith, I. F. C. (2002). Developing intelligent tensegrity structures with stochastic search. *Adv. Eng. Inform.* 16, 21–40. doi: 10.1016/S1474-0346(02)00003-4
- Sultan, C., Corless, M., and Skelton, R. E. (2002). Symmetrical reconfiguration of tensegrity structures. *Int. J. Solids Struct.* 39, 2215–2234. doi: 10.1016/S0020-7683(02)00100-2
- Sultan, C., and Skelton, R. (2003). Deployment of tensegrity structures. *Int. J. Solids Struct.* 40, 4637–4657. doi: 10.1016/S0020-7683(03)00267-1
- SunSpiral, V., Gorospe, G., Bruce, J., Iscen, A., Korbel, G., Milam, S., et al. (2013). “Tensegrity based probes for planetary exploration entry, descent and landing (EDL) and surface mobility analysis,” in *Proceedings of 10th International Planetary Probe Workshop* (San Jose, CA).
- Veuve, N., Safaei, S. D., and Smith, I. F. C. (2015). Deployment of a tensegrity footbridge. *J. Struct. Eng.* 141:04015021. doi: 10.1061/(ASCE)ST.1943-541X.0001260
- Wang, Z., Li, K., He, Q., and Cai, S. (2019). A light-powered ultralight tensegrity robot with high deformability and load capacity. *Adv. Mater.* 31:1806849. doi: 10.1002/adma.201806849
- Xu, X., and Luo, Y. (2009). Non-linear displacement control of prestressed cable structures. *Proc. Inst. Mech. Eng. Part G: J. Aerospace Eng.* 223, 1001–1007. doi: 10.1243/09544100JAERO455
- Xu, X., and Luo, Y. (2013). Collision-free shape control of a plane tensegrity structure using an incremental dynamic relaxation method and a trial-and-error process. *Proc. Inst. Mech. Eng. Part G: J. Aerospace Eng.* 227, 266–272. doi: 10.1177/0954410011433501
- Xu, X., Sun, F., Luo, Y., and Xu, Y. (2014). Collision-free path planning of tensegrity structures. *J. Struct. Eng.* 140:04013084. doi: 10.1061/(ASCE)ST.1943-541X.0000900
- Yu, Y., and Luo, Y. (2009). Finite particle method for kinematically indeterminate bar assemblies. *J. Zhejiang Univ. Sci. A* 10, 669–676. doi: 10.1631/jzus.A0820494
- Yu, Y., Paulino, G. H., and Luo, Y. (2011). Finite particle method for progressive failure simulation of truss structures. *J. Struct. Eng.* 137, 1168–1181. doi: 10.1061/(ASCE)ST.1943-541X.0000321
- Zhang, L., Maurin, B., and Motro, R. (2006). Form-finding of nonregular tensegrity systems. *J. Struct. Eng.* 132, 1435–1440. doi: 10.1061/(ASCE)0733-9445(2006)132:9(1435)
- Zhao, Y., Zhou, S., Lin, C., and Li, D. (2017). “An efficient locomotion strategy for six-strut tensegrity robots,” in *2017 13th IEEE International Conference on Control & Automation (ICCA) (Ohrd)*. doi: 10.1109/ICCA.2017.8003096

Conflict of Interest: The authors declare that the research was conducted in the absence of any commercial or financial relationships that could be construed as a potential conflict of interest.

Copyright © 2020 Cai, Wang, Xu and Luo. This is an open-access article distributed under the terms of the Creative Commons Attribution License (CC BY). The use, distribution or reproduction in other forums is permitted, provided the original author(s) and the copyright owner(s) are credited and that the original publication in this journal is cited, in accordance with accepted academic practice. No use, distribution or reproduction is permitted which does not comply with these terms.



Integrating Ionic Electroactive Polymer Actuators and Sensors Into Adaptive Building Skins – Potentials and Limitations

Raphael Neuhaus^{1*}, Nima Zahiri², Jan Petrs², Yasaman Tahouni³, Jörg Siegert¹, Ivica Kolaric¹, Hanaa Dahy² and Thomas Bauernhansl¹

¹ Functional Materials, Institute of Industrial Manufacturing and Management (IFF), University of Stuttgart, Stuttgart, Germany,

² Institute of Building Structures and Structural Design (itke), Biobased Materials and Materials Cycles in Architecture

(BioMat), University of Stuttgart, Stuttgart, Germany, ³ Institute for Computational Design and Construction (ICD), University of Stuttgart, Stuttgart, Germany

OPEN ACCESS

Edited by:

Gennaro Senatore,
École Polytechnique Fédérale de
Lausanne, Switzerland

Reviewed by:

Paolo Milani,
University of Milan, Italy
Roel Loonen,
Eindhoven University of
Technology, Netherlands
Alvo Aabloo,
University of Tartu, Estonia

*Correspondence:

Raphael Neuhaus
raphael.neuhaus@iff.uni-stuttgart.de

Specialty section:

This article was submitted to
Structural Sensing,
a section of the journal
Frontiers in Built Environment

Received: 27 March 2020

Accepted: 27 May 2020

Published: 02 July 2020

Citation:

Neuhaus R, Zahiri N, Petrs J, Tahouni Y, Siegert J, Kolaric I, Dahy H and Bauernhansl T (2020) Integrating Ionic Electroactive Polymer Actuators and Sensors Into Adaptive Building Skins – Potentials and Limitations. *Front. Built Environ.* 6:95. doi: 10.3389/fbuil.2020.00095

Building envelopes separate the confined interior world engineered for human comfort and indoor activity from the exterior world with its uncontrollable climatic forces and man-made immission. In the future, active, sustainable and lightweight building skins are needed to serve as an adaptive interface to govern the building-physical interactions between these two worlds. This article provides conceptual and experimental results regarding the integration of ionic electroactive polymer sensors and actuators into fabric membranes. The ultimate goal is to use this technology for adaptive membrane building skins. These devices have attracted high interest from industry and academia due to their small actuation voltages, relatively large actuation and sensing responses and their flexible and soft mechanical characteristics. However, their complex manufacturing process, sophisticated material compositions and their environmental sensitivity have limited the application range until now. The article describes the potentials and limitations of employing such devices for two different adaptive building functionalities: first, as a means of ventilation control and humidity regulation by embedding small actuated apertures into a fabric membrane, and second, as flexible, energy- and cost-efficient distributed sensors for external load monitoring of such structures. The article focusses on designing, building and testing two experimental membrane demonstrators with integrated polymer actuators and sensors. It addresses the challenges encountered and draws conclusions for potential future optimization at the device and system level.

Keywords: electroactive polymer (EAP) actuators, adaptive building envelope, integration concepts, switchable breathability, smart material actuator, wind load sensing, ventilation

INTRODUCTION

Many scientists, governments and international institutions predict a global population growth of up to 2.2 billion people between 2017 and 2050 (United Nations, 2017). Regarding this demographic increase, it is self-evident that additional buildings, roads, bridges, tunnels, and other infrastructure facilities have to be built to provide future generations with the same or higher housing standards and societal living conditions prevalent today (Tauber et al., 2019).

The construction of new buildings and infrastructure and particularly the modernization of the already existing building stock entail a growing demand for construction materials and energy resources. Even today, the construction industry is responsible for ~60% of global resource consumption, 50% of mass waste occurrence and 35% of both energy consumption and global emissions (Abergel et al., 2017).

Considering those numbers, it is necessary to find answers to the most urgent ecological and societal question of our time for the construction industry: How can we create – in view of a growing world population and shrinking resources – more sustainable housing with less material and energy consumption in the future? Employing lightweight structural systems and integrating adaptive elements into enveloping systems is considered an important approach (Klein and Knaack, 2015; Sobek, 2015; Košir, 2016).

Building envelopes, besides being exposed to climatic impacts like rain, wind and wide temperature ranges, are regulating thermal insulation, light transmission, humidity transport and ventilation. Thus, they are significantly involved in controlling the thermal and energy balance of the building. Nevertheless, their distinct features and operation principles are usually based on either high material usage (thermal energy storage, noise protection) or high energy usage (heating, cooling, ventilation, illumination). As a direct consequence, building envelopes not only contribute to the total energy and material resource consumption of the building, but their building-physical qualities strongly determine the physical and mental well-being of the users and residents. New ideas in designing lightweight and energy-efficient building envelopes go way beyond today's passive membrane structures, with some approaches currently exploring active concepts that include adaptive building-physical functionalities that can promote comfortable indoor settings (Aelenei et al., 2016; Attia et al., 2018).

One approach is being presented in this research paper, namely employing bio-inspired smart materials for adaptive ultra-lightweight building skins. The overarching objective is to present experimental methods and results regarding the integration of carbon nanotube based electroactive polymers that can be used as soft and flexible actuators and sensors in fabric membrane structures.

STATE OF THE ART

Structural Membranes as Building Envelopes

Since the second half of the 20th century lightweight building skins such as multi-layer fabric or foil-based membrane structures have been in the focus of architects and engineers and increasingly found their way into airport façade systems, roofing structures for stadiums and iconic temporary or stationary public buildings around the globe (Habermann and Koch, 2004).

New advances in polymer technology have brought new membrane materials to the market, accounting for improved life spans, optimized mechanical properties, dirt-repellent and UV-resistant characteristics and the very important features of

translucency (fabrics) and transparency (foils). They usually make use of multifunctional single-layer membranes and profit from their low material thicknesses of usually below 1 mm. The resulting low weight of the membrane cover leads to a relief of the load-bearing structures and thus to a reduction of necessary construction materials (Paech, 2016).

The Need for Adaptivity

Recent works have been published on design and optimization methods to reduce material and energetic impacts of civil structures through integration of active control (Senatore et al., 2018a,b, 2019). The building-physical properties and other distinct features of membrane skins, however, are usually static and non-changeable. They are designed and installed for specific use cases to operate within certain climatic conditions which are strongly related to the building's geographic location. Often no adaptive functionality is required, because energy-intensive artificial climate control still dominates the current practices in regulating comfort settings. However, in order to yield maximum energy efficiency and building performance, the building envelope needs to respond dynamically to changing environmental conditions and user comfort requirements.

Adaptivity in building skins can provide diverse functionalities: A controlled breathability may be desired to manage hygrothermal conflicts such as specific humidity and ventilation requirements or to prevent interstitial condensation in multi-layer membrane structures (Janssens, 1998; Cremers et al., 2016). The inflexible light transmission rates of construction membranes may be met with novel adaptive shading strategies involving kinetic devices or actuators directly integrated into the building skin. A geometric deformation of distributed façade elements may have many functions simultaneously, e.g., a variable sun shading function, a means of ventilation and humidity control or an induced change in local wind pressure forces by adjusting the building surface topology (Loonen et al., 2015).

Traditional actuators that were proposed for such tasks include pneumatic and electronic actuators, electro-magnetic motors and hydraulic cylinders (Janocha, 2004; Haase et al., 2011). However, the weight and size penalties, complex transmissions, high induced noise levels, restrictive shapes and the need for resource-intensive maintenance of such actuators have led researchers to investigate alternative technologies for more effective substitutes with larger mechanical flexibility and compliance, down-scalability, high power-to-weight and power-to-volume ratios and high efficiency. Finding such substituting systems is specifically necessary for the application in lightweight membrane building skins where traditional rigid actuators are difficult to integrate.

In recent years, a number of smart materials have been proposed for the integration into adaptive building envelopes, some of which could also be employed as sensors. Integrated sensors in building skins are useful to monitor external wind and snow loads, manage its energy demand and empower occupants or intelligent systems to take action.

Responsive and Smart Materials

It is desired to have soft and flexible actuators and sensors to avoid complex mechanical parts within adaptive building skin elements. A variety of smart materials have been proposed in this regard. Among the most interesting materials are thermally triggered bi-metal actuators and shape memory alloys (SMA) which both react to ambient temperature changes and have been suggested for adaptive ventilation and shading systems in architectural skins (Sung, 2011; Dewidar, 2013). Hygroscopic wooden bilayer composites have been explored to enable adaptive apertures that react to changing humidity and temperature conditions (Reichert et al., 2015). Such self-controlled materials, however, only respond to ambient environmental parameters and cannot be directly stimulated or controlled by humans.

For this reason, electroactive polymers (EAP) have attracted global interest among scientists and are believed to have a potential role in civil engineering and architectural applications (Kretzer and Rossi, 2012; Juaristi et al., 2018). These soft and flexible smart material systems exhibit a reversible change in size or shape when stimulated by an electric field. Despite their advantageous capability to combine sensor and actuator functionalities, they have not yet seen any commercial deployment in a wider architectural context.

Electroactive Polymers

There are two main groups of EAP prevailing in R&D today. The first and largest group – by numbers of publications and proposed applications – are the dielectric elastomer actuators (DEA) whose operation mode is based on purely physical effects. The second group consists of various sub-types of ionic EAP (IEAP), where actuation is based on electrochemical working principles.

DEA have a passive elastomer film with a high dielectric constant sandwiched between two compliant electrodes. Upon applying high electric voltages, the elastomer film is squeezed by the electrostatic pressure between the electrodes and therefore expands in size in planar direction. Regarding applications in built environment, they have only been proposed as an air flow actuator in HVAC systems by Berardi (2010), for daylighting control systems in homeostatic façades (Decker, 2013) and for a dynamic and responsive indoor arts installation mounted to a room ceiling in the project “Reef” by Mossé et al. (2012). Deformations of DEA are well-controlled, reversible, and capable of high-frequency operation, but they require very high driving voltages of several kilovolts for actuation. In this regard the operation of DEA as soft actuators in building envelopes may potentially be harmful for the residents and is thus not considered in this research paper.

Unlike DEA, IEAP operate on the principle of electrically controlled ion transport within a bi- or tri-layer setup and in most cases perform a bimorph bending motion. Some exhibit large deformation and medium force transmission at low operational power (<3 V), making them highly attractive for many applications where soft, non-hazardous and noise-free actuation is desired. Although several IEAP materials and their properties have been known for many decades, they have found very limited applications and have not replaced traditional actuators (electromagnetic, pneumatic, hydraulic, and

piezoelectric) because of complex manufacturing techniques, costly materials or poor actuation performance (Chang et al., 2018).

Focus – Specific Target Applications

Integrating soft and flexible actuators and sensors into membrane building skins can provide a variety of adaptive functionalities (see section The Need for Adaptivity). For this article, we focus on two application scenarios:

Switchable Breathability

Especially during winter time the temperature drop between the inside and the outside of a building skin can be significant. If humidity is trapped inside a confined multi-layer membrane structure and if the vapor pressure sets below the saturation pressure, condensation may occur. Condensation is an unwanted phenomenon as it may cause dampness, mold health issues, corrosion, material fatigue, and energy penalties due to increased heat transfer (Haase et al., 2011). Contemporary multi-layer membrane structures cannot breathe like conventional masonry walls, where humidity is simply dried out over time due to capillary diffusion processes. For this reason mechanical air heaters are often used to blow hot air through the interstitial space removing humidity. In view to avoid such energy intensive systems in the future, the first application scenario is an adaptively breathable membrane lowering the risk of interstitial condensation. This can be achieved by controlling the hygrothermal balance via integrated switchable apertures enabled by soft and flexible IEAP actuators.

Wind Load Monitoring

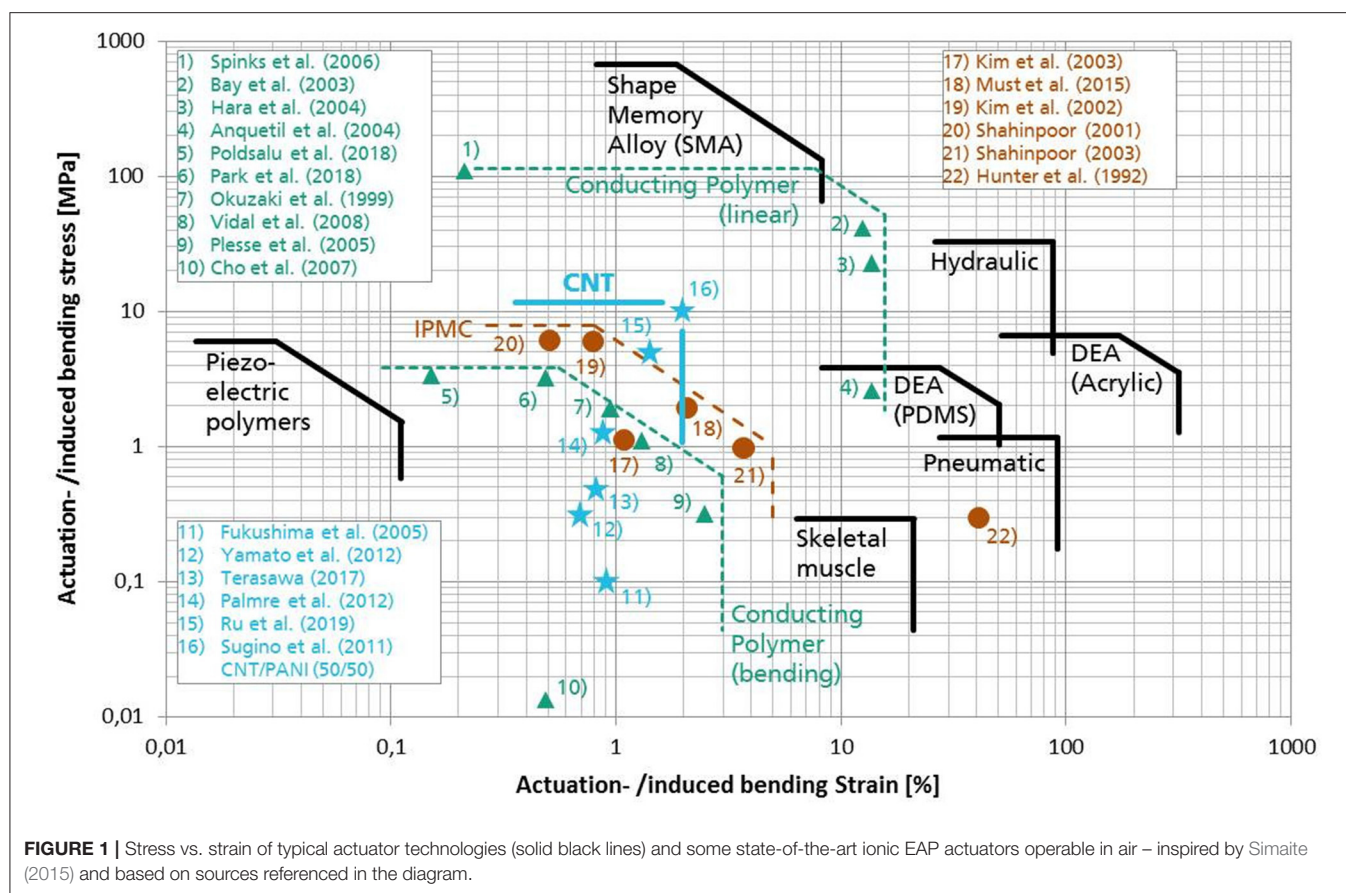
The second application scenario addresses load and stress sensing for fabric or foil-based membrane building skins. Strong wind loads, for example, first need to be detected before potential countermeasures can be taken. It is often desired to have locally resolved data about induced mechanical stresses inside membrane structures for health monitoring purposes and to ensure the serviceability and safety of the structure (Tang et al., 2019). We propose soft and flexible IEAP sensors for direct integration into tensile membrane structures as a viable alternative to the installation of conventional acceleration sensors and displacement meters.

SELECTION, MANUFACTURING AND TESTING OF SOFT ACTUATORS AND SENSORS

Types of Ionic EAP

Various types of IEAPs that can be operated under low voltage conditions have been developed, including conducting or conjugated polymers (CPs), ionic polymer–metal composites (IPMCs), carbon nanotube (CNT-) or Bucky gel polymers, and interpenetrating polymer networks (IPNs).

Conjugated polymers (CPs) represent a class of intrinsically conducting polymers such as polypyrrole, polyaniline, PEDOT:PSS and polythiophene that have unique actuation properties (Melling et al., 2019). Their working principle is based



on volume change in the electrodes due to the insertion and extraction of counter ions into the polymer matrix. In contrast to other IEAP, chemical oxidation and reduction processes occur at the ion-polymer interfaces. CPs usually operate in liquid electrolyte environments and are thus often proposed for biomedical applications, where the surrounding fluids (e.g., blood) can serve as an electrolyte. There are concepts of in-air operating CP actuators using an Interpenetrating Polymer Network (IPN) that contains the liquid electrolyte (Plesse et al., 2005). Such IPNs use one polymer network as ion conducting material and a second polymer network to provide the required mechanical properties. Newer research has proposed ink-jet printing of PEDOT:PSS on IPN networks for mass production of air-operating artificial muscles and supercapacitors (Nakshatharan et al., 2018). Other findings provided fast and durable CP actuators using graphene and a percolation network of silver nanowires to enhance the conductivity of the PEDOT:PSS electrodes (Park et al., 2018). An advantageous feature of CPs is that they hold their produced strain under DC voltage and at open circuit states.

The most commonly known IEAP is the ionic polymer-metal composite (IPMC) which is predominantly used as an actuator. IPMCs are composed of an ionic polymer membrane, typically Nafion, sandwiched between a pair of noble metal electrodes (Nakshatharan et al., 2018; Tamagawa et al., 2019).

When a voltage is applied to the metal electrodes of an IPMC, it causes directional motion of mobile cations together with water molecules from the ionic membrane to the electrode surfaces, where they form an electrochemical double layer. The excess of cations and water near the negatively charged electrode causes swelling which results in bending toward the positive electrode. IPMCs are, like CNT- or Bucky gel actuators, capable of self-sensing (Kruusamäe et al., 2015).

Unlike IPMCs, CNT-based IEAPs employ a pair of polymer supported Bucky gel electrodes containing CNTs instead of noble metal electrodes. Bucky gel is a highly viscous and electrically conductive gel obtained by physical cross-linking of highly entangled CNT bundles in the presence of imidazolium-based ionic liquids (IL). Such gels are stable at wide temperature ranges and do not shrink or dry out under reduced pressure due to the non-volatility of the ionic liquid. They can also be incorporated into a polymeric composite matrix to form free-standing conductive electrodes, which were used to build the first Bucky gel actuator that could operate in air without external electrolytes at comparably low applied voltages (± 3.0 V) (Fukushima et al., 2005).

The bending motion of CNT- or Bucky gel actuators is mainly caused by three superimposing effects, the first being the electrostatic attraction (or repulsion) between differently (or equally) charged neighboring CNTs within the Bucky gel

electrodes (Baughman et al., 1999). The second effect is caused by dimensional changes within individual CNTs themselves due to C-C bond elongation upon charge injection (Roth and Baughman, 2002). The third effect is due to transport of oppositely charged ions of different sizes to the cathodic and anodic side of the actuator, where they form electrochemical double layers with the positively and negatively charged CNTs. Since the BMI^+ cation is much larger than the BF_4^- anion in the ionic liquid, the ion transport leads to swelling of the cathode and shrinking of the anode side, respectively. Consequently, the actuator bends toward the anode side.

Benchmarking Performance Characteristics of IEAP

For a decision about which type of IEAP is most suitable for the desired target applications it was deemed necessary to compare their performance characteristics. To generate apertures in fabric membranes for building envelopes, long operation life-times and reproducibly strong forces and displacements are necessary. Slow actuation responses on the other hand should not have a negative impact, because changes in ambient temperature and humidity are also slow. Maximum internal material strains are key performance indicators for IEAP bending actuators. They indicate the unidirectional change of length within the electrode layers and, therefore, relate directly to the induced stress due to ionic transport forces. Induced bending strain and stress values are independent of the size or geometry of IEAP actuators, thus they can be used for direct comparison of their performance.

For benchmarking purposes, induced strain and stress values of different reported IEAP species have been collected from a variety of publications and are assembled in **Figure 1**. The illustrated performance boundaries take into consideration actuators operable in air only and depict values obtained under very low actuation frequencies (<0.1 Hz). Other actuator technologies such as SMA, DEA, skeletal muscles and others are also included for comparison.

Most IEAP species exhibit similar stress/strain combinations around 1 MPa and 1%, respectively, however CNT Bucky gel actuators appear to be especially promising. Furthermore, most reported IPMC actuators exhibit substantial back-relaxation effects, which is the unwanted behavior of a DC-excited actuator to slowly relax back toward its initial shape instead of holding its bent state (Vunder et al., 2012). Research on CP actuators has made tremendous progress in counteracting delamination and improving the electromechanical coupling efficiency and their cycle stability. However, the complex manufacturing techniques required for synthesizing and doping conductive polymers such as polypyrrole or PEDOT:PSS as well as the laboratory production of typically very thin actuators resulting in relatively low blocking forces have so far hindered a greater commercial adoption of this IEAP technology. CNT actuators on the other hand have reproducibly delivered strong actuation merits in previous projects (Addinall et al., 2014) and the authors believe that their simple and up-scalable manufacturing techniques, their proven in-air operability and

their sensory capabilities are important features when assessing their application potential for civil engineering structures. Without eliminating the possibility of other IEAP species also being compatible for the described application scenarios, CNT actuators were regarded as a premium choice for this project.

Figure 2 shows the electrochemical processes inside the three layer system leading to deformation of CNT actuators.

All IEAP species are reported to have lifetime expectancies (sometimes referred to as “cycle life”) of 10^4 – 10^7 working cycles, depending on the test environment, the applied power settings and choice of materials. Given an estimated average actuation frequency of five cycles per day the proposed application scenarios would yield a minimum lifetime expectancy of more than 5 years.

The authors would like to emphasize that in the following sections of this article the expression “actuator” always refers to IEAP with both actuator and sensor capabilities.

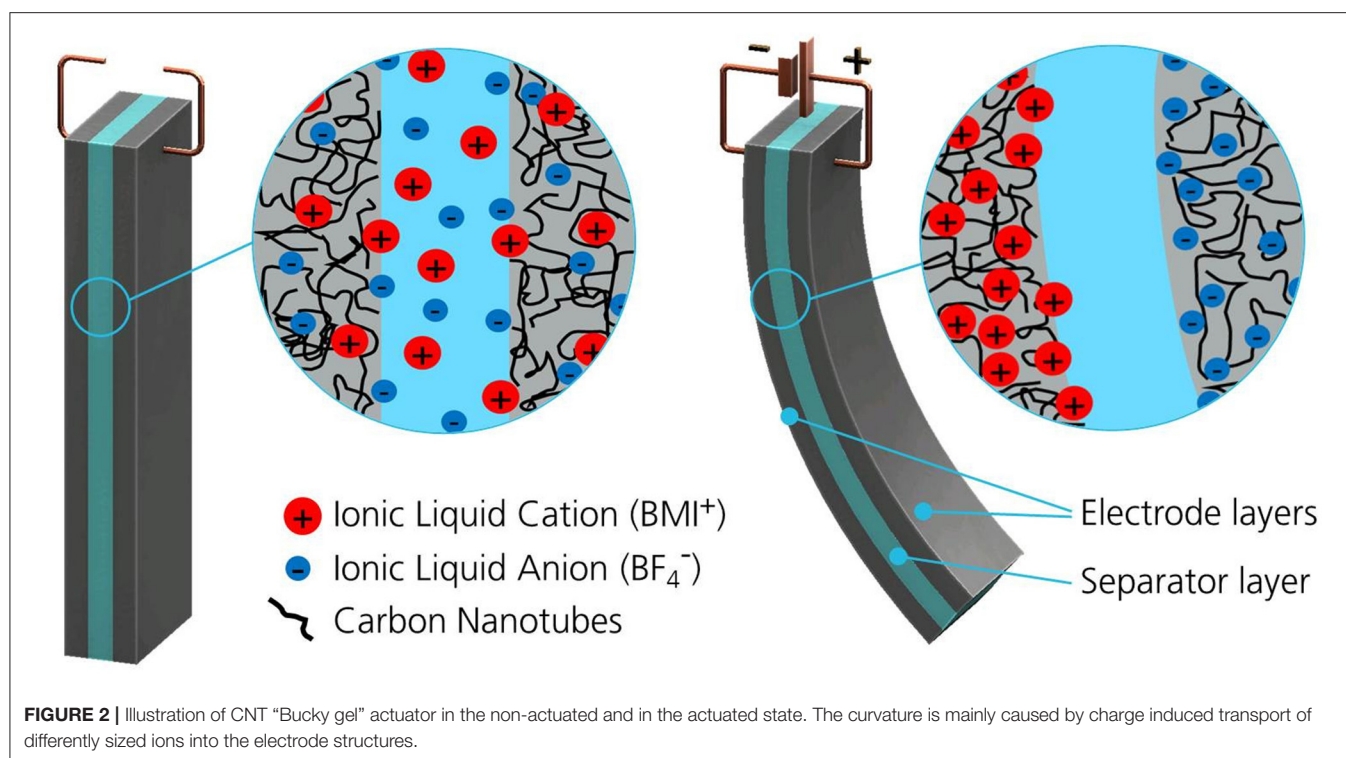
Manufacturing Methods of Ionic CNT Actuators

Until recently, the manufacturing process of CNT-based EAP actuators was a lab-scale fabrication method using small batches of raw materials and involving manual dispersion, casting and handling techniques. The authors have studied industrial dispersion and manufacturing techniques that enhanced the performance reproducibility of CNT-based actuators while simultaneously increasing the manufacturing speed and decreasing material costs. The findings of Sugino et al. (2011) served as a baseline for obtaining optimized material compositions for the actuators (**Figure 1**). Parts of the manufacturing procedure have been published by the authors in Neuhaus et al. (2019b).

Dispersion Techniques

The first step in actuator fabrication is to make homogeneous dispersions for both actuator electrodes and separators. In order to yield large electrochemical effects in the actuator electrodes – and thus high internal material strain for actuator deflection – a thorough separation of CNT agglomerates and an even distribution of all material components in the final dispersion is essential. Through the Design of Experiments (DoE) method it was possible to replace single-walled CNTs (SWCNTs) with much cheaper multi-walled CNTs (MWCNTs) that are easier to produce and available in large commercial quantities.

The fabrication of actuator electrodes and separators starts by dissolving polyvinylidene fluoride-cohexafluoropropylene [PVDF(HFP)] in the organic solvent 4-methyl-2-pentanone (4M2P). The polymer later serves as a matrix for the ionic liquid and the carbonaceous additives and is responsible for the actuator's stiffness. The room temperature ionic liquid 1-Butyl-3-methylimidazolium tetrafluoroborate (BMI-BF_4) is added to both dispersions and constitutes a non-volatile electrolytic ion reservoir. The electrode dispersion receives MWCNTs as the main active material (Nanocyl® NC7000) for sufficient specific surface area and Polyaniline (PANI) for enhanced electrode conductivity. Stirring of the dispersions and subsequent high frequency treatment in an ultrasonic bath has been reported to



last up to 72 h to yield sufficient homogenization (Sugino et al., 2011; Palmre et al., 2012). By applying high-power dispersion devices such as an ultrasonic sonotrode it was possible to reduce the overall dispersion time to <3 h, which is a significant improvement compared to conventional techniques.

Printing CNT Actuators

Printing of electrode and separator layers was performed with the discontinuous coating machine Easycoater EC 63 from Coatema Coating Machinery GmbH (Germany) that was specifically set up and re-designed for this project. Electrode and separator dispersions can be pumped separately into two different slot-die nozzles allowing for automated layer-by-layer printing without changing the slot-die configurations between different layers. Both slot-dies have a nozzle length of 200 mm. The width of the nozzle slot is 250 μm for the electrode slot-die and 100 μm for the separator slot-die. When the layers are applied onto the heated printing table with exactly controllable wet layer thickness, hot-air assisted drying accelerates the evaporation of the solvent. After 10 min, the layers are dry enough for the next layer to be printed. Alternatively, layers can be printed individually and later hot-pressed together for assembly of actuators and sensors.

Actuator Assembly – Separating Mechanical and Electrical Contacts

After printing the actuator layers, usually small rectangular pieces are cut out of the tri-layer compound. These actuators are not yet fitted with electric connections. For testing purposes, the bare electrode surfaces are mechanically clamped in between two conductive voltage terminals to perform their bimorph bending

motion. However, future applications require reliable electric contacts for simplified system integration and to improve the contact resistance between the main conductor (e.g., a cable) and the polymer electrodes. For testing such electric contacts, different flexible conductors were integrated into the actuator electrodes during and after the printing process. Silver plated conductive threads (Madeira HC 12 & HC 40), desoldering copper braid (Soder-Wick Rosin 50-6-25), adhesive copper foils (3M™ 11816 copper tape with acrylic conductive adhesive) and conductive epoxy glue (CircuitWorld CW2400) were tested for their applicability as embedded conductors. Dimension and resistivity parameters of all investigated conductive contact materials can be found in **Table 1**.

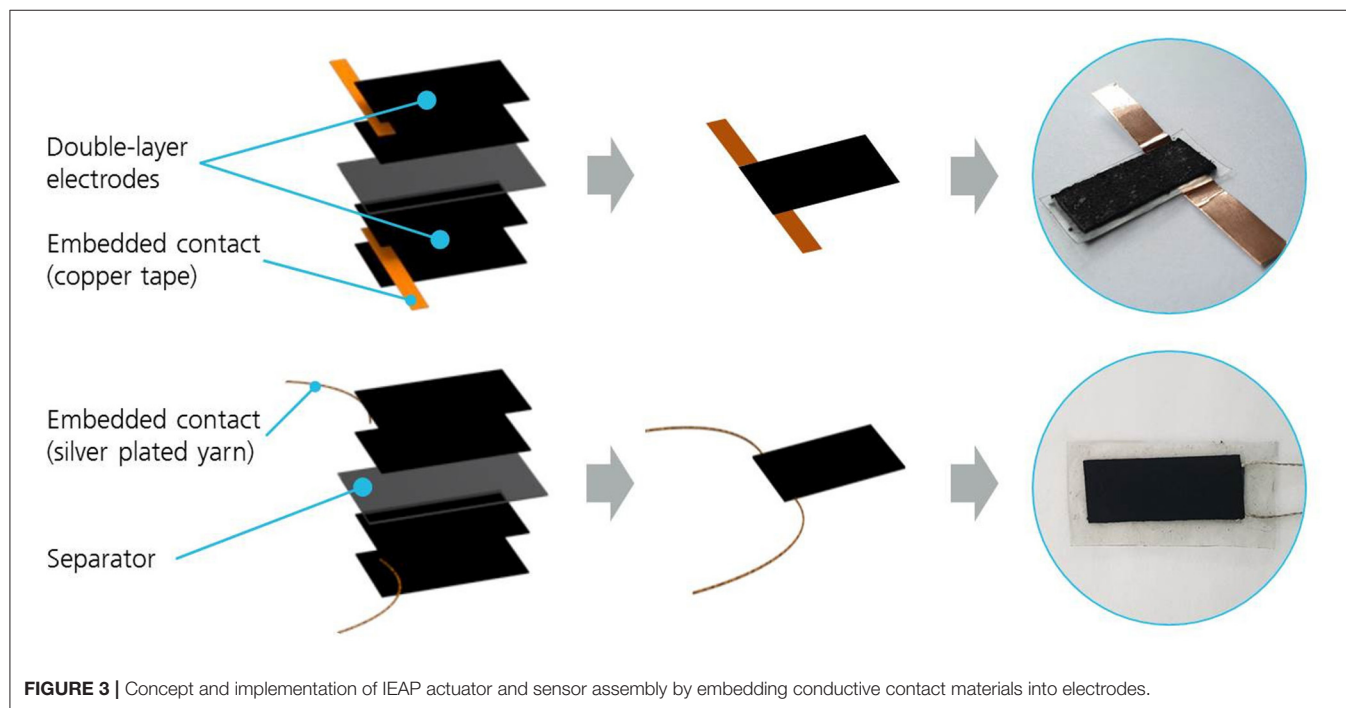
The solid conductors (yarn, desoldering braid, copper tape) were initially integrated into the wet electrode layers by placing them inside the printing mask where they were submerged by the electrode dispersion during stencil printing trials (Neuhaus et al., 2019a). After adoption of the new automated slot-die printing process, the conductors were sandwiched in between two printed and dried electrode layers of preferred shape and hot-pressed together. The resulting thick double-layer electrodes now featured firmly embedded electric contacts. The final assembly of the electrode-separator-electrode actuator composite was again done by hot pressing and produced a complete tri-layer actuator with two embedded electrode contacts for facilitated system integration (**Figure 3**).

Automated Actuator Testing

A fully automated test setup has been implemented for CNT actuator performance measurements. Actuators are clamped into

TABLE 1 | Dimension and resistivity values of commercial conductive materials used for embedding electric contacts into IEAP actuators and sensors.

Conductive contact material	Thickness/diameter	Electric resistivity
Madeira HC12/HC40 yarn	Ø 0.35/0.18 mm	<100/<300 Ω/m
Soder-Wick Rosin 50-6-25	0.7 mm	2.1 Ω/m
3M™ 11,816 copper tape	0.07 mm	0.043 Ω/m (5 mΩ contact res.)
CW2400 epoxy glue	–	1 mΩ·cm (specific resistance)



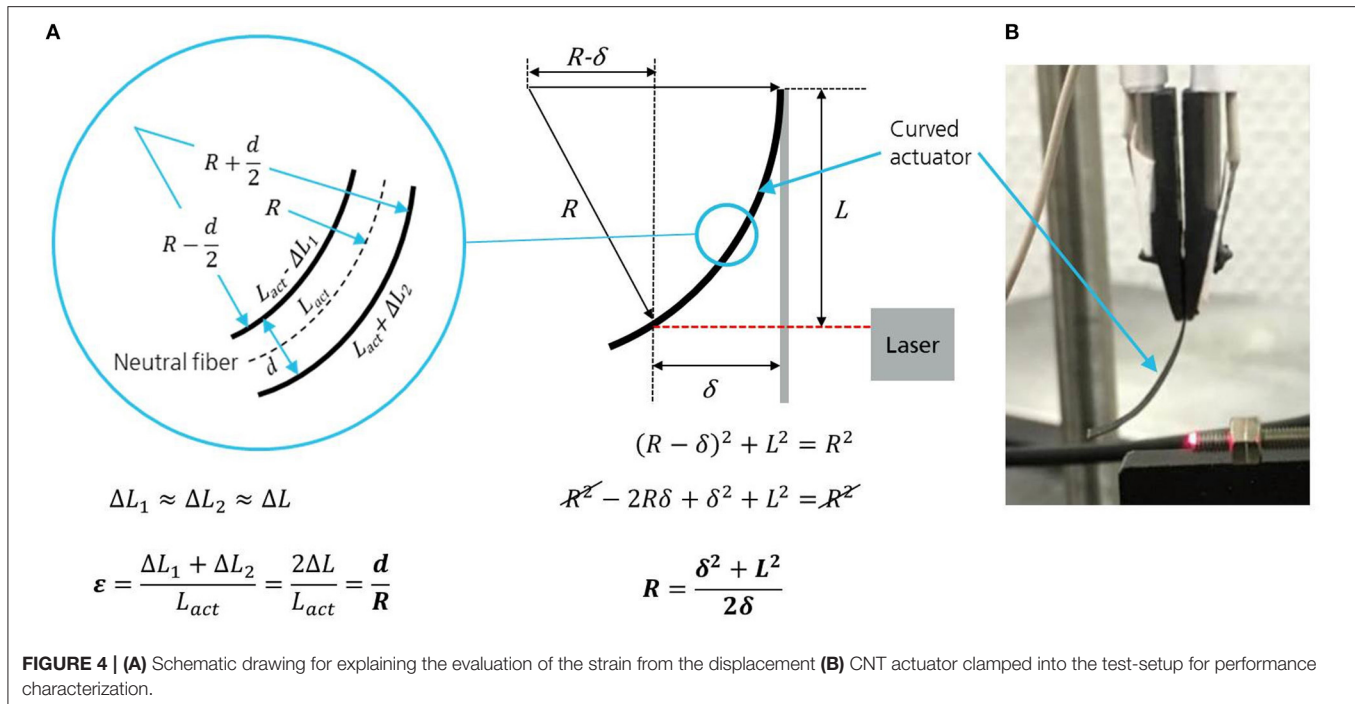
a fixture which provides electric contacts to both electrodes as depicted in **Figure 4A**, allowing the actuator to bend in both directions. The bending displacement is measured via optical laser triangulation (MicroEpsilon OptoNCDT 1302) with a range of 20 mm and an accuracy of $\pm 4 \mu\text{m}$. Lateral bending curvatures as depicted in **Figure 4B** are neglected in this measurement setup. A force sensor (KYOWA LTS20GA, 500, 0.01 mN resolution) is mounted on the moving part of a horizontally adjustable servo slide (Nanotec Munich KOWI), providing position resolved blocking force measurements on one side of the actuator specimen. A potentiostat triggers the actuation by providing a predefined tunable voltage level with high accuracy, varying the electric current according to the actuator's present impedance. Other parameters obtained by the measurement setup are electric current values, motor positions, temperature variations and heat radiation images, which are not further illuminated in this article. All measurement devices are connected to a National Instruments NI PCIE-6363 DAQ card and linked with a connector block NI SCB-68A for signal-PC-interface to the motherboard. All parameters and devices are controlled by a

central LabVIEW interface for direct display and automated data storage.

For thin actuator strips the induced strain difference ε can be directly calculated by measuring the free tip displacement δ of a clamped actuator using equation 1:

$$\varepsilon = \frac{2d\delta}{L^2 + \delta^2} \cdot 100\% \quad (1)$$

L is a fixed distance from the clamping of the actuator, marking the free length where the tip displacement δ is measured, whereas d is the thickness of the actuator strip. **Figure 4A** helps to understand the relationship between bending curvature and induced strain difference. R is the curvature radius and ΔL_1 , ΔL_2 are the induced length changes in each electrode. Equation (1) holds for small deflections so that it can be assumed that the neutral fiber does not change its length after bending and deforms into an arc. Thus a uniform bending curvature has been assumed for the actuator displacement, which is fairly accurate for fully actuated bending states. By measuring the Young's modulus of the stretched or squeezed electrode layers it is possible to obtain



the induced stress values of each actuator. Tested actuators that were assembled with fully printed MWCNT electrode layers showed induced bending strains of 1.4% and blocking forces of up to 30 mN at ± 2.5 V_{pp} applied square-wave voltage and 0.05 Hz actuation frequency at room temperature. Thicker actuator electrodes lead to higher bending forces while an overall thinner actuator results in a faster speed and larger displacement.

Actuator Encapsulation

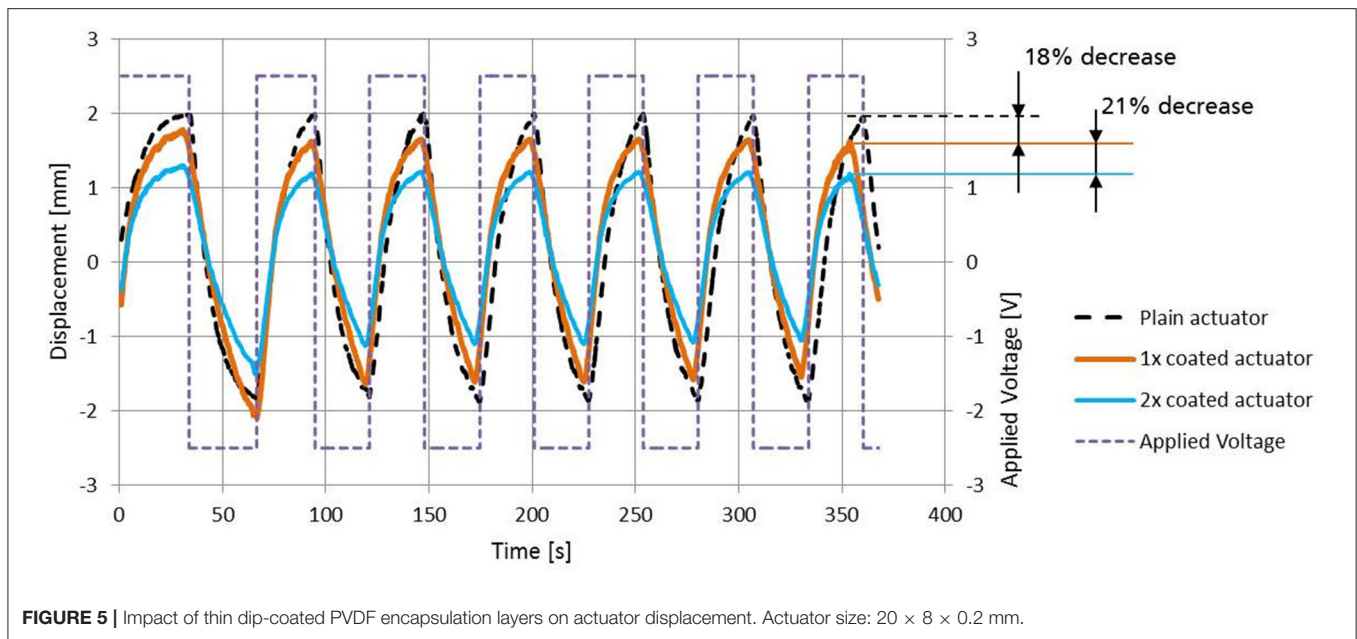
After assembly of the active layers and embedding the electric contact materials, the actuators are still in their natural form and their conductive electrode surfaces are directly exposed to air and humidity and thus capable of interacting with the surrounding environment. Encapsulation is deemed necessary for (a) providing a strong and anti-abrasive but flexible guard layer against mechanical disruption forces and (b) protecting the complex electrochemical processes inside the IEAP actuators and sensors from the influence of ambient humidity and (c) for electrical insulation and safety purposes. Various encapsulation materials like PDMS, PU, nitrocellulose, and paraffin-composites have been tested (Rinne et al., 2019). For this project it was determined to choose PVDF for encapsulation, because this material already serves as the backbone polymer for both electrode and separator layers. A good adhesion of the encapsulation layer to the actuator surface was expected. It was found that dip-coating of single actuator elements into a solution of PVDF in 4M2P (0.5 wt%) resulted in a thin layer (10–25 μ m) of PVDF deposited around the actuator. Tests showed that such encapsulation yields a moderate dielectric behavior for electrical insulation and slows down the penetration of water vapor into the active layers of the actuator (Punning et al., 2014). However, the free-tip bending displacement of coated actuators decreases

considerably with each additional encapsulation layer applied (Figure 5). This is because the bending resistance grows with an increase in non-active material thickness.

DESIGN, MANUFACTURING AND TESTING OF ACTIVE BUILDING SKIN DEMONSTRATORS

Evaluation of Aperture Actuation Kinematics

There are many possibilities to create controllable apertures in tensioned membrane surfaces using soft bimorph bending actuators. Depending on their shape, their mechanical attachment to the membrane and their power capabilities, different deformation characteristics can be achieved. It was generally assumed that the passage of air should be permitted in the actuated state (open) and blocked in the non-actuated state (closed). The process of opening will be performed by applying a voltage of certain polarity to the actuator while the process of closing will be accomplished (or assisted) by switching to the opposite polarity. Apertures can be created by widening slots that were originally closed, lifting flaps that were flush with the surrounding surface or by bending of formerly plain strips covering a hole in the membrane surface. Figure 6A shows a variety of potential motion principles that could be accomplished with IEAP bending actuators. The depicted shape-changing surface elements can either consist of thin IEAP actuators themselves or they are a passive flexible material (possibly the same material as the membrane) and their deformation is induced by buckling, bending or twisting motions of IEAPs attached underneath. Some of the geometric patterns could also



be used for sensing differences in air pressure produced by wind loads onto the membrane.

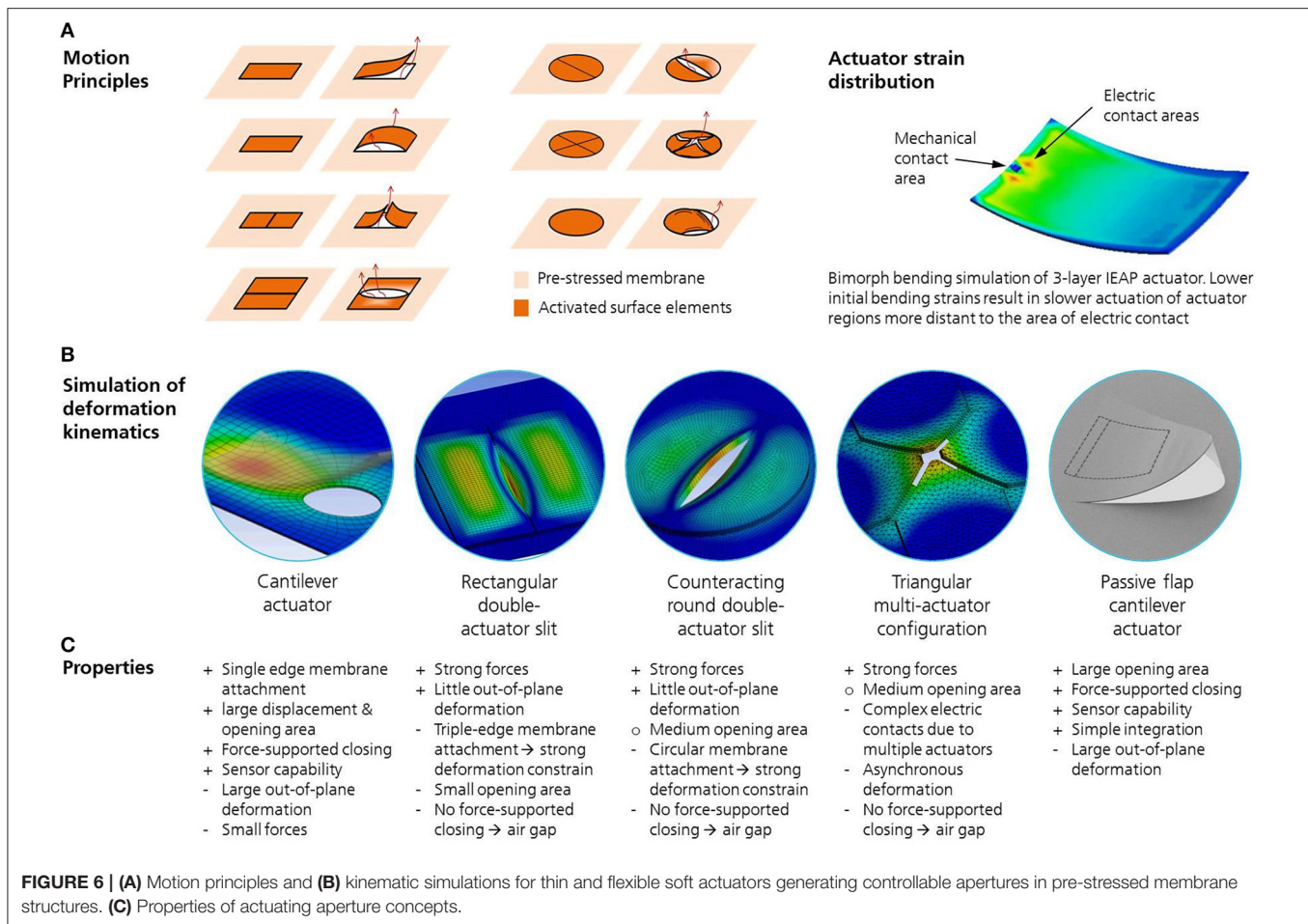
The finite element method (FEM) has been chosen to yield viable information about the deformation kinematics of IEAP actuators of different configurations attached to tensioned membranes (**Figure 6B**). Using ANSYS Workbench, the actuation is virtually initiated by a thermal load assigned to the electric contacts of the actuator. It causes the actuator electrodes to expand and to shrink, respectively, due to different thermal expansion coefficients assigned to the two electrodes (Addinall et al., 2014). By matching the thermal conductivity parameters of the electrode material with measured deformation data from rectangular bending actuators, a realistic simulation model could be implemented that is able to predict the motion kinematics of any actuator shape. A transient thermal simulation was performed that takes into consideration the transmission-line effect, which attributes for the slower actuation of actuator regions more distant to the area of electric contact. The main simulation target was to find suitable arrangements, sizes and shapes of IEAP actuators that produce the largest ratio of projected opening area per membrane area occupied by the actuator arrangement. The actual number of adaptive apertures needed per total membrane area depends on the climatic conditions of the target building and other construction settings such as the façade orientation, the volume of the interstitial membrane space and desired thermal insulation properties.

As a result of the analysis several actuator shapes and deformation kinematics materialized as viable configurations for the proposed application scenarios. The most efficient aperture configuration yielding the largest projected opening area was found to be the forced out-of-plane deflection of passive flaps being bent by soft actuators attached to their lower surface (passive flap cantilever actuator, **Figure 6**). The aperture configuration with the least out-of-plane motion and

yet considerable opening characteristics was found to be a slit expansion generated by two counteracting actuators positioned underneath the edges of the slit. Initial plans to utilize the actuators themselves as opening flaps or slit generators were discarded in regards to the much larger actuator sizes required, rendering their higher material costs and energy demand as inefficient.

Demonstrator Design

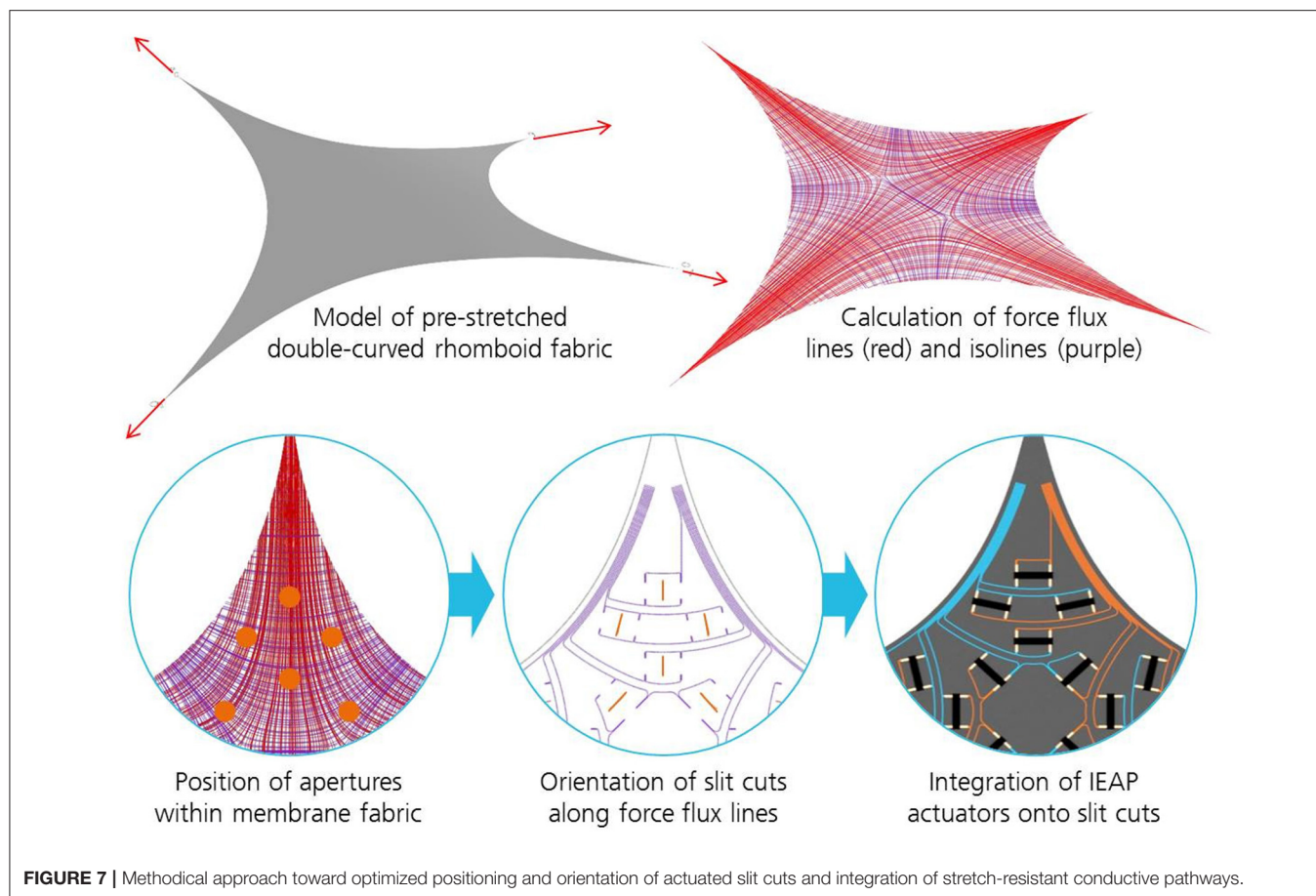
Two demonstrators were designed to investigate the actuation and sensing behavior of IEAPs integrated into a fabric membrane skin. The first demonstrator comprises a double-curved multilayer membrane with controllable apertures in the inner layer. These apertures allow for a controlled ventilation of the interstitial space between the two layers and thus prevent the necessity of mechanical air blowers currently employed to avoid condensation. This setup represents a new approach to accomplish a switchable breathability in building skins. The reason for the targeted double curvature was to demonstrate the potential of soft IEAP actuators being employed despite complex membrane shapes and in the presence of multilateral tensile forces. A rhomboid shaped fabric with four equally dished edges was chosen because it permits the creation of a double curvature by pulling apart the two pairs of opposite corners, each with divergent vertical components. In this pre-stressed double-curved state, all apertures in the fabric must remain closed if not actuated. One solution is to orientate linear slit cuts (as presented in **Figure 6**) in the direction of the main flux of forces within the fabric so that lateral forces are minimized and the edges of each slit are not pulled apart (**Figure 7**). The stress distribution was analyzed using parameterized geometric models compiled in Karamba3D and running optimization algorithms regarding the positioning and orientation of the slit cuts. Karamba3D is a parametric structural engineering tool



(Preisinger, 2019) that can run optimization loops on mechanical problems by changing structural parameters such as material thicknesses, cross sections, numbers of load bearing elements and spacing and positioning of these elements within given boundary conditions for internal stresses, strains and structural dimensions. It also proposes auxiliary construction measures if the solution space within a constrained approximation loop is empty. The objective of the optimization for this project was to fill the available fabric area with fifty apertures per square meter that preferably are evenly spaced, translating to twenty properly oriented slit cuts that had to be distributed evenly on the fabric's surface of ~ 0.45 square meters. Additionally, the routing design of the conductive pathways powering the apertures should have minimal length and run either parallel or perpendicular to the local main flux of forces to minimize cable distortion and seam failure when the membrane is stretched into a 3D shape. Another aim of an optimized routing pattern was to have two spatially separated connection areas on the demonstrator membrane, each one collecting all conductive pathways of the same polarity. This arrangement prevents the complex routing patterns that would emerge if each actuator's electric connections had individually separated access points. Furthermore, separated connection areas make it

easier to attach electronic control units to power the individual actuators (or to monitor the sensor signals, respectively). Some actuators are connected individually and others are combined to actuator clusters with a single pair of electric connections. A change in routing patterns can easily be implemented due to digital design methods that allow a straightforward transfer to automated fabrication techniques. The conceptual design approach of actuator integration and distribution is depicted in **Figure 8** for both demonstrators. The opening of the slit cut will be triggered by one actuator positioned on each side of a slit cut, one bending upwards and one downwards. Due to their flexibility the actuators will adapt to the local curvature of the membrane fabric without losing their motoric functionality.

The second demonstrator will show both actuator and sensor functionalities in a single planar membrane. Parabola-shaped passive flaps are intended to deflect outwards when the IEAP actuator mounted underneath creates a bending movement. Under wind loads, the flaps should deflect inwards and provide an electrical signal that can be processed by an electronic monitoring and control unit. 17 flap cuts with three different sizes are distributed in a regular pattern on the fabric surface, without any need for algorithm-assisted optimization.



Demonstrator Manufacturing

This subsection describes the materials, techniques and manufacturing procedures that were used to build the physical demonstrators taking into consideration the findings in simulation-assisted design of aperture kinematics and electric routing patterns described above.

Preparation of Textile Membrane Fabric

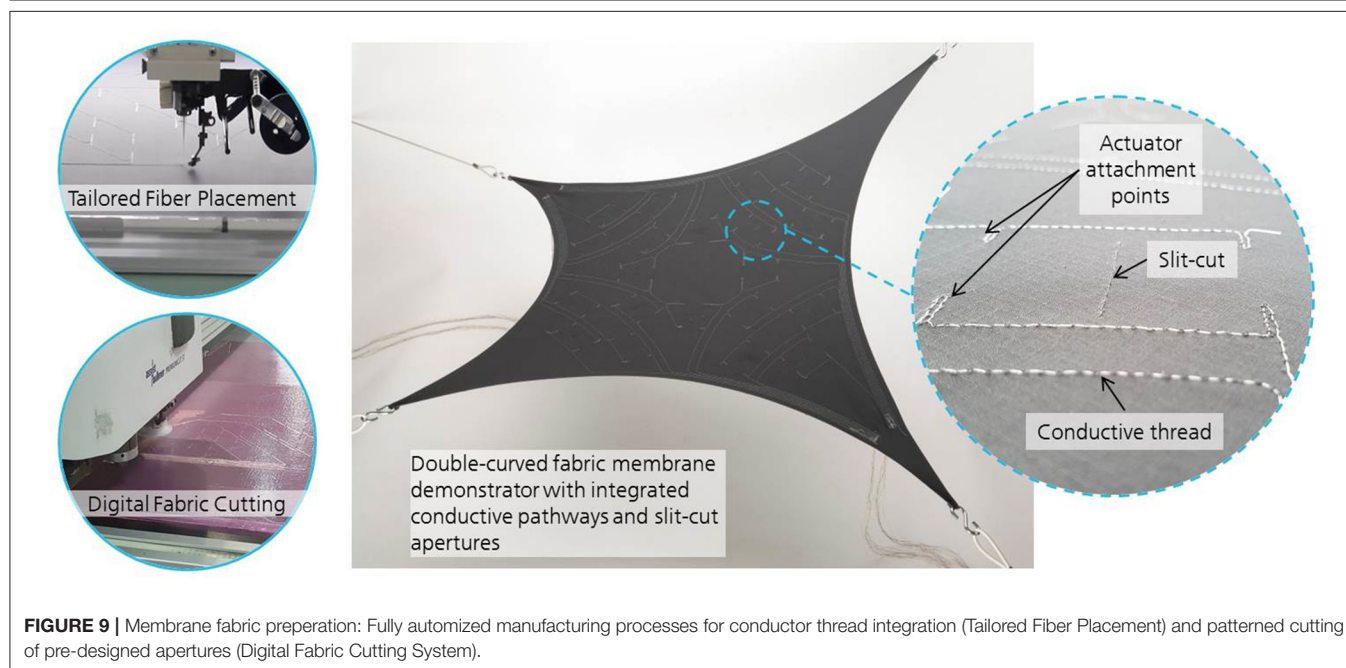
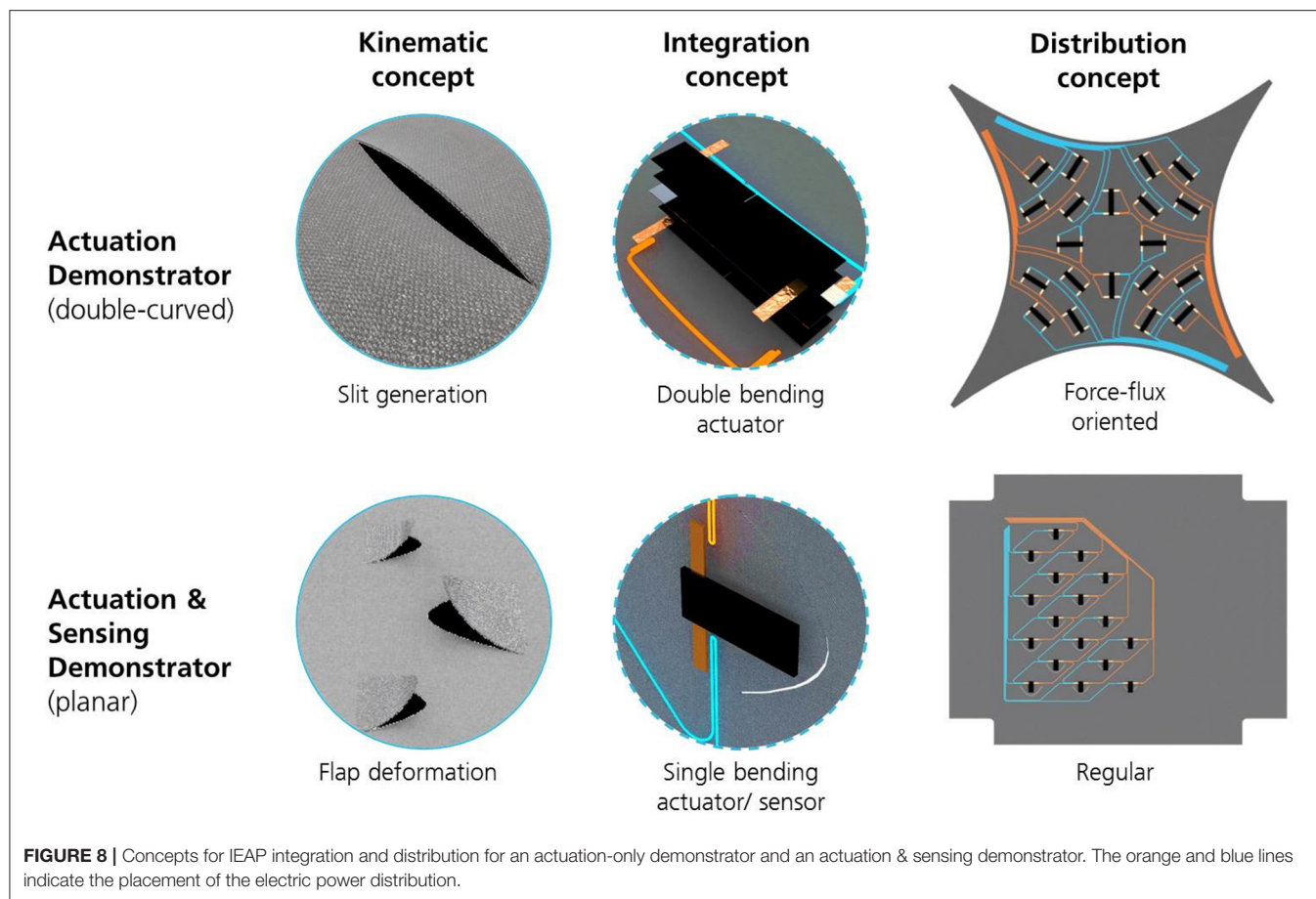
For the demonstrator membrane material a gray-colored high-strength polymeric fabric made of 47% polyester, 39% polyurethane, and 14% polyamide was purchased from Tolko Stoffe GmbH in Germany. The fabric contains two thin layers of a waterproof Gore-Tex membrane (expanded Polytetrafluoroethylene - ePTFE) and is fitted with interwoven ripstop reinforcement threads in a crosshatch pattern making it highly resistant to tearing and ripping. This fabric was used for both demonstrators. By employing the same automated methods for the two fabric membranes, they were fitted with electric conductors for power distribution and received their individual patterns of aperture cuts. The conductive pathways were formed by the same conductive threads previously tested for the integrated IEAP contacts (Madeira HC 12 silver plated conductive thread). Following the pre-designed electric routing pattern, the threads were attached onto the fabric using a fully

automated Tailored Fiber Placement (TFP) machine (Tajima 4-head embroidery machine). In this process the thicker conductor thread is uncoiled from the reel and placed onto the fabric by a cantilever which is attached to the machine's moving stitching head. Simultaneously, a thin auxiliary thread is alternately stitched over the conductor thread locking it firmly into place onto the fabric underneath. This stitching process proved to be a simple and effective method to generate arbitrary yet precise conductive pathways on any fabric surface.

The aperture cuts were made with a fully automated digital 2-axis multi-ply cutting machine (Assyst Bullmer Premiumcut ST). Via software interface it was possible to automatically assign the cutting patterns that were developed during the design stage to the machine's itinerary and transfer them onto the membrane fabric. **Figure 9** illustrates the automated manufacturing steps for the first demonstrator and depicts the resulting membrane fabric equipped with conductive pathways, actuator attachment points and integrated slit cuts.

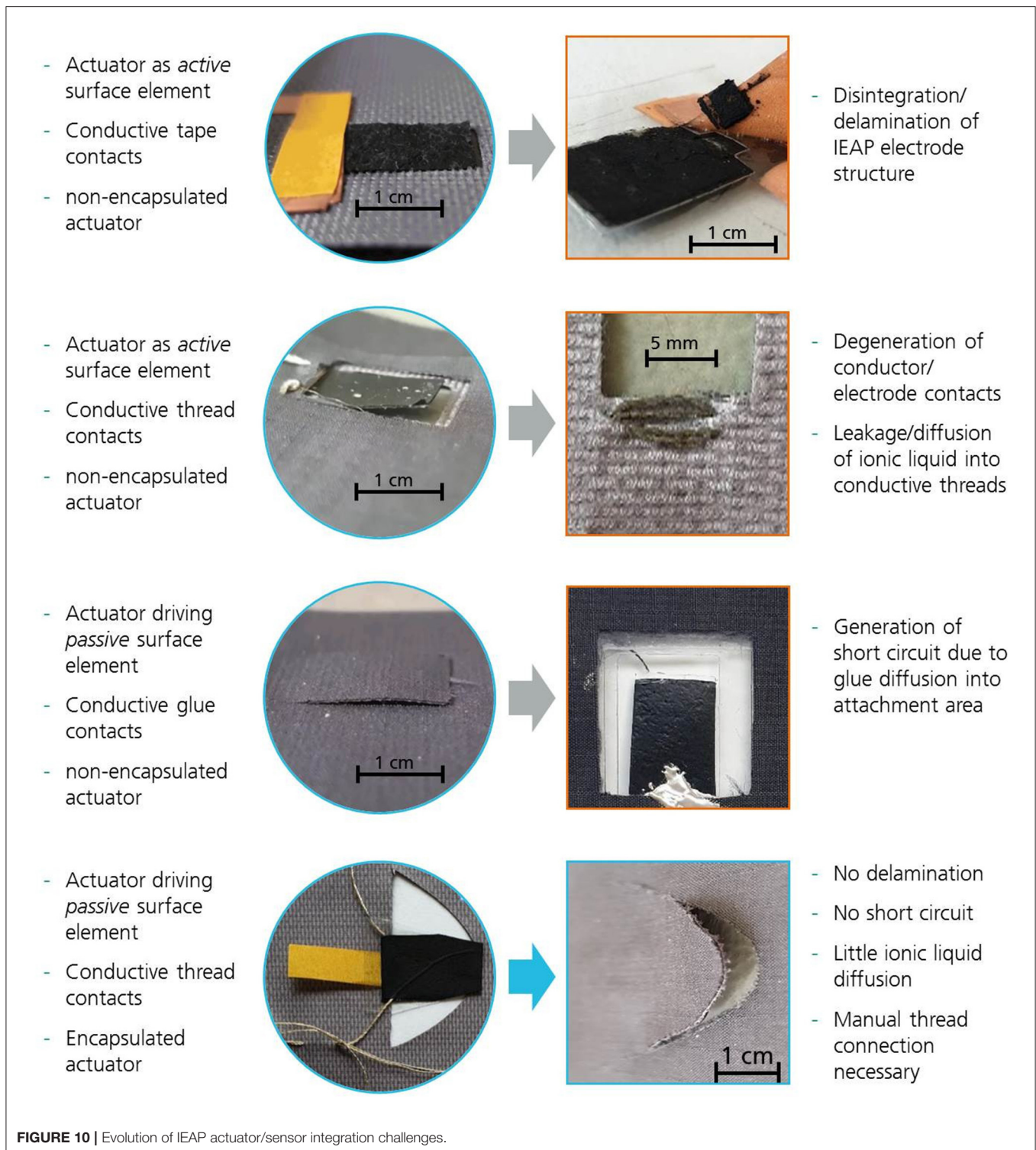
Actuator Integration

Before turning to the actual demonstrators for IEAP integration, lab-scale tests with individual actuator geometries, aperture designs and electrical connection alternatives were performed (**Figure 10**). Initially, the focus was on integrating rectangular non-encapsulated CNT actuators with no external electric



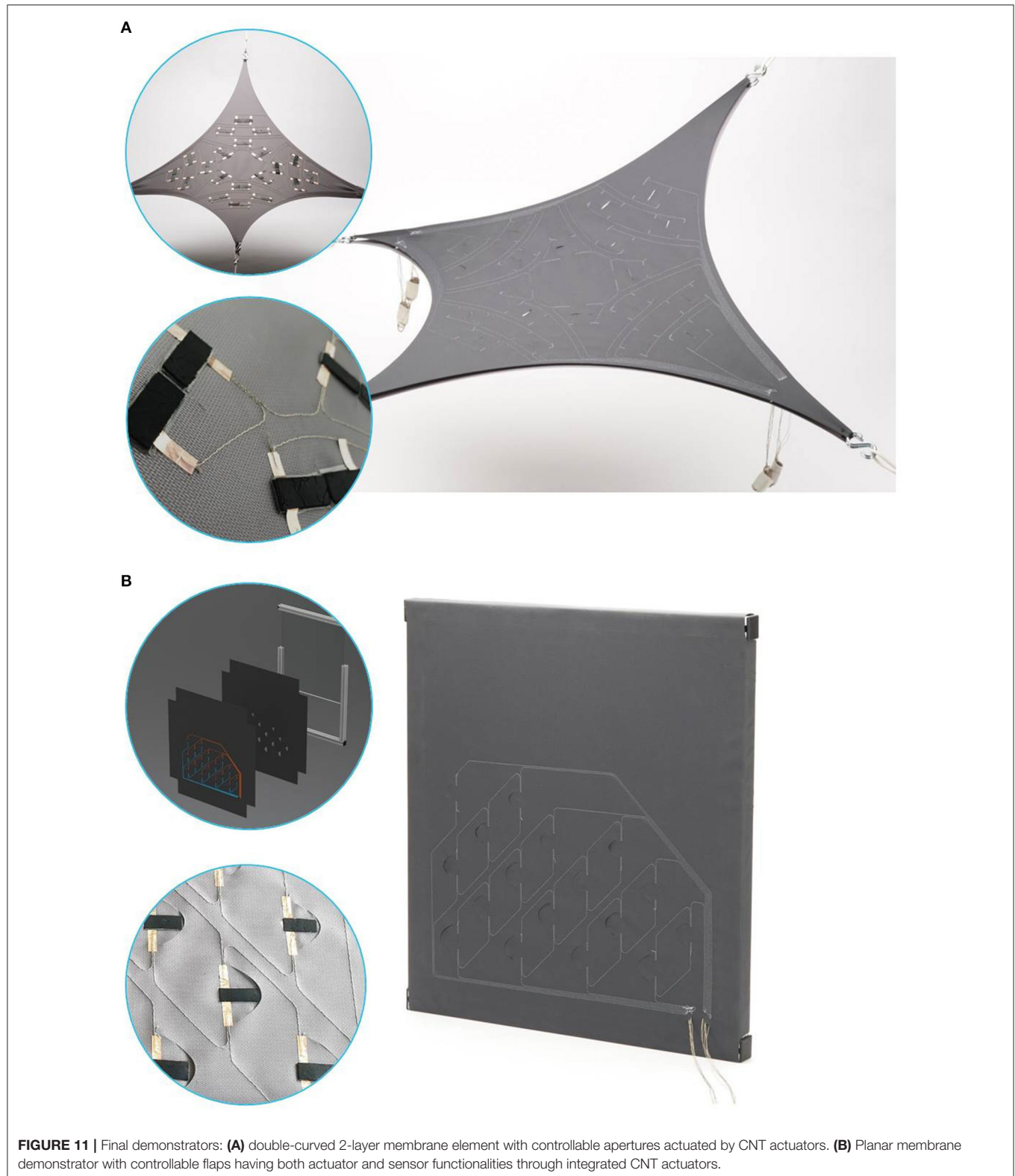
contacts by means of conductive epoxy glue applied to the electrode surfaces. The solvent-based glue, despite its low contact resistance, diffused into the fabric and beyond the intended

attachment area during pressure-assisted curing and in many cases caused a short circuit between the two actuator electrodes. Tests with encapsulated and thread-contacted specimen showed



no short circuit, but their electrical connection to the conductive pathways is only feasible by manually knotting the threads together. The most simple and robust integration method found was to apply the copper adhesive contact tapes to the provided conductor threads stitched into the fabric. The

positive connection between the fabric and the actuator surface was ensured by a thin layer of double-sided adhesive tape. 40 equally shaped CNT actuators for 20 distributed apertures were integrated into the rhomboid-shaped membrane fabric of the first demonstrator and 17 actuators having the same size



completed the second demonstrator with its 17 parabola-shaped flaps of three different sizes. Both demonstrators – equipped with integrated IEAP actuators – are depicted in **Figure 11**.

Experimental Testing

The displacement and blocking force of all actuators were measured using the LabVIEW-controlled automated test setup

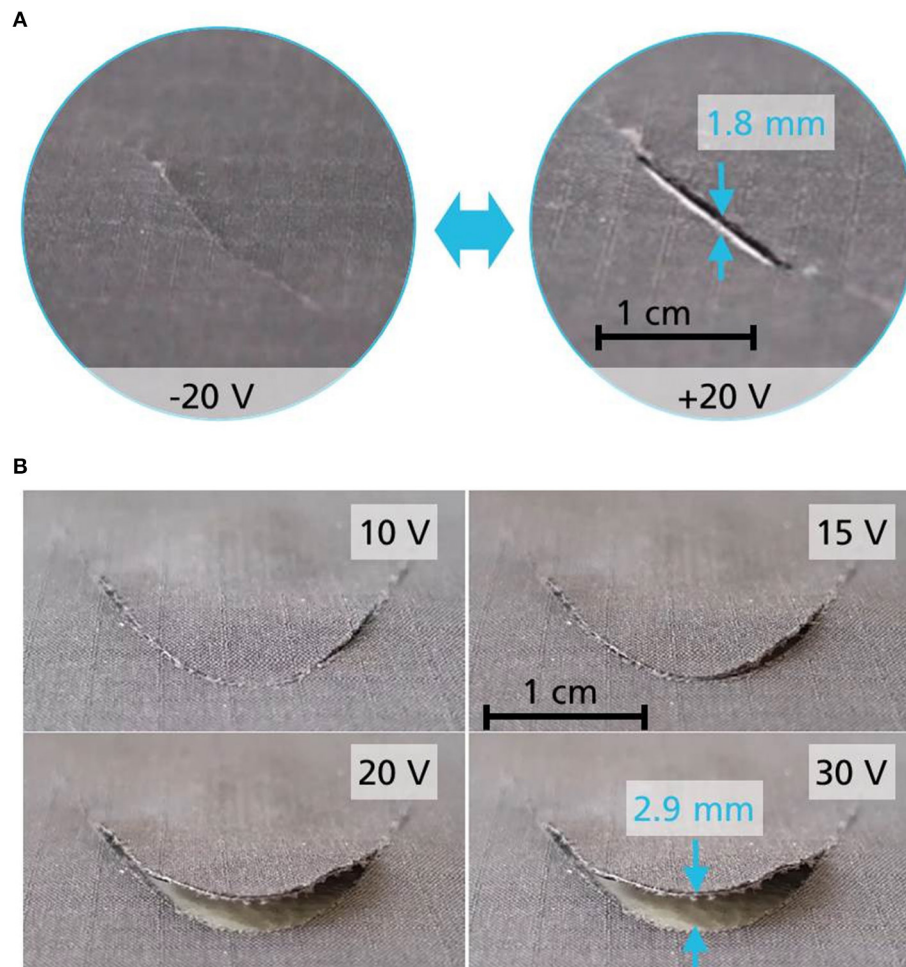


FIGURE 12 | Examples of successfully controlled membrane apertures in **(A)** the double-curved slit cut demonstrator and **(B)** the planar flap cut demonstrator.

before they were integrated into the demonstrators. All actuators produced for both demonstrators had a default length of 2.5 cm, a width of 1 cm and a thickness of 300–400 μm . Both bending displacements and blocking forces were measured at 10 mm distance from the clamping (electric contact area). The measured displacement values were converted into induced bending strain values following Equation (1). Out of more than 100 actuator specimens made, only those that yielded reproducible bending strains between 0.8 and 1.2% and blocking forces between 10.5 and 21.5 mN were selected. These results were obtained with an applied square wave voltage of 2.5 V and 0.05 Hz actuation frequency. Due to encapsulation, these performance values were slightly lower compared to those of non-encapsulated printed actuators (1.4% and up to 32 mN, respectively).

For measuring the actuation performance of the integrated actuators, the pairs of conductor threads leading to the distributed apertures were connected one by one to an adjustable power source. Due to the varying length of the conductor threads and the high contact resistances at the actuator interfaces it was necessary to adjust the applied voltage levels to much

higher values for the actuators to react. For the double-curved demonstrator, the maximum opening distances of the slit-cuts were measured at the actuation peak. For the flap demonstrator, the maximum tip deflection was measured.

On behalf of testing the sensing capabilities of the IEAPs integrated into the second demonstrator, the loose ends of all conductor threads leading to the distributed flaps were connected to the channels of a high-precision galvanostat/potentiostat analysis device (Ivium Octostat 5000) with low current and low voltage measurement capability. The voltage range set to 10 mV and 500 Hz sampling rate, it is possible to detect and measure very low potential differences as low as 0.01 mV with a sufficient time resolution required to resolve high-frequency phenomena during sensitivity testing. Two different test scenarios were performed.

In a first scenario, the flaps were subjected to a smooth and controlled alternating displacement in both inward and outward direction, simulating an external wind pressure. It is clear that this experimental approach does not accurately reproduce actual deformations induced by environmental forces, but this

procedure was imposed to generally investigate the nature of the feedback response. The displacement and output signal were simultaneously measured. According to Kamamichi et al. (2007) a small voltage should be measured as an output signal which is expected to have almost proportional values to the displacement of the IEAP sensor. In a second scenario, a sudden forced displacement of rectangular pattern was applied to the tip of a sensing flap resting in neutral position (flush with the membrane surface). This pulsed stimulus was repeated irregularly over a 50 s period and varying holding durations. The voltage response signals of both scenarios are depicted in **Figure 13**.

Power Consumption and Life Cycle Assessment (LCA) of Membrane Elements With Integrated CNT Actuators

The environmental impact of an adaptive IEAP-enhanced building skin element has been analyzed by a “cradle to grave” LCA approach, taking into account all energy and materials needed during production, operation and end-of-life treatment. For all three stages the cumulative energy demand (CED) and the carbon dioxide equivalent (CDE) were calculated with the aid of an LCA software tool called GaBi-ts 2019 from spheraTM. The CDE describes the global warming potential (GWP) of the energy and materials released during the system’s life cycle and thus better reflects the long-term effects of the proposed system. The calculation of CED and CDE was based on the German electricity mix in 2016 and is thus in accordance with reference scenarios recommended by the European Union.

The CED to produce such a system involves the whole inventory of materials and energy necessary for synthesis, dispersion and printing processes required to build the proposed components and structures. The amount of raw materials was calculated for a scenario with fifty actuators built into one square meter of fabric membrane, one actuator consisting of two electrodes and one electrolyte layer (separator), having total dimensions of 2.5 x 1.0 cm x 380 μ m. For making one electrode, one needs 1.9 mg of NC7000TM MWCNTs, 8.6 mg of polyaniline, 13.7 mg of PVDF (HFP) backbone polymer, 20.8 mg ionic liquid BMI-BF₄, 1.075 g of 4M2P organic solvent, 0.2 g copper adhesive tape, 0.1 g silver coated conductive thread and negligible amounts of dispersing agents. For making one separator, 18 mg of PVDF (HFP), 18 mg of BMI-BF₄ and 220 mg of 4M2P solvent are needed. Assumptions were made for the silver content of the conductive threads (10%), the exact material thickness of the fabric membrane’s top layer (50 μ m) and the energy demand for the catalytic carbon vapor deposition (CCVD) process for synthesizing MWCNTs, which was interpolated from bibliographical references. All catalytic materials needed for the CCVD process such as cobalt, manganese and magnesium, however, were accurately taken into account. Furthermore it was assumed that the full amount of solvent will evaporate into the air during the drying process after the electrode and separator layers are printed.

The calculation of the CED during system operation was based on the assumption of five actuation events with a determined holding period of 30 min per day, on average. Furthermore, a

total of 8,000 cycles was considered to be a realistic assessment of the actuator’s capabilities, yielding a service life of 4.4 years. The energy needed for opening and closing procedures were calculated by the amount of charge inserted into one actuator. The opening and closing requires 4.78 Joules while the holding period requires 81 Joules, which accumulates to a total of 22.6 and 8.26 MJ per year for the fifty actuators integrated into one square meter.

For the calculation of the CED for the end-of-life treatment it was determined that all materials shall be classified as hazardous waste and be disposed accordingly. Considering the fact that carbon nanotubes are considered as potentially hazardous and that there are indications that some species of ionic liquid – even at rare circumstances – may recombine to neurotoxic substances, this assumption is justified.

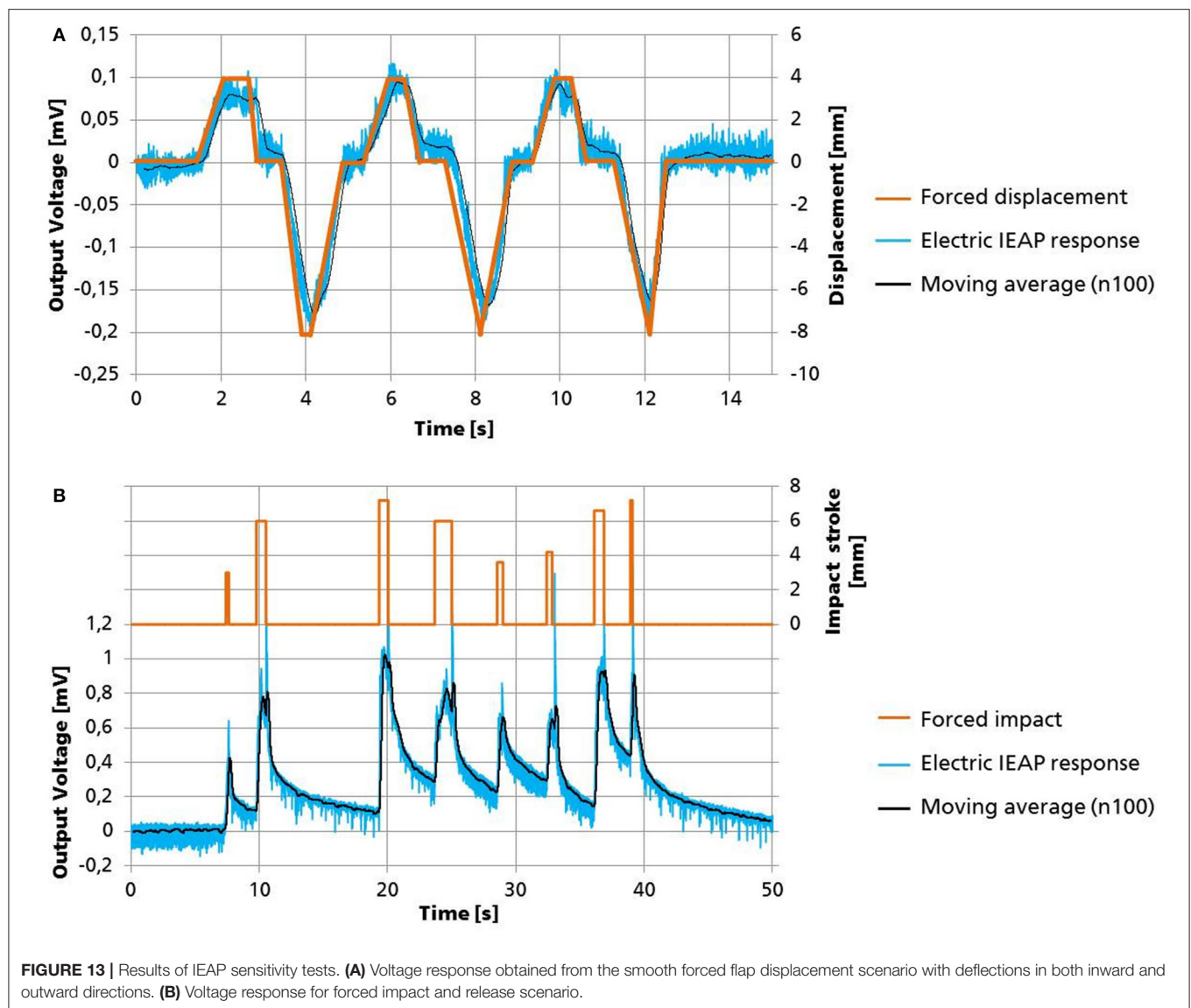
RESULTS

Actuation Properties of Integrated IEAPs

When directly connected to a constant voltage source (3 V), an actuator of the specified size will take ~20 s until it reaches full bending displacement. During this charging time a peak current of 0.8 A is measured that exponentially decreases to values of 15 mA and below where it will remain for the duration of the measurement. The amount of charge entering the actuator within the first twenty seconds was measured to be in the range of 3.18 Coulomb, resulting in a total actuator capacitance of 1.06 Farads and an energy input of ca. 4.77 Joules.

To counteract the low thread conductivities and high contact resistances in both demonstrators, the square wave voltage levels applied to the individual conductive pathways were slowly increased in a cautious approach of 5 V steps. Every test was conducted twice, first maintaining the testing frequency of 0.05 Hz and second holding the voltage levels at constant polarity until no further reaction could be detected. For the double-curved demonstrator, no displacement response of any IEAP actuator was observed below 10 V. At 15 V some membrane deformation was visible around individual slits, but only at 20 V a true separation of the first slit edges could be identified. The maximum slit opening distance obtained was 3.2 mm at 35 V for one aperture, measured between the highest and the lowest point of the upward and downward bending slit edge, respectively. Eleven actuators out of 40 did not perform any bending motion. Out of 20 apertures only 12 generated true openings, most of which did not exceed a maximum opening distance of 2.0 mm even at higher voltage levels. **Figure 12A** shows a slit cut aperture generating a gap of 1.8 mm upon polarity switching of \pm 20 V.

The same procedure was applied to the second demonstrator with passive flaps. Here again, the first out-of-plane flap deformations were observed at 15 V with no actual separation of the flap from the membrane surface. At the 20 V level six out of 17 flaps produced small openings allowing for air to pass through the membrane while at 30 V all flaps but one visibly bent out of the surface with tip deflections between 2.1 and 3.4 mm. The highest tip deflection of 4.6 mm was measured at 40 V applied to one of the larger flaps located close to the voltage source connector. Some flaps showed a strong bending curvature



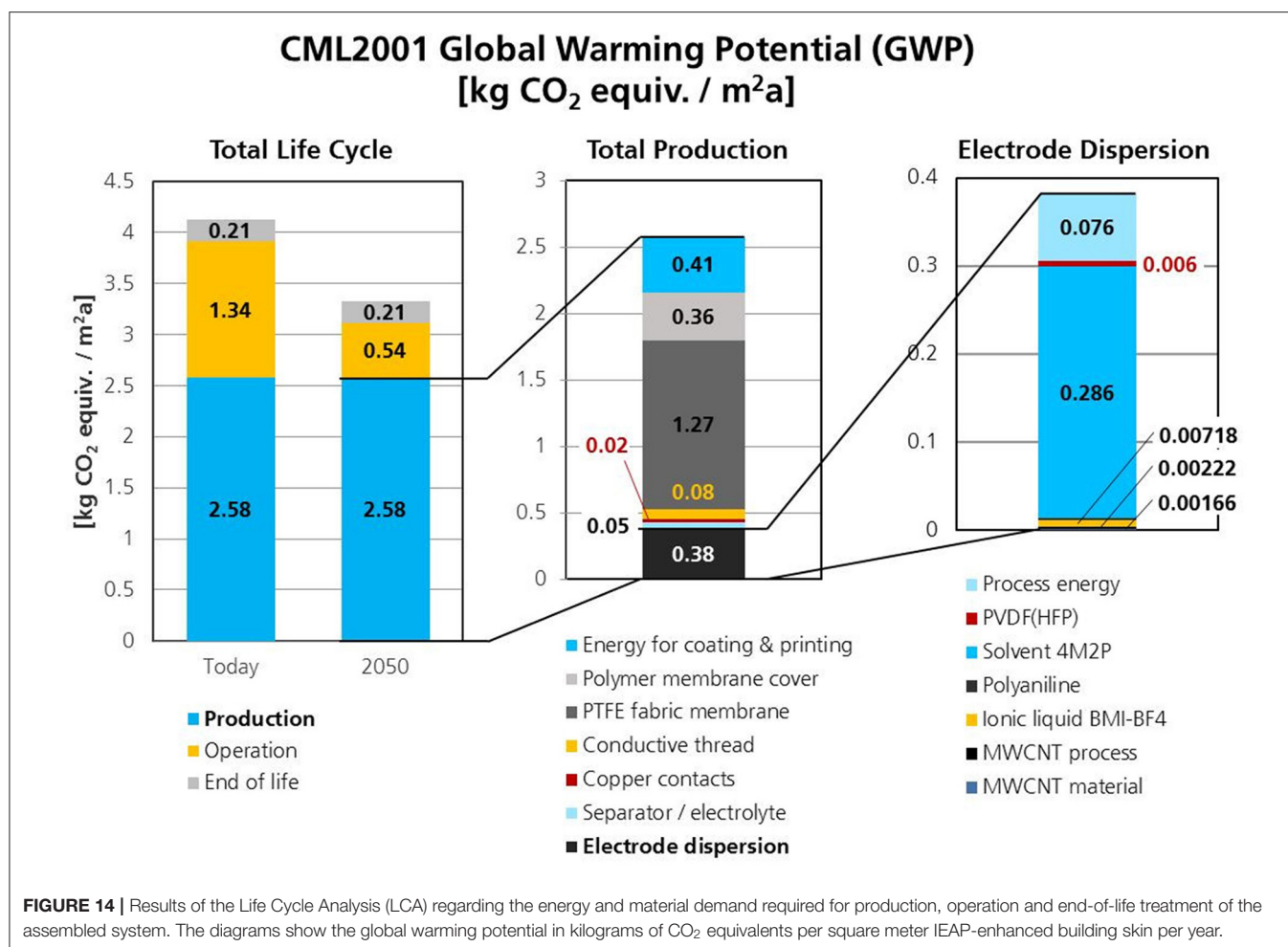
but did not open because the edges of the parabola shaped cuts in the fabric did not separate due to friction. Upon switching the polarity all previously deformed IEAPs performed a reverse closing motion until they passed the neutral position flush with the membrane surface. **Figure 12B** shows the actuation behavior of a medium-sized flap at different voltage levels applied to the conductive pathways, generating a 2.9 mm tip deflection at 30 V.

Sensing Properties of Integrated IEAPs

The scenario with a smooth displacement exerted on the membrane flaps with IEAPs attached underneath triggers a voltage signal that is almost perfectly proportional to the displacement, with only minor latency. The output signal is depicted in **Figure 13A** and goes well in line with the findings of Kamamichi et al. (2007). During the short holding intervals and at neutral displacement position the signal appears more rugged than during the active shifting periods. Furthermore,

at neutral position the signal offset increases as it appears to react with a shallower relaxation toward charge equilibrium. This proves that the electrochemical reactions within the IEAP react to the stop of motion in almost real time. The highest measured voltage levels obtained with this test did not exceed 0.1 V for an outward deflection of 4 mm and -0.2 V for an inward deflection of 8 mm. In general, sensors with longer conductive pathways transmitted lower voltage signals compared to sensors closer to the connectors of the measurement device. When they are connected with high-resistance conductive pathways, the increased voltage drop must be taken into consideration for the design and calibration of such membrane sensors.

The forced impact scenario depicted in **Figure 13B** triggers a sharp voltage rise of up to 1 mV at the beginning of the mechanical impacts, followed by a jagged holding period that ends with another sharp spike when the impact stroke is released. After the spike, the voltage level asymptotically decreases as the



flaps slowly relax back to their neutral position. Neither the impact stroke nor different holding periods seem to affect the slope of the relaxation curve. The relaxation curve shows about the same rate of decay for all performed impacts, even if the time intervals between impacts vary and one impact interrupts the relaxation phase of the previous impact. This is a sign for robust sensor functionality without hysteresis of such systems.

Life Cycle Assessment Results

The results of the LCA are given in **Figure 14**. For a realistic assessment of the true energy demand, the calculated CED values for the three stages of production, operation and end-of-life treatment were converted to total primary energy from non-renewable resources (PENRT) values. This was done considering a total energy conversion efficiency of 50% from the caloric energy content of the fuel to the energy output of the power plant. With this in mind, the physical unit of “mega Joules” (CED and PENRT) was converted into the more meaningful unit “kg CO₂ equivalents per square meter per year” (CDE and GWP) in consideration of the functional LCA unit being one square meter of membrane element per 1 year of operation for a total impact

period of 100 years. The PENRT values are 47.94 MJ/m²a for production, 16.5 MJ/m²a for operation and 0.66 MJ/m²a for end-of-life treatment. The GWP values are 2.58 kg CO₂ eq./m²a for production, 1.34 kg CO₂ eq./m²a for operation and 0.21 kg CO₂ eq./m²a for end-of-life treatment.

DISCUSSION

Summary

This article provides information about methods and results regarding the integration of soft and flexible IEAP actuators into planar and double-curved pre-stretched membranes. The scientific goal was to prove that IEAPs are principally capable of generating controllable apertures and to demonstrate that they have a promising potential to provide sensor functionality for adaptive building skins. In this article the complete process chain is described, including benchmarking of IEAP technologies, raw material selection, optimization of dispersion and printing techniques, application-specific post-treatment of IEAPs, system integration methods and automated testing procedures. Industrial manufacturing methods are presented including the adoption of cost-efficient substitute materials

and additives that are essential to produce CNT-type IEAP actuators and sensors faster and with better performance reproducibility and enhanced environmental stability. The described simulation assisted design approaches comprise the evaluation and verification of aperture actuation kinematics and the conceptual strategy for the positioning and distribution of actuators.

Evaluation of Actuation Performance

The general actuation behavior of integrated CNT actuators corresponds with the predicted actuation kinematics obtained via simulations. However, for the slit cut apertures of the first demonstrator their overall performance fell short of expectations, and especially the amount of dysfunctional actuators came as a surprise.

The causes of failure are manifold and range from electrode contacts detaching during the first operation cycle, electrode delamination and actuator deterioration due to electric hot spots within the electrode structure all the way to diffusion of heated electrolyte into the contacting threads and short circuits induced by manual handling and integration of actuators. Some of these phenomena such as hot spot generation are well-known from laboratory-scale prototypes and have been reported elsewhere. Other failure phenomena such as diffusion of heated ionic liquid into conductors are specific to this project and – to the best of the authors' knowledge – were encountered for the first time. Regarding actuators that failed during the first operation cycle, the high voltage levels applied to overcome the high contact and line resistances of the conductive pathways proved to be detrimental for some of the actuators. The voltage drop over line and contact resistances is proportional to the electric current flowing through the circuit (and thus through the actuator). Similar to charging a supercapacitor, the initial charging current will quickly decrease as electrochemical double layers form within the actuator electrodes. This decrease in current will cause a smaller voltage drop and consequently much higher given voltage levels at the actuator. Ultimately the voltage level will be much higher than the electrochemical potential window of the ionic liquid permits. Even though the given voltage levels were reduced manually during the actuation period, some actuators were destroyed by overvoltage before any deformation could be observed.

Evaluation of Sensing Performance

The proposed sensing functionalities of IEAPs integrated into membrane skins have been verified. Since the correlations between mechanical input and electric output are known and have now been confirmed, IEAPs might actually pose a viable alternative to other transducers, especially in areas where soft and flexible sensors have an advantage over their rigid and stiff counterparts, for example as health monitoring unit in soft membrane structures. Instead of employing high precision laboratory measurement equipment it is of course desirable to have compact analysis devices that are capable to measure and interpret the small voltage signals generated by deflected IEAPs. Field tests with optimized demonstrators exposed to real wind loads have yet to be conducted. A decline of the sensor

functionality over longer operation periods will most likely occur and should be investigated.

Derived Measures for CNT Actuator Optimization and Integration

The authors agree that it is essential to approach potential optimization measures concerning integrated IEAPs in two separate areas: actuator optimization and actuator integration. Regarding the actuator optimization, it is obvious that complex structures such as IEAP will not last forever, due to the decomposition of the polymer matrix and slow evaporation or leakage of electrolytes. As a result, the performance of IEAPs will in most cases decrease over time. The rate of performance drop depends mainly on the number of performed work cycles. This means that IEAPs need to be precisely tailored and optimized to fit their planned application scenario. The ionic liquid BMI-BF₄ has been chosen for this project because it provides a wide operational temperature window suitable for building applications. However, other types of ionic liquid have shown greater electrochemical activity and faster ion exchange rates that are more suitable for applications requiring higher actuation displacements and speeds. Optimization measures such as highly impermeable IEAPs encapsulations, force enhancement through actuator stacking and new electrochemically active nano materials and composites are currently explored by the authors and other scientists.

Regarding the actuator integration part, it is self-evident that conductive pathways with much higher electric conductivities are needed to power distributed actuators and sensors. The unpredictable contact resistances and low conductivities of the conductive threads triggered unprecise power settings for the connected IEAPs and resulted in unknown system states. It is essential to transfer sensor signals and electric power more reliably and over much longer distances. Thin copper cables might be a solution with similar automatable handling characteristics (TFP). Furthermore, these conductors should have electrical insulation just as the copper tapes used for integrated electrode contacts in order to shield them from environmental influences. Concerning the parabola shaped flaps in the second demonstrator the friction between the edges needs to be reduced to allow for a smoother and unobstructed opening.

General Evaluation of Potentials and Limitations and Future Outlook

This first-ever experimental approach of using IEAP technology in a building related application has shown that a practicable and reliable integration of such complex electrochemical devices remains a challenge, particularly because their performance is still highly sensitive to many non-application related factors. Material compositions, manufacturing techniques, auxiliary treatments and power controls have to be carefully designed and accurately tailored to yield desired performance characteristics in the first place. The main draw-back of IEAPs is their generally weak force generation, which was again demonstrated by this research. The improvements achieved in performance reproducibility and manufacturability came at a cost of even

lower bending forces which probably poses the greatest limitation for most potential future applications. In regards to building applications, the hydrophilicity of the ionic liquids may cause performance degradation over time due to humidity inevitably entering the three layer compound. If engaged for building physical outdoor missions, UV stability is also a topic that still needs to be addressed. Another question that will arise in this context is whether IEAP actuators or sensors will be affected by particle contamination and acidic or basic soiling. Overall, the results obtained for the actuation and sensing capabilities have demonstrated that it is principally possible to use IEAPs for generating controllable apertures in fabric tensile membranes. However, it requires further efforts of optimization to transfer the new discoveries to actual building envelopes.

Nevertheless the authors believe that the technical readiness of IEAPs is constantly improving and that more and more research related to macroscopic applications will emerge within the next few years. Now is the time to intensify the efforts to exploit their unique characteristics and to experiment with them in different areas of technology. They might have particularly high potential in areas where high forces are not required. Actuator arrays could be implemented for morphing indoor surfaces and structures, enabling novel ways of system interaction between users and technical appliances. For years car manufacturers and interior designers have been looking for soft materials that are capable of creating visual or haptic feedback via surface texturing. Once the accuracy and reliability has reached a sufficient state, these transducers may be employed in miniaturized high-precision applications such as optical systems, microscopic sample manipulation and biomedical use cases. The intrinsic sensor properties of IEAPs may promote intelligent fabrics in the field of textile engineering and wearables and provide integrated monitoring functionalities.

Investigations on building related usability of IEAPs in general and CNT based sensors and actuators in particular will be continued by the authors of this manuscript. The interdisciplinary collaboration with architects, process engineers and experts in building physics resulted in a very fruitful and enriching scientific environment with much room for new ideas and great infrastructure for generating and testing hardware. The learning curve has been steep so far, and everyone involved shares one common goal: to accelerate the rugged course toward real-world applications and market adoption of ionic electroactive polymers.

REFERENCES

- Abergel, T., Dean, B., and Dulac, J. (2017). *Towards a Zero-Emission, Efficient, and Resilient Buildings and Construction Sector*. Global Status Report 2017. International Energy Agency; United Nations Environment Programme.
- Addinall, R., Sugino, T., Neuhaus, R., Kosidlo, U., Tonner, F., Glanz, C., et al. (2014). "Integration of CNT-based actuators for bio-medical applications — Example printed circuit board CNT actuator pipette," in *International Conference on Advanced Intelligent Mechatronics*, (Besacon), 1436–1441.
- Aelenei, D., Aelenei, L., and Vieira, C. P. (2016). Adaptive façade: concept, applications, research questions. *Energy Proc.* 91, 269–275. doi: 10.1016/j.egypro.2016.06.218
- Anquetil, P. A., Rinderknecht, D., Vandesteeg, N. A., Madden, J. D., and Hunter, I. W. (2004). "Large strain actuation in polypyrrole actuators," in: *Smart Structures and Materials 2004: Electroactive Polymer Actuators and Devices (EAPAD)*, ed Y. Bar-Cohen (San Diego, CA), 380. doi: 10.1117/12.540141
- Attia, S., Bilir, S., Safy, T., Struck, C., Loonen, R., and Goia, F. (2018). Current trends and future challenges in the performance assessment of adaptive façade systems. *Energy Buildings* 179, 165–182. doi: 10.1016/j.enbuild.2018.09.017

DATA AVAILABILITY STATEMENT

The raw data supporting the conclusions of this article will be made available by the authors, without undue reservation.

AUTHOR CONTRIBUTIONS

RN: EAP benchmarking, simulation of actuation kinematics, electrical measurements, actuator manufacturing, printing technology, life cycle assessment, and conclusion. NZ: actuator manufacturing, actuator testing, dispersion technology, actuator integration, and electric contact integration. JP: membrane fabrics, architectural input, and soft robotics. YT: introduction and target specification. JS: actuator manufacturing and industrial upscaling. IK: carbon nanotubes and dispersion technology. HD: bioinspired materials, benchmarking, master thesis supervisor, and adaptive architecture. TB: project leader, industrial manufacturing and upscaling, production efficiency, and soft robotics. All authors contributed to the article and approved the submitted version.

FUNDING

The research presented in this paper was conducted within the framework of the Collaborative Research Center CRC 1244 (SFB1244, sub-project C03) Adaptive skins and structures for the built environment of tomorrow installed at the University of Stuttgart in the year 2017, which is supported by the German Research Foundation (DFG).

ACKNOWLEDGMENTS

The authors are indebted to the German Research Foundation and all partners that contributed to the development of industrialized dispersion and manufacturing processes of ionic electroactive polymers. A special thanks goes to the Fraunhofer Institute for Manufacturing Engineering and Automation IPA for providing parts of the necessary manufacturing and measurement equipment needed to build and characterize these novel materials. The authors would also like to thank Prof. Dr. Werner Sobek, head of the Institute for Lightweight Structures and Conceptual Design (ILEK) at the University of Stuttgart and Speaker of the CRC 1244 for the exchange of ideas and for providing valuable input regarding architectural standards and building-physical specifications.

- Baughman, R. H., Cui, C., Zakhidov, A. A., Iqbal, Z., Barisci, J. N., Spinks, G. M., et al. (1999). Carbon nanotube actuators. *Science* 284, 1340–1344. doi: 10.1126/science.284.5418.1340
- Bay, L., West, K., Sommer-Larsen, P., Skaarup, S., and Benslimane, M. (2003). A conducting polymer artificial muscle with 12% linear strain. *Adv. Mater.* 15, 310–313. doi: 10.1002/adma.200390075
- Berardi, U. (2010). Dielectric electroactive polymer applications in buildings. *Intellig. Buildings Int.* 2, 167–178. doi: 10.3763/inbi.2010.0043
- Chang, L., Liu, Y., Yang, Q., Yu, L., Liu, J., Zhu, Z., et al. (2018). Ionic electroactive polymers used in bionic robots: a review. *J. Bio. Eng.* 15, 765–782. doi: 10.1007/s42235-018-0065-1
- Cho, M., Seo, H., Nam, J., Choi, H., Koo, J., and Lee, Y. (2007). High ionic conductivity and mechanical strength of solid polymer electrolytes based on NBR/ionic liquid and its application to an electrochemical actuator. *Sens. Actuators B. Chem.* 128, 70–74. doi: 10.1016/j.snb.2007.05.032
- Creemers, J., Palla, N., Buck, D., Beck, A., Biesinger, A., and Brodkorb, S. (2016). Analysis of a translucent insulated triple-layer membrane roof for a sport centre in Germany. *Proc. Eng.* 155, 38–46. doi: 10.1016/j.proeng.2016.08.005
- Decker, M. (2013). “EMERGENT FUTURES: nanotechnology and emergent materials in architecture,” in *Conference of Technics of Teaching* (Newport, UK: Building Technology Educators Society).
- Dewidar, K. (2013). “Living Skins: A New Concept of Self Active Building Envelope Regulating Systems. (United Arab Emirates).
- Fukushima, T., Asaka, K., Kosaka, A., and Aida, T. (2005). Fully plastic actuator through layer-by-layer casting with ionic-liquid-based bucky gel. *Angew. Chem. Int. Ed. Engl.* 44, 2410–2413. doi: 10.1002/anie.200462318
- Haase, W., Klaus, T., Schmid, F., Sobek, W., Sedlbauer, K., Schmidt, T., et al. (2011). Adaptive textile und folienbasierte gebäudehüllen. *Bautechnik* 88, 69–75. doi: 10.1002/bate.201110005
- Habermann, K. J., and Koch, K.-M. (2004). *Membrane Structures: Innovative Building With Film and Fabric*. Munich: Prestel Publishing Ltd.
- Hara, S., Zama, T., Takashima, W., and Kaneto, K. (2004). Artificial muscles based on polypyrrole actuators with large strain and stress induced electrically. *Polym. J.* 36, 151–161. doi: 10.1295/polymj.36.151
- Janocha, H. (2004). *Actuators: Basics and Applications*. Heidelberg: Springer.
- Janssens, A. (1998). *Reliable Control of Interstitial Condensation in Lightweight Roof Systems: Calculation and Assessment Methods*. Leuven: s.n.
- Juaristi, M., Monge-Barrio, A., Knaack, U., and Gómez-Acebo, T. (2018). Smart and Multifunctional Materials and their possible application in façade systems. *J. Facade Design Eng.* 6, 19–33. doi: 10.7480/jfde.2018.3.2475
- Kamamichi, N., Yamakita, M., Asaka, K., Luo, Z.-W., and Mukai, T. (2007). “Sensor property of a novel EAP device with ionic-liquid-based bucky gel,” in: *IEEE Sensors*, (Atlanta, GA, USA), 221–224.
- Kim, B., Mok, B., Ryu, U., Oh, I.-H., Lee, S. K., Cha, S.-E., et al. (2003). “Analysis of mechanical characteristics of the ionic polymer metal composite (IPMC) actuator using cast ion-exchange film,” in *Proceedings of SPIE - The International Society for Optical Engineering*, Vol. 5051. doi: 10.1117/12.484296
- Kim, K., and Shahinpoor, M. (2002). A novel method of manufacturing three-dimensional ionic polymer-metal composites (IPMCs) biomimetic sensors, actuators and artificial muscles. *Polymer* 43, 797–802. doi: 10.1016/S0032-3861(01)00648-6
- Klein, T., and Knaack, U. (2015). Adaptive building envelopes, component development as well as implementation strategies. *J. Facade Design Eng.* 3:2. doi: 10.7480/jfde.2015.2.1011
- Košir, M. (2016). “Adaptive Building envelope: an integral approach to indoor environment control in buildings,” in *Automation and Control Trends*, eds P. Ponce, A. M. Gutierrez, L. M. Ibarra (InTech), 121–148. doi: 10.5772/64951
- Kretzer, M., and Rossi, D. (2012). ShapeShift. *Leonardo* 45, 480–481. doi: 10.1162/LEON_a_00451
- Kruusamäe, K., Punning, A., Aabloo, A., and Asaka, K. (2015). Self-sensing ionic polymer actuators: a review. *Actuators* 4, 17–38. doi: 10.3390/act4010017
- Loonen, R. C. G. M., Favoino, F., Rico-Martinez, J. M., and Brzezicki, M. (2015). “Design for façade adaptability: towards a unified and systematic characterization,” in *10th Conference on Advanced Building Skins* (Bern), 1284–1294.
- Melling, D., Martinez, J. G., and Jager, E. W. H. (2019). Conjugated polymer actuators and devices: progress and opportunities. *Adv. Mater. Weinheim* 31:e1808210. doi: 10.1002/adma.201808210
- Mossé, A., Gauthier, D., and Kofod, G. (2012). Towards interconnectivity: appropriation of responsive minimum energy structures in an architectural context. *Stud. Mater. Think.* 7, 1–11.
- Must, I., Kaasik, F., Pöldsalu, I., Mikkels, L., Johanson, U., Punning, A., et al. (2015). Ionic and capacitive artificial muscle for biomimetic soft robotics. *Adv. Eng. Mater.* 17, 84–94. doi: 10.1002/adem.201400246
- Nakshatharan, S., Vunder, V., Pöldsalu, I., Johanson, U., Punning, A., and Aabloo, A. (2018). Modelling and control of ionic electroactive polymer actuators under varying humidity conditions. *Actuators* 7:7. doi: 10.3390/act7010007
- Neuhaus, R., Bitzer, V., Jablockin, J., Glanz, C., Kolaric, I., Siegert, J., et al. (2019a). “Ionic CNT actuators and arrays – towards cost-efficient manufacturing through scalable dispersion and printing processes,” in *2019 IEEE/ASME International Conference on Advanced Intelligent Mechatronics (AIM)* (IEEE), 56–61.
- Neuhaus, R., Glanz, C., Kolaric, I., and Bauernhansl, T. (2019b). “Electroactive CNT-polymer-actuators: state of science and technology and their slow approach into architectural applications,” in *NanoCarbon Annual Conference*, Nanoinitiative Bayern GmbH/Cluster Nanotechnology (Würzburg).
- Okuzaki, H., and Funasaka, K. (1999). Electrically driven polypyrrole film actuator working in air. *J. Intellig. Mater. Syst. Struct.* 10, 465–469.
- Paech, C. (2016). Structural membranes used in modern building facades. *Proc. Eng.* 155, 61–70. doi: 10.1016/j.proeng.2016.08.007
- Palmre, V., Torop, J., Arulepp, M., Sugino, T., Asaka, K., Jänes, A., et al. (2012). Impact of carbon nanotube additives on carbide-derived carbon-based electroactive polymer actuators. *Carbon* 50, 4351–4358. doi: 10.1016/j.carbon.2012.04.071
- Park, M., Kim, J., Song, H., Kim, S., and Jeon, M. (2018). Fast and stable ionic electroactive polymer actuators with PEDOT:PSS/graphene-Ag-nanowires nanocomposite electrodes. *Sensors* 18:3126. doi: 10.3390/s18093126
- Plesse, C., Vidal, F., Randriamahazaka, H., Teyssié, D., and Chevrot, C. (2005). Synthesis and characterization of conducting interpenetrating polymer networks for new actuators. *Polymer* 46, 7771–7778. doi: 10.1016/j.polymer.2005.03.103
- Pöldsalu, I., Rohtlaid, K., Nguyen, T. M. G., Plesse, C., Vidal, F., Khorram, M. S., et al. (2018). Thin ink-jet printed trilayer actuators composed of PEDOT:PSS on interpenetrating polymer networks. *Sens. Actuators B: Chem.* 258, 1072–1079. doi: 10.1016/j.snb.2017.11.147
- Preisinger, C. (2019). *Karamba3D: Parametric Engineering*. Vienna: Bollinger und Grogmann ZT GmbH.
- Punning, A., Must, I., Pöldsalu, I., Vunder, V., Temmer, R., Kruusamäe, K., et al. (2014). Lifetime measurements of ionic electroactive polymer actuators. *J. Intellig. Mater. Syst. Struct.* 25, 2267–2275. doi: 10.1177/1045389X14546656
- Reichert, S., Menges, A., and Correa, D. (2015). Meteorosensitive architecture: biomimetic building skins based on materially embedded and hygroscopically enabled responsiveness. *Comp. Aid Design* 60, 50–69. doi: 10.1016/j.cad.2014.02.010
- Rinne, P., Pöldsalu, I., Johanson, U., Tamm, T., Pöhako-Esko, K., Punning, A., et al. (2019). Encapsulation of ionic electromechanically active polymer actuators. *Smart Mater. Struct.* 28:74002. doi: 10.1088/1361-665X/ab18c0
- Roth, S., and Baughman, R. H. (2002). Actuators of individual carbon nanotubes. *Curr. Appl. Phys.* 2, 311–314. doi: 10.1016/S1567-17390200116-5
- Ru, J., Bian, C., Zhu, Z., Wang, Y., Zhang, J., Horiuchi, T., et al. (2019). Controllable and durable ionic electroactive polymer actuator based on nanoporous carbon nanotube film electrode. *Smart Mater. Struct.* 28:85032. doi: 10.1088/1361-665X/ab2a28
- Senatore, G., Duffour, P., and Winslow, P. (2018a). Energy and cost assessment of adaptive structures: case studies. *J. Struct. Eng.* 144:4018107. doi: 10.1061/ASCEST.1943-541X.0002075
- Senatore, G., Duffour, P., and Winslow, P. (2018b). Exploring the application domain of adaptive structures. *Eng. Struct.* 167, 608–628. doi: 10.1016/j.engstruct.2018.03.057

- Senatore, G., Duffour, P., and Winslow, P. (2019). Synthesis of minimum energy adaptive structures. *Struct. Multidisc. Optim.* 60, 849–877. doi: 10.1007/s00158-019-02224-8
- Shahinpoor, M., and Kim, K. J. (2001). Ionic polymer-metal composites: I. Fundamentals. *Smart Mater. Struct.* 10, 819–833. doi: 10.1088/0964-1726/10/4/327
- Shahinpoor, M., Kim, K. J., and Leo, D. J. (2003). Ionic polymer-metal composites as multifunctional materials. *Polym. Compos.* 24, 24–33. doi: 10.1002/pc.10002
- Simaite, A. (2015). *Development of Ionic Electroactive Actuators With Improved Interfacial Adhesion: Towards the Fabrication of Inkjet Printable Artificial Muscles*. Toulouse: INSA de Toulouse, Micro and nanotechnologies/Microelectronics.
- Sobek, W. (2015). *Das Triple Zero-Gebäude: Null Energie, Null Emissionen, null Abfall*. 15. Münchner Wissenschaftstage: Städte der Zukunft.
- Spinks, G. M., Mottaghitalab, V., Bahrami-Samani, M., Whitten, P. G., and Wallace, G. G. (2006). Carbon-nanotube-reinforced polyaniline fibers for high-strength artificial muscles. *Adv. Mater.* 18, 637–640. doi: 10.1002/adma.200502366
- Sugino, T., Kiyohara, K., Takeuchi, I., Mukai, K., and Asaka, K. (2011). Improving the actuating response of carbon nanotube/ionic liquid composites by the addition of conductive nanoparticles. *Carbon* 49, 3560–3570. doi: 10.1016/j.carbon.2011.04.056
- Sung, D. K. (2011). “Skin deep: making building skins breathe with smart thermobimetals,” in *Where do you stand: 99th ACSA annual meeting, March 3–6, 2011, Montréal, Canada*, eds A. Pérez Gómez, A. Cormier, and A. Pedret (Washington, DC: ACSA Press), 145–152.
- Tamagawa, H., Okada, K., Mulembo, T., Sasaki, M., Naito, K., Nagai, G., et al. (2019). Simultaneous enhancement of bending and blocking force of an ionic polymer-metal composite (IPMC) by the active use of its material characteristics change. *Actuators* 8:29. doi: 10.3390/act8010029
- Tang, T., Yang, D.-H., Wang, L., Zhang, J.-R., and Yi, T.-H. (2019). Design and application of structural health monitoring system in long-span cable-membrane structure. *Earthq. Eng. Eng. Vib.* 18, 461–474. doi: 10.1007/s11803-019-0484-y
- Tauber, M., Feldkamp, D., Christian, G., Ailke, H., Till, Z., and Tobias, S. (2019). *Building the Housing of the Future*. Munich: Boston Consulting Group.
- Terasawa, N. (2017). High-performance ionic and non-ionic fluoropolymer/ionic liquid gel hybrid actuators based on single-walled carbon nanotubes. *RSC Adv.* 7, 2443–2449. doi: 10.1016/j.matpr.2019.10.044
- United Nations (2017). *World Population Prospects: The 2017 Revision: Key Findings and Advance Tables*. New York, NY: United Nations.
- Vidal, F., Plesse, C., Palaprat, G., Jüger, J., Citerin, J., Kheddar, A., et al. (2008). Synthesis and characterization of IPNs for electrochemical actuators. *AST* 61, 8–17. doi: 10.4028/www.scientific.net/AST.61.8
- Vunder, V., Punning, A., and Aabloo, A. (2012). Mechanical interpretation of back-relaxation of ionic electroactive polymer actuators. *Smart Mater. Struct.* 21:115023. doi: 10.1088/0964-1726/21/11/115023
- Yamato, K., Mukai, K., Hata, K., and Asaka, K. (2012). Fast-moving bimorph actuator based on electrochemically treated millimeter-long carbon nanotube electrodes and ionic liquid gel. *Int. J. Smart Nano Mater.* 3, 263–274. doi: 10.1080/19475411.2011.652992

Conflict of Interest: The authors declare that the research was conducted in the absence of any commercial or financial relationships that could be construed as a potential conflict of interest.

Copyright © 2020 Neuhaus, Zahiri, Peters, Tahouni, Siegert, Kolaric, Dahy and Bauernhansl. This is an open-access article distributed under the terms of the Creative Commons Attribution License (CC BY). The use, distribution or reproduction in other forums is permitted, provided the original author(s) and the copyright owner(s) are credited and that the original publication in this journal is cited, in accordance with accepted academic practice. No use, distribution or reproduction is permitted which does not comply with these terms.



Fast and Optimized Calculation of the Cable Pretension Forces in Arch Bridges With Suspended Deck

Mariano Modano¹, Arnas Majumder², Filipe Santos³, Raimondo Luciano⁴ and Fernando Fraternali^{2*}

¹ Department of Structures for Engineering and Architecture, University of Naples Federico II, Naples, Italy, ² Department of Civil Engineering, University of Salerno, Fisciano, Italy, ³ CERIS and Departamento de Engenharia Civil, Faculdade de Ciências e Tecnologia da Universidade Nova de Lisboa, Caparica, Portugal, ⁴ Department of Engineering, University of Naples "Parthenope", Naples, Italy

OPEN ACCESS

Edited by:

Gennaro Senatore,
École Polytechnique Fédérale
de Lausanne, Switzerland

Reviewed by:

Francesco Tornabene,
University of Salento, Italy
Nizar Bel Hadj Ali,
École Nationale d'Ingénieurs
de Gabès, Tunisia
Philippe Van Bogaert,
Ghent University, Belgium

*Correspondence:

Fernando Fraternali
f.fraternali@unisa.it

Specialty section:

This article was submitted to
Computational Methods in Structural
Engineering,
a section of the journal
Frontiers in Built Environment

Received: 24 March 2020

Accepted: 22 June 2020

Published: 16 July 2020

Citation:

Modano M, Majumder A,
Santos F, Luciano R and Fraternali F
(2020) Fast and Optimized Calculation
of the Cable Pretension Forces
in Arch Bridges With Suspended
Deck. *Front. Built Environ.* 6:114.
doi: 10.3389/fbuil.2020.00114

This paper presents with an effective and fast approach to the optimization of the pretension forces in arched bridges with suspended deck, which makes use of the influence matrix method (IMM). The given cable-tensioning procedure leads to a linear system of equations with a reduced number of unknowns and can be effectively implemented within active control procedures that handle time-varying loading conditions. This method produces a target bending moment distribution (TBMD) over the structure, which significantly mitigates the state of stress of the deck. Numerical simulations referred to a Nielsen arch bridge illustrate the versatility of the proposed approach when dealing with different loading conditions.

Keywords: arch bridges, pretension, target bending moment distribution, influence matrix, Nielsen bridge

INTRODUCTION

There are several adaptive applications of cable-stayed structures in the field of bridge construction (Simões and Negrão, 1995; Freire et al., 2006; Fabbrocino et al., 2017; Song et al., 2018; Reksowardojo et al., 2019). An adaptive design searches for the optimal configuration of these structures, which in most cases is not unique. Therefore, it is important to have effective methods to design cable-stayed bridges that are capable of responding in real time to changing loading conditions, with the aim of designing structural systems capable of responding in real time to the change of the design parameters, due, e.g., to the time-variation of the loading condition. It is also worth observing that recent history is full of dramatic examples of structural breakdowns or collapses of cable-stayed and suspended bridges, demonstrating that such structures require critical maintenance intervention and structural strengthening. Notable recent bridge collapses are that of the Polcevera viaduct, also known as Ponte Morandi, in Genoa, Italy (2019), and that involving the Chirajara bridge in Guayabetal, Colombia (2018).

Cable-stayed bridges, suspension bridges and arched bridges (e.g., the Langer, Lohse, and Nielsen types) have made rapid technological progress over the past century and their numbers have increased rapidly. There are two main reasons for their success: the first is aesthetic, due to their elegant appearance; the second is economic, due their efficient use of structural material (during construction) and reduced maintenance costs (Simões and Negrão, 1995; Freire et al., 2006; Song et al., 2018). Suspended deck bridges have also excellent anti-seismic and stabilizing properties and offer some notable practical advantages. For example, they do not require access from below,

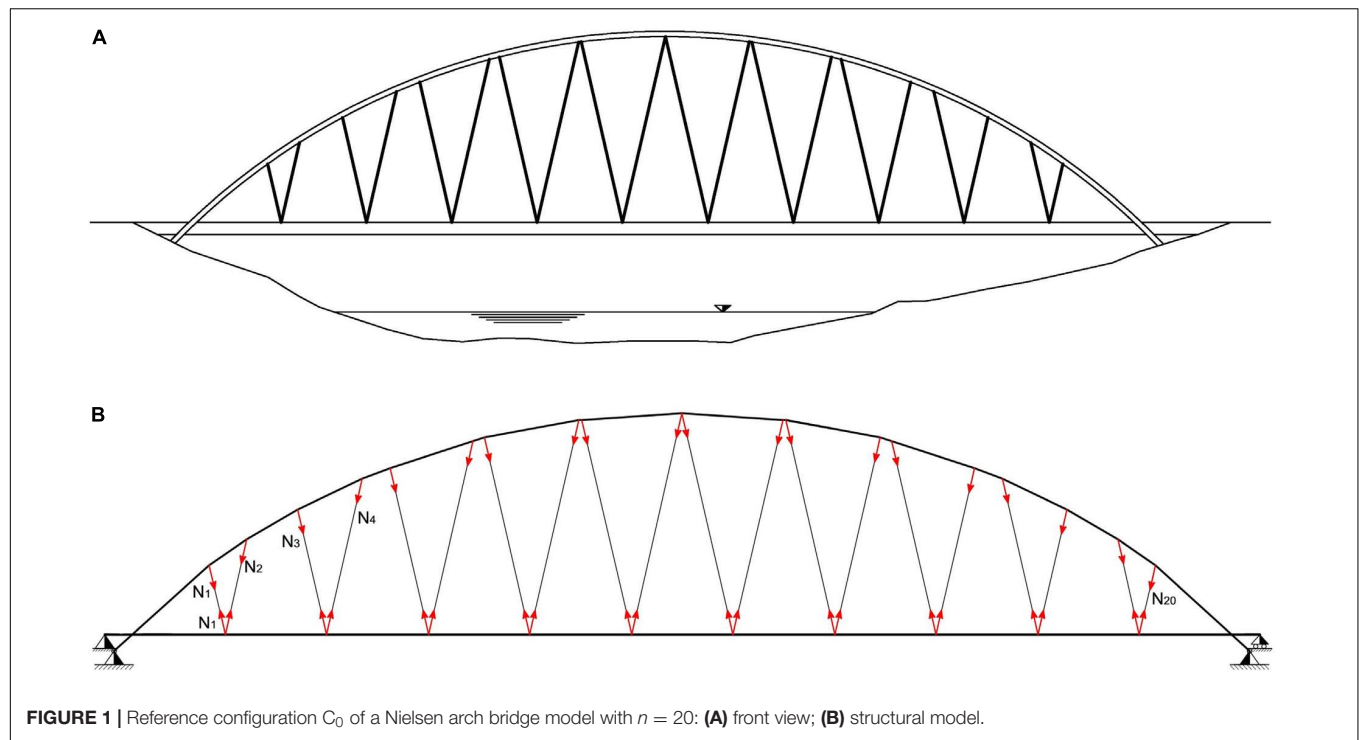


FIGURE 1 | Reference configuration C_0 of a Nielsen arch bridge model with $n = 20$: (A) front view; (B) structural model.

and the erection process is relatively straightforward. Despite all these positive aspects, they are highly sensitive to the load distribution, as well as to dynamic loads, such as wind. Additionally, they exhibit non-linear structural behavior that derive mainly from the changes in geometry, cable failure, etc. (Wang and Yang, 1996). From a mechanical point of view, suspended deck bridges are statically indeterminate structures that often exhibit a high degree of static indeterminacy. Their structural behavior is strongly influenced by the arrangement and the pre-tensioning forces of the cables, as well as by the distribution of stiffness in the load-bearing elements (cables, deck, support arch, etc.) (Lee et al., 2008). Therefore, the tendency has been to improve the structural behavior by using a variety of optimization methods (Sung et al., 2006; Lonetti and Pascuzzo, 2014).

The load balancing method introduced by Lazar et al. (1972) is one of the oldest available approaches for the optimization of the cable pretension forces. It assumes that such forces are responsible for reducing the bending moments and displacements of the deck. Lazar and co-authors base their optimization procedure on the bending moment influence

matrix, which is computed by applying a unit force to each suspension cable in turn (Lazar et al., 1972). Another approach, known as the Zero Displacement Method, was initially proposed by Wang et al. (1993) and recently improved by Zhang and Au (2014). Four different optimization methods are compared by Wang et al. (1997), which are minimization of the sum of the squares for vertical movements along the beam (MSSVD); minimization of the maximum beam moment (MMM); the continuous beam method (CBM); and the simple beam method (SBM). The study presented in Wang et al. (1997) concludes that the best approach to get accurate results with minimum effort is SBM, which describes the deck as a continuous beam on elastic supports, by neglecting non-linearities. Another available approach is the Force Equilibrium Method (Chen et al., 2000), which models for the unknown cable pretension forces through an iterative approach. It is well known that suspended deck bridges are lightweight structures, and that the structure's ability to actively respond to external stresses is a key requirement for this bridge typology.

The present work applies the Influence Matrix Method (IMM) presented in Fabbrocino et al. (2017) and Mascolo and Modano (2020) for an effective design of the pretension forces in cable-stayed arch bridges. An optimized cable-pretension

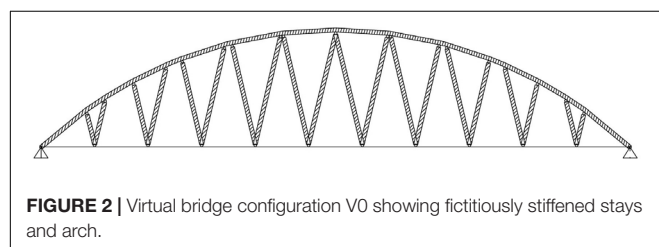


FIGURE 2 | Virtual bridge configuration V0 showing fictitiously stiffened stays and arch.

TABLE 1 | Main geometric parameters of the analyzed bridge model.

Bridge length	140.8 (m)
Maximum arch height	28 (m)
The deck width	13.90 (m)
Roadway width	7.50 (m)

procedure is proposed to produce a target bending moment distribution (TBMD) over the deck, which approximates that exhibited by a continuous beam. It provides a fast design tool that can be enforced within closed-loop active control procedures, making use of active tendons, and weight-in-motion (WIM) technologies (Jacob and Feypell-de La Beaumelle, 2010; Preumont, 2011; Reksowardojo et al., 2018, 2019; Senatore et al., 2018a,b, 2019). The traditional designing and sizing of a bridge is based on the worst expected load scenario. Contrary to such a conventional approach, the pretension design procedure here proposed allows the structure to cope with variable load scenarios. It can be profitably used as a tool to increase the load bearing capacity of the structure through a geometric-stiffness approach, during events that might result in the partial loss of the load bearing capacity (Casas, 2015).

COMPUTATION OF CABLE PRETENSION FORCES

Let us examine the arched bridge model in **Figure 1**, whose deck is suspended on a number n of stays. The bridge has been fully designed in terms of sizing of the structural members and it is subjected to a given loading condition. We distinguish the following three macrostructural elements: the arch structure E_1 , the deck E_2 , and the stays E_3 . The reference configuration C_0 of the bridge, in absence of cable pretensions, is obtained by assembling such macro-elements. The arch E_1 shows pinned supports at both ends, while the deck E_2 features a pinned

support at one end and a roller support at the other end (**Figure 1B**). Such boundary conditions imply that the deck can be regarded as a statically determinate structure, when one knows the tension forces N_1, \dots, N_n acting in the stays. The vector N_0 collects the forces acting in the cables for the reference configuration C_0 .

We aim at identifying convenient values of the pretension forces to be applied to the stays that lead us to obtain a desired bending moment distribution (BMD) over the deck. A convenient BMD is that corresponding to a deck responding as a continuous beam supported over the hanging points of the stays (*continuous-beam deck configuration*). One could obtain this TBMD through a material stiffening procedure, by significantly increasing the size of the cross-section of the stays and the arch, and/or using a very stiff material for such members. Let E_i^* denote a fictitious configuration of the i -th macro-element, which corresponds to assuming the Young modulus of the material 1000 times larger than the real value. We introduce the virtual configuration V_0 of the bridge, which is formed by the assembling of E_1^* , E_2 and E_3^* , which is a good approximation of the desired continuous-beam deck configuration (**Figure 2**). The vector N_d collects the cable forces for configuration V_0 . We refer to such forces as the “*optimal pretension forces*” in the remainder of the paper.

A geometric-stiffening approach to the TBMD consists of applying a suitable state of self-stress to C_0 , while leaving material properties and member sizing unchanged (Skelton and de Oliveira, 2010). The state of self-stress to be applied follows from the application of suitable axial forces to the stays, so that

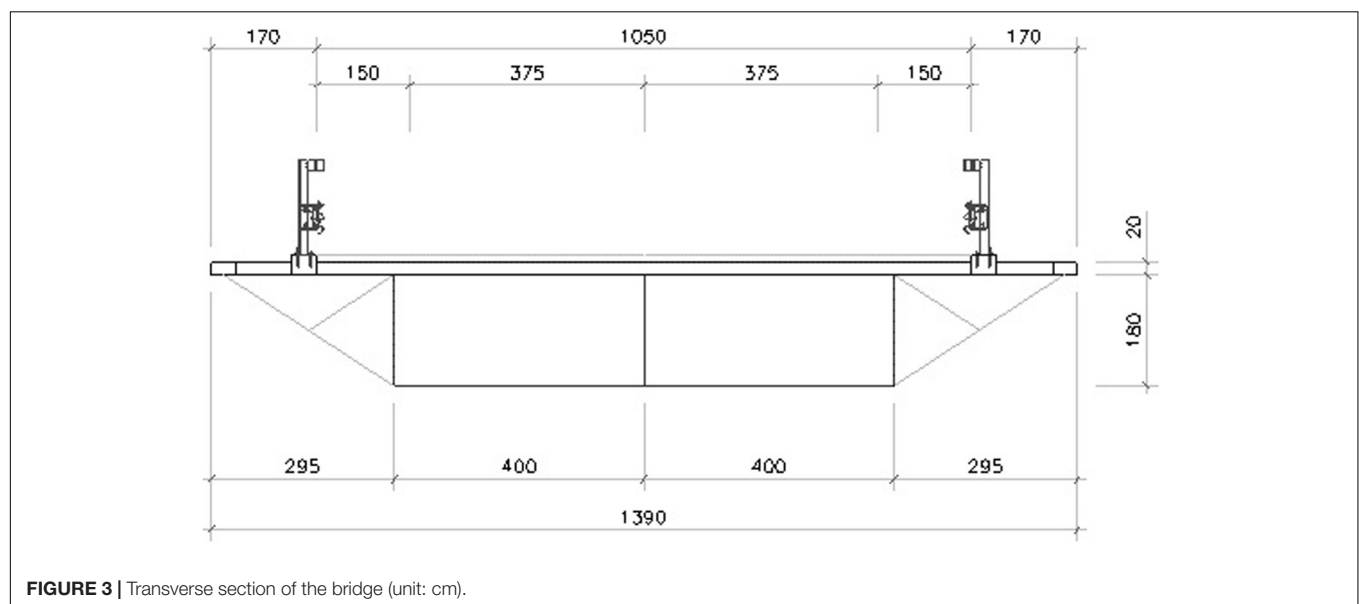


TABLE 2 | Mechanical properties of the employed finite element model of the bridge.

Structural member	Cross-section	Steel-Type	E (Nmm-1)	A (m ²)	I _y (m ⁴)
Arch	Tubular	S355	2,10E + 05	8,16E-02	2,68E-02
Deck	2-Cell Box	S355	2,10E + 05	6,96E-01	6,00E-01
Cables	Circular	$f_{yd} = 772$ MPa	2,10E + 05	5,027 E-3	2,011 E-6

TABLE 3 | Influence matrix of the analyzed finite element model (unit: kN).

	N 1	N 2	N 3	N 4	N 5	N 6	N 7	N 8	N 9	N 10	N 11	N 12	N 13	N 14	N 15	N 16	N 17	N 18	N 19	N 20
CABLE 1	1,000	-0,898	-0,201	0,115	0,016	0,039	-0,017	0,015	-0,014	0,009	-0,008	0,005	-0,004	0,003	-0,002	0,001	-0,001	0,001	0,000	0,001
CABLE 2	-0,469	1,000	-0,282	-0,035	0,016	0,002	0,012	-0,004	0,003	-0,003	0,002	-0,001	0,001	-0,001	0,001	0,000	0,000	0,000	0,000	0,000
CABLE 3	-0,228	-0,611	1,000	-0,380	-0,249	0,098	0,006	0,038	-0,016	0,014	-0,015	0,008	-0,008	0,005	-0,004	0,002	-0,002	0,001	-0,001	0,001
CABLE 4	0,105	-0,061	-0,306	1,000	-0,434	-0,127	0,016	-0,017	0,044	-0,017	0,017	-0,011	0,009	-0,005	0,005	-0,003	0,002	-0,002	0,001	-0,001
CABLE 5	0,020	0,040	-0,277	-0,601	1,000	-0,186	-0,274	0,100	-0,011	0,042	-0,022	0,016	-0,018	0,009	-0,009	0,005	-0,004	0,003	-0,001	0,002
CABLE 6	0,046	0,005	0,103	-0,166	-0,176	1,000	-0,493	-0,207	0,003	-0,032	0,072	-0,026	0,031	-0,017	0,014	-0,009	0,007	-0,004	0,002	-0,003
CABLE 7	-0,023	0,032	0,007	0,024	-0,298	-0,569	1,000	-0,092	-0,286	0,105	-0,027	0,046	-0,028	0,018	-0,020	0,010	-0,008	0,006	-0,002	0,004
CABLE 8	0,021	-0,011	0,046	-0,026	0,108	-0,238	-0,092	1,000	-0,509	-0,259	-0,009	-0,036	0,087	-0,028	0,036	-0,020	0,013	-0,010	0,003	-0,006
CABLE 9	-0,021	0,008	-0,021	0,069	-0,012	0,004	-0,301	-0,538	1,000	-0,054	-0,287	0,109	-0,038	0,049	-0,032	0,019	-0,017	0,010	-0,004	0,007
CABLE 10	0,013	-0,007	0,018	-0,027	0,048	-0,040	0,111	-0,274	-0,054	1,000	-0,518	-0,288	-0,010	-0,029	0,088	-0,025	0,028	-0,020	0,005	-0,011
CABLE 11	-0,011	0,005	-0,020	0,028	-0,025	0,088	-0,029	-0,010	-0,288	-0,518	1,000	-0,054	-0,274	0,111	-0,040	0,048	-0,027	0,018	-0,007	0,013
CABLE 12	0,007	-0,004	0,010	-0,017	0,019	-0,032	0,049	-0,038	0,109	-0,287	-0,054	1,000	-0,538	-0,301	0,004	-0,012	0,069	-0,021	0,008	-0,021
CABLE 13	-0,006	0,003	-0,010	0,013	-0,020	0,036	-0,028	0,087	-0,036	-0,009	-0,259	-0,509	1,000	-0,092	-0,238	0,108	-0,026	0,046	-0,011	0,021
CABLE 14	0,004	-0,002	0,006	-0,008	0,010	-0,020	0,018	-0,028	0,046	-0,027	0,105	-0,286	-0,092	1,000	-0,569	-0,298	0,024	0,007	0,032	-0,023
CABLE 15	-0,003	0,002	-0,004	0,006	-0,009	0,014	-0,017	0,031	-0,026	0,072	-0,032	0,003	-0,207	-0,493	1,000	-0,175	-0,166	0,103	0,005	0,046
CABLE 16	0,002	-0,001	0,003	-0,004	0,005	-0,009	0,009	-0,018	0,016	-0,022	0,042	-0,011	0,100	-0,274	-0,186	1,000	-0,601	-0,277	0,040	0,020
CABLE 17	-0,001	0,001	-0,002	0,002	-0,003	0,005	-0,005	0,009	-0,011	0,017	-0,017	0,044	-0,017	0,016	-0,127	-0,434	1,000	-0,305	-0,060	0,105
CABLE 18	0,001	-0,001	0,001	-0,002	0,002	-0,004	0,005	-0,008	0,008	-0,015	0,014	-0,016	0,038	0,006	0,098	-0,249	-0,379	1,000	-0,612	-0,228
CABLE 19	0,000	0,000	0,000	0,000	0,000	0,001	-0,001	0,001	-0,001	0,002	-0,003	0,003	-0,004	0,012	0,002	0,016	-0,035	-0,282	1,000	-0,469
CABLE 20	0,001	0,000	0,001	-0,001	0,001	-0,002	0,003	-0,004	0,005	-0,008	0,009	-0,014	0,015	-0,017	0,039	0,016	0,116	-0,201	-0,898	1,000

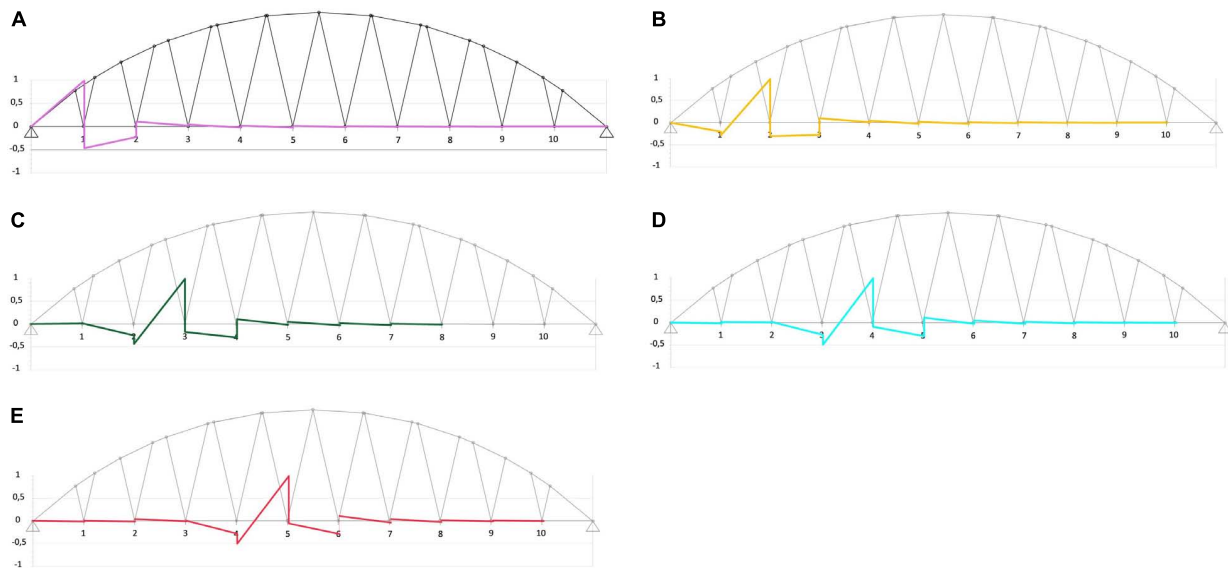


FIGURE 4 | Diagrams of the axial forces acting in all the cables when a selected cable is subject to a unit pre-tension. **(A)** Effects of a unit pre-tension of cable # 1. **(B)** Effects of a unit pre-tension of cable # 3. **(C)** Effects of a unit pre-tension of cable # 5. **(D)** Effects of a unit pre-tension of cable # 7. **(E)** Effects of a unit pre-tension of cable # 9.

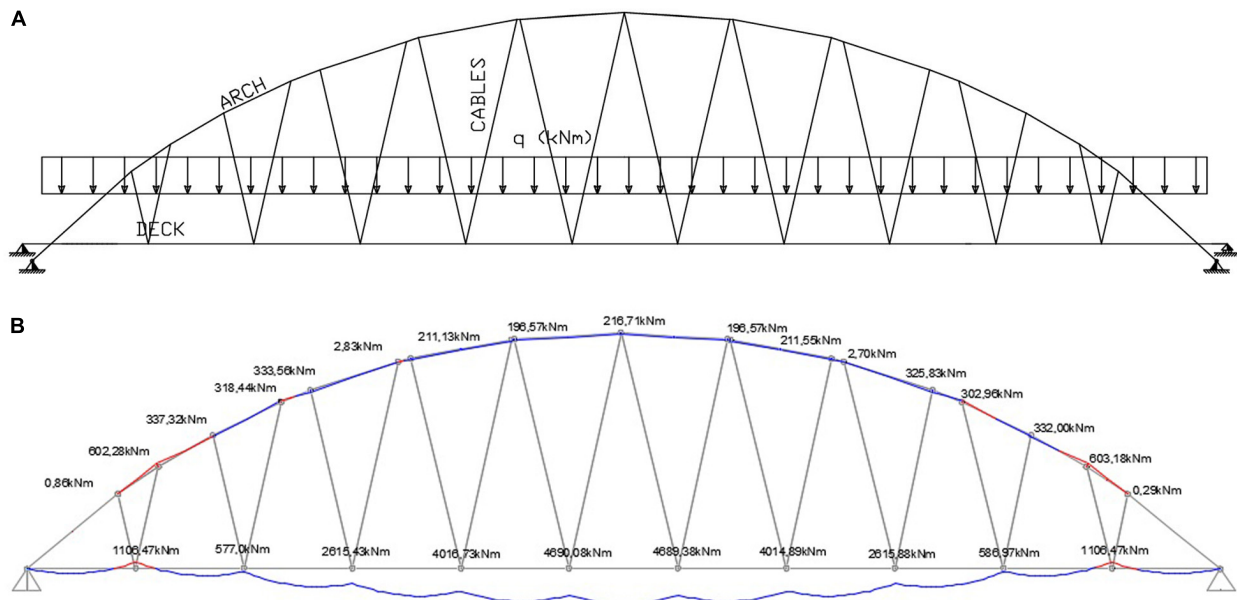


FIGURE 5 | Illustration of load case 1. **(A)** Load distribution. **(B)** Bending moment distribution over the deck and the arch in absence of cable pre-tension.

the final forces acting in such members will be equal to N_d . Due to the above mentioned static determinacy of E_2 (when the forces acting in the stays are known), the action of the forces N_d ensures that the BMD over the deck closely approximates the TBMD.

We determine the optimal pretension forces by solving a set of n elementary elastic problems, each of which corresponds to the application of a unit force in a single stay. Let us introduce the $n \times n$ influence matrix A whose entry A_{ij} is equal to the axial force acting in the j -th cable of C_0 when the i -th cable is subject to

a unit pretension force, and no external loads are applied to the bridge. It is an easy task to verify that it results

$$A^T x = N_d - N_0 \quad (1)$$

Equation (1) rules the cable pretension algorithm adopted in the present study, which returns the desired *optimal pretension factors* \bar{x} . It is worth observing that the influence matrix A is an intrinsic property of the bridge. As a consequence, the application

of Eqn. (1) to different loading conditions is an easy task, once the vectors N_0 and N_d have been computed through an elastic analysis of C_0 and V_0 , respectively. The linear nature of Eqn. (1), and the limited number of cables that characterize real-life suspended bridges, allow us to conclude that, in most cases, it is possible to solve such an equation with running time less than 1 s.

We have already observed that the deck is a statically determinate structure when the forces in the stays N are known. One can therefore easily obtain the vector M collecting all the deck bending moments at the cables' hanging points through the following linear equation

$$M = B N \quad (2)$$

where B is a suitable $n \times n$ equilibrium matrix. Let us consider now the following quadratic programming problem

$$\min_{N \in \mathbb{R}^n} N^T B^T B N, \text{ subject to } N \leq N_y \quad (3)$$

where N_y denotes the vector of the yielding forces of the stays. Such a problem searches for the cable forces that minimize the sum of squares of the deck bending moments M . Its solution requires the adoption of iterative solution procedures (refer, e.g., to Gill et al., 1981). Assuming that it results $N_d \leq N_y$, the vector N_d lead us to an approximate solution of problem (3). The accuracy of the approximation scheme based on setting $N = N_d$ is highlighted by the numerical results presented in Section "Numerical Results." Such results indeed show that the pretension forces obtained through the linear system (1) induce a

significant reduction of the bending moments acting on the deck, as compared to the BMD in absence of cable pre-tension. We let C_d denote the configuration of the bridge that features $N = N_d$.

FINITE ELEMENT MODEL

This section presents the numerical implementation of the analytical method given in Section "Computation of Cable Pretension Forces" with reference to a case study of a Nielsen arch bridge featuring a span of 140.8 m and an aerodynamic shape. The deck is suspended to a steel arch by 20 cables, which form ten V-shaped elements made of steel, as it is shown in **Figure 1** (refer to **Table 1** for the main geometric parameters). The deck rests on a two-cell box girder made of steel, which is locally reinforced to avoid local instability, and has a total width of 8.0 m and height of 1.8 m. The deck houses a 7.5 m wide roadway, two side platforms of 1.50 m each, and two pedestrian walkways of 1.70 m each (**Figure 3**). The latter are made with a metal grating that rests on cantilevered steel beams. The arch has a tubular section with a diameter of 1.50 m and it is constrained by hinge connections at its ends. Local stiffeners secure the cables (or tie rods) to the arch during the construction phase. The deck can be described as a beam on continuous supports with a pitch of 12.80 m, which is the distance between two consecutive suspension cables.

The static indeterminacy of the overall bridge structure is equal to the number of cables + 1 (i.e., 21). We refer the reader to Falanga (2019) for an in-depth description of the bridge model under examination. A two-dimensional finite element

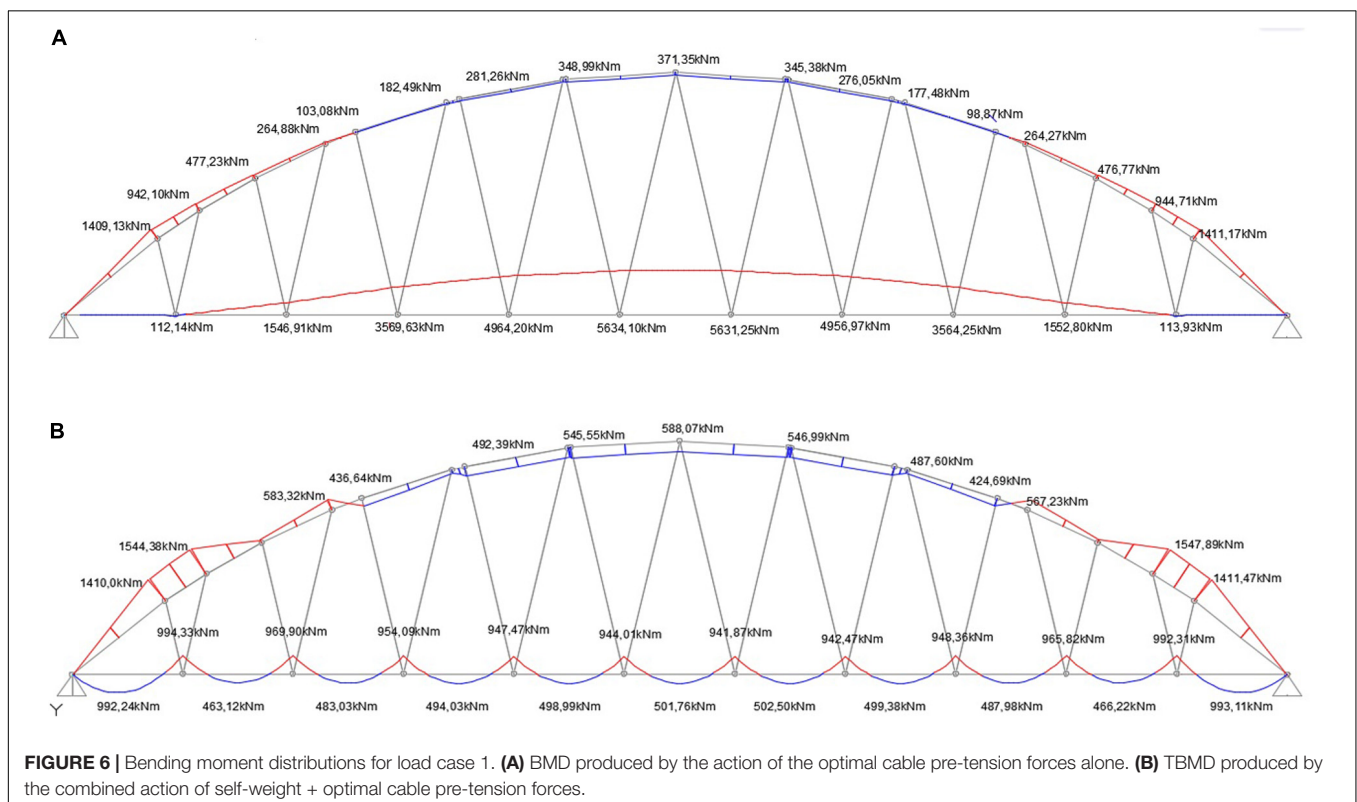


FIGURE 6 | Bending moment distributions for load case 1. **(A)** BMD produced by the action of the optimal cable pre-tension forces alone. **(B)** TBMD produced by the combined action of self-weight + optimal cable pre-tension forces.

model featuring the properties described in **Table 2** is employed to predict the response of the bridge under assigned loading conditions. It is worth observing that the adopted cross-section of the arch carries a maximum bending moment of $3,16 \times 10^4$ kNm in the fully elastic regime; the cross-section of the deck carries a maximum elastic bending moment of $2,25 \times 10^5$ kNm; and the cables can carry a maximum elastic tensile force of $N_y = 3,88 \times 10^3$ kN. The influence matrix associated with the present bridge model is given in **Table 3**, and one observes that such a matrix is dense. A graphical illustration of the effects produced in all cables by the application of a unit pretension of selected cables is given in **Figure 4**. The results presented in **Table 3** highlight that the influence matrix has leading diagonal terms, which implies that problem (1) is well conditioned.

NUMERICAL RESULTS

The following sections illustrate a collection of numerical results, which examine the effects of different loading conditions on the bridge model described in the previous section. The first

example deals with a uniformly distributed load (UDL) that corresponds to the self-weight of the structure (Section “Load Case 1”), while the second and third examples analyze the action of a partially distributed uniform load (PUDL) in proximity to the middle span (Section “Load Case 2”), and over one half of the span of the deck (Section “Load Case 3”), respectively. The 4th loading condition refers to a moving UDL superimposed to permanent loads (Section “Load Case 4”). Such a condition simulates the effects of traffic due to moving cars and lorries, assuming that dynamic amplification effects can be ignored (refer, e.g., to variable Load Model 1 of the European Standards EN 1991-2, 2003).

Load Case 1

The first example refers to the application of UDL with a magnitude of 70 kN/m over the deck (see **Figure 5**). The procedure described in Section “Computation of Cable Pretension Forces” results in the cable pretension forces given in **Figure 6A**, and the TBMD illustrated in **Figure 6B**. The increases of the bending moments carried by the arch, which are produced by the optimal pre-tensioning of the cables (compare

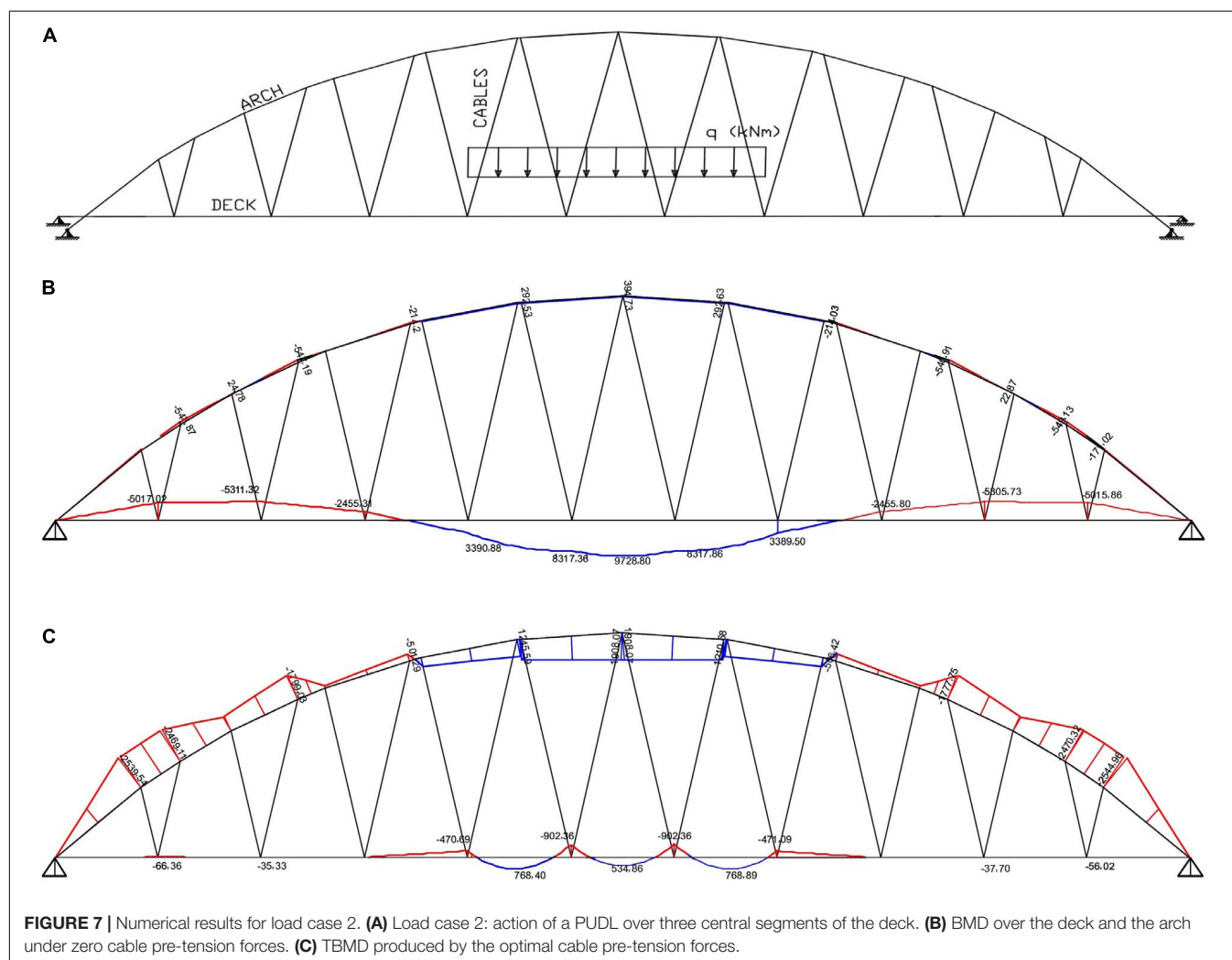


Figure 6B with **Figure 5B**), can be safely supported by the cross-section adopted for this member (cf. **Table 2**), since the maximum bending moment that the arch can carry in the fully elastic phase is equal to $3,16 \times 10^4$ kN m (cf. Section “Finite Element Model”). The maximum force in the stays $N_{d,max}$ is equal to 1.14×10^3 kN (cable #6). Such a force is significantly lower than the yielding force $N_y = 3,88 \times 10^3$ kN (cf. Section “Finite Element Model”).

Load Case 2

Load case 2 is a PUDL of 70 kN/m applied to the three central segments of the deck. The application of an optimization procedure similar to that presented with reference to load case 1 leads to the results illustrated in **Figure 7**. One observes that the BMD produced by the optimal pre-tension of the cables (**Figure 7C**) features peak values whose intensity is reduced by approximately 10 times, for both positive and negative values, as compared to the BMD associated with zero pre-tension forces (**Figure 7B**). Conversely, the bending moments in the arch increase in magnitude under optimal pretension forces, comparing with the case with zero pre-tensions. This is not a concern for the current design strategy, since the final bending moments in the arch are not dramatically high (peaks of the order of 2500 kNm), and can be safely sustained by this member

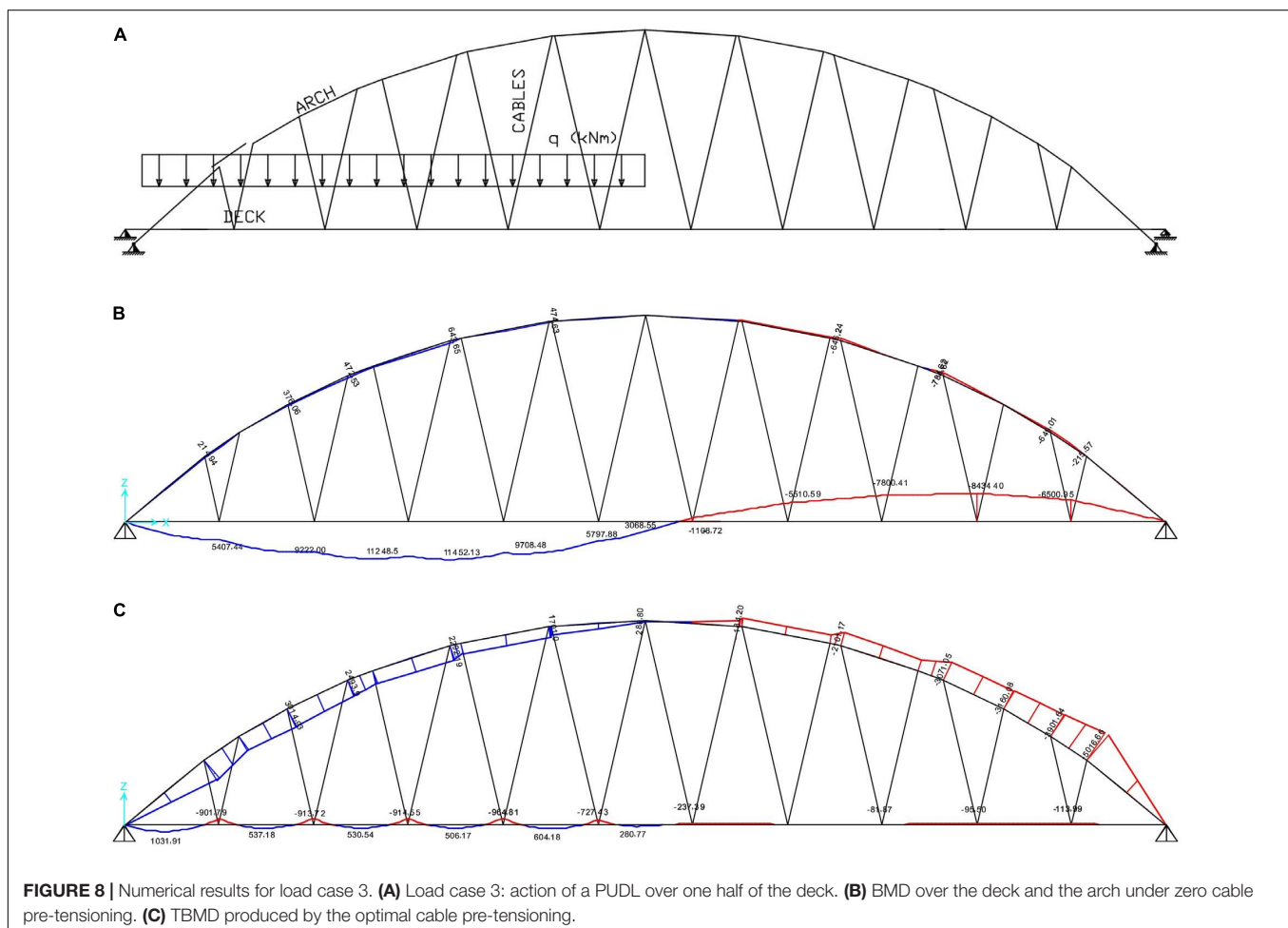
in the elastic regime (maximum elastic bending moment equal to $3,16 \times 10^4$ kNm, cf. Section “Finite Element Model”). In the present case, we observe $N_{d,max} = 1.31 \times 10^3$ kN in cable #11.

Load Case 3

Load case 3 is a PUDL of 70 kN/m applied on one half of the deck. The results of the optimization procedure referred to such a loading condition is illustrated in **Figure 8** ($N_{d,max} = 0.93 \times 10^3$ kN in cable #18). The TBMD produced by the optimal pre-tensioning of the cables shows peaks at the hanging points of the cables (**Figure 8C**), which are about 1/10 of the analogous peaks of the BMD corresponding to zero pre-tension forces (**Figure 8B**). The bending moment carried out by the arch increases moderately when pre-tension forces are applied.

Load Case 4

Load case 4 simulates vertical loads caused by vehicular traffic and lorries through a PUDL $q_a = 70$ kN/m that moves from left to right, and covers the entire span of the bridge. Such a load is superimposed to a UDL $q_p = 80$ kN/m corresponding to the summation of all the permanent loads.



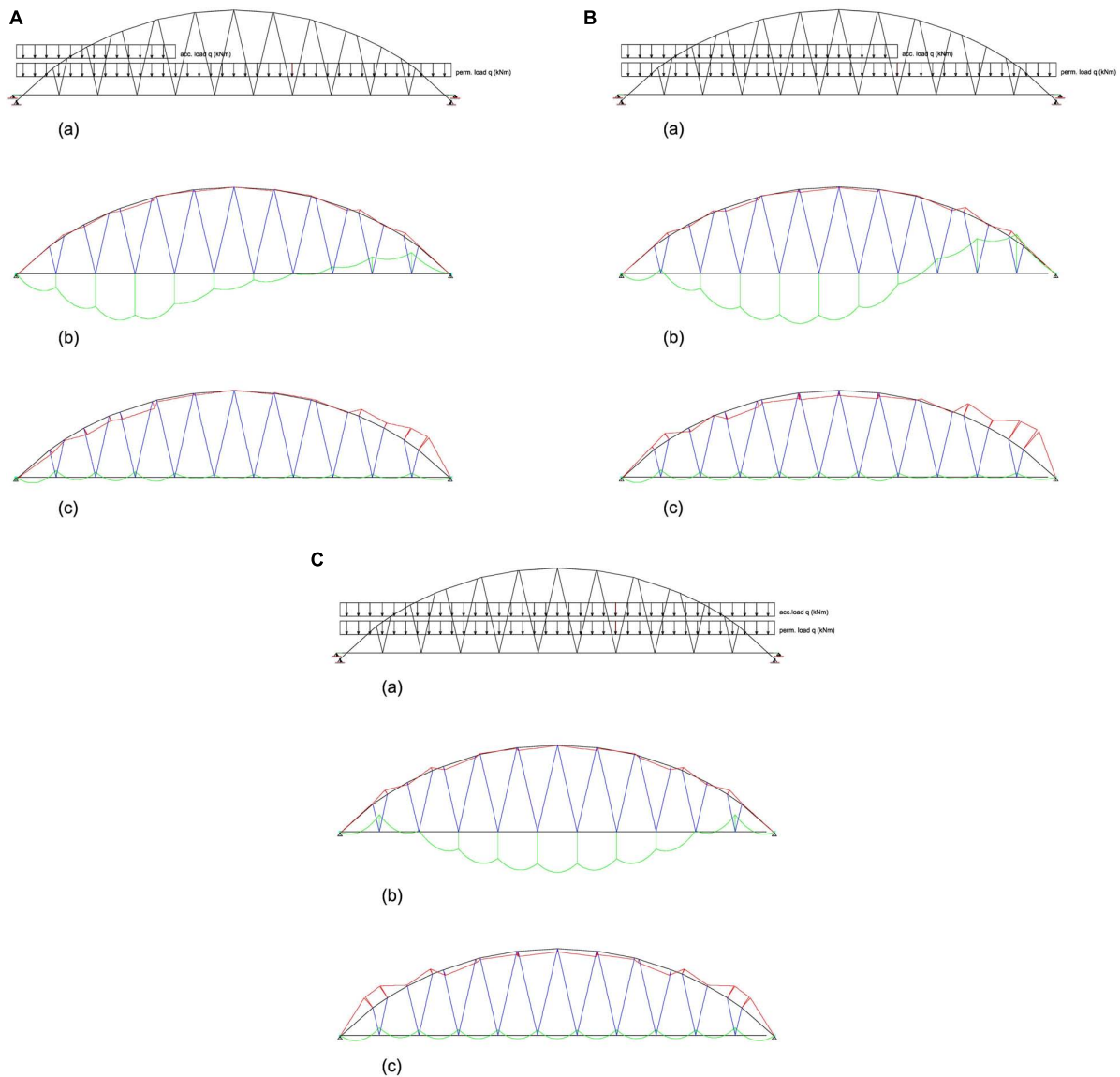


FIGURE 9 | Numerical results for load case 4. **(A):** current load distribution; **(B):** BMD over the deck and the arch under zero cable pre-tensioning; **(C)** TBMD produced by the optimal cable pre-tension forces.

Figure 9 illustrates the TBMDs induced by the optimal pretension forces that are associated with the three different positions of the moving load. Labels 4.1, 4.2, and 4.3 indicate loading scenarios which feature q_a distributed over 1/3, 2/3 and the entire span of the bridge, respectively. The TBMD bending moment peaks reduce by approximately 1/10 with respect to the case where no cable pretension is applied (BMD). One again observes that the peaks of the TBMDs exhibit the peaks of the bending moments that are reduced by $\approx 1/10$ with respect to those of the BMD without cable pretensioning, for each examined loading scheme. **Table 4** reports the optimal pretension factors corresponding to the TBMDs in **Figure 9**. We observe values of $N_{d,max}$ equal to 1.67×10^3 kN (cable #1), 1.98×10^3 kN (cable #13) and

1.86×10^3 kN (cable #18) in the load conditions 4.1, 4.2, and 4.3, respectively.

The results in **Figure 9** suggest that Eqn. (1) can be usefully employed within a closed loop active control system of the bridge under examination. Let us assume that the road pavement has been equipped with a WIM technology that allows the vehicles to be continuously weighed during traffic flow (refer, e.g., to Jacob and Feypell-de La Beaumelle, 2010 for an overview of available WIM technologies). In addition, let us suppose that all the stays have been equipped with hydraulic actuators, so as to behave as active tendons (Preumont, 2011; Coelho et al., 2015). One could design an active control system that operates according to the following methodology: (i) WIM sensors measure the variations of the moving loads on selected sections of the bridge

TABLE 4 | Optimal pretension factors corresponding to the TBMDs in **Figure 9**.

	4.1	4.2	4.3
\bar{x}_1	16,42	9,47	−4,77
\bar{x}_2	10,98	7,13	−1,38
\bar{x}_3	15,56	12,46	1,42
\bar{x}_4	10,85	9,84	3,28
\bar{x}_5	13,69	14,10	5,92
\bar{x}_6	9,52	11,27	6,78
\bar{x}_7	10,38	13,84	8,18
\bar{x}_8	6,88	11,09	8,59
\bar{x}_9	7,18	12,59	9,30
\bar{x}_{10}	3,97	9,61	9,39
\bar{x}_{11}	4,44	10,09	9,42
\bar{x}_{12}	1,36	6,78	9,31
\bar{x}_{13}	1,80	6,01	8,61
\bar{x}_{14}	−1,56	1,91	8,20
\bar{x}_{15}	−1,10	0,65	6,79
\bar{x}_{16}	−5,21	−4,80	5,94
\bar{x}_{17}	−4,91	−5,92	3,29
\bar{x}_{18}	−10,32	−13,41	1,44
\bar{x}_{19}	−9,19	−13,03	−1,36
\bar{x}_{20}	−16,61	−23,56	−4,75

and send the data to a controller; (ii) the controller solves Eqn. (1), determining the optimal pretension forces to be applied to the stays, and sends this information to the hydraulics actuators mounted on the stays; (iii) the actuators apply the optimal pretension forces to all the stays, determining the achievement of the TBMD over the deck. Additional mechanical and optical sensors measuring the forces in the stays and the deflections of the deck should also be integrated to ensure the system operates within required limit states. Assuming that dynamic effects as well as errors between the model and the real physical structure are compensated by other means, the proposed control strategy could be employed to mitigate the effect of loading on arch bridges with suspended deck. Time delay due to data transmission from the WIM sensors to the controller and from the controller to the actuators could be reduced by predicting the load distribution from previous measurements through vehicle speed estimation methods (Lu et al., 2020).

CONCLUSION

This paper has developed a linear elastic analysis for suspended deck arch bridges, which generalizes the studies presented in Fabbrocino et al. (2017) and Mascolo and Modano (2020) for beam bridges. By employing an engineering approximation to the mathematical optimization problem of the cable-pretension forces, an IMM has been formulated to determine a TBMD along the deck, which mimics a continuous-beam-type of response. Since the IMM is a linear system of equations with a reduced number of unknowns with respect to the full optimization problem, it could be suitable to be employed as part of a strategy for real-time

control. Assuming a linear behavior, the coefficient matrix of such a system is an intrinsic property of the bridge, and therefore it does not need to be modified when dealing with moving loads.

The results given in Section “Numerical Results” allow us to conclude that the cable pre-tensioning procedure presented in this study can be usefully employed within active control systems of cable-stayed bridges subject to moving vertical loads, when dynamic amplification effects can be neglected. It is aimed at controlling the response of the structure under ordinary service conditions, leading to the following key results: (a) to effectively “correct” the configuration of the bridge after completion of the construction process (Van Bogaert and De Backer, 2019); (b) to increase the load-bearing capacity when significant variations in mobile loads are to be expected, new vehicles are put into circulation or new technical regulations are enforced; (c) to strengthen new and existing structures by suitably reducing the peaks of the BMDs through an optimized cable pre-tensioning. We address such applications of the current research to future work, through analytical and experimental studies (Reksowardojo et al., 2018, 2019; Senatore et al., 2018a,b, 2019). Additional future research lines may include an iterative, incremental formulation of the optimization procedure presented in Section “Computation of Cable Pretension Forces,” to be aimed at handling dynamic effects (such as wind- or accidental-load-induced vibrations); time-dependent phenomena (viscous response of the materials of the arch and the deck, relaxation of the pre-stress of the tendons, etc.); and/or geometric non-linearities. Finally, we plan to compare different engineering strategies for the choice of the TBMD in future studies dealing with different typologies of suspended beam and arch bridges.

DATA AVAILABILITY STATEMENT

The original contributions presented in the study are included in the article/supplementary material, further inquiries can be directed to the corresponding author.

AUTHOR CONTRIBUTIONS

MM and FF led the mechanical modeling phases of the present study. MM designed and carried out the numerical simulations. AM collaborated to development of the numerical results. FS, RL, and FF supervised all the phases of the project. All authors contributed to the article and approved the submitted version.

FUNDING

AM and FF acknowledge financial support from the MIUR under the PRIN 2017 National Grant “Multiscale Innovative Materials and Structures” (grant number 2017J4EAYB).

REFERENCES

- Casas, J. R. (2015). The bridges of the future or the future of bridges? *Front. Built Environ.* 1:3. doi: 10.3389/fbuil.2015.00003
- Chen, D. W., Au, F. T. K., Tham, L. G., and Lee, P. K. K. (2000). Determination of initial cable forces in prestressed concrete cable-stayed bridges for given design deck profiles using the force equilibrium method. *Comput. Struct.* 74, 1–9. doi: 10.1016/S0045-7949(98)00315-0
- Coelho, H., Resende, A., Carvalho, D., and Soares, I. (2015). “High productivity in bridge construction,” in *Proceedings of the OPS effect - Multi-Span Large Bridges*, eds P. Pacheco and F. Magalhães (London: Taylor & Francis Group).
- EN 1991-2 (2003). *Eurocode 1: Actions on structures - Part 2: Traffic loads on bridges*. Brussels: European Union.
- Fabbrocino, F., Modano, M., Farina, I., Carpentieri, G., and Fraternali, F. (2017). Optimal prestress design of composite cable-stayed bridges. *Composite Struct.* 169, 167–172. doi: 10.1016/j.compstruct.2016.09.008
- Falanga, V. (2019). Procedura di ottimizzazione per ponti ad arco tipo Nielsen per la mitigazione delle sollecitazioni dovute alle modalità di varo. MSc Thesis, University of Naples, Federico II.
- Freire, A. M. S., Negrão, J. H. J. O., and Lopes, A. V. (2006). Geometrical nonlinearities on static analysis of highly flexible steel cable-stayed bridge. *Comput. Struct.* 84, 2128–2140. doi: 10.1016/j.compstruc.2006.08.047
- Gill, P. E., Murray, W., and Wright, M. H. (1981). *Practical Optimization*. Cambridge, MA: Academic Press.
- Jacob, B., and Feypell-de La Beaumelle, V. (2010). Improving truck safety: Potential of weigh-in-motion technology. *IATSS* 34, 9–15. doi: 10.1016/j.iatssr.2010.06.003
- Lazar, B. E., Troitsky, M. S., and Douglass, M. M. (1972). Load balancing analysis of cable-stayed bridges. *J. Struct. Divis.* 98, 1725–1740.
- Lee, T. Y., Kim, Y. H., and Kang, S. W. (2008). Optimization of tensioning strategy for asymmetric cable-stayed bridge and its effect on construction process. *J. Struct. Multidiscipl. Optim.* 35, 623–629. doi: 10.1007/s00158-007-0172-9
- Lonetti, P., and Pascuzzo, A. (2014). Optimum design analysis of hybrid cable-stayed suspension bridges. *Adv. Eng. Softw.* 73, 53–66. doi: 10.1016/j.advengsoft.2014.03.004
- Lu, S., Wang, Y., and Song, H. (2020). A high accurate vehicle speed estimation method. *Soft Comput.* 24, 1283–1291. doi: 10.1007/s00500-019-03965-w
- Mascolo, I., and Modano, M. (2020). Optimisation of suspended-deck bridge design: a case study. *Aust. J. Struct. Eng.* 2020:1778433. doi: 10.1080/13287982.2020.1778433
- Preumont, A. (2011). *Vibration Control of Active Structures*, 3rd Edn. Berlin: Springer.
- Reksowardojo, A. P., Senatore, G., and Smith, I. F. C. (2018). “Actuator layout optimization for adaptive structures performing large shape changes,” in *Advanced Computing Strategies for Engineering. EG-ICE 2018. Lecture Notes in Computer Science, 10864, Lausanne*, eds I. F. C. Smith and B. Dömer (Cham: Springer), 111–129. doi: 10.1007/978-3-319-91638-5_6
- Reksowardojo, A. P., Senatore, G., and Smith, I. F. C. (2019). Experimental testing of a small-scale truss beam that adapts to loads through large shape changes. *Front. Built Environ.* 5:93. doi: 10.3389/fbuil.2019.00093
- Senatore, G., Duffour, P., and Winslow, P. (2018a). Energy and cost analysis of adaptive structures: case studies. *J. Struct. Eng.* 144:04018107. doi: 10.1061/(asce)st.1943-541x.0002075
- Senatore, G., Duffour, P., Winslow, P., and Wise, C. (2018b). Shape control and whole-life energy assessment of an “Infinitely Stiff” prototype adaptive structure. *Smart Mater. Struct.* 27:015022. doi: 10.1088/1361-665x/aa8cb8
- Senatore, G., Duffour, P., and Winslow, P. (2019). Synthesis of minimum energy adaptive structures. *Struct. Multidiscipl. Optim.* 60, 849–877. doi: 10.1007/s00158-019-02224-8
- Simões, L. M. C., and Negrão, J. H. J. O. (1995). “Optimization of Cable-Stayed Bridges Subjected to Dynamic Loading,” in *Proceedings of Conference: The First World Congress on Structural and Multidisciplinary Optimization*, Goslar, 1–7.
- Skelton, R. E., and de Oliveira, M. C. (2010). *Tensegrity Systems*. Berlin: Springer.
- Song, C., Xiao, R., and Sun, B. (2018). Optimization of cable pre-tension forces in long-span cable stayed bridge considering the counterweight. *Eng. Struct.* 172, 919–928. doi: 10.1016/j.engstruct.2018.06.061
- Sung, Y. C., Chang, D. W., and Teo, E. H. (2006). Optimum post-tensioning cable forces of Mau-Lo His cable-stayed bridge. *J. Eng. Struct.* 28, 1407–1417. doi: 10.1016/j.engstruct.2006.01.009
- Van Bogaert, P., and De Backer, H. (2019). Continuous prestress in launched extradosed bridges. *Front. Built Environ.* 5:81. doi: 10.3389/fbuil.2019.00081
- Wang, P. H., Tseng, T. C., and Yang, C. G. (1993). Initial shape of cable-stayed bridges. *Comput. Struct.* 46, 1095–1106. doi: 10.1016/0045-7949(93)90095-u
- Wang, P. H., and Yang, C. G. (1996). Parametric studies on cable-stayed bridges. *Comput. Struct.* 60, 243–260. doi: 10.1016/0045-7949(95)00382-7
- Wang, Y. C., Vlahinos, A. S., and Shu, H. S. (1997). “Optimization of cable preloading on cable-stayed bridges. In Proc. SPIE. Smart Structures and Materials 1997,” in *Proceedings of the Smart Systems for Bridges, Structures, and Highways*, Vol 3043, San Diego, CA, 248–259. doi: 10.1117/12.274650
- Zhang, J., and Au, F. T. K. (2014). Calibration of initial cable forces in cable-stayed bridge based on Kriging approach. *Finite Element Anal. Design* 92, 80–92. doi: 10.1016/j.finela.2014.08.007

Conflict of Interest: The authors declare that the research was conducted in the absence of any commercial or financial relationships that could be construed as a potential conflict of interest.

Copyright © 2020 Modano, Majumder, Santos, Luciano and Fraternali. This is an open-access article distributed under the terms of the Creative Commons Attribution License (CC BY). The use, distribution or reproduction in other forums is permitted, provided the original author(s) and the copyright owner(s) are credited and that the original publication in this journal is cited, in accordance with accepted academic practice. No use, distribution or reproduction is permitted which does not comply with these terms.



Force and Shape Control Strategies for Minimum Energy Adaptive Structures

Gennaro Senatore* and Arka P. Reksowardojo*

Applied Computing and Mechanics Laboratory (IMAC), School of Architecture, Civil and Environmental Engineering (ENAC), Swiss Federal Institute of Technology (EPFL), Lausanne, Switzerland

OPEN ACCESS

Edited by:

Nikos D. Lagaros,
National Technical University of
Athens, Greece

Reviewed by:

Marios C. Phocas,
University of Cyprus, Cyprus
Maria Matheou,
University of Stuttgart, Germany

*Correspondence:

Gennaro Senatore
gennaro.senatore@epfl.ch
Arka P. Reksowardojo
arka.reksowardojo@epfl.ch

Specialty section:

This article was submitted to
Computational Methods in Structural
Engineering,
a section of the journal
Frontiers in Built Environment

Received: 27 March 2020

Accepted: 04 June 2020

Published: 22 July 2020

Citation:

Senatore G and Reksowardojo AP
(2020) Force and Shape Control
Strategies for Minimum Energy
Adaptive Structures.
Front. Built Environ. 6:105.
doi: 10.3389/fbuil.2020.00105

This work presents force and shape control strategies for adaptive structures subjected to quasi-static loading. The adaptive structures are designed using an integrated structure-control optimization method developed in previous work, which produces minimum “whole-life energy” configurations through element sizing and actuator placement optimization. The whole-life energy consists of an embodied part in the material and an operational part for structural adaptation during service. Depending on the layout, actuators are placed in series with the structural elements (internal) and/or at the supports (external). The effect of actuation is to modify the element forces and node positions through length changes of the internal actuators and/or displacements of the active supports. Through active control, the stress is homogenized and the displacements are kept within required limits so that the design is not governed by peak demands. Actuation has been modeled as a controlled non-elastic strain distribution, here referred to as *eigenstrain*. Any *eigenstrain* can be decomposed into two parts: an impotent *eigenstrain* only causes a change of geometry without altering element forces while a nilpotent *eigenstrain* modify element forces without causing displacements. Four control strategies are formulated: (C1) force and shape control to obtain prescribed changes of forces and node positions; (C2) shape control through impotent *eigenstrain* when only displacement compensation is required without affecting the forces; (C3) force control through nilpotent *eigenstrain* when displacement compensation is not required; and (C4) force and shape control through operational energy minimization. Closed-form solutions to decouple force and shape control through nilpotent and impotent *eigenstrain* are given. Simulations on a slender high-rise structure and an arch bridge are carried out to benchmark accuracy and energy requirements for each control strategy and for different actuator configurations that include active elements, active supports and a combination of both.

Keywords: adaptive structures, shape control, force control, *eigenstrain*, force method

INTRODUCTION

The construction sector is an important field of action in the on-going global effort to reduce anthropogenic greenhouse gas emissions (GHG) that aims to mitigate the potential consequence of climate crisis (I. E. Agency, 2018). Efforts to reduce building GHG emissions have focused mainly on operational emissions such as those that arise from heating/cooling, ventilation, lighting etc.

However, a significant share of buildings and structures GHG life cycle emissions is embodied because it arises from the manufacturing of components, construction, transport and demolition (Bekker, 1982). Recent studies have highlighted that the average embodied share of life cycle GHG emissions is 45–50% for energy-efficient buildings and that considering a service life of 50 years, the contribution of embodied GHG emissions can reach and surpass a ratio of 1:1 (embodied:operational) (Röck et al., 2020). Load-bearing systems have an important share of the environmental impact embodied in the built environment due to the large amount of material required for their construction and energy-intensive fabrication processes (Cole and Kernan, 1996; Kaethner and Burridge, 2012). According to the International Energy Agency (IEA), the embodied carbon (EC) of building structures, substructures and enclosures is responsible for 28% of global building sector emissions (I. E. Agency, 2018). Rapid growth population in conjunction with current and future energy depletion and material scarcity (I. E. Agency, 2017), call for new and radical solutions to reduce structures material usage and environmental impact. Despite this, best practice in structural design has led to significant oversizing because the structure is designed to withstand worst-case loads with long return periods such as high winds, earthquakes, heavy snow and large crowds. Since load-bearing structures are typically subjected to loads that are significantly lower than the design loads, it means that most structures are overdesigned for the majority of their service life.

Active structural control through sensing and actuation has been investigated as a strategy to meet safety and serviceability requirements under strong loading events such as high winds, earthquakes and unusual crowds (Soong, 1988; Casciati et al., 2012). Adaptive structures can control forces and deflections to stay within required limits such that the effect of external loading is reduced instead of relying only on passive load-bearing resistance. Several systems have been studied to control the structural response including building frames equipped with active bracings/columns (Reinhorn et al., 1993; Wagner et al., 2018; Weidner et al., 2018) and variable stiffness joints (Wang et al., 2020) as well as bridges equipped with active cable-tendons (Rodellar et al., 2002; Xu et al., 2003). Through integrated structure-control optimization (Smith et al., 1991; Begg and Liu, 2000; Soong and Cimellaro, 2009; Frohlich et al., 2019) civil structures can be designed to adapt (e.g., react positively) to rare loading events of high intensity in order to operate closer to required limits, which results in a better material utilization compared to equivalent weight-optimized passive structures (Teuffel, 2004; Sobek, 2016; Böhm et al., 2019). Material savings, however, are only possible at a cost of energy that is required to operate the adaptive system.

A new integrated structure-control optimization method has been formulated by Senatore et al. (2019), which produces minimum “whole-life” energy structures. The whole-life energy consists of the energy embodied in the material for material extraction, fabrication and construction as well as the operational energy for control. The whole-life energy is a new design criterion that allows to obtain adaptive structural systems with a significantly reduced material mass and which are minimum energy solutions thus reducing environmental impacts

with respect to conventional passive structures. Extensive numerical and experimental studies (Senatore et al., 2018a,c) have demonstrated that adaptive structures designed through the method given in Senatore et al. (2019), have significantly improved performances including reduced material mass, increased slenderness and increased stiffness as deflections are controlled within tight limits. In parallel, minimum energy adaptive structures have a lower environmental impact as the total energy can be reduced by up to 70% for slender configurations with respect to equivalent weight-optimized passive structures (Senatore et al., 2018b). Structural adaptation is particularly beneficial for stiffness governed design problems where it is challenging to reduce deflections within required limits for passive load-bearing systems. Instead, a well-designed adaptive structure can compensate for deflections actively at the cost of a small amount of operational energy. High-rise structures, long-span bridges and self-supporting roof systems are generally stiffness governed and therefore they are could greatly benefit from adaptive design strategies. Structural adaptation through geometric non-linear control has been further investigated in Reksowardojo et al. (2019, 2020a). Numerical and experimental studies have shown that when the structure is designed to be controlled into shape configurations that are optimal to counteract the effect of the external load, the stress can be effectively homogenized and minimized under different loading conditions. This leads to significant embodied energy savings with respect to adaptive structures limited to small shape changes as well as to weight-optimized passive structures.

The effect of actuation can be thought of as a non-elastic deformation that is similar to the strain caused by a lack of fit, thermal loading, plastic deformation or creep. This approach was taken in Ramesh and Utku (1991) and Lu et al. (1992) for force and geometry control as well as to formulate actuator placement optimization procedures. This type of non-elastic deformation has been referred to as *eigenstrain* in Mura (1991) and Irschik and Ziegler (2001). Nyashin et al. (2005) have shown that an *eigenstrain* can be decomposed into two main types: an *impotent eigenstrain* causes displacements without producing a stress change while a *nilpotent eigenstrain* changes the stress without causing displacements. This decomposition is of particular relevance in the context of active structural control because through inducing an impotent or a nilpotent *eigenstrain*, it is possible to control independently the external geometry and the forces, respectively.

The formulation of four control strategies is given in this paper: (C1) force and shape control to obtain prescribed changes of forces and node positions; (C2) shape control through impotent *eigenstrain* when only displacement compensation is required; (C3) force control through nilpotent *eigenstrain* when displacement compensation is not required and (C4) force and shape control through operational energy minimization. This work extends the integrated structure-control optimization method given in Senatore et al. (2019) with the formulation of control strategies C2, C3, and C4.

Depending on the actuator layout, actuators can be placed in series with the structural elements (internal actuator) and/or at the supports (external actuator). With a few exceptions such as in

Neuhaeuser et al. (2013), force and shape control through active supports has received little attention. In Senatore et al. (2019) it was shown that the length change of a linear actuator integrated in a reticular structure, can be conveniently modeled through an *eigenstrain* assignment which becomes part of the external load. This work extends the force and shape control formulation given in Senatore et al. (2019) to include the action (controlled displacements) of active supports.

This paper is arranged in six sections. Section Synthesis of Minimum Energy Adaptive Structures gives a summary of the design method adopted in this work. Section Structural Adaptation Process defines the structural adaptation process and it outlines the main formulation adopted in this work for structural analysis and control. Section Control Strategies gives the formulation of control strategies C1, C2, C3, and C4. In Section Case Studies, strategies C1, C2, C3, and C4 are applied to the control of a slender high-rise structure and an arch-truss bridge. Section Discussion and Conclusions conclude the paper.

SYNTHESIS OF MINIMUM ENERGY ADAPTIVE STRUCTURES

This work builds on the design method for adaptive structures given in Senatore et al. (2019). This method synthesizes adaptive structures through minimization of the whole-life energy (or total energy). The ability to actively counteract the effect of loading generally results in large savings of material and thus embodied energy. To minimize the consumption of operational energy for control, the structure is designed to rely on passive load-bearing capacity under normal loading conditions while adaptation is employed under strong loading events that occur rarely. This way, the embodied energy in the material is reduced at a small cost of operational energy. The formulation has been implemented for reticular structures with the assumption of small strains and small displacements. Note that it is assumed the dynamic response is not controlled through the active system. For the same reason, seismic design criteria are not included. Also, since adaptation is only necessary against strong but rare loads, it is assumed that fatigue is not a critical limit state.

The design variables are the element cross-section areas, the element forces, the actuator placement and the control commands. The objective is to minimize embodied and operational energy subject to ultimate and serviceability limit states under a randomly varying external load. Optimization is carried out through a nested scheme. Embodied and operational energy optimization are coordinated through two auxiliary variables: a design variable denoted as Material Utilization (*MUT*) factor which can be thought of as demand over capacity ratio defined for the structure as a whole; a state variable denoted as Load Activation Threshold (*LAT*) which is the lowest intensity loading event that causes a violation of a limit state. In the outer process, the *MUT* is varied in the range of $0\% < MUT \leq 100\%$ to obtain the minimum energy configuration. Figure 1A shows a notional relationship of the whole-life energy as a function of the *MUT*. A small *MUT* produces a very light-weight structure which has a small embodied energy but it might require large

control energy to satisfy stress and displacements limits during service (i.e., low level of *LAT*). Vice versa, a high *MUT* results into a stiffer structure which embodies larger energy in the material but it requires smaller control energy (i.e., high level of *LAT*).

For each *MUT* three steps are carried out: (1) embodied energy minimization, (2) actuator placement optimization, and (3) operational energy computation.

Step 1: Embodied Energy Optimization

The embodied energy is minimized through optimization of the element cross-section sizing and the internal load path (i.e., element forces). The embodied energy is computed for each element by scaling its mass with a material energy intensity factor which is the energy per unit mass for extraction and manufacturing taken from the *Inventory of Carbon and Energy (ICE)* (Hammond and Jones, 2008). For clarity, when all the structural elements are made of a single material, the embodied energy is equal to the mass scaled by a single factor.

This process can be thought of as a mapping between external loads, element forces and nodal displacements:

$$\begin{aligned} \chi : \mathbf{p}_j &\rightarrow (\mathbf{f}_j^t, \mathbf{d}_j^t) \quad \forall j = 0, 1, \dots, n^p, \\ \mathbf{p}_j &\mapsto \mathbf{f}_j^t(\mathbf{p}_j), \\ \mathbf{p}_j &\mapsto \mathbf{d}_j^t(\mathbf{p}_j), \end{aligned} \quad (1)$$

the index j refers to the j^{th} load case and n^p is the total number of load cases. The superscript t stands for *target* to denote the optimal internal load path. The outputs of this process are the cross-section areas and target forces \mathbf{f}^t under each load case.

Embodied energy optimization is carried out subject to equilibrium and ultimate limit state (ULS) constraints which include admissible stress and element buckling. However, geometric compatibility and deflection limits i.e., serviceability limit state (SLS) are not part of the optimization constraints. This means that when the load is applied and geometric compatibility is considered, the forces \mathbf{f} will be, in general, different to the target ones \mathbf{f}^t obtained through χ and the node displacements \mathbf{d} might not be within the required serviceability limits \mathbf{d}^t . The computation of \mathbf{d}^t requires selecting the controlled nodes (or controlled degrees of freedoms, denoted with cd) which is an input to the optimization process. The choice of cd depends on the type of structure as well as serviceability criteria. When the load causes a violation of an ultimate and/or a serviceability limit state, the forces and node positions will be controlled through actuation.

Step 2: Actuator Placement Optimization

The actuator layout comprises linear actuators which are assumed to be installed in series with the structure elements as shown by the illustrations in Table 1. The action of a linear actuator is to expand or retract, which is simulated through a non-elastic change of length Δl of the element onto which is fitted. The effect of the actuator length changes is to cause a change of forces $\Delta \mathbf{f}$ and node positions $\Delta \mathbf{d}^c$ (i.e., a change of shape). When the load causes a violation of an ultimate and/or a serviceability limit state, appropriate actuator commands Δl are computed to cause a change of forces

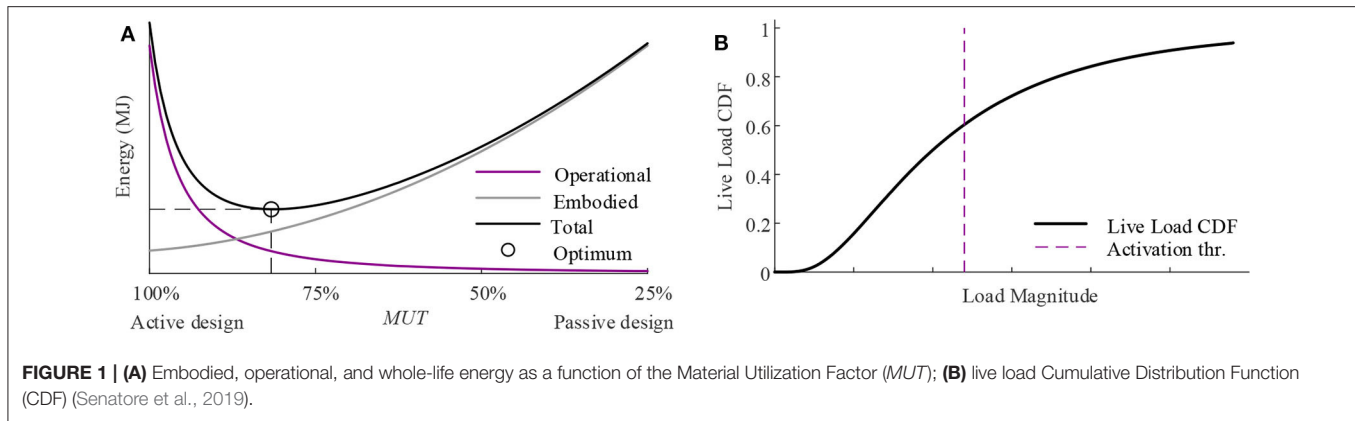


TABLE 1 | Structural adaptation process.

State	Displacement	Forces
(A) CONTROLLED SHAPE UNDER PERMANENT LOAD		
	$\mathbf{d}^n = 0$	\mathbf{f}^n
(B) DEFORMED SHAPE UNDER LIVE LOAD		
	\mathbf{d}^p	\mathbf{f}^p
(C) CONTROLLED SHAPE UNDER LIVE LOAD		
	$\mathbf{d}^c = \mathbf{d}^p + \Delta \mathbf{d}^c$	$\mathbf{f}^c = \mathbf{f}^p + \Delta \mathbf{f}^c$
(D) RESIDUAL EFFECT OF ACTUATION AFTER THE LIVE LOAD IS REMOVED		
	$\Delta \mathbf{d}^c$	$\Delta \mathbf{f}^c$

Actuators are represented by thick lines placed in the middle of the element.

$\Delta \mathbf{f}^t = \mathbf{f}^t - \mathbf{f}$ from a compatible state \mathbf{f} to the target state \mathbf{f}^t (obtained through χ) and a change of shape $\Delta \mathbf{d}^t = \mathbf{d}^t - \mathbf{d}$ from the deformed shape \mathbf{d} to the target one \mathbf{d}^t required by SLS.

The actuator placement optimization is a combinatorial problem which involves placing a certain number of linear actuators within a set of available sites (the structural elements or the supports). In order to improve computational efficiency, this binary problem has been relaxed into a continuous form through sensitivity analysis (Senatore et al., 2019). The actuators are placed through ranking by employing a control efficacy measure which evaluates the contribution of each actuator toward the attainment of the target change of forces $\Delta \mathbf{f}^t$ and node positions $\Delta \mathbf{d}^t$. The objective is to obtain an actuator

layout so that the change of forces $\Delta \mathbf{f}^c$ and node positions $\Delta \mathbf{d}^c$ caused by $\Delta \mathbf{l}$ are as close as possible to the required $\Delta \mathbf{f}^t$ and $\Delta \mathbf{d}^t$, respectively:

$$\vartheta : (\mathbf{f}_j^t, \mathbf{d}_j^t) \rightarrow \text{ACT} \quad \forall j = 0, 1, \dots, n^p, \quad (2)$$

where $\text{ACT} \in \mathbb{Z}^{n^{\text{act}}}$; $\text{ACT} \subseteq \{1, \dots, n^e\}$ is the set which contains the element indices that denote the actuator locations. When the actuator placement is known, suitable actuator commands $\Delta \mathbf{l}$ are obtained to control the structure through the target change of forces $\Delta \mathbf{f}^t$ and node positions $\Delta \mathbf{d}^t$. This is an inverse problem which has been solved through constrained optimization as described in section Control to Target Forces and Shapes (C1).

Once the actuator layout is known, it is possible to compute the actuation system embodied energy which is added to the structure embodied energy obtained from step 1. The same applies to the mass of the adaptive solution which is the sum of the structure mass and the actuation system mass. Generally, it is reasonable to assume that the actuator embodied energy (and thus its mass) increases as the actuator force capacity increases. In Senatore et al. (2019), it has been assumed that an actuator is entirely made of steel with an energy intensity of 35 MJ/kg (Hammond and Jones, 2008) and its mass is proportional to the required force capacity (i.e., the maximum force required through control) with a constant of 0.1 kg/kN (e.g., an actuator with a push/pull load of 10,000 kN has a mass of 1,000 kg) (ENERPAC, 2016).

Embodied energy optimization and actuator layout optimization are interrelated because the actuation system is an integral part of the structure. The layout of the structure (produced by process χ in Step 1) is obtained with the assumption that serviceability requirements are met through active control. Conversely, the optimal actuator placement that is determined through process ϑ depends on the layout of the structure produced by process χ . The actuator efficacy to control internal forces and displacements depends on its location in the structure as well as the position of the control nodes. The actuator optimal layout changes as the MUT is varied during energy optimization because the material distribution changes and therefore also the required force control and displacement compensation change.

Step 3: Operational Energy Computation

The structure is subjected to a permanent (self-weight + dead load) and a randomly fluctuating live load. For simplicity, all loads that are not permanent are considered live loads including events such as high winds, unusual crowds etc. The probability distribution of the live load is modeled with a log-normal function which is suitable to model a generic random occurrence. **Figure 1B** shows the plot of a generic log-normal cumulative distribution where the load activation threshold LAT is indicated by a dashed line. The LAT is the lowest level of the load probability distribution that causes a state of stress and/or displacement to violate a limit state. The design load is set as the characteristic value which corresponds to the 95th percentile of the associated normal distribution. Since the operational energy is computed during service, the characteristic value is the design load without load factors (i.e., SLS load case). The load probability distribution is discretized into n^d bins, the load corresponding to the k^{th} bin (i.e., occurrence) is denoted as \mathbf{p}_{jk} . The discretized probability density is scaled by the expected service life of the structure which is usually set to 50 years. The duration of each loading event Δt_{jk} is obtained through scaling the expected service life of the structure with the probability of the k^{th} occurrence for the j^{th} load case. The total operational energy is the sum of the energy required for force and displacement compensation for all the load occurrences above that corresponding to the LAT .

Steps 1 to 3 are repeated for each MUT to obtain the configuration of minimum energy. Although embodied and operational energy optimization are not carried out

simultaneously (nested approach), it has been proven by Wang and Senatore (2020) that solutions produced by this method are only marginally different in energy terms to those produced by an All-in-One implementation of the same method through Mixed-Integer Non-linear Programming.

Structural Adaptation Process

Table 1 gives an illustration of the four main states of the adaptation process considered in this work. The structure is controlled to move from the state (a) to state (d) for each load case. There are two phases of adaptation: (1) in the 1st phase (b–c), the structure is controlled to counteract the effect of the live load, (2) in the 2nd phase (d–a), the structure is controlled to eliminate the residual effect caused by actuation in the first phase, after the live load is removed.

The formulation presented in this study is implemented with the assumption of small strains and small displacements, and thus superposition applies. \mathbf{f}^{in} denote the forces when the structure is subjected only to permanent load which is assumed to be counteracted through actuation before the live load is applied. This can be thought of as a pre-cambering so that the structure undeformed (the displacements are reduced to zero, i.e., $\mathbf{d}^{in} = 0$) when the live load is applied. \mathbf{f}^p and \mathbf{d}^p denote forces and displacements caused by the external load \mathbf{p} . $\Delta \mathbf{f}^c$ and $\Delta \mathbf{d}^c$ are the change of forces and displacements caused by the actuator commands $\Delta \mathbf{l}$. The forces and displacements at the start (b) and end (c) of the 1st phase are $\mathbf{f}^p, \mathbf{d}^p$ and $\mathbf{f}^c, \mathbf{d}^c$, respectively. The forces and displacements at the start (d) and end (a) of the 2nd phase are $\mathbf{f}^{in} + \Delta \mathbf{f}^c, \mathbf{d}^{in} + \Delta \mathbf{d}^c$ and $\mathbf{f}^{in}, \mathbf{d}^{in}$, respectively.

ANALYSIS AND CONTROL OF ADAPTIVE STRUCTURES

Force Method

The analysis and control strategies implemented in this work use a force method formulation based on singular value decomposition of the equilibrium conditions in matrix form (Pellegrino and Calladine, 1986; Pellegrino, 1993), which is here referred to as SVD-FM. In previous own work (Reksowardojo and Senatore, 2020), it was proven that the SVD-FM is equivalent to the Integrated Force Method (IFM) (Patnaik, 1973) that was employed in Senatore et al. (2019) for design and control of adaptive structures. Both SVD-FM and IFM offer an effective way to predict the static response of a reticular structure subjected to external load and actuator actions. With these methods, actuation can be modeled as the effect of an imposed strain distribution i.e., *eigenstrain*, which is assigned directly as part of the external load. Although the IFM has a simpler and more intuitive formulation, the SVD-FM offers a way to derive closed-form solutions for control strategies C2 and C3 (impotent and nilpotent *eigenstrain*) which is the main reason it has been adopted in this work.

Given a pin-jointed structure made of n^e elements, n^n nodes in dim dimensions and thus having $n^d = dim \cdot n^n$ degrees of freedom, force-equilibrium conditions at nodes are:

$$\mathbf{A}\mathbf{f} = \mathbf{p} \quad (3)$$

where $\mathbf{p} \in \mathbb{R}^{n^d \times 1}$ is the external load vector. $\mathbf{A} \in \mathbb{R}^{n^d \times (n^e + n^{sd})}$ is an extended equilibrium matrix which concatenates $\mathbf{A}^{el} \in \mathbb{R}^{n^d \times n^e}$ and $\mathbf{A}^{sup} \in \mathbb{R}^{n^d \times n^{sd}}$:

$$\mathbf{A} = [\mathbf{A}^{el} \mid \mathbf{A}^{sup}]. \quad (4)$$

\mathbf{A}^{el} is the familiar equilibrium matrix which contains the element direction cosines. Details regarding the computation of \mathbf{A}^{el} can be found in Pellegrino and Calladine (1986) and Achtziger (2007). \mathbf{A}^{sup} is a matrix that contains the support reaction direction cosines for n^{sd} constrained degrees of freedom. The supports are effectively thought of as infinitely rigid elements which constrain the rigid body motion of the structure. When the support reaction directions coincide with the global axes, as in most cases, \mathbf{A}^{sup} is a matrix containing zeros and ones.

The vector of forces $\mathbf{f} \in \mathbb{R}^{(n^e + n^{sd}) \times 1}$ is the concatenation of the internal element forces $\mathbf{f}^{el} \in \mathbb{R}^{n^e \times 1}$ with the support reactions $\mathbf{f}^{sup} \in \mathbb{R}^{n^{sd} \times 1}$:

$$\mathbf{f} = \begin{Bmatrix} \mathbf{f}^{el} \\ \mathbf{f}^{sup} \end{Bmatrix}. \quad (5)$$

Depending on the actuator layout, actuators can be placed in series with the structural elements (internal actuator) and/or at the supports (external actuator). An internal actuator is a linear actuator that can either extend or reduce the length of the element onto which it is fitted. An external actuator instead moves the position of a support which can be thought of as an induced differential settlement. The vector of actuator commands $\Delta \mathbf{l} \in \mathbb{R}^{(n^e + n^{sd}) \times 1}$ is defined as the concatenation of the internal actuator length changes $\Delta \mathbf{l}^{el} \in \mathbb{R}^{n^e \times 1}$ with the support displacements caused by external actuators (or active supports) $\Delta \mathbf{d}^{sup} \in \mathbb{R}^{n^{sd} \times 1}$:

$$\Delta \mathbf{l} = \begin{Bmatrix} \Delta \mathbf{l}^{el} \\ \Delta \mathbf{d}^{sup} \end{Bmatrix}. \quad (6)$$

Note that, once the actuator placement is determined, the actuator command vector $\Delta \mathbf{l}$ reduces its dimension to $\mathbb{R}^{(n^{act}) \times 1}$ by including only the entries that correspond to the selected internal or external actuators.

Denote with r the rank of the equilibrium matrix \mathbf{A} , then the number of self-stress states is $s = (n^e + n^{sd}) - r$ and the number of mechanism modes is $m = n^d - r$ (including rigid body motion). Depending on the structural topology and the number of supports, static indeterminacy is caused by internal s^{int} and/or external s^{ext} self-stress states such that $s = s^{int} + s^{ext}$.

The singular value decomposition of \mathbf{A} gives the following:

$$\mathbf{A} = [\mathbf{U}_r \mid \mathbf{U}_m] \begin{bmatrix} \mathbf{V}_r & \mathbf{0} \\ \mathbf{0} & \mathbf{0} \end{bmatrix} [\mathbf{W}_r \mid \mathbf{W}_s]^T. \quad (7)$$

$[\mathbf{U}_r \mid \mathbf{U}_m] \in \mathbb{R}^{n^d \times n^d}$, $[\mathbf{W}_r \mid \mathbf{W}_s] \in \mathbb{R}^{(n^e + n^{sd}) \times (n^e + n^{sd})}$ and $\mathbf{V}_r \in \mathbb{R}^{(n^e + n^{sd}) \times (n^e + n^{sd})}$ are the left singular vectors, right singular

vectors and singular values of \mathbf{A} , respectively. The term $\mathbf{U}_r \in \mathbb{R}^{n^d \times (n^d - m)}$ is the basis of the load components that are in equilibrium with the forces lying in the space spanned by $\mathbf{W}_r \in \mathbb{R}^{(n^e + n^{sd}) \times (n^e + n^{sd} - s)}$ which is the basis of the row space $\mathcal{R}(\mathbf{A})$ of \mathbf{A} . The term $\mathbf{W}_s \in \mathbb{R}^{(n^e + n^{sd}) \times s}$ is the basis of the null space of \mathbf{A} . The columns of \mathbf{W}_s are s linear independent states of self-stress. The term $\mathbf{U}_m \in \mathbb{R}^{n^d \times m}$ is the basis of the left null space of the equilibrium matrix $\mathcal{N}(\mathbf{A}_t)$. The columns of \mathbf{U}_m are m independent nodal displacement modes which do not cause first-order deformation of the elements i.e., the inextensional mechanism basis. If the external load has components that lie in the space spanned by \mathbf{U}_m , it will excite one or more mechanisms and therefore the structure will not be able to take the load in its original configuration. If only first-order infinitesimal mechanisms exist, appropriate prestress might be applied to stabilize the structure (Pellegrino, 1990). For kinematically determinate structures, \mathbf{U}_m does not exist. This work only considers structures with static indeterminacy but not kinematic indeterminacy. For the full static and kinematic interpretation of the terms obtained from the SVD of the equilibrium matrix, the reader is referred to Pellegrino (1993).

Recalling the equilibrium conditions in Equation 3, there is an infinite number of non-trivial solutions for the homogeneous system $\mathbf{A}\mathbf{f} = \mathbf{0}$ which are linear combinations of the self-stress vectors:

$$\mathbf{f}^{\mathcal{N}(\mathbf{A})} = \mathbf{W}_s \boldsymbol{\mu} \in \mathcal{N}(\mathbf{A}) \quad (8)$$

The particular solution instead is:

$$\mathbf{f}^{\mathcal{R}(\mathbf{A})} = \mathbf{A}^+ \mathbf{p} \in \mathcal{R}(\mathbf{A}) \quad (9)$$

where \mathbf{A}^+ is the Moore-Penrose pseudoinverse of \mathbf{A} , which can be computed as:

$$\mathbf{A}^+ = \mathbf{W}_r \mathbf{V}_r^{-1} \mathbf{U}_r^T \quad (10)$$

The general solution is the sum of the particular and homogeneous solutions:

$$\mathbf{f} = \mathbf{A}^+ \mathbf{p} + \mathbf{W}_s \boldsymbol{\mu} \in \mathcal{R}(\mathbf{A}) \oplus \mathcal{N}(\mathbf{A}) \quad (11)$$

where the operator \oplus indicates a vector space addition. The linear coefficient vector $\boldsymbol{\mu}$ is:

$$\boldsymbol{\mu} = -(\mathbf{W}_s^T \mathbf{G} \mathbf{W}_s)^{-1} \mathbf{W}_s^T [\Delta \mathbf{l} + \mathbf{G} \mathbf{A}^+ \mathbf{p}], \quad (12)$$

which is obtained by substituting $\mathbf{A}^+ \mathbf{p} + \mathbf{W}_s \boldsymbol{\mu}$ into the compatibility conditions:

$$\mathbf{W}_s^T (\mathbf{G} \mathbf{f} + \Delta \mathbf{l}) = \mathbf{0} \quad (13)$$

and then solving for $\boldsymbol{\mu}$. The term $\mathbf{G} \in \mathbb{R}^{(n^e + n^{sd}) \times (n^e + n^{sd})}$ is the member flexibility matrix. For reticular structures \mathbf{G} is a diagonal matrix with entries $l_i / (E_i \alpha_i)$, where l_i , E_i and α_i are

the length, Young's modulus and cross-section area of the i^{th} element of the structure $\forall i \leq n^e$. The entries of \mathbf{G} are zeros for the supports i.e., $\forall i > n^e$, since supports are assumed to be infinitely stiff. The s compatibility conditions in Equation 13 can be derived from virtual work or alternatively as shown in Pellegrino (1993) from the orthogonality between the compatible strains $\boldsymbol{\varepsilon} = \mathbf{G}\mathbf{f} + \Delta\mathbf{I}$ and the basis of incompatible strains \mathbf{W}_s (\mathbf{W}_s can be interpreted as both the self-stress and incompatible strain basis). Note that since the equilibrium matrix includes the support reaction direction cosines (Equation 4), each column of \mathbf{W}_s includes support reactions that are in equilibrium with the self-stress state. The term $\boldsymbol{\varepsilon}$ includes the elastic strain $\mathbf{G}\mathbf{f}$ caused by the internal forces as well as the effect of a non-elastic strain $\Delta\mathbf{I}$, i.e., *eigenstrain*, which could be produced by a lack of fit or thermal loading or, following Senatore et al. (2019), by the length change of internal actuators and/or external actuators (i.e., displacements of the active supports). Through Equation 11, the forces \mathbf{f} caused by the combined effect ($\mathbf{f}^p + \Delta\mathbf{f}^c$) of the external load \mathbf{p} and actuator commands $\Delta\mathbf{I}$ are computed through a single statement. When the actuator commands are included in Equation 11, the forces are denoted as \mathbf{f}^c i.e., controlled forces and otherwise as \mathbf{f}^p .

Considering only kinematically determinate structures and recalling the compatibility conditions $\mathbf{A}^T\mathbf{d} = \mathbf{G}\mathbf{f} + \Delta\mathbf{I}$, the node displacements $\mathbf{d} \in \mathbb{R}^{n^d}$ caused by the combined effect ($\mathbf{d}^p + \Delta\mathbf{d}^c$) of the external load \mathbf{p} and the actuator commands $\Delta\mathbf{I}$ are obtained as:

$$\mathbf{d} = (\mathbf{A}^T)^+ (\mathbf{G}\mathbf{f} + \Delta\mathbf{I}) \in \mathcal{R}(\mathbf{A}^T) \quad (14)$$

For kinematically determinate structure \mathbf{A}^T is a full column rank matrix and hence its pseudoinverse is unique. When the actuator commands $\Delta\mathbf{I}$ are included in Equation 14, the displacements are denoted as \mathbf{d}^c i.e., controlled displacements (or shape) and otherwise as \mathbf{d}^p .

Force and Shape Influence Matrices

Assuming small deformations, control through the actuator commands $\Delta\mathbf{I}$ (internal + external) causes a change of forces $\Delta\mathbf{f}^c$ and shape $\Delta\mathbf{d}^c$, which can be expressed in matrix-vector product form as:

$$\mathbf{S}_f \Delta\mathbf{I}^{all} = \Delta\mathbf{f}^c, \quad (15)$$

$$\mathbf{S}_d \Delta\mathbf{I}^{all} = \Delta\mathbf{d}^c, \quad (16)$$

where $\mathbf{S}_f \in \mathbb{R}^{(n^e+n^{sd}) \times (n^e+n^{sd})}$ and $\mathbf{S}_d \in \mathbb{R}^{n^d \times (n^e+n^{sd})}$ are defined as the force and shape influence matrix, respectively. Note that in Equations 15 and 16, $\Delta\mathbf{I}^{all} \in \mathbb{R}^{(n^e+n^{sd}) \times 1}$ contains control commands for all the elements and supports as if they were all active.

The force and shape influence matrices can be obtained by collating column-wise the effect of a unitary length change of each element and a unitary displacement of each support in turn on forces (Equation 11) and node positions (Equation 14) without applying any external load \mathbf{P} (Senatore et al., 2019). However, from Equations 11 and 14, \mathbf{S}_f and \mathbf{S}_d can be

also computed directly (as also shown in Yuan et al., 2016; Reksowardojo and Senatore, 2020):

$$\mathbf{S}_f = -\mathbf{W}_s (\mathbf{W}_s^T \mathbf{G} \mathbf{W}_s)^{-1} \mathbf{W}_s^T, \quad (17)$$

$$\mathbf{S}_d = (\mathbf{A}^+)^T (\mathbf{G} \mathbf{S}_f + \mathbf{I}), \quad (18)$$

where \mathbf{I} denotes an identity matrix of dimensions $(n^e + n^{sd}) \times (n^e + n^{sd})$.

CONTROL STRATEGIES

The four strategies described in this section solve a common problem, which is the computation of suitable control commands given an actuator layout and a control objective. As anticipated in Step 2: Actuator Placement Optimization, following the method given in Senatore et al. (2019) control commands are computed to cause a simultaneous change of forces and node positions (C1) at the occurrence of a load above the activation threshold (*LAT*). However, in other cases, it might not be necessary to obtain a prescribed change of forces and node positions simultaneously. For example, it might be desirable to control only the node positions to satisfy deflection limits without affecting the forces if they are already within required limits (stress and stability). This can be achieved by applying an impotent *eigenstrain* through actuation (C2). Conversely, when it is only necessary to control the forces, for example, to reduce the stress under critical loading conditions but displacement compensation is not required, a possible strategy is to apply a nilpotent *eigenstrain* through actuation (C3). Finally, when the energy consumption of the actuation system is of primary concern, an alternative strategy is to obtain control commands through minimization of the work done by the actuators (C4) to minimize the operational energy during service.

Control to Target Forces and Shapes (C1)

Following the method given in Senatore et al. (2019) when the load causes a violation of an ultimate and/or a serviceability limit state, appropriate actuator commands $\Delta\mathbf{I}$ are computed to cause a change of forces $\Delta\mathbf{f}^t$ from a compatible state to the target state (obtained through χ) and a change of shape $\Delta\mathbf{d}^t$ from the deformed shape to the target one required by SLS. For control strategy C1 (as well as C2 and C3), it is useful to distinguish between target change of forces $\Delta\mathbf{f}^t$ and shape $\Delta\mathbf{d}^t$ and controlled change of forces $\Delta\mathbf{f}^c$ and shape $\Delta\mathbf{d}^c$. The target state is given as an input. The objective is to obtain control commands $\Delta\mathbf{I}$ whose effect is to cause a $\Delta\mathbf{f}^c$ and $\Delta\mathbf{d}^c$ which are as close as possible to $\Delta\mathbf{f}^t$ and $\Delta\mathbf{d}^t$. This objective can be fulfilled with an accuracy that depends on the actuator layout.

The combined number of internal and external actuators is denoted as n^{act} i.e., $n^{act} = n^{act,int} + n^{act,ext}$. The number of controlled degrees of freedom is denoted as n^{cd} . Recalling Equations 17 and 18, the force and shape influence matrices are computed assuming that all elements and supports are active. However, in practice only some of the elements and supports are equipped with actuators $n^{act} \leq n^e + n^{sd}$ and it

is required to control only some of the degrees of freedoms $n^{cd} \leq n^d$. Assume an actuator layout with n^{act} actuators and n^{cd} controlled degree of freedom. The force influence matrix is reduced to $\mathbf{S}_f^* \in \mathbb{R}^{(n^e+n^{sd}) \times n^{act}}$ which contains only the columns corresponding to the active elements and supports. Similarly, the shape influence matrix is reduced to $\mathbf{S}_d^* \in \mathbb{R}^{n^{cd} \times n^{act}}$ which contains only the rows corresponding to controlled degrees of freedom and the columns corresponding to active elements and supports. The target shape change is also reduced to $\Delta \mathbf{d}^{t*} \in \mathbb{R}^{n^{cd}}$ which contains only the entries corresponding to the controlled degrees of freedom. The same applies to the controlled shape change which is reduced to $\Delta \mathbf{d}^{c*} \in \mathbb{R}^{n^{cd}}$.

Since it is generally desirable to control structures with a simple (i.e., low number of actuators) actuation system, \mathbf{S}_f^* and \mathbf{S}_d^* are usually rectangular matrices with significantly more rows than columns (i.e., an over determinate linear system). A general formulation to compute actuator commands $\Delta \mathbf{l}$ to cause $\Delta \mathbf{f}^t$ and $\Delta \mathbf{d}^t$ is through a constrained least square optimization:

$$\min_{\Delta \mathbf{l}} \|\mathbf{S}_d^* \Delta \mathbf{l} - \Delta \mathbf{d}^{t*}\|_2 \quad (19)$$

s.t.

$$\mathbf{S}_f^* \Delta \mathbf{l} = \Delta \mathbf{f}^t. \quad (20)$$

The actuator commands $\Delta \mathbf{l}$ produced as the solution to this problem cause the required change of target force $\Delta \mathbf{f}^t$ and shape $\Delta \mathbf{d}^{t*}$. Generally, the rank of the reduced force and shape influence matrices \mathbf{S}_f^* and \mathbf{S}_d^* are equal to the degree of static indeterminacy s and the number of controlled degrees of freedom n^{cd} , respectively. When this is the case, depending on a well-chosen actuator placement, if the number of actuators is set to $n^{act} = s + n^{cd}$ the problem stated in Equations 19 and 20 admits a unique solution with low residuals ($\Delta \mathbf{f}^c = \Delta \mathbf{f}^t$; $\Delta \mathbf{d}^{c*} \approx \Delta \mathbf{d}^{t*}$). However, in practice it is generally preferable to reduce the number of actuators as much as possible. If the number of actuators is kept in the range $s < n^{act} \leq s + n^{cd}$, generally force control can be carried out accurately (the equality constraint in Equation 20 is satisfied) but shape control will be approximate ($\Delta \mathbf{f}^c = \Delta \mathbf{f}^t$; $\Delta \mathbf{d}^{c*} \sim \Delta \mathbf{d}^{t*}$). Depending on the choice of the controlled degrees of freedom and the actuator placement, there are cases in which \mathbf{S}_f^* or \mathbf{S}_d^* might be ill-conditioned. In these cases, adding more actuators might help to solve numerical issues.

Control Through Impotent and Nilpotent *eigenstrain*

In this work, the effect of actuation is modeled as a non-elastic deformation that is similar to the strain caused by thermal effect, plastic deformation or creep. This type of non-elastic deformation has been referred to as *eigenstrain*. Any *eigenstrain* can be uniquely decomposed into two distributions (Nyashin et al., 2005): impotent *eigenstrain* change the node positions without producing stress while nilpotent *eigenstrain* redistribute the stress without causing displacements. Impotent *eigenstrain* through actuation is useful when it is required to control the node

positions without affecting the forces. Conversely, when it is only necessary to control the forces, a nilpotent *eigenstrain* could be applied through actuation.

Shape Control Through Impotent *eigenstrain* (C2)

An impotent *eigenstrain* is produced by actuator commands that cause a required change of node positions $\Delta \mathbf{d}^t$ without changing the forces, therefore:

$$\min_{\Delta \mathbf{l}^{all}} \|\mathbf{S}_d \Delta \mathbf{l}^{all} - \Delta \mathbf{d}^t\|_2, \quad (21)$$

s.t.

$$\mathbf{S}_f \Delta \mathbf{l}^{all} = \mathbf{0}. \quad (22)$$

Equation 22 is a homogeneous linear equation system whose trivial solution is $\Delta \mathbf{l}^{all} = \mathbf{0}$. Assuming that all elements and supports are active, there is an infinite number of non-trivial solutions:

$$\Delta \mathbf{l}^{all} = \mathbf{W}_r \boldsymbol{\beta}, \quad (23)$$

where \mathbf{W}_r is the basis of the row space of the equilibrium matrix \mathbf{A} which is defined in section Analysis and Control of Adaptive Structures. Recalling Equation 17 for the force influence matrix \mathbf{S}_f , the product of \mathbf{W}_s^T with any linear combination of \mathbf{W}_r vanishes since by definition the row space is orthogonal to the null space. Therefore, if the actuator command components lie in the space spanned by \mathbf{W}_r , it will produce an impotent *eigenstrain*. Replacing Equation 23 in Equation 21 and then solving for $\boldsymbol{\beta}$:

$$\boldsymbol{\beta} = (\mathbf{S}_d \mathbf{W}_r)^+ \Delta \mathbf{d}^t. \quad (24)$$

Therefore, $\Delta \mathbf{l}^{all}$ to produce an impotent *eigenstrain* is:

$$\Delta \mathbf{l}^{all} = \mathbf{W}_r (\mathbf{S}_d \mathbf{W}_r)^+ \Delta \mathbf{d}^t. \quad (25)$$

Assuming small deformations, Equation 25 gives actuator commands $\Delta \mathbf{l}^{all}$ which cause the required change of node positions $\Delta \mathbf{d}^c = \Delta \mathbf{d}^t$ and no change of forces $\Delta \mathbf{f}^c = \mathbf{0}$. This means that the node positions change only through non-elastic deformations that do not cause any elastic deformation of the elements.

If only selected elements are actuators and only selected degrees of freedom are controlled, the non-trivial solutions of Equation 22 are actuator commands whose components lie in the null space of the reduced force influence matrix \mathbf{S}_f^* :

$$\Delta \mathbf{l} = \mathbf{W}_s^{S_f^*} \boldsymbol{\beta}, \quad (26)$$

Replacing Equation 26 in Equation 21 and solving for $\Delta \mathbf{l}$:

$$\Delta \mathbf{l} = \mathbf{W}_s^{S_f^*} \left(\mathbf{S}_d^* \mathbf{W}_s^{S_f^*} \right)^+ \Delta \mathbf{d}^{t*} \quad (27)$$

where $\mathbf{W}_s^{S_f^*}$ is the basis of the null space of \mathbf{S}_f^* i.e., $\mathcal{N}(\mathbf{S}_f^*)$. Equation 27 gives actuator commands $\Delta \mathbf{l}$ which cause a change

TABLE 2 | Shape control through impotent *eigenstrain*.

Configuration	n^{act}	$\Delta \mathbf{l}$	$\mathbf{S}_f^* \Delta \mathbf{l}$	$\mathbf{S}_d^* \Delta \mathbf{l}$
Only internal actuators	$n^{act,int} = n^e$	Equation 25	$= \mathbf{0}$	$= \Delta \mathbf{d}^{t*}$
	$s^{int} < n^{act,int} \leq n^e$	Equation 27 ^a ; else Equations 28, 29	$= \mathbf{0}$	$\approx \Delta \mathbf{d}^{t*}$
	$n^{act,int} \leq s^{int}$	Equations 28, 29	$\approx \mathbf{0}$	$\sim \Delta \mathbf{d}^{t*}$
Only external actuators	$s^{ext} < n^{act,ext} \leq n^{sd}$	Equation 27 ^a ; else Equations 28, 29	$= \mathbf{0}$	$\approx \Delta \mathbf{d}^{t*}$
	$n^{act,ext} \leq s^{ext}$	Equations 28, 29	$\approx \mathbf{0}$	$\sim \Delta \mathbf{d}^{t*}$
Internal + external actuators	$n^{act,int} + n^{act,ext} = n^e + n^{sd}$	Equation 25	$= \mathbf{0}$	$= \Delta \mathbf{d}^{t*}$
	$s^{ext} < n^{act,ext} \cup s^{int} < n^{act,int}$	Equation 27 ^a ; else Equations 28, 29	$= \mathbf{0}$	$\approx \Delta \mathbf{d}^{t*}$

^ayield $\Delta \mathbf{l} \rightarrow \infty$ when \mathbf{S}_f^* is ill-conditioned.

of node positions $\Delta \mathbf{d}^{c*} \sim \Delta \mathbf{d}^{t*}$ and no change of forces $\Delta \mathbf{f}^c = 0$. $\Delta \mathbf{d}^{c*}$ caused by $\Delta \mathbf{l}$ is not exactly $\Delta \mathbf{d}^{t*}$ because only some of the elements or supports are active, the degree of accuracy depends on the actuator placement and the number of actuators. Note that Equation 27 produces a non-zero $\Delta \mathbf{l}$ vector provided that the nullity of \mathbf{S}_f^* is not zero. Since $\mathbf{S}_f \in \mathbb{R}^{(n^e+n^{sd}) \times (n^e+n^{sd})}$ is a rank deficient matrix of rank s (i.e., the degree of static indeterminacy), the nullity of $\mathbf{S}_f^* \in \mathbb{R}^{(n^e+n^{sd}) \times n^{act}}$ is greater than zero only if the number of internal actuators is greater than s^{int} i.e., $n^{act,int} > s^{int}$. Otherwise when $n^{act,int} \leq s^{int}$, the columns of \mathbf{S}_f^* are linearly independent and therefore the nullity is zero i.e., the linear system $\mathbf{S}_f^* \Delta \mathbf{l} = \mathbf{0}$ admits only the trivial solution of $\Delta \mathbf{l} = \mathbf{0}$. When external actuators (i.e., active supports) are employed, the requirement $n^{act,int} > s^{int}$ does not apply. Instead, impotent *eigenstrain* can be caused by actuator commands computed through Equation 27 if the number of active supports is greater than s^{ext} i.e., $n^{act,ext} > s^{ext}$. When internal and external actuators are employed in combination, Equation 27 can be used if $s^{ext} < n^{act,ext} \cup s^{int} < n^{act,int}$ is true.

For the case when the nullity of \mathbf{S}_f^* is zero ($n^{act,ext} \leq s^{ext} \cup n^{act,int} \leq s^{int}$) and if a small change of forces is admissible, displacements can be controlled through an approximate impotent *eigenstrain* by solving the following constrained optimization problem:

$$\min_{\Delta \mathbf{l}} \left\| \mathbf{S}_f^* \Delta \mathbf{l} \right\|_2, \quad (28)$$

s.t.

$$\mathbf{S}_d^* \Delta \mathbf{l} = \Delta \mathbf{d}^{t*}. \quad (29)$$

The actuator commands $\Delta \mathbf{l}$ obtained from the solution of the problem stated in Equations 28 and 29 cause the required change of node positions $\Delta \mathbf{d}^{c*} = \Delta \mathbf{d}^{t*}$ through a minimum change of forces $\Delta \mathbf{f}^c \sim 0$, which can be thought of as the effect of an approximate impotent *eigenstrain*. Similar to C1, if the number of actuators is set to $n^{act} = s + n^{cd}$ the problem stated in Equations 28 and 29 admits a unique solution with low residuals ($\Delta \mathbf{f}^c \approx 0$; $\Delta \mathbf{d}^{c*} = \Delta \mathbf{d}^{t*}$). However, note that a significant change of forces may occur when $n^{act,int} \leq s^{int}$. Equations 28 and 29 may also be used in cases where Equation 27 yields $\Delta \mathbf{l} \rightarrow \infty$ because \mathbf{S}_f^* is ill-conditioned. Table 2 gives a summary of the

different approaches to obtain control commands that cause an impotent *eigenstrain*. Control accuracy decreases as the number of actuators reduces from $n^{act,int} = n^e$ or $n^{act,ext} = n^{sd}$ (all elements or supports are active) to $n^{act,int} = s^{int}$ or $n^{act,ext} = s^{ext}$ in which cases it is no longer possible to control the shape without also causing a change of forces.

Force Control Through Nilpotent *eigenstrain* (C3)

A nilpotent *eigenstrain* is produced by actuator commands that cause a change of forces but no change of displacements:

$$\min_{\Delta \mathbf{l}^e} \left\| \mathbf{S}_f \Delta \mathbf{l}^{all} - \Delta \mathbf{f}^t \right\|_2, \quad (30)$$

s.t.

$$\mathbf{S}_d \Delta \mathbf{l}^{all} = \mathbf{0}. \quad (31)$$

Equation 31 has a trivial solution for $\Delta \mathbf{l}^{all} = \mathbf{0}$. Assuming that all elements and supports are active, there is an infinite number of non-trivial solutions:

$$\Delta \mathbf{l}^{all} = \mathbf{G} \mathbf{W}_s \delta. \quad (32)$$

Equation 32 can be derived by expanding Equation 31 through Equations 17 and 18 and replacing $\Delta \mathbf{l}^{all}$ with $\mathbf{G} \mathbf{W}_s \delta$:

$$\mathbf{S}_d \mathbf{G} \mathbf{W}_s \delta = (\mathbf{A}^+)^T \left(-\mathbf{G} \mathbf{W}_s \left(\mathbf{W}_s^T \mathbf{G} \mathbf{W}_s \right)^{-1} \mathbf{W}_s^T \mathbf{G} \mathbf{W}_s \delta + \mathbf{G} \mathbf{W}_s \delta \right) \quad (33)$$

The underlined term is an identity matrix and therefore the right-hand term vanishes. This proves that any $\Delta \mathbf{l}^{all}$ spanning $\mathbf{G} \mathbf{W}_s$ causes no change of node positions. Replacing Equation 32 into Equation 30 and then solving for δ :

$$\delta = (\mathbf{S}_f \mathbf{G} \mathbf{W}_s)^+ \Delta \mathbf{f}^t. \quad (34)$$

Therefore, $\Delta \mathbf{l}^{all}$ to produce a nilpotent *eigenstrain* is:

$$\Delta \mathbf{l}^{all} = \mathbf{S}_f \mathbf{G} \mathbf{W}_s (\mathbf{S}_f \mathbf{G} \mathbf{W}_s)^+ \Delta \mathbf{f}^t. \quad (35)$$

Assuming small deformations, Equation 35 gives actuator commands $\Delta \mathbf{l}^{all}$ which cause the required change of forces $\Delta \mathbf{f}^c = \Delta \mathbf{f}^t$ and no change of shape $\Delta \mathbf{d}^{c*} = \mathbf{0}$. Note that force control through nilpotent *eigenstrain* can be performed

TABLE 3 | Force control through nilpotent *eigenstrain*.

Configuration	n^{act}	$\Delta \mathbf{l}$	$\mathbf{S}_f^* \Delta \mathbf{l}$	$\mathbf{S}_d^* \Delta \mathbf{l}$
Only internal actuators	$n^{\text{act,int}} = n^e$	Equation 35	$= \Delta \mathbf{f}^t$	$= \mathbf{0}$
	$n^{cd} < n^{\text{act,int}} \leq n^e$	Equation 37 ^a ; else Equations 38, 39	$\approx \Delta \mathbf{f}^t$	$= \mathbf{0}^b$
	$n^{\text{act,int}} \leq n^{cd}$	Equations 38, 39	$\sim \Delta \mathbf{f}^t$	$\approx \mathbf{0}$
Only external actuators	$n^{\text{act,ext}} > 0$	Equations 38, 39	$\approx \Delta \mathbf{f}^t$	$\sim \mathbf{0}$
Internal + external actuators	$n^{\text{act,int}} > 0 \cap n^{\text{act,ext}} > 0$	Equations 38, 39	$\approx \Delta \mathbf{f}^t$	$\approx \mathbf{0}$

^ayield $\Delta \mathbf{l} \rightarrow \infty$ when the matrix \mathbf{S}_d^* is ill-conditioned.

^b $\approx \mathbf{0}$ with Equations 38 and 39.

with good accuracy only if the target force change is a linear combination of the s column vectors of \mathbf{W}_s .

If only selected elements are actuators the non-trivial solutions of Equation 31 are actuator commands whose components lie in the null space of the reduced shape influence matrix \mathbf{S}_d^* .

$$\Delta \mathbf{l} = \mathbf{W}_s^* \delta, \quad (36)$$

Replacing Equation 36 in Equation 30 and solving for $\Delta \mathbf{l}$:

$$\Delta \mathbf{l} = \mathbf{W}_s^* (\mathbf{S}_f^* \mathbf{W}_s^*)^+ \Delta \mathbf{f}^t \quad (37)$$

where \mathbf{W}_s^* is the basis of the null space of \mathbf{S}_d^* i.e., $\mathcal{N}(\mathbf{S}_d^*)$. Equation 37 gives actuator commands $\Delta \mathbf{l}$ that cause a change of forces $\Delta \mathbf{f}^c \sim \Delta \mathbf{f}^t$ and no change of shape $\Delta \mathbf{d}^{c*} = 0$. $\Delta \mathbf{f}^c$ caused by $\Delta \mathbf{l}$ is not exactly $\Delta \mathbf{f}^t$ because only some of the elements or supports are active, the degree of accuracy depends on the actuator placement. Note that Equation 37 produces a non-zero $\Delta \mathbf{l}$ vector provided that the nullity of \mathbf{S}_d^* is not zero. Referring to the rank-nullity theorem, since $\mathbf{S}_d \in \mathbb{R}^{n^d \times (n^e + n^{sd})}$ is a full row rank matrix, the nullity of $\mathbf{S}_d^* \in \mathbb{R}^{n^{cd} \times n^{\text{act}}}$ is greater than zero only if the number of internal actuators is greater than the number of controlled degrees of freedom i.e., $n^{\text{act,int}} > n^{cd}$. Otherwise when $n^{\text{act,int}} \leq n^{cd}$, \mathbf{S}_d^* becomes a full rank matrix which has a nullity of zero and thus the linear system $\mathbf{S}_d^* \Delta \mathbf{l} = \mathbf{0}$ can only admit the trivial solution $\Delta \mathbf{l} = \mathbf{0}$. Note that it is not possible to obtain actuator commands that cause a nilpotent *eigenstrain* through Equation 37 when active supports are employed. This is because the effect of an active support is to move the node position and therefore by definition it cannot be employed to produce a nilpotent *eigenstrain*. In addition, in some configurations that include internal and external actuators, \mathbf{S}_d^* might be ill-conditioned. In this case, Equation 37 yields $\Delta \mathbf{l} \rightarrow \infty$.

For the case when the nullity of \mathbf{S}_d^* is zero because $n^{\text{act,int}} \leq n^{cd}$ and when active supports are employed, if a small change of shape is admissible, forces can be controlled through an approximate nilpotent *eigenstrain* by solving the following constrained optimization problem:

$$\min_{\Delta \mathbf{l}} \|\mathbf{S}_d^* \Delta \mathbf{l}\|_2, \quad (38)$$

s.t.

$$\mathbf{S}_f^* \Delta \mathbf{l} = \Delta \mathbf{f}^t. \quad (39)$$

The actuator commands $\Delta \mathbf{l}$ obtained from the solution of the problem stated in Equations 38 and 39 cause the required change of forces $\Delta \mathbf{f}^c = \Delta \mathbf{f}^t$ through a minimum change of node positions $\Delta \mathbf{d}^{c*} \sim 0$, which can be thought of as the effect of an approximate nilpotent *eigenstrain*. Similar to C1 and C2, if the number of actuators is set to $n^{\text{act}} = s + n^{cd}$ the problem stated in Equations 38 and 39 admits a unique solution with low residuals ($\Delta \mathbf{f}^c = \Delta \mathbf{f}^t$; $\Delta \mathbf{d}^{c*} \approx 0$). However, note that a significant change of node positions may occur when $n^{\text{act,int}} < n^{cd}$. Equations 38 and 39 may also be used in cases where Equation 37 yields $\Delta \mathbf{l} \rightarrow \infty$ because \mathbf{S}_d^* is ill-conditioned.

Table 3 gives a summary of the different approaches to obtain control commands that cause a nilpotent *eigenstrain*. Control accuracy decreases as the number of actuators reduces from $n^{\text{act,int}} = n^e$ (all elements are active) to $n^{\text{act,int}} = n^{cd}$ in which case it is no longer possible to control the forces without also causing a change of node positions. It is generally not possible to compute control commands that cause a nilpotent *eigenstrain* through Equation 37 if active supports are employed. However, active supports can be used through Equations 38 and 39.

Control Through Operational Energy Minimization (C4)

When operational energy consumptions are of primary concern, control commands $\Delta \mathbf{l}$ can be obtained through minimization of the work done by the actuators subject to stress and deflection limits. In this case, no target change of forces $\Delta \mathbf{f}^t$ and node positions $\Delta \mathbf{d}^t$ are supplied as inputs. The objective is to obtain suitable control commands so that forces \mathbf{f}^c and displacements \mathbf{d}^c are controlled as required by ULS and SLS, respectively, using minimum energy. Assuming small deformations and a linear elastic force-displacement relationship, the actuator work is made of two parts:

$$W_i = W_i^p + W_i^c, \quad (40)$$

$$W_i^p = \begin{cases} 0 & \text{if } \text{sgn}(f_i^p) = \text{sgn}(\Delta l_i) \\ \left| (f_i^p)^T \Delta l_i \right| & \text{otherwise} \end{cases}, \quad (41)$$

$$W_i^c = \begin{cases} 0 & \text{if } \text{sgn}(\Delta f_i^c) = \text{sgn}(\Delta l_i) \\ \frac{1}{2} \left| (\Delta f_i^c)^T \Delta l_i \right| & \text{otherwise} \end{cases}, \quad (42)$$

where \mathbf{f}^p are the forces before control which are assumed constant during actuation and $\Delta \mathbf{f}^c$ is the change of forces caused by the actuator commands $\Delta \mathbf{l}$. The objective function is sign-dependent because an actuator does work only when the applied forces and the length (internal) or displacement (support) changes are of opposite signs. For example, work is done when an internal actuator is required to extend under compression or to contract under tension and an external actuator is required to move the support in the opposite direction of the force it receives from the structure (opposite in sign of the support reaction). Otherwise, theoretically there would be a release of energy but since this study does not consider energy harvesting solutions, it is assumed that no energy gain can be made.

The total operational energy during service is computed as:

$$E^{opr} = \sum_{i \in \Delta \mathbf{CT}} \sum_j^{np} \sum_{k*}^{nb} \frac{(W_{ijk}^{(1)} + W_{ijk}^{(2)}) \Delta t_{jk} \omega}{\eta} \quad (43)$$

$W_{ijk}^{(1)}$ and $W_{ijk}^{(2)}$ are the work done during the first (1) and second (2) phase of adaptation (see section Structural Adaptation Process), respectively, by the i^{th} actuator, under the j^{th} load case for the k^{th} occurrence (i.e., bin) of the load probability distribution which, in this work, is assumed to be a log-normal distribution as defined in Step 3: Operational Energy Computation. Δt_{jk} is the duration of the load occurrence which is obtained through scaling the expected life-span of the structure with the probability of the k^{th} occurrence for the j^{th} load case p_{jk} . As discussed in Step 3: Operational Energy Computation, only load occurrences that are above the load activation threshold (LAT), which is denoted by k^* , are accounted for. The actuator working frequency ω is assumed to be identical to the 1st natural frequency which is likely to dominate the response of the structure. The actuator mechanical efficiency η is set depending on the actuator specification. For more details regarding the computation of the operational energy, the reader is referred to Senatore et al. (2019).

Minimization of the operational energy is subject to stress and displacement constraints to satisfy ULS and SLS:

$$\min_{\mathbf{x}} E^{opr} \quad (44)$$

s.t.

$$f_{ijk}^p + \mathbf{S}_f^* \Delta \mathbf{l}_{ijk} \leq \sigma_i^+ \alpha_i \quad (45)$$

$$f_{ijk}^p + \mathbf{S}_f^* \Delta \mathbf{l}_{ijk} \geq \max \left(\sigma_i^- \alpha_i, -\frac{\pi^2 E I_i}{l_i^2} \right) \quad (46)$$

$$-\mathbf{d}_{jk}^{SLS} \leq \mathbf{d}_{jk}^p + \mathbf{S}_d^* \Delta \mathbf{l}_{jk} \leq \mathbf{d}_{jk}^{SLS} \quad (47)$$

$$-\Delta \mathbf{l}^{lim} \leq \Delta \mathbf{l}_{jk} \leq \Delta \mathbf{l}^{lim} \quad (48)$$

$$\overline{W}_{ijk}^{p(1)} \leq (f_{ijk}^{in} + f_{ijk}^p) \Delta l_{ijk} \quad (49)$$

$$\overline{W}_{ijk}^{c(1)} \leq \frac{1}{2} \Delta f_{ijk}^c \Delta l_{ijk} \quad (50)$$

$$\overline{W}_{ijk}^{p(2)} \leq (f_{ijk}^{in} + \Delta f_{ijk}^c) (-\Delta l_{ijk}) \quad (51)$$

$$\overline{W}_{ijk}^{c(2)} \leq \frac{1}{2} (-\Delta f_{ijk}^c) (-\Delta l_{ijk}) \quad (52)$$

$$\overline{W}_{ijk}^{p(1)} \leq 0; \overline{W}_{ijk}^{c(1)} \leq 0 \quad (53)$$

$$\overline{W}_{ijk}^{p(2)} \leq 0; \overline{W}_{ijk}^{c(2)} \leq 0 \quad (54)$$

This formulation follows a Simultaneous Analysis and Design approach (Haftka, 1985) which was developed in previous own work (Wang and Senatore, 2020). The design variables vector \mathbf{x} comprises the actuator work as well as the control commands:

$$\mathbf{x} = [\overline{W}^p \ \overline{W}^c \ \Delta \mathbf{l}] \quad (55)$$

The actuator work is reformulated using two auxiliary variables:

$$W_{ijk} = -(\overline{W}_{ijk}^p + \overline{W}_{ijk}^c) \quad (56)$$

subject to auxiliary constraints (Equations 49–54). The auxiliary variables \overline{W}^p , \overline{W}^c and constraints are introduced to handle the sign-dependency of the optimization objective in order to formulate it as a continuous function. Note that Equation 56 is satisfied only at convergence i.e., when $-(\overline{W}^p + \overline{W}^c)$ reaches a minimum. The superscript (1) and (2) in the auxiliary constraints refer to the 1st and 2nd phase of the adaptation process (Section Structural Adaptation Process).

Similar to C1, C2, and C3, stress and displacement constraints in Equations 45–47 employ the force \mathbf{S}_f^* and shape and \mathbf{S}_d^* influence matrices to relate the actuator commands $\Delta \mathbf{l}$ to the controlled change of forces $\Delta \mathbf{f}_{jk}^c = \mathbf{S}_f^* \Delta \mathbf{l}_{jk}$ and node positions $\Delta \mathbf{d}_{jk}^c = \mathbf{S}_d^* \Delta \mathbf{l}_{jk}$, respectively. The change of forces $\Delta \mathbf{f}^c$ is obtained so that the controlled forces $\mathbf{f}^c = \mathbf{f}^p + \Delta \mathbf{f}^c$, where \mathbf{f}^p are the forces caused by the external load before control, are constrained by stress and stability limits (Equation 45 and 46). The change of node positions $\Delta \mathbf{d}^c$ is obtained so that the controlled displacements $\mathbf{d}^c = \mathbf{d}^p + \Delta \mathbf{d}^c$, where \mathbf{d}^p are the displacements caused by the external load before control, are bounded by SLS limits (Equation 47). The actuator commands $\Delta \mathbf{l}$ are also constrained to stay within required limits which are specific to the selected actuation system (Equation 48).

The optimization problem stated in Equations 44 to 54 has been successfully solved for the case studies presented in this work using the Sequential Quadratic Programming (SQP) algorithm built-in Matlab. Note that since the problem is generally non-convex, the optimal solutions obtained through SQP are local minima. Since control commands obtained through C4 require minimum operational energy, this strategy will be used to benchmark the energy requirements of C1, C2, and C3.

CASE STUDIES

The structure-control optimization method outlined in section Synthesis of Minimum Energy Adaptive Structures (Senatore et al., 2019) combined with the control strategies given in section Control Strategies has been applied to the design of a high-rise structure and an arch bridge. The main objective of

the comparative study presented in this section is to benchmark the control strategies to evaluate energy requirements and control accuracy.

Scope of Comparative Study

The four control strategy described in section Control Strategies are compared: (C1) force and shape control to obtain prescribed changes of forces and node positions, (C2) shape control through impotent *eigenstrain*, (C3) force control through nilpotent *eigenstrain*, and (C4) force and shape control through operational energy minimization. For all control strategies, three actuator configurations (AC) are considered: only internal actuators (AC1), only external actuators (AC2) and a combination of both (AC3). The control strategies and related actuator configurations are compared in terms of:

- Maximum controlled displacement $\max(|\mathbf{d}^p + \Delta \mathbf{d}^c - \mathbf{d}^{in}|)$ to evaluate if the required SLS limit is met
- Control residuals with respect to target force $\|\mathbf{S}_f^* \Delta \mathbf{l} - \Delta \mathbf{f}\|_2$ and shape $\|\mathbf{S}_d^* \Delta \mathbf{l} - \Delta \mathbf{d}^t\|_2$ changes
- Maximum element force change $\max(|\Delta \mathbf{f}|)$ caused by actuation
- Maximum shape change $\max(|\Delta \mathbf{d}^c|)$ caused by actuation
- Maximum actuator force capacity $\max(|\mathbf{f}|) \forall i \in \text{ACT}$
- Maximum internal actuator length extension $\max(\Delta \mathbf{l}^{el})$ and reduction $\min(\Delta \mathbf{l}^{el})$
- Maximum active support displacement $\max(\Delta \mathbf{d}^{sup})$; $\min(\Delta \mathbf{d}^{sup})$
- Embodied and operational energy as well as mass and energy savings with respect to the passive solution
- Computation time to obtain control commands $\Delta \mathbf{l}$.

Since actuators are assumed to be installed in series, they have to carry the full force in the corresponding element or support. For this reason, the maximum actuator force capacity is computed as the maximum force (in absolute value) that an actuator has to withstand over the entire adaptation process, namely the maximum among \mathbf{f}^{in} , \mathbf{f}^p , \mathbf{f}^c and $\mathbf{f}^{in} + \Delta \mathbf{f}^c$ (see section Analysis and Control of Adaptive Structures). For simplicity of notation, this is indicated as $\max(|\mathbf{f}|)$. With regard to the internal actuator length changes, a positive sign indicates an extension whereas a negative sign a length reduction. For external actuators, a positive sign indicates that the displacement is applied in the same direction of the support axis.

Material and Loading Assumptions

In both cases studies, the structures are made of circular hollow section elements. The minimum radius is set to 50 mm and 100 mm for the high-rise structure and the arch bridge configurations, respectively. To limit optimization complexity, the wall thickness is set to 10% of the external radius. The element material is structural steel with a Young's modulus of 210 GPA, a density of 7,850 kg/m³ and an energy intensity of 36.5 MJ/kg (Hammond and Jones, 2008). Following Senatore et al. (2019), it is assumed that the actuators are made of steel with an energy intensity factor of 36.5 MJ/kg and the actuator mass is linearly proportional to the required force capacity (i.e., maximum force

TABLE 4 | Load combination cases.

Limit state	Load case	Load combination
ULS	LC0	1.35 (SW + DL)
	LC1, LC2,...	1.35 (SW + DL) + 1.5 (LL1, LL2,...)
SLS	LC0	SW + DL
	LC1, LC2	SW + DL + (LL1, LL2,...)

required during control) with a coefficient of 0.1 kg/kN (e.g. an actuator with a push/pull load of 10,000 kN has a mass of 1,000 kg) (ENERPAC, 2016). Note that the mass of the adaptive configuration includes the mass of the actuation system layout. The same applies to the embodied energy. Similarly, the self-weight of the adaptive configuration comprises the weight of the structure and that of the actuation system.

The structure is subjected to a permanent load, which comprises self-weight (SW) and dead load (DL), as well as to a randomly fluctuating live load (LL) whose frequency of occurrence is modeled with a log-normal probability distribution (see section Step 3: Operational Energy Computation). The load combination cases considered in the case studies are summarized in **Table 4**.

High-Rise Structure

The vertical cantilever truss considered in this study can be thought of as the primary structure of a multi-story building reduced to two dimensions. The geometry of the structure is illustrated in **Figure 2A** which shows dimensions, support and loading conditions. The horizontal displacements of all free nodes are set as controlled degrees of freedom for a total of $n^{cd} = 16$. The controlled nodes are indicated by circles. The serviceability limit is set to $H / 500 = 200$ mm, where $H = 100$ m is the height of the structure. The degree of static indeterminacy (s) is $s^{int} = 7$ internally and $s^{ext} = 1$ externally.

The structure is designed to support a permanent and a live load. The permanent load consists of self-weight (SW), which includes the weight of the actuators, and dead load (DL). The dead load is set to 2.94 kN/m² (300 kg/m²) resulting in a uniformly distributed load of 22 kN/m (assuming 7.5 m of cover out of plane) applied every 4 m for each floor. The live loads, LL1 and LL2, are horizontally distributed in opposite direction (**Figure 2A**) with an intensity which is a function of the square root of the height to approximate a wind pressure distribution. The live-to-dead-load ratio is set to 1 and hence the live load maximum intensity is 2.94 kN/m². The live load frequency of occurrence is modeled with a log-normal probability distribution (see section Step 3: Operational Energy Computation).

The adaptive solution is compared to a weight-optimized passive solution of identical topology subjected to the same loading and limit states. The passive solution has been optimized using a method given in Senatore et al. (2019) that produces similar results to the Modified Fully Utilized Design method (Patnaik et al., 1998). **Figures 2B,C** show the passive and adaptive solution, respectively. The optimal adaptive solution has been obtained for $MUT = 28\%$ (see **Table 8**). For the passive solution, the equivalent $MUT = 13\%$ thus showing that material is better utilized in the adaptive solution. Line thickness variation

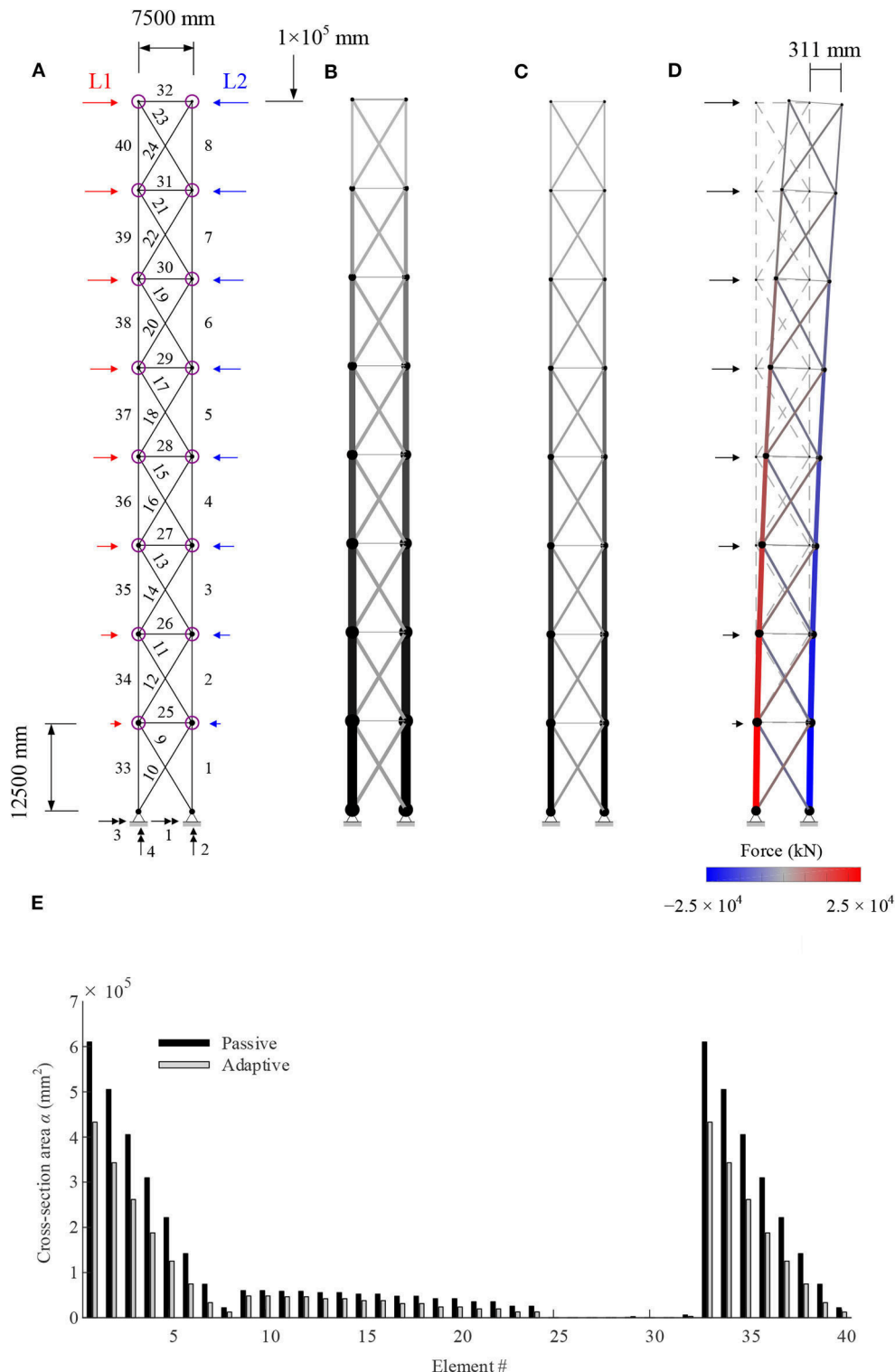


FIGURE 2 | Multi-story building: (A) dimensions, controlled nodes, and loading; (B) passive; (C) adaptive (MUT 28%); (D) deformed shape and element forces of the adaptive solution under LC1 before control (magnification $\times 20$); (E) element cross-section area passive vs. adaptive.

indicates the element diameter while the cross-section area is represented through a color gradient whereby a larger area is assigned a darker gray shade. The element cross-section area

for both passive and adaptive solutions are also indicated by the bar chart shown in **Figure 2E**. With regard to the adaptive solution, elements #1, #33 and #25 have the largest and smallest

diameter which are 1,707 and 100 mm, respectively. On average, the elements of the adaptive solution have a cross-section area and external diameter that are 45 and 23% smaller, respectively, with respect to the weight-optimized passive solution. **Figure 2D** shows the deformed shape of the adaptive solution under LC1 for the SLS case before control. As expected, the maximum deflection is 311 mm which is above the serviceability limit (200 mm). The internal forces are indicated by color shading; red is for tension and blue for compression. Since the deformed shape under LC2 mirrors that under LC1, for brevity it is not illustrated.

The objective of this case study is to benchmark energy requirements between control strategies C1, C2, and C4. The configuration shown in **Figure 2** (structure dimensions + loading) has been selected for this case study because it allows the application of control strategy C2. C2 can be only employed when displacement compensation is required but it is not necessary to control the forces because stress and stability limits are met without the contribution of the active system. The configuration selected for this case study met this condition for an *MUT* in the range $0 \leq MUT \leq 33\%$. In such range of the solution domain, which contains the optimal solutions for all cases considered in this study, the design for this configuration is purely stiffness governed thus allowing to benchmark control strategy C2 against C1 and C4.

The number of actuators for the different configurations are varied according to the conditions given for C1 and C2 (**Table 2**). For actuator configuration AC1 (only internal) three sub-cases are considered by decreasing the number of internal actuators from $n^{act,int} = n^e$ to $s^{int} \leq n^{act,int} \leq n^e$ and finally to $n^{act,int} < s^{int}$. For AC2 (only external) the number of external actuators is set to the number of constrained degrees of freedom $n^{act,ext} = n^{sd} = 4$. For AC3 (combination of internal and external) two sub-cases are considered by setting the number of external actuators $n^{act,ext} = n^{sd} = 4$ ($n^{act,ext} > s^{ext}$) and reducing the number of internal actuators from $s^{int} \leq n^{act,int} \leq n^e$ to $n^{act,int} < s^{int}$.

Tables 5–7 give results with regard to the metrics of interest for AC1, AC2, and AC3, respectively. The illustrations in **Table 8** show the controlled shapes and the actuator layout for each configuration. In addition, labels indicate the actuators that are subjected to the most demanding control requirements including maximum force capacity and maximum length change/support displacement. For brevity, illustrations in **Table 8** are only given for strategy C2 under load case LC1 (which is symmetrical to LC2).

AC1: Active Elements (Internal Actuators)

AC1a: $n^{act,int} = n^e$

In this configuration all elements are active. The actuator commands for C2 are computed through Equation 25 (**Table 2**). The optimal design has been obtained for *MUT* = 25%.

For all control strategies, the maximum deflection $\max(|\mathbf{d}^p + \Delta \mathbf{d}^c - \mathbf{d}^{in}|)$ (free-end) is reduced from 376 mm before control to 200 mm after control as required by SLS. Stress and stability limits are met through all control strategies. Good control accuracy is achieved through C1 and C2, as indicated by low residuals for force and shape control. In C4, control

residuals are not computed because the target shape and forces are not supplied.

The largest force change $\max(|\Delta \mathbf{f}|)$ is required in C1 at element #9. This is because in C1 the forces are constrained to be equal to the target forces obtained through load-path optimization χ . Instead, shape control through C2 causes a zero change of forces. Control through energy minimization C4 also gives actuator commands that cause a minimum (practically zero) change of forces. The maximum force capacity $\max(|\mathbf{f}|)$ is required in all strategies for the actuator placed at element #1 under LC1 and element #33 under LC2. The mass of the actuators subjected to maximum force capacity requirements is 2200 kg (see assumption given in section Material and Loading Assumptions). The maximum absolute length change is required in C4 for the actuator placed at element #39.

The actuation system embodied energy (and thus the mass) is on average 8% of the total (structure + actuation system) embodied energy among all control strategies. As expected, energy savings are the highest when the structure is controlled through C4. The operational energy for C4 is 53% of that required by C1. However, C2 is also efficient in terms of energy requirements. As expected, the computation time to obtain control commands through C4 is significantly higher than that required for C1 and C2.

AC1b: $s^{int} \leq n^{act,int} \leq n^e$

In this configuration $n^{act,int}$ is set to $n^{act,int} = n^{cd} + s = 24$ which is the required number of actuators to obtain a unique solution for C1 [Section Control to Target Forces and Shapes (C1)]. Actuator commands for C2 are obtained through Equation 27 (**Table 2**). The optimal design has been obtained for *MUT* = 28%.

The maximum deflection $\max(|\mathbf{d}^p + \Delta \mathbf{d}^c - \mathbf{d}^{in}|)$ is reduced from 415 mm before control to 200 mm after control through all strategies since the number of actuators meets the minimum requirement for accurate shape control. Low residuals indicate a good control accuracy through C1 and C2. Stress and stability limits are met through all control strategies.

Control strategy C4 requires the largest force change $\max(|\Delta \mathbf{f}|)$ at element #18. Control through C2 produces no change of forces while C4 causes a small force change compared to C1. The maximum force capacity $\max(|\mathbf{f}|)$ is required in all strategies for the actuator placed at element 1 under LC1 and element 33 under LC2. The mass of the actuator subjected to maximum force capacity requirements is 2,200 kg. The maximum absolute length change is required in C4 for the actuator placed at element #39.

The actuation system embodied energy (and thus the mass) is on average 8% of the total (structure + actuation system) embodied energy among all control strategies. The computation time for C4 is lower than that in AC1a because the number of actuators is lower and thus the number of optimization variables (Equation 44 to 54) is reduced.

AC1c: $n^{act,int} < s^{int}$

In this configuration $n^{act,int}$ is set to 6, which is lower than the degree of internal static indeterminacy ($s^{int} = 7$). Actuator commands for C2 are computed through Equations 28, 29 (**Table 2**). The optimal design has been obtained for *MUT* =

TABLE 5 | AC1 results.

	Passive	C1	C2	C4
Maximum deflection (mm)				
AC1a	200	200	200	200
AC1b	200	200	200	200
AC1c	200	211	211	200
Residual $\ S_d^* \Delta I - \Delta d^c\ _2$ (mm)				
AC1a	–	~0	~0	n/a
AC1b	–	~0	~0	n/a
AC1c	–	20.7	20.7	n/a
Residual $\ S_f^* \Delta I - \Delta f^c\ _2$ (kN)				
AC1a	–	~0	~0	n/a
AC1b	–	~0	~0	n/a
AC1c	–	75.1	68	n/a
max (Δf^c) (kN)				
AC1a	–	775 (el# 9)	~0	~0
AC1b	–	227 (el# 10)	~0	888 (el# 18)
AC1c	–	89.4 (el# 9)	21.7 (el# 10)	250.4 (el# 14)
max (f) $\forall i \in \text{ACT}$ ($\times 10^4$ kN)				
AC1a	–	2.20 (el# 1, LC1; el# 33, LC2)	2.20 (el# 1, LC1; el# 33, LC2)	2.20 (el# 1, LC1; el# 33, LC2)
AC1b	–	2.20 (el# 1, LC1; el# 33, LC2)	2.20 (el# 1, LC1; el# 33, LC2)	2.20 (el# 1, LC1; el# 33, LC2)
AC1c	–	2.23 (el# 1, LC1; el# 33, LC2)	2.23 (el# 1, LC1; el# 33, LC2)	2.23 (el# 1, LC1; el# 33, LC2)
max (Δl^{el}); min (Δl^{el}) (mm)				
AC1a	–	10 (el# 6); –10 (el# 38)	10 (el# 6); –10 (el# 38)	1 (el# 31); –27 (el# 39)
AC1b	–	17 (el# 6); –12 (el# 38)	17 (el# 6); –11 (el# 38)	0 (el# 18); –24 (el# 39)
AC1c	–	3 (el# 34); –3 (el# 2)	3 (el# 34); –3 (el# 2)	0 (el# 34); –2 (el# 2)
Embodied energy (MJ)				
Total; Actuators				
AC1a	1.95×10^7	1.14×10^7 ; 9.51×10^5	1.14×10^7 ; 9.40×10^5	1.14×10^7 ; 9.40×10^5
AC1b	1.95×10^7	1.04×10^7 ; 8.53×10^5	1.04×10^7 ; 8.46×10^5	1.04×10^7 ; 8.50×10^5
AC1c	1.95×10^7	1.85×10^7 ; 5.76×10^5	1.85×10^7 ; 5.76×10^5	1.85×10^7 ; 5.79×10^5
Operational energy (MJ)				
AC1a	–	4.45×10^6	3.55×10^6	2.40×10^6
AC1b	–	6.38×10^6	5.35×10^6	3.53×10^6
AC1c	–	7.27×10^5	7.10×10^5	1.59×10^5
Energy savings				
AC1a	–	18%	23%	28%
AC1b	–	14%	19%	24%
AC1c	–	n/a	n/a	n/a
Mass savings				
AC1a	–	41%	41%	41%
AC1b	–	47%	47%	47%
AC1c	–	n/a	n/a	5%
Computation time (s)				
AC1a	–	0.02	0.01	20.2
AC1b	–	0.02	0.01	2.6
AC1c	–	0.03	0.03	0.11

15%. The maximum deflection $\max(|\mathbf{d}^p + \Delta \mathbf{d}^c - \mathbf{d}^{in}|)$ cannot be reduced from 260 mm to the serviceability limit (200 mm) because the number of actuators is significantly lower than the minimum requirement for accurate shape control. Control accuracy in AC1c is generally poor as indicated by higher control residuals than those given for AC1a and AC1b. Control residuals

for C1 and C2 are similar, indicating a comparable performance for shape control through both strategies. Stress and stability limits are met through all control strategies.

The highest force change $\max(|\Delta \mathbf{f}^c|)$ is required by C4 at element #14. Since the number of actuators is lower than the minimum requirement to cause an impotent *eigenstrain*

TABLE 6 | AC2 results.

	Passive	C1	C2	C4
Maximum deflection (mm)	200	233	233	200
Residual $\ S_d^* \Delta \mathbf{l} - \Delta \mathbf{d}^{t*}\ _2$ (mm)	–	61.6	61.6	n/a
Residual $\ S_f^* \Delta \mathbf{l} - \Delta \mathbf{f}^t\ _2$ (kN)	–	272.1	~0	n/a
$\max(\Delta \mathbf{f}^t)$ (kN)	–	244.9 (el# 9)	~0	~0
$\max(\mathbf{f}) \forall i \in \mathbb{A} \mathbb{C} \mathbb{T}^{ext}$ ($\times 10^4$ kN)	–	2.44 (sup# 2, LC1; sup# 4, LC2)	2.44 (sup# 2, LC1; sup# 4, LC2)	2.44 (sup# 2, LC1; sup# 4, LC2)
$\max(\Delta \mathbf{d}^{sup}); \min(\Delta \mathbf{d}^{sup})$ (mm)	–	3 (sup# 3); –2 (sup# 4)	0 (sup# 3); –3 (sup# 4)	0 (sup# 3); –5 (sup# 4)
Embodied energy (MJ)	1.95×10^7	1.55×10^7 ; 2.78×10^5	1.55×10^7 ; 2.78×10^5	1.55×10^7 ; 2.78×10^5
Total; Actuators				
Operational energy (MJ)	–	9.23×10^5	3.06×10^6	1.18×10^6
Energy savings	–	n/a	n/a	14%
Mass savings	–	n/a	n/a	20%
Computation time (s)	–	0.03	0.03	0.12

(Table 2), a relatively small change of force is also produced through C2. The maximum force capacity $\max(|\mathbf{f}|)$ is required in C1, C2, and C4 for the actuator placed at element #1 under LC1 and element #33 under LC2. The mass of the actuator subjected to maximum force capacity requirements is 2,230 kg. The maximum absolute length change is required in C1 and C2 for the actuator placed at elements #34.

The actuation system embodied energy (and thus the mass) is on average 3% of the total (structure + actuation system) embodied energy among all control strategies. Since SLS has not been met for this configuration in C1 and C2, energy and mass savings are not given.

AC2: Active Supports (External Actuators)

In this configuration, there are no internal actuators and all supports are set to active $n^{act,ext} = 4$. Actuator commands for C2 are computed through Equation 27 (Table 2). The optimal design has been obtained for $MUT = 18\%$. The maximum deflection $\max(|\mathbf{d}^p + \Delta \mathbf{d}^c - \mathbf{d}^{in}|)$ can be reduced from 260 mm to the serviceability limit (200 mm) through C4, but not C1 or C2. Control accuracy in AC2 is generally poor for C1 and C2 as indicated by higher control residuals than those given for AC1. Control residuals $\|S_d^* \Delta \mathbf{l} - \Delta \mathbf{d}^{t*}\|_2$ for C1 and C2 are identical, indicating a comparable performance for shape control. Stress and stability limits are met through all control strategies.

The highest force change $\max(|\Delta \mathbf{f}^t|)$ is required in C1 at element #9. Since the number of actuators is higher than the degree of external indeterminacy $n^{act,ext} > s^{ext}$, it is possible to produce an impotent *eigenstrain* through C2 and thus there is no change of forces. The active supports provide a force couple that opposes the action of the external load. Under LC1, the vertical displacements are opposite (upward for support 2 and downward for support 4) (see illustration in Table 8). Identical but opposite in sign is the reaction of the active supports under LC2. The maximum force capacity $\max(|\mathbf{f}|)$ is required in C1 and C2 for the actuator placed at support 2 (vertical direction) under LC1 and support 4 (vertical direction) under LC2. The mass of the actuators subjected to maximum force capacity requirements is 2,440 kg. The maximum absolute displacement

is required in C1 for the external actuator placed at support #3 (horizontal direction).

The actuation system embodied energy (and thus the mass) is on average 2% of the total (structure + actuation system) embodied energy among all control strategies. Since SLS has not been met for this configuration in C1 and C2, energy and mass savings are not given.

AC3: Combination of Active Elements and Supports (Internal and External Actuators)

$$AC3a: s^{int} \leq n^{act,int} \leq n^e, n^{act,ext} = 4$$

In this configuration n^{act} is set to $n^{act} = n^{cd} + s = 24$ which is the required number of actuators to obtain a unique solution for C1. In this case $n^{act} = n^{act,int} + n^{act,ext}$ where $n^{act,int} = 20$ and $n^{act,ext} = 4$. Actuator commands for C2 are computed through Equation 27 (Table 2). The optimal design has been obtained for $MUT = 28\%$. The maximum deflection $\max(|\mathbf{d}^p + \Delta \mathbf{d}^c - \mathbf{d}^{in}|)$ is reduced from 415 mm to within serviceability limits (200 mm) for all strategies. Stress and stability limits are met through all control strategies. Control residuals are relatively low, indicating a good control accuracy for C1 and C2. Shape control residuals for C2 are lower than those for C1.

Control strategy C4 requires the largest force change $\max(|\Delta \mathbf{f}^t|)$ at element #18. The change of force in C1 is lower than that in C4. Control through C2 instead produces no change of forces. The maximum force capacity $\max(|\mathbf{f}|)$ is required in all strategies for the actuators placed at element #1 and support #2 under LC1 and element #33 and support #4 under LC2. The mass of the actuators subjected to maximum force capacity requirements is 2,200 kg for the internal type and 2370 kg for the external one. The maximum absolute length change is required in C4 for the internal actuator placed at element #39. The active support displacements are practically zero for all strategies hence no action is required for the external actuators.

The actuation system embodied energy (and thus the mass) is on average 10% of the total (structure + actuation system) embodied energy among all control strategies. The energy savings are the highest for C4, which requires only 53% of the operational energy required by C1. Due to high force requirements that result

TABLE 7 | AC3 results.

	Passive	C1	C2	C4
Maximum deflection (mm)				
AC3a	200	200	200	200
AC3b	200	210	210	200
Residual $\ S_d^* \Delta I - \Delta d^t\ _2$ (mm)				
AC3a	–	~0	~0	n/a
AC3b	–	20.5	20.5	n/a
Residual $\ S_f^* \Delta I - \Delta f^t\ _2$ (kN)				
AC3a	–	~0	~0	n/a
AC3b	–	75.1	~0	n/a
max (Δf^t) (kN)				
AC3a	–	227 (el #9)	~0	929.2 (el #18)
AC3b	–	89.3 (el #10)	~0	250.4 (el# 14)
max (f) $\forall i \in \text{ACT}^{int}$ ($\times 10^4$ kN)				
AC3a	–	2.20 (el# 1, LC1; el# 33, LC2)	2.20 (el# 1, LC1; el# 33, LC2)	2.20 (el# 1, LC1; el# 33, LC2)
AC3b	–	2.23 (el# 1, LC1; el# 33, LC2)	2.23 (el# 1, LC1; el# 33, LC2)	2.23 (el# 1, LC1; el# 33, LC2)
max (f) $\forall i \in \text{ACT}^{ext}$ ($\times 10^4$ kN)				
AC3a	–	2.37 (sup# 2, LC1; sup# 4, LC2)	2.37 (sup# 2, LC1; sup# 4, LC2)	2.37 (sup# 2, LC1; sup# 4, LC2)
AC3b	–	2.48 (sup# 2, LC1; sup# 4, LC2)	2.48 (sup# 2, LC1; sup# 4, LC2)	2.48 (sup# 2, LC1; sup# 4, LC2)
max (ΔI^{el}); min (ΔI^{el}) (mm)				
AC3a	–	16 (el# 6); –12 (el# 38)	17 (el# 6); –11 (el# 38)	3 (el# 23); –25 (el# 39)
AC3b	–	7 (el# 34); –6 (el# 2)	7 (el# 34); –7 (el# 2)	0 (el# 34); –2 (el# 35)
max (Δd^{sup}); min (Δd^{sup}) (mm)				
AC3a	–	~0	~0	~0
AC3b	–	0 (sup# 3); –1 (sup# 2);	0 (sup# 3); –1 (sup# 2);	~0
Embodied energy (MJ)				
Total; Actuators				
AC3a	1.95×10^7	1.06×10^7 ; 1.11×10^6	1.06×10^7 ; 1.10×10^6	1.06×10^7 ; 1.11×10^6
AC3b	1.95×10^7	1.88×10^7 ; 8.57×10^5	1.88×10^7 ; 8.57×10^5	1.88×10^7 ; 8.62×10^5
Operational energy (MJ)				
AC3a	–	6.79×10^6	5.87×10^6	3.62×10^6
AC3b	–	1.90×10^6	1.90×10^6	1.59×10^5
Energy savings				
AC3a	–	10%	15%	27%
AC3b	–	n/a	n/a	3%
Mass savings				
AC3a	–	45%	45%	45%
AC3b	–	n/a	n/a	4%
Computation time (s)				
AC3a	–	0.02	0.01	1.9
AC3b	–	0.03	0.02	0.19

in large operational energy consumption, the active supports do not contribute to displacement control in C4 i.e., control commands for the external actuators obtained through C4 are practically zero. As for previous cases, the computation time required by C4 is significantly higher than that for C1 and C2.

AC3b: $n^{act,int} < s^{int}$, $n^{act,ext} = 4$

In this configuration $n^{act} = n^{act,int} + n^{act,ext} = 10$ where $n^{act,int} = 6$ and $n^{act,ext} = 4$. Actuator commands for C2 are obtained through Equations 28, 29 (Table 2). The optimal design is obtained for $MUT = 15\%$. The maximum deflection

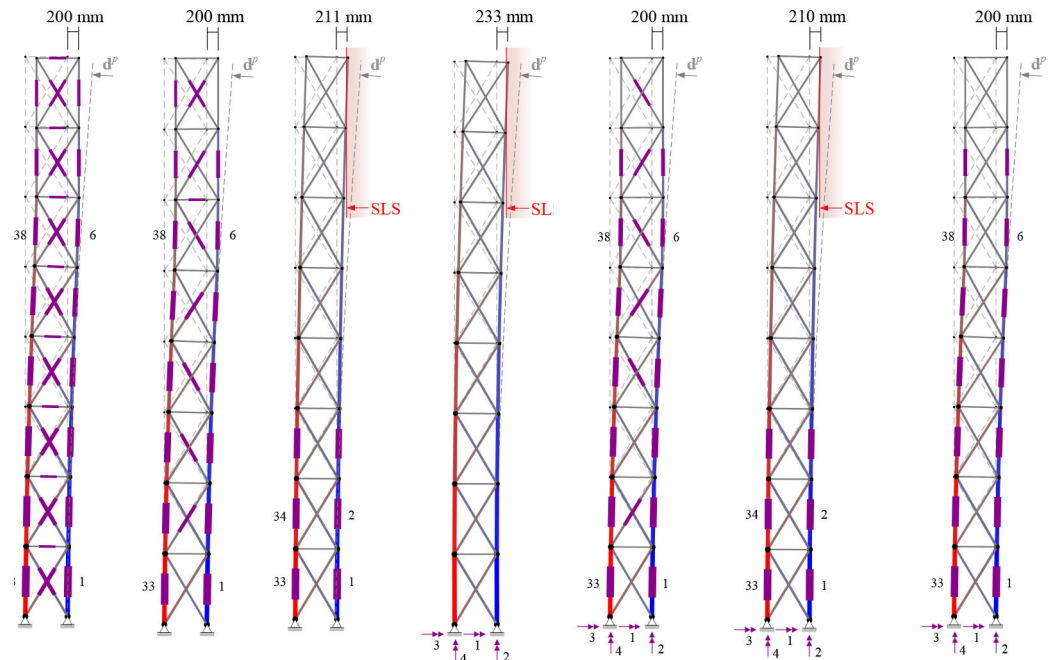
$\max(|d^p + \Delta d^c - d^{in}|)$ can be reduced from 260 mm to the serviceability limit (200 mm) through C4, but not C1 and C2.

Control strategy C4 requires the largest force change $\max(|\Delta f^t|)$ at element #14. Control through C2 instead produces no change of forces because the total number of actuators is $n^{act} > s$ (Table 2). The maximum force capacity $\max(|f|)$ is required in all strategies for the actuators placed at element #1 and support #2 under LC1 and element #33 and support #4 under LC2. The mass of the actuators subjected to maximum force capacity requirements is 2,230 kg for the internal type and

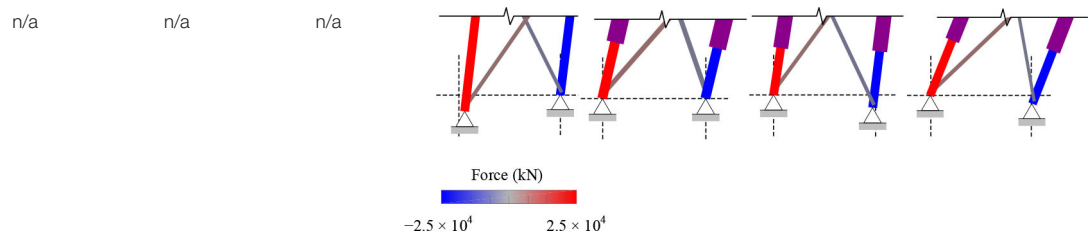
TABLE 8 | Multi-story structure: summary of results.

	AC1a	AC1b	AC1c	AC2	AC3a	AC3b	AC3c
<i>MUT</i>	25%	28%	15%	18%	28%	15%	28%
$n^{act,int}$	40	24	6	0	20	6	14
$n^{act,ext}$	0	0	0	4	4	4	4
SLS satisfied?	Yes	Yes	Yes (C4 only)	Yes (C4 only)	Yes	Yes (C4 only)	Yes
$\ S_d^* \Delta l - \Delta d^t\ _2$ (mm)							
C1	0	0	20.7	61.6	0	20.5	2.3
C2	0	0	20.7	61.6	0	20.5	1.5
$\ S_r^* \Delta l - \Delta f^t\ _2$ (kN)							
C1	0	0	75.1	272.1	0	75.1	117.2
C2	0	0	0	0	0	0	0
$\max(f) \forall i \in \text{ACT}^{int}$ ($\times 10^4$ kN)							
C1	2.20	2.20	2.23	–	2.20	2.23	2.20
C2	2.20	2.20	2.23	–	2.20	2.23	2.20
C4	2.20	2.20	2.23	–	2.20	2.23	2.20
$\max(f) \forall i \in \text{ACT}^{ext}$ ($\times 10^4$ kN)							
C1	–	–	–	2.44	2.37	2.48	2.37
C2	–	–	–	2.44	2.37	2.48	2.37
C4	–	–	–	2.44	2.37	2.48	2.37
Energy/mass savings							
C1	18%/41%	14%/47%	n/a	n/a	10%/45%	n/a	n/a
C2	23%/41%	19%/47%	n/a	n/a	15%/45%	n/a	n/a
C4	28%/41%	24%/47%	4%/5%	14%/20%	27%/45%	3%/4%	26%/46%

Actuator layouts and controlled shapes (mag. $\times 20$) (LC1, C2)



Active support displacements (mag. $\times 400$) (LC1, C2)



2,480 kg for the external one. The maximum absolute length change is required in C1 and C2 for the internal actuator placed at element #34. The maximum absolute displacement is required in C1 and C2 for the external actuator placed at support #2 (vertical direction).

The actuation system embodied energy (and thus the mass) is on average 5% of the total (structure + actuation system) embodied energy among all control strategies. Since SLS has not been met for this configuration in C1 and C2, energy and mass savings are not given.

Summary of Results

A comparison of the results obtained for configurations AC1, AC2 and AC3 is given in **Table 8**. The actuator placement and controlled shapes under LC1 are illustrated for each configuration. For brevity, only the configurations for C2 are illustrated. The internal actuators are represented by thicker lines placed in the middle of the elements while the external actuators are represented by arrows placed in proximity of the supports.

Generally, accurate control is only possible through C4 if the number of internal actuators is lower than the degree of internal static indeterminacy $n^{act,int} < s^{int}$. For this case study, the

external actuators are not as effective as the internal ones. In AC2, although all supports are active, the SLS limit could only be met through C4, but not C1 and C2. Control accuracy improves when external actuators are employed in combination with a sufficient number of internal actuators $n^{act,int} > s^{int}$ (AC3a).

The actuation system embodied energy (and thus the total mass of the actuators) is only a fraction of the total embodied energy (structure + actuation system). The actuation system is AC3a embodies the highest energy which, nonetheless, is only 10% of the total embodied energy for this configuration.

For all configurations, C4 produces solutions with the lowest operational energy requirement. However, since C4 is based on a non-convex optimization that employs explicit constraints on displacements, the computation time to obtain control commands is on average 2,020 times higher than that required for C1 and C2. C2 is also efficient with regard to operational energy requirement which is always lower than that required by C1. Note that C2 can be employed when displacement compensation is required but it is not necessary to control the forces because stress and stability limits are met without the contribution of the active system.

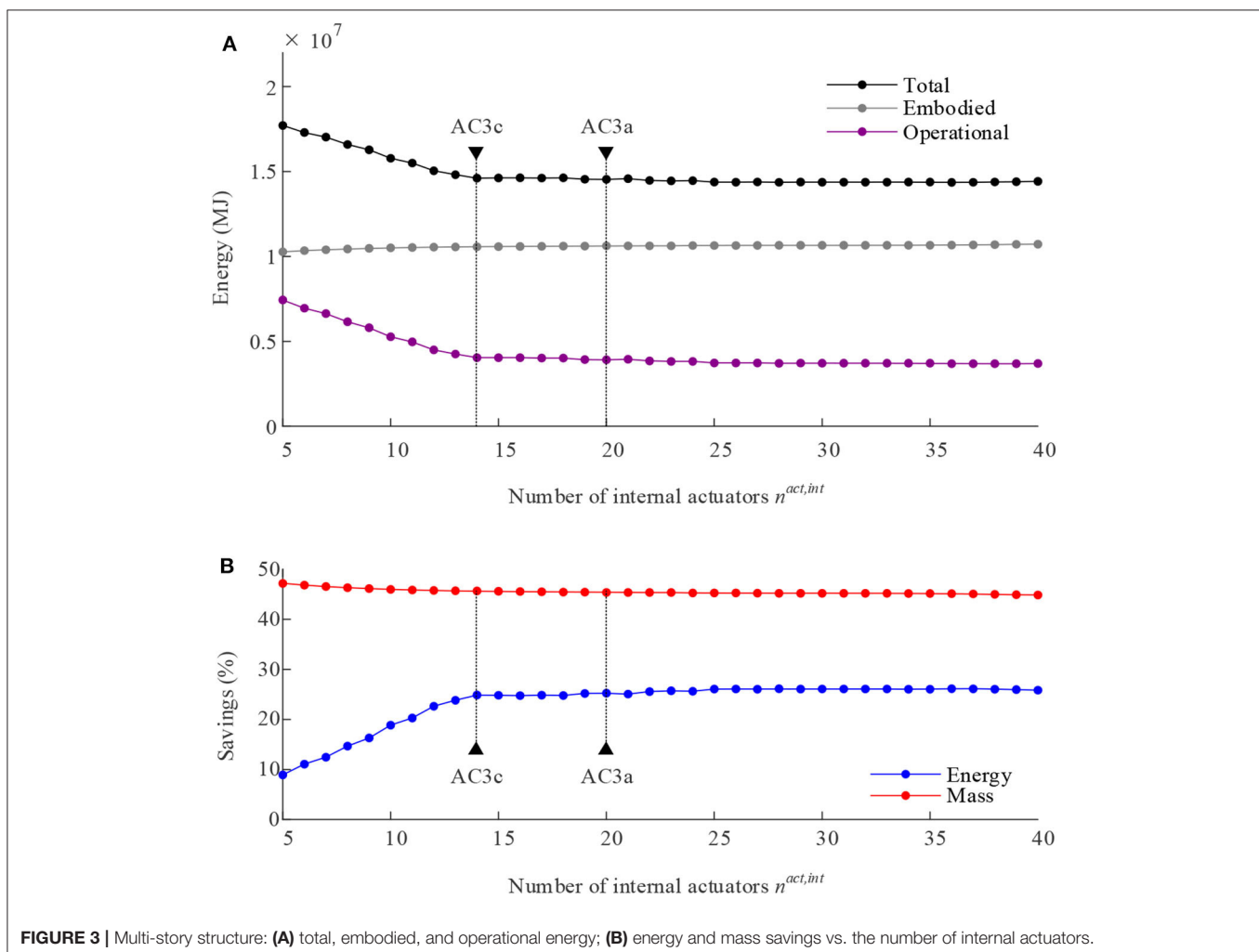


FIGURE 3 | Multi-story structure: **(A)** total, embodied, and operational energy; **(B)** energy and mass savings vs. the number of internal actuators.

Operational energy requirements when using external actuators are generally higher, which results in lower energy and mass savings for AC3a compared to AC1b. In AC3a ($n^{act,int} = 20, n^{act,ext} = 4$) using control strategy C4, the combination of internal and external actuators produce a small increase (3%) of the energy savings with respect to AC1b ($n^{act,int} = 24$) at the cost of a marginal reduction of mass savings (2%). This is because generally, the maximum force capacity of external actuators is higher than that of internal actuators.

A parametric study has been carried out to evaluate the sensitivity of energy requirements, as well as mass and energy savings, with respect to the number of internal actuators $n^{act,int}$. An adaptive structure solution has been obtained for each configuration by setting $MUT = 28\%$, which is kept constant. The number of internal actuators $n^{act,int}$ varies from $n^{act,int} = n^e$ to $n^{act,int} = s^{int}$ while the number of external actuators is kept constant $n^{act,ext} = n^{cd} = 4$. The control strategy adopted in this parametric study is C4. **Figure 3** shows (a) the variation of energy requirements as well as (b) energy and mass savings with respect to $n^{act,int}$. The embodied energy (and thus the mass) remains almost constant because the MUT is kept constant. The slight increase of embodied energy with the number of actuators is due to the increase of the actuation system embodied energy. Operational energy requirements increase as $n^{act,int}$ reduces from $n^{act,int} = n^e$; conversely, energy savings decrease. However, energy savings decrease significantly only after the number of internal actuators is further reduced from $n^{act,int} = 14$. This configuration is denoted as AC3c. Metrics of interest for AC3c are given in **Table 8** which includes an illustration of the actuator placement and controlled shape obtained through C2 under LC1. AC3c can be regarded as the best overall configuration because it achieves very similar energy and mass savings to AC3a (which has the highest energy savings), albeit using 30% fewer actuators.

Arch Bridge

The arch truss considered in this study can be thought of as an arch bridge reduced to two dimensions. The geometry of the structure is illustrated in **Figure 4A** which shows dimensions, support and loading conditions. The vertical displacement of all free nodes of top and bottom chords are set as controlled degrees of freedom for a total of $n^{cd} = 19$. The controlled nodes are indicated by circles. The serviceability limit is set to $S/1,000 = 100$ mm, where $S = 100$ m is the span of the bridge. The degree of static indeterminacy (s) is $s^{int} = 0$ internally and $s^{ext} = 3$ externally. The structure is designed to support a permanent and a live load. The permanent load consists of self-weight (SW), which includes the weight of the actuators, and dead load (DL). The dead load (DL) is uniformly distributed on the top chord nodes with an intensity of 10 kN/m. There are three uniformly distributed live loads (LL) cases. LL1 is applied on the whole span while LL2 and LL3 are applied on one-half of the span. The live-to-dead-load ratio is set to 1 for LL1 to simulate normal traffic conditions and to 1.25 for LL2 and LL3 to simulate asymmetric loadings due to vehicular traffic. The live load frequency of occurrence is modeled with a log-normal probability distribution (see section Step 3: Operational Energy Computation).

Figure 4B shows the adaptive solution which has been obtained for $MUT = 68\%$. Element diameters are indicated by line thickness variation, cross-section areas and element forces are indicated by color shading as for the previous case study (Section High-Rise Structure). Elements #11, #21 and #28, #35, #42, #43 have the largest and smallest diameter, which are 1,210 and 200 mm, respectively. **Figure 4C** shows the deformed shape under LC2 (before control). The maximum nodal displacement is 92 mm, which is lower than the required serviceability limit (100 mm), hence there is no need for active compensation of displacements. For this reason, the focus of this study will be on force control through strategy C3 i.e., nilpotent *eigenstrain*. In this case, the control objective is to maintain an optimal load-path under multiple load cases without causing any (or minimal) change of the node positions. Since the structure works as an arch bridge, an optimal load-path is when both top and bottom chords work in compression even under asymmetric loading. The target forces $\Delta \mathbf{f}$ are obtained through process χ (Section Step 1: Embodied Energy Optimization) by adding extra constraints that limit the forces in the top and bottom chord elements to compression.

The number of actuators for the different configurations are varied according to the conditions given in **Table 3**. For actuator configuration AC1 (only internal) three sub-cases are considered by decreasing the number of internal actuators from $n^{act,int} = n^e$ to $n^{cd} < n^{act,int} \leq n^e$ and finally to $n^{act,int} \leq n^{cd}$. For AC2 (only external) the number of external actuators is set to the number of constrained degrees of freedom $n^{act,ext} = n^{sd}$. For AC3 (combination of internal and external) two sub-cases are considered by setting the number of external actuators $n^{act,ext} = n^{sd}$ ($n^{act,ext} > s^{ext}$) and reducing the number of internal actuators from $n^{act,int} > s + n^{cd}$ to $n^{act,int} < s + n^{cd}$.

Control strategy C3 is benchmarked against C4. For both strategies, the change of forces $\Delta \mathbf{f} = \Delta \mathbf{f}^p + \Delta \mathbf{f}^c$ should be such that all elements of top and bottom chords are in compression under all load cases. Control accuracy is evaluated through a measure of the maximum change of displacements which should be as small as possible i.e., $\max(|\Delta \mathbf{d}^c|) \approx 0$. Results for AC1 to AC3 are summarized in **Table 9**. Each configuration is illustrated in **Figure 5**, which shows the actuator layout, element forces and controlled shapes.

In AC1a, since all elements are set to active (43 actuators, **Figure 5A**) control commands for C3 are obtained through Equation 35. Both strategies produce actuator commands that cause a nilpotent *eigenstrain* and top and bottom chord elements are controlled in compression under all load cases. Accurate force control for C3 is indicated by low residuals $\|\mathbf{S}_f^* \Delta \mathbf{l} - \Delta \mathbf{f}^t\|_2$. The operational energy for C4 is 11% of that required by C3. the computation time to obtain control commands through C4 is significantly higher than that required for C3.

In configuration AC1b, $n^{act,int} = 24 > s + n^{cd}$ (**Figure 5B**). Similar to AC1a, it is possible to obtain control commands that do not cause any change of node positions and to control the internal forces so that all elements of top and bottom chords are in compression. The operational energy for C4 is 26% of that

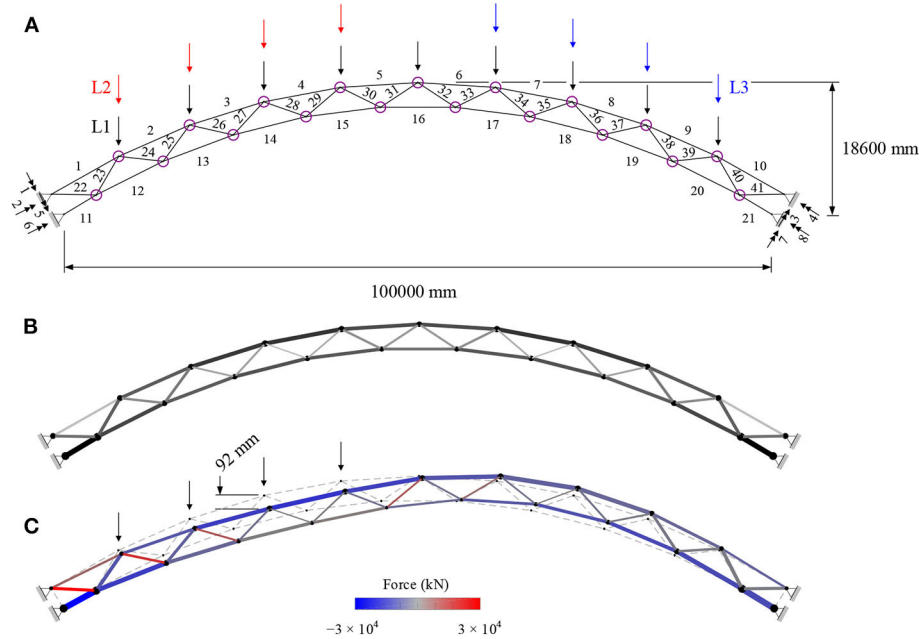


FIGURE 4 | Arch bridge: **(A)** dimensions, controlled nodes, and loading; **(B)** adaptive; **(C)** deformed shape and element forces under LC2 before control (magnification $\times 20$).

required by C3. Similar to AC1a, the computation time for C4 is significantly higher than that for C3.

In AC1c, $n^{act,int} = 10$ (Figure 5C). In this case, it is not possible to obtain control commands that do not cause any change of node positions through neither C3 nor C4. Control strategy C3 requires a change of node position $\max(|\Delta \mathbf{d}^c|) = 21.8 \text{ mm}$ which results in a violation of the serviceability limit (100 mm). As indicated by high residuals $\|\mathbf{S}_d^* \Delta \mathbf{l} - \Delta \mathbf{d}^{t*}\|_2$, control accuracy is poor due to the low number of actuators employed in this configuration. Through both strategies, top and bottom chord elements are controlled in compression under all load cases. The operational energy for C4 is 12% of that required by C3. In AC1c, the computation time is significantly lower than that required in configurations with more actuators such as AC1a and AC1b.

In AC2, all supports are set to active for a total of $n^{act,ext} = 8$ (Figure 5D). In this case, it is not possible to obtain control commands that do not cause any change of node positions through neither C3 nor C4. As discussed in section Force Control Through Nilpotent Eigenstrain (C3), the effect of an active support is to move the node positions and therefore it cannot be employed to produce a nilpotent eigenstrain. Although the serviceability limit (100 mm) is still respected, control strategy C3 requires the largest change of node position $\max(|\Delta \mathbf{d}^c|)$ of 39.9 mm. Similar to AC1c, high residuals $\|\mathbf{S}_d^* \Delta \mathbf{l} - \Delta \mathbf{d}^{t*}\|_2$ indicate poor control accuracy. Similar to AC1c, top and bottom chords are in compression under all load cases through both control strategies. The operational energy for C4 is only 1% of that required by C3. In AC2, the computation time is comparable to AC1c.

In AC3a and AC3b, all supports are set to active for a total of $n^{act,ext} = 8$ in combination with $n^{act,int} = 24 > s + n^{cd}$ and $n^{act,int} = 6$ internal actuators (Figures 5E,F). When $n^{act,int} < n^e$ or when the supports are active (AC2, AC3a, and AC3b) control commands are computed through Equations 38 and 39, which produce an approximate nilpotent eigenstrain. No significant change of shape occurs in AC3a for both C3 and C4, while in AC3b it is not possible to obtain control commands that do not cause any change of node positions through neither C3 nor C4. Although the serviceability limit (100 mm) is still respected in AC3b, control strategy C3 requires the largest change of node position $\max(|\Delta \mathbf{d}^c|) = 10.4 \text{ mm}$. High residuals $\|\mathbf{S}_d^* \Delta \mathbf{l} - \Delta \mathbf{d}^{t*}\|_2$ in AC3b indicate poor control accuracy due to the low number of actuators. In both AC3a and AC3b, and with both control strategies, top and bottom chords are in compression under all load cases. The operational energy for C4 is only 14% and 1% of that required by C3 in AC3a and AC3b, respectively.

The largest change of node positions occurs in AC2, where the actuators are only placed at the supports. No change of node positions occurs in AC1a, AC1b, and AC3a where the number of actuators $n^{act} = 24 > s + n^{cd}$ satisfies the condition to obtain a unique solution with low residuals for C1, C2, and C3 (see section Control Through Impotent and Nilpotent Eigenstrain).

The maximum force capacity $\max(|\mathbf{f}|)$ is required in AC1c for the actuators placed at element #25 and #38 under LC2 and LC3, in AC2, AC3a, and AC3b for the actuators placed at support #5 and 7 under LC2 and LC3. The mass of the actuators subjected to maximum force capacity requirements is 4,410 kg for the internal type and 1710 kg for the external one. The maximum absolute

TABLE 9 | Arch bridge: summary of results.

	AC1a	AC1b	AC1c	AC2	AC3a	AC3b
$n^{act,int}$	43	24	10	0	24	6
$n^{act,ext}$	0	0	0	8	8	8
Maximum deflection (mm)						
C3	92	92	103	90	90	95
C4	92	100	100	88.1	100	100
Residual $\ S_d^* \Delta I - \Delta d^{t*}\ _2$ (mm)						
C3	~0	~0	47.1	87.7	~0	24.4
Residual $\ S_f^* \Delta I - \Delta f^t\ _2$ (kN)						
C3	~0	~0	~0	~0	~0	~0
$\min(f^c) \forall i \in \{1, \dots, 21\}$ (kN)						
C3	-150	-150	-150	-150	-150	-150
C4	-0.1	-0.1	-0.1	-0.1	-0.1	-0.1
$\max(\Delta d^c)$ (mm)						
C3	~0	~0	21.8	39.9	~0	10.4
C4	~0	~0	25.9	20.4	~0	12
$\max(f) \forall i \in \text{ACT}^{int}$ ($\times 10^4$ kN)						
C3	1.99 (el# 11, LC2 ; el# 21, LC3)	1.06 (el# 3, LC2 ; el# 8, LC3)	4.41 (el# 25, LC2 ; el# 38, LC3)	—	1.07 (el# 3, LC2 ; el# 8, LC3)	2.29 (el# 30, LC2 ; el# 33, LC3)
C4	1.99 (el# 11, LC2 ; el# 21, LC3)	1.06 (el# 3, LC2 ; el# 8, LC3)	4.41 (el# 25, LC2 ; el# 38, LC3)	—	1.07 (el# 3, LC2 ; el# 8, LC3)	2.16 (el# 30, LC2 ; el# 33, LC3)
$\max(f) \forall i \in \text{ACT}^{ext}$ ($\times 10^4$ kN)						
C3	—	—	—	1.71 (sup# 5, LC2; sup# 7, LC3)	1.71 (sup# 5, LC2; sup# 7, LC3)	1.71 (sup# 5, LC2; sup# 7, LC3)
C4	—	—	—	1.71 (sup# 5, LC2; sup# 7, LC3)	1.71 (sup# 5, LC2; sup# 7, LC3)	1.71 (sup# 5, LC2; sup# 7, LC3)
$\max(\Delta I^{el}); \min(\Delta I^{el})$ (mm)						
C3	3 (el#1); -1 (el #12)	9 (el#19); -5 (el #25)	18 (el#34); -15 (el #25)	—	5 (el#19); -4 (el #8)	12 (el#37); 0 (el #1)
C4	4 (el#1); -1 (el #29)	6 (el#26); -4 (el #25)	19 (el#26); -23 (el #29)	—	3 (el#19); -2 (el #29)	9 (el#33); 0 (el #1)
$\max(\Delta d^{sup}); \min(\Delta d^{sup})$ (mm)						
C3	—	—	—	27 (sup# 1); -62 (sup# 4)	3 (sup# 1); -3 (sup# 7)	9 (sup# 1); -25 (sup# 4)
C4	—	—	—	6 (sup# 1); -13 (sup# 7)	4 (sup# 2); 0 (sup# 3)	5 (sup# 1); 0 (sup# 4)
Embodied energy ($\times 10^6$ MJ)						
Total; Actuators						
C3	5.24; 1.39	4.39; 0.53	3.99; 0.13	4.24; 0.39	4.78; 0.92	4.31; 0.46
C4	5.19; 1.34	4.37; 0.51	3.99; 0.13	4.24; 0.39	4.76; 0.90	4.31; 0.46
Operational energy (MJ)						
C3	6.80×10^6	8.61×10^6	6.61×10^6	6.50×10^7	8.26×10^6	2.38×10^7
C4	7.33×10^5	2.21×10^6	7.69×10^5	6.75×10^5	1.16×10^6	2.52×10^5
Total energy (MJ)						
C3	1.20×10^7	1.30×10^7	1.06×10^7	6.93×10^7	1.30×10^7	2.81×10^7
C4	5.93×10^6	6.57×10^6	4.75×10^6	4.92×10^6	5.91×10^6	4.56×10^6
Computation time (s)						
C3	0.01	0.002	0.003	0.003	0.002	0.003
C4	11.8	7.6	0.3	0.3	15	2

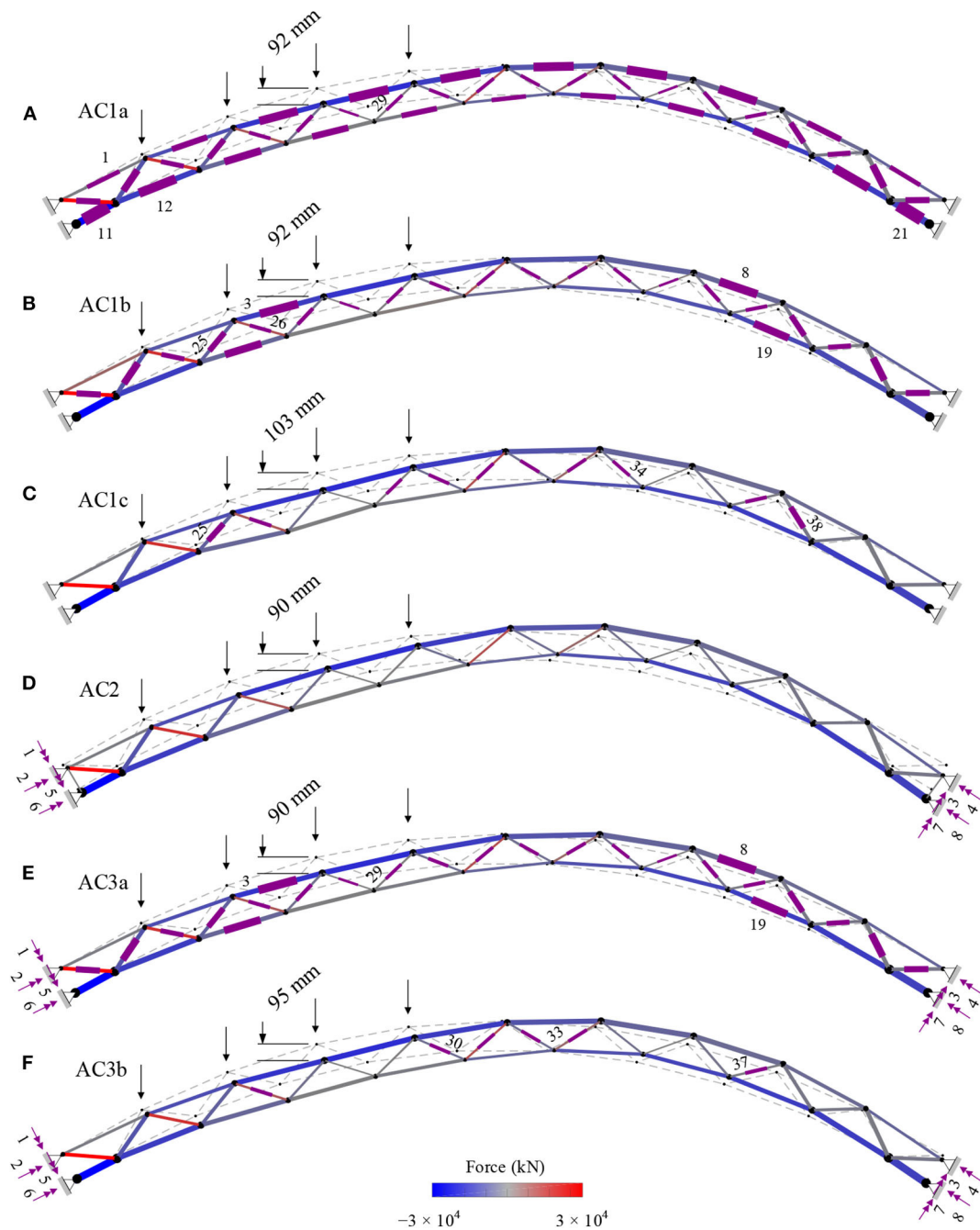


FIGURE 5 | Arch bridge: actuator layout, element forces, and controlled shapes (magnification $\times 20$) under LC2 for AC1a-c (only internal actuators), AC2 (only external actuators) and AC3a-b (combination of internal and external actuators).

length change is required for the actuator placed at element #34 in AC1c where the number of internal actuators is the lowest. Generally, the active supports move inward to counteract the effect of the external load as shown in **Figure 5D** for AC2. The maximum absolute support displacement occurs in AC2 for the external actuator placed at support #4.

In all configurations and under all load cases, top and bottom chords are controlled to stay in compression. Accurate force

control in C3 is indicated by the residual $\|S_f^* \Delta I - \Delta f^t\|_2$, which is practically zero for all cases (**Table 9**) including AC2 where only active supports are employed. **Figure 6** shows a bar chart of the internal forces for top and bottom chord elements #1 to #21 before control (black), after control through C3 (light gray) and after control through C4 (dark gray). For brevity, only forces for load case LC2 and configuration AC1b are given. The maximum force after control through C3 among the top and

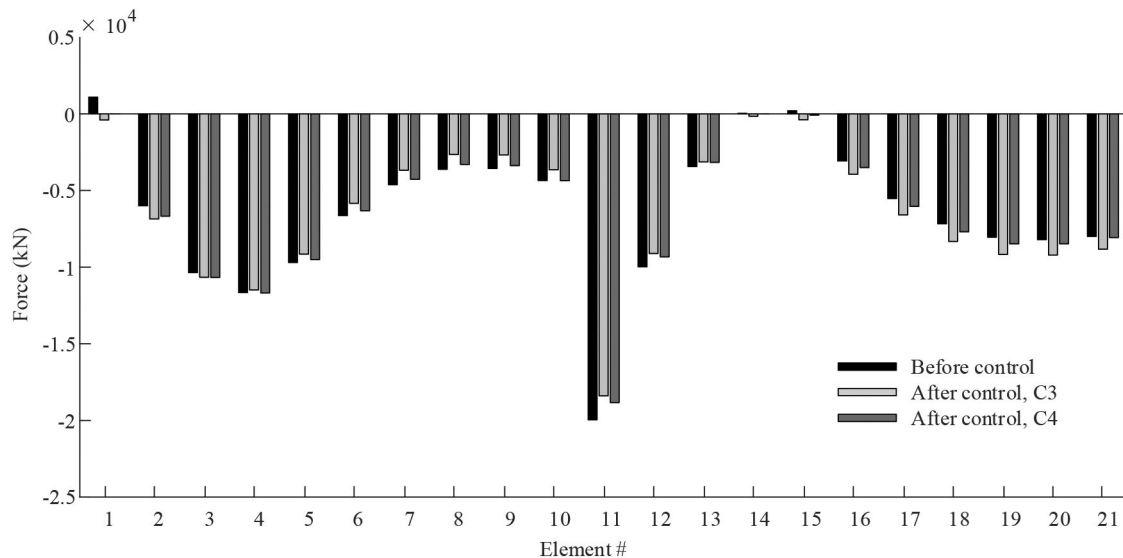


FIGURE 6 | Arch bridge: internal forces in the top and bottom chord elements for AC1b under LC2.

bottom chord elements, $\max(\mathbf{f}^c) \forall i \in \{1, \dots, 21\}$, is -150 kN in all configurations. The maximum force after control through C4 among the top and bottom chord elements, $\max(\mathbf{f}^c) \forall i \in \{1, \dots, 21\}$, is -0.1 kN in all configurations.

The embodied energy (and thus the mass) is lower for AC1c, AC2, and AC3b compared to the other configurations, which employ more actuators. This is because in AC1a, AC1b, and AC3a, actuators are placed on elements subjected to high forces such as element #11, #21, #3, #8, #13 and #19, which causes the actuation system embodied energy to reach 27%, 12% and 20% of the total (structure + actuation system) embodied energy, respectively. For AC1c, AC2 and AC3b instead, the actuation system embodied energy is 3, 9, and 10% of the total embodied energy.

Through strategies C3 and C4, the structure is controlled as required so that top and bottom chords are in compression even under asymmetrical load cases. Both strategies produce actuator commands that generally cause a minimal change of shape, which, in this case, was not needed as deflection limits are met without the contribution of the active system. The computation time to obtain a solution through C4 is on average 1,180 times higher than that required by C3. However, control through C4 requires significantly less operational energy which is on average only 9% of that required by C3.

Operational energy requirements are the highest in AC2 through C3 because the external actuators are required to work against high forces and to perform larger displacements compared to those required by the other configurations. Combination of internal and external actuators in AC3a is effective to reduce the operational energy requirement with respect to AC1b without reducing shape control accuracy (the maximum change of node positions and shape control residuals are practically zero for AC1b and AC3a). Configuration AC3b ($n^{act,int} = 6$, $n^{act,ext} = 8$) is the best overall configuration

because its embodied energy (and thus the mass) is only 8% higher than that of the minimum embodied energy configuration (AC1c) and its operational, as well as total energy, are the lowest among all configurations. In addition, AC3b employs fewer actuators compared to other configurations e.g. 43 actuators in AC1a, 24 in AC1b, 32 in AC3a vs. 14 actuators in AC3b.

DISCUSSION

Decoupling Force and Shape Control

Closed-form solutions to decouple force and shape control through impotent and nilpotent *eigenstrain* have been presented through strategies C2 and C3. Within the assumption of small deformations, impotent (C2) and nilpotent (C3) *eigenstrain* can be caused through actuation exactly ($\Delta \mathbf{f}^c = 0$; $\Delta \mathbf{d}^{c*} = 0$, respectively) provided that the null space of the force $\mathbf{S}_f^* \in \mathbb{R}^{(n^e + n^{sd}) \times n^{act}}$ and shape $\mathbf{S}_d^* \in \mathbb{R}^{n^{cd} \times n^{act}}$ influence matrices exist. The nullity of \mathbf{S}_f^* is greater than zero if the number of actuators is higher than the degree of static indeterminacy i.e. $s^{ext} < n^{act,ext} \cup s^{int} < n^{act,int}$; the nullity of \mathbf{S}_d^* is greater than zero if the number of internal actuators is higher than the number of controlled degrees of freedom i.e., $n^{act,int} > n^{cd}$. When these conditions are met, generally, force and shape control can be decoupled i.e., forces can be controlled without changing the shape through a nilpotent *eigenstrain* ($\Delta \mathbf{f}^c \approx \Delta \mathbf{f}^t$; $\Delta \mathbf{d}^{c*} = 0$) and the shape can be controlled without changing the forces through an impotent *eigenstrain* ($\Delta \mathbf{f}^c = 0$; $\Delta \mathbf{d}^{c*} \approx \Delta \mathbf{d}^t$). In some cases, depending on the actuator layout and the position of the controlled degrees of freedom, the basis of the null space of the force \mathbf{W}_s^f and shape \mathbf{W}_s^d influence matrices may be ill-conditioned. In such cases, and when the number of actuators does not meet required conditions (Tables 2, 3), control

commands to cause an approximate impotent and nilpotent *eigenstrain* can be obtained through optimization as shown in section Shape Control Through Impotent Eigenstrain (C2) and Force Control Through Nilpotent Eigenstrain (C3), respectively. Note that it is not possible to obtain actuator commands that cause an exact ($\Delta \mathbf{d}^{c*} = 0$) nilpotent *eigenstrain* when active supports are employed i.e., $n^{act,ext} > 0$. In such case, nilpotent *eigenstrain* can only be approximated through optimization in order to control the forces as required albeit causing a small change of shape.

Summary of Comparative Study Results

The structure-control optimization method given in Senatore et al. (2019) combined with the control strategies presented in section Control Strategies has been applied to the design of a high-rise structure and an arch bridge to benchmark control accuracy and energy requirements. Actuator layouts that include active elements (internal actuators), active supports (external actuators) and combination of both have been tested. For all control strategies, the actuator placement has been obtained through the method given in Senatore et al. (2019) and control commands are obtained so that that ULS and SLS are respected. Information regarding control requirements in terms of actuator maximum force capacity and length change has also been given for each configuration.

Since C4 is based on a non-convex optimization problem, the computation time to obtain control commands is significantly higher than that required for C1, C2, and C3. C1, C2, and C3 are convex problems that comprise either constraints on forces or displacements but not simultaneously and thus an approximate solution can be obtained in lower computation time. Owing to the simplicity and computational efficiency of C1 and C2, they have been successfully applied to linear (Senatore et al., 2018c) and geometric non-linear (Reksowardojo et al., 2020b) real-time control of experimental adaptive structures equipped with linear actuators.

The operational energy required by C2 and C4 is lower than that required by C1. Control through C1 aims to cause a prescribed change of forces and node positions and thus it involves more stringent constraints with respect to C4 in which forces and displacements are only constrained as required by ULS and SLS, respectively. This is the main reason C1 requires larger operational energy with respect to C2 and C4. While C4 always requires the least energy, C2 has comparable operational energy requirements. In addition, C2 is significantly more efficient in computation time terms which is on average 0.05% with respect to C4. That being said, C2 can only be employed when displacement compensation is required but it is not necessary to control the forces because stress and stability limits are met without the contribution of the active system. In these conditions, shape control through impotent *eigenstrain* (C2) should be employed instead of C1 or C4. This is an important finding because, since high-intensity loads occur rarely, it is only necessary to reduce displacements within SLS limits without affecting the internal forces under most occurrences of the load probability distribution which are above the load activation threshold (*LAT*) (see section Step 3: Operational

Energy Computation). This is particularly relevant to stiffness governed structures for which non-controlled displacements are likely to violate SLS limits before any critical stress condition might occur. In addition, when fail-safe constraints that account for control system failure and power breakdown are added to the structural optimization process outlined in section Synthesis of Minimum Energy Adaptive Structures (Senatore et al., 2019; Wang and Senatore, 2020), ULS is met without the contribution of the active system and thus only displacement compensation is required under SLS load cases.

In general, external actuators require higher operational energy than internal actuators since forces acting on the supports are usually higher than the element forces. However, a layout that combines external and internal actuators may require lower operational energy compared to one which comprises only internal actuators. For example, for the arch bridge case study, simulations have shown that it is effective to use external actuators in combination with internal actuators to lower the control energy.

A parametric study has been carried out to evaluate the sensitivity of energy requirements, as well as mass and energy savings, with respect to the number of internal actuators $n^{act,int}$. Embodied (and thus material mass) and operational energy requirements increase as $n^{act,int}$ reduces from $n^{act,int} = n^e$. Conversely, mass and energy savings decrease. However, mass and energy savings decrease significantly only when the number of internal actuators is significantly lower than $n^{act} = s + n^{cd}$ (static indeterminacy + controlled degrees of freedom), which is the condition to obtain a unique solution with low residuals for C1, C2, and C3 (see section Control Strategies).

CONCLUSIONS

This work has presented the formulation of four control strategies for adaptive structures equipped with linear actuators: (C1) force and shape control to obtain prescribed changes of forces and node positions; (C2) shape control through impotent *eigenstrain* when displacement compensation is required without affecting the forces; (C3) force control through nilpotent *eigenstrain* when displacement compensation is not required and (C4) force and shape control through operational energy minimization. These control strategies have been integrated within a previously developed structure-control optimization method (Senatore et al., 2019) which produces adaptive structural configurations that outperform equivalent weight-optimized passive structures on a variety of aspects: the adaptive solutions embody a significantly reduced material mass, they can be much more slender, they have a higher stiffness because deflections are controlled within tight limits, they are minimum energy solutions thus reducing environmental impacts.

The main contributions of this work are: (1) formulation of three new control strategies C2, C3 and C4 which extend the integrated structure-control optimization method given in Senatore et al. (2019); (2) derivation of closed-form solutions and formulation of optimization methods to decouple force and shape control through nilpotent and impotent *eigenstrain*; (3)

extension of the force and shape control formulation given in Senatore et al. (2019), which considered only internal actuators (i.e., active elements), to include the action of external actuators placed at supports (i.e., active supports).

The following conclusions are drawn from the analytic and numerical studies presented in this paper:

- A necessary condition to decouple force and shape control is the existence of the null space of the force and shape influence matrices defined in Force and Shape Influence Matrices. Therefore, it follows that: (1) the shape can be controlled as required without changing the forces through an impotent *eigenstrain* if the number of actuators is higher than the degree of static indeterminacy i.e., $s^{ext} < n^{act,ext} \cup s^{int} < n^{act,int}$; (2) forces can be controlled as required without changing the shape through a nilpotent *eigenstrain* if the number of internal actuators is higher than the number of controlled degrees of freedom i.e., $s^{ext} < n^{act,ext} \cup s^{int} < n^{act,int}$.
- Energy savings increase as the number of actuators increases from $n^{act} = s$. However, no further significant savings are gained as the number of actuators increases from $n^{act} = s + n^{cd}$ that is the sum of the degree of static indeterminacy and the number of controlled degree of freedom.
- When displacement compensation is required but no change of forces is needed, shape control through impotent *eigenstrain* (C2) is an effective strategy. C2 has comparable energy requirements to C4, which produces control solutions of minimum energy, and it is significantly more efficient than C4 with regard to computation time.

Future work could look into applying the methods formulated in this paper to other structural configurations with the aim to evaluate in which conditions the interaction of internal and external actuators is most beneficial in energy/mass savings terms as well as to increase structural performance for example of slender high-rise structures or long-span bridges. In this work,

actuators are assumed to be installed in series, and thus they have to carry the full force in the corresponding element. Another approach is to consider the actuators in parallel with the elements thereby decoupling the active elements from load transfer (Weidner et al., 2018; Böhm et al., 2020). This approach could be beneficial for control through nilpotent *eigenstrain* where the main objective is force control. Future work could extend the design and control strategies given in this paper to consider actuators installed in parallel. Extensions of the control strategies presented in this work to include geometric non-linear shape control (Reksowardojo et al., 2020a) as well as consideration of dynamics could also be subject of future investigations.

DATA AVAILABILITY STATEMENT

The raw data, including source code, which supports the conclusions of this article will be made available by the authors, without undue reservation. For up to date contact information visit <http://www.gennarosenatore.com>.

AUTHOR CONTRIBUTIONS

GS set up research objectives and directions. Method implementation was carried out by AR and GS. AR carried out simulations and wrote the first draft of the paper with GS actively involved in the rest of the writing process. All authors contributed to the manuscript revision, and reviewed and approved the final version.

FUNDING

The authors thankfully acknowledge the Swiss National Science Foundation who provided core funding for this research via project 200021_182033 (*Structural Adaptation through Large Shape Changes*).

REFERENCES

- Achtziger, W. (2007). On simultaneous optimization of truss geometry and topology. *Structural and Multidisciplinary Multidisc. Optimization*. 33, 285–304. doi: 10.1007/s00158-006-0092-0
- Begg, D. W., and Liu, X. (2000). On simultaneous optimization of smart structures - part II: algorithms and examples. *Comput. Methods Appl. Mech. Eng.* 184, 25–37. doi: 10.1016/S0045-7825(99)00317-5
- Bekker, P. C. F. (1982). A life-cycle approach in building. *Build. Environ.* 17, 55–61. doi: 10.1016/0360-1323(82)90009-9
- Böhm, M., Steffen, S., Geiger, F., Sobek, W., Bischoff, M., and Sawodny, O. (2020). "Input modeling for active structural elements – extending the established FE-Workflow for modeling of adaptive structures," in *International Conference on Advanced Intelligent Mechatronics*, (Boston, MA).
- Böhm, M., Wagner, J., Steffen, S., Sobek, W., and Sawodny, O. (2019). "Homogenizability of element utilization in adaptive structures," in *15th International Conference on Automation Science and Engineering (CASE)*, (Vancouver, BC). doi: 10.1109/COASE.2019.8843066
- Casciati, F., Rodellar, J., and Yildirim, U. (2012). Active and semi-active control of structures - theory and applications: a review of recent advances. *J. Intell. Mater. Syst. Struct.* 23, 1181–1195. doi: 10.1177/1045389X12445029
- Cole, R. J., and Kernan, P. C. (1996). Life-cycle energy use in office buildings. *Build. Environ.* 31, 307–317. doi: 10.1016/0360-1323(96)00017-0
- ENERPAC (2016). *E328e Industrial Tools - Europe*. Available online at: <http://www.enerpac.com/en-us/downloads>. (accessed December 07, 2017).
- Frohlich, B., Gade, J., Geiger, F., Bischoff, M., and Eberhard, P. (2019). Geometric element parameterization and parametric model order reduction in finite element based shape optimization. *Computational Comput. Mechanics*. 63, 853–868. doi: 10.1007/s00466-018-1626-1
- Haftka, R. (1985). Simultaneous analysis and design. *AIAA Journal*. 23, 1099–1103. doi: 10.2514/3.9043
- Hammond, G. P., and Jones, C. I. (2008). Embodied energy and carbon in construction materials. *Proceedings of the Institution of Civil Engineers-. Energy*. 161, 87–98. doi: 10.1680/ener.2008.161.2.87
- I. E. Agency. (2017). *2017 Global Status Report*. UN Environment Programme.
- I. E. Agency. (2018). *2018 Global Status Report*. UN Environment Programme.
- Irschik, H., and Ziegler, F. (2001). Eigenstrain without stress and static shape control of structures. *AIAA Journal*. 39, 1985–1990. doi: 10.2514/2.1189
- Kaethner, S., and Burrige, J. (2012). Embodied CO₂ of structural frames. *The Structural Engineer*. 90, 33–40.
- Lu, L. Y., Utku, S., and Wada, B. (1992). On the placement of active members in adaptive truss structures for vibration control. *Smart Materials and Structures*. 1, 8–23. doi: 10.1088/0964-1726/1/1/003
- Mura, T. (1991). *Micromechanics of Defects in Solids*, (2nd Edition). Dordrecht: Martinus Nijhoff.

- Neuhaeuser, S., Weickgenannt, M., and Witte, C. (2013). Stuttgart SmartShell – a full scale prototype of an adaptive shell structure. *J. of the International Association for Shell and Spatial Structures*. 548, 259–270.
- Nyashin, Y., Lokhov, V., and Ziegler, F. (2005). Decomposition method in linear elastic problems with eigenstrain. *Journal of Applied Appl. Mathematics and Mechanics*. 85, 557–570. doi: 10.1002/zamm.200510202
- Patnaik, S. (1973). An integrated force method for discrete analysis. *Int. J. Numer. Methods Eng.* 6, 237–251. doi: 10.1002/nme.1620060209
- Patnaik, S., Gendy, A., Berke, S., and Hopkins, D. (1998). Modified Fully Utilized Design (MFUD) method for stress and displacement constraints. *International Int. Journal for Numerical Numer. Methods in Engineering*. 41, 1171–1194.
- Pellegrino, S. (1990). Analysis of prestressed mechanisms. *Int. J. Solids Struct.* 26, 1329–1350. doi: 10.1016/0020-7683(90)90082-7
- Pellegrino, S. (1993). Structural computations with the singular value decomposition of the equilibrium matrix. *International Int. Journal of Solids and Structures*. 30, 3025–3035. doi: 10.1016/0020-7683(93)90210-X
- Pellegrino, S., and Calladine, C. (1986). Matrix analysis of statically and kinematically indeterminate frameworks. *International Int. Journal of Solids and Structures*. 22, 409–428. doi: 10.1016/0020-7683(86)90014-4
- Ramesh, A. V., and Utku, S. (1991). Real-time control of geometry and stiffness in adaptive structures. *Comput. Methods Appl. Mech. Eng.* 90, 761–779. doi: 10.1016/0045-7825(91)90183-7
- Reinhorn, A. M., Soong, T. T., Riley, M. A., and Lin, R. C. (1993). Full-scale implementation of active control. II: installation and performance. *Journal of Structural Struct. Engineering*. 119, 1935–1960. doi: 10.1061/(ASCE)0733-9445(1993)119:6(1935)
- Reksowardojo, A., Senatore, G., Srivastava, A., Smith, I. F. C., Unterreiner, H., and Carroll, C. (2020b). “Design and control of a prototype structure that adapts to loading through large shape changes,” in *Proceedings of the 21st International Federation of Automatic Control World Congress*, (Berlin).
- Reksowardojo, A. P., and Senatore, G. (2020). A proof of equivalence of two force methods for active structural control. *Mech. Res. Commun.* 103:103465. doi: 10.1016/j.mechrescom.2019.103465
- Reksowardojo, A. P., Senatore, G., and Smith, I. F. C. (2019). Experimental testing of a small-scale truss beam that adapts to loads through large shape changes. *Frontiers in Built Environment*. 5:93. doi: 10.3389/fbuil.2019.00093
- Reksowardojo, A. P., Senatore, G., and Smith, I. F. C. (2020a). Design of structures that adapt to loads through large shape changes. *Journal of Structural Struct. Engineering (ASCE)*. 146:04020068. doi: 10.1061/(ASCE)ST.1943-541X.0002604
- Röck, M., Saade, M. M., Balouktsi, M., Rasmussen, F. R., Birgisdottir, H., Frischknecht, R., et al. (2020). Embodied GHG emissions of buildings – the hidden challenge for effective climate change mitigation. *Appl. Energy*. 258:114107. doi: 10.1016/j.apenergy.2019.114107
- Rodellar, J., Mañosa, V., and Monroy, C. (2002). An active tendon control scheme for cable-stayed bridges with model uncertainties and seismic excitation. *Structural Struct. Control and Health Monitoring*. 9, 75–94. doi: 10.1002/stc.4
- Senatore, G., Duffour, P., and Winslow, P. (2018a). Energy and cost analysis of adaptive structures: case studies. *Journal of Structural Struct. Engineering Eng. (ASCE)*. 144:04018107. doi: 10.1061/(ASCE)ST.1943-541X.0002075
- Senatore, G., Duffour, P., and Winslow, P. (2018b). Exploring the application domain of adaptive structures. *Engineering Eng. Structures*. 167, 608–628. doi: 10.1016/j.engstruct.2018.03.057
- Senatore, G., Duffour, P., and Winslow, P. (2019). Synthesis of minimum energy adaptive structures. *Structural and Multidisciplinary Multidiscip. Optimization*. 60, 849–877. doi: 10.1007/s00158-019-02224-8
- Senatore, G., Duffour, P., Winslow, P., and Wise, C. (2018c). Shape control and whole-life energy assessment of an “infinitely stiff” prototype adaptive structure. *Smart Materials and Structures*. 27:015022. doi: 10.1088/1361-665X/aa8cb8
- Smith, M. J., Grigoriadis, K. M., and Skelton, R. E. (1991). “The optimal mix of passive and active control in structures” in *American Control Conference* (Boston, MA). doi: 10.23919/ACC.1991.4791625
- Sobek, W. (2016). Ultra-lightweight construction. *International Int. Journal of Space Structures*. 31, 74–80. doi: 10.1177/0266351116643246
- Soong, T., and Cimellaro, G. (2009). Future directions in structural control. *Structural Struct. Control Cont. and Health Monitoring*. 16, 7–16. doi: 10.1002/stc.291
- Soong, T. T. (1988). Active structural control in civil engineering. *Engineering Eng. Structures*. 10, 74–84. doi: 10.1016/0141-0296(88)90033-8
- Teuffel, P. (2004). *Entwerfen adaptiver strukturen* [Doctoral dissertation]. University of Stuttgart - ILEK, Stuttgart, Germany.
- Wagner, J. L., Gade, J., Heidingsfeld, M. F., Geiger, F., von Scheven M, Böhm M, et al. (2018). On steady-state disturbance compensability for actuator placement in adaptive structures. *Automatisierungstechnik*. 66, 591–603. doi: 10.1515/auto-2017-0099
- Wang, Q., Senatore, G., Jansen, K., Habraken, A., and Teuffel, P. (2020). Design and characterization of variable stiffness structural joints. *Materials and Design*. 187:108353. doi: 10.1016/j.matdes.2019.108353
- Wang, Y., and Senatore, G. (2020). Minimum energy adaptive structures – all-in-one problem formulation. *Computers and Structures*. 236:106266. doi: 10.1016/j.compstruc.2020.106266
- Weidner, S., Kelleter, C., Sternberg, P., Haase, W., Geiger, F., Burghardt, T., et al. (2018). The implementation of adaptive elements into an experimental high-rise building. *Steel Construction: Design and Research*. 11, 109–117. doi: 10.1002/stco.201810019
- Xu, B., Wu, S. Z., and Yokoyama, K. (2003). Neural networks for decentralized control of cable-stayed bridge. *Journal of Bridge Engineering (ASCE)*. 8, 229–236. doi: 10.1061/(ASCE)1084-0702(2003)8:4(229)
- Yuan, X., Liang, X., and Li, A. (2016). Shape and force control of prestressed cable-strut structures based on nonlinear force method. *Advances in Structural Struct Engineering*. 19, 1917–1926. doi: 10.1177/1369433216652411

Conflict of Interest: The authors declare that the research was conducted in the absence of any commercial or financial relationships that could be construed as a potential conflict of interest.

Copyright © 2020 Senatore and Reksowardojo. This is an open-access article distributed under the terms of the Creative Commons Attribution License (CC BY). The use, distribution or reproduction in other forums is permitted, provided the original author(s) and the copyright owner(s) are credited and that the original publication in this journal is cited, in accordance with accepted academic practice. No use, distribution or reproduction is permitted which does not comply with these terms.

NOMENCLATURE

$\mathbf{A} \in \mathbb{R}^{n^d \times (n^e + n^{sd})}$	Equilibrium matrix	$\mathbf{p} \in \mathbb{R}^{n^d}$	External load
$\mathbf{A}^{el} \in \mathbb{R}^{n^d \times n^e}$	Element direction cosines	$\mathbf{p}_{jk} \in \mathbb{R}^{n^d}$	k^{th} occurrence of the load probability distribution for the j^{th} load case
$\mathbf{A}^{sup} \in \mathbb{R}^{n^d \times n^{sd}}$	Support direction cosines	$s \in \mathbb{Z}$	Degree of static indeterminacy
$\mathbf{G} \in \mathbb{R}^{(n^e + n^{sd}) \times (n^e + n^{sd})}$	Flexibility matrix	$\mathbf{W} \in \mathbb{R}^{n^{act}}$	Actuator work
$\mathbf{S}_d \in \mathbb{R}^{n^d \times (n^e + n^{sd})}$	Shape influence matrix	$\alpha \in \mathbb{R}$	Cross-section area
$\mathbf{S}_f \in \mathbb{R}^{(n^e + n^{sd}) \times (n^e + n^{sd})}$	Force influence matrix	β	Impotent <i>eigenstrain</i> coefficient vector
$\mathbf{S}_d^* \in \mathbb{R}^{n^{cd} \times n^{act}}$	Reduced shape influence matrix	δ	Nilpotent <i>eigenstrain</i> coefficient vector
$\mathbf{S}_f^* \in \mathbb{R}^{(n^e + n^{sd}) \times n^{act}}$	Reduced force influence matrix	$\boldsymbol{\varepsilon} \in \mathbb{R}^{(n^e + n^{sd})}$	Compatible strains
$\mathbf{U}_f \in \mathbb{R}^{n^d \times (n^d - m)}$	Basis of the column space of the equilibrium matrix	$\boldsymbol{\mu} \in \mathbb{R}^s$	Self-stress states coefficient vector
$\mathbf{U}_m \in \mathbb{R}^{n^d \times m}$	Basis of the left null space of the equilibrium matrix i.e., m linear independent inextensional mechanisms	χ	Optimization of load path and element sizing
		ϑ	Optimization of actuator layout
$\mathbf{V}_r \in \mathbb{R}^{(n^e + n^{sd}) \times (n^e + n^{sd})}$	Equilibrium matrix singular values		
$\mathbf{W}_r \in \mathbb{R}^{(n^e + n^{sd}) \times (n^e + n^{sd} - s)}$	Basis of the row space of the equilibrium matrix		
$\mathbf{W}_s \in \mathbb{R}^{(n^e + n^{sd}) \times s}$	Basis of the null space of the equilibrium matrix i.e., s linear independent states of self-stress		
$\mathbf{d} \in \mathbb{R}^{n^d}$	Displacements (or shape)		
$\mathbf{d}^c \in \mathbb{R}^{n^d}$	Controlled displacements (or shape)		
$\mathbf{d}^i \in \mathbb{R}^{n^d}$	Initial displacements (or shape)		
$\mathbf{d}^p \in \mathbb{R}^{n^d}$	Displacements (or deformed shape) caused by external loads		
$\mathbf{d}^t \in \mathbb{R}^{n^d}$	Target displacements (or shape)		
$\Delta \mathbf{d}^c \in \mathbb{R}^{n^d}$	Change of shape through actuation		
$\Delta \mathbf{d}^{c*} \in \mathbb{R}^{n^{cd}}$	Change of shape through actuation reduced to the controlled degrees of freedom		
$\Delta \mathbf{d}^{sup} \in \mathbb{R}^{n^{sd}}$	Change of constrained node positions through actuation (active support displacements)		
$\Delta \mathbf{d}^t \in \mathbb{R}^{n^d}$	Target change of shape		
$\Delta \mathbf{d}^{t*} \in \mathbb{R}^{n^d}$	Target change of shape reduced to the controlled degrees of freedom		
$\mathbf{f} \in \mathbb{R}^{(n^e + n^{sd})}$	Forces (internal forces + support reactions)		
$\mathbf{f}^c \in \mathbb{R}^{(n^e + n^{sd})}$	Controlled forces		
$\mathbf{f}^{el} \in \mathbb{R}^{n^e}$	Internal forces		
$\mathbf{f}^i \in \mathbb{R}^{(n^e + n^{sd})}$	Initial forces		
$\mathbf{f}^p \in \mathbb{R}^{(n^e + n^{sd})}$	Forces caused by external loads		
$\mathbf{f}^{sup} \in \mathbb{R}^{n^{sd}}$	Support reactions		
$\Delta \mathbf{f}^c \in \mathbb{R}^{(n^e + n^{sd})}$	Change of forces through actuation		
$\Delta \mathbf{f}^t \in \mathbb{R}^{(n^e + n^{sd})}$	Target change of forces		
$i \in \mathbb{Z}$	i^{th} element		
$\mathbf{l} \in \mathbb{R}^{n^e}$	Element lengths		
$\Delta \mathbf{l} \in \mathbb{R}^{n^{act}}$	Actuator commands (element length changes + active support displacements)		
$\Delta \mathbf{l}^{all} \in \mathbb{R}^{(n^e + n^{sd})}$	Actuator commands, all elements and support as active		
$\Delta \mathbf{l}^{el} \in \mathbb{R}^{n^e}$	Internal actuators length changes		
$n^{act} \in \mathbb{Z}$	Number of actuators		
$n^{cd} \in \mathbb{Z}$	Number of controlled degrees of freedom		
$n^d \in \mathbb{Z}$	Number of degrees of freedom		
$n^e \in \mathbb{Z}$	Number of elements		
$n^n \in \mathbb{Z}$	Number of nodes		



Adaptive Concrete Beams Equipped With Integrated Fluidic Actuators

Christian Kelleter^{1*}, Timon Burghardt², Hansgeorg Binz², Lucio Blandini¹ and Werner Sobek¹

¹ Institute for Lightweight Structures and Conceptual Design—ILEK, University of Stuttgart, Stuttgart, Germany, ² Institute for Engineering Design and Industrial Design—IKTD, University of Stuttgart, Stuttgart, Germany

OPEN ACCESS

Edited by:

Gennaro Senatore,
École Polytechnique Fédérale de
Lausanne, Switzerland

Reviewed by:

Marios C. Phocas,
University of Cyprus, Cyprus
Mohamed Hechmi Elouni,
King Khalid University, Saudi Arabia

*Correspondence:

Christian Kelleter
christian.kelleter@ilek.uni-stuttgart.de

Specialty section:

This article was submitted to
Structural Sensing,
a section of the journal
Frontiers in Built Environment

Received: 07 April 2020

Accepted: 26 May 2020

Published: 22 July 2020

Citation:

Kelleter C, Burghardt T, Binz H,
Blandini L and Sobek W (2020)
Adaptive Concrete Beams Equipped
With Integrated Fluidic Actuators.
Front. Built Environ. 6:91.
doi: 10.3389/fbuil.2020.00091

The rapidly growing world population is a great challenge for the building industry. Due to the impending scarcity of resources, it is not possible to provide the growing mankind with sufficient living and work places and infrastructure with current construction methods. For wide-spanning beams and slabs, the decisive design criteria are mainly determined by deformations rather than stresses, since deflections must be limited. This leads to structural elements, which are not fully utilized. However, if the deformations can be reduced, significant material savings can be achieved. Sensors, actuators, and a control unit enable components subjected to bending to adapt to high but rare loads. This article presents a solution that allows beams to react actively to loads by use of integrated actuators. The newly developed integrated hydraulic actuators allow the structure to react specifically to a wide range of load cases, by adjusting the internal hydraulic pressure. This is a clear advantage in load-bearing systems because there is often no dominant load case. This internal actuation concept is a new approach, as previous adaptive structures either have externally added actuators or are composed of truss structures in which single bars are actuated. In this paper, the concept is explained analytically, simulated with the finite element method and validated experimentally.

Keywords: adaptivity, lightweight construction, beams, slabs, simulation

INTRODUCTION

The increasing world population, the growing urbanization, and the rising standard of living in large parts of the world confront the construction industry with a great challenge, which cannot be solved with conventional methods (Curbach, 2013; Sobek, 2016). Mineral building materials, especially sand, the main component of concrete, are already becoming scarce in some regions of the world (United Nations Environment Programme, 2014). However, extraction is not decreasing and is twice as high as the natural supply (Milliman and Syvitski, 1992). In addition, the cement production alone accounts for about 10% of the total anthropogenic CO₂ emissions and subsequently 6% of the anthropogenic greenhouse gases (Scrivener et al., 2016). The entire construction industry is even responsible for 40% of all greenhouse gas emissions (European Commission, 2019). With concrete being the most widely used building material (Mitchel, 2008), alternative design and construction methods must be developed, especially for concrete structures. Therefore, the following investigations are carried out for the material of concrete.

Passive structures are very often oversized for most of their lifetime, as the loads they are designed for rarely or never occur. To give an example, the snow and wind loads for Germany, which are defined in the European codes, have a statistical probability of occurrence once every

50 years (DIN Deutsches Institut für Normung, 2009). This is an annual exceedance probability of just 2%. Nevertheless, of course, structures have to withstand any occurring load, independently of their frequency of occurrence.

Adaptive structures can react to these rare, but usually high loads and allow structures to be designed with less material and therefore with fewer resources and embodied emissions. By means of a smart interaction between actuators, sensors, and a control unit, adaptive structures can reduce stresses, deformations, and vibrations. First concepts of combining such active components with load-bearing structures into a control loop can be found in Yao (1972). However, the motivation behind it was to extend the limiting height of tall buildings rather than saving building materials. Previous studies on adaptive structures, which were not limited to vibration control, can be divided into two categories.

The first category accounts for truss structures in which individual single bars are actuated (contracted or extended). In Weidner et al. (2018), a large-scale prototype of an adaptive high-rise building is presented, in which the deformations and vibrations of the structure can be reduced by active columns and bracing elements. In another example, displacement control has been used to completely compensate for the deflection of an adaptive truss with electrical linear actuators (Senatore et al., 2018).

Senatore et al. (2019) introduce a new method for the design of minimum energy adaptive structures. Embodied energy in the material and operational energy for control units are minimized through combined optimization of structural sizing and actuator placement. Potential reduction of mass and energy consumption of engineering structures through adaptivity has also been investigated via Life Cycle Analysis applied to an adaptive high-rise building (Schlegel et al., 2019).

The second group of studies employs the principle of adaptivity by installing actuators to the structures externally (Domke et al., 1981; Domke, 1992). This means that the whole structure can be manipulated with few actuators. For example, experimental testing on a small-scale prototype has shown that it is possible to manipulate the deformations of a bridge with only one actuator that rotates one of the bridge's bearings (Teuffel, 2004). Experimental testing on a large-scale prototype, an adaptive shell structure, has shown that a significant reduction of stress can be achieved through a translation of the supports, which are equipped with actuators (Sobek et al., 2013; Neuhäuser, 2014).

Further examples for external actuation are structures with variable prestress devices (Pacheco et al., 2010; Schnellenbach-Held et al., 2014). Here, the level of prestressing is adjusted at the anchorage according to the external load. However, the characteristics of the stresses determined by the curved tendons cannot be changed.

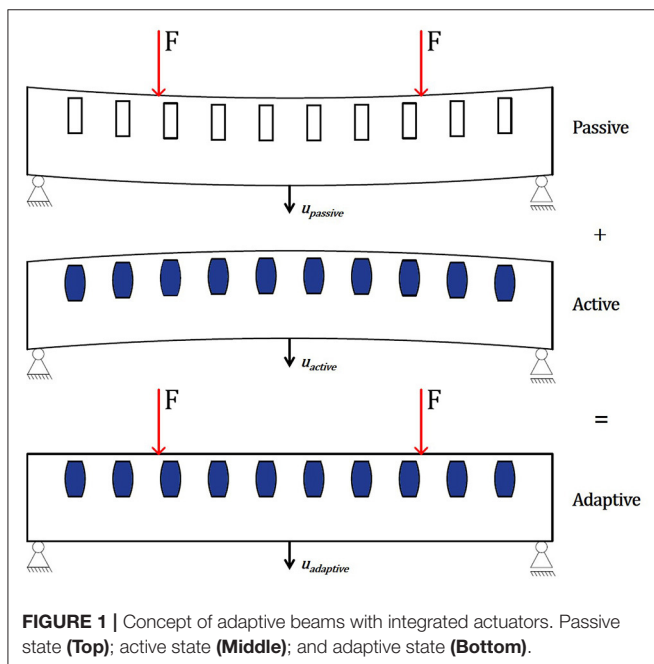
In the presented concept, load-bearing structures and actuators are not separated. Several actuators are integrated into the cross-section of a beam, thus allowing for a section-wise manipulation and therefore specific reactions to a wide range of load cases. The focus in many studies is to adapt the whole load-bearing structure, whereas in this paper, the aim is to manipulate beams as a part of an overall structure.

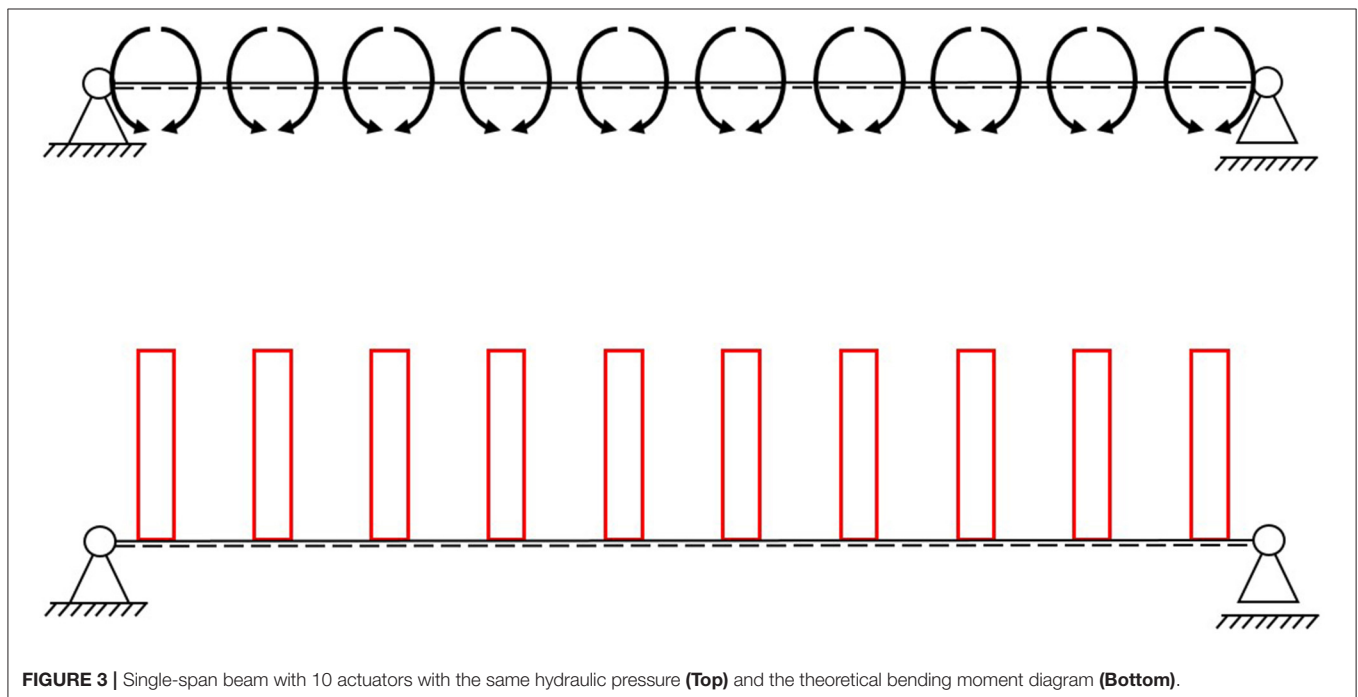
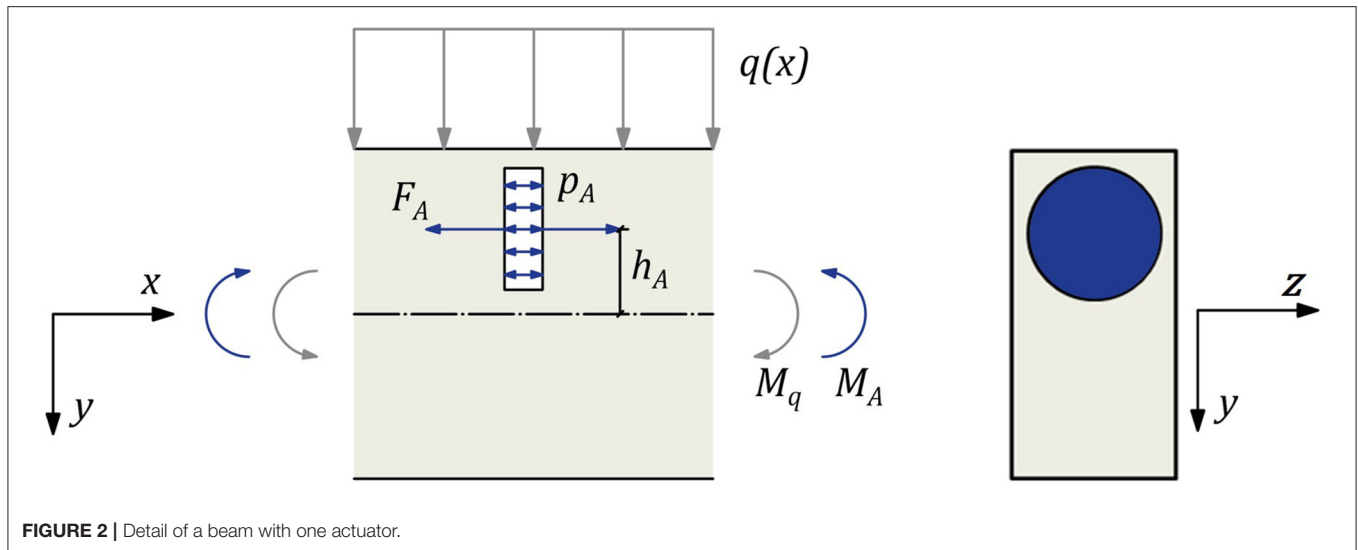
OBJECTS OF INVESTIGATION

A look at the built environment reveals that almost every building (whether residential or office) consists of components subjected to bending. These are mostly beams that act as downstand beams or rafters of frames or slabs in the form of floor slabs. In skeleton structures, which are very often used in non-residential buildings, components subjected to bending make up over 50% of the total mass (Berger et al., 2013). Depending on the height of the building and its number of stories, it may increase to up to or over 75% (Block et al., 2017). In order to save material and therefore reduce embodied emission, components subjected to bending should be intensively considered.

In most cases, those components are flat structural elements that are easily manufactured and, unlike shells, for example, are ideal for use as floor levels. So far, the load transfer of components subjected to bending is inefficient (especially with the small inner levers of beams and slabs). In the neutral fiber, the incorporated material is hardly or not used at all during the linear transition from compressive to tensile strain (Gross et al., 2018). Mass reduction through adaptation of high-performance concrete is possible. However, since self-weight is reduced, variable loading events such as payloads or snow loads become dominant. In these cases, when strong loads that do not occur frequently are dominant, an adaptive beam concept could significantly improve the performance of the structure.

A further important aspect in the design and dimensioning of the beams and slabs is that the governing limitation is not stress but rather deformations to ensure the serviceability, e.g.,



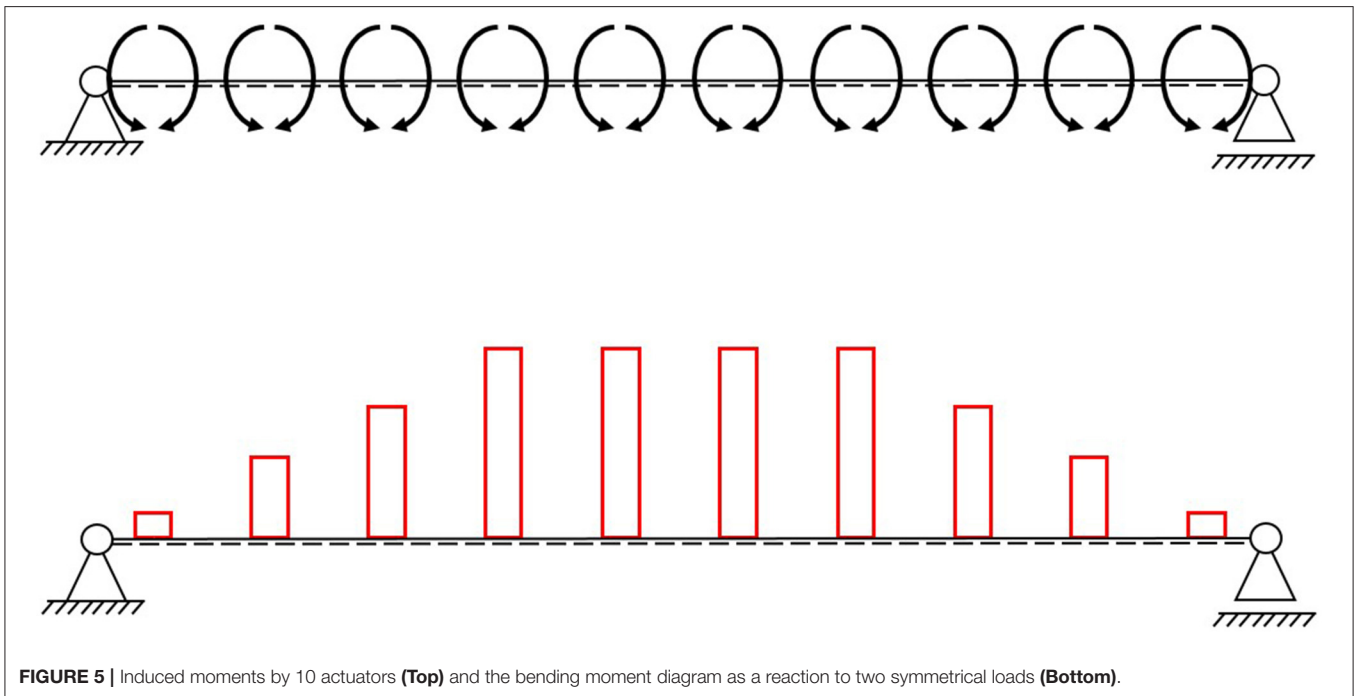
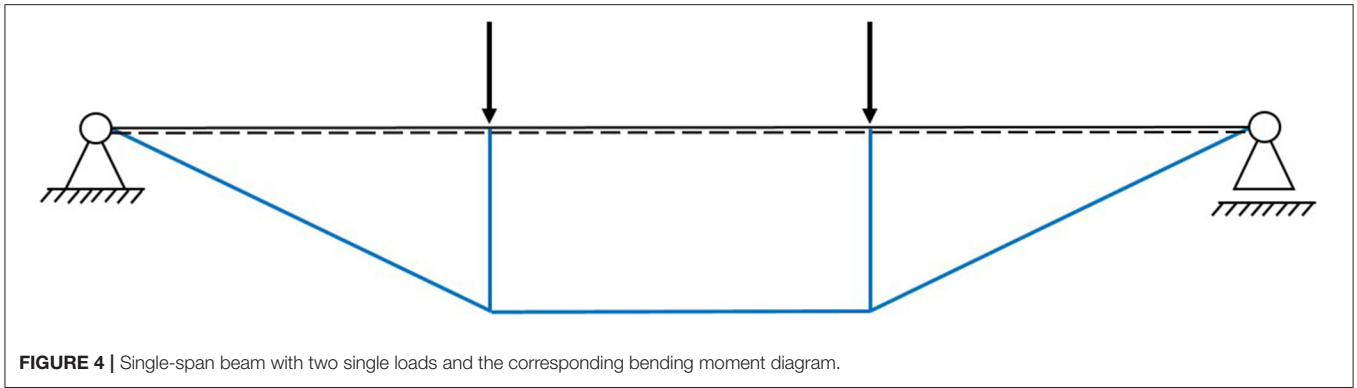


avoid damage to non-load-bearing partition walls (Setareh and Darvas, 2016). This results in a stiffness problem, not a strength problem. In order to adhere to these limits, an adequate stiffness of the structural element has to be achieved by an increase of the element's cross-section and therefore mass. In the presented alternative, adaptive structures can reduce the deformation to the desired minimum through actuation. Actuators induce a counter-deformation, increasing the stiffness of beams, when external loads occur. Therefore, reduction of the deflection at mid span is defined as the target of control.

Adaptive beams and slabs have a great mass saving potential by compensating for deflection actively, which could change the design of these components from stiffness to stress governed.

CONCEPT

Passive beams, as utilized today, deform under their own weight and under a possible external load (passive state). In order to compensate for this deflection, a concept has been developed in which the beam is deformed in the opposite direction by integrated actuators (active state). A superposition of these two states, a positive curvature and a negative curvature, results in zero deflection at any time (adaptive state). Sensors detect whether an external load acts on the beam and transmit that information to a control unit, which forwards a command to the actuators if necessary. A similar concept was already developed with the focus on stress control in Sobek (2016).



Since deformation limits are often governing for dimensioning components subjected to bending, in this work, the focus is on control of deflections. **Figure 1** shows a visualization of this concept.

$$u_{passive} + u_{active} = u_{adaptive} \quad (1)$$

The deflection in the passive state $u_{passive}(F)$ depends on the external load F . In the active state, the deflection $u_{active}(p)$ depends primarily on the hydraulic pressure p through actuation. The forces generated this way counteract the deflection in the passive state. The adaptive state $u_{adaptive}(F, p)$ is dependent on both the external load F and the pressure p inside the actuators.

$$u_{passive}(F) + u_{active}(p) = u_{adaptive}(F, p) \quad (2)$$

In the proposed concept, the pressure p is dependent on the external load F . If the external load F increases, the pressure p

must also increase to keep the deflection $u_{adaptive}$ low or zero. For a significant performance increase, $u_{adaptive}$ should be as low as possible.

$$u_{passive}(F) + u_{active}(p(F)) = u_{adaptive}(F, p(F)) \cong 0 \quad (3)$$

Depending on whether the actuators are placed in the compression or tension zone of the beam, an expansion or contraction is needed to counteract deflections. Placing actuators in both compression and tension zones is also possible (Kelleter et al., 2018). The presented investigations focus on an actuation in the compression zone.

To prove this concept, an analytical approach is derived in section Analytical Approach, which is numerically and experimentally validated on a $1,200 \times 200 \times 100$ [mm³] concrete beam in sections Numerical Simulation and Experimental Validation, using the finite-element method (FEM) and a universal testing machine (UTM), respectively.

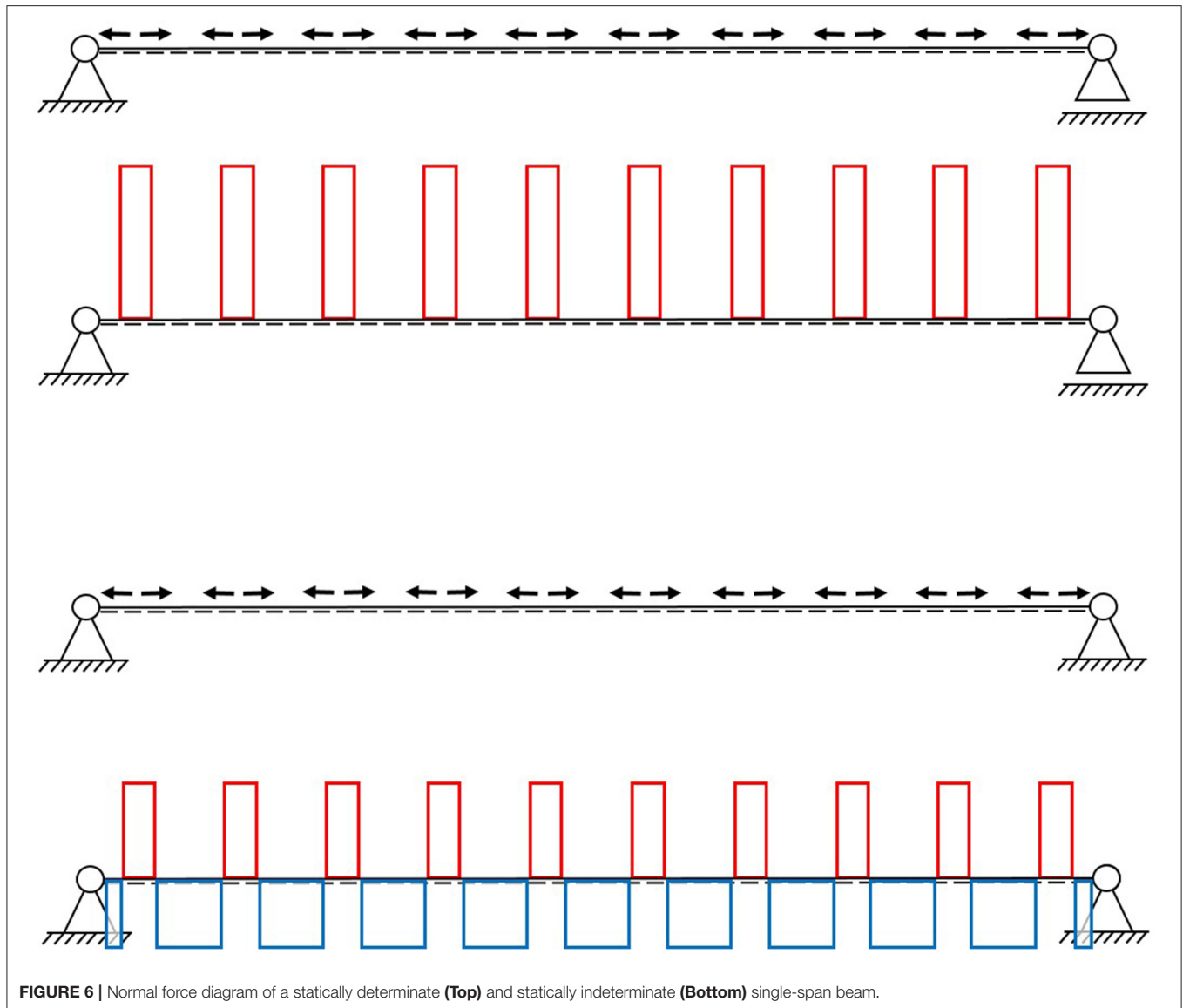


FIGURE 6 | Normal force diagram of a statically determinate (Top) and statically indeterminate (Bottom) single-span beam.

Analytical Approach

Each actuator induces a pair of normal forces $F_{A,i}$ and a pair of bending moments $M_{A,i}$. The actuation concept has no influence on the shear forces within the beam. The resulting force F_A induced into the cross-section via an actuator is calculated from the hydraulic pressure p_A and the available actuator cross-section A_A (Janocha, 2004). Design measures are taken to ensure that the hydrostatic stress state from the applied hydraulic pressure in the actuators is largely restricted to one predetermined axis. Thus, a distinct orientation of the resulting force F_A can be ensured, which lies strictly in the longitudinal axis of the beam. Since the actuator is located in the compression zone, the distance between the actuator center and the axis of gravity of the beam h_A results in a moment M_A (cf. Figure 2). For a single actuator i , the relationship can be written as:

$$M_{A,i} = F_{A,i} \cdot h_{A,i} = A_{A,i} \cdot p_{A,i} \cdot h_{A,i}. \quad (4)$$

A first approach to determine the necessary pressures p_A is to use an equilibrium of moments. The moment generated by the actuators M_A should be equal to the moment from external load M_q :

$$M_A + M_q = 0 \quad (5)$$

Theoretical Bending Moment Diagrams

If the passive moment M_q increases, the induced active moment must be raised accordingly by the same amount but with opposite sign. Since the active bending moment of one actuator $M_{A,i}$ only acts locally, more than one or rather multiple actuators should be arranged along the entire longitudinal axis of the component. The theoretical bending moment diagram for a one-dimensional beam, using a simple strut and tie model, with 10 actuators is shown in Figure 3.

TABLE 1 | Calculated hydraulic pressure in each actuator.

Actuator	x_i [mm]	$M_{q,i}$ [kNm]	$p_{A,i}$ [N/mm ²]	$p_{A,i}$ [bar]
1	50	0.20	0.80	8.0
2	150	0.60	2.39	23.9
3	250	1.00	3.98	39.8
4	350	1.33	5.31	53.1
5	450	1.33	5.31	53.1
6	550	1.33	5.31	53.1
7	650	1.33	5.31	53.1
8	750	1.00	3.98	39.8
9	850	0.60	2.39	23.9
10	950	0.20	0.80	8.0

For the building industry in particular, a prediction of the occurring loads is very difficult, in many cases even impossible. Therefore, an adjustment of the individual active bending moments $M_{A,i}$ generated by the actuators is desirable. This could be done by changing the distance h_A of the actuators to the neutral axis, by reducing the size of each actuator's area $A_{A,i}$ or by individually adjusting the pressure $p_{A,i}$. Of those parameters, only the adjustment of the hydraulic pressure $p_{A,i}$ can be repeatedly varied. Thus, this concept will be pursued further. By adapting the pressure, the bending moment diagram from the actuators can be adapted to counteract the bending moment caused by the external load.

Figure 4 shows the bending moment diagram of a four-point bending test. In this example, some actuators should be pressurized differently. The internal hydraulic pressure should be the same for all actuators between the application position of the two point loads and lower for the actuators toward the support, generating an oppositely directed bending moment diagram (see **Figure 5**).

Further examples can be found in Kelleter et al. (2019).

Theoretical Normal Force Diagram

This far, all shown examples (cf. section Theoretical Bending Moment Diagrams) are statically determined, which is often preferred to avoid restraint forces. The normal forces induced by the actuators are short-circuited locally, along each actuator, as the beam can expand or contract freely. This means that the areas between the actuators are theoretically stress free, while the areas around the actuators are not (see **Figure 6**).

If the beam elongation is constrained (statically indeterminate), not only the stress in the area of the actuators can be manipulated, but also the stresses between the actuators. More precisely, it is possible to compress the spaces between the actuators, due to an expansion of the latter (see **Figure 6**). Although constraints are usually avoided, for concrete beams with integrated actuators, this seems to lead to a distribution that consists of compression only.

The ratio of compressive forces in the beam in **Figure 6**, between the actuators (blue) and tensile forces (red) around the

actuators, is dependent on the ratio of stiffness of those areas. In previous studies on adaptive truss structures, a distinction was made between parallel and serial actuation (Weidner et al., 2019). With the actuator being surrounded by concrete on all sides, the shown actuation concept can be considered parallel (cf. **Figure 2**). If the stiffness around the actuators is zero, this actuation concept would be closer to a serial actuation. This article on integrated actuators focuses on reducing deflection and the bending moment; therefore, the normal and shear forces are not discussed further. The parallel and serial actuation of truss structures is examined in more detail in Steffen et al. (2020).

Example

The shown analytical approach is applied to the chosen adaptive beam ($1,200 \times 200 \times 100$ [mm³]), loaded in the four-point bending setup (cf. **Figures 1, 4**), with a distance between the supports of 1,000 mm (cf. section Experimental Validation), as a first simplified approach to determine the needed pressures. It is assumed that both point loads F are 4 kN, leading to a maximum bending moment M_q of 1.33 kNm.

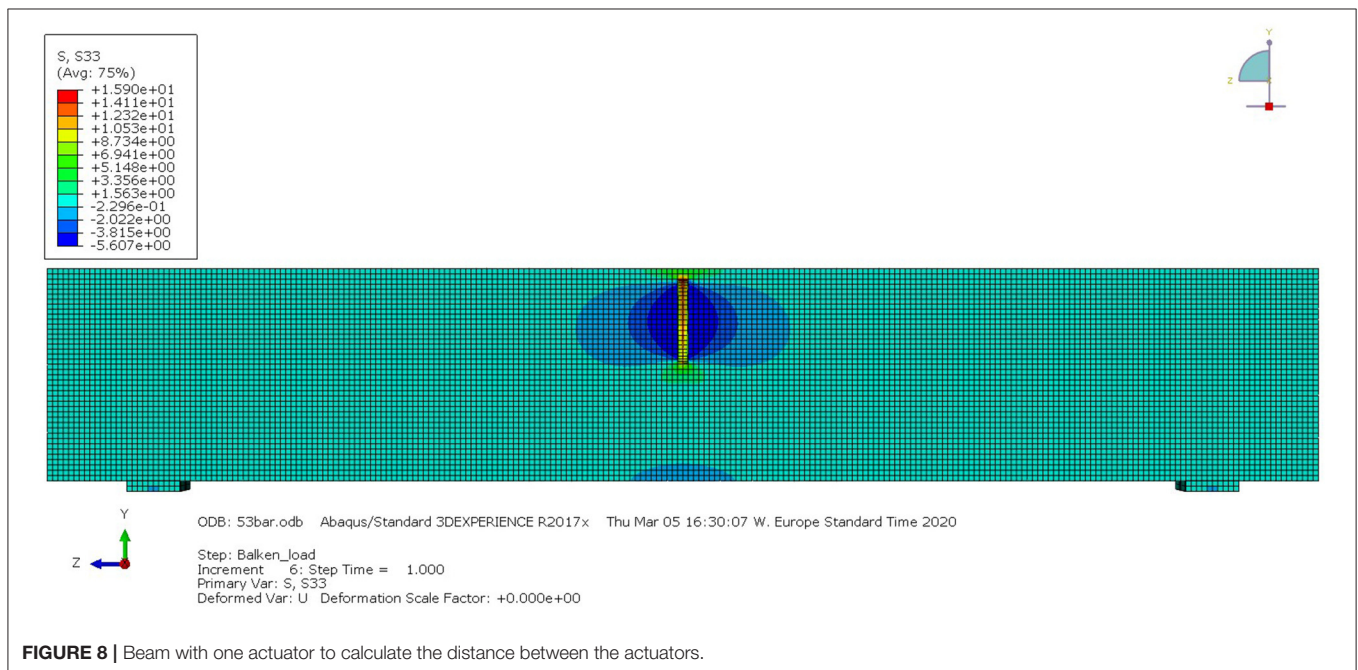
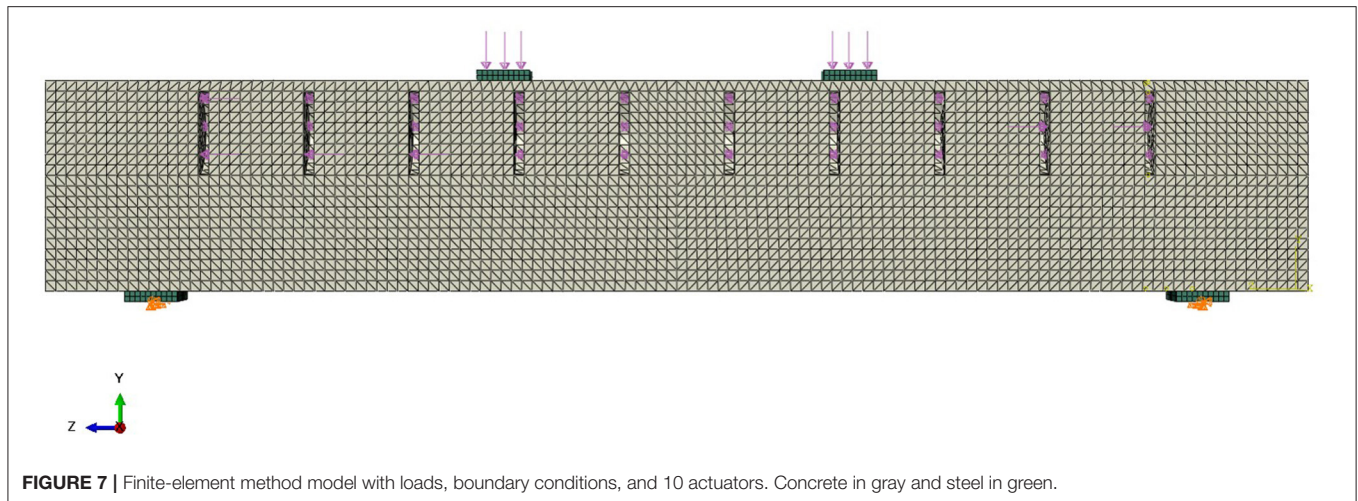
From the resulting passive bending moment diagram, the needed pressures can be calculated by solving Equation (4) for the pressure.

$$p_{A,i} = \frac{M_{q,i}}{A_{A,i} \cdot h_{A,i}} \quad (6)$$

All actuators are assumed to be thin cylindrical discs (cf. Section Experimental Validation), with a diameter of 80 mm, resulting in an area A_A of 5026.5 mm². Each actuator is positioned in the center of the upper half of the cross-section (cf. **Figure 2**), leading to an inner lever h_A of 50 mm. The position was chosen so that the lever arm h_A is maximized, while keeping the actuators evenly surrounded by concrete. Ten actuators are placed along the longitudinal axis of the beam with an interval of 100 mm, with the first actuator being placed at a distance of 50 mm from the first support. The equidistant arrangement was derived through FE analysis (cf. section Numerical Simulation). The calculated pressures are presented in **Table 1** and further used for the numerical simulations in section Numerical Simulation.

NUMERICAL SIMULATION

The example from Section Analytical Approach is further validated through numerical simulations through FE analysis. The determined hydraulic pressures are adjusted if necessary. The beam has been modeled with the software ABAQUS and consists of solid elements C3D10 with an approximate element size of 2 mm (cf. **Figure 7**). The C3D10 element is a second-order tetrahedral element with 10 nodes and four integration points. A comparison between a model in which the actuators were fully modeled and a model in which the actuators were simplified as a cavity in the beam showed that this simplification does not affect solution accuracy significantly. Therefore, the actuators were idealized as a cavity with a surface pressure applied on the xy -plane, which is set to the pressure given in **Table 1** (see **Figure 7**).

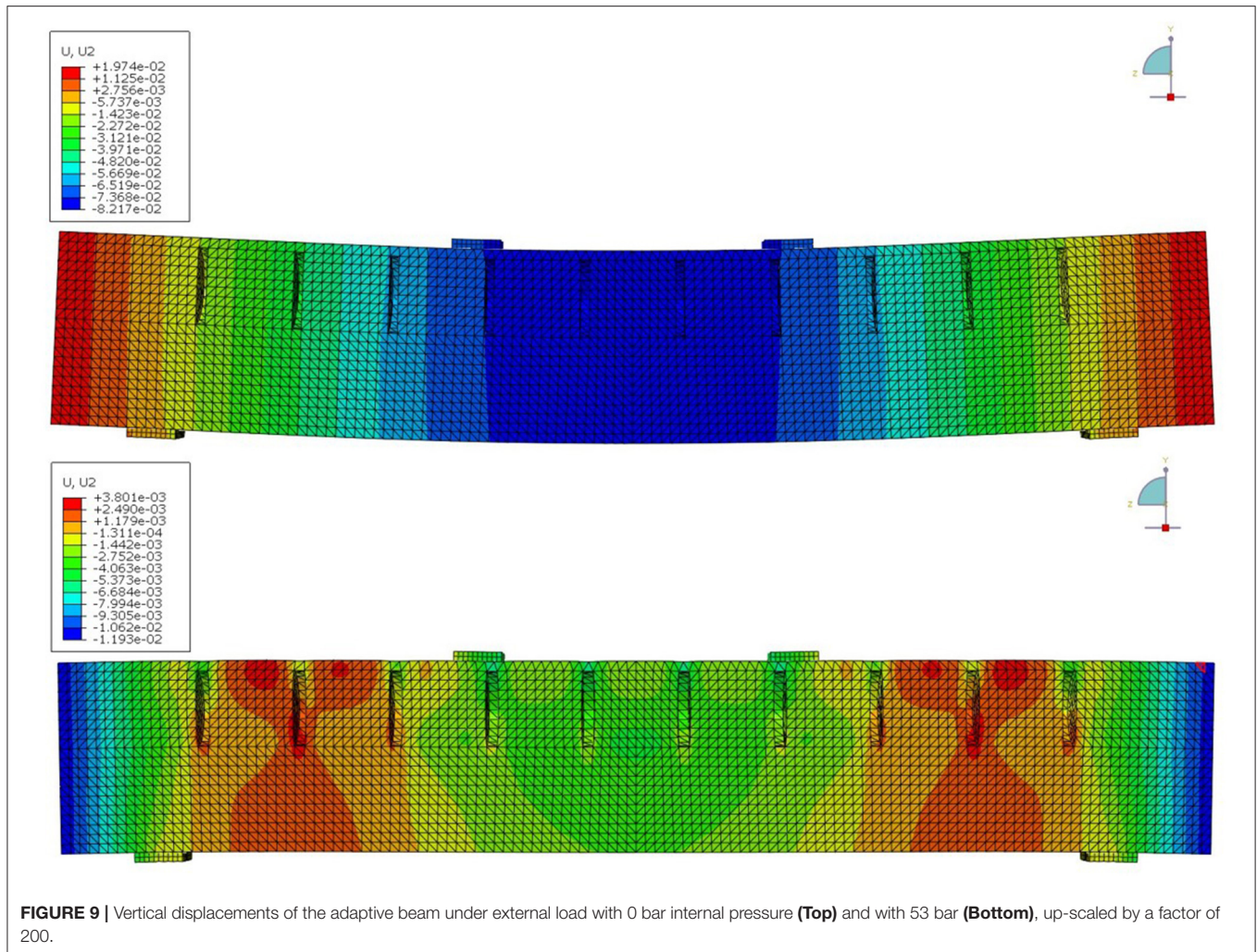


Since a linear elastic behavior is assumed (in the best-case scenario, the beam has no deflection at all), a linear elastic material is defined. A conventional concrete C35/45 is used, which is modeled with a modulus of elasticity of 34,000 N/mm². The support flats and load introduction flats were also modeled in accordance with the experimental setup of Section Experimental Validation. These flats were made of steel with a modulus of elasticity of 210,000 N/mm² and were meshed with eight node brick elements C3D8R.

The symmetry of the beam is used to save calculation time. Only half of the beam is created and provided with the necessary boundary conditions (displacement- x = rotation- y = rotation- z = 0) (see **Figure 7**). One support restricts vertical (displacement- y = 0) and horizontal (displacement- z =

0) movement, and the other one restricts vertical movement only. To allow for rotations of the supports, their translational boundary conditions are not applied over the entire surface of the support flat, but only along a line parallel to the x -axis (cf. **Figure 7**). Between the steel flats and the concrete beam, a frictionless surface-to-surface contact is defined to take the polytetrafluoroethylene layer into account, which will be placed between the steel flats and the cylinder segments in the experimental setup.

As explained in section Theoretical Normal Force Diagram, the forces induced by an actuator in the cross-section only act locally. Firstly, the stresses induced by each actuator decay or homogenize over the length of the beam, according to the principle of St. Venant (Mises, 1945). Secondly, the forces are short-circuited, since each actuator is surrounded



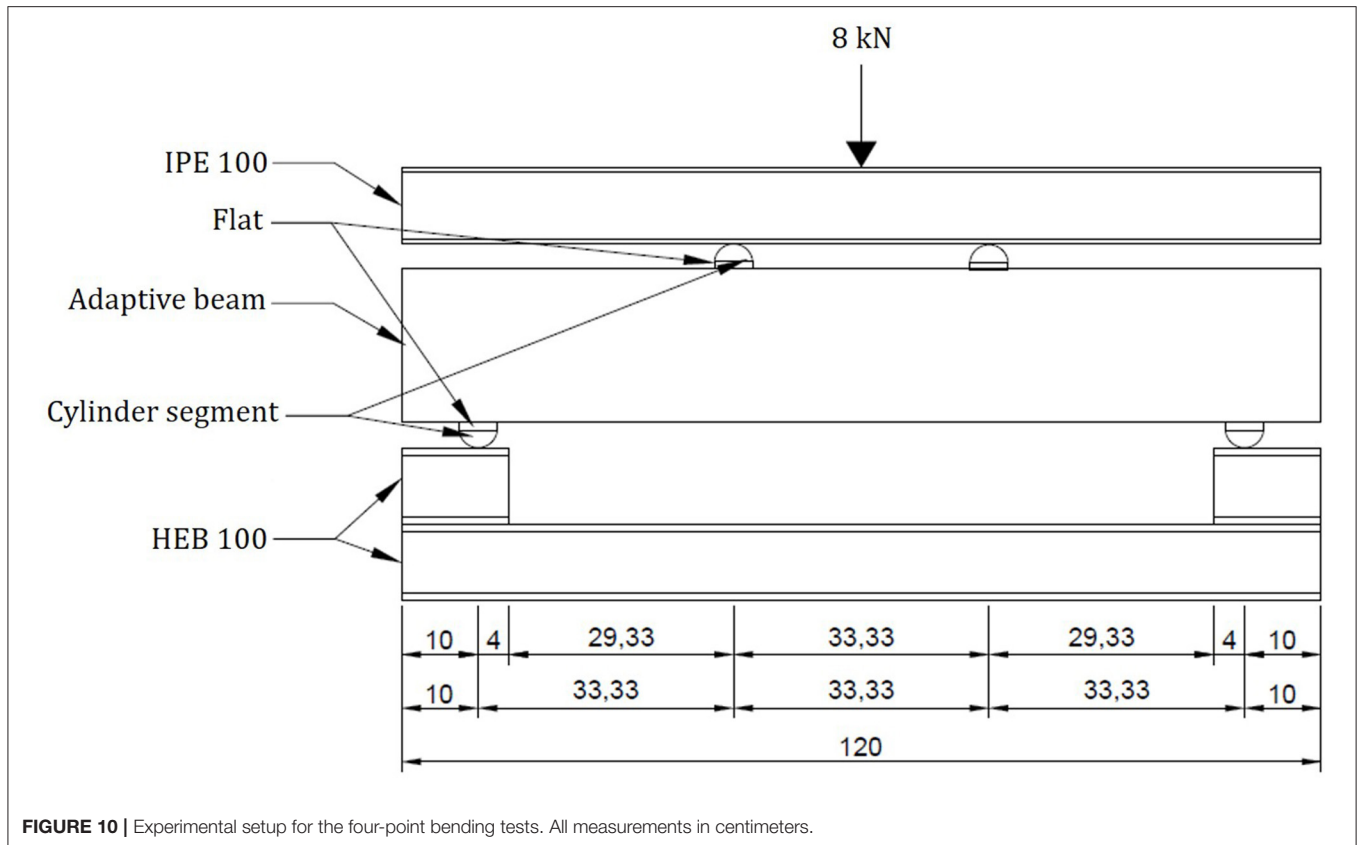
by concrete (parallel actuation). Multiple actuators should be spaced depending on this effect. Thus, a separate FE analysis was done to estimate the distances between the actuators. A beam with only one actuator with a hydraulic pressure of 53 bar (cf. **Table 1**) and no external load is simulated (see **Figure 8**). The maximum stress in longitudinal direction from actuation results in the area next to the actuator (5.3 N/mm^3). As the stress fields of two adjacent actuators overlap, the spacing of the actuators is chosen to be determined by the distance over which the maximum stress induced by one actuator reduces by at least 50%. In the given model, the maximum stress decreases from 5.3 N/mm^2 to 2.66 N/mm^2 over a distance of approximately 50 mm, resulting in a spacing of 100 mm for the actuators. This leads to 10 actuators for the given span of 1,000 mm. The quality of this estimation is evaluated through experimental investigations and modified if necessary.

The simulations with 10 actuators show that the deflection resulting from two external point loads of 4 kN each and the dead load of the beam can be reduced from $u_{\text{passive}} = 0.00815 \text{ mm}$ to $u_{\text{adaptive}} = 0.00285 \text{ mm}$ (see

Figure 9). In this simulation, all actuators have a hydraulic pressure of 53 bar, because in the tests, the pressure was not individually adjusted for each actuator (cf. section Experimental Validation).

EXPERIMENTAL VALIDATION

Results obtained from the FE analysis are experimentally validated in a four-point bending test series. The beam rests on two support plates, which, separated by an intermediate polytetrafluorethylene layer, rest on half cylinders. A UTM applies the external load via two steel plates and the deflection of the beam is measured at mid-span with two inductive displacement transducers. The experimental setup is visualized in **Figure 10**. The test is carried out by first letting the structure deform under the external load and then compensating the deflection by the hydraulic pressure in the actuators. This process takes place successively in order to observe the behavior of the beam in each state. For simplicity, in this series of test, the pressure is not varied for each

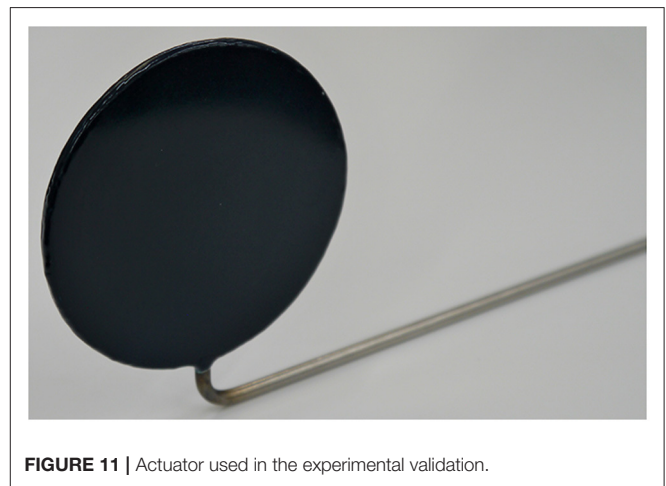


actuator individually, as shown in section Analytical Approach. Instead, the same pressure is applied to each actuator at the same time.

Actuators

The actuators were specifically developed for integration in concrete beams. As maintenance is not possible, no wear parts are used. Due to the minimal deformations of the concrete, the actuators also only have to generate minimal displacements. Thus, in order to completely eliminate the use of parts subjected to wearing, only the elastic deformations of the actuators are utilized. However, large forces must be generated to actuate the beam. Among the many actuator operating principles, hydraulic was chosen because it can generate the required forces and at the same time it can react quickly. In addition, hydraulic pressures can be transmitted directly to the concrete structure.

Each actuator consists of three layers, two external steel sheets with 1 mm wall thickness, and an internal core with 2 mm thickness, which stiffens the actuator in radial direction. Despite hydrostatic internal pressure, forces can be introduced exclusively in the axial direction of the beam, by positioning the actuators accordingly. The actuators are disc-shaped with a diameter of 80 mm (see **Figure 11**). The three layers are welded all around and connected to a supply line for the hydraulic oil with a diameter of 4 mm. A visual prototype, showing the section of a concrete beam, is depicted in **Figure 12**.



Each actuator is connected to a hydraulic power unit via its supply line pipe (cf. **Figure 11**). The pressure in each actuator can be individually adjusted via solenoid valves and hydraulic pressure transmitter, which are both attached to the hydraulic power unit (for simplicity, in this test series, the pressure in the actuators is not adjusted individually). The control loop with all additional components is shown in Kelleter et al. (2019).

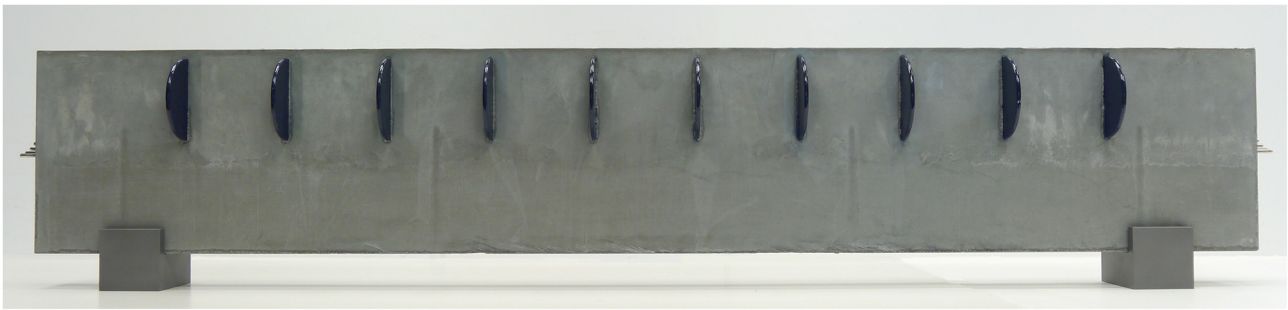


FIGURE 12 | Prototype with only one half poured with concrete and 10 integrated actuators. Length = 1,200 mm.

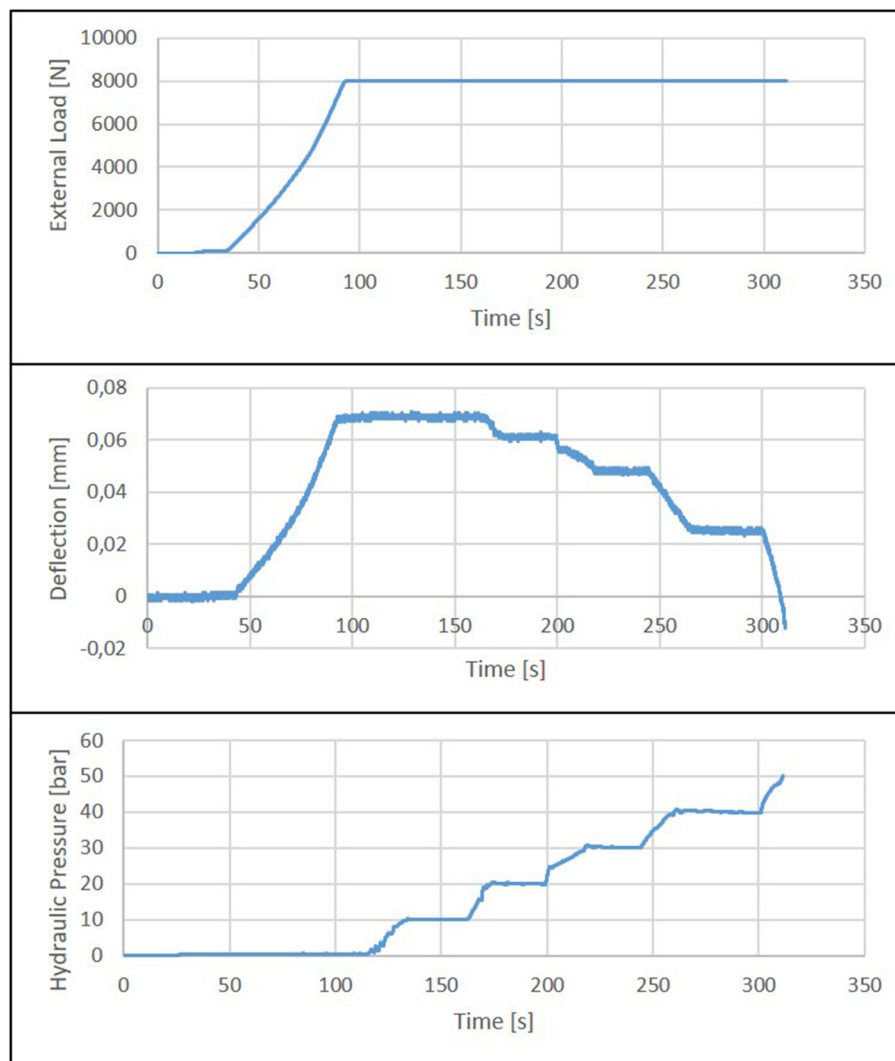


FIGURE 13 | Results of a four-point-bending test: external load (**Top**), mid-span deflections of the beam (**Mid**), hydraulic pressure inside the integrated actuators (**Bottom**).

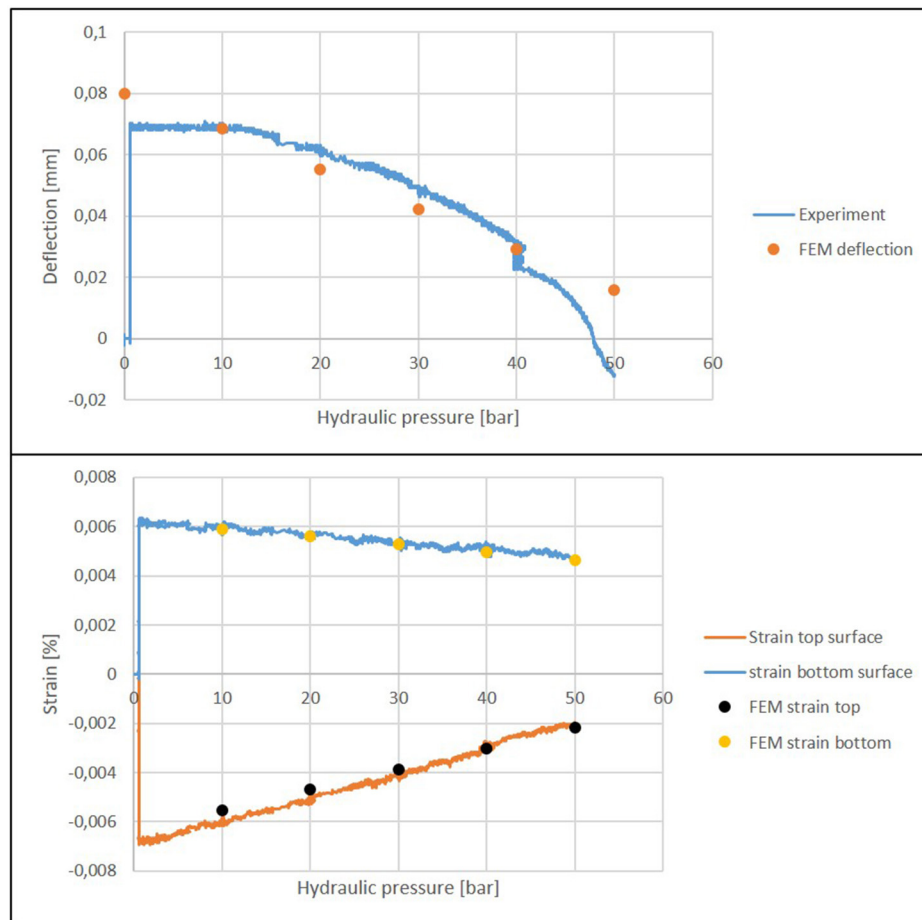


FIGURE 14 | Compensation of the deflection (**Top**) and strains (**Bottom**) as a result of hydraulic pressure.

Test Results

Figure 13 shows the measurement results of a test with an actuated beam under four-point bending load.

Initially, the beam is loaded with 8 kN. This load is kept constant under force control for the rest of the test duration. After reaching the maximum external force, the hydraulic pressure inside the integrated actuators is increased continuously in steps of 10 bar. As can be seen in the bottom diagram in **Figure 13**, the mid-span deflection is fully compensated at a pressure of approx. 47 bar. Increasing the pressure further, the beam can even be bent upwards (positive curvature).

At a pressure above 50 bar, the first cracks appear at the outer ends on the upper surface of the beam, i.e., in the normally compressed zone. This failure behavior coincides with the theory. Since there is less compressive stress due to the bending moment (above the supports, the bending moment is almost zero), the pressure of the actuators, which is not adapted to the moment characteristic, leads to failure in these areas. In the tested beams, there is no reinforcement in the upper part, which is compressed in the passive state and under tension when the beam has a negative vertical deflection, although in real beams, there is most

likely reinforcement in the compression and tension zone as a secondary reinforcement.

The test results and the results of the FEM simulation are compared in **Figure 14**. In the unpressurized state, the simulated deflection is greater than the measured deflection. This is due to the fact that the actuators are not modeled (see section Numerical Simulation) and therefore the supporting effect of the actuator housing is not taken into account. Between 10 and 40 bar, there is good accordance between numerical and experimental results. The deviation at 50 bar is due to the ideal elastic material model on which the simulation is based. Due to the cracking of the concrete, when the beam is rising upwards, this model cannot accurately predict the response of the structure.

Another parameter used for validation are the strains. Two strain gauges are attached to the beam. One on the top surface and one on the bottom surface, both placed in mid-span. The calculated strains are very close to the measured strains, verifying the FEM model (see **Figure 14**). Both strain values are significantly reduced. The strain at the top side of the beam is reduced much more than the strain at the bottom side. This observation is in good accordance with theoretical predictions.

This is because the actuators not only reduce the bending moment and therefore the deflection, but also induce a pair of normal forces (cf. section Numerical Simulation). At the top, where the actuator is closer to the surface, the effect of the elongation due to the pair of normal forces is higher than at the bottom (St. Venant principle).

CONCLUSION

In this paper, it was shown that the deflection of a concrete bending beam can be minimized by means of integrated fluidic actuators. Based on the presented example of a beam on a reduced scale, the concept was derived with analytical preliminary considerations and with FEM simulations. Simulation results were validated experimentally. There is good accordance between numerical and experimental results in the linear elastic range.

The entire compensation of the deflection of components subjected to bending allows a new way of dimensioning. The approach of integrating the actuators into the cross-section allows one to react, unlike many other adaptive structures, to a wide range of load cases in an optimal way. By transforming the stiffness problem of beams into a strength problem, this approach has a great mass and energy saving potential. How much material and energy are saved depends on the individual scenario (span, maximum load levels of external loads, probabilities of occurrence, etc.). In the example shown, however, the full compensation of deflection is highly promising.

The next step is to calculate the material savings that can be achieved through the shown concept. This is an iterative process, since a reduction of the cross-section means that the actuators must also be reduced in size. As a consequence, the resulting actuator force is lower for a given pressure. The proven concept

in this paper is limited to static loads, but the developed actuators can also compensate for vibrations. The hydraulic power unit can increase the pressure almost in real time, since small changes in volume are sufficient.

DATA AVAILABILITY STATEMENT

The original contributions presented in the study are included in the article/supplementary material, further inquiries can be directed to the corresponding author/s.

AUTHOR CONTRIBUTIONS

WS initiated the research project. TB and CK did the experimental testing under the guidance of WS, HB, and LB. The analytical approach was developed by CK. The numerical studies were done under the guidance of WS by CK. The first draft was written by TB and CK. All authors actively revised, reviewed, and approved the final submission.

FUNDING

The work described in this paper was conducted in the framework of the Collaborative Research Center 1244 Adaptive Skins and Structures for the Built Environment of Tomorrow/project C02 Integrated fluid-actuators funded by the German Research Foundation (DFG—Deutsche Forschungsgemeinschaft).

ACKNOWLEDGMENTS

The authors are grateful for the generous financial support and wish to express their gratitude therefor.

REFERENCES

- Berger, T., Patrick, P., and Hans Georg, R. (2013). Einsparung von grauer energie bei hochhäusern. *Beton Stahlbetonbau* 108, 395–403. doi: 10.1002/best.201300019
- Block, P., van Mele, T., Matthias, R., and Noelle, P. (2017). *Beyond Bending: Reimagining Compression Shells: DETAIL Special*. 1st Edn. Munich: Edition DETAIL.
- Curbach, M. (2013). Bauen für die zukunft. *Beton Stahlbetonbau* 108:751. doi: 10.1002/best.201390098
- DIN Deutsches Institut für Normung (2009). *Eurocode 1: Einwirkungen Auf Tragwerke – Teil 1-3: Allgemeine Einwirkungen, Schneelasten; Deutsche Fassung* (Berlin: Beuth Verlag GmbH).
- Domke, H. (1992). *Aktive Tragwerke*. Opladen: Westdeutscher Verlag.
- Domke, H., Backe, W., Meyr, H., Hirsch, G., and Goffin, H. (1981). Aktive verformungskontrolle von bauwerken. *Active deformation control of buildings. Bauingenieur* 56, 405–412.
- European Commission (2019). *Taking Action on the Total Impact of the Construction Sector.* level(s). unpublished manuscript. Available online at: [https://ec.europa.eu/environment/eussd/pdf/LEVEL\(S\)%20CONFERENCE%20REPORT.pdf](https://ec.europa.eu/environment/eussd/pdf/LEVEL(S)%20CONFERENCE%20REPORT.pdf) (accessed October 30, 2019).
- Gross, D., Werner, H., Schröder, J., Wall, W. A., and Javier, B. (2018). *Engineering Mechanics 2: Mechanics of Materials*. 2nd Edn. Berlin, Heidelberg: Springer Berlin Heidelberg.
- Janocha, H. (2004). *Actuators: Basics and Applications*. Berlin, Heidelberg: Springer.
- Kelleter, C., Timon, B., Hansgeorg, B., and Werner, S. (2018). “Actuation concepts for structural concrete elements under bending stress,” in *Proceedings of the 6th. European Conference on Computational Mechanics (Solids, Structures and Coupled Problems) ECCM 6*, edited by International Center for Numerical Methods in Engineering, eds. S.L. Huelva (Spain, Cornellà de Llobregat: Artes Gráficas Torres), 127–37. 9, 08940. Available online at: <http://www.eccm-ecfd2018.org/frontal/docs/Ebook-Glasgow-2018-ECCM-VI-ECFD-VII.pdf>
- Kelleter, C., Timon, B., Hansgeorg, B., and Werner, S. (2019). “Actuation of structural concrete elements under bending stress with integrated fluidic actuators,” in *Advances in Engineering Materials, Structures and Systems: Innovations, Mechanics and Applications: Proceedings of the 7th International Conference on Structural Engineering, Mechanics, and Computation (SEMC) 2019*, eds A. Zingoni (Boca Raton: CRC Press), 1005–1009.
- Milliman, J., and Syvitski, J. P. M. (1992). Geomorphic/tectonic control of sediment discharge to the ocean: the importance of small mountainous rivers. *J. Geol.* 100, 525–44. doi: 10.1086/629606
- Mises, R. V. (1945). On saint venant's principle. *Bull. Amer. Math. Soc.* 51, 555–563. doi: 10.1090/S0002-9904-1945-08394-3
- Mitchel, J. C. (2008). *The Concrete Conundrum. Chemistry World*, 62–68. Available online at: [https://www.rsc.org/images/Construction_tcm18-11\(4530\).pdf](https://www.rsc.org/images/Construction_tcm18-11(4530).pdf) (accessed August 27, 2019).
- Neuhäuser, S. (2014). *Untersuchungen zur homogenisierung von spannungsfeldern bei adaptiven schalentragwerken mittels auflagerverschiebung*. (Ph.D.

- Dissertation). Institut für Leichtbau Entwerfen, Konstruieren, Universität Stuttgart.
- Pacheco, P., André, A., Teresa, O., and Pedro, B. (2010). Automation robustness of scaffolding systems strengthened with organic prestressing. *Automat. Construct.* 19, 1–10. doi: 10.1016/j.autcon.2009.09.001
- Schlegl, F., Honold, C., Leistner, S., Albercht, S., Roth, D., Hasse, W., et al. (2019). Integration of LCA in the planning phases of adaptive buildings. *Sustainability* 11:4299. doi: 10.3390/su11164299
- Schnellenbach-Held, M., Daniel, S., Abdalla, F., and Oliver, K. (2014). Adaptive spannbetonstruktur mit lernfähigem fuzzy-regelungssystem. *Bauingenieur* 89, 57–66.
- Scrivener, K., Vanderley, J., and Ellis, G. (2016). Eco-efficient cements: potential economically viable solutions for a low-CO₂ cement-based materials industry. *Cement Concrete Res.* 114, 2–26. doi: 10.1016/j.cemconres.2018.03.015
- Senatore, G., Philippe, D., Pete, W., and Chris, W. (2018). Shape control and whole-life energy assessment of an 'Infinitely Stiff' prototype adaptive structure. *Smart Mater. Struct.* 27:1. doi: 10.1088/1361-665X/aa8cb8
- Senatore, G., Philippe, D., and Peter, W. (2019). Synthesis of minimum energy adaptive structures. *Struct. Multidisc Optim.* 60, 849–77. doi: 10.1007/s00158-019-02224-8
- Setareh, M., and Darvas, R. (2016). *Concrete Structures. 2nd Edn.* (Switzerland: Springer). doi: 10.1007/978-3-319-24115-9
- Sobek, W. (2016). Ultra-Lightweight construction. *Int. J. Space Struct.* 31, 74–80. doi: 10.1177/0266351116643246
- Sobek, W., Stefan, N., Walter, H., Oliver, S., and Martin, W. (2013). "Ultralightweight structures." in *Proceedings of IASS Annual Symposia* (Wrocław). 2013, 1–9.
- Steffen, S., Stefanie, W., Lucio, B., and Werner, S. (2020). Using influence matrices as a design and analysis tool for adaptive truss and beam structures. *Front. Built Environ.* 6, 1–12. doi: 10.3389/fbuil.2020.00083
- Teuffel, P. (2004). *Entwerfen adaptiver strukturen: lastpfadmanagement zur optimierung tragender leichtbaustrukturen.* (Ph.D. Dissertation). Institut für Leichtbau Entwerfen und Konstruieren, Universität Stuttgart.
- United Nations Environment Programme. (2014). "Sand, Rarer Than One Thinks: UNEP Global Environmental Alert Service. Available online at: [http://hdl.handle.net/20.500.11822/\(8665\)](http://hdl.handle.net/20.500.11822/(8665)) (accessed March 2014).
- Weidner, S., Simon, S., and Werner, S. (2019). The integration of adaptive elements into high-rise structures. *Int. J. High Rise Buildings* 8, 95–100. doi: 10.21022/IJHRB.2019.8.2.95
- Weidner, S., Christian, K., Paula, S., Walter, H., Florian, G., Timon, B., et al. (2018). The implementation of adaptive elements into an experimental high-rise building. *Steel Construct.* 11, 109–17. doi: 10.1002/stco.201810019
- Yao, J. T. P. (1972). Concept of structural control. *J. Struct. Division* 98, 1567–74.

Conflict of Interest: The authors declare that the research was conducted in the absence of any commercial or financial relationships that could be construed as a potential conflict of interest.

Copyright © 2020 Kelleter, Burghardt, Binz, Blandini and Sobek. This is an open-access article distributed under the terms of the Creative Commons Attribution License (CC BY). The use, distribution or reproduction in other forums is permitted, provided the original author(s) and the copyright owner(s) are credited and that the original publication in this journal is cited, in accordance with accepted academic practice. No use, distribution or reproduction is permitted which does not comply with these terms.



A Case Study on Design and Optimization of Adaptive Civil Structures

Florian Geiger*, Jan Gade, Malte von Scheven and Manfred Bischoff

Institute for Structural Mechanics, University of Stuttgart, Stuttgart, Germany

OPEN ACCESS

Edited by:

Gennaro Senatore,
École Polytechnique Fédérale de
Lausanne, Switzerland

Reviewed by:

M. Z. Naser,
Clemson University, United States
Izuru Takewaki,
Kyoto University, Japan

*Correspondence:

Florian Geiger
geiger@ibb.uni-stuttgart.de

Specialty section:

This article was submitted to
Computational Methods in Structural
Engineering,
a section of the journal
Frontiers in Built Environment

Received: 01 April 2020

Accepted: 26 May 2020

Published: 30 July 2020

Citation:

Geiger F, Gade J, von Scheven M and
Bischoff M (2020) A Case Study on
Design and Optimization of Adaptive
Civil Structures.
Front. Built Environ. 6:94.
doi: 10.3389/fbuil.2020.00094

Taking advantage of adaptivity in the field of civil engineering is a subject of ongoing research. Integration of adaptive elements in load-bearing structures is already well-established in many other engineering fields, albeit mostly for different purposes than withstanding predominantly static loads. Initial investigations have demonstrated potential for substantial material and energy savings also in the field of civil engineering, especially for high-rise buildings and wide-span structures, such as roofs or bridges. Adaptive civil structures show promise in tackling current challenges arising from emissions and shortages of materials. In this study, we compare the possible minimum-weight designs for different actuator placement approaches and for different structural topologies that satisfy various constraints for high-rise buildings. We use case studies as illustrative examples to show which advantages and disadvantages can be expected from a specific design. The overarching aim is to learn how truss and beam structures should be designed to perform well as adaptive structures.

Keywords: adaptive structures, structural optimization, integrative design approach, actuator modeling, adaptive truss, adaptive frame

1. INTRODUCTION

To tackle today's challenges arising from extensive material consumption, waste production, and emissions, innovative solutions are needed from the building industry. Nowadays, buildings are designed to withstand occurring loads and simultaneously satisfy defined conditions by using a large amount of material, leading to a large amount of emissions and waste. For most of a building's life span, some of this material is not needed, because extreme load conditions are not permanent. The incorporation of active elements in passive structures to make the structures adaptive offers a promising way of using material more efficiently. The resulting adaptive buildings therefore consist of passive elements, controllers, sensors, and actuators, which can influence the load-bearing and deformation behavior of the whole structure. The underlying idea is to significantly reduce embodied energy in built structures by avoiding the use of material that is necessary only in a small part of the building's life span to maintain, e.g., serviceability limits. The missing structural part is compensated for by using actuation energy, which affects the critical states that are assumed to overshoot defined limits. Preliminary investigations have demonstrated potential for significant material savings in the primary structure. In times of increasing demand for sand and other scarce raw materials, adaptive structures offer a very promising approach to more sustainable buildings.

However, compared to the design of passive structures, new challenges arise in the design of adaptive structures. Influences from architecture, structural engineering, mechanical engineering, and control engineering have to be integrated in order to design an optimal adaptive structure. To bring together specialists in all these different areas, the Collaborative Research Center SFB 1244, “Adaptive Skins and Structures for the Built Environment of Tomorrow,” was initiated in 2017 at the University of Stuttgart. Application of the design concepts in realistic scenarios and buildings is being researched and tested at the interdisciplinary Collaborative Research Center. A demonstrator high-rise will also be erected on the campus of the University of Stuttgart. Details are presented in Weidner et al. (2018). Apart from the aforementioned challenges in the design of the load-bearing structure, the research center conducts work on adaptive facades and adaptivity in the field of building physics.

The first designs to include active elements in civil structures were developed in the 1960s. Zuk and Clark (1970) presented the idea of an active tendon system for controlling static deformations and manipulating internal forces, which was the origin of much work on this topic. The early approaches focused on the control of vibrations in order to maintain defined limits of serviceability and safety (e.g., Soong and Manolis, 1987). Another research focus was deployable large-span space structures (e.g., Kwan and Pellegrino, 1993). Pertinent overviews can be found in Soong and Spencer (1992), Soong (1988), Utku (1998), and Korkmaz (2011).

In the present work, design and optimization of adaptive structures are addressed. Initial approaches to optimized adaptive structures were due to Kirsch and Moses (1977), who carried out an optimization for a given beam structure with fixed actuator position to determine the minimum cross-sectional dimensions. Optimization procedures involving simultaneous optimization of the controller and the structure were introduced by Hale et al. (1985). An overview of further optimization approaches can be found in Frecker (2003). Inspired by a separation of equilibrium and compatibility equations, introduced by Kirsch and Moses (1977), Teuffel (2004) proposed a workflow for designing ultra-light adaptive structures, additionally incorporating the problem of actuator placement in adaptive truss structures. This approach was adopted by Senatore et al. (2019) and extended to an “all in one” formulation of the design of adaptive structures which included whole-life energy assessment. Additional computational improvements were also obtained, and the results have been experimentally validated by Senatore et al. (2017). In contrast to the work of Senatore et al. (2019), the present article proposes not a workflow for designing minimum-energy adaptive structures, but rather a method for learning about fundamental properties of adaptive structures. The main goal of the method is to learn which types of structures are suitable, and especially, why. Therefore, some simplifications are needed (e.g., neglecting additional masses of actuators), which are stated in our assumptions and models, to be introduced in the appropriate sections. The problem of suitable actuator placement to achieve certain goals was addressed by Kawaguchi et al. (1996) and, from a system dynamics point of view recently, by Wagner et al.

(2018), among other authors. The influence of the design process of adaptive structures on adaptability, performance, and actuation energy demand was investigated by Geiger et al. (2020b) in a simple case study. Fröhlich et al. (2019) proposed a method for optimizing structures toward their efficiency, using a measure of the total energy demand as the objective function.

This paper’s focus is on incorporating adaptivity into the load-bearing structure, in order to manipulate structural behavior under different loading scenarios. Given a design task for a building, including, e.g., predefined overall dimensions and other structural constraints, finding the basic concept of the structure in terms of the topological layout of the structural members and the design of the load-bearing behavior is one of the most important tasks for the structural engineer. For conventional passive structures, layout and design strategies to produce structures that are efficient, reliable, redundant, cheap, etc., are well-known. With adaptive structures, however, building upon experience gained in the design of passive structures may lead to suboptimal results. Therefore, the aim of this research is to find design criteria and guidelines to determine whether the geometry and the topological layout of an optimal passive structure will lead to an optimal adaptive structure, and to identify how efficient adaptive structures can be characterized and designed. Preliminary studies can be found in Geiger et al. (2020a), which describes an approach to actuator placement using the redundancy matrix in a forward calculation without employing an optimization algorithm. Additionally, a proof-of-concept for the idea of transforming stiffness-governed structures into strength-governed structures is presented. The term stiffness-governed means that the stiffness of the structure against displacements is design decisive for the cross-section of structural members. It is shown that when adaptivity comes into play, this is not the case. This leads to the conclusion that the normal force and hence the maximum allowable stress of the used material is decisive for the cross-section of a bar, which is a characteristic of strength-governed problems. This transformation from stiffness-governed to strength-governed makes possible a more efficient utilization of the material and thus significant savings of material. The present work extends these basic studies, first to a systematic comparison of different assemblies in terms of topology for truss structures and then to an investigation of beam structures, in order to deduce new design guidelines.

The paper is structured as follows: In section 2 the methodology for the case study, basic assumptions, and details of the modeling are presented. Section 3 presents two different adaptive structures in various configurations. The overall mass-saving potentials are computed for the different layouts, and the design ideas deduced from them are discussed.

2. METHODOLOGY

In this section, the methodology of the case study is motivated, and the necessary actuator placement, structural and actuation models, and efficient solution process are presented.

2.1. Case Study

The aim of this research is to learn how to design adaptive structures. To derive design guidelines, a case study on different adaptive structures is conducted. The results are compared and the observations discussed with regard to insights gained into the characteristics of adaptive structures. This process requires objective measures that can be used to compare different adaptive structures and to determine which design is preferable. Comparison of adaptive structures gives rise to a new class of problems in the field of structural design, and new measures have to be defined. In the present approach, different variants of adaptive structures are compared using two values, which have to be calculated for all variants. To obtain comparable results, the outer dimensions of the variants are kept constant, and identical loading scenarios and structural constraints are used. The first measure is the mass-saving potential of the adaptive structure relative to the passive structure with the same topology but without actuation; each active element is treated as the corresponding passive element. The second measure is the total mass of the adaptive structure. We do not compare the whole-life energy demand of the structures, because this would require an additional quantification of the material saving vs. the energy saving, which would entail numerous additional assumptions, such as assumptions concerning the energy mix in the following years for different countries, and is thus beyond the scope of this study, which is dedicated to structural behavior and the corresponding potential of adaptation.

Firstly, for a given topology, the minimum-weight design of the structure without actuation is compared to the minimum-weight design of the same structure using actuators. These designs for the passive and the active structures are the solutions of two non-linear optimization problems, the formulation of which may be found in section 2.4.

Secondly, for given outer dimensions (e.g., height and width) and a given application of the adaptive structure (e.g., high-rise building), different topologies are compared to generate guidelines. The comparison makes use of insights from a structural mechanics point of view in conjunction with observations, comparing the computed results. In this process, the influence of known structural properties of the investigated topologies is examined. Among other factors, the degree of static indeterminacy is investigated. Therefore, starting from a basic configuration of an exemplary structure, different variants are generated by inserting or removing elements and/or supports. This generation process is motivated by the aim to verify or falsify hypotheses, which are presented and discussed.

2.2. Structural Model

The basic assumptions and modeling aspects are presented in this subsection. In the present investigation only structures consisting of truss and beam elements are considered, and only centric linear actuators are used, e.g., hydraulic cylinders in the center of a truss or beam element. To keep the computations as simple and fast as possible, small deformations and linear elastic isotropic material behavior are assumed. For a single element e , a linear elastic material model is chosen with Young's modulus E_e , tensile

strength $f_{y,e}$, mass density ρ_e , and Poisson's ratio ν_e . Dynamic effects are neglected in this case study. Under these assumptions, the discrete linear time-invariant equation of motion for the problem is given by

$$\mathbf{K}\mathbf{D} = \mathbf{F}. \quad (1)$$

The system stiffness matrix $\mathbf{K} \in \mathbb{R}^{n \times n}$ describes the correlation of load vectors gathered column-wise in a matrix $\mathbf{F} \in \mathbb{R}^{n \times l}$ and the solution vector gathered column-wise in a matrix $\mathbf{D} \in \mathbb{R}^{n \times l}$. The number of degrees of freedom in the model is represented by the variable n , and the number of load cases is represented by l . The load vector \mathbf{F} is the sum of the vector of external forces \mathbf{F}_{ext} , which collects the external forces for each degree of freedom, and the vector $\mathbf{F}_{\text{act}} = \mathbf{B}\mathbf{u}$, which contains the input matrix $\mathbf{B} \in \mathbb{R}^{n \times m}$ and the actuation input $\mathbf{u} \in \mathbb{R}^{m \times l}$. The number of actuators is represented by m . The load vector can therefore be expressed as a function of the actuation input, $\mathbf{F} = \mathbf{F}(\mathbf{u})$. The system stiffness matrix \mathbf{K} is assembled from all the element stiffness matrices, which depend on the cross-sections of the elements. Therefore, the system stiffness matrix is a function of the vector $\mathbf{a} \in \mathbb{R}^{n_{\text{le}}}$, which collects the cross-sectional areas of all elements, and of the vector \mathbf{i} , which collects the moments of inertia of all beam elements: $\mathbf{K} = \mathbf{K}(\mathbf{a}, \mathbf{i}) = \mathbf{K}(\mathbf{s})$. The vector of design variables relating to the cross-sections is defined as $\mathbf{s} := [\mathbf{a}, \mathbf{i}]^T$. The solution \mathbf{D} of Equation (1) gives the structural responses for all investigated load cases, which are used for further processing.

2.3. Actuator Model

For a proper and efficient simulation of the actuation, an active beam finite element is introduced, extending the active truss finite element presented in Geiger et al. (2020b). The aim is to apply a prescribed stroke u of an actuator directly, without further pre- and post-processing steps, for beam finite elements as well. **Figure 1** shows the element used. The derivation and particular modifications compared to the active truss are briefly discussed in the following. The starting point is the total potential energy functional Π^{tot} of a plane Bernoulli beam element, given by

$$\Pi^{\text{tot}}[d(x), w(x)] = \Pi^{\text{int}}[d(x), w(x)] + \Pi^{\text{ext}}[d(x), w(x)]. \quad (2)$$

The total potential energy consists of both internal and external potential energy and depends on the displacement fields in the axial direction $d(x)$ and the transverse direction $w(x)$. The element is in equilibrium if and only if the first variation of the total potential energy, $\delta \Pi^{\text{tot}}$, vanishes. The total potential energy functional has a minimum for these particular displacement fields. For the derivation we assume geometrically and materially linear behavior and that the displacement fields in the axial and transverse directions are decoupled. Therefore, the effects can be separated in the total potential energy functional:

$$\Pi^{\text{tot}}[d(x), w(x)] = \Pi^{\text{int},N}[d(x)] + \Pi^{\text{int},M}[w(x)] + \Pi^{\text{ext}}[d(x), w(x)]. \quad (3)$$

Quantities related to energy from axial forces in the beam, including all contributions from the actuation, are labeled with

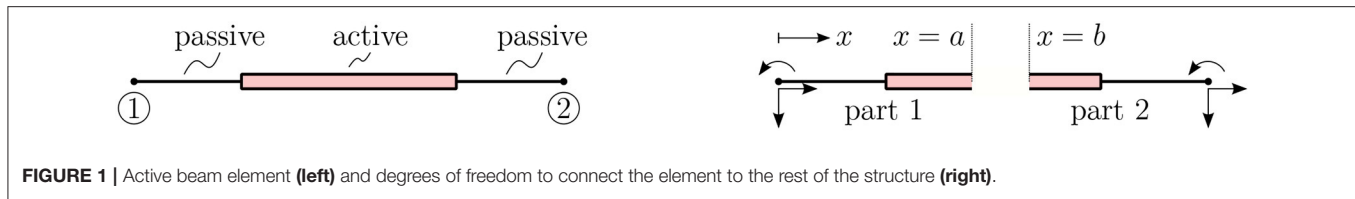


FIGURE 1 | Active beam element (left) and degrees of freedom to connect the element to the rest of the structure (right).

superscript N, and quantities related to bending energy are labeled with superscript M. Using this functional, the derivation simplifies to the separate derivation of the active truss element as shown in Geiger et al. (2020b) using the axial force part of the internal potential energy $\Pi^{\text{int},N}[d(x)]$. The actuation of the element is modeled as a discontinuity in the magnitude of the applied stroke u in the axial displacement field $d(x)$. In order to describe this jump, the element is cut into two parts, each part is modeled separately, and the connection is introduced by the additional coupling equation for displacements in the axial direction between points a and b ,

$$d(b) - d(a) = u, \quad (4)$$

as shown in **Figure 1**. Including the constraint equation by means of the Lagrangian multiplier λ yields the enhanced internal energy from axial forces:

$$\Pi^{\text{enh,int},N}[d(x), \lambda] = \Pi^{\text{int},N}[d(x)] + \lambda(d(b) - d(a) - u). \quad (5)$$

The Lagrangian functional yields

$$\begin{aligned} \mathcal{L}[d(x), w(x), \lambda] &= \Pi^{\text{enh,int},N}[d(x), \lambda] + \Pi^{\text{int},M}[w(x)] \\ &+ \Pi^{\text{ext}}[d(x), w(x)]. \end{aligned} \quad (6)$$

After applying the same procedure as in Geiger et al. (2020b), consisting of variation and discretization using linear ansatz functions, to the axial force part, the bending part $\Pi^{\text{int},M}[w(x)]$ can be treated separately, leading to the derivation of a passive beam element. No effects from the centric linear actuation have to be considered in this part. For further details on the derivation of the bending stiffness matrix, see e.g., Melosh (1963). For a single plane and a straight active beam element in horizontal orientation as shown in **Figure 1**, the derivation yields a linear system of equations at the element level:

$$\left(\begin{array}{cc} \tilde{\mathbf{k}}_N & \tilde{\mathbf{k}}_M \\ \left[\begin{array}{ccc} \mathbf{k}_{1,N} & \mathbf{0} & \mathbf{g}_{1,N}^T \\ \mathbf{0} & \mathbf{k}_{2,N} & \mathbf{g}_{2,N}^T \\ \mathbf{g}_{1,N} & \mathbf{g}_{2,N} & 0 \end{array} \right] & + \left[\begin{array}{ccc} \mathbf{k}_{1,M} & \mathbf{k}_{12,M}^T & \mathbf{0} \\ \mathbf{k}_{12,M} & \mathbf{k}_{2,M} & \mathbf{0} \\ \mathbf{0} & \mathbf{0} & 0 \end{array} \right] \end{array} \right) \begin{bmatrix} \mathbf{d}_1 \\ \mathbf{d}_2 \\ f_A \end{bmatrix} = \begin{bmatrix} \mathbf{f}_1 \\ \mathbf{f}_2 \\ u \end{bmatrix}. \quad (7)$$

Quantities for part 1 are labeled with subscript 1 and quantities for part 2 with subscript 2. The matrices $\mathbf{k}_{1,N}$ and $\mathbf{k}_{2,N}$ describe

the particular elastic axial stiffness matrices, and the vectors $\mathbf{g}_{1,N}$ and $\mathbf{g}_{2,N}$ are the corresponding coupling vectors. The matrices $\mathbf{k}_{1,M}$ and $\mathbf{k}_{2,M}$ describe the elastic bending stiffness matrices for the bending action and $\mathbf{k}_{12,M}$ the corresponding coupling matrix. Load and displacement vectors are separated into displacements of the two parts and the additional variables f_A and u . These parameters describe the discretized Lagrangian multiplier representing the actuator force f_A , which is therefore directly computed when solving the linear system of equations, and the applied stroke in the actuator u , respectively. It can be seen that there is a coupling of the bending part between the two separated element parts 1 and 2 introduced by the matrix $\mathbf{k}_{12,M}$. At the same position in the stiffness matrix for the axial part, there is no direct coupling. The coupling of the axial part is introduced by the additional condition and therefore by the vectors $\mathbf{g}_{1,N}$ and $\mathbf{g}_{2,N}$. The decoupling of axial force and bending within one element may not be seen in this representation. The element stiffness matrix $\tilde{\mathbf{k}}$ and the element load vector are used to assemble the global stiffness matrix \mathbf{K} and the global load vector \mathbf{F} . After assembly, the linear system of equations (1) can be solved for the global solution vector \mathbf{D} .

2.4. Structural Optimization

The minimum possible mass of the structure is computed by an optimization procedure using the total mass as the objective function and several non-linear constraints for displacements and stresses. Since we only look at plane examples, the feasibility of the stresses is evaluated at four particular positions of each element: at either end of the element at the upper and lower edges of the actual cross-section. To keep it simple, only nodal loads and no distributed loads are permitted, so that it is not necessary to check the stresses along the beam span. Additionally, each element in compression is checked for buckling. Therefore, Euler's critical buckling force $N_{b,e}$ is computed for the element's actual cross-section, and the absolute value of its normal force N_e may not exceed this value. Assumptions on the cross-sections are necessary to keep calculations simple and the number of design variables as small as possible. In the present paper, a square hollow section (SHS) is chosen, which can be described by only two independent variables, the cross-sectional area A and the moment of inertia I . The feasibility with maximum allowable displacements is checked at predefined degrees of freedom. The maximum displacement at those chosen degrees of freedom \mathbf{D}_c must not exceed the predefined limit.

2.4.1. Formulation of the Optimization Problem for the Passive Structure

The formulation of the resulting mass minimization problem for the passive structure reads

$$\begin{aligned}
 \min_{\mathbf{s}} \quad & m(\mathbf{a}) = \sum_{e=1}^{n_{\text{ele}}} l_e A_e \rho_e \\
 \text{subject to} \quad & \text{displacement constraint} \\
 & \|\mathbf{D}_c(\mathbf{s})\|_{\infty} \leq d_{\max} \\
 & \text{stress constraint} \\
 & \|\boldsymbol{\sigma}_e(\mathbf{s})\|_{\infty} \leq f_y \quad \forall e \\
 & \text{buckling constraint} \\
 & |N_e(\mathbf{s})| \leq N_{b,e}(\mathbf{s}) \quad \forall \{e \mid N_e(\mathbf{s}) < 0\}.
 \end{aligned} \quad (8)$$

2.4.2. Formulation of the Optimization Problem for the Active Structure

For the active structure, additionally the input strokes for the actuators is a design variable and part of the optimization. Therefore, the optimization problem reads

$$\begin{aligned}
 \min_{\mathbf{s}, \mathbf{u}} \quad & m(\mathbf{a}) = \sum_{e=1}^{n_{\text{ele}}} l_e A_e \rho_e \\
 \text{subject to} \quad & \text{displacement constraint} \\
 & \|\mathbf{D}_c(\mathbf{s}, \mathbf{u})\|_{\infty} \leq d_{\max} \\
 & \text{stress constraint} \\
 & \|\boldsymbol{\sigma}_e(\mathbf{s}, \mathbf{u})\|_{\infty} \leq f_y \quad \forall e \\
 & \text{buckling constraint} \\
 & |N_e(\mathbf{s}, \mathbf{u})| \leq N_b(\mathbf{s}) \quad \forall \{e \mid N_e(\mathbf{s}, \mathbf{u}) < 0\}.
 \end{aligned} \quad (9)$$

2.4.3. Solution Method for the Optimization Problems

To facilitate the simulation of several load cases in an efficient way, the solution procedure was implemented in MATLAB using vectorized solutions and post-processing. An SQP implementation available in MATLAB was chosen as the optimization algorithm, which requires the gradient and the Hessian of the objective function and of the constraint functions. The gradient of the objective function is calculated analytically and passed to the optimizer, and the gradient of the constraint functions is computed using a complex-step derivative approximation as in Squire and Trapp (1998), also vectorized for all design variables.

The attractive features of this type of numerical differentiation are briefly outlined in the following. The classical forward-difference formula for computing the first derivative of a function $f(x)$ reads

$$f'(x) = \frac{f(x+h) - f(x)}{h} + \mathcal{O}(h) \approx \frac{f(x+h) - f(x)}{h}. \quad (10)$$

Two errors occur in the approximation of the first derivative, namely the subtraction cancellation error, from taking the difference of two similar-valued numbers $f(x+h)$ and $f(x)$,

and the truncation error, from neglecting the $\mathcal{O}(h)$ part in the computation of the approximation. The step size has to be small enough to limit the truncation error but large enough to limit the error from subtraction cancellation, and it is not trivial to estimate the optimal compromise a priori. By using the complex-step derivative, the formula changes to

$$f'(x) = \frac{\text{Im}(f(x+ih))}{h} + \mathcal{O}(h^2) \approx \frac{\text{Im}(f(x+ih))}{h}. \quad (11)$$

This method does not suffer from the subtraction cancellation error, because no subtraction is needed. The truncation error is reduced significantly, because the truncated parts are of order $\mathcal{O}(h^2)$. In the following optimizations a step size of $h = 10^{-10}$ is used, so the truncation error can be neglected. For further reading, a derivation of the formula, and numerical examples, see Martins et al. (2003). The implementation in the MATLAB environment is not subject to major changes. Only computations of absolute values or transpositions that are suitable for complex-valued scalars, vectors, and matrices have to be implemented. The approximation of the Hessian is achieved by a Broyden-Fletcher-Goldfarb-Shanno (BFGS) algorithm; see Fletcher (2013). For future work, the Hessian can also be computed using complex numbers to achieve higher accuracy than the approximation and hence faster convergence of the optimization.

3. CASE STUDY AND DISCUSSION

The preliminary work of Geiger et al. (2020a) is used as a starting point for the formulation of hypotheses, which will be verified or falsified in two examples. Through this structured investigation, design guidelines are deduced. The preliminary work is extended to the comparison of different layouts for a truss structure in the first example and to the investigation of frame structures in the second example. In both examples, the mass savings achieved by adaptation and the minimized total masses are compared for several topological modifications of a basic structure exposed to the same load cases. Both constraints on maximum allowable stresses and constraints on maximum allowable displacements are met through active control. Failure of the actuators or of the control system is not considered in this case study.

The following assumptions hold for both examples. In all cases structural steel S235 with the following properties is chosen:

$$\begin{aligned}
 E &= 2.10 \cdot 10^8 \text{ kN/m}^2, \\
 f_y &= 2.35 \cdot 10^5 \text{ kN/m}^2, \\
 \rho &= 78.5 \text{ kN/m}^3, \\
 \nu &= 0.3.
 \end{aligned}$$

Square hollow sections with maximum outer dimensions of 0.50×0.50 m are used. The thickness of the walls is not limited until the box is fully filled with material, so the wall thickness is less than 0.25 m. The minimum outer edge length is fixed at 0.01 m, and the minimum wall thickness is defined as $1.0 \cdot 10^{-6}$ m. Penetration of material is prevented by a further constraint that requires twice the wall thickness to be less than or equal to the

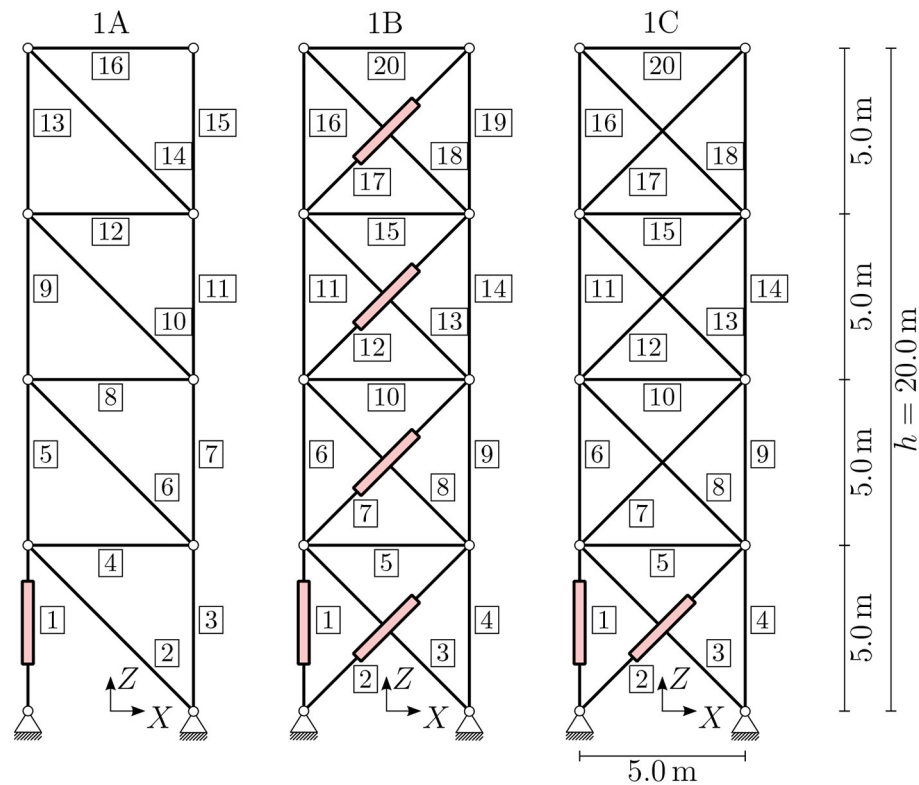


FIGURE 2 | Example 1, truss design: investigated variants with dimensions and actuator positions.

edge length. An element whose cross-section reaches the lower limit of the permissible range does not change the global results because of its low stiffness and low mass, but would regularize the stiffness matrix. Recall that the goal of the study is not to propose a directly buildable adaptive structure but to learn about adaptive structures. To keep things simple, the cross-section and the material model are assumed to be constant along the element axis in passive and in active elements. Additional masses of actuators are not considered here.

3.1. Example 1: Truss Design

As the first example, a structure is chosen that is inspired by high-rise buildings. The basic structure is shown in the left diagram of **Figure 2**. A similar structure was investigated by Geiger et al. (2020a). In a nutshell, their findings are that stiffness-governed design problems can be transformed into strength-governed design problems by manipulating the deformation state of the structure using active elements. This was also shown in Senatore et al. (2018), for example. For statically indeterminate structures, it is shown that the additional internal forces due to internal constraints, which arise from introducing a length change of an element as actuation, can be manipulated by additional actuators. If enough additional actuators are chosen, the reduction of the additional internal forces to zero is included in the design space but is not necessarily the optimal solution. This is also known as the introduction of “impotent eigenstrain”; see Furuhashi and Mura (1979). The results of the structural optimizations show

that the necessary amount of material for the primary structure can be reduced significantly. Mass-saving potentials of 65–70% are achievable by structural adaptation in such cases. Results of this magnitude were also reported by Senatore et al. (2019).

To obtain meaningful results for the mass-saving potential, three load cases are applied; these are shown in **Figure 3**. Two of the load cases (red and green) can be interpreted as wind loads with constant values of ± 15.0 kN/m in the X -direction along the height of the structure applied as nodal loads of ± 75.0 and ± 37.5 kN. The third load case (blue) is an additional load of -20.0 kN/m in the Z -direction on the horizontal floors, which results in nodal loads of 50 kN. All load cases are simulated separately. For simplicity, neither superposition nor safety factors are assumed. Additionally, the dead load of the members depending on the actual size of the cross-sectional area is considered in all load cases. For this example, horizontal deformations at all nodes, $\mathbf{D}_c = \mathbf{D}_{\text{horiz}}$, are constrained to a maximum absolute value of $d_{\text{max}} = h/500 = 20 \text{ m}/500 = 0.04 \text{ m}$, which is a reasonable assumption in high-rise design. Additional assumptions on, for example, inter-story drift or maximum accelerations are not considered here.

The first hypothesis arises from considering the essence of the design problem at hand. The resulting structure is subject to strict constraints on the allowable displacements, which are globally decisive for the dimensions of the cross-sections. Therefore, the aim of the actuation is efficient manipulation of the displacements. This implies the first hypothesis, H1, which is

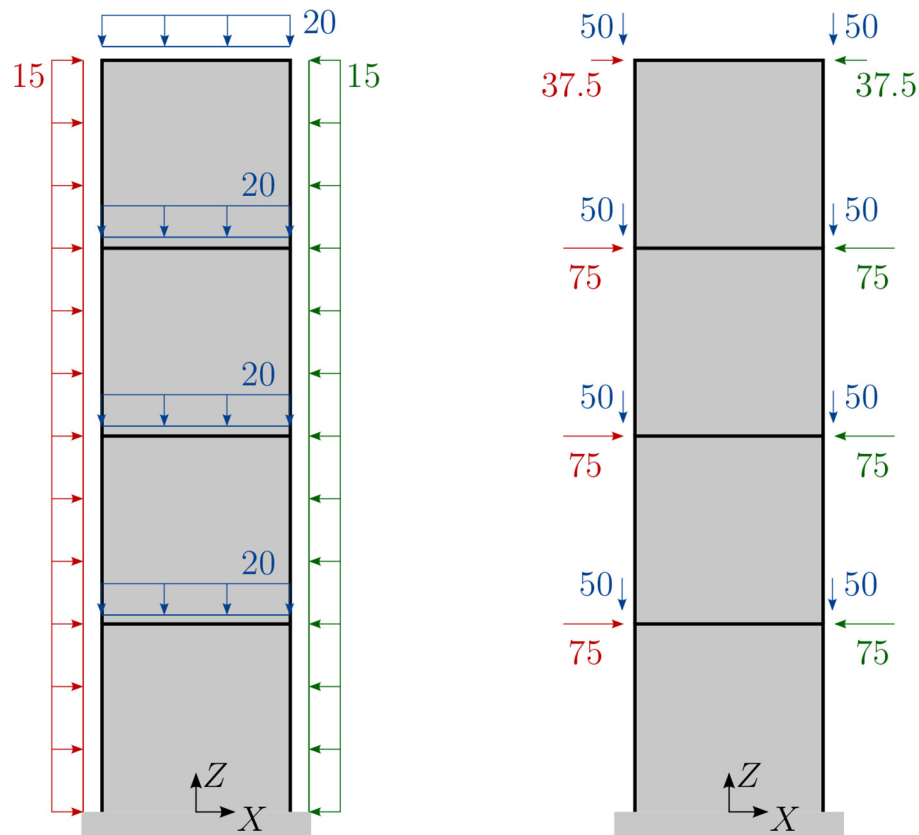


FIGURE 3 | Example 1, truss design: three investigated load cases (red, green, and blue), with line loads in kN/m and nodal forces in kN.

formulated as: “Statically determinate structures are advantageous compared to statically indeterminate one if an adaptive structure is used to solve a stiffness-governed design problem.” The second hypothesis applies when statically indeterminate structures are investigated. The question is whether it is sufficient to enable constraint-free manipulation of the displacements, or if additional actuators are needed to enable actuation of the stress state in the structure. Therefore, the second hypothesis, H2, is formulated as: “Implementing only as many actuators as necessary to enable constraint-free manipulation of the displacements performs worse than implementing n_s additional actuators to manipulate all forces arising from internal constraints.”

To test these hypotheses, several structures are compared. The basic structure, variant 1A, is shown in the left diagram of **Figure 2**. The figure also shows element numbers in rectangles. The truss structure is planar and consists of 16 single truss elements. Integrated actuators are shown in the figure. To determine actuator placement for the compensation of occurring deformations, methods from Wagner et al. (2018) are applied. A single actuator in element 1 is sufficient to restore about 95% of all deformations to the mean value for arbitrary load cases; therefore this actuator is chosen. As variant 1A is statically determinate, no additional

actuators are necessary to control internal forces arising from internal constraints.

Variant 1B is shown in the middle diagram of **Figure 2**. This variant incorporates additional diagonals into the basic structure to obtain a statically indeterminate structure. Following e.g., Senatore et al. (2019), for variant 1B with static indeterminacy of degree 4, a total of four additional actuators have to be implemented to manipulate all internal forces arising from internal constraints (cf. Pellegrino and Calladine, 1986). Therefore, variant 1B has a prescribed number of five actuators, placed as shown in **Figure 2** (middle). All additional elements are actuators. Variant 1C has the same topology as variant 1B but only one additional actuator to manipulate the internal forces arising from actuation. Additional information on actuator placement with the aim of compensating for introduced internal constraints can be found in Geiger et al. (2020a).

Results for the necessary mass of variant 1A in the passive state, displayed in **Figure 4** and **Table 1**, show that in order to deal with the constraints on the horizontal displacements, the stiffness of the statically determinate passive truss structure has to be very high. If the truss were simplified to a vertical cantilever beam, the moment of inertia of the cross-section at the basement would have to be large enough to keep the deformations small. Therefore, the cross-sectional areas

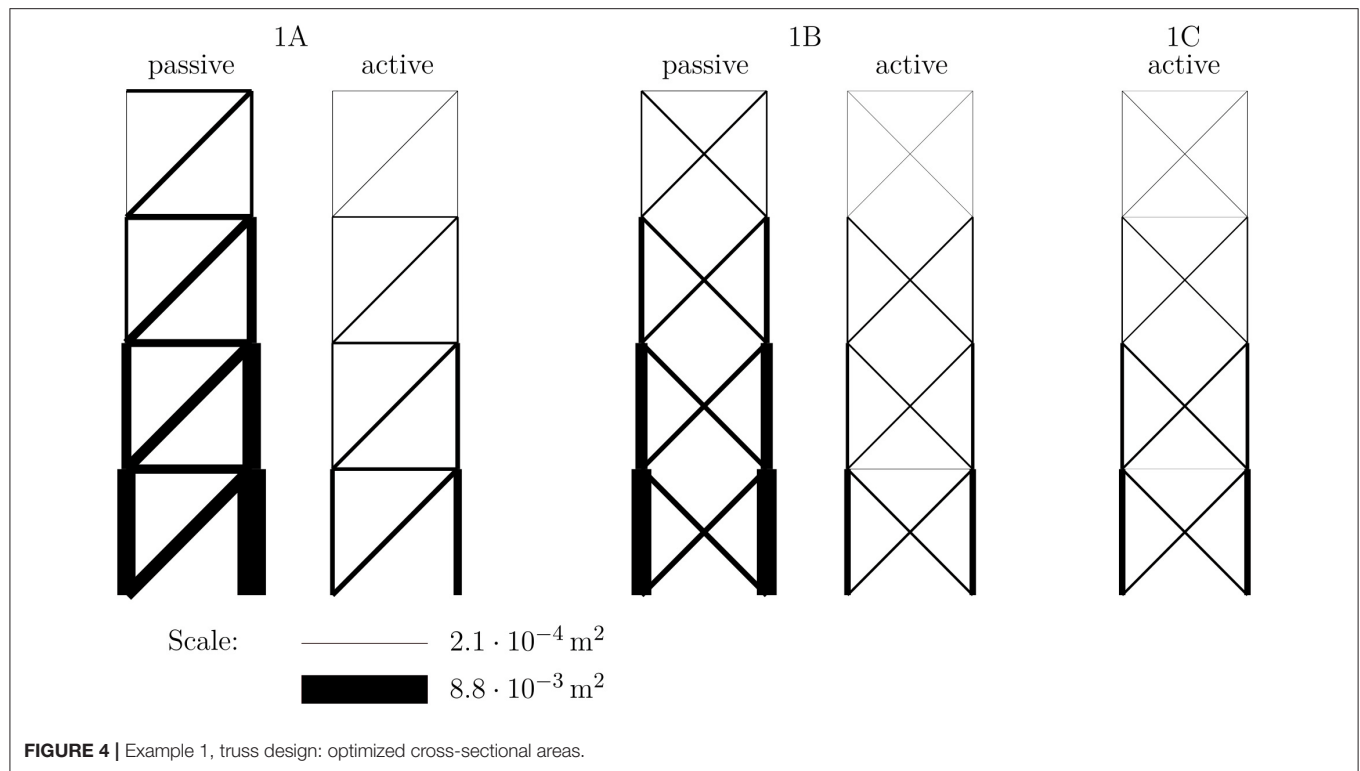


TABLE 1 | Example 1, truss design: total masses and mass-saving potentials (additional actuator mass not considered).

Variant	1A	1B	1C
m_{passive} (kg)	2,107	1,519	1,519
m_{active} (kg)	598	503	535
Mass-saving potential (%)	72	67	65

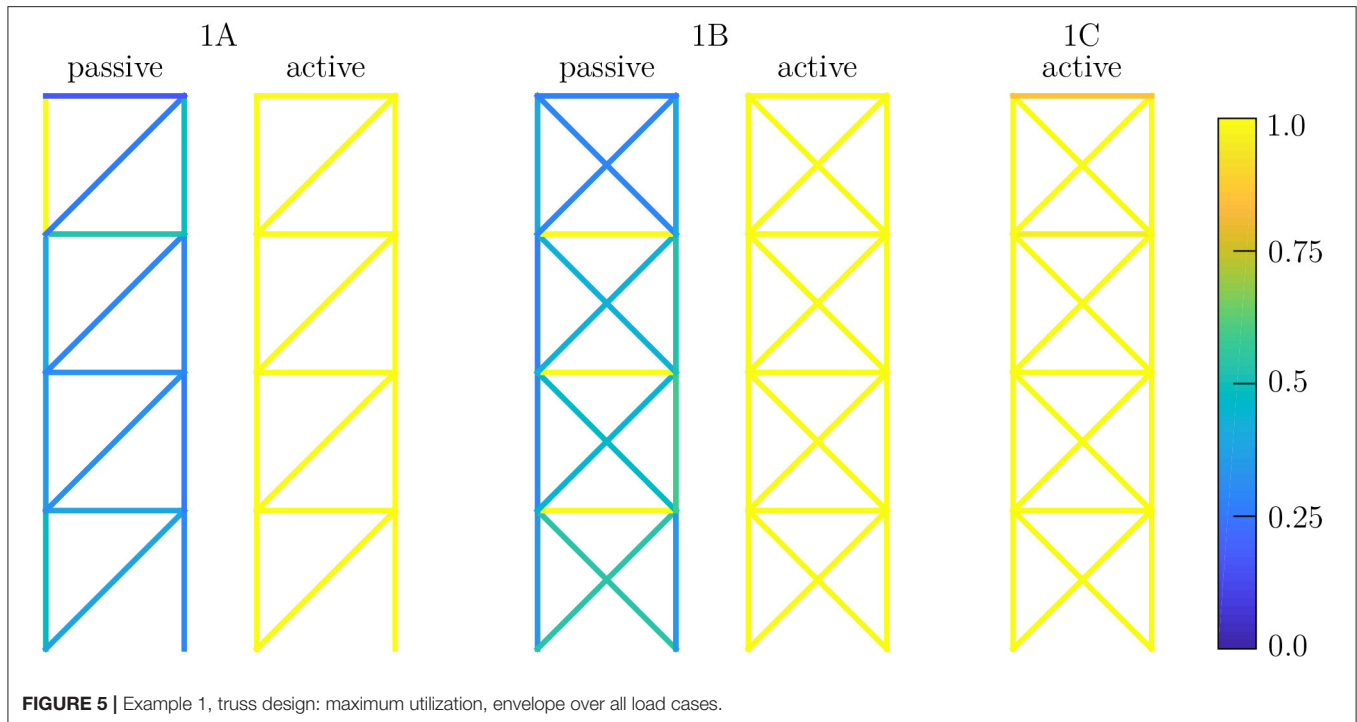
in the corresponding members are very large in the passive designs. **Figure 5** (1A passive) shows that it is not possible to exploit the maximum possible strength in all members. The amount of mass required is determined by the required axial stiffness.

The corresponding results for the adaptive structure 1A are shown in **Figure 4** (1A active) and **Table 1**. By incorporating the actuator in element 1, which can efficiently manipulate the horizontal displacements, it is now possible to satisfy the displacement constraints without large axial stiffness of the trusses. Therefore, the cross-sections can be utilized with their maximum strength capacity [see **Figure 5** (1A active)], and this comes with a significant reduction in cross-sectional areas and mass.

Analogous observations are obtained for variant 1B. In order to check the first hypothesis, the results for the variants are compared with each other. The mass-saving potential reduces from 72% for variant 1A to 67% for variant 1B, but the total minimum mass also decreases from 598 to 503 kg, or around 15% relative to variant 1A. It can therefore be concluded that in this case hypothesis H1 does not hold. The general validity

of this finding needs to be investigated in further work. Even though in both cases almost all elements are fully utilized in at least one load case, the statically indeterminate structure can carry the load to the supports using less material than the statically determinate variant. The intrinsically constraint-less actuation of the statically determinate case is not beneficial. Owing to actuation, the statically indeterminate structure also offers the possibility of constraint-free actuation. Additionally, several possible “load paths” are available to carry the load to the supports, and the manipulation of the internal constraint enables triggering of a normal force distribution that can be carried with less mass. This is not yet a universal design guideline, but it is a remarkable and somewhat counter-intuitive observation. Another notable observation is that for any actuator set, by using extra actuators starting from variant 1B no additional savings are possible. The complete actuation subspace is spanned by the chosen actuators, and any additional actuator is redundant.

Taking into account the results for variant 1C, it is found that the mass can be reduced by about 60 kg compared to variant 1A, but the minimum-weight design is not possible with only these two actuators. **Figure 5** (1C active) shows that not all members are utilized 100%. The mass can be reduced further by introducing additional actuators. Although actuation of element 1 can be constraint-free by a suitable action of the second actuator, the absolute mass minimum cannot be attained. To obtain the structure with the least amount of material, the state of internal forces also has to be manipulated by using additional actuators in statically indeterminate structures. This is in line with the findings from comparing the statically determinate case



1A, where member forces cannot be manipulated, with case 1B, where all of the internal constraints can be manipulated by adaptation. It can therefore be deduced that hypothesis H2 holds in this case.

Already for passive structures, the mass needed to cope with all constraints in all load cases can be reduced by 28% if the structure's degree of static indeterminacy is 4 instead of 0. Considering only a single load case without constraints on the displacements, the design with the least amount of mass would be statically determinate (see Kirsch, 1991). However, considering multiple load cases with constrained deformations, the additional internal constraint provides different "load paths" for carrying the external forces to the supports, and the extra stiffness introduced by the additional members is beneficial to meeting the constraints on the displacements.

3.2. Example 2, Frame Design

The second example through which we aim to investigate and learn the optimal design of adaptive structures is a frame structure with the same outer dimensions as the truss in Example 1. The applied nodal loads are taken from the previous example and shown in the right diagram of **Figure 3**. Bearing in mind that high-rise buildings are being considered, we adopt the commonplace assumption that distributed loads are transferred by a secondary structure, such as a facade, to the nodes, where they act as concentrated forces. The restrictions on horizontal deformations from the first example are also assumed to hold in the present example. Again a basic configuration, variant 2A, is defined, which is shown in the left diagram of **Figure 6**. The basic configuration in this case is statically indeterminate to degree 12.

The proof of stability for all beams is simplified on the safe side. For the computation of Euler's critical buckling load it is assumed that all beams are hinged at both ends and that the beam element with the smallest bending stiffness is decisive for the computation of the critical buckling load. The first assumption neglects the bending stiffness of the rigid joints; if all stiffnesses were correctly taken into account, the resistance of the beams against buckling would be higher. Therefore, the assumptions are on the safe side in this case. Regardless of these assumptions, the computations show that member buckling is not critical for design in the investigated cases. As mentioned before, no distributed loads are applied, so linearly varying bending moments are expected in the structure. To approximate a linearly varying cross-section along one beam, the beam is discretized using 10 beam finite elements of constant cross-section. Further improvements could be achieved by the introduction of e.g., linearly varying cross-sections or a finer discretization of the beam. In the following, the terms *beam element* and *element* specify a single finite element, and a *beam* connecting two loaded or supported nodes consists of 10 beam elements. **Figure 6** shows the positions of the actuators in varying beams of the frame structures. Since it suffices for only one element of a beam to be an active element, the exact position of the active element within one beam is not shown.

For frame structures, which are very typical for e.g., multi-story buildings, the degree of static indeterminacy is typically greater than for simple truss structures. The number of actuators needed to control all internal forces arising from constraints is significantly higher than for trusses. The assumption that only linear actuators in the central axis of an element are available is not suitable for frame structures, because, in contrast to truss structures, the degree of static indeterminacy

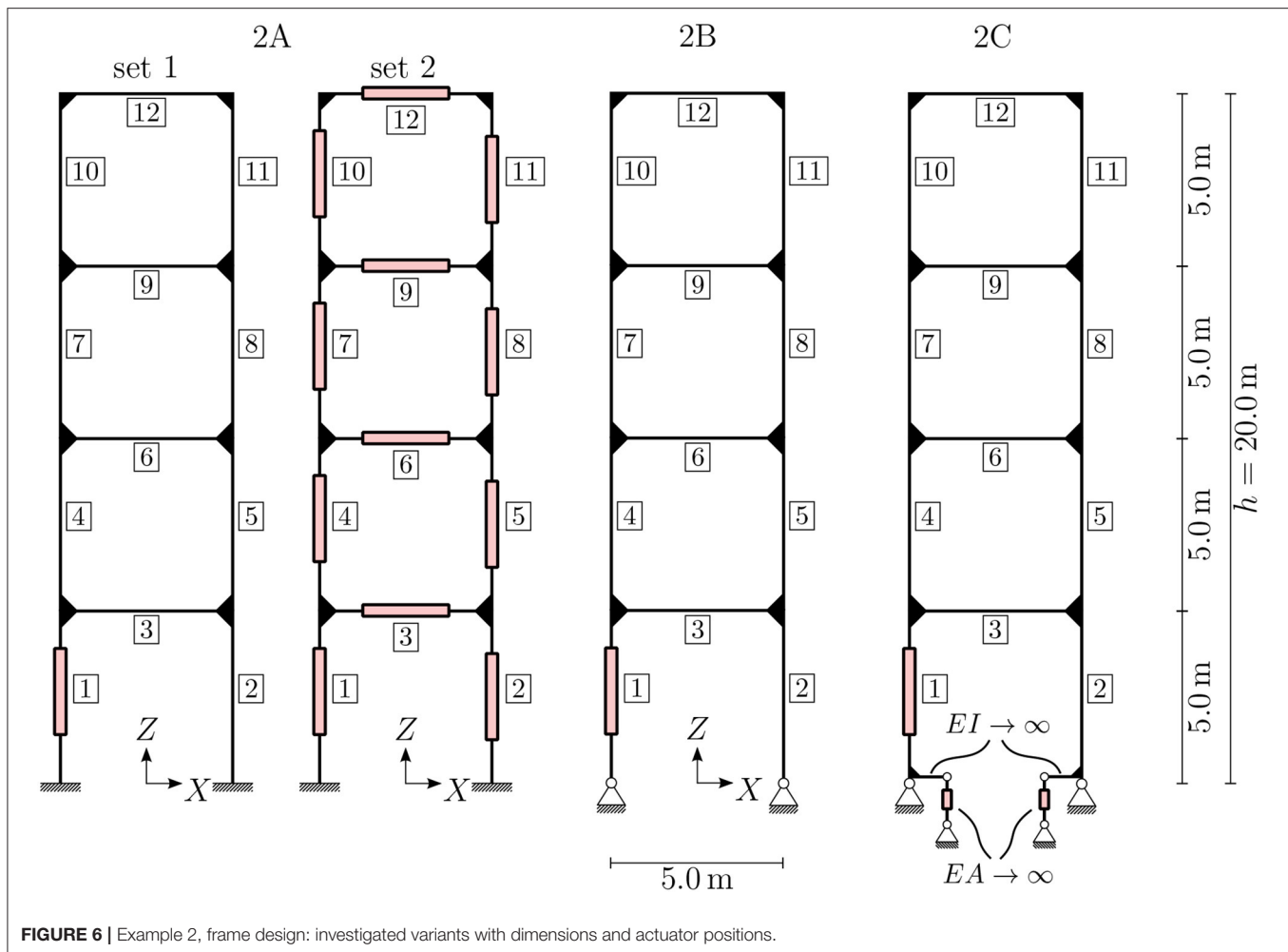


FIGURE 6 | Example 2, frame design: investigated variants with dimensions and actuator positions.

in frame structures can be greater than the number of elements. This leads to the hypothesis H3 for beam structures: “Actuation using only axial linear actuators is not sufficient to enable a well-performing adaptive frame structure. Direct manipulation of bending moments and transverse shear forces is necessary.”

In order to check this hypothesis, several variants of the structure are introduced. For the basic configuration, 2A, two actuator sets are compared. Set 1 has only one actuator, which can manipulate the displacements but will introduce additional internal forces due to internal constraints in the structure. Set 2 has a total of 12 actuators, one in each beam, to test whether it is possible to control the internal constraint completely. The setup of variant 2B is inspired by insights into load-bearing behavior from a structural mechanics point of view. The actuation of the structure can be constraint-free when using hinged supports, as shown in the middle diagram of **Figure 6**. The axial forces in both columns are statically determinate now, so there is no additional force arising from actuating one of these elements.

The resulting cross-sections from the optimization processes are shown in **Figure 7** (2A and 2B). Because of the missing clamping at the supports, and hence the missing stiffness for

preventing large deformations, the variant 2B performs worse in terms of the amount of material used, although the adaptation is constraint-free. As shown in **Table 2**, instead of 8,193 kg a total mass of 14,059 kg is needed to provide a functional passive building, and instead of 1,978 or 1,935 kg a new mass of 2,532 kg is needed for the adaptive structure. Relative to the passive structures, the mass-saving potentials of the adaptive structures are between 76 and 82%. This significant mass-saving potential can be traced back to the very inefficient load-bearing behavior of the passive construction. Horizontal deformation depends on the bending stiffness, which leads to an extensive need for material. Interestingly, the full actuation of the structure using set 2 does not yield significantly greater material savings.

To overcome this issue, adaptive clamping of the support is investigated. This can be represented in the model by starting with variant 2 and introducing two additional actuators at the bottom of elements 1 and 2; see the right diagram of **Figure 6**. These actuators can enable a constraint-free rotation of the beam at the support if they are controlled to introduce no actuation force. On the other hand, these actuators prevent (additional) rotation at the support if they are controlled to hold their actual stroke level. Therefore, variant 2C is an intermediate version

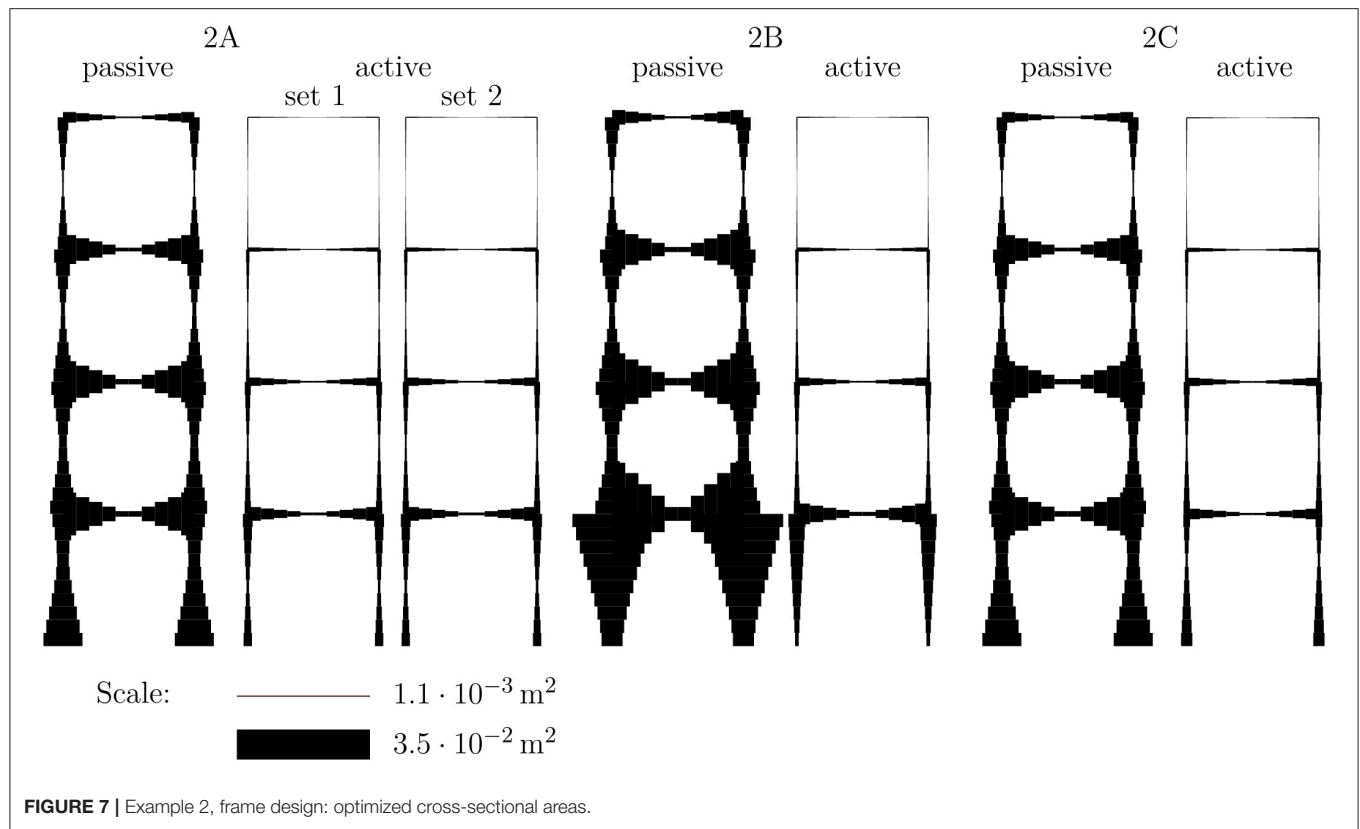


TABLE 2 | Example 2, frame design: total masses and mass-saving potentials (additional actuator mass not considered).

Variant	2A: set 1	2A: set 2	2B	2C
m_{passive} (kg)	8,193	8,193	14,059	8,193
m_{active} (kg)	1,978	1,935	2,532	1,883
Mass-saving potential (%)	76	76	82	77

between variants 2A and 2B. To preserve comparability of the results, the cross-section of these additional elements is taken to be very large compared to all the other elements and is assumed to be completely rigid. The mass of the additional elements is not considered, because the switchable clamping is part of the supporting structure, whose weight is also not considered in the other examples. Generally speaking, a clamping needs more mass than a hinged support.

The resulting structure after optimization of variant 2C is shown in the right diagram of **Figure 7**. The switchability of the clamping in the support offers the possibility of constraint-free manipulation of the displacements with the actuator in element 1, combined with the additional stiffness of the clamping. Therefore, this results in the adaptive structure having a total mass of 1,883 kg, which is 26% less than variant 2B and even 3% less than variant 2A. Even for a structure that is packed with active elements, such as variant 2A with actuator set 2, optimal performance in terms of mass-saving cannot be achieved. Actuators for direct manipulation of the bending

moments or transverse shear forces have to be introduced. The workaround we have introduced provides an easy way to model an actuator that can apply a bending moment at the support. It can be concluded that hypothesis H3 holds in this case.

4. CONCLUSIONS AND FURTHER WORK

New challenges arise in the design of adaptive structures compared to the design of passive structures. For classical passive structures, it is well-known how to lay out a structure so that it is efficient, reliable, redundant, cheap, etc. With adaptive elements coming into play, using intuition gained from the design of passive structures may lead to suboptimal results, because such intuition does not fully take into account the particular characteristics of adaptive structures. The two academic examples investigated in this study demonstrate the changes in the requirements, which are not necessarily obvious. The results represent an important step toward developing the needed design guidelines, although the process is still far from complete. The results presented in this paper can help to advance research into the optimal number and placement of actuators, while maintaining the reliability of the whole adaptive structure and, of course, controlling its cost. The results also highlight some opportunities that are opened up by the introduction of adaptive civil structures. Significant mass savings can be achieved, and serviceability can also be improved.

The results of this study provide new insights into the nascent field of designing adaptive structures. The first example investigates the incorporation of actuators into passive truss

structures, and the second example examines a similar procedure for frame structures. For both of the investigated structures, significant mass-saving potentials of more than 65% in the primary structure can be achieved by using actuators, compared to the passive version of the structure, under the given assumptions. The potential savings are greater for the frame structure than for the truss structure. These results apply to the utilization of adaptive structures in stiffness-governed design tasks. The examples look at only several different variants and do not yet provide a genuine process for designing an adaptive structure. More investigations have to be carried out in order to formulate a suitable design process. The aim would not be to design passive structures and make them adaptive afterwards, but rather to design adaptive structures in an integrative design process; this would be an important continuation of the present study to a more applicable setting.

For future work, the investigation of different actuation concepts for frame structures would be the most important extension of the present study. Therefore, non-linear actuation and elements for bending and shear actuation also need to be taken into account. The inclusion of non-linear effects for beam actuators represents the next challenge in the optimization of adaptive structures, because optimized adaptive structures are getting more and more slender and hence non-linearities have to be considered in the simulation process. Additionally, it is planned to extend these investigations to plates and shells.

REFERENCES

- Fletcher, R. (2013). *Practical Methods of Optimization*. Chichester: John Wiley & Sons, Ltd.
- Frecker, M. I. (2003). Recent advances in optimization of smart structures and actuators. *J. Intell. Mater. Syst. Struct.* 14, 207–216. doi: 10.1177/1045389X03031062
- Fröhlich, B., Gade, J., Geiger, F., Bischoff, M., and Eberhard, P. (2019). Geometric element parameterization and parametric model order reduction in finite element based shape optimization. *Comput. Mech.* 63, 853–868. doi: 10.1007/s00466-018-1626-1
- Furuhashi, R., and Mura, T. (1979). On the equivalent inclusion method and impotent eigenstrains. *J. Elast.* 9, 263–270. doi: 10.1007/BF00041098
- Geiger, F., Gade, J., von Scheven, M., and Bischoff, M. (2020a). “Anwendung der Redundanzmatrix bei der Bewertung adaptiver Strukturen [Application of the redundancy matrix in the assessment of adaptive structures],” in *Baustatik-Baupraxis*, eds B. Oesterle, M. von Scheven, and M. Bischoff, Vol. 14 (Stuttgart: Institute for Structural Mechanics, University of Stuttgart), 119–128.
- Geiger, F., Gade, J., von Scheven, M., and Bischoff, M. (2020b). *Optimal Design of Adaptive Structures vs. Optimal Adaption of Structural Design*. Berlin: IFAC-PapersOnLine.
- Hale, A. L., Lisowski, R. J., and Dahl, W. E. (1985). Optimal simultaneous structural and control design of maneuvering flexible spacecraft. *J. Guid. Control Dyn.* 8, 86–93. doi: 10.2514/3.19939
- Kawaguchi, K.-I., Hangai, Y., Pellegrino, S., and Furuya, H. (1996). Shape and stress control analysis of prestressed truss structures. *J. Reinf. Plast. Compos.* 15, 1226–1236. doi: 10.1177/073168449601501204
- Kirsch, U. (1991). Optimal design of structural control systems. *Eng. Optim.* 17, 141–155. doi: 10.1080/03052159108941066
- Kirsch, U., and Moses, F. (1977). Optimization of structures with control forces and displacements. *Eng. Optim.* 3, 37–44. doi: 10.1080/03052157708902375
- Korkmaz, S. (2011). A review of active structural control: challenges for engineering informatics. *Comput. Struct.* 89, 2113–2132. doi: 10.1016/j.compstruc.2011.07.010
- Kwan, A., and Pellegrino, S. (1993). Prestressing a space structure. *AIAA J.* 31, 1961–1963. doi: 10.2514/3.11876
- Martins, J. R. R. A., Sturdza, P., and Alonso, J. J. (2003). The complex-step derivative approximation. *ACM Trans. Math. Softw.* 29, 245–262. doi: 10.1145/838250.838251
- Melosh, R. J. (1963). Basis for derivation of matrices for the direct stiffness method. *AIAA J.* 1, 1631–1637. doi: 10.2514/3.1869
- Pellegrino, S., and Calladine, C. (1986). Matrix analysis of statically and kinematically indeterminate frameworks. *Int. J. Solids Struct.* 22, 409–428. doi: 10.1016/0020-7683(86)90014-4
- Senatore, G., Duffour, P., and Winslow, P. (2018). Energy and cost assessment of adaptive structures: case studies. *J. Struct. Eng.* 144:04018107. doi: 10.1061/(ASCE)ST.1943-541X.0002075
- Senatore, G., Duffour, P., and Winslow, P. (2019). Synthesis of minimum energy adaptive structures. *Struct. Multidiscipl. Optim.* 60, 849–877. doi: 10.1007/s00158-019-02224-8
- Senatore, G., Duffour, P., Winslow, P., and Wise, C. (2017). Shape control and whole-life energy assessment of an ‘infinitely stiff’ prototype adaptive structure. *Smart Mater. Struct.* 27:015022. doi: 10.1088/1361-665X/aa8cb8
- Soong, T. (1988). State-of-the-art review: active structural control in civil engineering. *Eng. Struct.* 10, 74–84. doi: 10.1016/0141-0296(88)90033-8
- Soong, T. T., and Manolis, G. D. (1987). Active structures. *J. Struct. Eng.* 113, 2290–2302. doi: 10.1061/(ASCE)0733-9445(1987)113:11(2290)
- Soong, T. T., and Spencer, B. F. (1992). Active structural control theory and practice. *J. Eng. Mech.* 118, 1282–1285. doi: 10.1061/(ASCE)0733-9399(1992)118:6(1282)

DATA AVAILABILITY STATEMENT

All datasets generated for this study are included in the article/supplementary material.

AUTHOR CONTRIBUTIONS

This research was initiated and globally supervised by MB. FG and JG developed the modeling, design strategies, and formulation, as well as executed the optimization processes together. FG contributed the selection and evaluation of the case study. The modeling and the case study were supervised by MB. MS supervised the optimization part. The first draft of the paper was written by FG. All authors actively revised, reviewed, and approved the final submission.

FUNDING

The work described in this paper was conducted in the framework of the Collaborative Research Center 1244 Adaptive Skins and Structures for the Built Environment of Tomorrow, within the projects A04 Form finding, structural optimization, and system optimization and B01 Characterization, modeling, and model order reduction, funded by the Deutsche Forschungsgemeinschaft (DFG, German Research Foundation) under project number 279064222. The authors were grateful for the generous support.

- Squire, W., and Trapp, G. (1998). Using complex variables to estimate derivatives of real functions. *SIAM Rev.* 40, 110–112. doi: 10.1137/S003614459631241X
- Teuffel, P. (2004). *Entwerfen Adaptiver Strukturen* (Ph.D. thesis). Stuttgart: Universität Stuttgart.
- Utku, Ş. (1998). *Theory of Adaptive Structures: Incorporating Intelligence Into Engineered Products. New Directions in Civil Engineering*. Boca Raton, FL: CRC Press.
- Wagner, J. L., Gade, J., Heidingsfeld, M., Geiger, F., von Scheven, M., Böhm, M., et al. (2018). On steady-state disturbance compensability for actuator placement in adaptive structures. *At Automatisierungstech.* 66, 591–603. doi: 10.1515/auto-2017-0099
- Weidner, S., Kelleter, C., Sternberg, P., Haase, W., Geiger, F., Burghardt, T., et al. (2018). The implementation of adaptive elements into an experimental high-rise building. *Steel Constr.* 11, 109–117. doi: 10.1002/stco.201810019
- Zuk, W., and Clark, R. H. (1970). *Kinetic Architecture*. New York, NY: Van Nostrand Reinhold.

Conflict of Interest: The authors declare that the research was conducted in the absence of any commercial or financial relationships that could be construed as a potential conflict of interest.

Copyright © 2020 Geiger, Gade, von Scheven and Bischoff. This is an open-access article distributed under the terms of the Creative Commons Attribution License (CC BY). The use, distribution or reproduction in other forums is permitted, provided the original author(s) and the copyright owner(s) are credited and that the original publication in this journal is cited, in accordance with accepted academic practice. No use, distribution or reproduction is permitted which does not comply with these terms.



Optimal Static Load Compensation With Fault Tolerance in Nonlinear Adaptive Structures Under Input and State Constraints

Julia L. Wagner*, Andreas Gienger, Charlotte Stein, Philipp Arnold, Cristina Tarin, Oliver Sawodny and Michael Böhm

Institute for System Dynamics, University of Stuttgart, Stuttgart, Germany

OPEN ACCESS

Edited by:

Gennaro Senatore,
École Polytechnique Fédérale de
Lausanne, Switzerland

Reviewed by:

Filippo Ubertini,
University of Perugia, Italy
Baki Ozturk,
Hacettepe University, Turkey

*Correspondence:

Julia L. Wagner
wagner@isis.uni-stuttgart.de

Specialty section:

This article was submitted to
Structural Sensing,
a section of the journal
Frontiers in Built Environment

Received: 28 February 2020

Accepted: 26 May 2020

Published: 15 September 2020

Citation:

Wagner JL, Gienger A, Stein C,
Arnold P, Tarin C, Sawodny O and
Böhm M (2020) Optimal Static Load
Compensation With Fault Tolerance in
Nonlinear Adaptive Structures Under
Input and State Constraints.
Front. Built Environ. 6:93.
doi: 10.3389/fbuil.2020.00093

Adaptive structures are conventional truss structures that are equipped with sensors, actuators, and a control unit. This offers the opportunity of reacting and adapting to external loads but raises nontrivial issues. When actuators are placed optimally within a structure, they can be individually integrated either parallel to or in series with elements of the original passive structure. Additionally, some of the elements might be tension-only elements and thus have to be treated as nonlinear, as their stiffness depends on the stress within the element itself. Input constraints naturally arise for actuators, e.g., due to the maximum pressure limit of a hydraulic system and displacement limits of the actuators. We present modeling approaches for an add-on inclusion of these different types of actuators in an existing finite-element model of a passive structure. We place special focus on the ability of the model to reproduce the correct behavior in case of an actuator reaching its displacement constraint within a tension-only element. When such an adaptive structure is subject to static loads, e.g., wind loads, it is required to respond using its actuators to keep the structure within given safety and comfort limits. These limits can be expressed as state constraints. We present a method for optimally compensating these static loads under the given input and state constraints along with experimental results on a scale model of an actual high-rise building. An important aspect regarding adaptive structures is that of their behavior in case of actuator faults. An obvious result is that a structure's performance degrades, and the controller needs to recognize faults and deal with it properly. Assuming a diagnosed actuator fault, we present results illustrating the performance degradation. The designed controller can reconfigure and reinitialize itself. The performance with and without applied reconfiguration to the nominal case is compared.

Keywords: adaptive structures, tension-only elements, static load compensation, fault tolerant control, optimal control, input/state constraints

1. INTRODUCTION

Lightweight structures are a reality for many mass-sensitive applications, such as large civil engineering structures. In the most cases, the designs of passive structures present a minimum in terms of required mass under given safety limitations and user comfort constraints. However, it is possible to stay within these limits while further reducing the total embodied mass significantly by introducing active structures, which is referred to as ultra-lightweight design. Through their various actuators, these structures can react and adapt to external loads and disturbances – both static and dynamic. This is done in order to minimize element stresses and at the same time maximize lifetime expectancy. Even lighter designs are possible compared to passive lightweight structures. In light of the expected construction activities within the next 20–30 years (OECD, 2015), and in line with the ongoing population growth as estimated by the UN (Department of Economic and Social Affairs), the world-wide trend of urbanization will further increase in pace, as projected by the UN (Department of Economic and Social Affairs). Ultra-lightweight designs can thus help save millions of tons of concrete and steel and significantly reduce waste production and CO₂-emissions of the construction industry.

One of the first research results on adaptive engineering structures was published by Yao (1972). Just a few years later, Kirsch and Moses (1977) proposed an active control strategy for a single beam subject to several single loads, but their findings strongly supported the idea of increased loading capacity or reduced cross section dimensions through the use of mechanisms for active compensation. Since then, the field has evolved, but it has nevertheless remained a rather small community, as it requires an interdisciplinary approach bringing together civil and control engineering. Recent overviews about structural control, including several passive, semi-active, and active approaches, have been provided by Korkmaz (2011), Housner et al. (1997), and Spencer and Nagarajaiah (2003). Most of the literature focuses on dynamic problems, i.e., active vibration control for damping oscillations. For example, Gawronski (2004) and Preumont (1997) use model-based approaches for the control design. Literature on the compensation of static loads by active structures is problem specific. A broad overview of current developments in structural control in Europe can be found in Basu et al. (2014), who give several case studies. Case studies that focus on energy and cost assessment of adaptive structures are presented in Senatore et al. (2018a). Insight into an approach for influence matrices is given in Reksowardojo and Senatore (2020), where the integrated force method is compared with a force method based on singular value decomposition.

From a practical point of view, the literature on active vibration control is manifold. Different aspects have to be taken into account such as input constraints due to actuator size, force limitations, as well as state constraints due to the need for keeping inhabitants comfortable. The authors of Johnson and Erkus (2002) present a semi-active optimal control approach for a structural control problem, for which the semi-active damping device is modeled by input constraints. Active vibration

control with active mass dampers of seismically excited multi-story building is done by Materazzi and Ubertini (2012). To incorporate input constraints in the proposed linear quadratic regulator (LQR), the problem is augmented, introduction of a virtual unsaturated input and a nonlinear map between augmented state and virtual input. For this system, the state-dependent Riccati equation is solved. A backstepping approach to control seismic motion of structures was proposed by Amini and Ghaderi (2013). This approach guarantees the limitation of control forces while at the same time improving closed loop system performance. The algorithm is illustrated on a three-story building.

There are tensegrity structures that can be associated, to a certain extent, with the structure considered in this contribution. Adam and Smith (2008) designed a multi-objective shape controller that selects a pareto optimum based on the applied load and is additionally improved by reinforcement learning. This approach is validated on an experimental setup of a tensegrity structure covering 15 m². Fest et al. (2003) specifically included geometric nonlinearities in their modeling approach of an active tensegrity structure and applied a stochastic search algorithm to determine the control inputs. In comparison to pure tensegrity structures, we consider a structure that is stiffened by tension-only diagonal bracings that are barely prestressed and therefore buckle under compression, which has been studied for tensegrities by Alart et al. (2007). Nevertheless, our structure also incorporates beam elements that bear tension, compression, and even bending and torsion, many strategies that work for tensegrities cannot thus be simply applied here.

Sobek and Teuffel (2001) proposed a method for static control of structures by minimizing element forces or displacements in a simple optimization without consideration of input or state constraints. In this paper, adaptivity is considered during the design process already, which eventually leads to a more sustainable structure. More recently, Neuhäuser et al. (2013) and Neuhäuser (2014) showed static load compensation for a double-curved shell in order to minimize peak stresses in the structure. Experimental validation is also given. Senatore et al. (2019) introduced a methodology for optimal design of adaptive structures while minimizing the whole-life energy consumption by regarding embodied energy and operational energy needed during operation to perform any necessary adaption. Their approach has been experimentally validated with an adaptive truss prototype, see Senatore et al. (2018b).

Static shape control is performed for two- and three-dimensional bodies such as beams, shells, or plates. For example, Irschik and Ziegler (2001) and Irschik et al. (2000) conducted static shape control by performing an eigenstrain analysis to determine the control forces that can compensate the quasi-static deflection of the body through external forces. Piezoelectric actuators are used to manipulate the body's stress distribution. The analysis and design are based on distributed parameters theory and thus cannot simply be transferred to our discretized finite element (FE) model. The authors of this publication have, however, also studied this aspect and Wagner et al. (2019b) presented an example for static load compensation on a beam modeled by a distributed parameters system.

The application of adaptive structures and static control is a wide field in aerospace engineering, regarding satellites with positioning of measurement equipment or wings of airplanes to adapt for wind flows. Sener et al. (1994) focused on statically indeterminate structures and investigated static control and actuator placement. As noted by Pellegrino (1990), it is important to separate between statically determinate and indeterminate structures because the number of independent force states in a structure is—as mentioned by Wagner et al. (2018)—coupled to the static indeterminacy. Sener et al. (1994) aimed at enlarging the stress in a structure. Therefore, the authors mainly work with statically indeterminate and prestressed structures. Several examples are given for illustration. For large space structures, Matunaga and Onoda (1995) presented a control law for optimal shape control with respect to modeling errors for elements and actuator forces. They further performed actuator placement by means of an integer optimization problem, where they specifically included several actuator failure cases in the optimization to increase the fault tolerance of the entire structure. This is highly relevant for space applications due to the limited maintenance options. A different approach of actuation was taken by Haftka and Adelman (1985), who used nonuniform heating to control deformation of adaptive structures governed by continuous or discrete equations. Saggere and Kota (1999) regarded an airplane wing as a smart structure, where principles of mechanics and kinematics are coupled with an optimization program to achieve smooth shape changes using a single actuator.

Previous works of our group have considered the problem of actuator placement for structures under static loads (e.g., Wagner et al., 2018; Böhm et al., 2019) and under dynamic loads (e.g., Heidingsfeld et al., 2017), as well as dynamic modeling and nonlinear damping control of structures with tension-only elements (e.g., Wagner et al., 2019a) and enhanced with decentralized control (e.g., Wagner et al., 2020). Böhm et al. (2020) focus on modeling and successful integration of different types of actuation principles into existing FE-models of passive structures. A relation is derived between actuators included in series and in parallel. First results on fault-tolerant control for active shape control of a double-curved shell were given by Heidingsfeld et al. (2015), where faults in actuators were treated as additional constraints in the optimization to derive the input signals. Recent results on fault detection and diagnosis were published by Gienger et al. (2020), and convolutional neural networks were used on the various input and sensor signals to detect and isolate actuator and sensor faults.

This article contributes to the modeling and control of adaptive structures with tension-only elements where some of these are equipped with serially integrated actuators, which renders the equations more complex and naturally leads to input constraints. More specifically, the main contribution of this article is the derivation and validation of a load compensation method based on numerical minimization of deformations due to static loads that particularly includes input and state constraints. Validation of the proposed algorithms is performed on an experimental setup with 25 actuators evaluating element forces and position measurements of the structure. Proving the real world applicability of the strategy, a 1:18 scale model is used.

Finally, the potential to rerun the optimization with a reduced set of actuators is demonstrated, which enhances the fault-tolerance of adaptive structures.

The article is organized as follows: Section 2 introduces the nonlinear modeling including tension-only elements for a given structure. Additionally, inputs and outputs are modeled. In section 3, the optimal control strategy is introduced to conduct static load compensation and the treatment of faults in actuators. Experimental and numerical results are illustrated and discussed in section 4. Finally, a conclusion and outlook are given.

2. SYSTEM MODELING

This section derives the nonlinear, stationary model equations of an adaptive high-rise structure. These serve as the basis for the following optimal load compensation. For the sake of completion, first, a linear system model is introduced, on top of which nonlinear structural elements are incorporated.

2.1. Linear Equations of Motion

Assuming stationary conditions, the physical states of a stationary civil engineering structure are computed by means of the finite element method (FEM). The vector $\mathbf{q} \in \mathbb{R}^n$ denotes the nodal degrees of freedom (DOF) in translational and rotational directions and is also called state of the system. In particular these modeling equations are represented by

$$\mathbf{K}\mathbf{q} = \mathbf{f}(\mathbf{u}) \quad \text{with} \quad \mathbf{f}(\mathbf{u}) = \mathbf{F}\mathbf{u} + \mathbf{E}\mathbf{z}, \quad \mathbf{y} = \mathbf{C}\mathbf{q}, \quad (1)$$

where $\mathbf{K} \in \mathbb{R}^{n \times n}$ is the stiffness matrix, and $\mathbf{f}(\mathbf{u})$ comprises actuator forces $\mathbf{u} \in \mathbb{R}^m$ and disturbances $\mathbf{z} \in \mathbb{R}^k$. The input matrix $\mathbf{F} \in \mathbb{R}^{n \times m}$ describes the actuator topology for m active elements. The disturbance matrix $\mathbf{E} \in \mathbb{R}^{n \times k}$ represents stationary external loads, for example, snow loads or static wind loads. Each column of this matrix, each contains the distribution of external forces over all degrees of freedom for a single load case. The overall external load is given as a linear combination of these individual disturbance vectors with the respective amplitudes defined in \mathbf{z} . The system's output $\mathbf{y} \in \mathbb{R}^l$ captures measurement values and can be calculated by means of the output matrix $\mathbf{C} \in \mathbb{R}^{l \times n}$ and the systems state.

2.2. Nonlinear Equations of Motion

In practice, structures may not be accurately represented by the linear system model (1). Common nonlinear structural elements are bracings, which serve the purpose of stiffening an entire structure. For example, a cable or flat steel both introduce nonlinearities because these elements can only bear tension forces and therefore slacken under compression. This effect leads to a state dependent stiffness matrix $\mathbf{K}(\mathbf{q})$. In the case of a compressed nonlinear bracing element, the corresponding entry k_i of the stiffness matrix does not contribute to the structure's stiffness:

$$k_i(\mathbf{q}) = \begin{cases} k_i, & \Delta l_i(\mathbf{q}) \geq 0 \\ 0, & \Delta l_i(\mathbf{q}) < 0 \end{cases} \quad i = 1, \dots, n_t. \quad (2)$$

The total amount tension-only elements is denoted by n_t . The switching condition between tension and compression depends on the length difference of an element

$$\Delta l_i(q) = \sqrt{\Delta \tilde{q}_i^T \Delta \tilde{q}_i} - \sqrt{\Delta q_{i,0}^T \Delta q_{i,0}} \quad (3)$$

The last term represents the initial length of an element with $\Delta q_{i,0} = q_{i,1,0} - q_{i,2,0}$, where $q_{i,1,0}$ and $q_{i,2,0}$ are the initial absolute positions given in a global coordinate system of the nodes to which element i is attached to. The first term yields the current length of the element i , where the individual positions of the associated nodes have to be represented in a global coordinate system.

$$\Delta \tilde{q}_i = \tilde{q}_{i,1} - \tilde{q}_{i,2} \quad (4)$$

In the above equation, the absolute reference position of the nodes $\tilde{q}_{i,1}$ and $\tilde{q}_{i,2}$ are equal to $\tilde{q}_{i,1} = q_{i,1,0} + q_{i,1}$ and $\tilde{q}_{i,2}$, respectively, where the relative displacements of the attachment nodes are a subset of the DOF vector, i. e., $q_{i,1} \subset q$ and $q_{i,2} \subset q$. If changes in the element's stiffness $k_i(q)$ in function (2) apply, the structure's stiffness matrix $K(q)$ has to be reassembled, leading to a state-dependent formulation of (1):

$$K(q) = f(u), \quad y = h(q, u). \quad (5)$$

Consequently, the system's output is stated as a general nonlinear function depending on the state and the input. Nevertheless, in most cases the output is given by a linear function of the form $h(q, u) = Cq$. Nonlinearities of the kind (2) can be considered in structural analysis using any common FE-software. The system formulation (5), however, is required for the purpose of model-based control design (ref. section 3) within a tool as Matlab or Python. A system formulation for dynamic analysis of this type of nonlinearities was derived by Wagner et al. (2019a, 2020).

2.3. Actuation Principles and Input Modeling

In this study, two actuation principles are introduced, and their implication on the adaptive structure is analyzed. The first principle, shown in **Figure 1A**, considers a force parallel actuator, which is essentially an additional (active) link that can influence

the truss structure. Changing the length of this actuator leads to the same length change in the parallel element due to the fact that both elements are attached to identical nodes. However, the forces in the actuator and the parallel (passive) element are potentially very different. These depend on the cross sectional areas of the active and passive element and are determined as a function of the actuator force, while the structure is required to reach an equilibrium state.

Due to the parallel elements, this actuation principle might seem to lead to an overdesigned configuration. However, it enables actuation of highly loaded elements and has benefits in terms of safety and fault tolerance. Such elements are mainly included in the load path to compensate a structure's dead load. Consequently, since the actuator is not required to completely bear the static dead load, it can be used for damping purposes or to generate small scale manipulations and structural deformations. Moreover, the actual passive element can be designed for much smaller dynamic loads because dynamic load components are transferred to the actuator. Together, both can be designed such that they are not necessarily heavier than a single passive column.

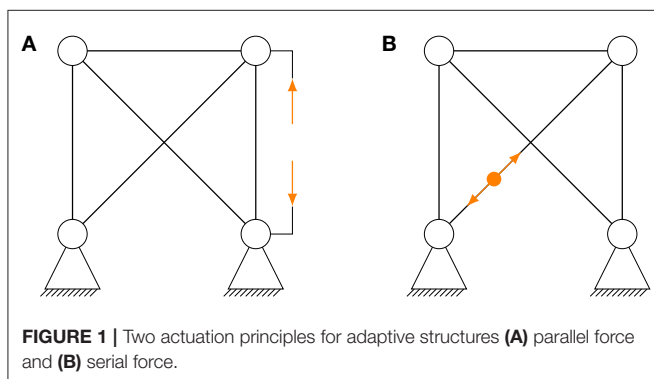
The second principle is the serial actuation depicted in **Figure 1B**. In this configuration, the actuator is included in the load path of an element so that the force in the element is directly set by and equal to the actuator's force. If the structure is not in an equilibrium, the element will extend or shorten its length until the element force is equal to the actuator's force. In duality with the parallel actuation principle, the displacement of the passive part of the element and the actuator add up to the total change in length between the two nodes (Böhm et al., 2020). The element and actuator force are equal. As it was concluded in Wagner et al. (2018), a serial actuation principle for bracing elements is preferred, which stiffen a structure. Regardless of the chosen principle, all actuator forces will be limited in practice according to the design. Since typical bracing elements can only be stressed in tension, as explained in section 2.2, serial actuators are not capable of exerting compression forces in such elements.

A mechanical limit in the actuators needs to be installed for safety reasons to prevent undesired large deformations of the structure. If the actuator hits its upper limit stop and the force within this active element is higher than the upper force limit of the actuator, an impact on the structure is not possible¹. Furthermore, actuation is lost, in the case of a fully contracted actuator, if the active element is compressed. Therefore, all inputs generated by actuators, which are connected in series, are state dependent. This is modeled by means of a state-dependent input matrix $B_s(q)$. The basic equations for including serial actuation into a given model are given by Böhm et al. (2020), and the input function can be separated as follows:

$$f(u_s, u_p) = B_s(q)u_s + B_p u_p + Ez. \quad (6)$$

Consider a number of serial actuators, m_s , and a number of parallel actuators, m_p . The causality between the actuation and the DOF is described by the respective input matrix

¹However, this would be a strong indicator for a poorly chosen actuator design.



$\mathbf{B}_s(\mathbf{q}) \in \mathbb{R}^{n \times m_s}$ and $\mathbf{B}_p \in \mathbb{R}^{n \times m_p}$. The input forces of both types of active elements are $\mathbf{u}_s \in \mathbb{R}^{m_s}$ and $\mathbf{u}_p \in \mathbb{R}^{m_p}$. The external loads, which cannot be affected, are captured in the last term $\mathbf{E}\mathbf{z}$. Given a parallel setup in which each individual actuation is represented by $\mathbf{b}_i^T \mathbf{u}_{p,i}$, the actuation force of a corresponding serial configuration (leading to the same equilibrium state of the structure) is calculated by

$$u_{s,i} = u_{p,i} - k_i \mathbf{b}_i^T \mathbf{q}. \quad (7)$$

if the element's stiffness k_i is known. The question of where the actuators are placed within the structure is addressed in earlier contributions. For active vibration control under dynamic loads, actuators can be placed according to Heidingsfeld et al. (2017) by means of the Gramian controllability matrix with integrated spillover reduction. For static load compensation, a placement strategy was proposed in Wagner et al. (2018) in which a cost function is derived based on certain load assumptions. Appropriate assumptions can be formulated in order to achieve optimality under a wide range of loading events. However, an adaptive structure's set of actuators needs to provide high performance for a variety of loads. The final choice of the actuator set for any kind of adaptive structure must be a combination of these results obtained for the various loads—static and dynamic—eventually considering symmetry and economic aspects as well.

2.4. Output Modeling

Different outputs may be considered in adaptive structures. This section focuses on two relevant types of outputs, which are used in optimization and for evaluation. These are the nodal displacements and the element forces.

2.4.1. Displacement

In civil engineering, rather strong restrictions apply to the displacements of high-rise buildings due to comfort reasons. A common rule is the horizontal displacement of the tip of a building is restricted within a range that does not exceed 0.2–0.5 % of the building's height. In order to test this restriction, we need to define the nodal displacement output:

$$\mathbf{y}_{\text{disp}} = \mathbf{C}_{\text{disp}} \mathbf{q}. \quad (8)$$

Only the translational DOFs are considered via the output matrix \mathbf{C}_{disp} , as there are typically no (strong) restrictions on the rotational DOFs.

2.4.2. Element Forces

As discussed in section 2.2, tension-only elements, common link elements, and different actuator types are complex to consider in terms of element forces in output modeling. Therefore, the N_e element forces are captured in $\mathbf{y}_{\text{force}}(\mathbf{q}) \in \mathbb{R}^{N_e}$, which comprises four parts. Firstly, element forces $\mathbf{y}_{\text{force},s}(\mathbf{q}) \in \mathbb{R}^{N_s}$ of tension-only elements with serial actuation are considered. Secondly, element forces $\mathbf{y}_{\text{force},p} \in \mathbb{R}^{N_p}$ of all (link or beam) elements with parallel actuation are included. Thirdly, element forces $\mathbf{y}_{\text{force},sp}(\mathbf{q}) \in \mathbb{R}^{N_{sp}}$

of tension-only elements without actuation are captured. Finally, the remaining element forces, $\mathbf{y}_{\text{force},r} \in \mathbb{R}^{N_r}$:

$$\mathbf{y}_{\text{force}}(\mathbf{q}) = [\mathbf{y}_{\text{force},s}^T(\mathbf{q}), \mathbf{y}_{\text{force},p}^T, \mathbf{y}_{\text{force},sp}^T(\mathbf{q}), \mathbf{y}_{\text{force},r}^T]^T. \quad (9)$$

All element forces are normal forces and are calculated in dependence of the actuation type and the element type. For tension-only elements actuated in series, where the actuator is operating within its stroke limits, the element force is equal to the actuator force. If the actuator hits the upper stroke limit, the force exerted on the element by the structure's displacement can be higher than the actuator force. This force is calculated in the same way as for passive elements using an adapted stiffness constant of the combined element. If the actuator is fully contracted and the element is slackend, no force is transmitted over the element. In summary, the force output of each individual element i is expressed:

$$\mathbf{y}_{\text{force},s,i}(\mathbf{q}) = \begin{cases} \mathbf{C}_{\text{force},s,i} \mathbf{q}, & \Delta l_i(\mathbf{q}) \geq 0 \\ u_{s,i}, & \Delta l_{i,\min} < \Delta l_i(\mathbf{q}) < 0, \\ 0, & \Delta l_i(\mathbf{q}) < \Delta l_{i,\min} \end{cases} \quad (10)$$

where $\Delta l_{i,\min}$ is the lower actuator stroke limit and 0 its upper stroke limit. For the elements actuated in parallel

$$\mathbf{y}_{\text{force},p} = \mathbf{C}_{\text{force},p} \mathbf{q} + \mathbf{D} \mathbf{u}_p \quad (11)$$

holds. The first term represents the force transferred through the passive part, while the second term represents the actuator force. With the notation adopted, the actuator force is positive when the actuator acts against its compression. Since compression forces are typically defined with a negative sign, the matrix \mathbf{D} is defined as $\mathbf{D} = -\mathbf{I}$. Any passive tension-only element only transfers forces if it is under tension, while the element forces are zero under compression:

$$\mathbf{y}_{\text{force},sp,i}(\mathbf{q}) = \begin{cases} \mathbf{C}_{\text{force},sp,i} \mathbf{q}, & \Delta l_i(\mathbf{q}) \geq 0 \\ 0, & \Delta l_i(\mathbf{q}) < 0. \end{cases} \quad (12)$$

The remaining elements are common tension and compression (link or beam) elements with

$$\mathbf{y}_{\text{force},r} = \mathbf{C}_{\text{force},r} \mathbf{q}. \quad (13)$$

Equations (9)–(13) are summarized in the nonlinear output function $\mathbf{h}(\mathbf{q})$ to obtain

$$\mathbf{y}_{\text{force}}(\mathbf{q}) = \mathbf{h}(\mathbf{q}) \mathbf{q}. \quad (14)$$

All output matrices $\mathbf{C}_{\text{force},(\cdot)} \in \mathbb{R}^{(\cdot) \times n}$ contain the matched stiffness and geometric information, i.e., the stiffness of the individual elements and to which nodes the respective elements are attached to.

3. CONTROL

In this section, a model-based control strategy for optimal static load compensation for nonlinear adaptive structures under state and input constraints is introduced. While for linear control, a variety of analytic control schemes are available, static compensation for the nonlinear model is best tackled by an optimization-based algorithm, as proposed in section 3.2. The required optimization metric is explained in section 3.1. Finally, a simple adaption scheme for reconfiguration of the compensation control is given for the case of actuator faults in section 3.3.

3.1. Optimization Metric

For this contribution, we chose to minimize the nodal displacements of the structure. Therefore, the cost function consists of the quadratic sum of all nodal displacements and is given by

$$J(\mathbf{q}) = \mathbf{y}_{\text{disp}}^T \mathbf{y}_{\text{disp}} = \mathbf{q}^T \mathbf{C}_{\text{disp}}^T \mathbf{C}_{\text{disp}} \mathbf{q}. \quad (15)$$

Another possible optimization metrics is the homogenization of element forces over all elements, which was used as a metric for actuator placement by Böhm et al. (2019). For this, the stress in an element is calculated and set in relation to its yield strength. This utilization quantity is homogenized over all elements by penalizing deviations from the mean utilization value in the cost function.

3.2. Static Load Compensation

Static load compensation is realized by minimizing the cost function introduced above under given constraints regarding the structure's displacement as well as state and input constraints. One common requirement for high-rise buildings is the limitation of the structure's displacement to 0.2–0.5 % of a building's height. In the following, the approach for optimal static load compensation including all constraints is given using the nonlinear model together with serial and parallel actuated elements.

3.2.1. Optimization

The optimization problem to determine the optimal parallel and serial inputs for a given static load by minimizing the displacement of the structure under constraints with the cost function taken from (15) described by

$$\{\mathbf{u}_s^*, \mathbf{u}_p^*, \mathbf{q}^*\} = \arg \min_{\mathbf{u}_s, \mathbf{u}_p, \mathbf{q}} J(\mathbf{q}) \quad (16)$$

$$\begin{aligned} \text{s.t.} \quad & \mathbf{K}(\mathbf{q}) = \mathbf{B}_s(\mathbf{q})\mathbf{u}_s + \mathbf{B}_p\mathbf{u}_p + \mathbf{E}z \\ & \mathbf{u}_{s,\min} \leq \mathbf{u}_s \leq \mathbf{0} \\ & \mathbf{u}_{p,\min} \leq \mathbf{u}_p \leq \mathbf{u}_{p,\max}. \end{aligned} \quad (17)$$

The optimization variables in (16) are the parallel and serial inputs \mathbf{u}_p and \mathbf{u}_s . Note, that the state-dependent stiffness matrix $\mathbf{K}(\mathbf{q})$ can become singular as soon as too many

tension-only elements are actually under compression. Thus, invertibility of $\mathbf{K}(\mathbf{q})$ cannot be guaranteed and therefore, the state vector \mathbf{q} cannot be calculated by inversion of $\mathbf{K}(\mathbf{q})$. We have thus reformulated the optimization with the steady state equation as an equality constraint rendering the state \mathbf{q} an additional optimization variable. This avoids inversion of $\mathbf{K}(\mathbf{q})$ but leads to a higher number of optimization variable as a consequence. The input constraints can be explained as follows: the serial input signals can only transmit tension forces and therefore must have a negative value. The largest tension force is given by $|\mathbf{u}_{s,\min}|$. The parallel actuators can generate tension and compression forces and stay within the limits of $\mathbf{u}_{p,\min}$ and $\mathbf{u}_{p,\max}$. Since only static loads are considered, constraints of time-dependent values, e.g., acceleration or velocities, can be neglected. In the present paper, we assume a known static load, while, in practice, static load estimation is a complex task that is beyond the scope of this contribution.

The optimization is started with an initial condition, corresponding to the state of the passive structure under the given load. The parallel and serial input \mathbf{u}_p and \mathbf{u}_s are concatenated to $\mathbf{u} = [\mathbf{u}_p, \mathbf{u}_s]$. The input \mathbf{u} is calculated analytically for the system linearized around $\mathbf{q} = \mathbf{0}$:

$$\mathbf{u} = -(\mathbf{CK}^{-1}(\mathbf{0})\mathbf{B})^+(\mathbf{CK}^{-1}(\mathbf{0})\mathbf{E}z), \quad (18)$$

where $\mathbf{B} = [\mathbf{B}_p, \mathbf{B}_s]$. Note that the initial conditions might not satisfy state and input constraints.

3.3. Fault Tolerance and Reconfiguration

In large and complex systems with many actuators and sensors, robustness with respect to faults is an important property. In this contribution, we focus on actuator faults and assume the detection of faults is available (e.g., as proposed by Gienger et al., 2020). Through the potential of the large number of actuators, it is possible to reconfigure control to provide high control performance despite faults. After detecting an actuator fault, an obvious approach is the recalculation of control signals with a reduced number of actuators. This is acceptable, if the calculation time of the optimization stays below the time constants of the system dynamics. In this article, we consider only quasi-stationary loads, which is an important load case for civil engineering structures, and the optimization program is solved in way shorter time. Furthermore, as initial condition, the preceding solution without actuator faults is used as the reconfigured solution is expected to be close. So, the optimization problem is solved for a changed actuator configuration using (16) and (17). In an additional step, it would be possible to include constraints induced through faulty actuators, e.g., an actuator cannot move further and remains at an arbitrary but fixed length.

4. NUMERICAL AND EXPERIMENTAL RESULTS

In this section, the numerical and experimental results are depicted and discussed. At first, the investigated structure is explained, and, subsequently, the results for optimal static load compensation and reconfiguration are given.

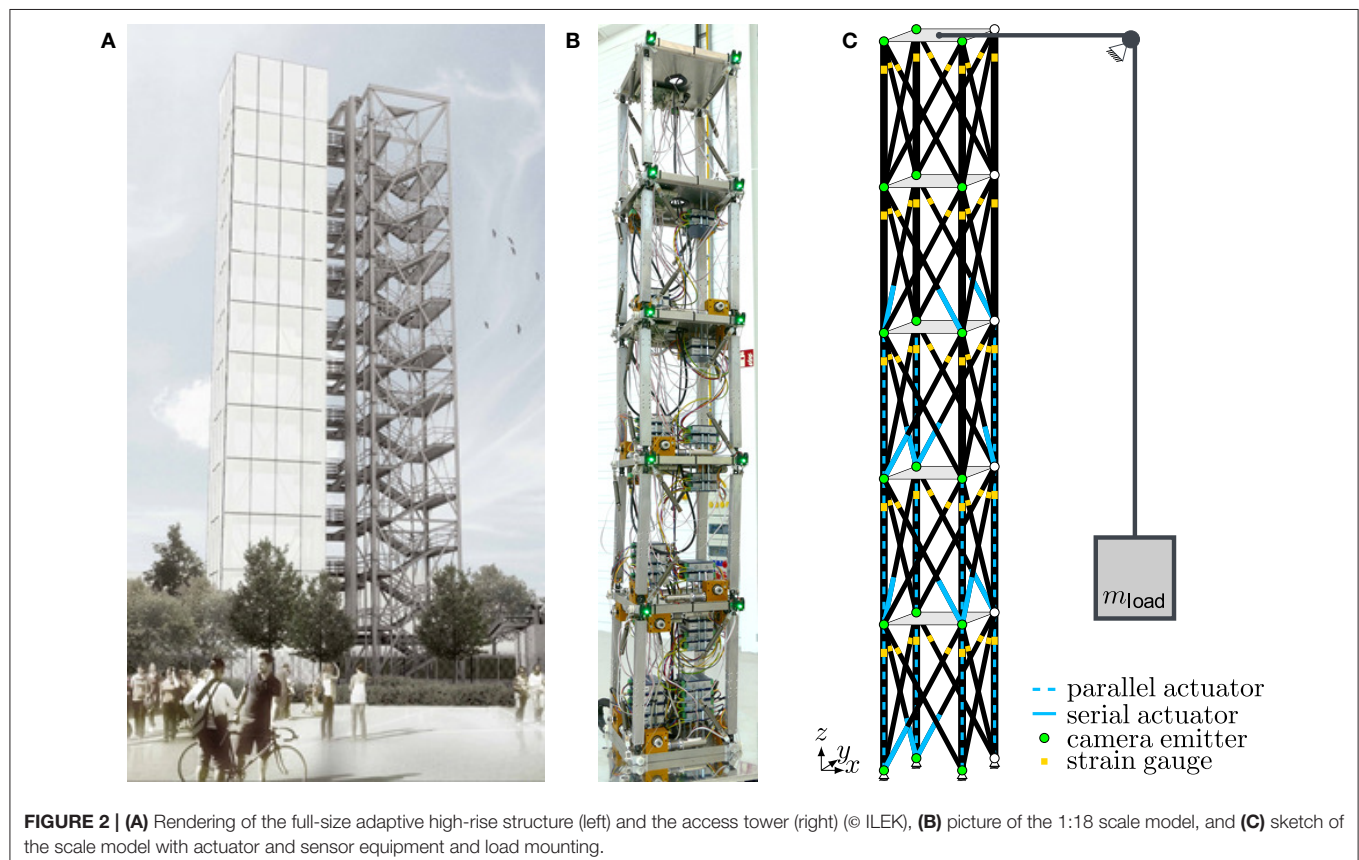
4.1. System Description

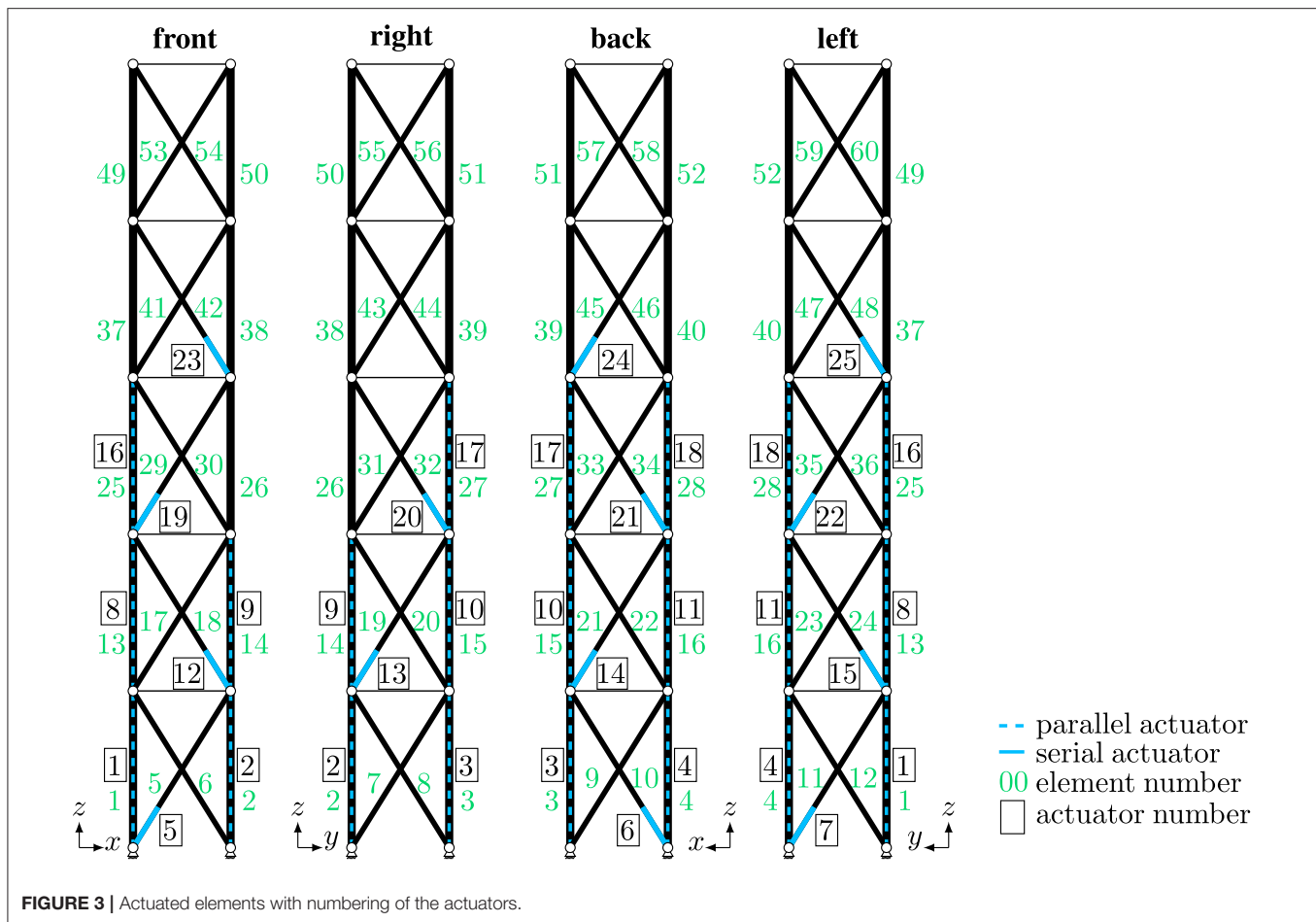
4.1.1. General Setup

To illustrate the results of optimal static load compensation, a scale model of an adaptive high-rise structure is used. The full size adaptive high-rise structure will be constructed on the site of the University of Stuttgart, rendered in **Figure 2A**. The structure will be a twelve story building with 36 m height covering a square base with side length of 4.7 m, detailed information is given by Weidner et al. (2018). The scale model investigated in this contribution is 18 times smaller, leading to a height of 2 m and a square ground base of 0.26×0.26 m (see **Figure 2B**). It is subdivided into five modules, where one module comprises two stories. The module and story numbering start at the bottom with index 1. The full-size building comprises four modules with three stories each.

Four vertical elements, eight diagonal bracings, and one plate are mounted per module, where the element numbering is given in **Figure 3**. Instead of plates, the full-size building will feature horizontal bracings where modules meet. Additionally, the plates are assumed to be very rigid and are therefore excluded in the calculation of element forces. Sensors are installed in terms of strain gauges in almost each vertical and diagonal element. Furthermore, an optical measurement system is installed to measure some of the nodal displacements (ref. **Figure 2**). Strain gauges are mounted onto the base material of the elements and the small measurement signals are amplified.

The optical sensors measure the nodal displacement of one side of the building (**Figure 2C**). The green light emitters are detected with a camera system (Ximea MC023MG-SY) on two sides of the building to get spatial information on the structure's displacement with submillimeter resolution. The full-scale building will be equipped with the same sensor setup, adapted to the larger scale. Additionally, sensors for wind, rain, and solar radiation will be installed to estimate external loads. A construction to excite the scale model statically is shown in the scheme. A weight of $m_{\text{load}} = 4$ kg, and, by this, about 40 N are applied to the top of the scale model horizontally in x -direction. In modeling, the load is divided upon the upper two nodes on the right side. A shaker table is installed below the scale model, exciting the structure in x - and y -direction for investigating the dynamic behavior. As providing this kind of excitation is too complex for the full-scale building, a subset of the integrated actuators will be used instead to simulate excitation. Every module incorporates a microcontroller, which communicates sensor and actuator signals to the central control unit. The optical measurement system directly communicates its measurements via ethernet to the central control unit. All microcontrollers are connected to the central control hardware (dSpace MicroLabBox DS1202) via CAN-bus. All algorithms are implemented using Matlab/Simulink and executed using the dSpace MicroLabBox along with the software dSpace ControlDesk. A summary of geometry and material parameters are given in **Table 1**.





4.1.2. Actuators

Parallel actuators are integrated in 11 vertical elements, as depicted in **Figure 2C**. The integration of active components in a column is shown at the top of **Figure 4**. A brushless DC motor (Faulhaber 2264W024BP4 3692—operated by a motor controller Faulhaber MC5010) is mounted at the bottom of each active column. The motor is coupled to a ball screw to transform rotation to a linear motion. The nut is clamped between two springs, which directly determine the stiffness of a column. The lower end of the lower spring and the upper end of the upper spring are connected via the housing and are referred to as grounding. Therefore, the springs are mounted in a parallel setup. The corresponding actuation principle is sketched in **Figure 1**. The structure also incorporates 14 active diagonal bracings, see **Figure 2C** for the locations. Diagonal elements are realized by steel cables, which are wound over a roll that is connected to a worm gear. A brushless DC motor is mounted on the other end of the worm gear. The top module is a passive part of the structure, i.e., no actuators are installed in the top module. Actuator and element numbers are given in **Figure 3**. The full-scale building includes a similar actuator set; however, due to the absence of the fifth module the following changes occur. The

third module does not include vertical actuators, and the fourth module contains no actuators at all, leading to only 24 active elements. These actuators will be realized as hydraulic cylinders. The full-scale model will be the main experimental setup to validate and evaluate all developed control algorithms, including static compensation as well as active vibration control, observer strategies and fault detection.

The values for inequality constraints are calculated based on **Table 1** such that $u_{s,\min} = -111 \text{ N}$, $u_{p,\min} = -296 \text{ N}$ and $u_{p,\max} = 296 \text{ N}$. The actuator forces in the setup for serial and parallel actuation cannot be measured directly. The motors are velocity controlled by the motor controllers. To apply the desired serial actuator force, an underlying PI-controller was designed for each motor, which uses the strain gauge measurement to control the current element force. Due to the strain gauge installation, the serial element force is measured, from which the corresponding parallel element force can be calculated using (7). The feedback gains for the parallel and serial actuators are designed separately. The error is defined as the difference between desired and measured value. The P- and the I-gains multiplied with the errors for the parallel actuators are $k_P = -1$ and $k_I = -10$ and for the serial actuators $k_P = -20$ and $k_I = -80$.

4.2. Static Load Compensation

The optimization problem (16), (17) was solved by means of an interior-point algorithm as proposed by Wächter and Biegler (2006)². On a development PC (Intel Core i@2.7GHz), computation time of the optimization for the given parameters and initial condition is approximately 3 s, which is sufficient for static adaption. Displacement results are presented for both the simulated and measured structures and an illustration of the measured element forces is provided.

4.2.1. Displacements

Figure 5 shows the qualitative results of the static load compensation of the experimental setup with the reference state in Figure 5A. The structure stands upright without actuation; however, serial actuation needs to be turned on and set to an initial value to apply a minimal prestress as a valid starting point

TABLE 1 | Geometry and material parameters of the scale model.

Description		Formula sign	Value	Unit
	Weight structure	m_{tot}	≈ 35	kg
	Weight load	m_{load}	4.0	kg
	Height structure	h_{tot}	2.0	m
Vertical elements	Length	l_v	0.4	m
	Stiffness	k_v	22124	N/m
Diagonal elements	Length	l_d	0.48	m
	Stiffness	k_d	18192	N/m
Plate elements	Side length	l_p	0.26	m
Actuation	Motor torque	M_m	0.059	Nm
	Ball screw diameter	d_v	0.006	m
	Ball screw slope	s_v	0.001	m
	Gearing ratio	i	65	
	Wheel radius	r_d	0.01	N/m

²We used here the implementation of the *OPTI Toolbox*, a free MATLAB Toolbox for Optimization by Inverse Problems Ltd. from 2014. More information can be found online at: <https://www.inverseproblem.co.nz/OPTI/index.php/Main/HomePage>.

from which to apply compensating input signals. The worm gear is self-locking, and the force is preserved without motor interference thereafter. Figure 5B displays the structure under the load without actuation. In Figure 5C, the displacements induced by the load are compensated by using the motors and the optimized input signals.

Position measurements are compared to the simulation results in Figure 6. These measurements are obtained from the cameras of the optical measurement system, and an offset is applied based on the reference state measurements. Figure 6A shows the measurement points in xz -plane for the reference, loaded, and compensated states. The effect of the load is almost completely compensated for, as seen by the reduction in displacement from 11.5 to 0.3 cm at the top. Deviations from the reference state are mainly visible in the middle of the structure, and they are reduced from 4.6 to 1.3 cm at the end of the second module. In general, perfect compensation cannot be reached for all loads. The deviation in the middle is due to the locations of the serial actuation. The actuated diagonal elements go from the bottom right to the top left in the second module and therefore they cannot counteract the induced displacement. Thus, only the actuation in the columns is available, which is not sufficient for the required compensation. Regarding actuator placement, various static loads were investigated justifying the present actuator configuration (Wagner et al., 2018). While, for this specific load, another actuator configuration would have been beneficial, the model's actuator setup is chosen as a compromise between the optimal placement for several different load cases. Figure 6B displays measurement and simulation results for the scale model under load. According to the simulation, the expected displacement is larger than the measured displacement. The simulation model assumes a homogenous structure with constant parameters for passive and active elements. However, the upper modules do contain mostly passive elements. Especially the diagonals in these modules are prestressed to avoid slack even in the initial straight upright position. Therefore, the upper modules seem more rigid and are not as much displaced in the experiments compared to the simulation results. Figure 6C shows the compensation of the displacement of the structure under load for the real setup and simulation. The optimization results are applied to the motors and almost completely

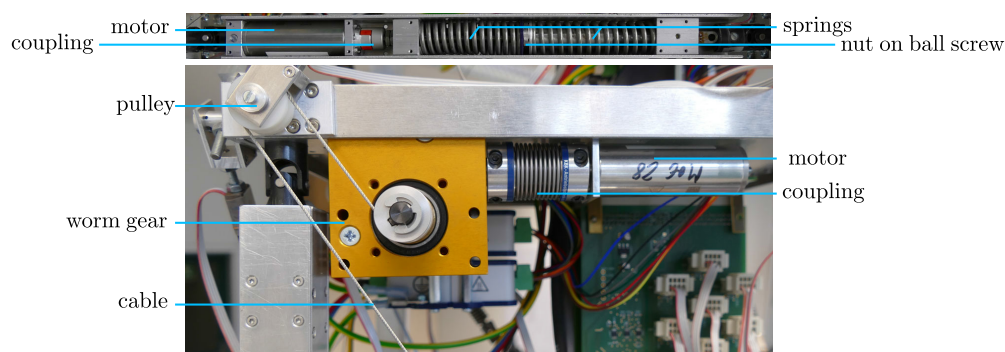


FIGURE 4 | Construction of parallel actuation in the columns (Top, rotated by 90°) and serial actuation for diagonal elements (Bottom).

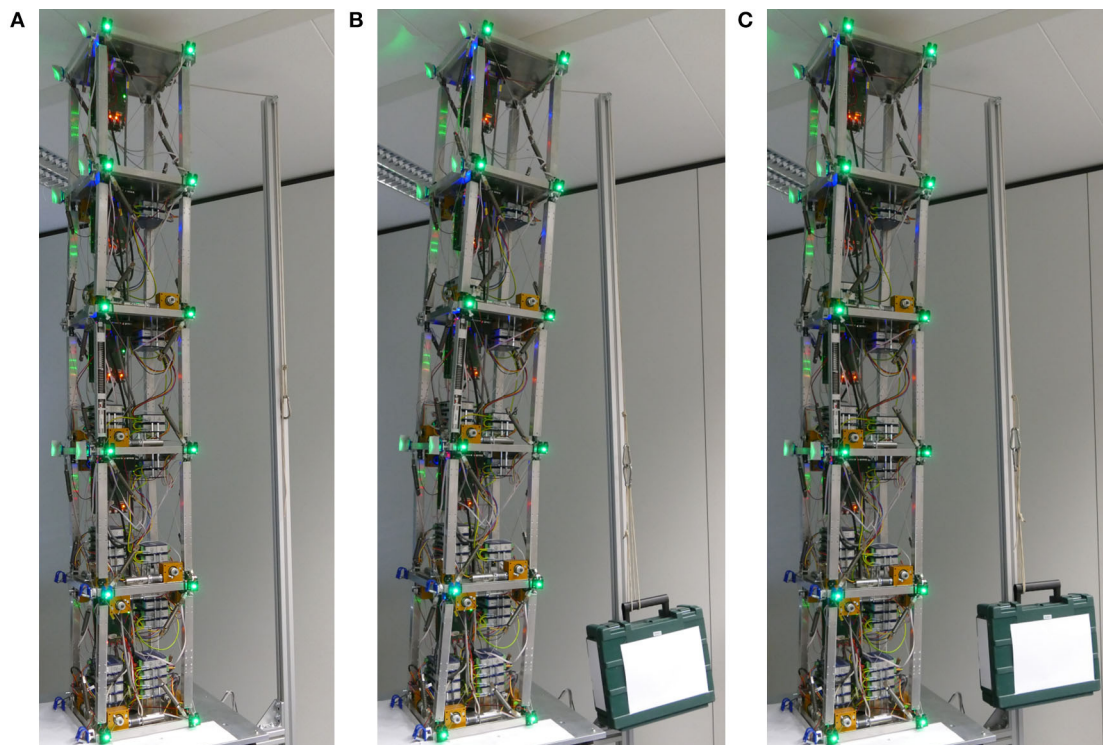


FIGURE 5 | Photographs of the experimental setup of the scale model. **(A)** Upright state as reference, **(B)** applied load without compensation, and **(C)** compensation of the displacement caused by the load.

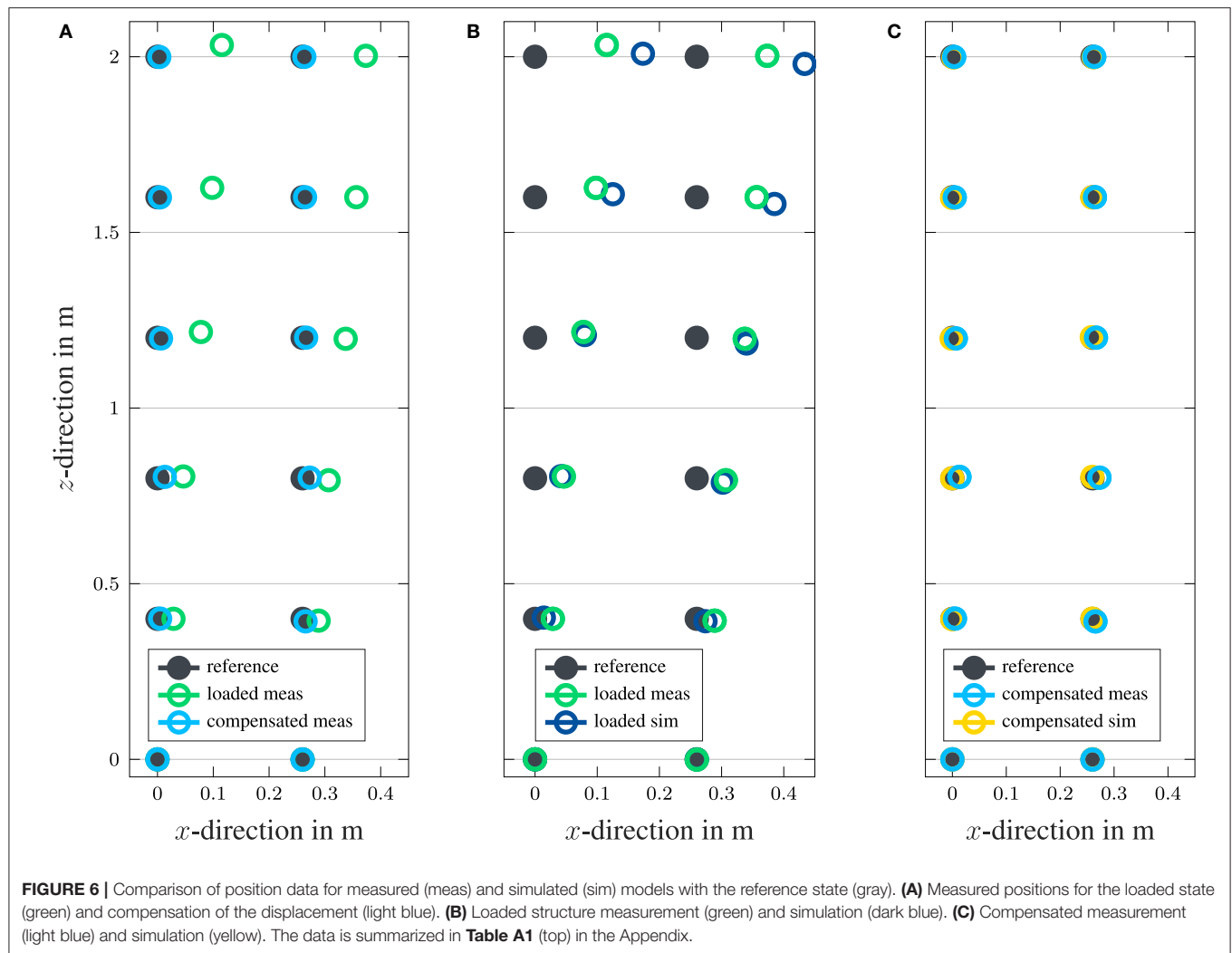
compensate for the initial displacement. The deviation from the reference state is not visible for the simulation. This discrepancy can be partly explained by asymmetric actuator placement in the model. Furthermore, a model is only a limited approximation of the real world behavior and leaves out effects, e.g., nonlinear effects, such as hysteresis and stick-slip in the actuated columns and diagonal bracings. In general, the results of the position measurements show sufficient accuracy and performance and a very good static load compensation.

4.2.2. Actuator Forces

For an illustration of the actuator forces, the parallel and serial inputs are named according to the actuator number in **Figure 3** and summarized to one sorted input u . **Figure 7** shows the actuator forces determined by the optimization algorithm. Serial forces are depicted directly, while parallel actuation forces are calculated with (7) to obtain the element force. As expected, under the given load, the actuators in columns 1, 4, 8, 11, 16, and 19 need to apply tension forces, while column actuators 2, 3, 9, 10, and 17 apply compression forces. All diagonal actuators show, as required, only non-positive forces (i.e., tension). All input constraints due to the actuator force limits are met. The asymmetry in the actuator forces is due to the asymmetric actuator locations. In module three, only three columns are actuated and in module one and four, three diagonals are actuated.

For the forces in the columns, the zero-offset value cannot be determined in the mounted state. Therefore, the reference value of the upright state is set as the zero-offset value. For active and passive tension-only elements, the zero-offset value was determined in advance by slackening the cables.

To evaluate the actuation forces, the desired and the measured element forces are depicted over the actuator number in **Figure 8**. Actuator numbers are given in **Figure 3**. Serial actuators are highlighted by a gray background. In **Figure 8A** the results for the structure under load are shown, where actuation for compensation is turned off. However, the serial actuated elements are controlled such that the element force from the prestress in the reference state is maintained. Otherwise, if these elements were fixed, they would be stretched and exhibit high element forces, induced by the load. That is the reason why desired element forces for the serial actuated elements are shown in this plot. Desired forces are matched by actual measured forces to a sufficient extent. Some of these actuated tension-only elements are slack, which is shown by values close to/below zero (see actuator 14, and 15). Values below zero are possible since the zero-offset value can only be determined within a few Newtons. Actuators 13, 20, 23, and 24 do not reach their desired forces due to the limited motor torque. Due to the loading, the structure stretches these elements. Therefore, higher forces cannot be reached. Actuator 6 is set to a lower tension force in the element, but does not achieve it. Due to safety reasons, a mechanical stroke limit stop was installed for the



serial actuators to avoid complete release of several tension-only elements, which would lead to a collapse of the structure. In the full-scale structure, mechanical stroke limits are installed as well to meet legal requirements. **Figure 8B** illustrates the forces of the actuated elements in the case of active load compensation. In columns 1, 2, 3, 4, and 8, the desired forces are reached with high accuracy. For columns 11, 16, and 17, small deviations from the desired values are visible; however, an acceptable accuracy is still achieved. The vertical elements 9, 10, and 18 show large discrepancies from the desired value. Possible reasons for this are mainly constraints in the motor torques, especially with respect to the reference state. Such constraints are considered in the optimization, but due to the unknown zero-offset value, the reference state may have had larger than anticipated initial loads.

4.2.3. Element Forces

To illustrate the effects of the load and the compensation on the whole structure, element forces are displayed by means of colored plots. Tension forces are depicted in red and compression forces

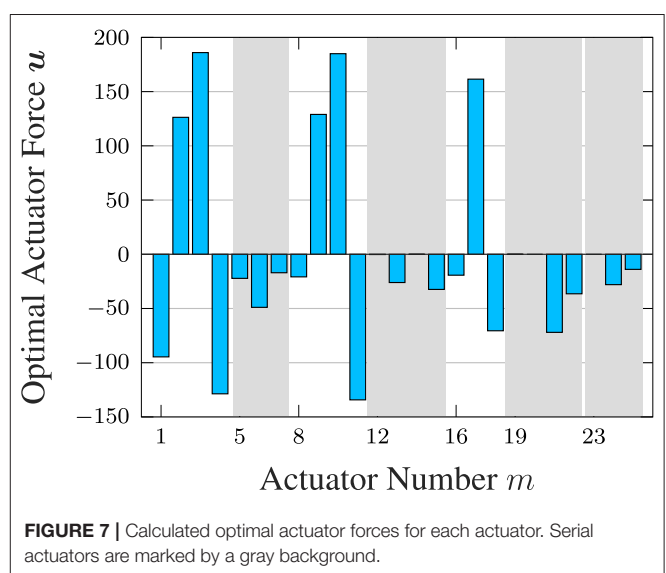
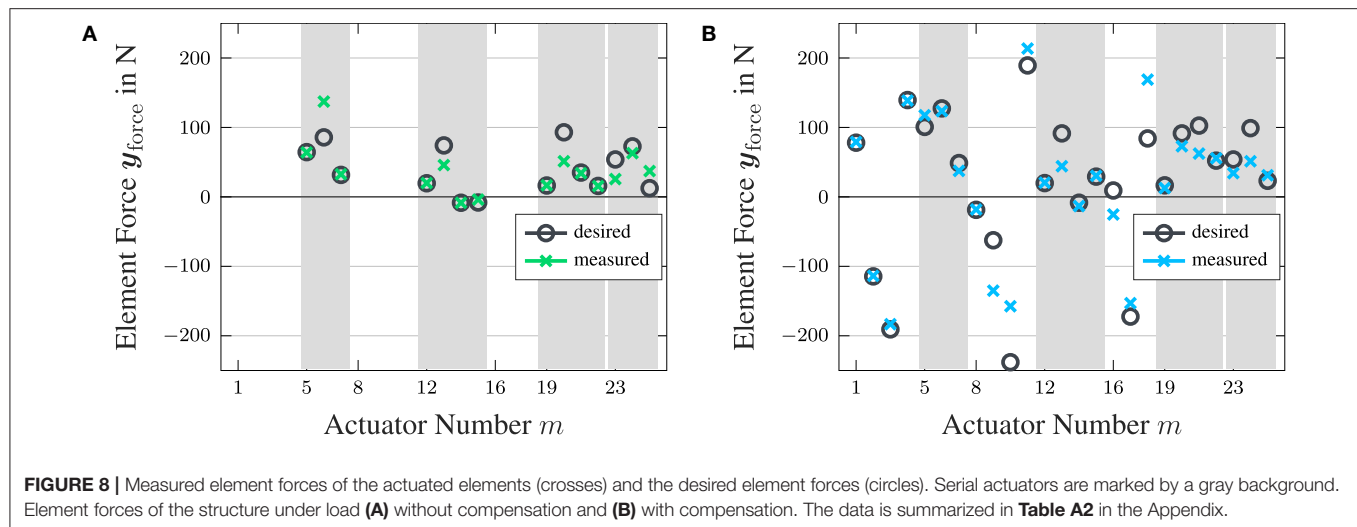


FIGURE 7 | Calculated optimal actuator forces for each actuator. Serial actuators are marked by a gray background.



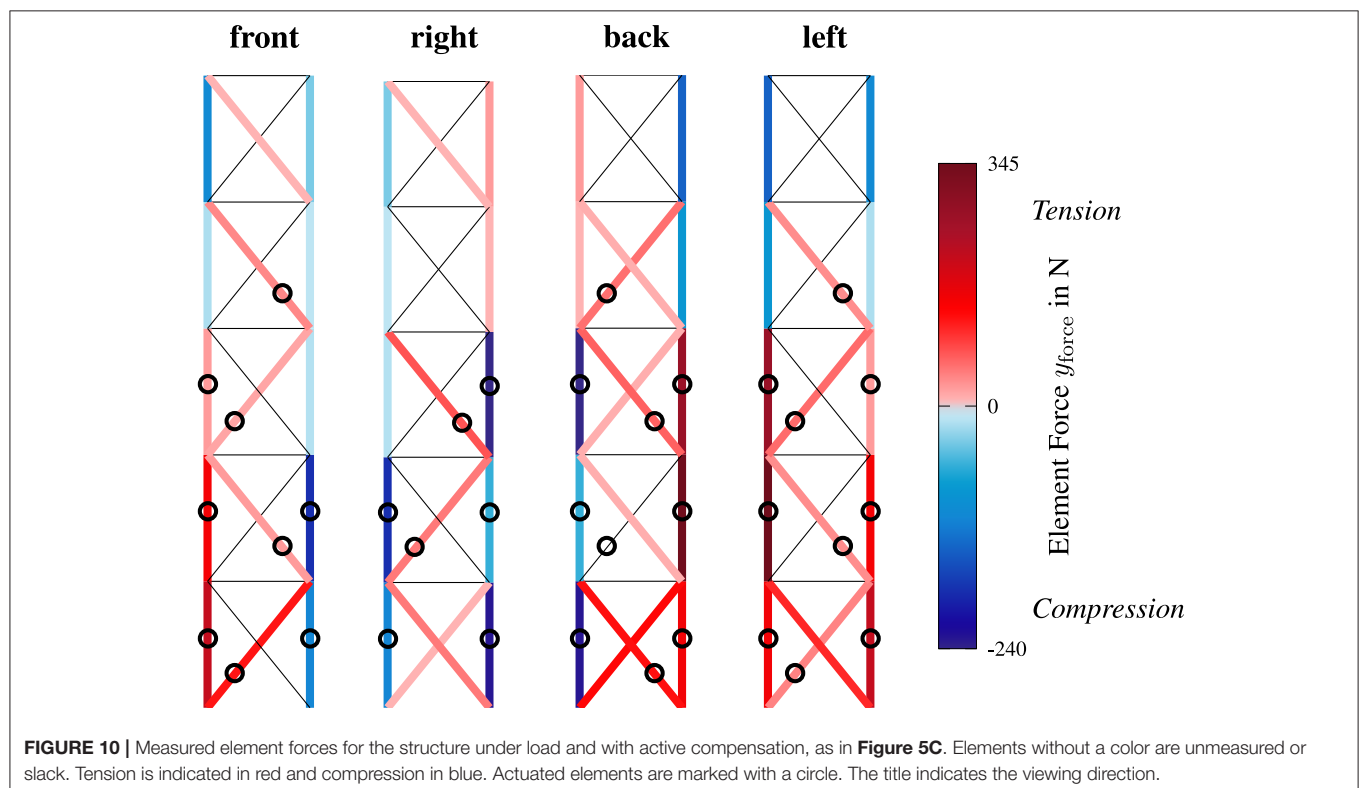
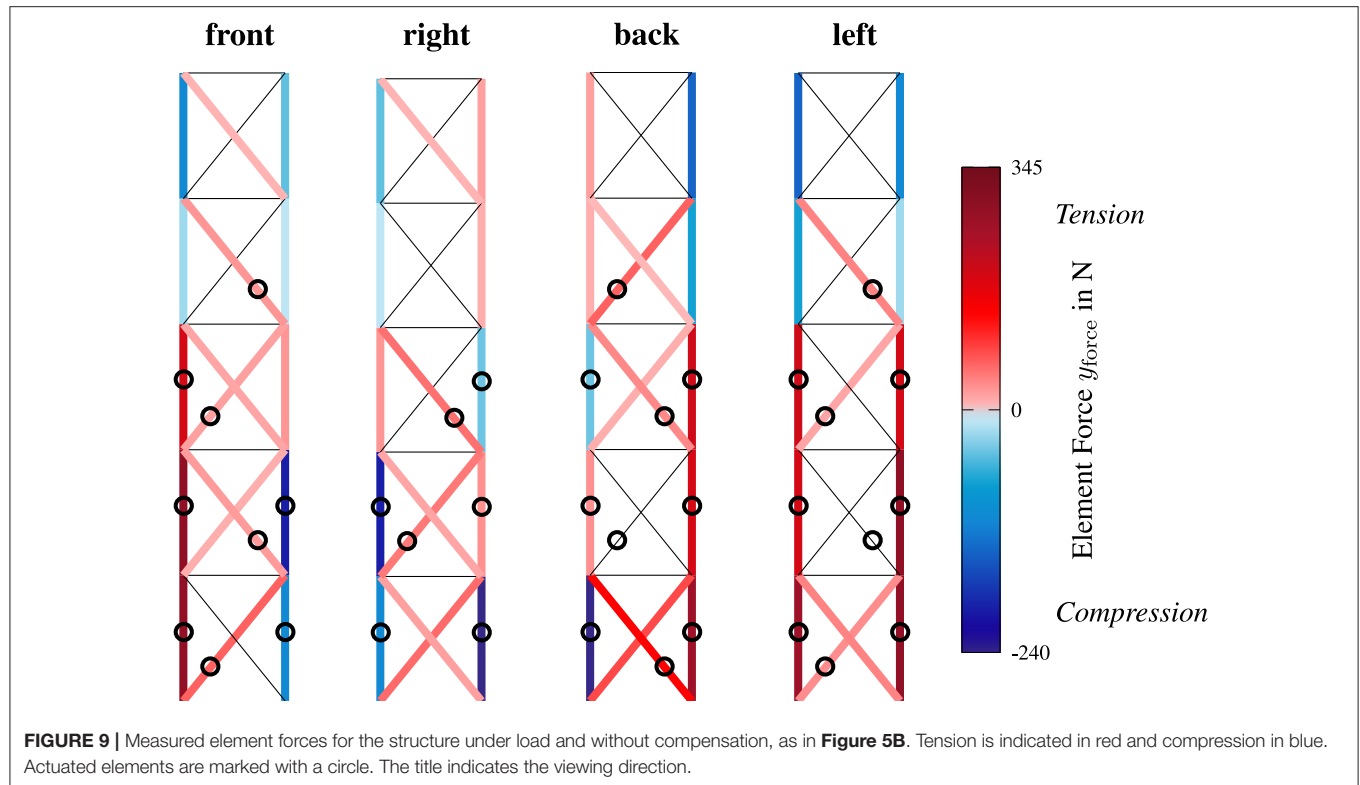
in blue. The darker the color, the higher the element's force. The plates are indicated by horizontal lines and are not equipped with sensors. Diagonal tension-only elements in black are slack. Two diagonal elements in the fifth module and one in the second module had faulty strain gauge sensors (see **Figure 2C**) and are also marked in black. Diagonal elements show absolute forces, while columns are shown in reference to the initial upright state because absolute force could not be determined in the mounted state. Active elements are marked by a circle, keeping in mind that the element force of diagonal elements is controlled solely by the motors. Active columns are only controlled in the compensated state.

When the load is applied, as shown in **Figure 9**, columns on the left side experience high tension forces, while columns on the right are mostly subject to compression forces. Small tension forces appear in element 15; however, in comparison to the reference state, compressive loading has reduced these forces. Element 26 is the only passive column in the third module and shows slightly different behavior than the active columns. Furthermore, this element is shorter by a few millimeters due to construction. The upper two modules seem to be stiffer, as already visible in **Figure 6A**, and bending of these modules is lower than expected from the simulation. This is caused by the construction of the passive columns. In **Figure 10**, the element forces of the structure under active load compensation are depicted. In the columns on the left, tension forces are reduced due to a more upright position compared to the uncompensated state. On the right side, compression forces are reduced for the same reason; however, in element 14, the force is reduced only marginally. Owing to the limitations of the motor torque, this compression force remains at a high level. Moreover, the column above, number 26, is the only passive column in module three. The fifth module is almost unchanged due to the absence of actuators. Regarding the columns, the fourth module also shows a similar force distribution with and without compensation.

When considering the diagonal elements, the prestress of each individual element has a large impact on the structure's behavior. Diagonal 5, which is also actuated, exhibits a higher

force when the compensation is enabled as is calculated through the optimization. Visually speaking, this diagonal pulls back the structure to an upright state, which appears intuitively right. Element 10 should show a similar behavior; however, this element is at its stroke limit in the uncompensated case, which can be seen in **Figure 8A**, since the desired force is not reached in that case. In general, actuators in diagonal bracings on the right can only marginally counteract the load-induced nodal displacements. Nevertheless, in the nonlinear model, a slight influence is present and actuation forces are obtained from the optimization (see **Figure 8**). In the second module, the active diagonals cannot counteract the displacement through the load due to their tension-only capability. Further tensioning of these active elements would enlarge the displacement, therefore, the optimized actuator forces are zero for elements 18 and 21, which corresponds to actuator number 12 and 14 (see **Figure 7**). Element 22, which contains actuator number 15, exhibits zero force in the uncompensated load case due to the low prestress in the reference state. During compensation, the optimal actuator force is reached, and the element is under tension. The third module shows similar behavior as the first module because the actuator configuration is similar. Element 30 is slack in the uncompensated load case but is under tension in the compensated state.

In general, evaluation of this multiple input multiple output (MIMO) system is quite challenging because small changes in a single actuator influence many elements. Furthermore, the sheer amount of output data complicates evaluation and bookkeeping of the system and its measurements. However, the experiment provides a proof of concept and showed that using the proposed method of optimal static load compensation for structures with tension-only elements and feasible input and state constraints, a significant reduction of nodal displacements could be achieved in the experimental testing. Force distribution in active and passive elements is reasonable and the structural behavior that is to be expected for the actual high-rise demonstrator is also well-illustrated.



4.3. Fault Tolerance and Reconfiguration

It is assumed that faults are detected in the column actuators 3 and 4 and are therefore no longer functional. The optimization

problem as defined by (16), (17) is adapted and rerun with updated parameters compensating for the missing actuators. The displacement results are shown in **Figure 11**. The displacements

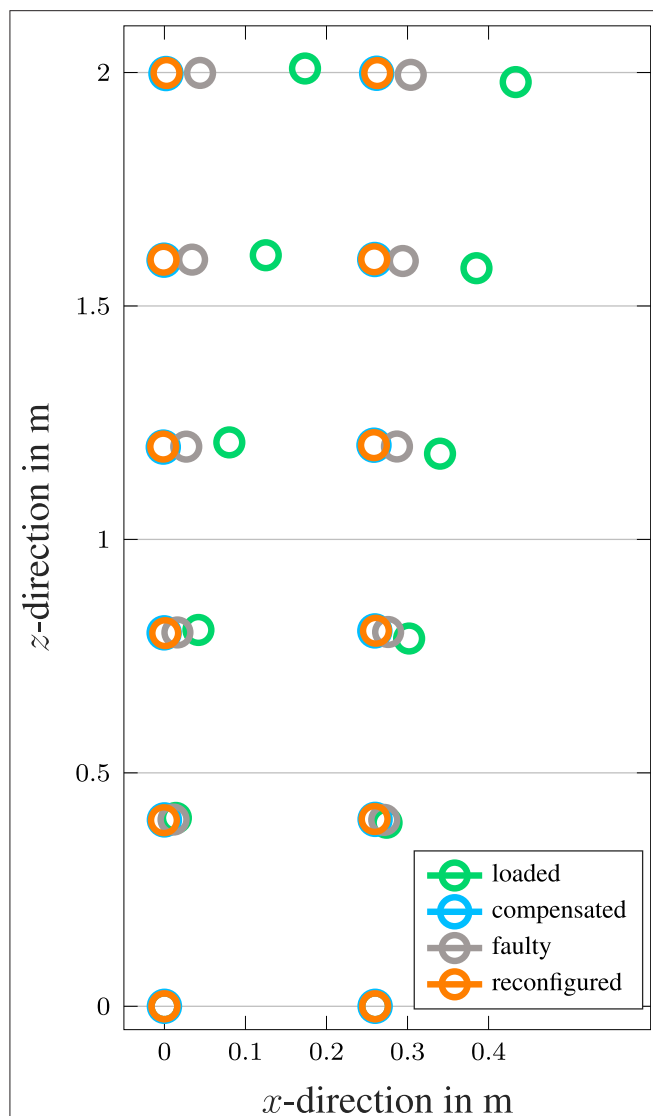


FIGURE 11 | Position data for a reduced actuator set due to actuator faults: the optimal input including all actuators (gray), the reconfigured optimal input for the reduced actuator set (orange), passive structure under load (green), and compensated state where all actuators are functional (light blue). The reduced actuator set does not include column actuator 3 and 4 due to actuator faults. The data is summarized in **Table A1** (bottom) in the Appendix.

of the structure using the optimal actuation signals under the assumption of faulty actuators are shown against the compensation assuming fully functioning actuators. On a development PC (Intel Core i@2.7GHz), computation time of the optimization is approximately 2 s. The lower value is mainly due to using the preceding solution as the initial condition, obtained for the faultless case. After reconfiguration and calculation of actuator signals for the current actuator set, the performance of load compensation is comparable to the performance with all actuators. For a small number of faulty actuators, it is possible to still achieve a very good load compensation due to the large overall amount of actuators. With an increasing number of

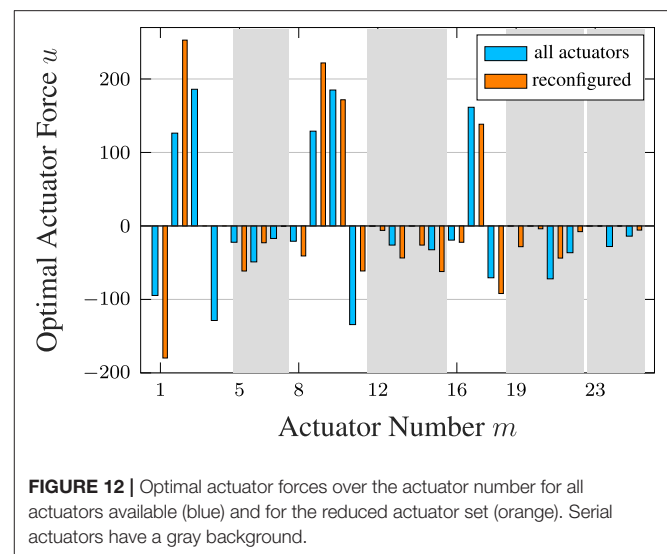


FIGURE 12 | Optimal actuator forces over the actuator number for all actuators available (blue) and for the reduced actuator set (orange). Serial actuators have a gray background.

faulty actuators, it will become difficult to maintain functionality. However, when faults occur, prompt actuator maintenance will be implemented such that safety of inhabitants and surrounding structures and persons is guaranteed. **Figure 12** depicts actuator signals of the adapted configuration in comparison to the optimal result with all actuators. Actuation signals for actuator 3 and 4 are missing. Actuation force of other actuators rise, especially in the first module where the faulty actuators are located. Diagonal tension-only actuator efforts that contribute to pulling the structure back into an upright position, e.g., actuators 5, 8, 12–15, 19, and 20, are increased to compensate for the missing actuators. Other actuation forces are reduced such that the structure is not deformed in an undesired way. Forces from diagonal actuators 6 and 7 are reduced and are directly interacting with the faulty actuators. Tension from these actuators, adds forces in the negative x - and z -directions of the element with faulty actuator 3. This would align the structure more upright; however, it would also pull down the z -coordinate. To balance this, the optimization returns no input signal for actuator 7. Reconfiguration under a small number of faulty actuators is an important capability because performance losses can be avoided and functionality and safety can be maintained until maintenance.

5. CONCLUSION AND OUTLOOK

In this work, we have presented a modeling approach for adaptive structures comprising of tension-only elements with serial and parallel actuation. Based on this model, an optimization-based approach for optimal static load compensation was introduced and demonstrated by means of an experimental setup. A drastic reduction of the structure's displacements was achieved such that safe operation of an adaptive building can be guaranteed, establishing a comfortable environment for inhabitants. Input constraints due to actuator saturation and state constraints due to comfort limits of a structure were both considered in the optimization formulation and were not violated by the results.

The measured compensation results were all well within a limit of $h_{\text{tot}}/100$. Results from the simulation and experiment aligned, however, there were errors as it seems the overall stiffness is higher than in simulation since the simulated displacements due to the applied load are clearly higher than the measured displacements. This holds especially for the upper two modules. Despite containing only three actuators, the results obtained from the optimization using the simulation model still provided a very good compensation. The performance of the algorithm degrades when faulty actuators are present. However, when these faults can be detected and the control signals are reconfigured accordingly, it is possible to restore the original performance, provided there is a sufficient number of remaining actuators. This kind of fault tolerance is a necessary property in control of civil engineering structures.

In this context, eigenstrain analysis can be an applicable tool. However, one has to investigate the feasibility with respect to the present nonlinearities. A proper starting point could be the method presented in Reksowardojo et al. (2020), which considered eigenstrain analysis geometric nonlinearities due to large shape changes. Furthermore, measurements regarding the energy consumption of the static control strategy on the scale model are planned. For the next step, we will integrate the load estimation to achieve applicability in a full size adaptive structure. We plan to apply this strategy to the full size adaptive structure and provide the respective experimental validation.

REFERENCES

- Adam, B. and Smith, I. F. (2008). Active tensegrity: a control framework for an adaptive civil-engineering structure. *Comput. Struct.* 86, 2215–2223. doi: 10.1016/j.compstruc.2008.05.006
- Alart, P., Dureisseix, D., Laniel, R., and Pagano, S. (2007). “Wires and cables in some discrete structures of civil engineering,” in *6th Eurosim Congress on Modelling and Simulation* (Ljubljana).
- Amini, F., and Ghaderi, P. (2013). Seismic motion control of structures: a developed adaptive backstepping approach. *Comput. Struct.* 114, 18–25. doi: 10.1016/j.compstruc.2012.09.011
- Basu, B., Bursi, O. S., Casciati, F., Casciati, S., Del Grosso, A. E., Domaneschi, M., et al. (2014). A European association for the control of structures joint perspective. Recent studies in civil structural control across Europe. *Struct. Control Health Monit.* 21, 1414–1436. doi: 10.1002/stc.1652
- Böhm, M., Steffen, S., Gade, J., Geiger, F., Sobek, W., Bischoff, M., et al. (2020). “Input modeling for active structural elements—extending the established Fe-workflow for modeling of adaptive structures,” in *International Conference on Advanced Intelligent Mechatronics* (Vancouver, BC).
- Böhm, M., Wagner, J., Steffen, S., Sobek, W., and Sawodny, O. (2019). “Homogenizability of element utilization in adaptive structures,” in *IEEE 15th International Conference on Automation Science and Engineering (CASE)* (Boston), 1263–1268.
- Fest, E., Shea, K., Domer, B., and Smith, I. F. C. (2003). Adjustable tensegrity structures. *J. Struct. Eng.* 129, 515–526. doi: 10.1061/(ASCE)0733-9445(2003)129:4(515)
- Gawronski, W. (2004). *Advanced Structural Dynamics and Active Control of Structures*. New York, NY: Springer Science & Business Media. doi: 10.1007/978-0-387-72133-0
- Gienger, A., Ostertag, A., Böhm, M., Bertsche, B., Sawodny, O., and Tarín, C. (2020). Data-based distributed fault diagnosis for adaptive structures using convolutional neural networks. *Unmanned Syst.* 8, 221–228. doi: 10.1142/S2301385020500156
- Haftka, R. T., and Adelman, H. M. (1985). An analytical investigation of shape control of large space structures by applied temperatures. *AIAA J.* 23, 450–457. doi: 10.2514/3.8934
- Heidingsfeld, M., Arnold, E., Tarín, C., and Sawodny, O. (2015). “Actuator fault-tolerant control of the stuttgart smartshell,” in *2015 IEEE Conference on Control Applications* (Sydney), 996–1001. doi: 10.1109/CCA.2015.7320742
- Heidingsfeld, M., Rapp, P., Böhm, M., and Sawodny, O. (2017). “Gramian-based actuator placement with spillover reduction for active damping of adaptive structures,” in *Proc. of the IEEE/ASME International Conference on Advanced Intelligent Mechatronics* (Munich), 904–909. doi: 10.1109/AIM.2017.8014133
- Housner, G., Bergman, L., Caughey, T., Chassiakos, A., Claus, R., Masri, S., et al. (1997). Structural control: past, present, and future. *J. Eng. Mech.* 123, 897–971. doi: 10.1061/(ASCE)0733-9399(1997)123:9(897)
- Irschik, H., Krommer, M., and Pichler, U. (2000). Shaping distributed piezoelectric self-sensing layers for static shape control of smart structures. *J. Struct. Control* 7, 173–189. doi: 10.1002/stc.4300070204
- Irschik, H., and Ziegler, F. (2001). Eigenstrain without stress and static shape control of structures. *AIAA J.* 39, 1985–1990. doi: 10.2514/2.1189
- Johnson, E., and Erkus, B. (2002). “Structural control with dissipative damping devices,” in *Proc. of the American Control Conference, Vol. 3* (Anchorage, AK: IEEE), 2463–2468. doi: 10.1109/ACC.2002.1024013
- Kirsch, U., and Moses, F. (1977). Optimization of structures with control forces and displacements. *Eng. Optim.* 3, 37–44. doi: 10.1080/03052157708902375
- Korkmaz, S. (2011). A review of active structural control: challenges for engineering informatics. *Comput. Struct.* 89, 2113–2132. doi: 10.1016/j.compstruc.2011.07.010
- Materazzi, A. L., and Ubertini, F. (2012). Robust structural control with system constraints. *Struct. Control Health Monit.* 19, 472–490. doi: 10.1002/stc.447
- Matunaga, S., and Onoda, J. (1995). Actuator placement with failure consideration for static shape control of truss structures. *AIAA J.* 33, 1161–1163. doi: 10.2514/3.12540
- Neuhäuser, S. (2014). *Untersuchungen zur homogenisierung von spannungsfeldern bei adaptiven schalentragwerken mittels auflagerverschiebung* (Dissertation). Lightweight Structures and Conceptual Design, University of Stuttgart, Stuttgart, Germany.

Static load compensation and active vibration control need to be incorporated in a single control scheme, such that the effect of various loads can be compensated.

DATA AVAILABILITY STATEMENT

All data used in and recorded for this study are available from the authors upon request.

AUTHOR CONTRIBUTIONS

MB, JW, and AG contributed to the presented methodology. CS, JW, AG, and MB conducted the implementations. JW, AG, and MB wrote sections of the manuscript. PA was responsible for the experimental hardware where measurements were conducted. OS and CT provided approval for publication. All authors intensively and critically discussed the content, contributed to manuscript revision, read, and approved the submitted version.

FUNDING

The authors gratefully acknowledge the generous funding of this work by the German Research Foundation (DFG—Deutsche Forschungsgemeinschaft) as part of the Collaborative Research Centre 1244 (SFB) Adaptive Skins and Structures for the Built Environment of Tomorrow, B04, B03, A06, Z01.

- Neuhäuser, S., Weickgenannt, M., Witte, C., Haase, W., Sawodny, O., and Sobek, W. (2013). Stuttgart smartshell-a full scale prototype of an adaptive shell structure. *J. Int. Assoc. Shell Spat. Struct.* 54, 259–270.
- OECD (2015). *Material Resources, Productivity and the Environment*. OECD Publishing. doi: 10.1787/9789264190504-en
- Pellegrino, S. (1990). Analysis of prestressed mechanisms. *Int. J. Solids Struct.* 26, 1329–1350. doi: 10.1016/0020-7683(90)90082-7
- Preumont, A. (1997). *Vibration Control of Active Structures, Vol. 2*. Berlin; Heidelberg: Springer. doi: 10.1007/978-94-011-5654-7
- Reksowardojo, A. P., and Senatore, G. (2020). A proof of equivalence of two force methods for active structural control. *Mech. Res. Commun.* 103:103465. doi: 10.1016/j.mechrescom.2019.103465
- Reksowardojo, A. P., Senatore, G., and Smith, I. F. (2020). Design of structures that adapt to loads through large shape changes. *J. Struct. Eng.* 146:04020068. doi: 10.1061/(ASCE)ST.1943-541X.0002604
- Saggere, L., and Kota, S. (1999). Static shape control of smart structures using compliant mechanisms. *ALAA J.* 37, 572–578. doi: 10.2514/2.775
- Senatore, G., Duffour, P., and Winslow, P. (2018a). Energy and cost assessment of adaptive structures: case studies. *J. Struct. Eng.* 144:04018107. doi: 10.1061/(ASCE)ST.1943-541X.0002075
- Senatore, G., Duffour, P., and Winslow, P. (2019). Synthesis of minimum energy adaptive structures. *Struct. Multidisc. Optim.* 60, 849–877. doi: 10.1007/s00158-019-02224-8
- Senatore, G., Duffour, P., Winslow, P., and Wise, C. (2018b). Shape control and whole-life energy assessment of an-infinitely stiff-prototype adaptive structure. *Smart Mater. Struct.* 27:015022. doi: 10.1088/1361-665X/aa8cb8
- Sener, M., Utku, S., and Wada, B. K. (1994). Geometry control in prestressed adaptive space trusses. *Smart Mater. Struct.* 3:219. doi: 10.1088/0964-1726/3/2/018
- Sobek, W., and Teuffel, P. (2001). Adaptive systems in architecture and structural engineering. *Proc. SPIE*. 4330, 36–45. doi: 10.1117/12.434141
- Spencer, B. Jr, and Nagarajaiah, S. (2003). State of the art of structural control. *J. Struct. Eng.* 129, 845–856. doi: 10.1061/(ASCE)0733-9445(2003)129:7(845)
- UN, Department of Economic and Social Affairs, Population Division (2015). *World Urbanization Prospects: The 2014 Revision*. ST/ESA/SER.A/36.
- UN, Department of Economic and Social Affairs, Population Division (2017). *World Population Prospects: The 2017 Revision, Key Findings and Advanced Tables*. Working Paper No. ESA/P/WP/248.
- Wächter, A., and Biegler, L. T. (2006). On the implementation of an interior-point filter line-search algorithm for large-scale nonlinear programming. *Math. Programm.* 106, 25–57. doi: 10.1007/s10107-004-0559-y
- Wagner, J. L., Böhm, M., and Sawodny, O. (2019a). “Nonlinear modeling and control of tension-only elements in adaptive structures,” in *SMART, 9th ECCOMAS Thematic Conference on Smart Structures and Materials* (Paris), 90–101.
- Wagner, J. L., Böhm, M., and Sawodny, O. (2020). “Decentralized control design for adaptive structures with tension-only elements,” in *Proc. of IFAC World Congress* (Berlin).
- Wagner, J. L., Gade, J., Heidingsfeld, M., Geiger, F., von Scheven, M., Böhm, M., et al. (2018). On steady-state disturbance compensability for actuator placement in adaptive structures. *At-Automatisierungstechnik* 66, 591–603. doi: 10.1515/auto-2017-0099
- Wagner, J. L., Schmidt, K., Böhm, M., and Sawodny, O. (2019b). “Optimal actuator placement and static load compensation for Euler-Bernoulli beams with spatially distributed inputs,” in *IFAC Symposium on Mechatronic Systems* (Wien). doi: 10.1016/j.ifacol.2019.11.723
- Weidner, S., Kelleter, C., Sternberg, P., Haase, W., Geiger, F., Burghardt, T., et al. (2018). The implementation of adaptive elements into an experimental high-rise building. *Steel Construct.* 11, 109–117. doi: 10.1002/stco.201810019
- Yao, J. (1972). Concept of structural control. *ASCE J. Struct. Div.* 98, 1567–1574.

Conflict of Interest: The authors declare that the research was conducted in the absence of any commercial or financial relationships that could be construed as a potential conflict of interest.

Copyright © 2020 Wagner, Gienger, Stein, Arnold, Tarín, Sawodny and Böhm. This is an open-access article distributed under the terms of the Creative Commons Attribution License (CC BY). The use, distribution or reproduction in other forums is permitted, provided the original author(s) and the copyright owner(s) are credited and that the original publication in this journal is cited, in accordance with accepted academic practice. No use, distribution or reproduction is permitted which does not comply with these terms.

APPENDIX

TABLE A1 | Values according to **Figure 6** (top) and **Figure 11** (bottom).

Point	Ref. (mm)	Displacements under load			Displacements with compensation			
		Sim. (mm)	Meas. (mm)	Diff. to sim. (%)	Sim. (mm)	Meas. (mm)	Diff. to sim. (%)	Diff. to ref. (%)
1	0	0	0	0.0	0	0	0.0	0.0
2	260	260	260	0.0	260	260	0.0	0.0
3	0	14	29	0.7	0	5	0.2	0.2
4	260	274	289	0.7	260	265	0.3	0.3
5	0	42	46	0.2	0	13	0.7	0.7
6	260	302	307	0.2	260	273	0.6	0.7
7	0	80	78	−0.1	−1	6	0.3	0.4
8	260	340	337	−0.1	259	266	0.3	0.4
9	0	125	98	−1.4	0	4	0.2	0.2
10	260	385	356	−1.4	260	264	0.2	0.2
11	0	173	115	−2.9	2	3	0.2	0.1
12	260	433	373	−3.0	262	263	0.2	0.1

Point	Ref. (mm)	Compensation		Faulty compensation		Reconfigured compensation	
		Meas. (mm)	Diff. (%)	Faulty (mm)	Diff. (%)	Reconfigured (mm)	Diff. (%)
1	0	0	0.0	0	0.0	0	0.0
2	260	260	0.0	260	0.0	260	0.0
3	0	5	0.2	11	0.6	−1	0.0
4	260	265	0.3	271	0.6	259	0.0
5	0	13	0.7	16	0.8	1	0.1
6	260	273	0.6	276	0.8	261	0.1
7	0	6	0.3	27	1.3	−1	−0.1
8	260	266	0.3	287	1.3	259	−0.1
9	0	4	0.2	34	1.7	−1	−0.1
10	260	264	0.2	294	1.7	259	−0.1
11	0	3	0.2	44	2.2	3	0.1
12	260	263	0.2	304	2.2	263	0.1

Simulated and measured displacements are given in (mm). The differences are given as percentage (%) with respect to the height of the scale model (2 m).

TABLE A2 | Table displaying the data of **Figure 8**.

Actuator	Act. type	Actuator forces under load			Actuator forces under compensation		
		Desired (N)	Actual (N)	Diff. (%)	Desired (N)	Actual (N)	Diff. (%)
1	Parallel				78.0	79.1	1.3
2	Parallel				−114.5	−113.8	−0.6
3	Parallel				−190.8	−183.3	−3.9
4	Parallel				139.4	138.7	−0.5
5	Serial	64.4	64.0	−0.7	100.8	117.5	16.6
6	Serial	85.7	137.3	60.2	127.4	123.5	−3.1
7	Serial	31.7	32.6	2.9	48.7	37.4	−23.2
8	Parallel				−18.6	−18.1	−2.6
9	Parallel				−62.5	−135.0	116.2
10	Parallel				−238.1	−157.5	−33.8
11	Parallel				189.3	213.6	12.8
12	Serial	19.6	20.0	1.7	19.9	20.5	3.0
13	Serial	74.1	45.8	−38.2	91.4	44.1	−51.8
14	Serial	−8.4	−8.5	0.6	−8.4	−13.3	57.8
15	Serial	−8.1	−3.9	−52.3	29.2	30.3	3.9
16	Parallel				9.2	−25.4	−375.2
17	Parallel				−172.4	−153.1	−11.2
18	Parallel				84.2	168.9	100.6
19	Serial	16.4	16.6	1.4	16.6	12.7	−23.9
20	Serial	93.0	51.3	−44.8	91.4	72.8	−20.3
21	Serial	35.0	34.1	−2.6	102.7	62.3	−39.3
22	Serial	15.8	15.6	−1.3	52.2	55.6	6.4
23	Serial	53.9	25.6	−52.4	53.9	34.2	−36.6
24	Serial	72.7	63.0	−13.4	99.0	51.3	−48.2
25	Serial	12.5	37.2	196.6	23.2	31.1	34.2

All actuator forces are given in (N). The differences are given as percentage (%) with respect to the desired values.



Vibration Suppression Through Variable Stiffness and Damping Structural Joints

Qinyu Wang^{1*}, Gennaro Senatore^{2*}, Kaspar Jansen³, Arjan Habraken¹ and Patrick Teuffel¹

¹ Department of Built Environment, Chair of Innovative Structural Design (ISD), Eindhoven University of Technology, Eindhoven, Netherlands, ² Applied Computing and Mechanics Laboratory, School of Architecture, Department of Civil and Environmental Engineering, Swiss Federal Institute of Technology (EPFL), Lausanne, Switzerland, ³ Department of Industrial Design Engineering, Delft University of Technology, Delft, Netherlands

OPEN ACCESS

Edited by:

Dryver R. Huston,
University of Vermont, United States

Reviewed by:

Shinta Yoshitomi,
Ritsumeikan University, Japan
Christian Málaga-Chuquitaype,
Imperial College London,
United Kingdom
Wei Song,
University of Alabama, United States

*Correspondence:

Qinyu Wang
q.wang2@tue.nl
Gennaro Senatore
gennaro.senatore@epfl.ch

Specialty section:

This article was submitted to
Structural Sensing,
a section of the journal
Frontiers in Built Environment

Received: 10 April 2020

Accepted: 03 September 2020

Published: 30 October 2020

Citation:

Wang Q, Senatore G, Jansen K, Habraken A and Teuffel P (2020) Vibration Suppression Through Variable Stiffness and Damping Structural Joints. *Front. Built Environ.* 6:550864. doi: 10.3389/fbuil.2020.550864

This paper introduces a new semi-active strategy for vibration control of truss and frame structures equipped with variable stiffness and damping joints which consist of a shape memory polymer (SMP) core reinforced by an SMP-aramid composite skin. When the joints are actuated to the transition temperature through thermal actuation, the SMP core transitions from a glassy to a rubbery state through a viscoelastic region, which causes a stiffness reduction and an increase of damping. The mechanic behavior of the joint can be thought of as transitioning from a moment to a pin connection. This way, it is possible to cause a shift of the structure natural frequencies and to increase damping, which is employed to obtain a significant reduction of the dynamic response. This paper comprises two parts: (1) characterization of a variable stiffness and damping material model through experimental testing; (2) numerical simulations of a truss bridge and a four-story frame, which are equipped with variable stiffness and damping joints. The truss bridge (case A) is subjected to a resonance and a moving load while the four-story frame (case B) is subjected to El Centro earthquake loading. For case A under resonance loading, the dynamic response can be reduced exclusively through a frequency shift and ignoring viscoelastic effects. For case A under moving load and case B under earthquake loading, vibration suppression is mostly caused by the increase of damping due to viscoelastic effects. Control time delays due to joint heating have been included in the analysis. When the joints are actuated to the transition range 55°C–65°C, which is specific to the SMP adopted in this study, the acceleration peak amplitude reduces by up to 95% and 87%, for case A and case B, respectively. For both cases, damping increases by up to 2.2% from undamped conditions (25°C). This work has shown that the adoption of variable stiffness and damping structural joints has great potential to enable a new and effective semi-active control strategy to significantly reduce the structure response under a wide range of dynamic loading conditions.

Keywords: adaptive structures, variable stiffness and damping joint, frequency shift, viscoelastic material, structural dynamics, vibration control

INTRODUCTION

Adaptive Structures

Adaptive structures are equipped with actuators, sensors, and controllers to maintain optimal performance under changing loading conditions. Through mechanical actuation the state of the structure (stress and deformation) can be modified to counteract actively the effect of loading. Structural control strategies have been categorized in four types: active, semi-active, passive, and hybrid (Soong and Spencer, 2000; Preumont and Seto, 2008). Numerical and experimental studies on active bracing for buildings and active tendons for bridges have shown that active control systems can be effectively employed for vibration suppression under strong loading such as high wind or earthquakes (Soong, 1988; Reinhorn et al., 1993; Xu et al., 2003; Mirfakhraei et al., 2019).

Benchmark control problem studies for seismic (Spencer et al., 1998; Ohtori et al., 2004) and wind excited (Yang et al., 2004) buildings have shown that through active control, the structure response (e.g., displacement, acceleration, and inter-story drift) can be reduced significantly more than through passive control. Although active controlled systems are more effective to suppress vibrations than passive ones, they generally require high power density supply and they might require a large energy consumption during service. In addition, due to latency and model inaccuracy, the control forces might cause instability of the structure-control system (Kinay and Turan, 2012; Wang et al., 2017). Semi-active control systems, such as magnetorheological (MR) dampers, require less energy compared to active systems. In addition, they are as reliable as passive devices while maintaining some of the versatility and adaptability of fully active systems (Dyke et al., 1996; Symans and Constantinou, 1999; Yang et al., 2002; Zhao et al., 2019). Generally, closed-loop semi-active control systems perform better than passive ones. Although passive control systems such as base isolation (Huang et al., 2014), viscoelastic and elastoplastic dampers (Kasai et al., 1998) require no control power, they have limited capabilities compared to active and semi-active systems. Hybrid control systems (for example hybrid mass dampers) might combine passive, semi-active and active control strategies and devices (Spencer and Sain, 1997; Kinay and Turan, 2012). For example, a hybrid vibration control system which combines a base isolator and an active tuned mass damper was investigated in Djedoui et al. (2017). This hybrid system was able to reduce by more than 70% the base isolator displacement while keeping the base acceleration within an acceptable range, which was more effective than the response reduction obtained through a passive control system made of a base isolator and a passive tuned mass damper (Djedoui et al., 2017). However, hybrid control systems are generally complex and might involve significant maintenance costs (Gkatzogias and Kappos, 2016).

The ability to counteract the effect of loading actively through control of internal forces and the external geometry, has been employed in integrated structure-control design to produce efficient configurations with a significantly better material utilization (Teuffel, 2004) and a lower whole-life energy (Senatore et al., 2019; Senatore and Reksowardojo, 2020;

Wang and Senatore, 2020) than conventional passive structures. The whole-life energy comprises the energy embodied in the material and the operational energy for control. Extensive numerical (Senatore et al., 2018a,b) and experimental studies (Senatore et al., 2018c) have shown that minimum energy adaptive structures have a lower environmental impact as the total energy requirement can be reduced by up to 70% compared to weight-optimized passive structures. Structural adaptation is particularly beneficial for stiffness governed design problems such as slender high-rise structures, long-span bridges and self-supporting roof systems. When the structure is designed to counteract the effect of loading through controlled large shape changes, further material and embodied energy savings are obtained compared to adaptive structures limited to small shape changes as well as to passive structures (Reksowardojo et al., 2019, 2020). This way, the structure is controlled into optimal shapes as the external load changes so that the stress is significantly homogenized, and the design is not governed by strong loading events which occur rarely. Shape control has also been employed to reduce the dynamic response through shifting the structure natural frequencies (Bel Hadj Ali and Smith, 2010; dos Santos et al., 2015; dos Santos and Cismaşiu, 2017) and for the control of direct daylight in buildings through adaptive façade systems (Lienhard et al., 2011; Lignarolo et al., 2011).

One of the most important aspects in the design of adaptive structures is to consider the mechanical behavior of the joints. Since active control requires some degree of geometry reconfiguration, the joints should be designed to be flexible during control in order to prevent stress build-up and to reduce control energy requirements. Joint mechanisms based on pin-joints or linkages could be employed, however, these systems often add a substantial weight penalty and they are generally complex devices which require maintenance (Campanile, 2005). To address this challenge, a new type of variable stiffness and damping joint has been proposed in previous work (Senatore et al., 2017). The joint has been modeled to have two states: in the “locked” state, it behaves as a moment connection and in the “released” state, it behaves as a pin connection. A numerical study on a Warren truss has shown that by selectively switching the joint states, the structure natural frequencies could be controlled to shift significantly (Wang et al., 2018). In practice, transition from a moment to a pin connection has been realized through control of the joint stiffness (Wang et al., 2020). The joint is made of a polyurethane based shape memory polymer (SMP) core that is reinforced by an SMP-aramid skin. Stiffness variation has been achieved through resistive heating of the joint core material. When the SMP core is heated up to the transition temperature (65°C), a change from a glassy to a rubbery state occurs, which causes a significant stiffness reduction of the joint and a parallel damping increase due to viscoelastic effects. The material behavior has been fully characterized through Dynamic Mechanical Analysis (Wang et al., 2020).

Most semi-active control strategies aim to mitigate the structure response by appropriate adjustments of the magnitude of control forces that develop through motion (e.g., electrorheological dampers, magnetorheological dampers, fluid viscous dampers). Semi-active strategies based on stiffness and

damping control instead, aim to mitigate the structure response by tuning its dynamics characteristics. Existing semi-active stiffness and damping control devices comprise several parts and require complex joint detailing to be installed (Kobori et al., 1993; Sarlis et al., 2013; Shu et al., 2017). The ability to tune stiffness and damping of the joint itself, as formulated in this work, allows for a new type of semi-active stiffness and damping control device. In this case the device is completely integrated because it is part of the structure i.e., the joint is the semi-active device. Numerical simulations on a planar frame equipped with two variable stiffness and damping joints have shown that it is possible to significantly reduce the structure response under resonance loading solely through thermal actuation of the joints. The state change of the joints caused up to 8.72% shift of the first natural frequency and an increase of damping up to 1.2% from undamped conditions (25°C) due to viscoelastic effects (Wang et al., 2020).

Smart Materials for Structural Control

Smart materials such as magnetorheological elastomers, shape memory alloys and polymers have been employed for shock isolation (Ledezma-Ramirez et al., 2011), vibration suppression (Bonello et al., 2005) and shape control applications (Kuder et al., 2013). Shape memory alloy (SMA) linear actuators were applied in shape control of a tensegrity tower to mitigate the structure dynamic response (dos Santos et al., 2015). Magnetorheological elastomer elements have been used as tunable springs to design vibration isolators with tunable stiffness and damping (Du et al., 2011; Liao et al., 2012). Shape memory polymers (SMPs) can move from a deformed shape to an undeformed stress-free shape through thermal, electric and magnetic actuation (Leng et al., 2011; Meng and Li, 2013). SMPs feature large stiffness variation (up to 1,000 times) between a glassy and a rubbery state (Liu et al., 2006; Hu et al., 2017b). Below the transition temperature T_g , the polymer is stiff with a modulus of approximately 1 GPa whereas above T_g , the polymer has a rubbery elastic behavior with a modulus which is approximately two decades (i.e., order of magnitude) lower. SMPs have received attention for application as actuators and smart textiles in deployable and morphing structures (Liu et al., 2011). For example, SMA stripes have been embedded in a SMP matrix for a wind-responsive façade system (Lignarolo et al., 2011). A fiber reinforced SMP hinge has been tested to control the orientation of a solar array prototype in order to maximize solar gain (Lan et al., 2009). It was possible to change the orientation of the solar array by 90° in 80 s. However, application of SMPs in load-bearing structures has been limited due to low mechanical strength. The addition of continuous fibers (for example carbon, glass, and aramid fibers) significantly increases mechanical strength in the fiber direction while keeping the shape memory effect in the transverse direction (Gall et al., 2000; Lan et al., 2009). Generally, shape memory polymer composites (SMPC) are more suitable for application in load-bearing structures (Liu et al., 2011; Hu et al., 2017a).

Outline

Own previous work (Wang et al., 2020) focused on design and characterization of variable stiffness and damping structural

joints to be employed as semi-active control devices. This work builds on and generalizes the conclusions reached in Wang et al. (2020) by evaluating the capability of this new semi-active stiffness and damping control device through simulations on more complex structural configurations and loading scenarios. This paper is arranged as follows. Section “Variable Stiffness and Damping Joint” describes the main features of the variable stiffness and damping joint material including characterization through Dynamic Mechanical Analysis. Section “Thermal Actuation” describes numerical simulations of a truss bridge subjected to a resonance and a moving load. Section “Case Study B: Four-Story Frame” describes numerical simulations of a four-story frame subjected to earthquake loading. Both structures are equipped with variable stiffness and damping joints. Joint stiffness and damping control are employed as a strategy to reduce the structure dynamic response through a shift of the natural frequencies as well as an increase of damping due to viscoelastic effects. Section “Discussion” and “Conclusion” conclude this paper.

VARIABLE STIFFNESS AND DAMPING JOINT

The variable stiffness and damping joints considered in this study consists of an SMP core and an SMP-aramid composite skin which acts as a reinforcement (see section “SMP-aramid Skin: Isotropic Elastic Material Model”). **Figure 1** shows an example of such joint. The joints were manufactured to be integrated in a 650 mm × 650 mm × 1325 mm three-story frame prototype which is shown in **Figure 1A** for illustration purposes. **Figure 1B** shows an example of a joint core. The core is fabricated through fused deposition modeling (FDM). The filament used for 3D printing is obtained from a polyurethane-based SMP (MM5520) which is made by SMP Technologies Inc. MM5520 is a pellet type SMP with a nominal transition temperature of 55°C (as reported by the manufacturer). A 1 mm diameter resistive heating wire is passed through the joint core through a series of holes which have been made through selective deposition. **Figure 1C** shows the heating wire weave pattern from the back side of the joint core. **Figure 1D** shows a joint core connected to four aluminum tubes using structural glue (Pattex 100%). **Figure 1E** shows the assembly (joint + elements) after the reinforcement skin is applied (Wang et al., 2020).

Material Characterization

Polymers are materials whose stiffness depends on temperature as well as time (creep) and loading frequency. The standard procedure to characterize viscoelastic behavior is to use a setup in which loading frequency and temperature are varied systematically (Menard, 2008). In previous work (Wang et al., 2020), the thermomechanical properties of a 3D printed SMP strip have been fully characterized through Dynamic Mechanical Analysis (DMA) using a Q800 tester. **Figure 2A** shows the plots of storage modulus E' , loss modulus E'' and $\tan \delta$ as functions of the temperature at 1 Hz. The storage modulus E characterizes the

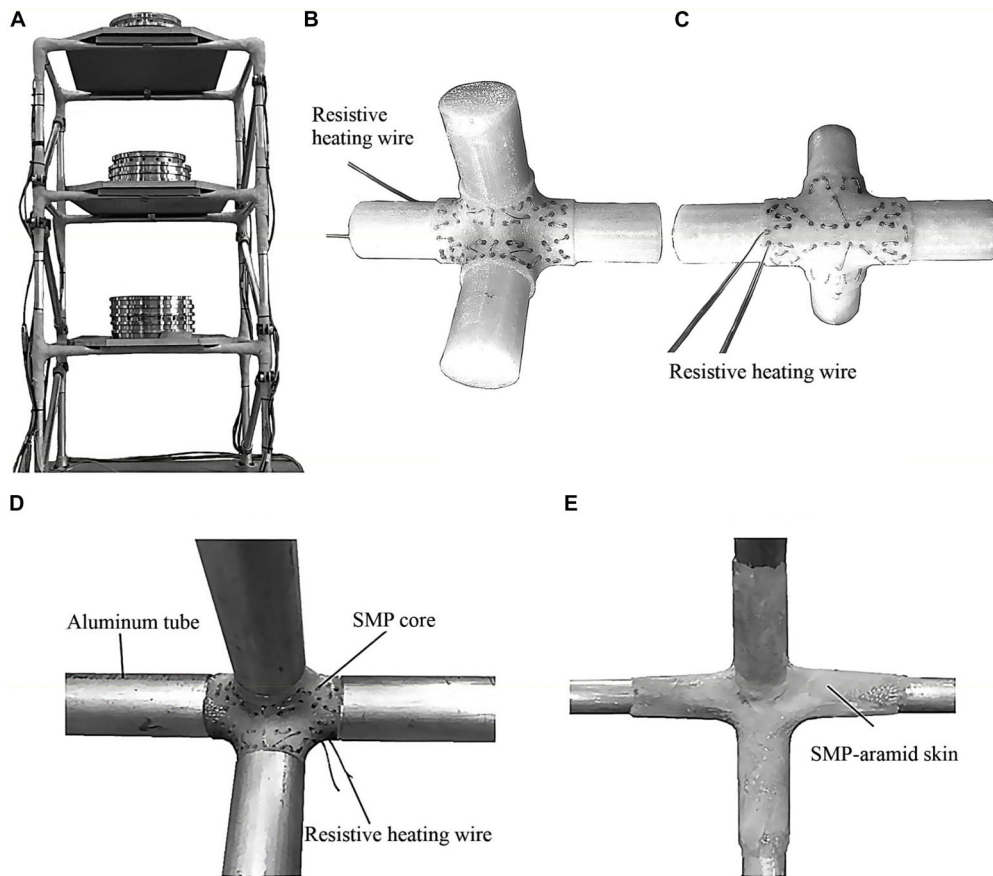


FIGURE 1 | (A) Integration of variable stiffness and damping joints into a 3-story prototype frame; **(B,C)** SMP core with heating wire; **(D)** joint core connected to four aluminum tubes; **(E)** SMP-aramid reinforcement skin (Wang et al., 2020).

elastic part of the material behavior in which strain and stress are in phase as for any other elastic material.

When the material enters the viscoelastic region (opaque region in **Figure 2A**), caused by an increase of temperature, strain and stress are out of phase, which is indicated by the loss modulus E'' . The ratio $\tan \delta = E''/E'$ is a measure of damping (Menard, 2008; ISO-6721-1, 2011). Through DMA testing, it was found that the transition temperature is 65°C (Wang et al., 2020). During glass transition (40°C – 65°C), the storage modulus drops from 1,340 to 37 MPa while damping increases significantly (approximately by a factor of 60). However, as the temperature is increased above the transition value, damping decreases because the material enters the rubbery state which has an elastic behavior.

Time-temperature superposition principle is employed in order to map experimental data obtained at different temperatures and frequencies on a single master curve (Ferry, 1980), which is shown in **Figure 2B**. **Figure 2B** also shows the plot of the shift factor curve which relates the change of stress relaxation rate with temperature. The shift factor curve is used to extrapolate to frequencies other than those tested experimentally in order to characterize the viscoelastic behavior in the entire temperature-frequency domain, i.e., to obtain the master curve.

The dashed lines in **Figure 2B** are the storage modulus curves measured in the frequency range 0.32–32 Hz and temperature range 40°C – 85°C . The shift factor curve has been approximated by fitting the Williams–Landel–Ferry (WLF) function to the measured data:

$$\log(a_T) = \frac{-C_1(T - T_{ref})}{C_2 + (T - T_{ref})} \quad (1)$$

where a_T is the shift factor. The constants C_1 and C_2 , which have been calculated through fitting, are 14.6 and 24.2, respectively. At the reference temperature $T_{ref} = 50^{\circ}\text{C}$ the shift factor is set to 1. The storage modulus curve in this case is indicated by square markers. The moduli at a temperature and at a frequency that have not been tested through DMA, are obtained by shifting along the frequency axis using the shift factor curve. For example, at 60°C the shift factor a_T is approximately 10^4 which means that stress relaxation is faster by a factor of 10^4 . Consequently, the storage modulus curve at 60°C , which is indicated by circle markers, shifts by a factor of 10^4 to the left to form the master curve. For a more detailed description of the material model the reader is referred to (Wang et al., 2020).

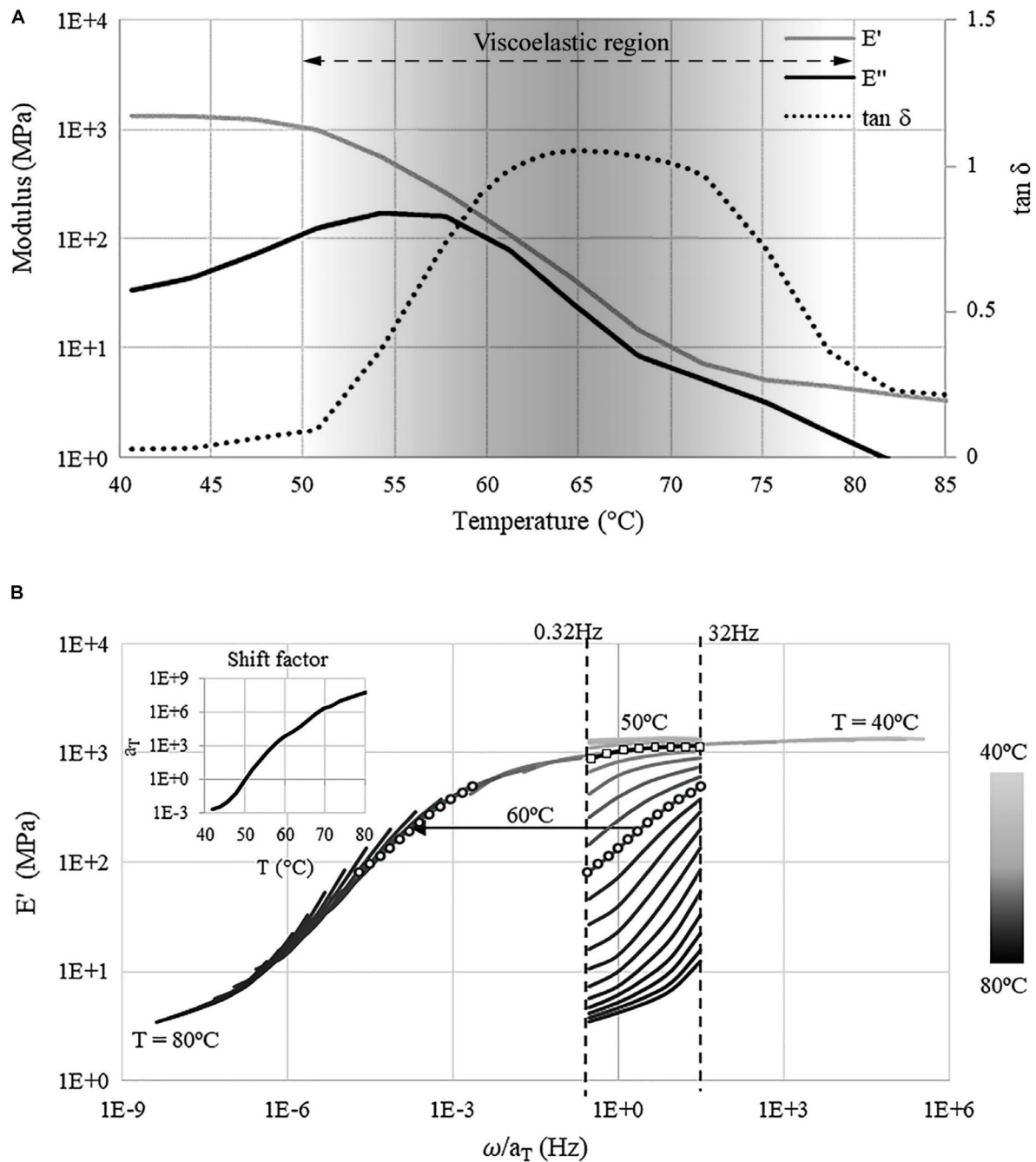


FIGURE 2 | (A) Storage E' , loss E'' modulus, and $\tan \delta$ vs. temperature at 1 Hz; **(B)** master and shift factor curves ($T_{ref} = 50^\circ\text{C}$). Both **(A,B)** have been obtained through experimental testing (Wang et al., 2020).

In addition to the viscoelastic material model, a simpler thermo-elastic model is considered in which frequency dependent effects are neglected and thus the modulus only changes with temperature. For this temperature-only dependent elastic model, the storage modulus curve measured at 1 Hz (Figure 2) is adopted. This way, stiffness variation through temperature is decoupled from damping variation due to viscoelasticity. This simplified material model will be employed

for modal analysis as well as transient analysis through mode superposition for the truss bridge (case A) under resonance loading. For the configurations under moving (case A) and earthquake loading (multi-story frame, case B), full transient analysis will be carried out using both thermo-elastic and viscoelastic material model in order to evaluate the combined effect of frequency shift and damping variation on the structure response.

SMP-aramid Skin: Isotropic Elastic Material Model

To reduce potentially excessive deformations of the joint core when it is thermally actuated in the transition range, a reinforcement skin is applied. This skin consists of a stack of woven aramid fabric layers which are impregnated with SMP material to form a stiff and thin composite. The individual fabric layers have fibers oriented at 0° and 90° which feature an anisotropic behavior to loading. Generally, the joints have a complex geometry to connect multiple elements and hence they are likely to be subjected to bending and torsion. For this reason, the reinforcement skin should behave as an isotropic material. Therefore, two additional fabric layers with a 45° orientation have been added, which has resulted in a quasi-isotropic skin with a modulus of approximately 8,320 MPa and a thickness of 1.72 mm (Wang et al., 2020). Thicker skins may be needed to prevent excessive deformation of the joint if high loads are applied, in which case additional 0° and 45° layers might be added. The reader is referred to (Wang et al., 2020) for more information regarding the reinforcement skin design and related experimental testing.

SEMI-ACTIVE CONTROL STRATEGY

Feedforward Control

It is clear from material characterization (section “Material Characterization”) that the damping ratio increase caused by viscoelastic effects is the highest when the joint core is thermally actuated in the transition range. It will be shown through full transient analysis (sections “Thermal Actuation” and “Case Study B: Four-Story Frame”) that mitigation of the structure response under dynamic excitation is mostly caused by the increase of damping of the joints. Under excitations that have several high-energy frequency components (e.g., earthquake loading), generally the effect of damping is dominant even when, due to the structure frequency shift that is caused by joint stiffness reduction, a temporary resonance condition arises. For this reason, a simple feedforward control scheme is proposed to mitigate the structure response through thermal actuation of the joints.

Assume a generic multi-story building which is equipped with variable stiffness and damping joints. Accelerometers are installed at each floor. Thermocouples are embedded during fabrication in the core of each joint to monitor the temperature. **Figure 3A** shows an example of a seismic excitation (in this case El Centro earthquake loading). **Figure 3B** shows the non-controlled as well as controlled acceleration response of the structure. **Figure 3C** shows the temperature control law for the joints. Thermal actuation of the joints is switched on when the ground acceleration is higher than a set threshold (point 1). The set-point for the joint temperature is set to the transition value. The joint temperature is regulated independently through feedback control. Once the joint temperature reaches the transition value (point 2), the temperature is kept constant. The response of the structure is reduced through the combined effect of frequency shift and damping increase. Once the ground

acceleration reduces below the set threshold (point 3), the joint temperature is kept at the transition value for a certain time period (stand-by) after which, if no further increase of ground acceleration is measured, thermal actuation is switched off (point 4). The joint temperature reduces to the field temperature through natural cooling (point 5). **Figure 3D** shows a schematic flow-chart of the feedforward control scheme including the feedback loop for joint temperature modulation.

Thermal Actuation

Generally, the temperature increase rate through thermal actuation depends on the type of heat transfer technology and activation stimulus of the SMP material (e.g., resistive and magnetic actuation). Assuming thermal actuation through resistive heating, the energy required to actuate the joint from ambient to transition temperature is:

$$Q_1 = cm\Delta T \quad (2)$$

where c is the specific heat capacity of the joint core material and ΔT is the required temperature change. The heat energy generated through resistive heating is:

$$Q_2 = \frac{U^2}{R}t = Pt \quad (3)$$

where U is the power supply voltage; R is the resistance of the heating element; t is the heating time and $P = \frac{U^2}{R}$ is the power rating of the heating element. If heat transfer time and energy dissipation are ignored, let $Q_1 = Q_2$. For the case studies considered in this work, the average mass of the joints is 9 kg. Assuming the specific heat capacity of SMP joint core is 1.4 kJ/(kg°C), a rough estimate of the heat energy it takes to actuate the joint from ambient (25°C) to transition temperature (65°C) is 504 kJ. Assuming an appropriate power supply, five heating elements with a power rate of 20 kW suffice to limit the required heating time to 5 s.

Note that a transition temperature of 65°C is specific to the type of SMP that is adopted in this study which was selected primarily based on commercial availability. However, there exist several other SMP materials which feature a transition temperature that varies from 10°C to 178°C (Kusy and Whitley, 1994; Takahashi et al., 1996; Kumar et al., 2014). The SMP material specifics can be therefore chosen depending on location to minimize control effort and energy requirements by limiting interference with field temperature and the effect of seasonal temperature variation.

CASE STUDY A: TRUSS BRIDGE

Model Features

Structural Model

The structure considered in this study is a simply supported planar truss which is designed as a truss bridge reduced to two dimensions. **Figure 4A** shows dimensions and support conditions. The span and rise of the truss are 8 and 0.5 m, respectively. The structure is equipped with seven variable stiffness and damping joints which are indicated by the yellow

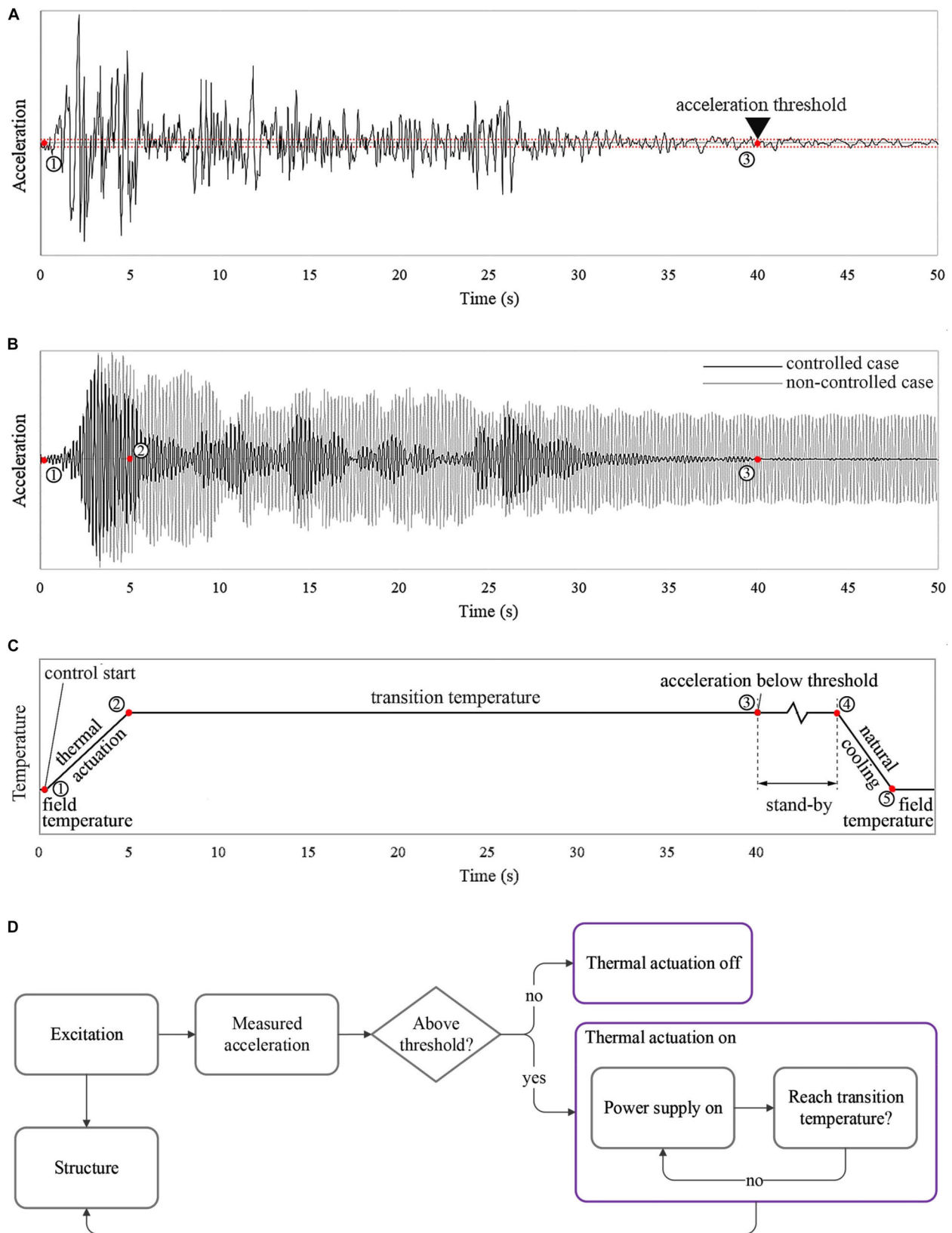
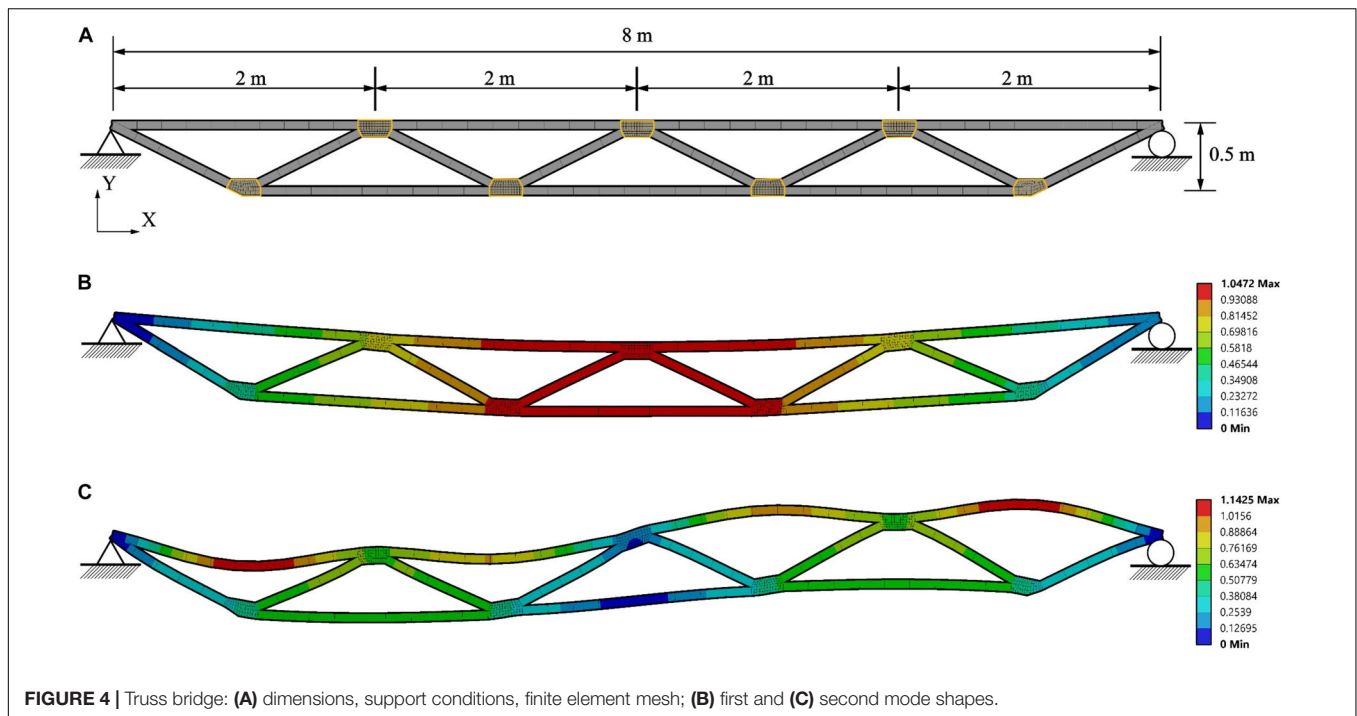


FIGURE 3 | Semi-active control strategy: **(A)** ground acceleration; **(B)** non-controlled and controlled acceleration response; **(C)** joint temperature control law; **(D)** control strategy flow-chart.



contour lines in **Figure 4A**. The adaptive joints are installed at all nodes except for the supports. The finite element model comprises beam elements of type BEAM188 for the chords and bracings as well as solid elements of type SOLID186 for the joints. The beam element material is structural steel S355. The beams have a 60 mm × 60 mm square hollow section and a wall thickness of 8 mm. The joint element material is the SMP material described in section “Variable Stiffness and Damping Joint.” Each solid element is a cuboid with edges of approximately 20 mm to mesh the joint geometry. The joint geometry has been obtained so that the beam elements connect to it through a section perpendicular to their axis. The beam sections are connected to the joint elements through a fixed contact. The reinforcement skin is modelled with “surface coating” elements of type SURF156 with a thickness of 5.16 mm which is obtained by stacking three layers of the SMP-aramid composite described in section “SMP-aramid Skin: Isotropic Elastic Material Model” (1.72 mm per layer). Since the skin is applied on the outer surface of the joint where the temperature is the lowest, it is assumed that the skin material is always in the glass state and therefore it has an elastic and temperature independent behavior. A modulus of 8320 MPa and an ultimate stress of 107 MPa is assumed for the reinforcement skin material based on experimental data (Wang et al., 2020).

Loading and Analysis Setting

The structure is subjected to a dead load which is uniformly distributed on the top chord members with an intensity of 200 kg/m² and assuming 2 m of cover. Depending on the analysis type, additional loading will be applied. Static analysis is carried out under a uniformly distributed live load to evaluate the static response as the joint temperature increases. Transient analysis

with mode superposition is carried out under resonance loading to test vibration control through frequency shift but ignoring damping variation due to viscoelastic effects. Full transient analysis using the viscoelastic material model is carried out to test the combined effect of frequency shift and damping variation on the structure dynamic response under a moving load. Since the location of the degree of freedom subjected to maximum displacement and acceleration changes with time, an average value among all degrees of freedom is taken because it is more representative of the dynamic response. The average value of the displacements is denoted as “deformation.”

In each analysis the joints are assumed to be actuated through resistive heating from ambient 25°C to transition temperature 65°C. Two types of thermal load are considered: (1) a constant thermal load is applied to increase the joint temperature in discrete steps; (2) following from the assumptions made in section “Thermal Actuation” with regard to the thermal actuation system, a time-linear thermal load is applied to increase the joint temperature from 25°C to 65°C in 5 s. Under constant thermal load the joints are assumed to be at a prescribed temperature when the load is applied and therefore the time it takes to increase the temperature is not taken into account. Under time-linear thermal load, time delays due to heating are included in the analysis.

All simulations are carried out in Ansys Workbench.

Static Analysis

In addition to the dead load defined in section “Model Features,” a uniformly distributed live load with an intensity of 350 kg/m² and assuming 2 m of cover is applied on the top chord members. A comparison between with and

without reinforcement skin is carried out. When the joints are actuated from 25°C to 65°C, the maximum static deformation of the structure increases from 44.7 to 1095.8 mm without reinforcement skin and from 23.2 to 33.5 mm with reinforcement skin. This clearly indicates the importance of applying the SMP-aramid reinforcement skin to reduce excessive deformation of the joints which occurs when they are thermally actuated to the transition range. Due to stiffness reduction caused by temperature increase, the maximum stress (von Mises) in the joint core decreases significantly from 11.1 to 1.2 MPa. Conversely, the maximum stress (von Mises) in the skin increases from 57.1 to 88.2 MPa.

Frequency Shift and Damping Variation

Joint stiffness variation causes a simultaneous shift of the structure natural frequencies and a damping variation. In this section these two effects are studied separately. Modal analysis is carried out using the thermo-elastic material model for the joints to evaluate the frequency shift caused by joint stiffness variation but ignoring frequency dependent effects. A free vibration test is carried out through full transient analysis using the viscoelastic material model for the joints in order to evaluate how the damping varies due to viscoelastic effects.

Frequency Shift

The first and second modes are observed as the joints are actuated from ambient to transition temperature (25–65°C). The natural frequencies and frequency shifts are indicated by $\omega_1 - S_{\omega 1}$ and $\omega_2 - S_{\omega 2}$ for the first and second mode, respectively. Results are given in **Table 1**. Due to the joint stiffness reduction, the structure natural frequency shifts up to 16.5% for the first mode and 10.24% for the second mode. The first and second mode shapes of the truss at 25°C are shown in **Figures 4B,C**.

Damping Variation

To quantify the damping variation caused by viscoelastic effects, a free vibration test is simulated. The joints are actuated from ambient to transition temperature (25°C–65°C). A 1 N impulse is applied in the middle of the bottom chord elements for 0.01 s in order to excite the first mode. The average deformation as a function of time for 40°C, 45°C, 50°C, 55°C, 60°C, and 65°C is shown in **Supplementary Figure A1**. The deformation vs. frequency curves shown in **Table 1** are obtained from Fast Fourier transform (FFT). The peak indicates the structure natural frequency which reduces (shift to the left) when the joint temperature increases from 40°C to 65°C. Results from the free vibration test simulation in terms of frequency shift are in good accordance to what has been observed through modal analysis. At 40°C, the first mode frequency computed through modal analysis and FFT is 5.75 and 5.67 Hz, respectively. The difference in percentage terms is 1.4%. At 55°C, this difference reaches a maximum value of 2.5% (5.23 Hz from modal analysis and 5.36 Hz from FFT).

The half-power bandwidth method is employed to compute the damping ratio. This method can be applied to a multi-degree-of-freedom system when the modes are well-separated. For unnormalized spectra, the damping ratio ζ can be computed from Eq. 4 (Butterworth et al., 2004). It is assumed that half the total power dissipation occurs between f_1 and f_2 which are the frequencies corresponding to an amplitude of $f_{res}/\sqrt{2}$ where f_{res} is the frequency corresponding to the peak (i.e., resonance) (Butterworth et al., 2004).

$$\zeta = \frac{f_{res}(f_1 - f_2)}{(f_1^2 + f_2^2)} \quad (4)$$

The half-power bandwidth frequencies for the first mode at 65°C and the damping ratios at different temperatures are given in **Table 1**. The structure damping increases by up to 2.22% from undamped conditions (25°C) as the joints are actuated to 60°C and then it decreases as the temperature increases further. This trend is in accordance to what has been observed in section “Material Characterization.” Above transition temperature (65°C) damping decreases because the SMP material leaves the viscoelastic region and it enters the rubbery state (elastic). This explains why the peak amplitude for the deformation vs. frequency curve at 65°C is higher than that at 60°C (**Table 1**). At 65°C, the damping ratio (1.4%) is lower than that of 60°C (2.22%), hence the peak amplitude is higher.

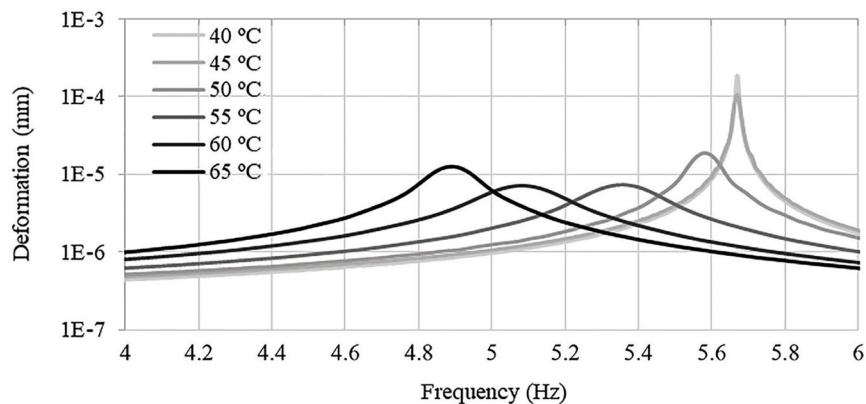
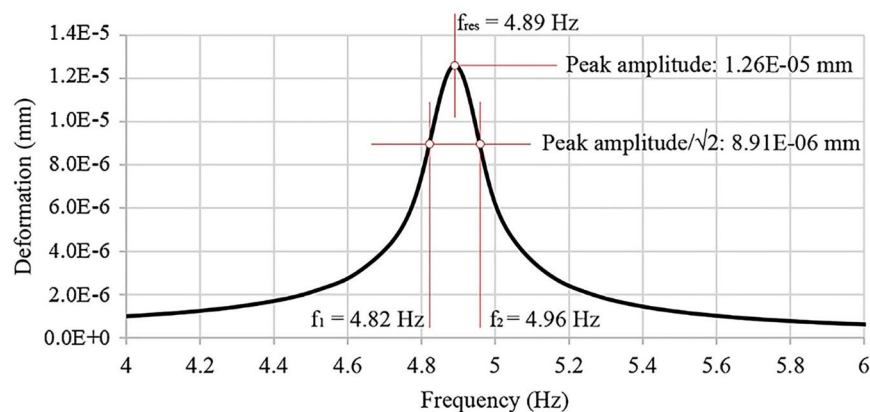
Vibration Control Under Resonance Loading

Mode superposition analysis is carried out to evaluate dynamic response mitigation under resonance loading through frequency shift. A sinusoidal load $q_s = A \sin(2\pi\omega_e t)$ with an amplitude $A = 500$ N is linearly distributed on the top chord elements in order to excite the first mode. The excitation frequency is identical to the structure first natural frequency at 25°C $\omega_1 = \omega_e = 5.85$ Hz. **Figure 5** shows the average deformation vs. time at 25°C, 45°C, 50°C, 55°C, 60°C, and 65°C. At 25°C, the deformation amplitude of the truss increases steadily because of resonance. When the joints are actuated to 45°C, the deformation peak decreases significantly due to a 2.14% frequency shift (see **Table 1**). As the temperature increases, the frequency shift increases and therefore the average deformation peak amplitude reduces by 82% (from 141 mm after 5 s at 25°C to 25 mm at 65°C). In addition, since the natural frequency reduces, the period of the single cyclic pulsation (the so called “beat”) $T_b = 1/|\omega_1 - \omega_e|$ also reduces progressively as shown in **Figures 5C–F**.

As the stiffness of the joint decreases with the temperature, the maximum stress (von Mises) in the joint decreases from 91 MPa at 25°C to 1.2 MPa at 65°C. Since the reinforcement skin is stiffer than the joint, it takes most of the stress which also decreases as the temperature increases due to the reduction of deformation caused by the frequency shift. The maximum stress in the reinforcement skin decreases from 477 MPa (resonance case) to 315 MPa at 40°C, 256 MPa at 45°C, 147 MPa at 50°C, 97 MPa at 55°C, 93 MPa at 60°C, and 94 MPa at 65°C.

TABLE 1 | Truss bridge: frequency, frequency shift, and first modal damping ratio.

	25°C	40°C	45°C	50°C	55°C	60°C	65°C
ω_1 (Hz)	5.85	5.75	5.72	5.59	5.23	4.98	4.88
ω_2 (Hz)	15.88	15.74	15.71	15.50	14.91	14.45	14.26
S_{ω_1} (%)	–	1.67	2.14	4.50	10.62	14.89	16.50
S_{ω_2} (%)	–	0.88	1.13	2.44	6.15	9.06	10.24
ζ_1 (%)	–	0.09	0.10	0.73	1.94	2.22	1.40

Deformation vs frequency from FFT for 1st modeHalf-power bandwidth frequencies from deformation spectrum for 1st mode

Note that, when the joints are actuated to 55°C, the stress decreases to a value which is lower than the skin material ultimate stress of 107 MPa.

Vibration Control Under Moving Load

A moving load of 350 kg/m² is applied on the top chord elements. The load moves from the pin (left side in **Figure 6**) to the roller support (right side) and then backwards. Two speeds are tested: 1× = 1.4 m/s (walking pace) and 10× = 14 m/s (typical car speed on residential roads 50 km/h). The load is applied on each top chord element (2 m in length). To simulate the transition from one element to the next, the load intensity varies from 0 to 350 kg/m² (max) as the application position approaches the middle of the element and then from 350 kg/m² (max) to 0 when

the application position reaches the element end. This load profile is illustrated in **Figure 6** for the 1.4 m/s speed case.

Mitigation of the dynamic response through frequency shift and damping variation is evaluated. Full transient analysis is carried out using both the thermo-elastic and viscoelastic material model. **Figure 7** shows the plots of the average acceleration and deformation vs. time, under 1× and 10× speed load cases when the joints are actuated to 40°C, 55°C, and 65°C.

Under the 1× speed load, at a temperature lower than 50°C, the dynamic response obtained using the elastic and viscoelastic material model is similar (**Figure 7A**). However, when the joints are actuated to and above 55°C (**Figure 7C**), the dynamic response reduces significantly only for the viscoelastic case which accounts for the increase of damping that occurs

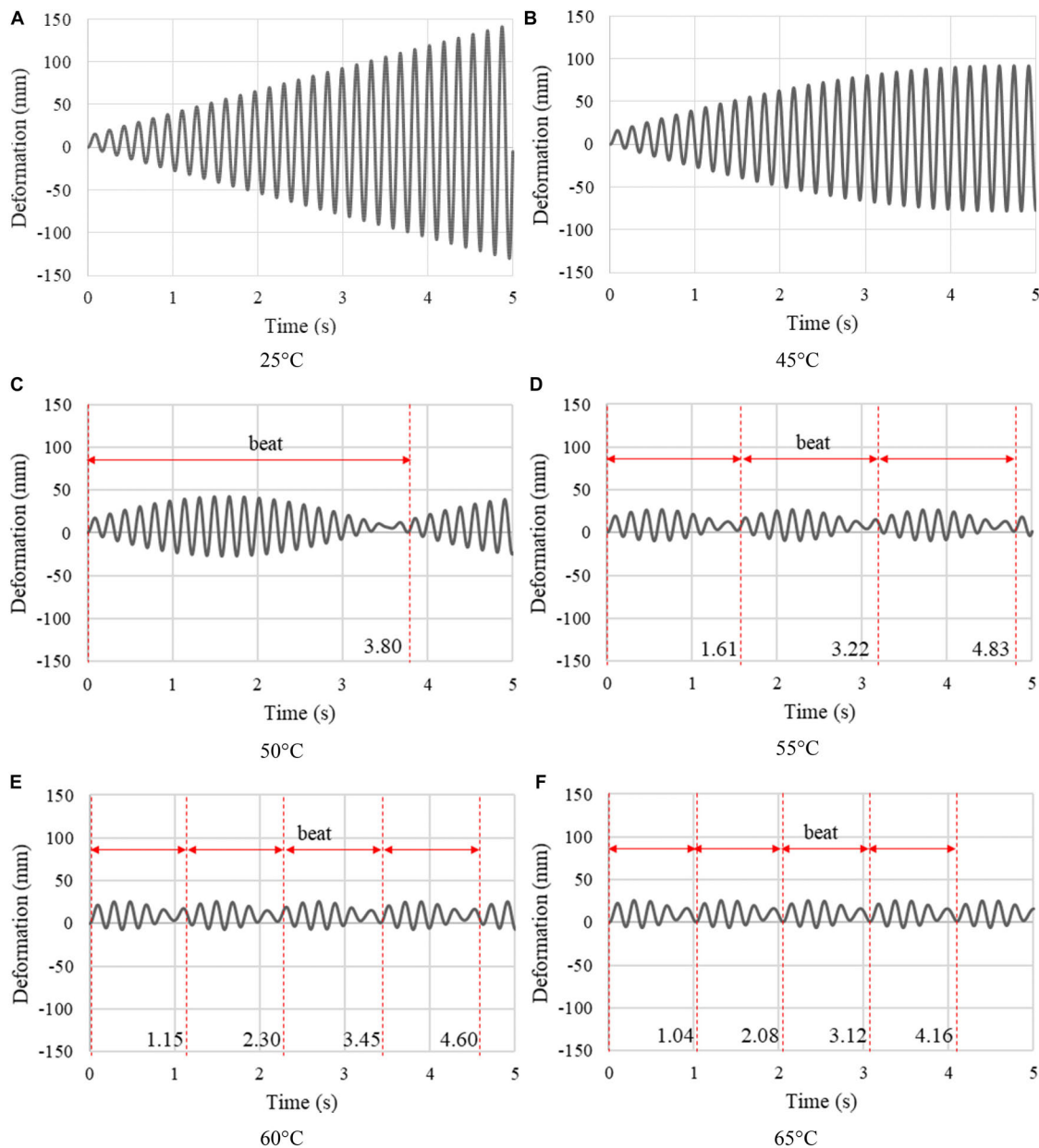


FIGURE 5 | Truss bridge: (A–F) Average deformation vs. time at 25°C, 45°C, 50°C, 55°C, 60°C, and 65°C under resonance load.

because the SMP is in the viscoelastic region (from 50°C to 65°C). At 60°C, the average acceleration and deformation peak amplitudes reduce by 95% and 20%, respectively, compared to the non-controlled case (25°C) after 4.2 s. Instead, for the elastic case, the deformation peak amplitude increases due to the stiffness reduction of the joints. In this case, frequency shift does not contribute significantly to vibration suppression while the increase of damping due to viscoelastic effects is dominant.

A different behavior is observed under the 10× speed load. The dynamic response for the elastic and viscoelastic case features a similar beat when the joints are actuated to 40°C (Figure 7D). When the joints are actuated to 55°C, resonance conditions occur

due to the frequency shift. The deformation and acceleration for the viscoelastic case are larger than those for the elastic case because the excitation frequency is the closest to the natural frequency at 54°C using the viscoelastic model. Instead, using the elastic model, the excitation frequency is the closest to the natural frequency at 52°C. When the joints are actuated to 65°C (Figure 7F), the dynamic response reduces for both elastic and viscoelastic case, and more prominently for the latter due to the combined effect of frequency shift and damping increase. The average acceleration and deformation peak amplitudes reduce by 69% and 22%, respectively, compared to the non-controlled case (25°C) after 4.2 s.

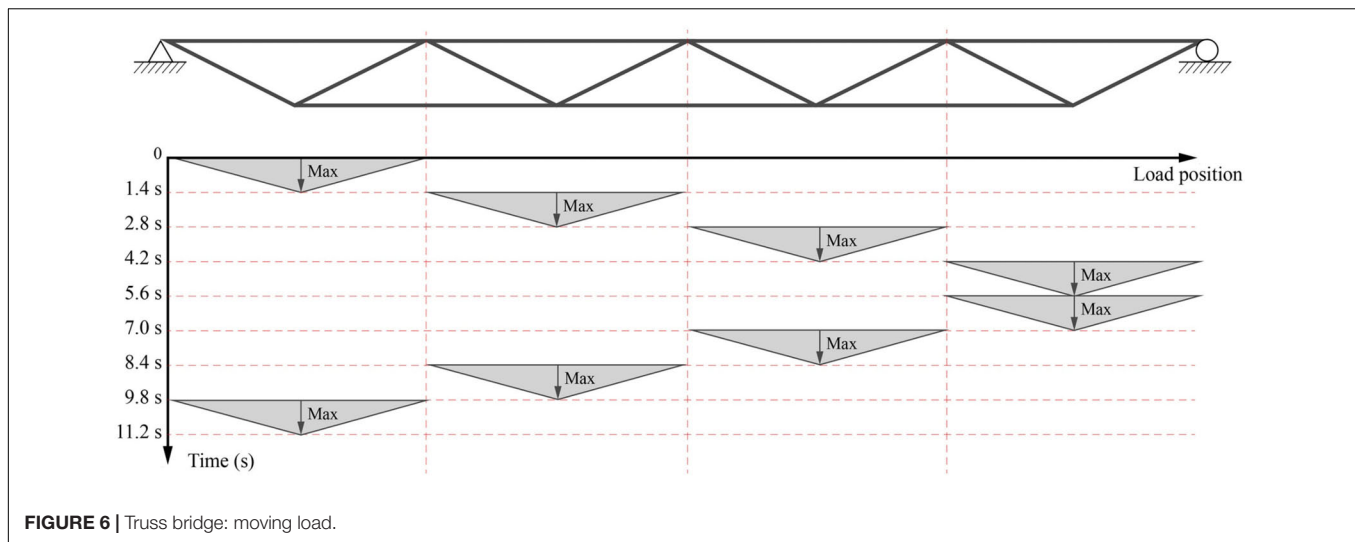


FIGURE 6 | Truss bridge: moving load.

Vibration Control Under Moving Load Considering Time Delays Due to Heating

In order to account for time delays due to heating, vibration control simulation under the $1\times$ speed moving load is carried out by applying a time-linear thermal load that increases the joint temperature from 25°C to 65°C in 5 s (see assumptions regarding the thermal actuation system given in section “Thermal Actuation”). Acceleration and displacement responses are shown in **Figures 8A,B**, respectively. The non-controlled case (25°C) is indicated by a gray curve while controlled cases with constant thermal load at 65°C and linear thermal load (25°C – 65°C in 5 s) are indicated by a black-dashed and an orange curve, respectively. During the first 3 s (25°C – 50°C), since the joint core material has not entered the viscoelastic region (see **Figure 2A**), the structure response is very similar to the non-controlled state. From 3 to 5 s (50°C – 65°C) the core material is in the viscoelastic region; the structure response starts to reduce rapidly owing to the increase of damping. Compared to the constant thermal load at 65°C , the acceleration decay is faster under the time-linear load because as discussed in section “Frequency Shift,” the damping ratio is higher at 55°C and 60°C than that at 65°C . After 5 s, when the joint core material reaches the transition temperature of 65°C , the structure response becomes very similar to that controlled by applying a constant thermal load at 65°C . Considering a time delay of 5 s, results in a marginally higher controlled acceleration compared to the case without time delay. Similar conclusion applies to the displacement response. Note that, when the linear thermal load is applied, the peak displacements are smaller than those under the constant thermal load because the structure is stiffer in the first 5 s.

When considering time delay due to heating, vibration suppression becomes effective once the joint core material enters the viscoelastic region.

Joint and Element Utilization

Supplementary Figure A2 shows the plot of the average von Mises stress vs. strain for the joint core and reinforcement skin

at 40°C , 55°C , and 65°C under the $1\times$ speed load. At 40°C the behavior of the SMP core material is almost purely elastic hence the stress vs. strain curve is a straight line. When the joints are actuated to 50°C and above, stress and strain are out of phase and hence the curves feature hysteresis loops. The stress in the joint core decreases as the temperature increases due to loss of stiffness. The SMP-aramid skin is modeled as an elastic material and therefore the stress vs. strain curve is linear at all temperatures. As expected, the stress in the reinforcement skin increases when the temperature increases due to loss of stiffness of the joint core.

Maximum demand over capacity for the truss elements under tension, compression, bending, shear and buckling are evaluated using BS EN 1993-1-1 (Eqs 5–9) from ambient to transition temperature (25°C – 65°C) under the moving load ($1\times$ speed). The utilization factors given in **Table 2** are obtained from full transient analysis using the viscoelastic material model.

$$\text{Tension} \quad \frac{N_{Ed}}{N_{t,Rd}} \leq 1 \quad (5)$$

$$\text{Compression} \quad \frac{N_{Ed}}{N_{c,Rd}} \leq 1 \quad (6)$$

$$\text{Bending} \quad \frac{M_{Ed}}{M_{c,Rd}} \leq 1 \quad (7)$$

$$\text{Shear} \quad \frac{V_{Ed}}{V_{c,Rd}} \leq 1 \quad (8)$$

$$\text{Buckling} \quad \frac{N_{Ed}}{\chi N_{c,Rd}} + \frac{M_{y,Ed}}{\chi_{LT} M_{c,Rd}} \leq 1 \quad (9)$$

N_{Ed} and M_{Ed} are the maximum for tension/compression and bending moment computed through transient analysis ($1\times$ speed load); $N_{t,Rd}$, $N_{c,Rd}$, and $M_{c,Rd}$ are the tension, compression and moment resistance. χ and χ_{LT} are the reduction factors for axial and torsional buckling. The elements with the highest utilization

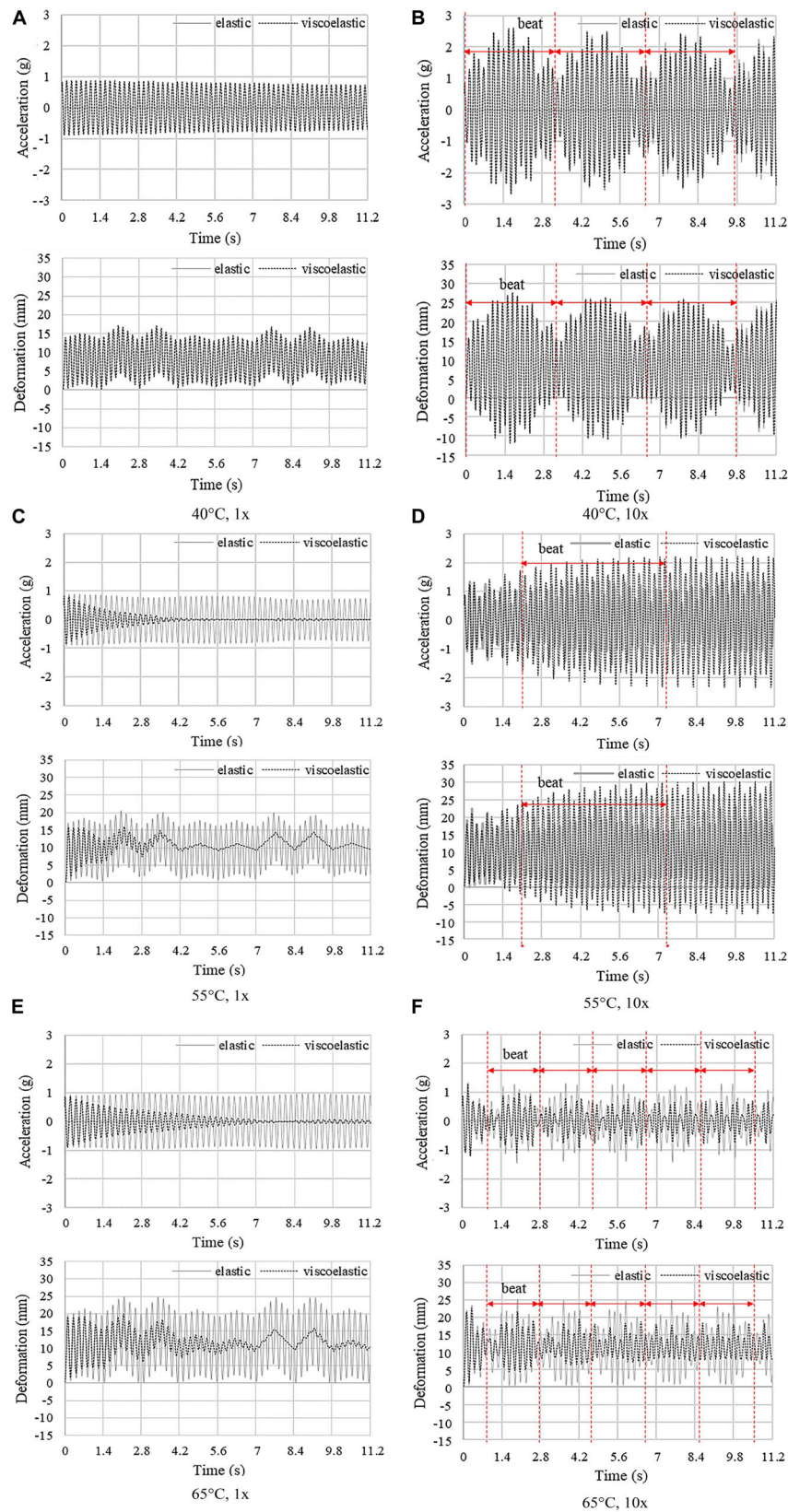


FIGURE 7 | Truss bridge: average deformation and acceleration vs. time at 40°C, 55°C, and 65°C under 1 × -speed load (A,C,E) and under 10 × -speed load (B,D,F).

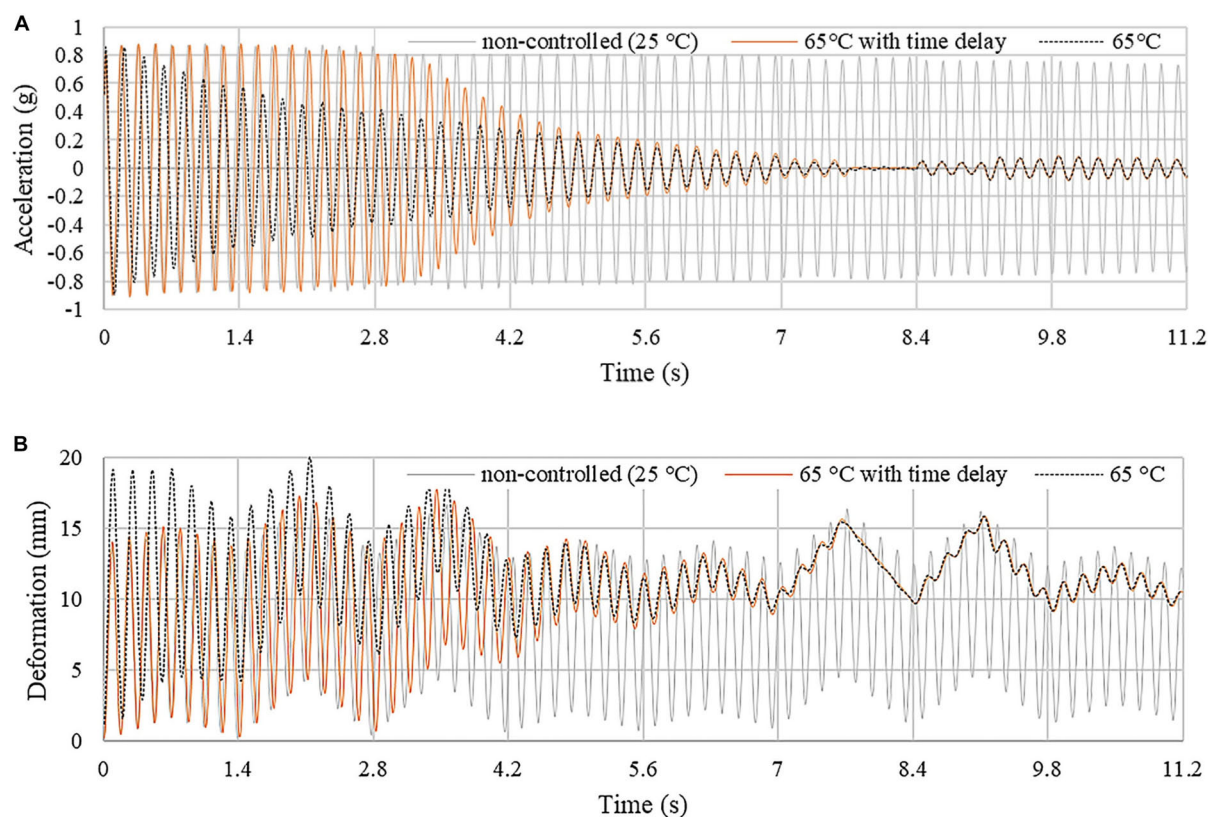


FIGURE 8 | Truss bridge: **(A)** acceleration and **(B)** displacement response. The joints are actuated through a time-linear thermal load which increases the core temperature from 25°C to 65°C in 5 s.

TABLE 2 | Utilization factors for chord and bracing elements.

	25°C	40°C	45°C	50°C	55°C	60°C	65°C
Tension	0.166	0.166	0.164	0.147	0.129	0.128	0.138
Compression	0.319	0.318	0.314	0.283	0.247	0.247	0.265
Bending	0.181	0.179	0.178	0.163	0.161	0.158	0.153
Shear	0.042	0.041	0.041	0.038	0.038	0.038	0.037
Buckling	0.823	0.821	0.812	0.735	0.622	0.608	0.684

are the top and bottom chord elements at mid span (**Figure 4**). Generally, element utilization decreases as the joints are actuated from ambient to 60°C and then increases slightly due to the decrease of damping when the SMP core approaches the rubbery state (see section “Material Characterization”). On average, the utilization factors reduce by 23% for tension and compression, 13% for bending, 10% for shear, and 26% for buckling at 60°C, with respect to the non-controlled state (25°C).

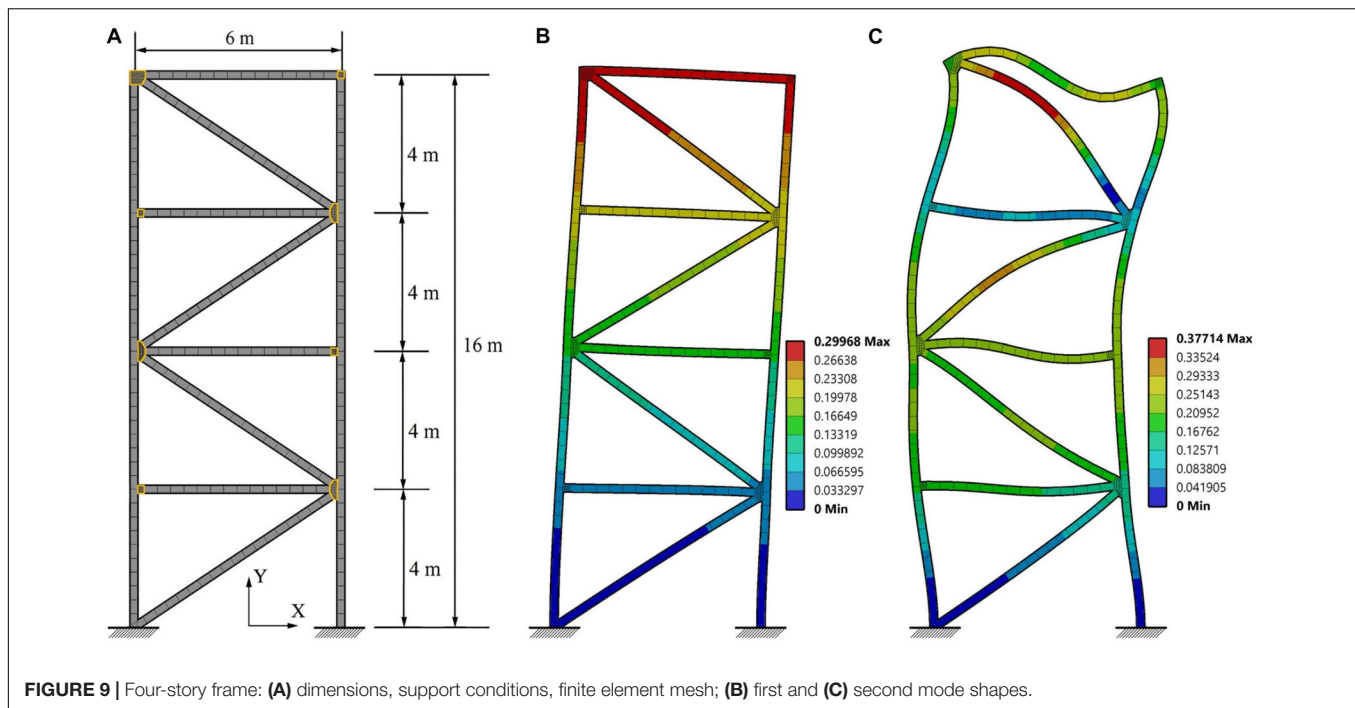
CASE STUDY B: FOUR-STORY FRAME

Model Features

Structural Model

The structure considered in this study is a 6 m (width) × 16 m (height) planar frame which is designed as a 4-story building

reduced to two dimensions. **Figure 9A** shows dimensions and support conditions. The frame is equipped with eight variable stiffness and damping joints which are installed at all nodes except for the supports. The adaptive joints, which are indicated by yellow contour lines, are fitted between the bracing and the floor beams without interrupting column continuity. The finite element mesh comprises elements of type BEAM188 for the columns and floor beams and elements of type SOLID186 for the joints. The beam element material is structural steel S355. The beams have a 200 mm × 200 mm square hollow section and a wall thickness of 10 mm. The joint element material is the SMP material described in section “Variable Stiffness and Damping Joint.” The joint elements and geometry have been modeled similarly to the truss bridge case study. The reinforcement skin is modeled with “surface coating” elements of type SURF156 with a thickness of 6.88 mm which is obtained by stacking four layers



of the SMP-aramid composite described in section “SMP-aramid Skin: Isotropic Elastic Material Model” (1.72 mm per layer). The skin element material is the same of that used for the truss bridge case study.

Loading and Analysis

The structure is subjected to a dead load which is uniformly distributed on each floor beam with an intensity of 300 kg/m² and assuming 6 m of cover. Full transient analysis using the viscoelastic material model is carried out to test vibration control under El-Centro earthquake loading. Since the location of the degree of freedom subjected to maximum displacement and acceleration changes with time, an average value among all degrees of freedom is taken because it is more representative of the dynamic response. The average value of the displacements is denoted as “deformation.”

In each analysis the joints are assumed to be actuated through resistive heating from ambient 25°C to transition temperature 65°C in discrete steps. The same types of thermal load considered in the truss bridge case study (section “Case Study A: Truss Bridge”) are applied here: (1) a constant thermal load is applied to increase the joint temperature in discrete steps; a time-linear thermal load is applied to increase the joint temperature from 25°C to 65°C in 5 s.

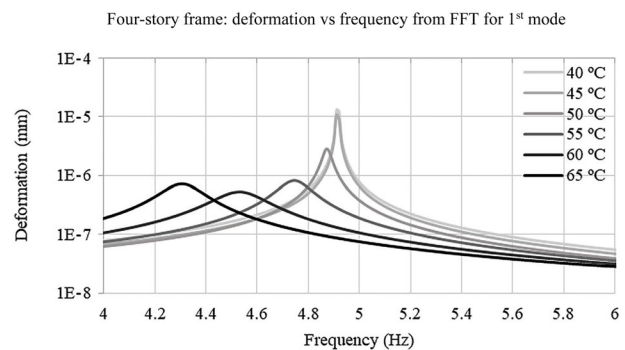
All simulations are carried out in Ansys Workbench.

Frequency Shift and Damping Variation

Modal analysis and a free vibration test have been carried out to evaluate frequency shift and damping variation for first and second modes. The joints are actuated from ambient to transition temperature (25–65°C). The free vibration test is carried out by applying a horizontal 1 N impulse force to the middle node

TABLE 3 | Four-story frame: frequency, frequency shift, and first modal damping ratio.

	25°C	40°C	45°C	50°C	55°C	60°C	65°C
ω_1 (Hz)	5.01	4.97	4.95	4.89	4.66	4.40	4.27
ω_2 (Hz)	15.84	15.71	15.67	15.46	14.68	13.80	13.35
$S_{\omega 1}$ (%)	–	0.78	1.01	2.30	6.96	12.1	14.8
$S_{\omega 2}$ (%)	–	0.79	1.03	2.37	7.32	12.9	15.7
ζ_1 (%)	–	0.18	0.18	0.41	1.37	2.26	1.88



of the left column elements in order to excite the first mode. Modal analysis is carried out using the thermo-elastic material model for the joints while the free vibration test is carried out through full transient analysis using the viscoelastic material model for the joints. The first two mode frequencies ω_1 , ω_2 , and frequency shifts $S_{\omega 1}$, $S_{\omega 2}$ are given in Table 3. Due to joint stiffness reduction, the structure natural frequency shifts up to 14.8% for the first mode and 15.7% for the second mode. The first and second mode shapes are shown in Figures 9B,C, respectively.

The deformation vs. frequency curves for the first mode are shown in **Table 3**. At 40°C, the first mode frequency computed through modal analysis and FFT is 4.97 and 4.91 Hz, respectively. The difference in percentage terms is 1.2%. At 60°C, this difference reaches a maximum value of 3.0% (4.40 Hz from modal analysis and 4.53 Hz from FFT). The damping ratio ζ_1 has been obtained through the half-power bandwidth method (Eq. 4). The damping ratio increases by up to 2.26% from undamped conditions (25°C) as the joints are actuated to 60°C and then it decreases as the temperature increases further. This explains why the peak amplitude for the deformation vs. frequency curve at 65°C is higher than that at 60°C. As observed previously (see section “Material Characterization”), above transition temperature (65°C) damping decreases, as the SMP material leaves the viscoelastic region and enters the rubbery state. The deformation vs. time curves for the free vibration test are shown in **Supplementary Figure A3**.

Vibration Control Under Earthquake Loading

Mitigation of the dynamic response under El Centro earthquake loading through frequency shift and damping variation is evaluated. The joints are actuated from ambient to transition temperature (25–65°C). Full transient analysis is carried out using both the thermo-elastic and viscoelastic material model for the joints.

Figure 10 shows the horizontal component (axis \times in **Figure 9**) of the average acceleration (absolute) and deformation relative to the ground vs. time for all temperatures in the considered range 25°C, 40°C, 45°C, 50°C, 55°C, 60°C, and 65°C. For the elastic case, the dynamic response increases significantly at 45°C, 50°C, and at 60°C due to resonance. In the frequency range 4–5 Hz, the load has high energy components at 4.94, 4.89, and 4.38 Hz which are very close to the natural frequency at 45°C (4.95 Hz), 50°C (4.89 Hz), and 60°C (4.40 Hz), respectively. For the viscoelastic case instead, the dynamic response reduces significantly. The average acceleration (absolute) peak amplitude reduces from 1.6 g at 25°C to 0.6 g at 60°C. However, due to resonance conditions caused by the frequency shift, the response increases at 40°C and 45°C. When the temperature reaches 50°C, resonance is avoided, and the effect of damping becomes dominant. The slight increase of acceleration and deformation at 65°C is due to the decrease of damping as the SMP enters the rubbery state (see section “Material Characterization”). Despite this, at 65°C, the average acceleration (absolute) and deformation peak amplitudes reduce by 87% and 83%, respectively, compared to the non-controlled case (25°C) after 35 s.

For seismic design, the inter-story drift d_r should be contained within the damage limitation (European Committee for Standardization [CEN], 2004):

$$\frac{d_r v}{h} \leq \alpha, \quad (10)$$

where h is the story height; v is the reduction factor which accounts for the return period of the seismic action associated with damage limitation requirements and α is a factor which

considers non-structural element types (i.e., elements that do not add stiffness to the structure). The recommended value for v is 0.4 for buildings with importance class III and IV and 0.5 for importance class I and II. The recommended value for α is 0.005, 0.0075, and 0.01 for elements made of brittle materials, ductile elements, and fixed elements, respectively. The value for v and α is set to 0.5 and 0.005, respectively. The maximum inter-story drift d_r reduces from 6.3 mm between second and third floor at 25°C to 3.3 mm (48% reduction) between first and second floor at 60°C. However, due to resonance conditions caused by the frequency shift, d_r reaches a maximum of 7.52 mm at 40°C between second and third floor. From Eq. 10 $\frac{d_r v}{h} = 0.00282 < 0.005$, hence the structure can be regarded as safe with respect to the damage limitation requirement under El Centro earthquake load.

The difference between results obtained using elastic and viscoelastic material models, indicates that the dynamic response reduces primarily because of the increase of damping. As the temperature of the joints is increased, the frequency shift might cause resonance. However, as shown by full transient analysis using the viscoelastic material model, the effect of damping becomes dominant when the joints are actuated to a temperature above 50°C, which causes a significant reduction of the dynamic response.

Vibration Control Under Earthquake Loading Considering Time Delay

In order to account for time delays due to heating, vibration control simulation under El Centro earthquake loading is carried out by applying a time-linear thermal load that increases the joint temperature from 25°C to 65°C in 5 s (see assumptions regarding the thermal actuation system given in section “Thermal Actuation”). Acceleration (absolute) and displacement responses are shown in **Figures 11A,B**, respectively. The non-controlled case (25°C) is indicated by a gray curve while controlled cases with constant thermal load at 65°C and linear thermal load (25°C–65°C in 5 s) are indicated by a black-dashed and an orange curve, respectively. As observed for the truss bridge case study, the structure response is very similar to the non-controlled state until the joint core is actuated to the viscoelastic region (first 3 s). After 5 s, when the joint core material reaches the transition temperature of 65°C, the structure response becomes very similar to that controlled by applying a constant thermal load at 65°C. When considering time delay due to heating, vibration suppression becomes effective once the joint core material enters the viscoelastic region.

Joint and Element Utilization

Similar considerations to the truss bridge case study apply with regard to the average von Mises stress vs. strain for the joint core and reinforcement skin (see **Supplementary Figure A4**). The SMP core behaves almost as a purely elastic material at 40°C and when the temperature increases, stress and strain go out of phase because the material enters the viscoelastic region. While the stress in the joint decreases, the stress in the reinforcement

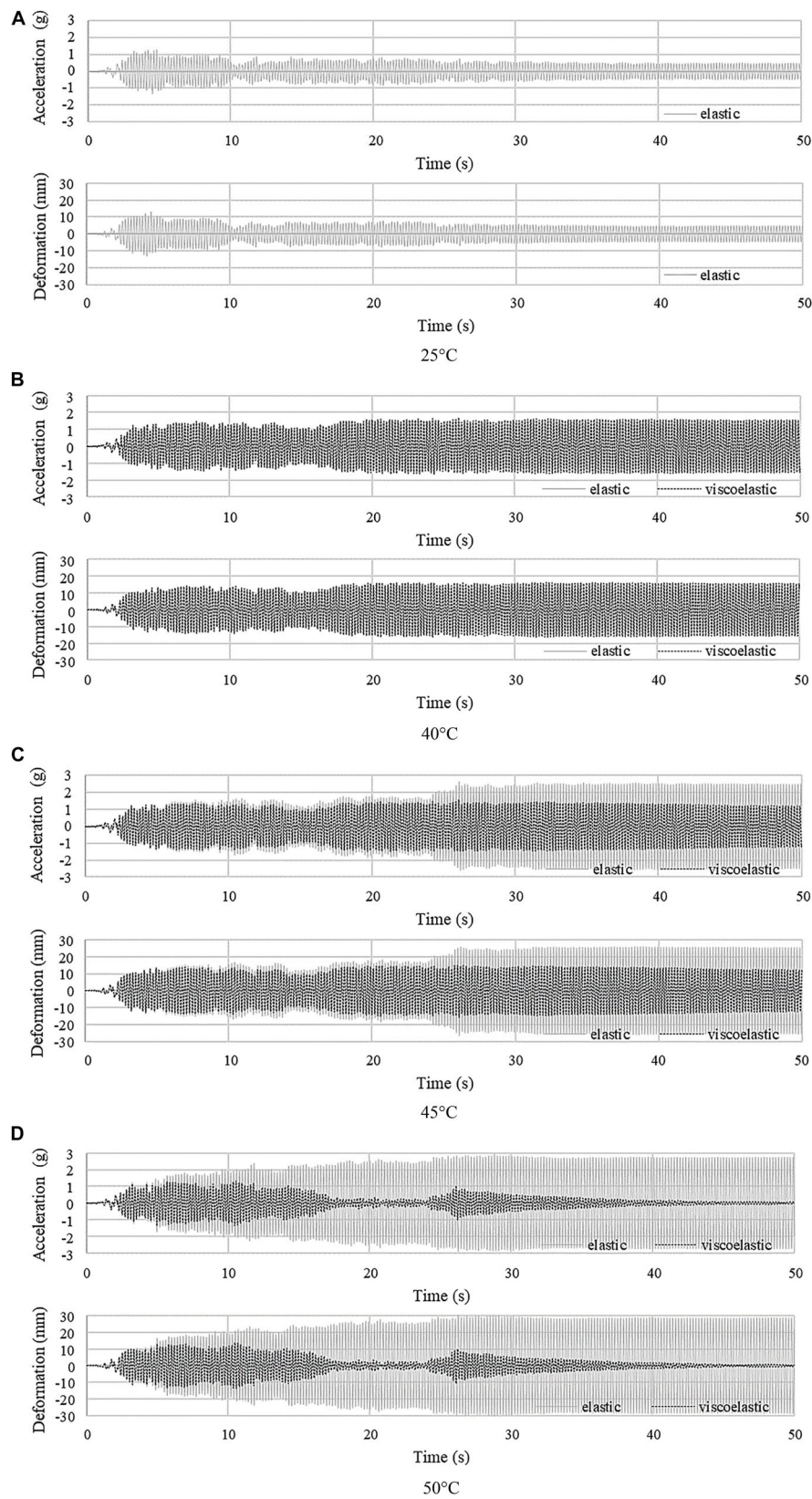


FIGURE 10 | Continued

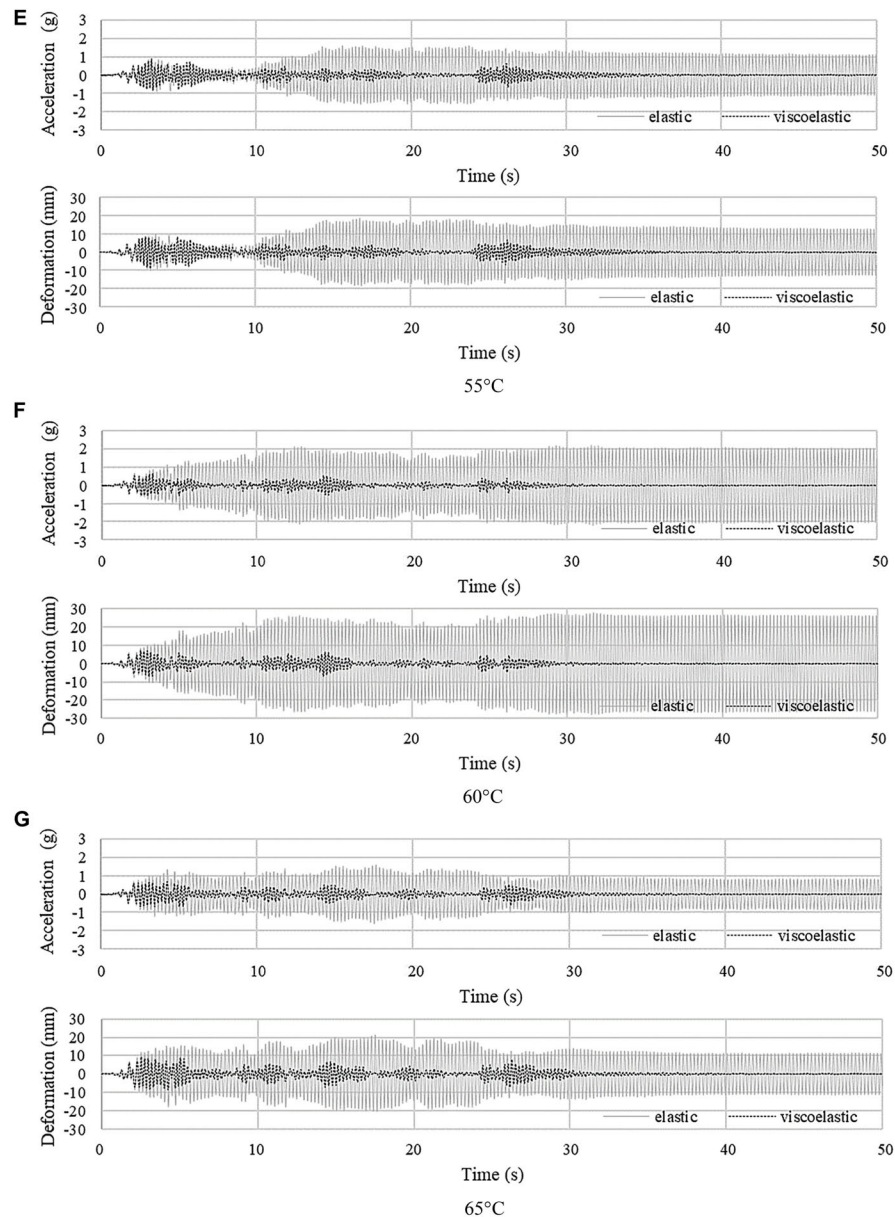


FIGURE 10 | Four-story frame (A–G): average acceleration (absolute) and deformation (\times component relative to the ground) vs. time under El Centro NS at 25°C, 40°C, 45°C, 50°C, 55°C, 60°C, and 65°C.

skin increases as the temperature increases due to the loss of stiffness of the joint core.

Maximum demand over capacity for the column, bracing and floor beam elements are evaluated using BS EN 1993-1-1 (Eqs 5–9). The utilization factors given in **Table 4** are obtained through full transient analysis using the viscoelastic material model for the joints. The elements with the highest utilization are the first-floor bracing and right column elements. Generally, element utilization decreases as the joints are actuated from ambient to 60°C and then increases slightly due to the decrease of damping when the SMP core approaches the rubbery state (see section “Material Characterization”). The initial increase from

25°C to 40°C is caused by resonance conditions that occur due to frequency shift. On average, the utilization factors are reduced by 72% for tension, 56% for compression, 21% for bending, 25% for shear, and 53% for buckling at 60°C, with respect to the non-controlled state (25°C).

DISCUSSION

This paper has presented a new semi-active vibration control device for truss and frame structures. The variable stiffness and damping joint discussed in this work comprises a SMP core

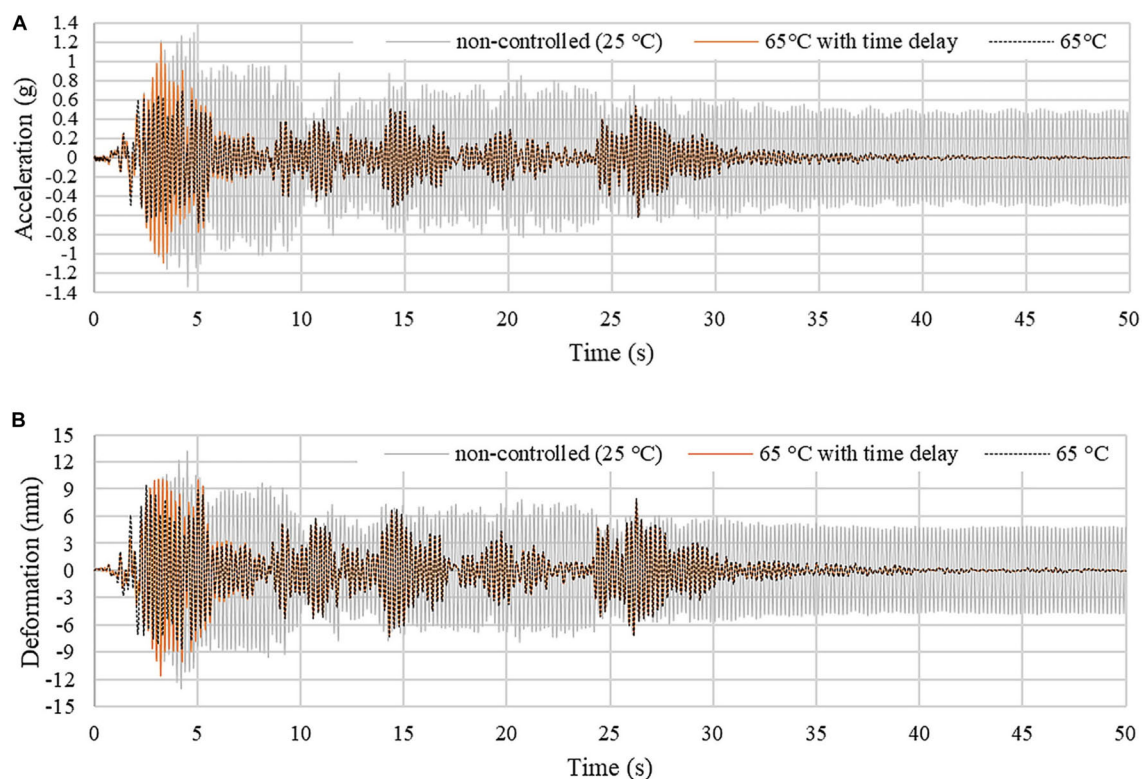


FIGURE 11 | Four-story frame: **(A)** average acceleration (absolute) and **(B)** displacement response. The joints are actuated through a time-linear thermal load which increases the core temperature from 25°C to 65°C in 5 s.

TABLE 4 | Utilization factors for columns, bracing, and floor beams.

	25°C	40°C	45°C	50°C	55°C	60°C	65°C
Tension	0.222	0.282	0.249	0.216	0.106	0.080	0.086
Compression	0.351	0.448	0.407	0.368	0.246	0.199	0.236
Bending	0.376	0.384	0.377	0.351	0.319	0.304	0.310
Shear	0.107	0.107	0.105	0.095	0.085	0.080	0.082
Buckling	0.582	0.718	0.674	0.587	0.407	0.338	0.389

which is reinforced by an SMP-aramid composite skin. The joints are assumed to be actuated through resistive heating. When the joints are actuated, the stiffness decreases and in parallel damping increases due to viscoelastic effects. The combined effect is a significant shift of the structure natural frequencies and an increase of damping. Simulations on a truss bridge and a four-story frame equipped with such variable stiffness and damping joints, have shown that this strategy is effective to mitigate the dynamic response under different loading scenarios including resonance, transient and earthquake loading.

Simulation results of a truss bridge under resonance loading have shown that the response is reduced significantly when the joints are actuated to 50°C and above. The average acceleration and deformation peak amplitudes reduce by 91% and 82% with respect to the non-controlled case (25°C). Under resonance loading, frequency shift caused by the joint stiffness reduction is effective to avoid resonance.

When viscoelastic effects (frequency dependency) are ignored, the frequency shift due to joint stiffness reduction, might cause resonance if the excitation has important frequency components which are relatively close to the structure natural frequencies. However, when the effect of damping is considered through the viscoelastic material model, the overall effect is a significant reduction of the dynamic response. When the joints are actuated to 60°C, the damping ratio for the first mode increases by up to 2.2% and 2.3% from undamped conditions (25°C) for the truss bridge and four-story building, respectively.

For both case studies, the joints are assumed to be actuated through resistive heating from ambient 25°C to transition temperature 65°C. Thermal actuation of the joints has been simulated by applying two types of thermal load: (1) a constant thermal load is applied to increase the joint temperature in discrete steps without accounting for time delays due to heating;

(2) a time-linear thermal load is applied to increase the joint temperature from 25°C to 65°C in 5 s. For the truss bridge under moving load, the average acceleration peak amplitude reduces by up to 95% with respect to the non-controlled case (25°C) in approximately 7 s with and without including time delays due to heating. Compared to the constant thermal load (65°C), the acceleration decay is faster under the time-linear load because the damping ratio is higher at 55°C and 60°C than that at 65°C. For the four-story building under earthquake loading and joints actuated to the transition temperature (65°C), the average acceleration (absolute) and deformation peak amplitudes and the inter-story drift reduce by 87%, 83%, and by 32%, respectively, with respect to the non-controlled case (25°C) after 35 s. Also in this case, the response reduction is very similar with and without accounting for time delays except in the first 5 s. When considering time delay due to heating, vibration suppression becomes effective once the joint core material enters the viscoelastic region (in this case after 3 s).

A transition temperature of 65°C is specific to the type of SMP adopted in this study which was selected primarily based on commercial availability. SMPs characteristics should be chosen appropriately depending on location in order to minimize control effort and energy requirements for thermal actuation by limiting interference with field temperature. For example, in cold regions, SMPs that feature a lower transition temperature should be selected. There exist several other SMP materials which feature a transition temperature that varies from 10°C to 178°C (Kusy and Whitley, 1994; Takahashi et al., 1996; Kumar et al., 2014). In addition, suitable insulation materials can be applied to the joints in order to reduce further interference with field temperature and the effect of seasonal temperature variation.

CONCLUSION

Dynamic response mitigation through control of variable stiffness and damping joints is possible due to a combination of frequency shift and damping variation. When the joints are actuated to the transition phase, the storage modulus (or stiffness) decreases while the material damping increases. When the excitation has a dominant frequency component that is close to the structure natural frequency, the response is reduced primarily through frequency shift. Conversely, when the excitation has several important frequency components, the response reduces primarily through the increase of damping due to viscoelastic effects. For the SMP material employed in this work, the response is reduced significantly using a control temperature between 55°C and 65°C. When considering time delay due to heating, vibration suppression becomes effective once the joint core material enters the viscoelastic region. SMPs characteristics should be chosen appropriately depending on location in order

to minimize control effort and energy requirements for thermal actuation by limiting interference with field temperature.

On-going work will further elaborate and investigate the semi-active control strategy proposed in this paper through experimental testing on a small scale three-story spatial frame (650 mm × 650 mm × 1325 mm). In order to generalize the conclusions reached in this paper, future work will look into applying joint stiffness and damping control to mitigate the response of spatial structural configurations that have a complex layout.

DATA AVAILABILITY STATEMENT

All datasets generated for in this study are included in the article/Supplementary Material.

AUTHOR CONTRIBUTIONS

QW, GS, and PT set up research objectives and directions with contribution from KJ and AH. QW carried out method implementation with support of GS, KJ, and AH. QW carried out numerical studies with support of GS, AH, and PT and experimental testing with support of KJ. QW wrote the first version of the manuscript with support of GS. GS actively contributed to writing the final version of the manuscript. All authors contributed to manuscript revision, reviewed, and approved the final version.

ACKNOWLEDGMENTS

We thankfully acknowledge China Scholarship Council and 4TU Federation who provided funding for this research via 4TU Lighthouse Project.

SUPPLEMENTARY MATERIAL

The Supplementary Material for this article can be found online at: <https://www.frontiersin.org/articles/10.3389/fbuil.2020.550864/full#supplementary-material>

Supplementary Figure A1 | Truss bridge: (a–f) free vibration at 40°C, 45°C, 50°C, 55°C, 60°C and 65°C.

Supplementary Figure A2 | Truss bridge: stress vs. strain at 40°C, 55°C and 65°C in SMP core (a,c,e) and SMP-aramid skin (b,d,f).

Supplementary Figure A3 | Four-story frame: (a–f) free vibration at 40°C, 45°C, 50°C, 55°C, 60°C and 65°C.

Supplementary Figure A4 | Four-story frame: stress vs strain in SMP core (a,c,e) and SMP-aramid skin (b,d,f) at 40°C, 55°C and 65°C.

REFERENCES

- Bel Hadj Ali, N., and Smith, I. F. C. (2010). Dynamic behavior and vibration control of a tensegrity structure. *Int. J. Solids Struct.* 47, 1285–1296. doi: 10.1016/j.jisolstr.2010.01.012
- Bonello, P., Brennan, M. J., and Elliott, S. J. (2005). Vibration control using an adaptive tuned vibration absorber with a variable curvature stiffness element. *Smart Mater. Struct.* 14:1055. doi: 10.1088/0964-1726/14/5/044
- Butterworth, J., Lee, J. H., and Davidson, B. (2004). “Experimental determination of modal damping from full scale testing,” in

- Proceedings of the 13th World Conference on Earthquake Engineering*, Vancouver.
- Campanile, L. F. (2005). Initial thoughts on weight penalty effects in shape-adaptable systems. *J. Intell. Mater. Syst. Struct.* 16, 47–56. doi: 10.1177/1045389X05046692
- Djedoui, N., Ounis, A., Pinelli, J. P., and Abdeddaim, M. (2017). Hybrid control systems for rigid buildings structures under strong earthquakes. *Asian J. Civil Eng.* 18, 893–909.
- dos Santos, F. A., and Cismaşiu, C. (2017). Adaptive underslung beam using shape-memory alloys for frequency-tuning. *J. Intell. Mater. Syst. Struct.* 28, 1260–1271. doi: 10.1177/1045389X16667558
- dos Santos, F. A., Rodrigues, A., and Micheletti, A. (2015). Design and experimental testing of an adaptive shape-morphing tensegrity structure, with frequency self-tuning capabilities, using shape-memory alloys. *Smart Mater. Struct.* 24:105008. doi: 10.1088/0964-1726/24/10/105008
- Du, H., Li, W., and Zhang, N. (2011). Semi-active variable stiffness vibration control of vehicle seat suspension using an MR elastomer isolator. *Smart Mater. Struct.* 20:105003. doi: 10.1088/0964-1726/20/10/105003
- Dyke, S. J., Spencer, B. F. Jr, Sain, M. K., and Carlson, J. D. (1996). Seismic response reduction using magnetorheological dampers. *IFAC Proc.* 29, 5530–5535. doi: 10.1016/S1474-6670(17)58562-6
- European Committee for Standardization [CEN] (2004). *Eurocode 8: Design of (structures) for Earthquake Resistance-part 1: General Rules, Seismic Actions and Rules For Buildings*, European Standard, 2004. Brussels: CEN.
- Ferry, J. D. (1980). *Viscoelastic Properties of Polymers*. Hoboken, NJ: John Wiley & Sons.
- Gall, K., Mikulas, M., Munshi, N. A., Beavers, F., and Tupper, M. (2000). Carbon fiber reinforced shape memory polymer composites. *J. Intell. Mater. Syst. Struct.* 11, 877–886. doi: 10.1106/EJGR-EWNM-6CLX-3X2M
- Gkatzogias, K. I., and Kappos, A. J. (2016). Semi-active control systems in bridge engineering: a review of the current state of practice. *Struct. Eng. Int.* 26, 290–300. doi: 10.2749/101686616X14555429844040
- Hu, J., Chen, W., Fan, P., Gao, J., Fang, G., Cao, Z., et al. (2017a). Uniaxial tensile tests and dynamic mechanical analysis of satin weave reinforced epoxy shape memory polymer composite. *Polym. Test.* 64, 235–241. doi: 10.1016/j.polymertesting.2017.09.038
- Hu, J., Chen, W., Fan, P., Gao, J., Fang, G., Cao, Z., et al. (2017b). Epoxy shape memory polymer (SMP): material preparation, uniaxial tensile tests and dynamic mechanical analysis. *Polymer Testing* 62, 335–341. doi: 10.1016/j.polymertesting.2017.07.001
- Huang, B., Zhang, H., Wang, H., and Song, G. (2014). Passive base isolation with superelastic nitinol SMA helical springs. *Smart Mater. Struct.* 23:065009. doi: 10.1088/0964-1726/23/6/065009
- ISO-6721-1. (2011). *Plastics Determination of Dynamic Mechanical Properties*. Geneva: ISO.
- Kasai, K., Fu, F., and Watanabe, A. (1998). Passive control systems for seismic damage mitigation. *J. Struct. Eng.* 124, 501–512. doi: 10.1061/(ASCE)0733-9445(1998)124:5(501)
- Kınay, G., and Turan, G. (2012). A hybrid control of seismic response by passive and semi-active control strategies. *J. Eng. Sci. Des.* 2, 27–36.
- Kobori, T., Takahashi, M., Nasu, T., Niwa, N., and Ogasawara, N. (1993). Seismic response controlled structure with active variable stiffness system. *Earth. Eng. Struct. Dyn.* 22, 925–941. doi: 10.1002/eqe.4290221102
- Kuder, I. K., Arrieta, A. F., Raither, W. E., and Ermanni, P. (2013). Variable stiffness material and structural concepts for morphing applications. *Prog. Aerospace Sci.* 63, 33–55. doi: 10.1016/j.paerosci.2013.07.001
- Kumar, K. S., Khatwa, A. K., and Nair, C. R. (2014). High transition temperature shape memory polymers (SMPs) by telechelic oligomer approach. *React. Funct. Polym.* 79, 7–13. doi: 10.1016/j.reactfunctpolym.2014.02.008
- Kusy, R. P., and Whitley, J. Q. (1994). Thermal characterization of shape memory polymer blends for biomedical implantations. *Thermochim. Acta* 243, 253–263. doi: 10.1016/0040-6031(94)85060-7
- Lan, X., Liu, Y., Lv, H., Wang, X., Leng, J., and Du, S. (2009). Fiber reinforced shape-memory polymer composite and its application in a deployable hinge. *Smart Mater. Struct.* 18:024002. doi: 10.1088/0964-1726/18/2/024002
- Ledezma-Ramirez, D. F., Ferguson, N. S., and Brennan, M. J. (2011). Shock isolation using an isolator with switchable stiffness. *J. Sound Vib.* 330, 868–882. doi: 10.1016/j.jsv.2010.09.016
- Leng, J., Lan, X., Liu, Y., and Du, S. (2011). Shape-memory polymers and their composites: stimulus methods and applications. *Prog. Mater. Sci.* 56, 1077–1135.
- Liao, G. J., Gong, X. L., Xuan, S. H., Kang, C. J., and Zong, L. H. (2012). Development of a real-time tunable stiffness and damping vibration isolator based on magnetorheological elastomer. *J. Intell. Mater. Syst. Struct.* 23, 25–33. doi: 10.1177/1045389X11429853
- Lienhard, J., Schleicher, S., Poppinga, S., Masselter, T., Milwich, M., Speck, T., et al. (2011). Flectofin: a hingeless flapping mechanism inspired by nature. *Bioinspirat. Biomimet.* 6, 1–7. doi: 10.1088/1748-3182/6/4/045001
- Lignarolo, L., Lelieveld, C., and Teuffel, P. (2011). “Shape morphing wind-responsive facade systems realized with smart materials,” in *Proceedings of the International Adaptive Architecture Conference*, London.
- Liu, Y., Du, H., Liu, L., and Leng, J. (2011). Shape memory polymers and their composites in aerospace applications: a review. *Prog. Mater. Sci.* 56, 1077–1135. doi: 10.1016/j.pmatsci.2011.03.001
- Liu, Y., Gall, K., Dunn, M. L., Greenberg, A. R., and Diani, J. (2006). Thermomechanics of shape memory polymers: uniaxial experiments and constitutive modeling. *Int. J. Plast.* 22, 279–313. doi: 10.1016/j.ijplas.2005.03.004
- Menard, K. P. (2008). *Dynamic Mechanical Analysis: A Practical Introduction*. Boca Raton, FL: CRC Press. doi: 10.1201/9781420053135
- Meng, H., and Li, G. (2013). A review of stimuli-responsive shape memory polymer composites. *Polymer* 54, 2199–2221. doi: 10.1016/j.polymer.2013.02.023
- Mirfakhraei, S. F., Andalib, G., and Chan, R. (2019). Numerical investigation on toggled actuator forces in active vibration control system. *Adv. Res. Civil Eng.* 1, 16–35. doi: 10.1007/s42452-019-0210-4
- Ohtori, Y., Christenson, R. E., Spencer, B. F. Jr., and Dyke, S. J. (2004). Benchmark control problems for seismically excited nonlinear buildings. *J. Eng. Mech.* 130, 366–385. doi: 10.1061/(ASCE)0733-9399(2004)130:4(366)
- Preumont, A., and Seto, K. (2008). *Active Control of Structures*. Hoboken, NJ: John Wiley & Sons. doi: 10.1002/9780470715703
- Reinhorn, A. M., Soong, T. T., Riley, M. A., Lin, R. C., Aizawa, S., and Higashino, M. (1993). Full-scale implementation of active control. II: installation and performance. *J. Struct. Eng.* 119, 1935–1960. doi: 10.1061/(ASCE)0733-9445(1993)119:6(1935)
- Reksowardojo, A. P., Senatore, G., and Smith, I. F. (2019). Experimental testing of a small-scale truss beam that adapts to loads through large shape changes. *Front. Struct. Sens.* 5:93. doi: 10.3389/fbuil.2019.00093
- Reksowardojo, A. P., Senatore, G., and Smith, I. F. C. (2020). Design of structures that adapt to loads through large shape changes. *J. Struct. Eng.* 146:04020068. doi: 10.1061/(ASCE)ST.1943-541X.0002604
- Sarlis, A. A., Pasala, D. T. R., Constantinou, M. C., Reinhorn, A. M., Nagarajaiah, S., and Taylor, D. P. (2013). Negative stiffness device for seismic protection of structures. *J. Struct. Eng.* 139, 1124–1133. doi: 10.1061/(ASCE)ST.1943-541X.0000616
- Senatore, G., Duffour, P., and Winslow, P. (2018a). Energy and cost analysis of adaptive structures: case studies. *J. Struct. Eng.* 144:04018107. doi: 10.1061/(ASCE)ST.1943-541X.0002075
- Senatore, G., Duffour, P., and Winslow, P. (2018b). Exploring the application domain of adaptive structures. *Eng. Struct.* 167, 608–628. doi: 10.1016/j.engstruct.2018.03.057
- Senatore, G., Duffour, P., and Winslow, P. (2019). Synthesis of minimum energy adaptive structures. *Struct. Multidiscipl. Optimiz.* 60, 849–877. doi: 10.1007/s00158-019-02224-8
- Senatore, G., Duffour, P., Winslow, P., and Wise, C. (2018c). Shape control and whole-life energy assessment of an infinitely stiff prototype adaptive structure. *Smart Mater. Struct.* 27, 015022. doi: 10.1088/1361-665X/aa8cb8
- Senatore, G., and Reksowardojo, A. P. (2020). Force and shape control strategies for minimum energy adaptive structures. *Front. Built Environ.* 6:105. doi: 10.3389/fbuil.2020.00105
- Senatore, G., Wang, Q., Bier, H., and Teuffel, P. (2017). “The use of variable stiffness joints in adaptive structures,” in *Proceedings of the IASS 2017, Hamburg*.
- Shu, Z., Zhang, J., and Nagarajaiah, S. (2017). Dimensional Analysis of Inelastic Structures with negative stiffness and supplemental damping devices. *J. Struct. Eng.* 143:04016184. doi: 10.1061/(ASCE)ST.1943-541X.0001658
- Soong, T. T. (1988). State of the art review: active structural control in civil engineering. *Eng. Struct.* 10, 74–84. doi: 10.1016/0141-0296(88)90033-8

- Soong, T. T., and Spencer, B. F. (2000). Active, semi-active and hybrid control of structures. *Bull. New Zeal. Soc. Earth. Eng.* 33:2000. doi: 10.5459/bnzsee.33.3.387-402
- Spencer, B. F. Jr, Christenson, R. E., and Dyke, S. J. (1998). "Next generation benchmark control problem for seismically excited buildings," in *Proceedings of the Second World Conference on Structural Control*, Kyoto.
- Spencer, B. F., and Sain, M. K. (1997). Controlling buildings: a new frontier in feedback. *IEEE Cont. Syst. Mag.* 17, 19–35. doi: 10.1109/37.642972
- Symans, M. D., and Constantinou, M. C. (1999). Semi-active control systems for seismic protection of structures: a state-of-the-art review. *Eng. Struct.* 21, 469–487. doi: 10.1016/S0141-0296(97)00225-3
- Takahashi, T., Hayashi, N., and Hayashi, S. (1996). Structure and properties of shape-memory polyurethane block copolymers. *J. Appl. Polym. Sci.* 60, 1061–1069. doi: 10.1002/(SICI)1097-4628(19960516)60:7<1061::AID-APP18>3.0.CO;2-3
- Teuffel, P. (2004). *Entwerfen Adaptiver Strukturen*. Stuttgart: University of Stuttgart – ILEK.
- Wang, L., Wang, X., Li, Y., Lin, G., and Qiu, Z. (2017). Structural time-dependent reliability assessment of the vibration active control system with unknown-but-bounded uncertainties. *Struct. Cont. Health Monit.* 24:e1965. doi: 10.1002/stc.1965
- Wang, Q., Senatore, G., Jansen, K., Habraken, A., and Teuffel, P. (2020). Design and characterization of variable stiffness structural joints. *Mater. Design* 187:108353. doi: 10.1016/j.matdes.2019.108353
- Wang, Q., Senatore, G., Kaymenaki, V., Habraken, A., and Teuffel, P. (2018). "A vibration control strategy using variable stiffness joints," in *Proceedings of the IASS 2018*, Boston.
- Wang, Y., and Senatore, G. (2020). Minimum energy adaptive structures – All-In-One problem formulation. *Comp. Struct.* 236:106266. doi: 10.1016/j.compstruc.2020.106266
- Xu, B., Wu, S. Z., and Yokoyama, K. (2003). Neural networks for decentralized control of cable-stayed bridge. *J. Bridge Eng.* 8, 229–236. doi: 10.1061/(ASCE)1084-0702(2003)8:4(229)
- Yang, G., Spencer, B. F. Jr., Carlson, J. D., and Sain, M. K. (2002). Large-scale MR fluid dampers: modeling and dynamic performance considerations. *Eng. Struct.* 24, 309–323. doi: 10.1016/S0141-0296(01)00097-9
- Yang, J. N., Agrawal, A. K., Samali, B., and Wu, J. C. (2004). Benchmark problem for response control of wind-excited tall buildings. *J. Eng. Mech.* 130, 437–446. doi: 10.1061/(ASCE)0733-9399(2004)130:4(437)
- Zhao, Y. L., Xu, Z. D., and Wang, C. (2019). Wind vibration control of stay cables using magnetorheological dampers under optimal equivalent control algorithm. *J. Sound Vib.* 443, 732–747. doi: 10.1016/j.jsv.2018.12.016

Conflict of Interest: The authors declare that the research was conducted in the absence of any commercial or financial relationships that could be construed as a potential conflict of interest.

Copyright © 2020 Wang, Senatore, Jansen, Habraken and Teuffel. This is an open-access article distributed under the terms of the Creative Commons Attribution License (CC BY). The use, distribution or reproduction in other forums is permitted, provided the original author(s) and the copyright owner(s) are credited and that the original publication in this journal is cited, in accordance with accepted academic practice. No use, distribution or reproduction is permitted which does not comply with these terms.



Inherent Adaptive Structures Using Nature-Inspired Compound Elements

Mohammad Reza Chenaghlou^{1*}, Mohammad Kheirollahi¹, Karim Abedi¹, Ahmad Akbari² and Aydin Fathpour¹

¹ Faculty of Civil Engineering, Sahand University of Technology, Tabriz, Iran, ² Faculty of Electrical Engineering, Sahand University of Technology, Tabriz, Iran

OPEN ACCESS

Edited by:

Gennaro Senatore,
École Polytechnique Fédérale de
Lausanne, Switzerland

Reviewed by:

Julio Alfonso Ramirez,
Purdue University, United States
Sung-Gul Hong,
Seoul National University, South Korea

*Correspondence:

Mohammad Reza Chenaghlou
mrchenaghlou@sut.ac.ir

Specialty section:

This article was submitted to
Structural Sensing,
a section of the journal
Frontiers in Built Environment

Received: 14 May 2020

Accepted: 08 October 2020

Published: 25 November 2020

Citation:

Chenaghlou MR, Kheirollahi M,
Abedi K, Akbari A and Fathpour A
(2020) Inherent Adaptive Structures
Using Nature-Inspired Compound
Elements.
Front. Built Environ. 6:561902.
doi: 10.3389/fbuil.2020.561902

Biomimicry studies have attracted significant attention in research and practice, leading to effective engineering solutions to develop new types of structures inspired by natural systems. The objective of this study is to employ natural structures' inherent adaptivity under changing loading conditions. Three new types of compound elements are proposed that are able to improve the structure load-bearing capacity through passive inherent adaptivity. A self-centering system, inspired by the human spine, which comprises a column pre-stressed through cables, is employed as a kinematic isolator. A similar self-centering system is applied to increase the load-bearing capacity of unreinforced masonry columns. An axially loaded element, inspired by the bamboo stem, which comprises a steel core reinforced by a series of cylindrical plates that are encased in a steel tube, is employed to control the onset of instability in long-span truss structures. Application to typical frame, masonry, and truss structures is investigated through finite element analysis. Results show that the proposed compound elements are effective to increase the structure load-bearing capacity and to reduce the response under seismic excitation owing to their inherent adaptive features.

Keywords: inherent adaptivity, compound element, self-centering system, masonry columns, truss structures, seismic excitation

INTRODUCTION

Structures capable of adapting by changing their properties or behavior in response to environmental stimuli are called adaptive structures (Wagg et al., 2008). "Structural response control" is an established field that is dedicated to the development of design methods and control systems with the objective to mitigate the structure response under external loading. Various investigations have been conducted on the application of structural control systems. Most of these systems are employed as additional components to influence the structure response. Structural control systems have been categorized as passive, semiactive, active, and hybrid. These systems can be defined as follows:

1. Passive systems reduce the structure response through employing either isolation devices (e.g., elastomeric bearings) or energy-dissipation devices (e.g., tuned mass dampers). The shared feature of these passive systems is that they do not require input energy.
2. Semiactive control systems (Symans and Constantinou, 1999, Gkatzogias and Kappos, 2016, Wang et al., 2020) employ adjustable energy-dissipation devices (e.g., magneto-rheological dampers). Sensors mounted on the structure measure acceleration and/or displacements at different locations, and based on a suitable control strategy, the semiactive device is adjusted to dissipate vibrational motion. A small amount of energy is required by the system to carry out the adjustment. Even if the adjustment mechanism fails, semiactive control systems can still function passively.
3. Active control systems (Reinhorn et al., 1993) (e.g., active mass drive or active bracing control) are capable of considerably mitigating structural vibrations using active control devices (e.g., electro-hydraulic actuators). These actuators, which are installed in the structure, provide control forces that directly reduce the structure response.
4. A hybrid control system is a combination of active and passive control strategies.

The control strategies described above are rank-ordered based on their dynamic mitigation capabilities. The reader is referred to Saeed et al. (2015), Eshaghi et al. (2016), Thieblemont et al. (2017), Yang and Yang (2018) for additional information on structural control strategies. While more effective in mitigating the effect of disturbances, active control systems are more complex and might require a large input energy. However, recent studies have shown that, through integrated structure-control design, it is possible to obtain adaptive structures that require minimum energy throughout service (Senatore et al., 2019, Senatore and Reksowardojo, 2020). Numerical simulations and experimental testing show that that, compared with a passive solution, significant (up to 50%) mass and total energy savings (embodied in the material plus operational energy for control) could be achieved through the proposed adaptive solution (Wang and Senatore, 2020).

Although significant advances have been made in the design and control of adaptive structures, reliability issues related to the structure-control system, instability, and maintenance costs might be perceived as barriers for a wide application of such active systems. For this reason, it is worth investigating new passive structural control strategies and devices. This paper investigates the use of passive control devices with inherent adaptive features that allow mitigation of the structure response with no energy input. In natural structures, adaptation is often inherently built in. “Inherent,” in its literal sense, refers to something that is “stuck” in something else so firmly that the two cannot be separated. There are many instances of inherent adaptivity in the natural world. Lindner et al. (2010) investigate the notion of inherent adaptivity in a study on trees and state that “the inherent adaptive capacity encompasses the evolutionary mechanisms and processes that permit tree species to adjust to new environmental conditions.”

An example of a biological system that has provided inspiration for this study is the human spine. The spine comprises a series of vertebrae that are held together by muscles and ligaments. The intervertebral disc, a fibro-cartilaginous joint, lies between two adjacent vertebrae to stabilize the vertebral column, and it also provides shock absorption capability. The central part of the intervertebral disc, the nucleus pulposus, has the capacity to distribute pressure evenly across the disc, preventing force concentrations (McCann et al., 2012). The ligaments are located in different parts of the spine. Anterior, posterior, and interspinous ligaments extend, respectively, along the front, behind, and between the spinous processes (Palastanga and Soames, 2011). In conjunction with the lumbar muscles, they are effective to bear loads. **Figures 1A,B** shows the vertebral ligaments and the components of a section of the vertebral column, respectively.

Natural structures are complex systems that are made of many parts (i.e., compound) whose properties have been fine-tuned through evolution to provide inherent adaptivity to changing external actions. In most civil structures, single-function elements, such as beams and columns, are used. The development of a new element with inherent adaptivity involves

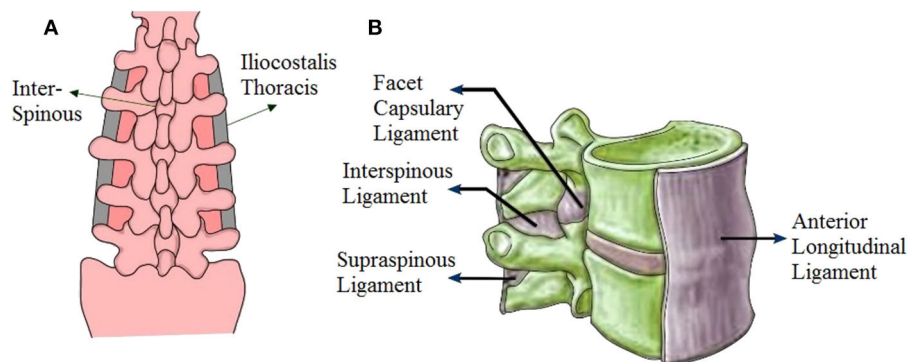


FIGURE 1 | Components of the human spine. **(A)** Vertebral ligaments, **(B)** components of a section of the vertebral column.

the use of more complex parts. In a compound element, it is the interaction between its parts that provides adaptive load-bearing capabilities in response to external loading. Generally, compound elements can be categorized as follows:

- 1- Compound connection element;
- 2- Compound beam element;
- 3- Compound column element;
- 4- Compound beam–column element;
- 5- Compound wall element;
- 6- Compound truss element.

Examples of existing compound elements are given in **Table 1**. The first element is a steel accordion force limiting device (AFLD), which has been designed based on buckling restrained bracing (Poursharifi et al., 2017, Poursharifi et al., 2020). This device can be used in place of critical compressive members in spatial structures. By controlling the instability onset of critical compressive members, AFLDs increase spatial structures’ load-bearing capacity.

The second element is a new concept named buckling-controlled member (BCM) (Chenaghlou et al., 2020). Compared to conventional truss members, the BCM offers a controlled post-buckling behavior that increases ductility and load-bearing capacity of the structure. One way to control buckling modes of compressive members is to add lateral constraints. In a BCM, this is achieved via a series of cylindrical plates (nuts) and an outer casing. Together, these components force the element to buckle through higher modes, ultimately increasing its load-carrying capacity.

In this paper, three passive compound elements with adaptive load-bearing capability are presented:

- 1. Compound column element inspired by the human spine;
- 2. Compound column element (masonry and cables) inspired by the human spine;
- 3. Compound truss element inspired by the bamboo stem.

Element 1 is a self-centering system inspired by the human spine, which comprises a column pre-stressed through cables. Element 1 is employed as a kinematic isolator. Element 2 is a similar self-centering system, which is applied to increase the load-bearing capacity of unreinforced masonry columns. Element 3 is an axially loaded element, inspired by the bamboo stem, which comprises a steel core reinforced by a series of cylindrical plates that are encased in a steel tube. Element 3 is employed to control the onset of instability in long-span truss structures. Application to typical frame, masonry, and truss structures is investigated through finite element analysis.

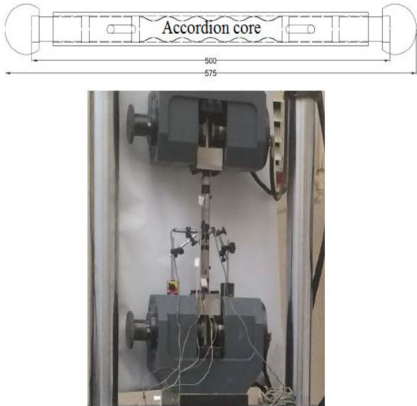
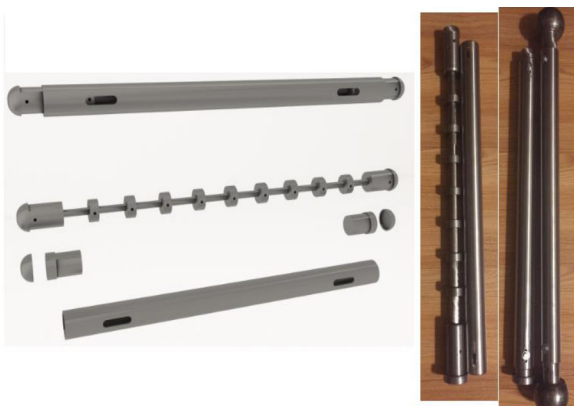
COMPOUND COLUMN ELEMENT INSPIRED BY THE HUMAN SPINE

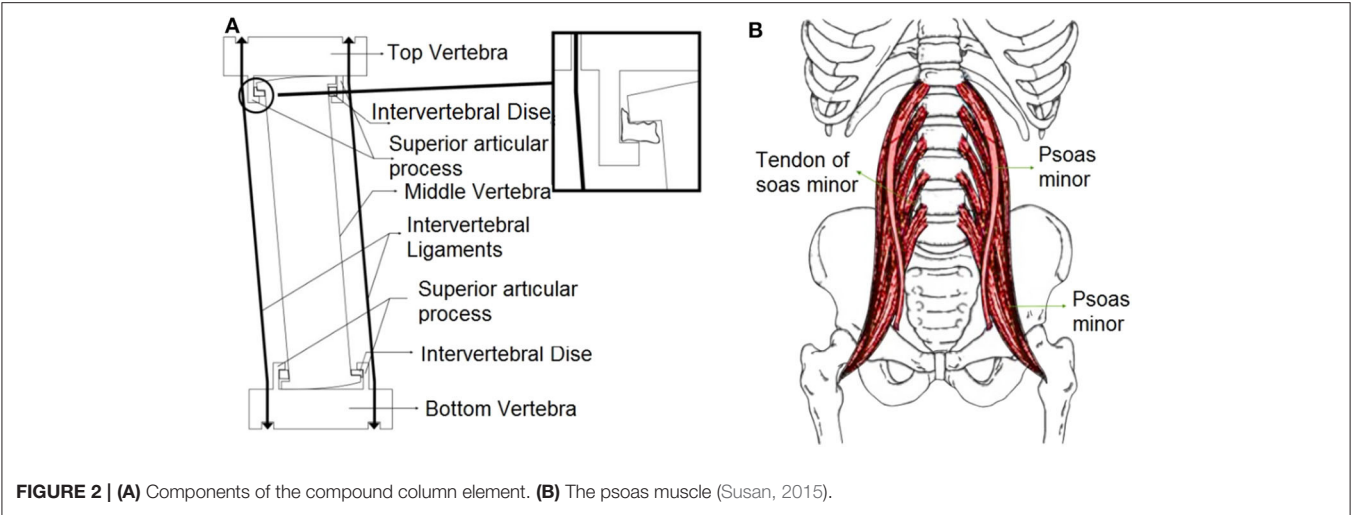
System Description

The compound column element is inspired by the human spine. It is a type of kinematic isolator, which was first proposed by Calafell et al. (2010). The compound column element is a self-centering system that comprises 4 main parts (see **Figure 2**): a vertical rod with rolling surfaces at both ends (similar to a lumbar vertebra), top and bottom capitals (similar to a half lumbar vertebra), circumferential cables (similar to vertebral ligaments and muscles), and top and bottom interface rubber-like material (similar to an intervertebral disc). The central rod can roll on the top and bottom surfaces of the capitals, and slippage can occur between the rolling surfaces. When the compound column is subjected to lateral loading, the tail-ends of the rolling surfaces of the central rod might come in contact with the movement restrainers of the top and bottom capitals, which function as kinematic constraints.

In the proposed column, interface rubber-like material is employed to bridge the gap between the tail-ends of the rolling surfaces with the capitals to prevent sudden impacts and also to reduce shock impact transfer to the superstructure.

TABLE 1 | Examples of compound elements.

Experimental and numerical studies		
Compound truss element		
	Steel accordion force limiting device (AFLD) (Poursharifi et al., 2017, 2020).	Buckling controlled member (BCM) (Chenaghlou et al., 2020).



By pre-stressing the circumferential cables, which is similar to the contraction of the muscle surrounding the spine, the column’s self-centering capability is obtained. The similarities of the proposed element to the human spine are listed in **Table 2**.

Finite Element Modeling

ABAQUS 6.12 has been employed to simulate the mechanical behavior of the compound column element. The components of the system, namely the top and bottom capitals, the central circular steel column, and the top and bottom interface rubber rings, have been modeled using the C3D8R element, an eight-node brick element with reduced integration. This element makes use of reduced integration algorithms to deal with shear locking issues (Simulia, 2012). Also, the T3D2 element, a three-dimensional, 2-node linear truss element, has been employed to model the circumferential cables. The mechanical properties of the top and bottom capitals and the central circular column are given in **Table 3**.

The Arruda and Boyce constitutive law (Arruda and Boyce, 1993) has been employed to model the behavior of the rubber rings. The material constant of the rubber material has been estimated based on guidelines recommended by the AASHTO 2000 standard (Pratt et al., 2000). The shear and bulk moduli of the rubber material with a hardness of 50 IHRD¹ have been set to 620 and 15×10^5 kN/m², respectively. All three translational degrees of freedom (u_x , u_y , u_z) of all the nodes at the bottom surface have been fixed (see **Figure 3**). The pre-stressed cables have been selected based on specifications by ASTM Grade 270 steel strand (ASTM A 416/A 416M). The diameter of the cables and their modulus of elasticity have been set to 9.53 mm and 200 GPa, respectively. The cables are anchored between top and bottom capitals. The cables have been pre-stressed using an initial tensile force of 10 kN. The interactions of the rolling surface of the central steel

TABLE 2 | The components of proposed compound element in comparison with human spine.

Proposed compound column element	Human spine
Circumferential cables	ligaments and muscles
Steel circular central column	vertebra
Top and bottom capitals	some portion of vertebrae
Interface rubber rings	intervertebral disc
Kinematic constraint of movement restrainer	interarticular processes

TABLE 3 | Compound column element mechanical properties.

Modulus of elasticity(E) MPa	Poisson's ratio (ν)	Yield stress (F_y) MPa	Coefficient of thermal expansion α 1/ $^{\circ}$ C	Mass density kg/m ³
2.1×10^5	0.3	240	12×10^{-6}	7,850

column with the top and bottom capitals have been accounted for using hard contact elements. Moreover, the interaction between the surfaces of the capitals and the column has been taken into account using kinematic contact elements. Also, the friction coefficient between the rolling surfaces and the capitals has been considered sufficiently high in order to avoid sliding. The other surfaces have been modeled with frictionless elements.

Numerical Simulation

Figure 3A shows the components of the compound column element. Two models are set up to investigate

- The behavior of a single compound column element
- Application of the compound column element as a kinematic isolator in a moment resisting frame.

¹International Rubber Hardness Degrees (ASTM D1415).

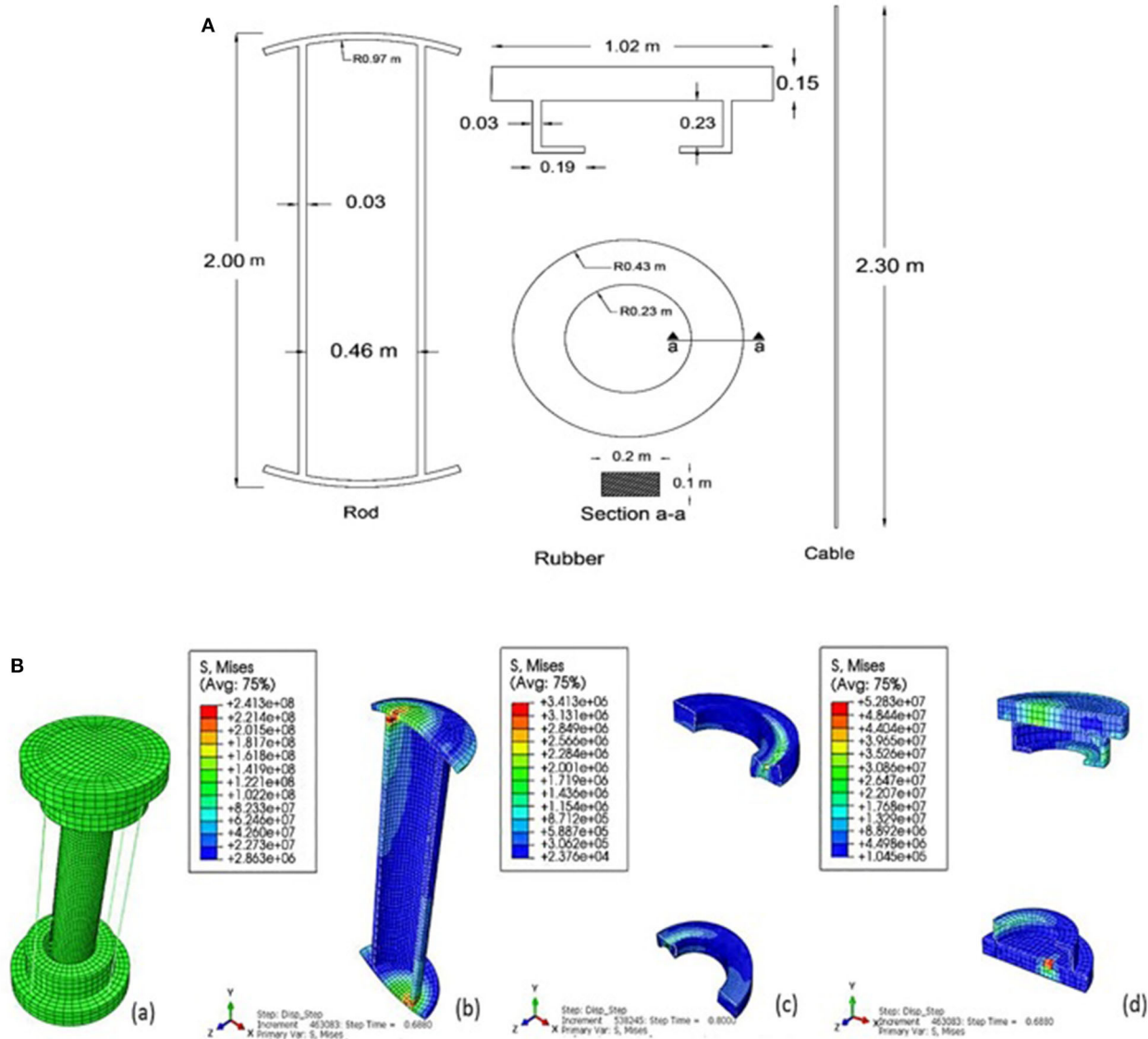


FIGURE 3 | (A) Components of the compound column element, **(B)** deformed shape and Von Mises stress contours.

Gravity load has been applied to the top surface of the column. A target displacement of ± 0.25 m has been defined. The force-displacement responses of the model have been determined in the following four cases:

1. With no pre-stressed cables as well as no top and bottom interface rubber rings.
2. Adding pre-stressed cables.
3. Adding top and bottom interface rubber rings.
4. Adding both pre-stressed cables as well as top and bottom interface rubber rings.

With the addition of the cables and the interface rubber rings, the capacity of the column progressively increases as

seen from **Figure 4A**. The inclusion of these elements has improved the performance of the column and eliminated residual displacements. The deformed shape and von Mises stress contours for case 4 are shown in **Figures 3B–D**.

Application of the compound column element to mitigate the structure response under seismic excitation has been studied. The compound element is employed as a kinematic isolator applied to the base of the columns of a moment resisting frame.

The behavior of the moment resisting frame is analyzed with/without the compound element. Two steel moment resisting frames (a one- and a two-story frame) are considered. Each of the two frames has four bays. As shown in **Figure 4B**, the span of the bays and the height of the stories are 5 and

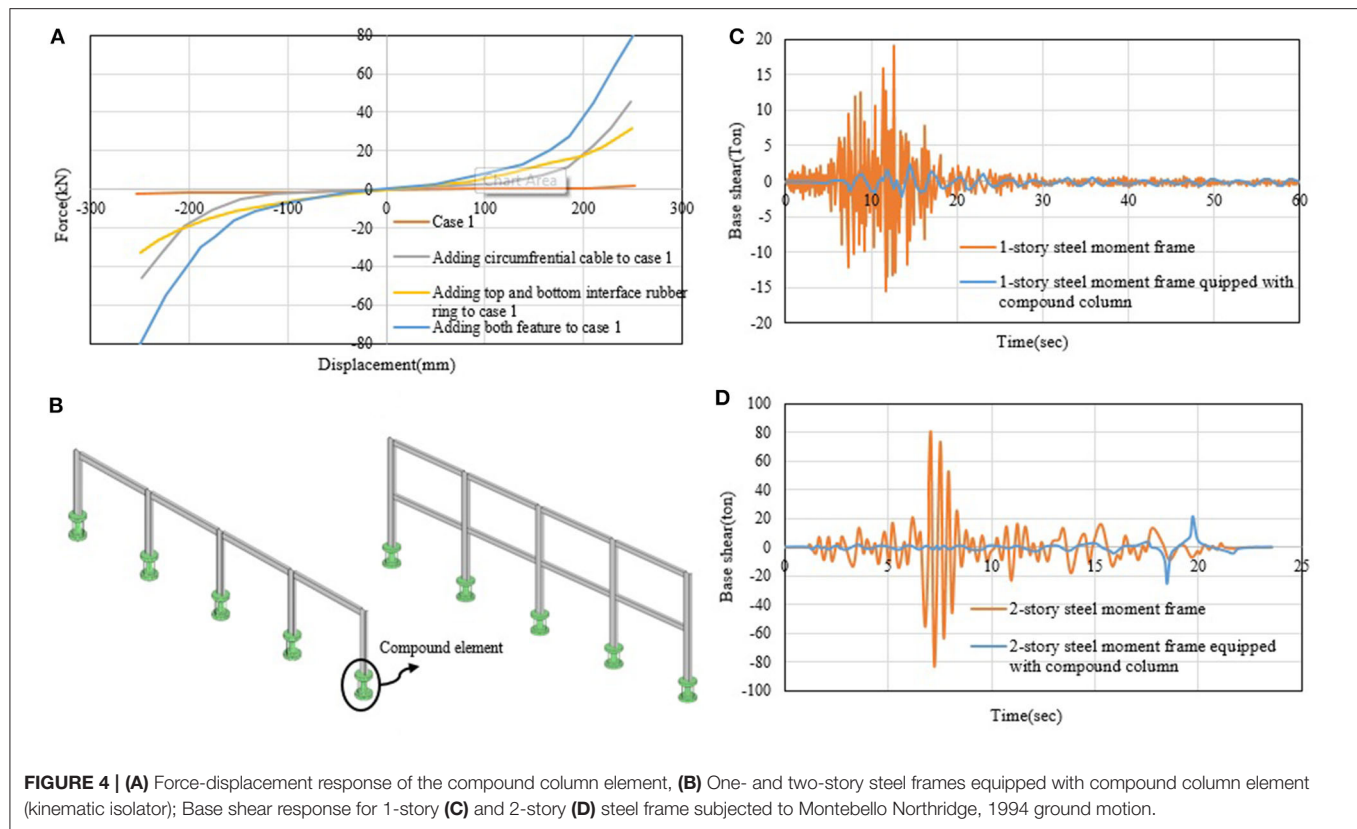


FIGURE 4 | (A) Force-displacement response of the compound column element, **(B)** One- and two-story steel frames equipped with compound column element (kinematic isolator); Base shear response for 1-story **(C)** and 2-story **(D)** steel frame subjected to Montebello Northridge, 1994 ground motion.

3.2 m, respectively. The magnitudes of the dead and live loads have been set to 650 and 200 kg/m², respectively. The seismic mass of the frame consists of the dead load in addition to 20% of the live load. Plastic hinges have been used to model the non-linear behavior of the structure. Plastic hinges have been used in the beams and columns based on guidelines by the ASCE 41-13 (ASCE, 2013) standard. For columns, the standard recommends the use of plastic hinges that are based on the interaction between axial forces and bending moments. The standard also recommends using bending moment-based plastic hinges for the beams. Non-linear time history analysis has been performed under 1994 Northridge ground motion. In the analysis, the Wilson- θ time integration method has been employed, whose stability and accuracy are determined by the parameter θ . This parameter and the damping ratio have been set to 1.4% and 5%, respectively. SAP2000 (Sap, 2016) has been used to carry out the non-linear time-history analysis. After evaluating the behavior of the steel frames, the compound element has been incorporated as a kinematic isolator placed at the base of the frame columns. Link elements have been used to model the column. The results of the analyses are shown in **Figures 4C,D**. The total base shear of the structure equipped with the compound element is significantly reduced (up to 87.26 and 95.86%, respectively) with respect to the original structure. This shows that the compound column element is an effective kinematic isolator, which is able to

reduce the seismic response of frame structures subjected to seismic excitation.

MASONRY COLUMN INSPIRED BY THE HUMAN SPINE

System Description

A similar self-centering system to that described in section Compound Truss Element is applied to improve load-bearing capability of masonry columns. In this compound element, cables can be thought of as the ligaments, the masonry column as the vertebral column, and top and bottom concrete capitals as the vertebrae of the human spine (see **Figure 5**). The behavior of this element has been analyzed through finite element modeling in ABAQUS 6.12 (Simulia, 2012). The results have been compared to the original masonry pier that is not equipped with pre-stressed cables. To model unreinforced masonry structures, different numerical approaches are employed. The following section gives details of the modeling procedure.

Modeling of Masonry Structure

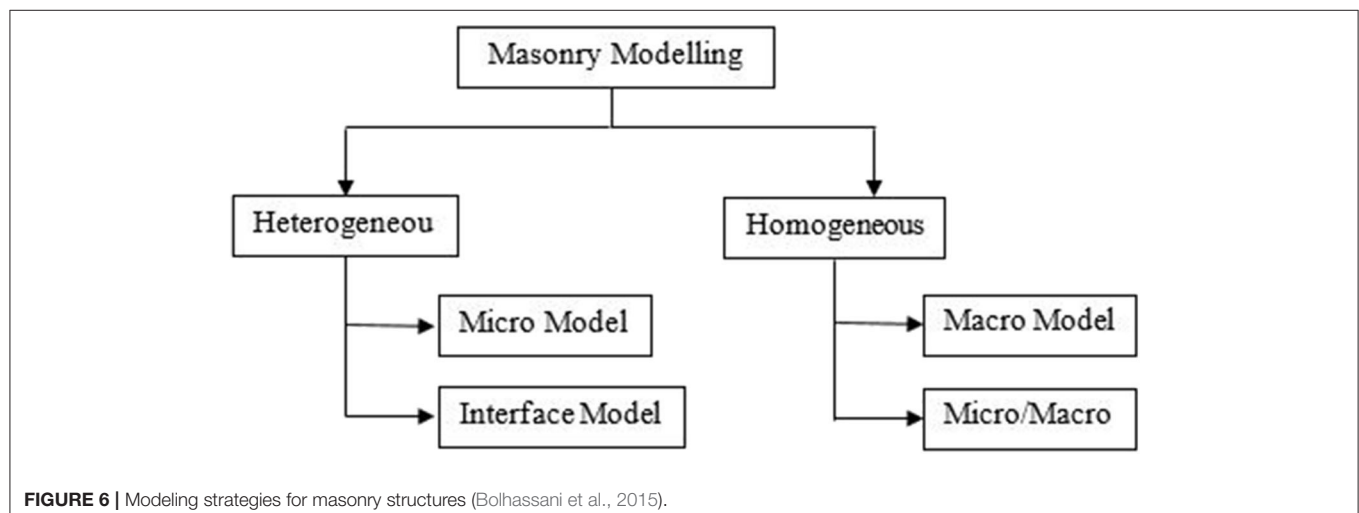
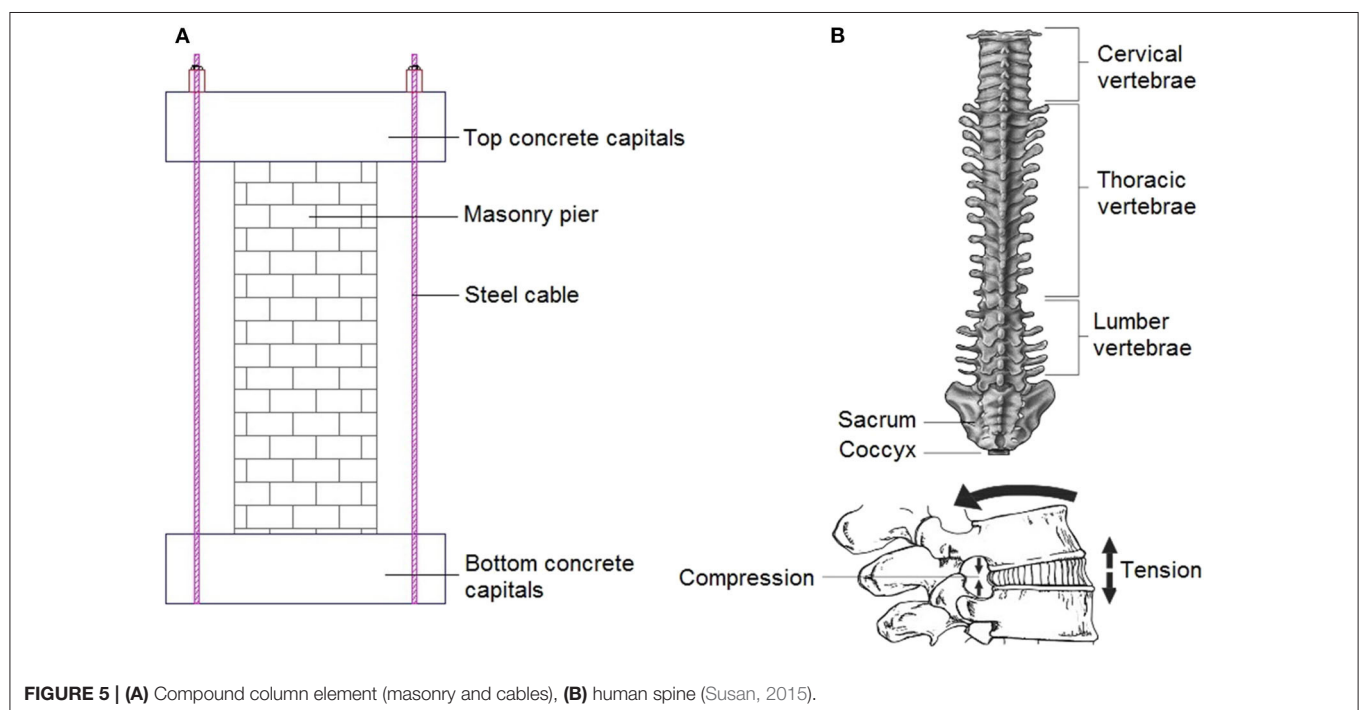
Masonry is one of the oldest materials used in construction. New methods of analyzing masonry structures have been the focus of recent studies (Lotfi and Shing, 1991, Lourenço and Rots, 1997, Shing et al., 1992, Berto et al., 2004, Milani, 2008, Milani, 2011a, Milani, 2011b, Stavridis and Shing, 2010, Minaie, 2010). The

finite element method (FEM) is a robust and powerful numerical method for the modeling of masonry structures (Bolhassani et al., 2015). FEM approaches for modeling masonry structures are classified into two categories: heterogeneous and homogeneous. In the heterogeneous approach, although collectively assumed as a single material, the mortar and the masonry units are considered as separate entities. Although the heterogeneous method of modeling masonry materials is generally more accurate compared to the homogeneous approach, it is far more time-consuming. Therefore, modeling masonry structures using either method depends on the level of desired accuracy.

Some of the procedures that may be adopted to model masonry structures are given in the flowchart of **Figure 6**. Among the most commonly used modeling procedures are

- The macro-modeling procedure, in which masonry units, mortar, and unit–mortar interfaces are merged in a homogeneous continuum.
- The detailed micro-modeling procedure, in which the masonry units and mortar joints—i.e., the mortar-filled intervals separating the bricks—are modeled using continuum elements. However, discontinuous elements are used for modeling unit–mortar interfaces.
- The simplified micro-modeling procedure, in which expanded units are represented by continuum elements, whereas the behavior of the mortar joints and unit–mortar interface is lumped in discontinuous elements (Laurenco et al., 1995).

According to the abovementioned methods, in this study, the simplified micro-modeling method has been adopted.



Numerical Simulation

The following models have been studied:

- 1- A masonry pier;
- 2- A masonry pier equipped with pre-stressed cables.

Non-linear static analysis has been performed on each model. The dimensions of the pier are $30 \times 30 \times 100$ cm. The brick sizes are $20 \times 10 \times 5$ cm and $10 \times 10 \times 5$ cm. The cables have a diameter of 10 mm. Material properties of the bricks, concrete capitals, and cables are given in **Table 4**. As mentioned before, the simplified micro-modeling technique has been used for the model. Also, concrete damage plasticity (CDP) has been employed to model the non-linear behavior of the masonry. Although this criterion is primarily used for isotropic brittle materials like concrete, it has also been extensively used for anisotropic materials such as masonry. The CDP model can take into account compressive and tensile strength with different damage parameters. In this model, tension and compression stress states are defined by the tensile damage index (d_t) and compressive damage index (d_c), respectively.

Material behavior in tension is linear up to the yield stress σ_{t0} . Above this value, cracks propagate, which is represented by a sudden drop of the stress–strain curve. The decay rate in the stress–strain curve is controlled by d_t (see **Figure 7A**). In compression, the behavior is linear until the yield stress σ_{c0} .

Then, hardening occurs before compressive crushing initiates. Above the peak stress σ_{cu} , the stress–strain curve drops due to softening. The rate of decay in the compressive stress–strain curve is controlled by d_c (see **Figure 7B**).

The damage parameters in tension (d_t) and compression (d_c) are defined by the following relationships:

$$\sigma_t = (1 - d_t) E_0 (\varepsilon_t - \varepsilon_t^{pl}), \quad (1)$$

$$\sigma_c = (1 - d_c) E_0 (\varepsilon_c - \varepsilon_c^{pl}), \quad (2)$$

wherein σ_t and σ_c are the tensile and compressive stresses; E_0 is the initial elastic modulus; ε_t and ε_c are, respectively, the total strain in tension and compression; and ε_t^{pl} and ε_c^{pl} are, respectively, the plastic strains in tension and compression. A summary of concrete damage parameters used in the non-linear analysis is given in **Table 5**.

The interaction between two brick units has been modeled by taking into account cohesion and friction. A sensitivity analysis has been carried out to achieve appropriate mesh sizing. Mortar material properties have been used in the simplified micro-modeling procedure. The model proposed by Mehrabi and Shing

TABLE 4 | Material properties of bricks, concrete capitals, and cables.

Masonry units			
Modulus of elasticity (E) (MPa)	Poisson's ratio (ν)	Compressive strength (MPa)	Tensile strength (MPa)
3980	0.15	7	0.7
Top and bottom concrete capitals			
Modulus of elasticity (E) (MPa)	Poisson's ratio (ν)	Compressive strength (MPa)	Tensile strength (MPa)
26139.8	0.2	24	2.4
Cables			
Modulus of elasticity (E) (GPa)	Poisson's ratio (ν)	Yield stress (MPa)	Mass density (Kg/m ³)
200	0.3	1,600	7,850

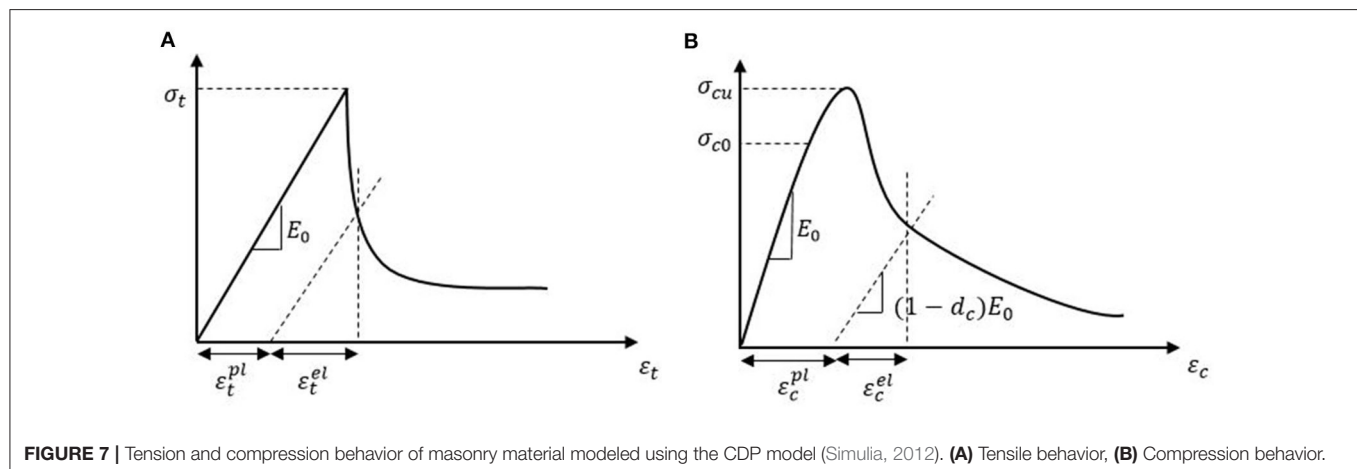


TABLE 5 | Concrete damage plasticity parameters for masonry units and concrete.

	Dilatation angle (ψ)	Eccentricity (ϵ)	$\frac{f_{bo}}{f_{co}}$	K_c	Viscosity parameter (α)
Masonry units	25°	0.1	1.16	0.67	0.002
Concrete capitals	38°	0.1	1.16	0.67	0.001

(1997) has been used to assign frictional, cohesive, and post-failure characteristics. A small non-zero value ($\cong 0.001$) has been used for the friction failure coefficient (Mehrabi and Shing, 1997). Also, the mortar tensile and shear stiffness have been determined using Equations (4) and (5), proposed by Furukawa et al. (2012):

$$\bar{k}_n = \frac{1}{\frac{l_A - t_M/2}{E_A/(1-\nu_A^2)} + \frac{t_M}{E_M/(1-\nu_M^2)} + \frac{l_B - t_M/2}{E_B/(1-\nu_B^2)}}, \quad (3)$$

$$\bar{k}_s = \frac{1}{\frac{l_A - t_M/2}{E_A/(1+\nu_A)} + \frac{t_M}{E_M/2(1+\nu_M)} + \frac{l_B - t_M/2}{E_B/2(1+\nu_B)}}, \quad (4)$$

wherein \bar{k}_n is the normal or tensile stiffness between the mortar layers, \bar{k}_s is the shear stiffness between the mortar layers, l_A and l_B are the distances from the surface of the masonry unit to its center, and t_M is the mortar layer thickness. E_A , E_B , and E_M are the elastic moduli of upper and lower masonry units and the mortar, respectively. ν_A , ν_B , and ν_M are the Poisson ratios of upper and lower masonry units and the mortar, respectively. **Table 6** gives cohesion and friction material properties adopted in the model.

The base of the masonry columns is fully fixed. A vertical gravity load has been applied to the top of the column and kept constant throughout the displacement-control analysis. A horizontal displacement of 20 cm has been applied to the top of the column. Von Mises stress contours are shown in **Figure 8A**. The masonry pier collapses in the absence of cables, while adding the cables increases significantly the load-bearing capacity. Also, the action of cables prevents cracks from propagating into the pier. Comparing the base shear-displacement curves in the two states shows that the pre-stressed cables have significantly increased the capacity of pier (see **Figure 8B**).

COMPOUND TRUSS ELEMENT

System Description

This compound element is inspired by the morphology of the bamboo stem. The proposed element comprises a steel core, adjustable cylindrical plates (nuts), and a steel casing. The similarity of the proposed element with the bamboo stems is illustrated in **Figure 9**. When the steel core alone is under the action of the compressive load P , it buckles easily. Addition of the cylindrical plates (i.e., nuts) between the core and the casing

TABLE 6 | Cohesive and frictional behavior of the numerical model.

Behavior			
Tangential behavior		Friction coefficient (μ)	0.7
Normal behavior		Hard contact	—
Cohesive behavior		Traction-separation behavior	
Stiffness coefficient (MN/m)	K_{nn}	K_{ss}	K_{tt}
		8.7	8.7
			0
Damage	Initiation	Normal (N/mm ²)	0.0611
		Shear I (N/mm ²)	0.09335
		Shear II (N/mm ²)	0.09335
	Evolution	Plastic Displacement (mm)	1
		Exponential parameter	10

is effective to postpone the onset of buckling of the steel core (Chenaghlou et al., 2020). The cylindrical plates (nuts) are fixed to the steel core similar to how a nut is fixed to a screw. The cylindrical nuts and the steel core are placed inside the steel casing. Compressive load is first applied to the steel core, and after it buckles, the load is transferred to the steel casing. There is a 1-mm gap between the steel casing and the steel core. In other words, there is no contact between the steel core and the steel casing prior to buckling. The gap allows the steel core to go through different buckling modes before making contact with the casing. This way, the member reacts to compressive loads in two stages. In the first stage, the after the steel core reaches its maximum capacity, it buckles. In the second stage, the two components (i.e., the core and the casing) come into contact, and the casing is only responsible for controlling post-buckling effects.

Application of this compound element has been investigated for long-span spatial structures, such as roof systems with a large cover. These structures tend to be brittle and go through progressive collapse when a number critical compressive members buckle (Schmidt et al., 1980, Schmidt et al., 1982). Several techniques have been developed to delay the onset of brittle collapse for these structures. One of these techniques is the application of a force limiting device (FLD) in the critical compressive members. The compound truss element presented in this section is a new FLD that can be employed to replace critical compressive members in spatial structures. This element is illustrated in **Figure 10A**. A double-layer flat roof is selected to investigate the efficacy of such compound element (see **Figure 10B**).

Numerical Simulation

The structure is designed to take dead and snow loads, which have been applied following the Iranian national code of buildings (Housing and Development, 2014). Non-linear analyses have been carried out using ABAQUS. Geometric and material non-linearity has been taken into account. Mechanical properties and cross-section properties of the structural elements are given in **Tables 7, 8**.

The compound element is first studied in isolation under compressive loading. A slenderness ratio of $\lambda = 85$ and

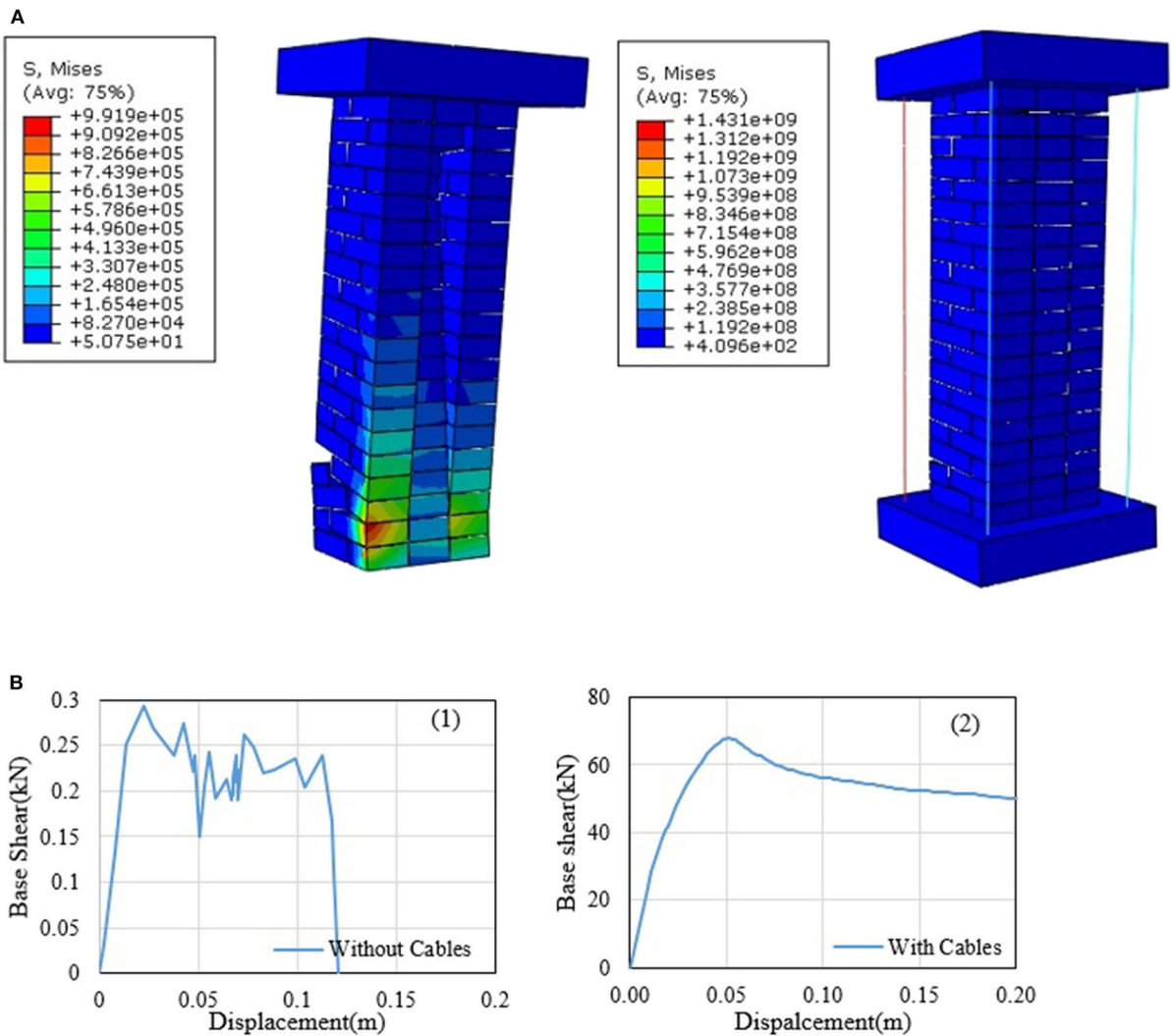


FIGURE 8 | (A) Von-Mises stress contours of the masonry pier. **(B)** Base shear-displacement curves of masonry pier (1) without cables, (2) with cables.

an initial geometrical imperfection of $0.001L$ applied at midlength have been considered. The axial displacement response of the encasing element (without nuts) is shown in **Figure 11A** and that of the compound element is shown in **Figure 11B**.

The obtained results show that, when the encasing reaches its critical capacity under compressive loading, it buckles and undergoes a sudden strength degradation. However, after the addition of the steel core, the brittle behavior of the casing changes to a ductile one, which persists until a strain of ~ 0.1 . At this point, the core and the casing come in contact, resulting in a sudden surge in strength of the member. After reaching a maximum stress of $\sim 1,200$ MPa, the member goes through failure.

The effect of using such a compound element in spatial structures has been evaluated. The location of buckled members

(see **Figure 12A**) and the collapse behavior of the structure have been determined using non-linear static analysis. Then, the proposed compound element has been used in place of the buckled members. Another non-linear static analysis has been carried out replacing the critical compressive elements with the proposed compound element. **Figure 12B** shows the force-displacement response of the spatial structure with and without compound elements. The effect of the compound elements has changed the structure behavior from brittle to ductile ultimately delaying significantly the onset of collapse. Simulation results indicate that application of the compound truss element improves energy absorption, ductility, stiffness, and capacity of the double-layer flat roof by up to 58, 64, 17, and 53%, respectively. Given that the proposed compound truss element is used in place of only a few critical members, the structure mass increases by 9.755%, which is not a significant penalty.

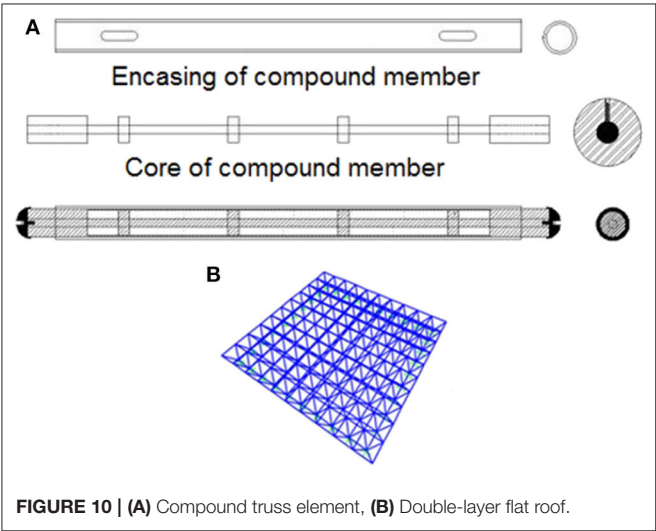
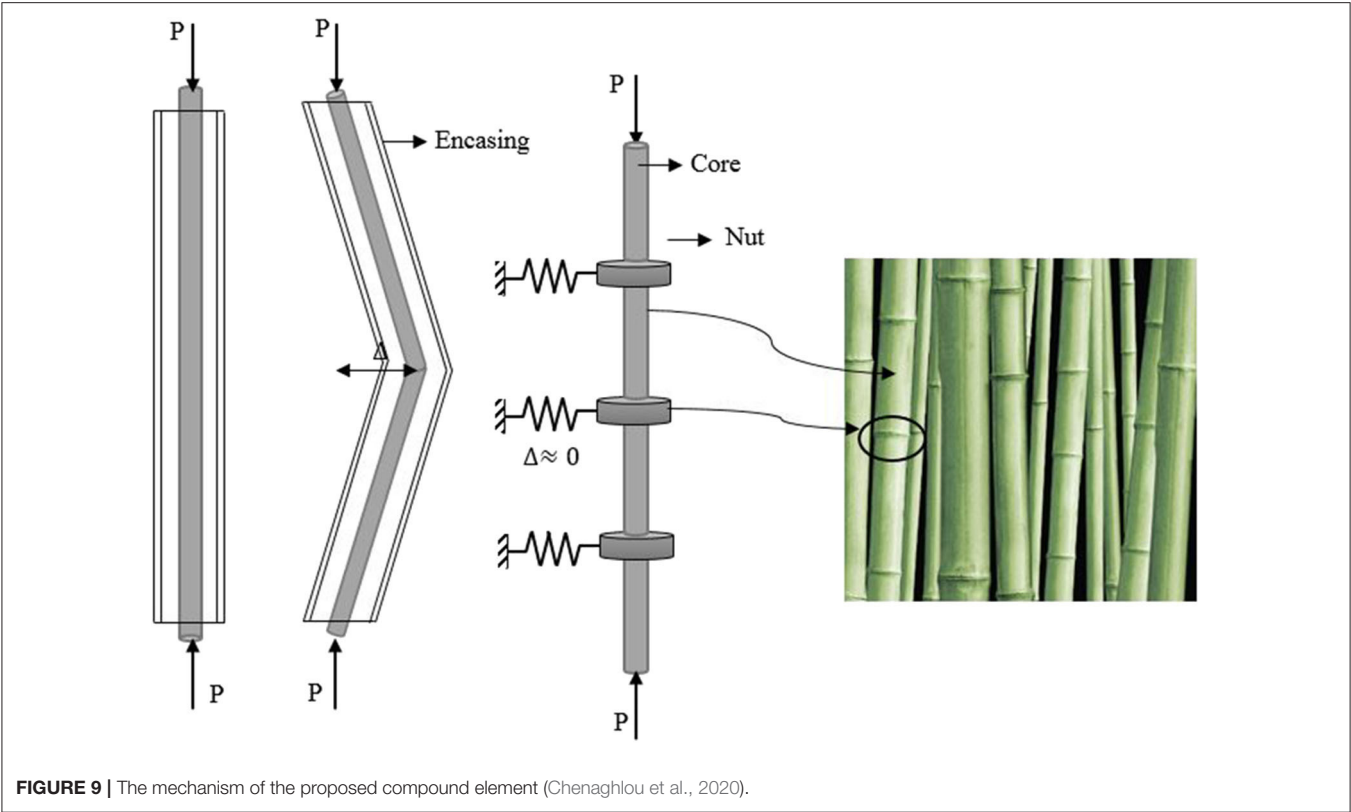


TABLE 7 | Material mechanical properties.

Modulus of elasticity (<i>E</i>) <i>MPa</i>	Poisson's ratio (<i>ν</i>)	Yield stress (<i>F_y</i>) <i>MPa</i>	Coefficient of thermal expansion (<i>α</i>) 1/° c	Mass density <i>kg/m³</i>
2.1 × 10 ⁵	0.3	240	12 × 10 ^{−6}	7,850

TABLE 8 | Spatial structure element cross-section section properties.

Range of section properties	Double-layer flat roof	
	Chord	Web
Section Area <i>A</i> (cm ²)	17.72	13.95
Diameter <i>D</i> (mm)	100	80
Thickness <i>t_w</i> (mm)	6	6

CONCLUSIONS

This study has taken inspiration from natural structures inherent adaptive capabilities. Three compound elements that improve structures' load-bearing capacity through passive inherent adaptivity have been proposed in this paper. These elements are (1) a self-centering column inspired by the human spine, (2) a self-centering unreinforced masonry pier with cables also

inspired by the human spine, and (3) an FLD (compound truss member) inspired by the bamboo stem.

The behavior of each compound element and its efficacy when employed as load-bearing member has been investigated through FEM. Based on the obtained results, the following conclusions can be drawn:

- Using the compound column element as a kinematic isolator is effective to mitigate the response of frame structures

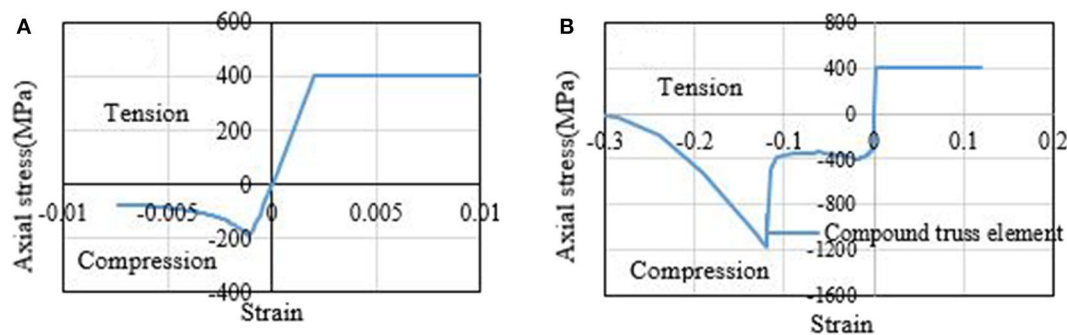


FIGURE 11 | Axial displacement response of (A) encasing member with a slenderness ratio of $\lambda = 85$ and (B) compound truss element.

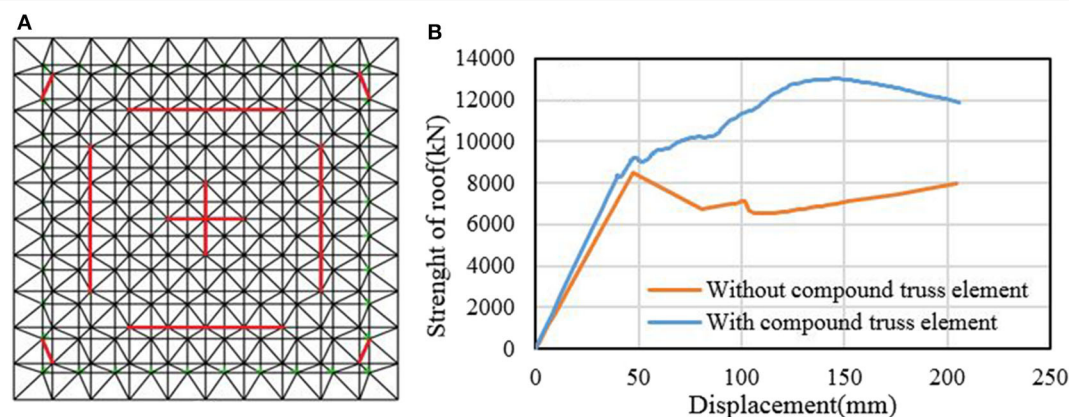


FIGURE 12 | (A) Location of critical compressive elements, (B) Force-displacement response with and without compound truss elements.

subjected to ground motion. Simulations on a one- and two-story moment resisting frames under seismic excitation have shown that the base shear decreases by 87.26 and 95.86%, respectively.

- The self-centering property of the compound masonry column element postpones collapse onset and prevents crack propagation. The effect of pre-stressed cables significantly increases the masonry column load-bearing capacity, which becomes twice as ductile compared to the masonry column that is not equipped with pre-stressed cables.
- Replacing critical compression members with the compound truss element is effective to increase ductility of long-span spatial structures as well as energy absorption, stiffness, and load-bearing capacity.

DATA AVAILABILITY STATEMENT

The raw data supporting the conclusions of this article will be made available by the authors, without undue reservation.

AUTHOR'S NOTE

The main objective of this paper is to show how the inspiration from the nature has influenced the designing of structures and discusses how the nature-inspired idea could convert into a new language for the future structural design industry. Also, the new concept for inherent adaptive control of structures and compound element based on natural creatures inspired from nature is introduced and compound element.

AUTHOR CONTRIBUTIONS

All authors listed have made a substantial, direct and intellectual contribution to the work, and approved it for publication.

ACKNOWLEDGMENTS

The authors gratefully acknowledge Maryam Chenaghloou, MD, cardiologist, fellowship of heart failure and transplantation at the Rajaie cardiovascular medical and research center, for her assistance.

REFERENCES

- Arruda, E. M., and Boyce, M. C. (1993). A three-dimensional constitutive model for the large stretch behavior of rubber elastic materials. *J. Mech. Phys. Solids* 41, 389–412. doi: 10.1016/0022-5096(93)90013-6
- ASCE (2013). *ASCE/SEI 41-13: Seismic Evaluation and Retrofit of Existing Buildings*. Reston, VA: American Society of Civil Engineers.
- Berto, L., Saetta, A., Scotta, R., and Vitaliani, R. (2004). Shear behaviour of masonry panel: parametric FE analyses. *Int. J. Solids Struct.* 41, 4383–4405. doi: 10.1016/j.ijsolstr.2004.02.046
- Bolhassani, M., Hamid, A. A., Lau, A. C., and Moon, F. (2015). Simplified micro modeling of partially grouted masonry assemblages. *Constr. Build. Mater.* 83, 159–173. doi: 10.1016/j.conbuildmat.2015.03.021
- Calafell, R. L., Roschke, P. N., and Juan, C. (2010). Optimized friction pendulum and precast-prestressed pile to base-isolate a Chilean masonry house. *Bull. Earthquake Eng.* 8, 1019–1036. doi: 10.1007/s10518-009-9163-0
- Chenaghloou, M. R., Kheirollahi, M., and Abedi, K. (2020). *Patent No. E04C 3/00;E04B 1/00, Patent and Trademark Office*. Tabriz-Iran patent application.
- Eshaghi, M., Sedaghati, R., and Rakheja, S. (2016). Dynamic characteristics and control of magnetorheological/electrorheological sandwich structures: a state-of-the-art review. *J. Intell. Mater. Syst. Struct.* 27, 2003–2037. doi: 10.1177/1045389X15620041
- Furukawa, A., Kiyono, J., and Toki, K. (2012). Numerical simulation of the failure propagation of masonry buildings during an earthquake. *J. Nat. Disaster Sci.* 33, 11–36. doi: 10.2328/jnds.33.11
- Gkatzogias, K. I., and Kappos, A. J. (2016). Semi-active control systems in bridge engineering: a review of the current state of practice. *Struct. Eng. Int.* 26, 290–300. doi: 10.2749/101686616X14555429844040
- Housing, M. O., and Development, U. (2014). *Iranian National Building Code (Part 6)*. 3rd ed. Ministry of Housing and Urban Development, Tehran, Iran.
- Laurenco, P., Rots, J. G., and Blaauwendraad, J. (1995). Two approaches for the analysis of masonry structures: micro and macro-modeling. *HERON* 40:1995.
- Lindner, M., Maroschek, M., Netherer, S., Kremer, A., Barbat, A., Garcia-Gonzalo, J., et al. (2010). Climate change impacts, adaptive capacity, and vulnerability of European forest ecosystems. *For. Ecol. Manage.* 259, 698–709. doi: 10.1016/j.foreco.2009.09.023
- Lotfi, H., and Shing, P. (1991). An appraisal of smeared crack models for masonry shear wall analysis. *Comput. Struct.* 41, 413–425. doi: 10.1016/0045-7949(91)90134-8
- Lourenço, P. B., and Rots, J. G. (1997). Multisurface interface model for analysis of masonry structures. *J. Eng. Mech.* 123, 660–668. doi: 10.1061/(ASCE)0733-9399(1997)123:7(660)
- McCann, M. R., Tamplin, O. J., Rossant, J., and Séguin, C. A. (2012). Tracing notochord-derived cells using a Noto-cre mouse: implications for intervertebral disc development. *Dis. Model. Mech.* 5, 73–82. doi: 10.1242/dmm.008128
- Mehrabi, A. B., and Shing, P. B. (1997). Finite element modeling of masonry-infilled RC frames. *J. Struct. Eng.* 123, 604–613. doi: 10.1061/(ASCE)0733-9445(1997)123:5(604)
- Milani, G. (2008). 3D upper bound limit analysis of multi-leaf masonry walls. *Int. J. Mech. Sci.* 50, 817–836. doi: 10.1016/j.ijmecsci.2007.11.003
- Milani, G. (2011a). Simple homogenization model for the non-linear analysis of in-plane loaded masonry walls. *Comput. Struct.* 89, 1586–1601. doi: 10.1016/j.compstruc.2011.05.004
- Milani, G. (2011b). Simple lower bound limit analysis homogenization model for in-and-out-of-plane loaded masonry walls. *Const. Build. Mater.* 25, 4426–4443. doi: 10.1016/j.conbuildmat.2011.01.012
- Minaie, E. (2010). *Behavior and vulnerability of reinforced masonry shear walls* (Ph.D. thesis). Drexel University.
- Palastanga, N., and Soames, R. (2011). *Anatomy and Human Movement, Structure and Function With PAGERBURST Access, 6: Anatomy and Human Movement*. London: Elsevier Health Sciences.
- Poursharifi, M., Abedi, K., Chenaghloou, M., and Fleischman, R. B. (2020). Introducing a new all steel accordion force limiting device for space structures. *Struct. Eng. Mech.* 74, 69–82. doi: 10.12989/sem.2020.74.1.069
- Poursharifi, M., Abedi, K., and Chenaghloou, M. (2017). 05.32: Experimental and numerical study on the collapse behavior of an all-steel accordion force limiting device. *ce/papers* 1, 1315–1324. doi: 10.1002/cepa.173
- Pratt, R. I., Roush, N. H., Ruff, W. T., Schneider, M. M. E. (2000). *American Association of State Highway and Transportation Officials*.
- Reinhorn, A., Soong, T., Riley, M., Lin, R., Aizawa, S., and Higashino, M. (1993). Full-scale implementation of active control. II: installation and performance. *J. Struct. Eng.* 119, 1935–1960. doi: 10.1061/(ASCE)0733-9445(1993)119:6(1935)
- Saeed, T. E., Nikolakopoulos, G., Jonasson, J.-E., and Hedlund, H. (2015). A state-of-the-art review of structural control systems. *J. Vibrat. Control* 21, 919–937. doi: 10.1177/1077546313478294
- Sap, C. (2016). *Integrated Finite Element Analysis and Design of Structures*. Version 18.0. Berkeley, CA: Computers and Structures Inc.
- Schmidt, L., Cogan, K., Morgan, P., and Omeagher, A. (1980). Ultimate load behaviour of a full scale space truss. *Proc. Institution Civil Eng.* 69, 97–109. doi: 10.1680/jicep.1980.2489
- Schmidt, L. C., Morgan, P., and Hanaor, A. (1982). Ultimate load testing of space trusses. *J. Struct. Division* 108, 1324–1335. doi: 10.1061/(ASCE)0733-9445(1983)109:5(1334.2)
- Senatore, G., Duffour, P., and Winslow, P. (2019). Synthesis of minimum energy adaptive structures. *Struct. Multidisciplinary Optimization* 60, 849–877. doi: 10.1007/s00158-019-02224-8
- Senatore, G., and Reksowardojo, A. (2020). Force and shape control strategies for minimum energy adaptive structures. *Front. Built Environ.* 6:105. doi: 10.3389/fbuil.2020.00105
- Shing, P., Lofti, H., Barzegarmehrabi, A. and Bunner, J. (1992). “Finite element analysis of shear resistance of masonry wall panels with and without confining frames,” in *Proceedings of the 10th World Conference on Earthquake Engineering*. Netherlands: AA Balkema Rotterdam, 2581–2586.
- Simulia, D. S. (2012). *Abaqus 6.12 Documentation*. Providence: Simulia Company, 261.
- Stavridis, A., and Shing, P. (2010). Finite-element modeling of nonlinear behavior of masonry-infilled RC frames. *J. Struct. Eng.* 136, 285–296. doi: 10.1061/(ASCE)ST.1943-541X.116
- Susan, J. H. (2015). *Basic Biomechanics*. New York, NY: McGraw-Hill Education.
- Symans, M. D., and Constantinou, M. C. (1999). Semi-active control systems for seismic protection of structures: a state-of-the-art review. *Eng. Struct.* 21, 469–487. doi: 10.1016/S0141-0296(97)00225-3
- Thieblemont, H., Haghighat, F., Ooka, R., and Moreau, A. (2017). Predictive control strategies based on weather forecast in buildings with energy storage system: a review of the state-of-the-art. *Energy Buildings*, 153, 485–500. doi: 10.1016/j.enbuild.2017.08.010
- Wagg, D., Bond, I., Weaver, P., and Friswell, M. (2008). *Adaptive Structures: Engineering Applications*. Chichester: John Wiley & Sons. doi: 10.1002/9780470512067
- Wang, Q., Senatore, G., Jansen, K., Habraken, A., and Teuffel, P. (2020). Design and characterization of variable stiffness structural joints. *Mater. Des.* 187:108353. doi: 10.1016/j.matdes.2019.108353
- Wang, Y., and Senatore, G. (2020). Minimum energy adaptive structures—All-In-One problem formulation. *Comput. Struct.* 236:106266. doi: 10.1016/j.compstruc.2020.106266
- Yang, Y., and Yang, J. P. (2018). State-of-the-art review on modal identification and damage detection of bridges by moving test vehicles. *Int. J. Struc. Stability Dynamics* 18:1850025. doi: 10.1142/S0219455418500256

Conflict of Interest: The authors declare that the research was conducted in the absence of any commercial or financial relationships that could be construed as a potential conflict of interest.

Copyright © 2020 Chenaghloou, Kheirollahi, Abedi, Akbari and Fathpour. This is an open-access article distributed under the terms of the Creative Commons Attribution License (CC BY). The use, distribution or reproduction in other forums is permitted, provided the original author(s) and the copyright owner(s) are credited and that the original publication in this journal is cited, in accordance with accepted academic practice. No use, distribution or reproduction is permitted which does not comply with these terms.



Motion Design with Efficient Actuator Placement for Adaptive Structures that Perform Large Deformations

Renate Sachse*, Florian Geiger, Malte von Scheven and Manfred Bischoff

Institute for Structural Mechanics, University of Stuttgart, Stuttgart, Germany

OPEN ACCESS

Edited by:

Gennaro Senatore,
École Polytechnique Fédérale de
Lausanne, Switzerland

Reviewed by:

David Lattanzi,
George Mason University,
United States
Philippe Duffour,
University College London,
United Kingdom

*Correspondence:

Renate Sachse
sachse@ibb.uni-stuttgart.de

Specialty section:

This article was submitted to
Computational Methods in Structural
Engineering,
a section of the journal
Frontiers in Built Environment

Received: 26 March 2020

Accepted: 21 May 2021

Published: 02 June 2021

Citation:

Sachse R, Geiger F, von Scheven M
and Bischoff M (2021) Motion Design
with Efficient Actuator Placement for
Adaptive Structures that Perform
Large Deformations.
Front. Built Environ. 7:545962.
doi: 10.3389/fbuil.2021.545962

Adaptive structures have great potential to meet the growing demand for energy efficiency in buildings and engineering structures. While some structures adapt to varying loads by a small change in geometry, others need to perform an extensive change of shape to meet varying demands during service. In the latter case, it is important to predict suitable deformation paths that minimize control effort. This study is based on an existing motion design method to control a structure between two given geometric configurations through a deformation path that is optimal with respect to a measure of control efficiency. The motion design method is extended in this work with optimization procedures to obtain an optimal actuation system placement in order to control the structure using a predefined number of actuators. The actuation system might comprise internal or external actuators. The internal actuators are assumed to replace some of the elements of the structure. The external actuators are modeled as point forces that are applied to the structure nodes. Numerical examples are presented to show the potential for application of the motion design method to non-load-bearing structures.

Keywords: motion design, optimization, adaptive structures, deployable structures, actuator placement

INTRODUCTION

Sustainability and energy efficiency have become important design requirements for engineering structures. The ability to adapt to changing loading conditions enables adaptive structures to achieve material and energy savings. Through sensing and actuation, adaptive structures are able to counteract deflections and to homogenize the stress under varying loading conditions as shown in Sobek and Teuffel (2001) and Senatore et al. (2018). In so doing significant mass, embodied energy and carbon can be saved compared to conventional passive structures. Since these studies were primarily concerned with adaptive load-bearing structures, adaptation was limited to relatively small shape changes.

Adaptive structures can also adapt to varying usage requirements during service, for example, deployable structures in the form of retractable roofs, folding bridges and adaptive façades (e.g., Knippers and Schlaich 2000; Knippers et al., 2013). In these cases, the structure adapts through a series of geometry configurations that might differ significantly from each other. Transitioning from one geometry configuration to another is typically carried out through articulations such as joints and hinges, or in the case of compliant structures, by a targeted stiffness reduction in the direction of the desired deformation (Kota et al., 2001). Compliant structures (also called morphing structures) are able to deform in required shapes through strategic distribution of stiffness as shown in Hasse and Campanile (2009), and Masching and Bletzinger (2016). Several studies also exist on truss (Inoue 2008; Sofla et al., 2009; Reksowardojo et al., 2019) and tensegrity structures (Wijdeven and Jager 2005; Masic and Skelton 2005) that are able to perform large shape changes.

A critical aspect in structural adaptation is to consider the transition between shapes (i.e., geometry configurations) because changing shape causes stresses and requires energy. The shape change can be realized through different actuation types. Discrete (e.g., linear) and continuous (e.g., piezoelectric, shape-memory alloy) actuators have been employed for shape control (Irschik 2002, Mohd Jani et al., 2014, Senatore et al., 2018). The way the actuators are controlled is important to achieve satisfactory shape-control efficiency. Other approaches combine optimal control with mechanics (Preumont 2011; Ibrahimbegovic et al., 2004) as well as stochastic optimization with path-planning and machine learning (Veuve et al., 2017; Sychterz and Smith 2018).

Optimal actuator placement is a key to shape control efficiency. This is a challenging task i.e., an active field of research. Generally, the better the choice of the actuator locations, the lower the energy for adaptation. Actuator placement has been carried out through numerical optimization formulations in Gupta et al. (2010) with a focus on the use of piezoelectric actuation. In Kwan and Pellegrino (1993), a simplex optimization approach was applied for actuator placement in pre-stressed deployable structures. Actuator placement formulations for discrete truss structures have been given by many. A genetic optimization algorithm was implemented for efficient structural vibration control in Abdullah et al. (2001). A greedy and inverse greedy algorithm was implemented by Wagner et al. (2018) for optimal compensation of external disturbances. In Teuffel (2004), optimal placement was implemented based on a heuristic measure of actuator efficacy for force and shape control. Senatore et al. (2019) and Wang and Senatore (2020) formulated new methods to design minimum energy adaptive structures. Embodied energy in the material and operational energy for control are minimized through combined optimization of structural sizing and actuator placement. Results have shown that minimum energy adaptive structures perform significantly better than conventional passive structures with regard to input material as well as energy and carbon requirements thus reducing adverse environmental impacts. These studies focused on load-bearing structures and thus were based on small strain and small displacement assumptions. Large deformations have been accounted for in Masching and Bletzinger (2016), where actuator locations were optimized based on a measure of control efficiency which is included in the shape optimization of shells. A multi-objective optimization formulation was given in Reksowardojo et al. (2020) to design truss structures that react to loading through shape adaptation accounting for large deformations. The structure is designed to “morph” into shapes that are optimal to take external loads. These target shapes are obtained through shape optimization. The actuator placement is then optimized so that the structure can be controlled into the target shapes. The inverse problem to obtain actuator commands that control the structure into the target shapes is solved through a Newton-Raphson scheme based on a geometrically nonlinear force method. It was shown that optimal shape adaptation enables significant stress homogenization which produces minimum mass structural solutions.

In this publication, heuristic algorithms for actuator placement are combined with an existing method for motion

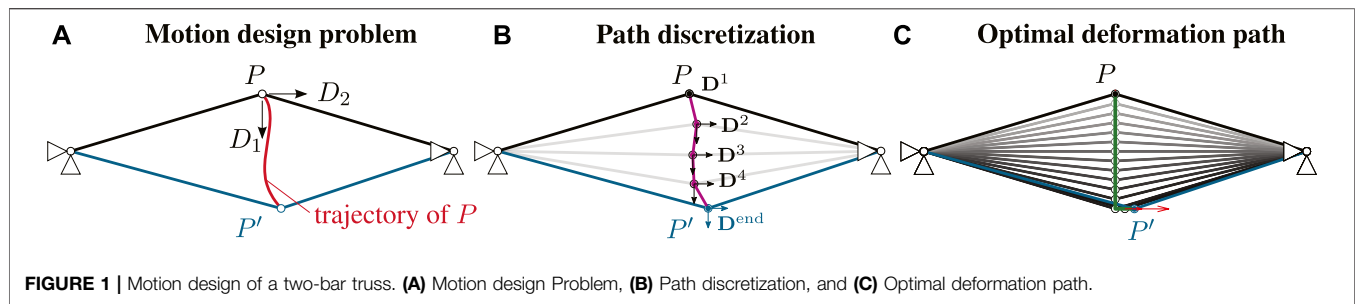
design presented in Sachse and Bischoff (2020) and further extended in Sachse et al. (2021). This method produces optimal deformation paths between two prescribed geometric configurations that might differ significantly from each other to meet varying demands during service. The method of motion design takes large deformations into account. Motion might involve element deformations, deployment through finite mechanisms and a combination of both. The integral of the strain energy over the deformation path is employed as the objective function, which is to be minimized. This objective can be interpreted as the “cost of deformation,” which is similar to the “cost of transport” employed in robotics (e.g., Seok et al., 2013). The “cost of deformation” gives an indication of the energy required to control the structure between two prescribed shapes. In Sachse and Bischoff (2020) this method was investigated for structures that move through finite mechanisms, incorporating instability behavior and inextensible deformations of shells. The optimal motion trajectory is first obtained. Then, actuation forces to realize such motion are back-calculated from equilibrium conditions. As a result, actuation forces may be required for all degrees of freedom, which is a limitation for most practical structures since the actuation system would be too complex. This limitation has been surpassed by adding suitable constraints to the motion design formulation so that resulting deformation paths can be realized through a specific number of external or internal actuators. The constrained motion design formulation is given in Sachse et al. (2021) and is summarized in *Motion Design of Structures With Constraints* of this paper for completeness. A method for optimal placement of external actuation forces to control the structure into required deformation paths is given in *Motion Through External Actuation*. In *Motion Through Internal Actuation*, a similar method is implemented for optimal placement of internal actuators.

In none of the methods presented in this work constraints on material strength and stability (local and global) are considered to ensure that structural integrity is preserved throughout the motion. Applying the formulation presented in this paper to load-bearing structures is not feasible and requires appropriate extensions.

MOTION DESIGN OF STRUCTURES WITH CONSTRAINTS

Basic Method of Motion Design

As described in Sachse and Bischoff (2020), the motion design method enables to identify an optimal deformation path between an initial undeformed geometry and a prescribed deformed configuration. **Figure 1A** shows an illustration of this method. The initial geometry (black), as well as the deformed final geometry (blue) of a two-bar truss, is given and the optimal trajectory of point *P* (red) is searched for. It is also possible to prescribe only parts of the end-configuration, e.g., only a vertical displacement. The method is developed for quasi-static problems that do not include dynamic effects and for geometrically nonlinear problems accounting for large deformations. The functional *J*,



i.e., the objective function that is to be minimized, is the integral of the strain energy Π_{int} over the deformation path s

$$J = \int_s \Pi_{\text{int}} ds \rightarrow \min. \quad (1)$$

Using the Green-Lagrange strain tensor \mathbf{E} , second Piola-Kirchhoff stress \mathbf{S} and the linear, elastic and isotropic St. Venant-Kirchhoff material law for large deformations with the elasticity tensor \mathbf{C} , the strain energy is therein defined as

$$\Pi_{\text{int}} = \int_{\Omega} \frac{1}{2} \mathbf{E}^T \mathbf{S} d\Omega = \int_{\Omega} \frac{1}{2} \mathbf{E}^T \mathbf{C} \mathbf{E} d\Omega \quad (2)$$

J is a measure for the “cost of deformation.” To solve this problem using variational calculus, two discretizations are introduced. The first is the well-known spatial discretization of the structure, i.e., the discretization with a number of finite elements n_{ele} . This allows the unknown displacement field to be approximated using n_{dof} discrete displacement degrees of freedom (i.e., nodal displacements), which are combined in the vector $\mathbf{D}(s)$. By using bar elements as in the illustrative example in **Figure 1**, the structure is already discretized in space by its nature. However, the method can also be used with other finite element formulations in two or three dimensions as well as with other spatial discretizations such as Lagrange and Non-Uniform Rational B-Spline (NURBS-) shape functions. The nodal displacements, i.e., the displacement field, are the variables that are searched for.

The nodal displacements are functions of the deformation path, since the displacement field changes throughout the motion. Due to this dependence on the motions, a second discretization of the deformation path is introduced, as illustrated in **Figure 1B**. This can be compared to space-time finite elements but differs in the fact that the deformation path depends on the displacement field while time is an autonomous value. The deformation path is discretized with \bar{n}_{ele} path elements between the initial configuration and the prescribed end-configuration. For clarity, n_{ele} denotes the number of structural elements while \bar{n}_{ele} the number of motion-path elements (for brevity path elements). This way the integral in the objective function can be split into a sum over all motion-path elements:

$$J = \int_s \Pi_{\text{int}} ds \approx \sum_{e=1}^{\bar{n}_{\text{ele}}} \int_{s_e} \Pi_{\text{int}} ds_e. \quad (3)$$

Considering a discretization with \bar{n}_{ele} path elements and associated \bar{n}_{node} path nodes, the total number of degrees of freedom increases to

$$\bar{n}_{\text{dof}} = \bar{n}_{\text{node}} \cdot n_{\text{dof}}. \quad (4)$$

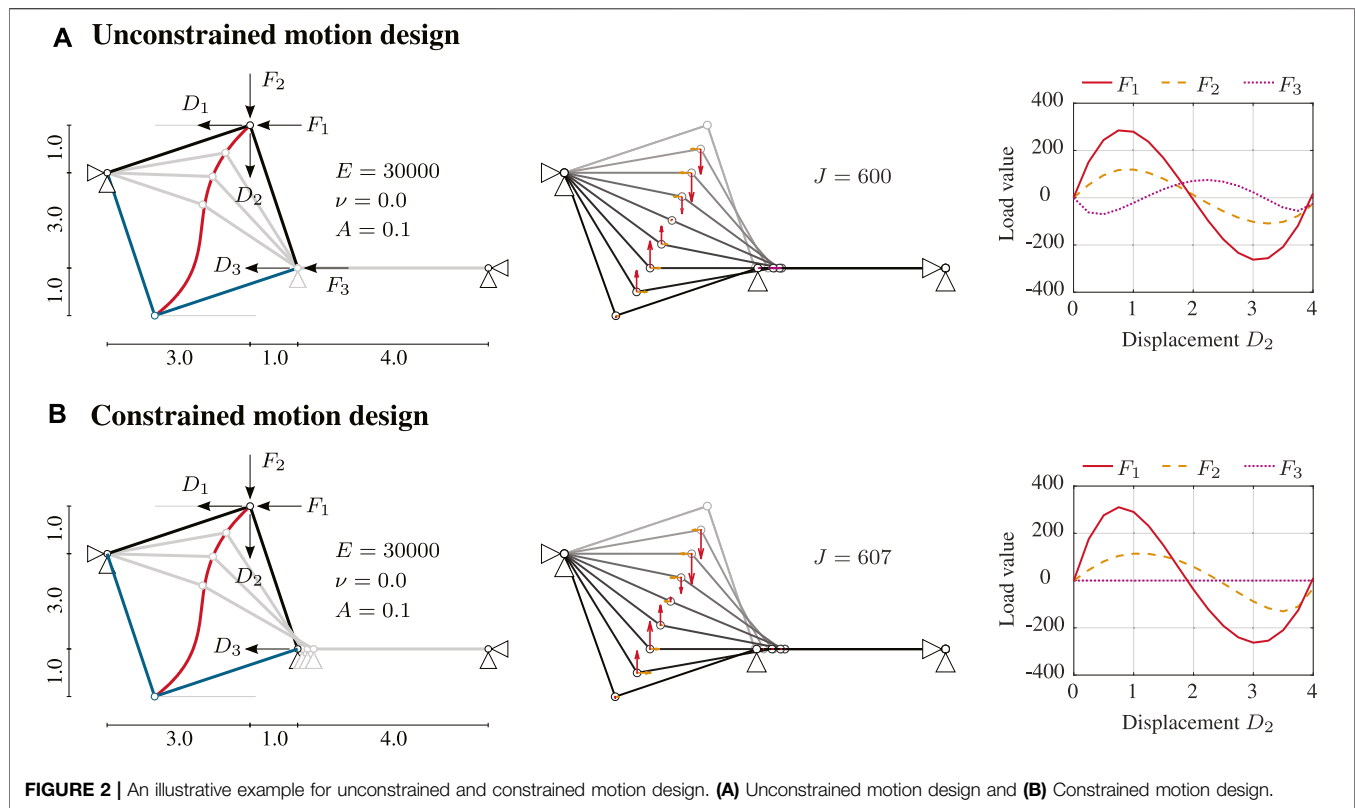
The motion-path nodes are intermediate geometric configurations that are encountered throughout the motion. The relationship between the number of motion-path nodes \bar{n}_{node} and elements \bar{n}_{ele} depends on the employed shape functions. The shape functions in this discretization interpolate the initial, intermediate and end-configuration. Generally, all types of shape functions, which interpolate the different geometric configurations, can be used for the deformation-path discretization, e.g., Lagrange polynomials as well as B-spline functions. Depending on the problem, a suitable discretization method should be chosen. The vector of total displacement degrees of freedom $\bar{\mathbf{D}}$ is extended since it contains degrees of freedom of all geometric configurations throughout the motion and therefore consists of \bar{n}_{node} vectors

$$\bar{\mathbf{D}} = \begin{bmatrix} \mathbf{D}^1 \\ \mathbf{D}^2 \\ \vdots \\ \mathbf{D}^{\bar{n}_{\text{node}}} = \mathbf{D}^{\text{end}} \end{bmatrix} \quad (5)$$

where $\mathbf{D}^1 = \mathbf{0}$ and \mathbf{D}^{end} refer to the initial (undeformed) and end-configuration (prescribed target shape), respectively. The constraint of reaching the target shape is included by prescribing the displacement values within the vector \mathbf{D}^{end} . In the example of **Figure 1B** a motion discretization of four linear elements is employed, which leads to

$$\bar{\mathbf{D}} = [\mathbf{D}_1^1 \ \mathbf{D}_2^1 \ \mathbf{D}_1^2 \ \mathbf{D}_2^2 \ \mathbf{D}_1^3 \ \mathbf{D}_2^3 \ \mathbf{D}_1^4 \ \mathbf{D}_2^4 \ \mathbf{D}_1^{\text{end}} \ \mathbf{D}_2^{\text{end}}]^T. \quad (6)$$

The superscripts indicate the geometric configuration throughout the motion while the subscripts indicate the nodal displacement degrees of freedom. Building the variation leads to a nonlinear system of equations that can be solved iteratively through linearization using the Newton-Raphson solution scheme. This way, the deformation path is obtained for all configurations at once rather than incrementally, as is the case in nonlinear structural analysis. As the end-configuration is prescribed, the value of the strain energy at the end of the deformation path cannot be changed. However, the intermediate configurations are varied such that the integral of the strain energy is minimized.



The solution of the motion of the two-bar-truss example using 14 linear path elements is illustrated in **Figure 1C**. A vertical snap-through with a successive motion to the right side causes less integrated strain energy than a linear interpolation between the initial and end-configuration. The solution is not unique because various discretizations may approximate the same curve. As a result, the problem is not well-posed and it has to be regularized by either enforcing equal size of the path elements or by controlling the increment of a chosen degree of freedom throughout the motion (Sachse and Bischoff, 2020).

The resulting motion is realized by applying forces to the structure. Equilibrium conditions have not been considered because equilibrium can be enforced for any resulting optimal deformation path since it is assumed that arbitrary forces can be applied at any degree of freedom. The internal forces are calculated throughout the entire deformation process using the displacement values. For equilibrium, the internal forces are then set as the external actuation forces required to realize the deformation path. In other words, external forces are determined that are in equilibrium with all deformed configurations. In practice, this means that external actuation forces (i.e., point forces at nodes), might need to be applied to all degrees of freedom. This is usually not of concern when the motion is realized through finite mechanisms (e.g., deployable structures). In such cases, considering frictionless finite mechanisms, absence of gravity and no external loading, the external actuation forces are zero. However, if the motion is not realized through finite mechanisms and for structures that are made of many elements, this assumption would lead to

prohibitively complex actuation systems. In such cases, it is possible to formulate suitable constraints so that the motion is controlled through a prescribed number of internal or external actuators. This approach has been presented in Sachse et al. (2021) and it is summarized in the following.

Constrained Motion Design With a Prescribed Number of Actuators

Consider the configuration illustrated in **Figure 2**. In unconstrained motion design, all free degrees of freedom are controlled by forces F_1 , F_2 , and F_3 as in **Figure 2A**. In constrained motion design, the deformation path is controlled through a subset of forces, F_1 and F_2 as shown in **Figure 2B**. Therefore, F_3 is set to zero throughout the motion. This is a constraint on the solution and can be introduced in the functional by different constraint-enforcement techniques such as the Lagrange multiplier method or the penalty method. Using the Lagrange multiplier method, the functional is extended by the product of the Lagrange multipliers λ and the vector of constraints in a residual form $\mathbf{g} = \mathbf{0}$ such as

$$\bar{J} = J + \lambda^T \mathbf{g}. \quad (7)$$

The vector of constraints contains the internal forces that must not contribute to motion and, therefore, are enforced to be zero during the entire deformation process. Enforcing this constraint also means that not all prescribed end-configurations can be reached using the available forces.

Depending on the prescribed end-geometry, two different processes may be required:

- If only a part of the end-geometry is prescribed, the rest of the deformed geometry can adjust to meet equilibrium conditions. However, the maximum number of prescribed displacement degrees of freedom must be smaller than the number of allowed actuation forces.
- If the complete end-geometry is prescribed, then such configuration must be in equilibrium with the allowed actuation forces. If this is not possible, a new end-configuration is calculated through shape optimization before starting the motion design process. The objective of this shape optimization process is to obtain an end-configuration i.e., as close as possible to the desired end-configuration (minimizing the norm of the difference of node positions) subject to equilibrium constraints with the allowed actuation forces.

Figure 2B shows the solution obtained when no constrain on forces is applied. The motion path so obtained requires a total strain energy of $J = 600$. When only F_1 and F_2 are employed, the optimal deformation path so obtained requires a total strain energy of $J = 607$, which is larger compared to the unconstrained motion solution. When only one force is applied, no design variable (i.e., the relation between available actuation forces) is left for optimization, and thus the optimal deformation path reduces to that obtained from nonlinear structural analysis.

In addition to external actuation, which is modeled through external point forces, also internal actuation is considered by using linear actuators installed in series with structural elements (Sachse et al., 2021). An actuator element formulation is employed that is based on a bar element (tension/compression) but includes an additional parameter for the length change. A linear actuator can expand and contract its length. The total strain E_d of an actuator element is divided into two parts: the elastic strain E_{el} and the actuation strain E_{act} :

$$E_d = E_{el} + E_{act}. \quad (8)$$

The actuation strain is not calculated from displacement values, but on the basis of a length change.

$$l_\alpha = (1 + \alpha)L. \quad (9)$$

The parameter α indicates the percentage of actuator length change, i.e., a value of $\alpha = 0.5$ results in 50% elongation for an actuator with free-free boundary conditions.

MOTION THROUGH EXTERNAL ACTUATION

In the constrained motion design method outlined in *Motion Design of Structures With Constraints*, the locations of actuation forces are predetermined. Reducing the number of actuation forces to control the structure deformation path, generally, results in an increase of the integrated strain energy. An optimization problem is formulated to

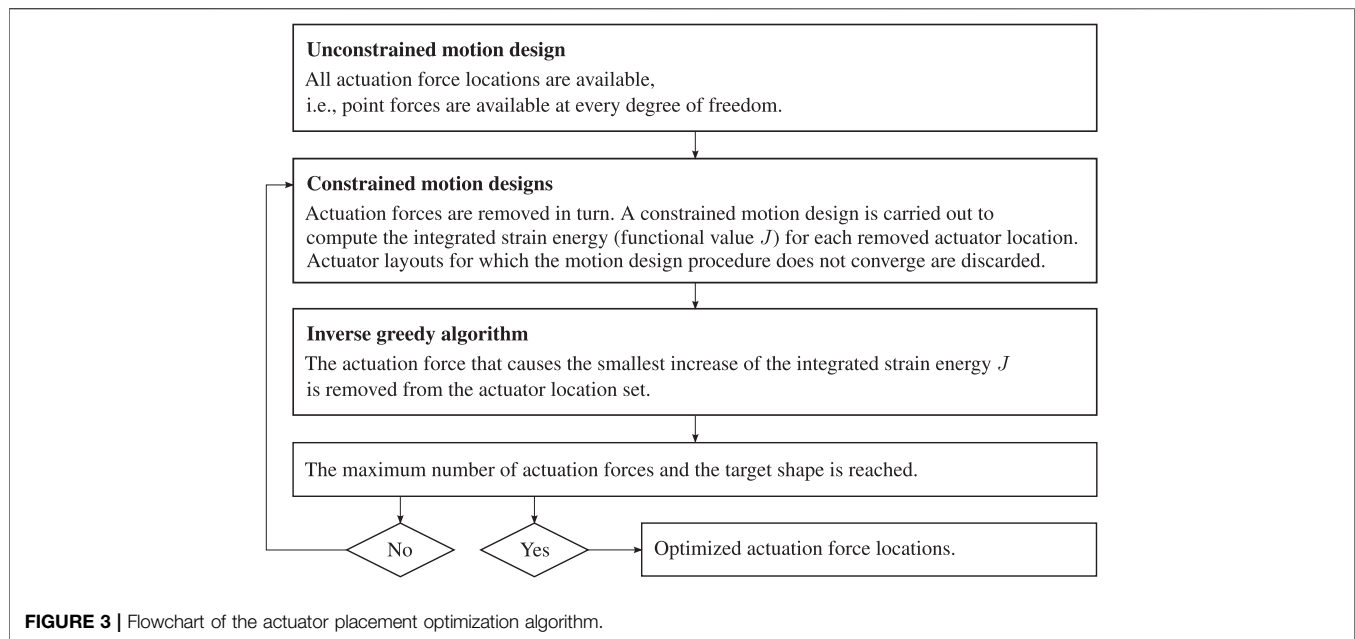
minimize such an increase of the integrated strain energy through optimal placement of external actuators. In this context the actuation forces are external point forces applied to the structure, i.e., the actuators are not included in the structure.

Efficient Placement of External Actuators

The calculation of an optimal set of actuation force locations is a discrete optimization problem. Due to a large number of possible combinations, a brute force approach is often not feasible. Depending on the problem formulation, various optimization methods could be applied to obtain a solution, such as genetic algorithms, mixed-integer programming, heuristic algorithms and gradient-based optimization algorithms of first and second order. The focus of this work is not on obtaining a global optimum of the actuator placement problem but rather a heuristic that can be conveniently employed with the constrained motion design method. A simple inverse greedy method that was first introduced in Kruskal (1956) and later used in Wagner et al. (2018) is adopted. The objective is to identify a feasible set of actuation force locations to control the structure through an optimal deformation path obtained by motion design. This inverse greedy algorithm is a robust heuristic that can be implemented with little effort. However, this algorithm cannot guarantee global optimality. Since the examples presented in this work are simple, solution quality can be assessed through a brute force search.

All possible actuation force locations are first considered, i.e., an unconstrained motion design is performed. The resulting unconstrained optimized motion serves as a predictor for a subsequent application of constrained motion design. Using the inverse greedy algorithm, the point forces are removed one by one and a constrained motion design is carried out for each force removal. The point force that causes the smallest increase of the objective function (strain energy integrated over the motion path) is removed from the set of applied actuation forces. Enough actuators are assumed to be available in order to reach the prescribed end displacement values exactly. This process is repeated until the desired number of actuation forces is reached. A flowchart of the actuator placement optimization process is given in **Figure 3**.

An illustrative example of a statically indeterminate extended two-bar truss is given in **Figure 4A**. Two shallow arches are connected by a stiff element that is modeled with a larger cross-section area. The upper midpoint is to be moved downwards, i.e., its vertical displacement is prescribed. There are four free degrees of freedom in total, the horizontal and vertical degrees of freedom located at the upper and lower midpoint, respectively. First, an unconstrained motion design is carried out and an optimized motion path is obtained that requires integrated strain energy of $J = 1,617$. In this case, the upper node first rotates around the lower node and is then further moved downwards. This way, the large stiffness element is subjected to minimum strain, which avoids a significant increase of integrated strain energy. This deformation path requires all four actuation forces, as seen in **Figure 4B1**. It can be noted that although the problem description is symmetric, unsymmetric motion is obtained minimizing the integrated strain energy.



Applying the inverse greedy algorithm, each actuation force is removed separately and a constrained motion design is carried out for each removal. The actuation force that causes the least deterioration of the functional value is then removed from the available actuation locations. In this example, the vertical force at the lower node has the least influence on the strain energy. By removing this force location, the integrated strain energy increases from $J = 1,617$ to $J = 1,621$, which is less than a 1% difference. The resulting motion is illustrated in **Figure 4B2**. The motion and the trajectory of both midpoints during deformation do not change significantly although only three forces instead of four forces are applied. This process repeats for the three remaining actuation force locations. In this second iteration, a more significant change can be observed in the trajectory of the two moving points, as shown in **Figure 4B3**. Also, the integrated strain energy increases to $J = 1789$ by approximately 11% compared to the unconstrained motion design. However, the overall motion path remains similar. The prescribed displacement values are reached exactly as their number is less than or equal to the number of actuation forces.

This example has shown that through the inverse greedy algorithm it is possible to identify the location of external actuation forces to perform an efficient motion between two prescribed geometries. This way, it is possible to further reduce the integrated strain energy compared to that required for a motion obtained with a predefined set of actuation force locations (as in Sachse et al., 2021).

Influence of the Prescribed End-Geometry

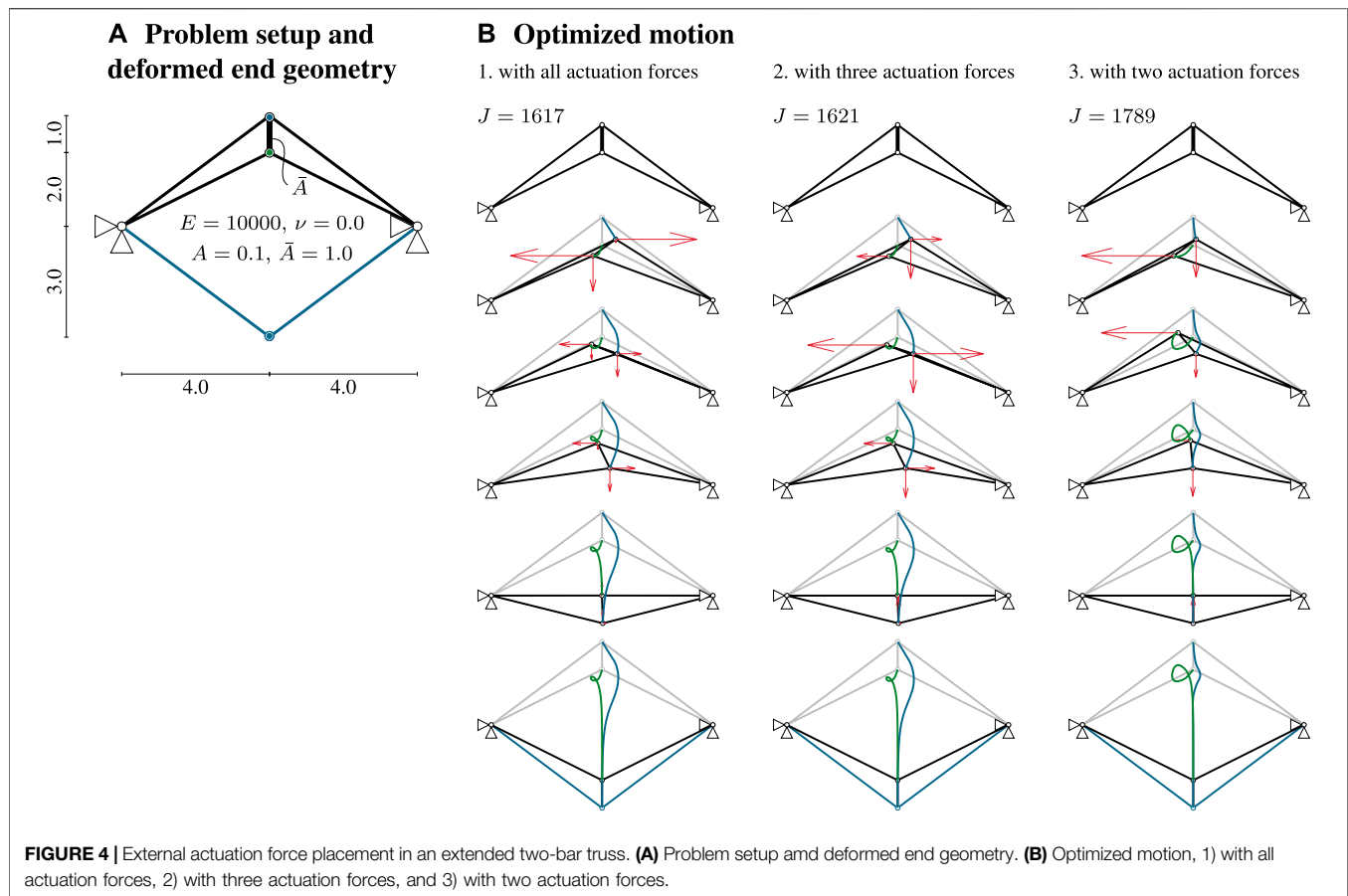
As explained in *Motion Design of Structures With Constraints*, it is possible to either fully prescribe the end-geometry or only parts of it. This choice has a significant influence on the actuator placement solution. Consider the simply supported truss example

shown in **Figure 5A**. The structure is modeled with bar elements (black). The objective is to move the free top-chord nodes upwards. The end-geometry is defined as the deformed configuration that is computed through geometrically nonlinear analysis by applying a force $F = 200$ to each free top-chord node simultaneously.

A motion path discretization with eight linear elements is chosen and the vertical displacement of the upper mid node is controlled. In order to obtain reference solutions, a constrained motion design and an unconstrained motion design with a specification of the entire end-geometry are performed. The solution obtained through constrained motion design using three vertical forces involves a simultaneous increase of the actuation forces during motion (see **Figure 5B**) and requires an integrated strain energy $J = 395$. This motion path is similar to that obtained through a nonlinear analysis during which the force applied to each node is increased simultaneously. In the unconstrained motion design (**Figure 5C**), the same end-configuration is reached. This happens because the end-configuration is fully prescribed and has been determined through analysis. However, additional forces are applied during the deformation process to enable a more efficient motion that requires lower strain energy. Accordingly, before reaching the end-geometry, the deformation path goes through an intermediate configuration where additional actuation forces are applied. This leads to a reduction of integrated strain energy from $J = 395$ for the constrained motion design solution to $J = 387$ for the unconstrained motion design solution.

To study the influence of the prescribed end-geometry, three different cases are investigated that differ in the number of prescribed displacement values.

1. **Figure 5D1**: the end-geometry is fully prescribed. In this case, since the number of prescribed displacements is higher than the number of actuators, it is in general not possible to reach



equilibrium in the target shape. For this reason, shape optimization is carried out before motion design (see *Constrained Motion Design With a Prescribed Number of Actuators*). Through shape optimization, a deformation state is obtained that is close to the desired end-geometry and in equilibrium with the current actuation forces. This leads to slightly modified end-geometries for each inverse greedy step. As a result, the final end-geometry can be realized through different actuation forces as those initially considered and it requires integrated strain energy $J = 392$, which is slightly lower than that required for case B.

2. **Figure 5D2:** only a part of the end-geometry is prescribed, in this case the vertical position of the upper chord nodes. The same actuation forces as in case B result from actuation placement optimization. The strain energy required in this case is identical to that for case B. In this case, the number of prescribed displacements and actuation forces is identical. As only some displacements are prescribed and not the entire end-geometry, these values are strictly enforced. Hence, actuation forces in other locations cannot control the structure into the prescribed end displacements and thus the solution is identical to that for case B.

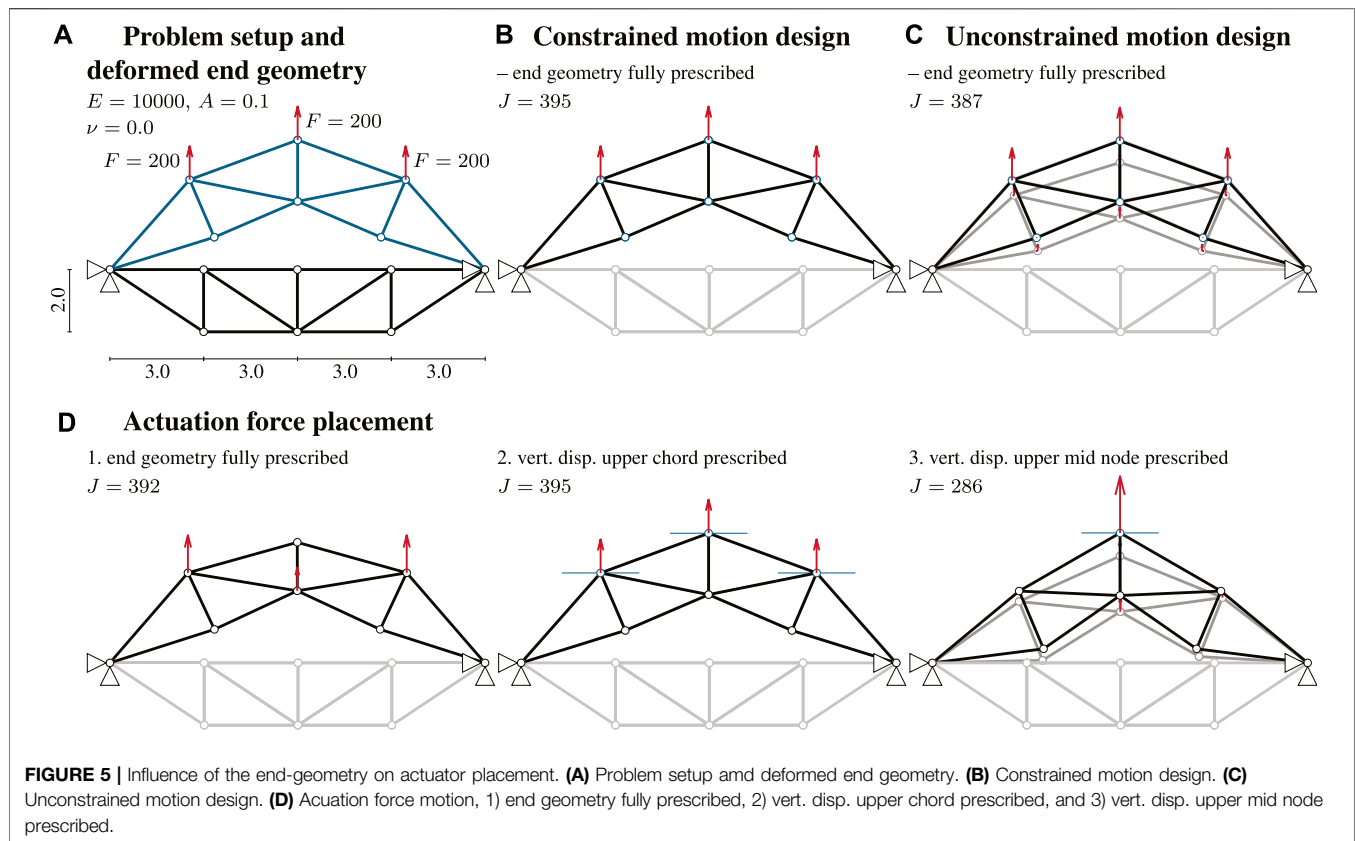
3. **Figure 5D3:** a lower number of displacements than actuation forces is prescribed. In this case, only the vertical displacement of the upper mid node is specified. This way, further end-geometry variations and thus actuation force

combinations are possible. A different end-geometry that requires significantly lower integrated strain energy $J = 286$ is obtained.

As expected, the prescribed end-geometry strongly influences the resulting actuation forces. In general, when more displacement values than available actuation forces are prescribed, shape optimization is employed to obtain a slightly different but feasible end-configuration that might require different actuation force locations compared to those initially assigned (**Figure 5D1**). When the prescribed number of displacements is equal to or lower than the available number of actuators, the prescribed end-configuration can be met exactly (**Figure 5D2**). Depending on design requirements, in order to reduce the integrated strain energy, the lowest number of displacements should be prescribed.

Morphing Cantilever

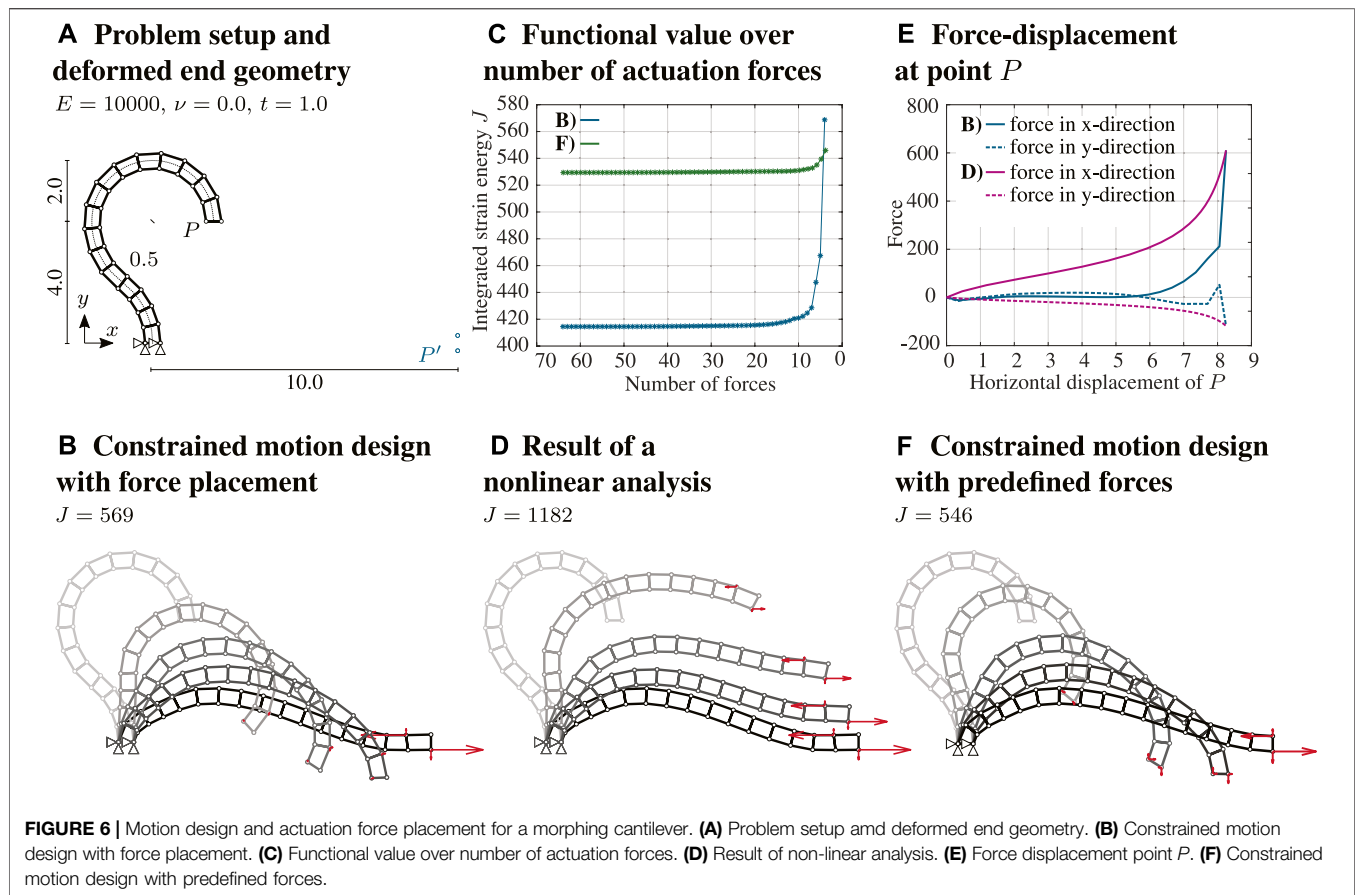
A morphing cantilever example is taken into consideration. The initial state is a hook-shaped configuration. The objective is to identify an efficient deformation path so that the free end-nodes reach the prescribed locations, as illustrated in **Figure 6A**. Motion is controlled through four actuation forces. The cantilever, which is fixed at the bottom, is modeled with 16 displacement-based plane four-node elements. The path is discretized with 18 linear elements.



First, an unconstrained motion design is carried out, whereby a deformation path is obtained so that the end-shape matches with the prescribed end-displacements. At this stage, all actuation forces are applied (*Basic Method of Motion Design*). The solution of this first process is given as starting point, i.e., a predictor motion, for a subsequent application of constrained motion design (*Constrained Motion Design With a Prescribed Number of Actuators*). In this second step, the motion is controlled through only four actuation forces, and therefore equilibrium constraints must be enforced throughout. The actuation force locations are identified through the placement method based on the inverse greedy algorithm (*Efficient Placement of External Actuators*). The solution of this second step is the location of the actuation forces as well as the deformation path enabled through such forces, as illustrated in **Figure 6B**. The four actuation forces are located at two nodes. The evolution of these four actuation forces throughout the deformation process is an output of motion design. The integrated strain energy required for this motion path is $J = 569$. The diagram in **Figure 6C** shows how the integrated strain energy varies as the actuation forces are removed (inverse greedy algorithm). This solution is compared to the result of a geometrically nonlinear analysis that is carried out by applying the same actuation forces obtained in B. Although the end-geometry is identical in both cases, the deformation path is dissimilar (cf. **Figure 6D**) because actuation forces are applied differently throughout the motion. In a geometrically nonlinear analysis, all forces are increased simultaneously and uniformly, whereas, through motion

design, actuation forces are varied independently or simultaneously as required. This effect can be observed in the force-displacement diagram shown in **Figure 6E**, where the horizontal and vertical forces at point P are plotted over the horizontal displacement. When the end-geometry is reached, the force-displacement curves come together to the same point. The deformation caused by a uniform increase of forces results in integrated strain energy $J = 1,182$, which is significantly larger than that required through motion design.

Another approach to identifying efficient actuation force locations is to consider the location set that requires the lowest strain energy in the deformed end-state. This approach does not consider the entire motion, but it minimizes the strain energy in the end-configuration. Consequently, another set of actuation forces is obtained. This solution is illustrated in **Figure 6F**. The motion path is similar to that of case B. Although the end-geometry varies slightly, the prescribed two free end-node locations are satisfied. The strain energy required in this case is lower than the energy required by the solution of motion design in case B. To compare both approaches, the evolution of integrated strain energy as the point forces are successively removed (in an inverse greedy algorithm scheme) until the prescribed set of four forces remains, is illustrated in **Figure 6C**. The end-geometry in this second approach requires lower strain energy. However, all other force location combinations that include more than four actuators, require larger strain energy for case F (cf. **Figure 6B**). Owing to the inability of the inverse greedy algorithm to guarantee solution



optimality, the location of some of the forces considered in case F has been removed during the optimization process, which explains the larger integrated strain energy for case B when the number of actuator forces is reduced to four. That being said, both approaches give a good estimation of an efficient motion design and actuation force placement.

MOTION THROUGH INTERNAL ACTUATION

Elastic and Actuation Energy

In previous examples, the motion path has been controlled through external actuation forces. However, also internal actuators can be employed. Internal actuator elements are modeled using the formulation given in Sachse et al. (2021) that has been summarized in *Constrained Motion Design With a Prescribed Number of Actuators*. In this formulation, the intended actuator length change is treated as an additional variable of the motion design process. The actuator length changes are varied to control the structure into the required deformation path. The optimal deformation path and actuator length changes are outputs of motion design. In previous examples, the objective has been the minimization of strain energy integrated over the deformation path. However, as presented in Sachse and Bischoff (2020), other objectives can

be employed, such as integrated stress or strain of the entire structure or only parts of it. The total strain energy is defined as

$$\begin{aligned}\Pi_{\text{int}} &= \int_{\Omega} \frac{1}{2} \mathbf{S}^T (\mathbf{E}_{\text{el}} + \mathbf{E}_{\text{act}}) d\Omega = \int_{\Omega} \frac{1}{2} \mathbf{E}_{\text{el}}^T \mathbf{C} (\mathbf{E}_{\text{el}} + \mathbf{E}_{\text{act}}) d\Omega \\ &= \int_{\Omega} \left(\frac{1}{2} \mathbf{E}_{\text{el}}^T \mathbf{C} \mathbf{E}_{\text{el}} + \frac{1}{2} \mathbf{E}_{\text{el}}^T \mathbf{C} \mathbf{E}_{\text{act}} \right) d\Omega\end{aligned}\quad (10)$$

where \mathbf{S} is the element stress and \mathbf{E} is the total strain which is divided into the elastic strain \mathbf{E}_{el} and the strain due to actuation \mathbf{E}_{act} . The elastic energy is defined as

$$\Pi_{\text{int,el}} = \int_{\Omega} \frac{1}{2} \mathbf{E}_{\text{el}}^T \mathbf{C} \mathbf{E}_{\text{el}} d\Omega \quad (11)$$

while the actuation energy is

$$\Pi_{\text{int,act}} = \int_{\Omega} \frac{1}{2} \mathbf{E}_{\text{el}}^T \mathbf{C} \mathbf{E}_{\text{act}} d\Omega. \quad (12)$$

In practice, even when the actuator moves under no force, a length change requires input energy, which could be included *via* an extra term in the actuation energy in **Equation 12**. However, this depends on the type of actuation technology. In the case of external actuation, the elastic energy is the total strain energy. In the general case, both energy shares are integrated over the deformation path and are a measure of the cost of

deformation. Depending on the problem and application, either of them may be used.

The actuation energy given in Eq. 12 does not differentiate between positive and negative actuation work. In other words, it is possible that through the deformation path, some of the elastic energy stored in a previous control step is released, because the model allows for energy harvesting. If energy harvesting is not possible, this formulation might lead to an underestimation of the actuation energy that is required to control the structure through the optimal deformation path. To avoid energy gains during motion, the objective function should become a discontinuous function as formulated in Senatore and Reksowardojo (2020), which, in this case, since large deformations are considered, would make the optimization formulation significantly more complex.

To reduce optimization complexity, in this work only the first energy share (elastic) is considered.

Efficient Placement of Internal Actuators

The location of internal actuators is sought to control the structure through the optimal deformation path using minimum elastic energy. For simplicity, only truss structures are investigated. The same example as that described in *Influence of the Prescribed End-Geometry* (Figure 5) is taken as a case study. The influence of different degrees of static indeterminacy is tested by adding two and four bars, which results in a degree of static indeterminacy of three and five, respectively. The specification of the end-geometry is carried out by prescribing one (as in Figure 5D2) and three end-displacements (as in Figure 5D3). As for the optimization of external actuator forces (*Efficient Placement of External Actuators*), it is assumed that enough actuators are available to reach the prescribed end-displacements exactly.

There are two ways to model internal actuators. Actuators can be installed in series and parallel with a truss element. With regard to parallel actuation, an actuator element is added in the same location of a truss element. Consequently, both elements are connected at the nodes and when the actuator element changes length, the truss element must also change length through deformation, which creates a resisting force. With regard to serial actuation as considered in this work, the actuator replaces (entirely or partially) a truss element. In this case, the actuator length change does not cause a deformation in a hosting truss element. However, deformation can still occur in the hosting element owing to resisting forces that develop through the stiffness of the rest of the structure.

Referring to the optimization method employed for the placement of external actuators (*Efficient Placement of External Actuators*), the application of an inverse greedy algorithm for internal actuator placement would require replacing all elements with actuators in the first step. In such a case, assuming that each actuator replaces its hosting element entirely, there would be no resistance from passive elements. Since the objective is the minimization of integrated elastic energy (no actuation energy is accounted for) and no stress/stability constraints are enforced, the motion design problem becomes highly ill-posed i.e., infinite optimal motion paths exist to reach the target geometry. Therefore, to avoid convergence issues, the

optimal actuator placement is carried out by adopting a brute force search combined with a greedy algorithm, whereby actuators are added one by one in turn:

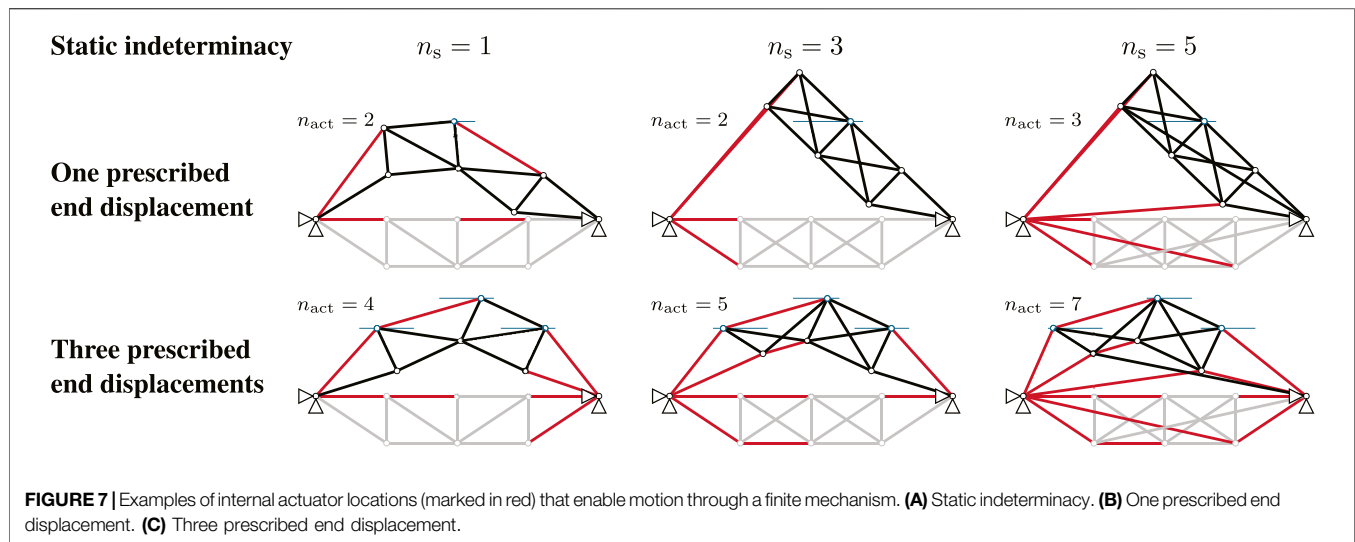
- Step 1: The number of actuators is progressively increased and all combinations are tested until the specified end-displacements are met.
- Step 2: If there are enough actuators such that the end-displacement specifications can be met, the combination that requires the lowest elastic energy is selected.
- Step 3: In case more actuators are considered, the solution obtained in step 2 is employed as a basis. The remaining truss elements are replaced by actuators in turn. The actuator location combination that results in the smallest functional value is selected. This step of the greedy algorithm is repeated until the desired number of actuators is reached.

An optimal actuator placement is sought that minimizes the elastic energy integrated over the motion path. Two cases are analyzed in the following. First, the minimum number and location of actuators are determined in order to reach the specified end-geometry through a finite mechanism. Second, an optimal placement of actuators is determined to reach the end-geometry through a deformation path that requires minimum elastic energy.

Minimum Number of Actuators to Enable Motion Through Finite Mechanisms

When a certain number of actuators replace truss elements a motion path through finite mechanisms can be identified that requires minimal (zero) strain energy (energy loss due to friction is not considered). However, whether such finite mechanisms exist depends on the structural topology, the degree of static indeterminacy n_s , the number and location of the actuators as well as the number of prescribed displacements of the end-configuration. The number of actuators required to enable motion through a finite mechanism is calculated within step 1 of the algorithm for efficient placement of internal actuators (*Efficient Placement of Internal Actuators*). The number of actuators is gradually increased and all combinations are tested until the prescribed end-displacements are reached through a finite mechanism which is identified when the integrated elastic energy is zero. Often there exist several actuator location combinations that enable motion through a finite mechanism. Figure 7 shows finite mechanisms resulting from actuator placement for three different structures, which differ in the degree of their static indeterminacy, $n_s = 1$, $n_s = 3$ or $n_s = 5$.

In all examples, the length of truss elements that are not replaced by actuators remains identical in the initial and end-geometry. Therefore, the elastic energy is zero and thus an elastic-energy-free motion is possible. The minimum number of actuators n_{act} to enable such a motion depends on the structure topology and the prescribed end-displacements. For example, when only one end-displacement is prescribed, two actuators are needed for the first two topology examples even



though the degree of static indeterminacy n_s is different. For the structure with $n_s = 5$, one additional actuator, i.e., three actuators are needed. In general, the more displacement values are prescribed, the more actuators are required. However, the actuator layout for a specific number of actuators n_{act} to enable a finite mechanism is not unique. Examples of possible actuator layouts are illustrated in **Figure 7**. There exist other actuator location combinations that fulfill the defined requirements.

Actuator Placement for Motion Through Deformation

If there are not enough actuators available to enable motion through finite mechanisms, the actuator locations can be selected based on their contribution to control the structure through the required deformation path using minimum elastic energy. The algorithm for efficient placement of internal actuators (*Efficient Placement of Internal Actuators*) is applied. An illustrative example is given in **Figure 8**. Three displacement values are prescribed and the degree of statistical indeterminacy is $n_s = 3$. The result of step 2 is shown in **Figure 8A**. The end-displacements are reached exactly using three actuators. From all combinations of three actuators (only some combinations are shown in **Figure 8**), the placement that results in the elastic energy integrated over the motion path ($J = 135$) is chosen. Starting from this configuration, one additional truss element is replaced by an actuator, and a new actuator layout is obtained which requires lower integrated elastic energy as shown in **Figure 8B**.

DISCUSSION

This work has presented an extension of previous methods for motion design through a combination of heuristic algorithms

for actuator placement. The methods presented in this paper are useful to identify a subset of external or internal actuator force locations that enable control of the structure through a required motion path between two significantly different geometric configurations. This work has focused on actuator placement through minimization of the elastic energy integrated over the motion path. No quantification of the actuation energy has been investigated. However, minimization of the integrated actuation energy in **Eq. 12** can also be used to obtain suitable actuator placements. The choice of objective function depends on the intended application. If large element deformations must be prevented, minimization of the elastic energy should be employed. On the other hand, minimization of actuation energy could be chosen when control of the motion path requires large actuation energy. Future work could look into the quantification of actuator energy and testing different actuation technologies.

An inverse greedy algorithm has been applied to identify optimal locations of external actuators. This algorithm cannot guarantee global optimality, i.e., important actuation force locations may be excluded early in the optimization process. A combination of brute force and a greedy algorithm has been employed for the placement of internal actuators. Similar limitations regarding solution quality apply in this case. Owing to the iterative nature of motion design and its sequential application in combination with the heuristics adopted for actuator placement, the overall procedure has a high computational cost. The overall number of iterations can be reduced by using the solution obtained from a previous motion design as a predictor (i.e., starting configuration) for a subsequent iterative cycle. This reduces the overall computation time compared to a single motion design that starts from a naïve predictor (e.g., linear interpolation). Future work could look into implementing different algorithms that are better suited for large-scale numerical optimization.

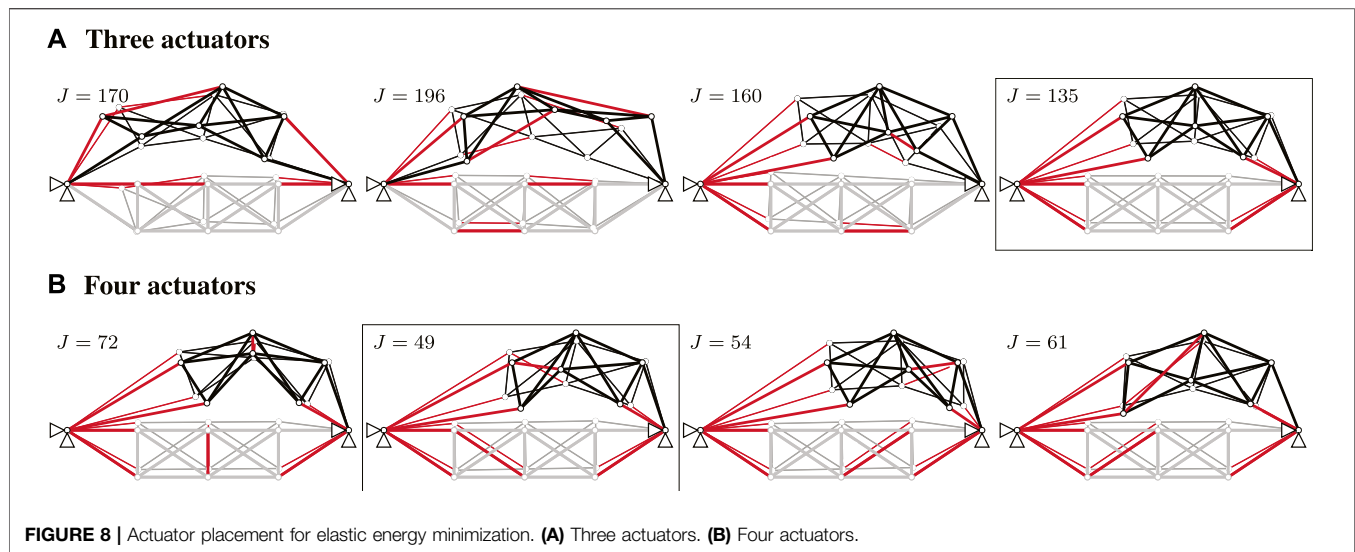


FIGURE 8 | Actuator placement for elastic energy minimization. **(A)** Three actuators. **(B)** Four actuators.

The presented work has aimed to evaluate the application feasibility of the proposed motion design method through numerical examples. Making this method more relevant to practical applications will be the subject of future work. Among possible extensions, constraints on actuation could be added, for example, to limit the actuator length changes. In addition, constraints on material strength, structural element stability should be added to ensure that structural integrity is preserved throughout motion. The proposed method is also suitable to identify inextensible deformations of shells, which could be employed to control large geometry changes with low control effort.

CONCLUSION

The method of motion design has been successfully combined with heuristic algorithms for optimal actuator placement. While the heuristics implemented in this work do not guarantee global optimality, they generally allow the identification of efficient actuator layouts that enable control of the structure through the required motion path.

Constrained motion design is able to identify motion paths that are more efficient than those obtained from intuitive approaches. Numerical simulations have shown that strategically restricting actuation to a limited number of locations (i.e., degrees of freedom) does not significantly change the overall motion path obtained with unconstrained motion design. A naïve proportional increase of actuation forces to control the structure into a given target configuration requires a significantly larger cost of deformation (i.e., indication of control energy) than that required by a motion design solution. This is because the motion design method takes into

account the entire deformation process, not only the final configuration. Generally, as expected, the fewer displacement values of the end-geometry are prescribed, the lower the cost of deformation.

DATA AVAILABILITY STATEMENT

The original contributions presented in the study are included in the article, further inquiries can be directed to the corresponding author.

AUTHOR CONTRIBUTIONS

RS did the development of the method and the investigation under a close guidance by MB and assistance of FG and MV.

FUNDING

This research work by RS was part of the collaborative project “Bio-inspirierte Materialsysteme und Verbundkomponenten für nachhaltiges Bauen im 21ten Jahrhundert” (BioElast) funded by the State Ministry of Baden-Wuerttemberg for Sciences, Research and Arts. Furthermore, the contribution of FG was conducted in the framework of the Collaborative Research Center 1244 “Adaptive Skins and Structures for the Built Environment of Tomorrow”/project B01 funded by the Deutsche Forschungsgemeinschaft (DFG, German Research Foundation)—project number 279064222. The authors are grateful for the generous support.

REFERENCES

- Abdullah, M. M., Richardson, A., and Hanif, J. (2001). Placement of Sensors/actuators on Civil Structures Using Genetic Algorithms. *Earthquake Engng. Struct. Dyn.* 30, 1167–1184. doi:10.1002/eqe.57
- Gupta, V., Sharma, M., and Thakur, N. (2010). Optimization Criteria for Optimal Placement of Piezoelectric Sensors and Actuators on a Smart Structure: A Technical Review. *J. Intell. Mater. Syst. Structures* 21, 1227–1243. doi:10.1177/1045389x10381659
- Hasse, A., and Campanile, L. F. (2009). Design of Compliant Mechanisms with Selective Compliance. *Smart Mater. Struct.* 18, 115016. doi:10.1088/0964-1726/18/11/115016
- Ibrahimbegovic, A., Knopf-Lenoir, C., Kueroš, A., and Villon, P. (2004). Optimal Design and Optimal Control of Structures Undergoing Finite Rotations and Elastic Deformations. *Int. J. Numer. Meth. Engng.* 61, 2428–2460. doi:10.1002/nme.1150
- Inoue, F. (2008). "Development of Adaptive Construction Structure by Variable Geometry Truss," in *Robotics and Automation in Construction*. Editors C. Balaguer and M. Abderrahim (London, United Kingdom: InTech). doi:10.5772/5543
- Irschik, H. (2002). A Review on Static and Dynamic Shape Control of Structures by Piezoelectric Actuation. *Eng. Structures* 24, 5–11. doi:10.1016/s0141-0296(01)00081-5
- Jani, J. M., Leary, M., Subic, A., and Gibson, M. A. (2014). A Review of Shape Memory alloy Research, Applications and Opportunities. *Mater. Des. (1980-2015)* 56, 1078–1113. doi:10.1016/j.matdes.2013.11.084
- Knippers, J., and Schlaich, J. (2000). Folding Mechanism of the Kiel Hörn Footbridge, Germany. *Struct. Eng. Int.* 10, 50–53. doi:10.2749/101686600780620991
- Knippers, J., Jungjohann, H., Scheible, F., and Oppe, M. (2013). Bio-inspirierte kinetische Fassade für den Themenpavillon "One Ocean" EXPO 2012 in Yeosu, Korea. *Bautechnik* 90 (6), 341–347. doi:10.1002/bate.201300034
- Kota, S., Joo, J., Li, Z., Rodgers, S. M., and Sniogowski, J. (2001). Design of Compliant Mechanisms: Applications to MEMS. *Analog Integrated Circuits Signal. Process.* 29, 7–15. doi:10.1023/a:1011265810471
- Kruskal, J. B. (1956). On the Shortest Spanning Subtree of a Graph and the Traveling Salesman Problem. *Proc. Amer. Math. Soc.* 7, 48. doi:10.1090/s0002-9939-1956-0078686-7
- Kwan, A. S. K., and Pellegrino, S. (1993). Prestressing a Space Structure. *AIAA J.* 31, 1961–1963. doi:10.2514/3.11876
- Masching, H., and Bletzinger, K.-U. (2016). Parameter Free Structural Optimization Applied to the Shape Optimization of Smart Structures. *Finite Elem. Anal. Des.* 111, 33–45. doi:10.1016/j.finel.2015.12.008
- Masic, M., and Skelton, R. E. (2005). Path Planning and Open-Loop Shape Control of Modular Tensegrity Structures. *J. Guidance, Control Dyn.* 28, 421–430. doi:10.2514/1.6872
- Preumont, A. (2011). *Vibration Control of Active Structures: An Introduction. Solid Mechanics and its Applications*. 3 edn. Dordrecht: Springer Netherlands. doi:10.1007/978-94-007-2033-6
- Reksowardojo, A. P., Senatore, G., and Smith, I. F. C. (2019). Experimental Testing of a Small-Scale Truss Beam that Adapts to Loads through Large Shape Changes. *Front. Built Environ.* 5, 93. doi:10.3389/fbuil.2019.00093
- Reksowardojo, A. P., Senatore, G., and Smith, I. F. C. (2020). Design of Structures that Adapt to Loads through Large Shape Changes. *J. Struct. Eng.* 146, 04020068. doi:10.1061/(asce)st.1943-541x.0002604
- Sachse, R., and Bischoff, M. (2020). A Variational Formulation for Motion Design of Adaptive Compliant Structures. *Int. J. Numer. Methods Eng.* 122, 972–1000. doi:10.1002/nme.6570
- Sachse, R., Geiger, F., and Bischoff, M. (2021). Constrained Motion Design with Distinct Actuators and Motion Stabilization. *Int. J. Numer. Methods Eng.* 122, 2712–2732. doi:10.1002/nme.6638
- Senatore, G., and Reksowardojo, A. P. (2020). Force and Shape Control Strategies for Minimum Energy Adaptive Structures. *Front. Built Environ.* 6, 105. doi:10.3389/fbuil.2020.00105
- Senatore, G., Duffour, P., Winslow, P., and Wise, C. (2018). Shape Control and Whole-Life Energy Assessment of an 'infinitely Stiff' Prototype Adaptive Structure. *Smart Mater. Structures* 27, 015022. doi:10.1088/1361-665x/aa8cb8
- Senatore, G., Duffour, P., and Winslow, P. (2019). Synthesis of Minimum Energy Adaptive Structures. *Struct. Multidisc Optim* 60 (3), 849–877. doi:10.1007/s00158-019-02224-8
- Seok, S., Wang, A., Meng Yee Chuah, M. Y., Otten, D., Lang, J., and Kim, S. (2013). *Design Principles for Highly Efficient Quadrupeds and Implementation on the MIT Cheetah Robot, 2013*. Karlsruhe, Germany: IEEE International Conference on Robotics and Automation, 3307–3312. doi:10.1109/ICRA.2013.6631038
- Sobek, W., and Teuffel, P. (2001). "Adaptive Systems in Architecture and Structural Engineering," in *Smart Structures and Materials 2001: Smart Systems for Bridges, Structures, and Highways*, 4330. Bellingham, Washington: International Society for Optics and Photonics, 36–46.
- Sofla, A. Y. N., Elzey, D. M., and Wadley, H. N. G. (2009). Shape Morphing Hinged Truss Structures. *Smart Mater. Structures* 18, 065012. doi:10.1088/0964-1726/18/6/065012
- Sychterz, A. C., and Smith, I. F. C. (2018). Deployment and Shape Change of a Tensegrity Structure Using Path-Planning and Feedback Control. *Front. Built Environ.* 4, 45. doi:10.3389/fbuil.2018.00045
- Teuffel, P. (2004). *Entwerfen Adaptiver Strukturen*. Stuttgart: Ph.D. thesis, University of Stuttgart. doi:10.2749/222137804796302004
- Veue, N., Sychterz, A. C., and Smith, I. F. C. (2017). Adaptive Control of a Deployable Tensegrity Structure. *Eng. Structures* 152, 14–23. doi:10.1016/j.engstruct.2017.08.062
- Wagner, J. L., Gade, J., Heidingsfeld, M., Geiger, F., von Scheven, M., Böhm, M., et al. (2018). On Steady-State Disturbance Compensability for Actuator Placement in Adaptive Structures. *at Automatisierungstechnik* 66, 591–603. doi:10.1515/auto-2017-0099
- Wang, Y., and Senatore, G. (2020). Minimum Energy Adaptive Structures - All-In-One Problem Formulation. *Comput. Structures*, vol. 236, p. 106266. doi:10.1016/j.compstruc.2020.106266
- Wijdeven, J. v. d., and Jager, B. d. (2005). "Shape Change of Tensegrity Structures: Design and Control," in *Proceedings of the 2005, 4, Portland, OR: American Control Conference*. 2522–2527.

Conflict of Interest: The authors declare that the research was conducted in the absence of any commercial or financial relationships that could be construed as a potential conflict of interest.

Copyright © 2021 Sachse, Geiger, von Scheven and Bischoff. This is an open-access article distributed under the terms of the Creative Commons Attribution License (CC BY). The use, distribution or reproduction in other forums is permitted, provided the original author(s) and the copyright owner(s) are credited and that the original publication in this journal is cited, in accordance with accepted academic practice. No use, distribution or reproduction is permitted which does not comply with these terms.

Advantages of publishing in Frontiers



OPEN ACCESS

Articles are free to read
for greatest visibility
and readership



FAST PUBLICATION

Around 90 days
from submission
to decision



HIGH QUALITY PEER-REVIEW

Rigorous, collaborative,
and constructive
peer-review



TRANSPARENT PEER-REVIEW

Editors and reviewers
acknowledged by name
on published articles

Frontiers

Avenue du Tribunal-Fédéral 34
1005 Lausanne | Switzerland

Visit us: www.frontiersin.org

Contact us: frontiersin.org/about/contact



REPRODUCIBILITY OF RESEARCH

Support open data
and methods to enhance
research reproducibility



DIGITAL PUBLISHING

Articles designed
for optimal readership
across devices



FOLLOW US

@frontiersin



IMPACT METRICS

Advanced article metrics
track visibility across
digital media



EXTENSIVE PROMOTION

Marketing
and promotion
of impactful research



LOOP RESEARCH NETWORK

Our network
increases your
article's readership